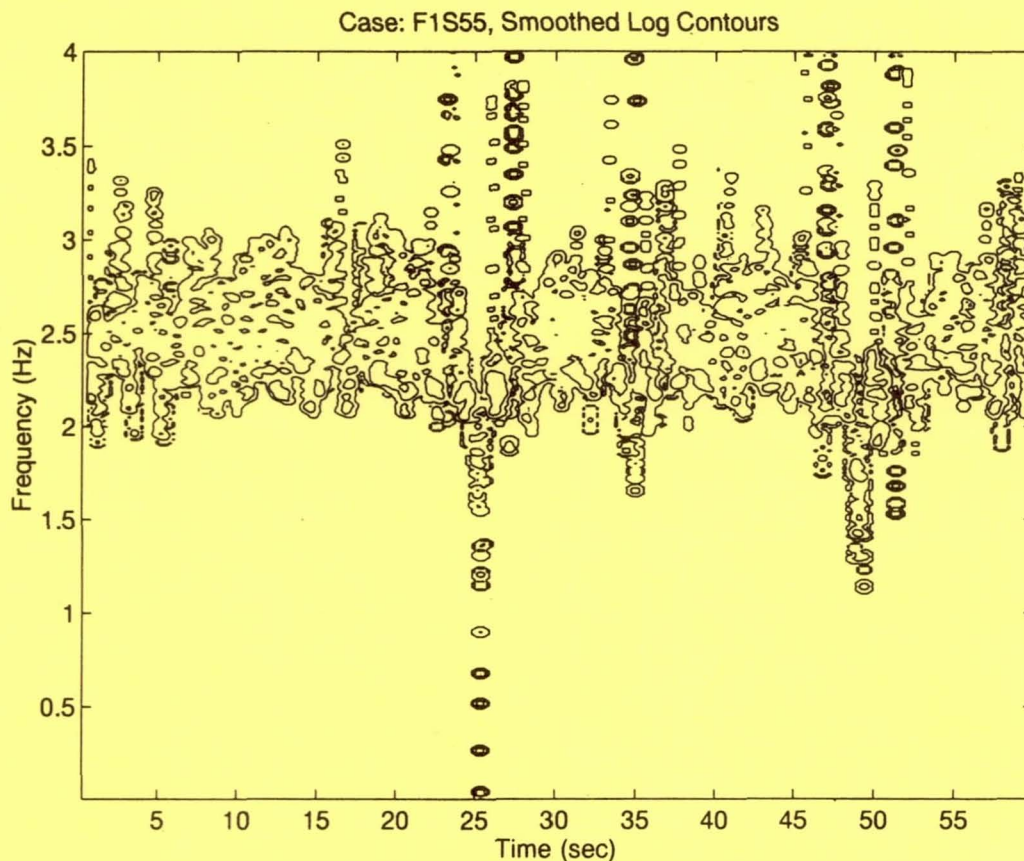


# LABORATORY FOR HYDROSPHERIC PROCESSES



## RESEARCH PUBLICATIONS 1997

NATIONAL AERONAUTICS AND SPACE ADMINISTRATION  
GODDARD SPACE FLIGHT CENTER  
GREENBELT, MARYLAND 20771  
301-286-6171



### Cover Figure Caption

Fig. 14. This is an example of a Hilbert Spectrum for laboratory wave data. The Hilbert Spectrum is a three dimensional presentation of an energy-frequency-time distribution. The analysis is based on the totally adaptive Empirical Mode Decomposition method from which the Intrinsic Mode Functions are extracted, and the frequency is defined by differentiation rather than convolution. Such a frequency not only has instantaneous meaning, but also can represent nonlinear distortion of waveform in terms of intra-wave frequency modulation rather than the traditional spurious harmonics from Fourier based analysis. This figure illustrates the range of intra-wave modulation for a nonlinear water wave train. The process of wave fusion, in which the two waves fused into one, is shown by the sudden drop in the instantaneous frequency value at the 25<sup>th</sup> second.

This cover figure is from the Laboratory's 1996 Peer Award for best publication by Drs. Norden E. Huang (Code 971), Stephen R. Long (Code 972), and Zheng Shen, entitled The mechanism for frequency downshift in nonlinear wave formation, *Advances in applied mechanics*, 12, 59-117.

## Laboratory for Hydrospheric Processes 1997 Publications

This document is a compilation of publications of the Goddard Space Flight Center Laboratory for Hydrospheric Processes for calendar year 1997. Each two-page entry is a cut-and-pasted extraction from a 1997 published journal article, book chapter, symposium or conference proceedings, or technical memorandum. This provides a quick, inexpensive way to communicate our research. If you wish further information, or a reprint, please contact the author of the article or the publisher. There are two sections, the first consisting of 76 journal articles and book chapters which are arranged according to the science priorities of NASA's Earth Science Enterprise:

- Land-Cover Change and Global Productivity
- Seasonal-to-Interannual Climate Prediction
- Natural Hazards
- Long-Term Climate Variability
- Atmospheric Ozone, and an additional category
- Sensor/Algorithm Development.\*

Each of these sections is preceded by a foreword.

A second section, consisting of 52 other contributions (e.g. conference/symposium proceedings and technical memoranda), provides additional scientific information to the outside community.

This document was initiated within the Earth Sciences Directorate at the NASA/Goddard Space Flight Center to provide internal communication. We anticipate it will prove useful to visitors and other people interested in our research. This is our fifth annual document.

The Laboratory for Hydrospheric Processes is one of the major elements of the Earth Sciences Directorate at NASA's Goddard Space Flight Center. Scientific investigations within the Division range from theoretical to experimental research dealing with oceanic/physical oceanography, hydrologic, and cryospheric sciences. The Laboratory currently has a staff of 60 civil servants and approximately 138 visiting scientists, postdoctoral fellows, and contractors. At various times throughout the year, the Laboratory hosts additional personnel through NASA and Goddard sponsored enrichment programs for high school, undergraduate and graduate students, and high school and university faculty. For further information see our web site at <http://neptune.gsfc.nasa.gov>.

*Antonio Busalacchi*

Dr. Antonio J. Busalacchi  
Chief, Laboratory for Hydrospheric Processes  
Code 970  
NASA Goddard Space Flight Center  
Greenbelt, MD 20771

\* This group title was added to provide a logical place for other studies that are done within the Division that don't readily fall within the five science priorities.

## Laboratory for Hydrospheric Processes Best Publication Awards

Each year, as part of our Peer Award process, the Laboratory selects an article and presents the author or authors an award to honor their publication efforts during the previous year. Listed below are the previous winners since we began compiling the Laboratories' publications in a booklet similar to this beginning with calendar year 1993.

1993

Robert J. Gurney, **James L. Foster**, and **Claire L. Parkinson**, *Atlas of satellite observations related to global change*, Cambridge University Press.

1994

**Kevin Arrigo**, Impact of ozone depletion on phytoplankton growth in the Southern Ocean: large-scale spatial and temporal variability, *Marine Ecology Progress Series*, **114**, 1-12.

1995

**William B. Krabill**, Robert H. Thomas, Chreston F. Martin, **Robert N. Swift**, and **Earl B. Frederick**, Accuracy of airborne laser altimetry over the Greenland ice sheet, *International Journal of Remote Sensing*, **16**(7), 1211-1222.

1996

**Norden E. Huang**, **Steven R. Long**, and Zheng Shen, The mechanism for frequency downshift in nonlinear wave evolution. *Advances in Applied Mechanics*, **32**, Eds. Hutchinson and Wu, Academic Press, 60-117 plus figures.



## TABLE OF CONTENTS

Cover Caption .....	inside front cover
Preface .....	i
Annual Best Publication Award .....	ii
Table of Contents .....	iii
Laboratory for Hydrospheric Processes Personnel .....	xiii
Journal Papers and Book Chapters .....	1
<b>Boldface</b> indicates Code 970 personnel.	

### LAND COVER CHANGE AND GLOBAL PRODUCTIVITY SUMMARY..... 3

<b>Arrigo, K.R., D.L. Worthen, M.P. Lizotte, P. Dixon, and G. Dieckmann, 1997:</b> Primary production in Antarctic sea ice. <i>Science</i> , <b>276</b> , 394-397. ....	5
Chen, D., <b>E.T. Engman</b> , and W. Brutsaert, 1997: Spatial distribution and pattern persistence of surface soil moisture and temperature over prairie from remote sensing. <i>Remote Sens. Environ.</i> , <b>61</b> , 347-360. ....	7
<b>Engman, E.T.</b> , 1997: Soil moisture, the hydrologic interface between surface and ground waters. <i>Remote Sensing and Geographic Information Systems for Design and Operation of Water Resources Systems</i> , M.F. Baumgartner, G.A. Schultz, and A.I. Johnson, Eds., IAHS Publication No. 242, 129-140. ....	9
Jackson, T.J., <b>P.E. O'Neill</b> , and C.T. Swift, 1997: Passive microwave observation of diurnal surface soil moisture. <i>IEEE Trans. Geosci. Remote Sens.</i> , <b>35</b> (5), 1210-1222. ....	11
Lehodey, P., M. Bertignac, J. Hampton, A. Lewis, and <b>J. Picaut</b> , 1997: El Niño Southern Oscillation and tuna in the western Pacific. <i>Nature</i> , <b>389</b> , 715-718. ....	13
Monger, B., <b>C. McClain</b> , and <b>R. Murtugudde</b> , 1997: Seasonal phytoplankton dynamics in the eastern tropical Atlantic. <i>J. Geophys. Res.</i> , <b>102</b> (C6), 12,389-12,411. ....	15

### SEASONAL-TO-INTERANNUAL CLIMATE VARIABILITY SUMMARY ..... 17

<b>Busalacchi, A.J.</b> , 1997: Oceanic observations. <i>J. Meteorol. Soc. of Japan</i> , <b>75</b> (1B), 131-154. ....	19
<b>Cavaleri, D.J., P. Gloersen, C.L. Parkinson, J.C. Comiso, and H.J. Zwally</b> , 1997: Observed hemispheric asymmetry in global sea ice changes. <i>Science</i> , <b>278</b> , 1104-1106. ....	21
Chen, D., S.E. Zebiak, M.A. Cane, and <b>A.J. Busalacchi</b> , 1997: Initialization and predictability of a coupled ENSO forecast model. <i>Mon. Wea. Rev.</i> <b>125</b> (5), 773-788. ....	23

- Chen, G., B. Chapron, J. Tournadre, K. Katsaros, and **D. Vandemark**, 1997: Global oceanic precipitation: A joint view by TOPEX and the TOPEX microwave radiometer. *J. Geophys. Res.*, **102**(C5), 10,457-10,471. ----- 25
- Chen, T.H., A. Henderson-Sellers, P.C.D. Milly, A.J. Pitman, A.C.M. Beljaars, J. Polcher, F. Abramopoulos, A. Boone, S. Chang, F. Chen, Y. Dai, C.E. Desborough, R.E. Dickinson, L. Dümenil, M. Ek, J.R. Garratt, N. Gedney, Y.M. Gusev, J. Kim, **R. Koster**, E.A. Kowalczyk, K. Laval, J. Lean, D. Lettenmaier, X. Liang, J.-F. Mahfouf, H.-T. Mengelkamp, K. Mitchell, O.N. Nasonova, J. Noilhan, A. Robock, C. Rosenzweig, J. Schaake, C.A. Schlosser, J.-P. Schulz, Y. Shao, A.B. Shmakin, D.L. Verseghy, P. Wetzel, E.F. Wood, Y. Xue, Z.-L. Yang, and Q. Zeng, 1997: Cabauw experimental results from the project for intercomparison of land-surface parameterization schemes. *J. Climate*, **10**(7), 1194-1215. ----- 27
- Choudhury, B.J.**, 1997: Global pattern of potential evaporation calculated from the Penman-Monteith equation using satellite and assimilated data. *Remote Sens. Environ.*, **61**, 64-81. ----- 29
- Geiger, C.A.**, S.F. Ackley, W.D. Hibler, III, 1997: Year-round pack ice in the Weddell Sea, Antarctica: response and sensitivity to atmospheric and oceanic forcing. *Ann. Glaciol.*, **25**, 269-275. ----- 31
- Giovinetto, M.B., G. Holdsworth, D.A. Fisher, N.M. Waters, and **H.J. Zwally**, 1997: An assessment of the regional distribution of the oxygen-isotope ratio in northeastern Canada. *Ann. Glaciol.*, **25**, 214-219. ----- 33
- Ho, D.T., **L.F. Bliven**, R. Wanninkhof, and P. Schlosser, 1997: The effect of rain on air-water gas exchange. *Tellus*, **49B**, 149-158. ----- 35
- Hooker, S.B.**, R.P. Mied, J.W. Brown, and A.D. Kirwan, Jr., 1997: Remote sensing of dipole rings. *IEEE Trans. Geosci. Remote Sens.*, **35**(6) 1394-1399. ----- 37
- Jacobs, S.S., and **J.C. Comiso**, 1997: Climate variability in the Amundsen and Bellingshausen Seas. *J. Climate*, **10**(4), 697-709. ----- 39
- Jouzel, J., R.B. Alley, K.M. Cuffey, W. Dansgaard, P. Grootes, G. Hoffmann, S.J. Johnsen, **R.D. Koster**, D. Peel, **C.A. Shuman**, M. Stievenard, M. Stuiver, and J. White, 1997: Validity of the temperature reconstruction from water isotopes in ice cores. *J. Geophys. Res.*, **102**(C12), 26,471-26,487. ----- 41
- Kalnay, E., D.L.T. Anderson, A.F. Bennett, **A.J. Busalacchi**, S.E. Cohn, P. Courtier, J. Derber, A.C. Lorenc, D. Parrish, J. Purser, N. Sato, and T. Schlatter, 1997: Data assimilation in the ocean and in the atmosphere: What should be next? *J. Meteorol. Soc. of Japan*, **75**(1B), 489-496. ----- 43
- Koster, R.D.**, and P.C.D. Milly, 1997: The interplay between transpiration and runoff formulations in land surface schemes used with atmospheric models. *J. Climate*, **10**, 1578-1591. ----- 45
- Kwok, R., and **J.C. Comiso**, 1997: The perennial ice cover of the Beaufort Sea from active- and passive-microwave observations. *Ann. Glaciol.*, **25**, 376-381. ----- 47
- Lakshmi, V., E.F. Wood, and **B.J. Choudhury**, 1997: A soil-canopy-atmosphere model for use in satellite microwave remote sensing. *J. Geophys. Res.*, **102**(D6), 6911-6927. ----- 49
- Lakshmi, V., E.F. Wood, and **B.J. Choudhury**, 1997: Investigation of effect of heterogeneities in vegetation and rainfall on simulated SSM/I brightness temperatures. *Int. J. Remote Sens.*, **18**(13), 2763-2784. ----- 51
- Lakshmi, V., E.F. Wood, and **B.J. Choudhury**, 1997: Evaluation of special sensor microwave/imager satellite data for regional soil moisture estimation over the Red River Basin. *J. Appl. Meteorol.*, **36**(10), 1309-1328. ----- 53



<b>Liu, A.K.</b> , S. Martin, and R. Kwok, 1997: Tracking of ice edges and ice floes by wavelet analysis of SAR images. <i>J. Atmos. Ocean. Technol.</i> , <b>14</b> , 1187-1198. -----	55
Miller, R.N., <b>A.J. Busalacchi</b> , and <b>E.C. Hackert</b> , 1997: Applications of data assimilation to analysis of the ocean on large scales. <i>J. Meteorol. Soc. of Japan</i> , <b>75</b> (1B), 445-462. -----	57
<b>Parkinson, C.L.</b> , 1997: Earth from above using color-coded satellite images to examine the global environment, University Science Books, Sausalito, California, 175 pp. -----	59
<b>Picaut, J.</b> , F. Masia, and Y. du Penhoat, 1997: An advective-reflective conceptual model for the oscillatory nature of the ENSO. <i>Science</i> , <b>277</b> , 663-666. -----	61
Pinkel, R., M. Merrifield, M. McPhaden, <b>J. Picaut</b> , S. Rutledge, D. Siegel, and L. Washburn, 1997: Solitary waves in the western equatorial Pacific Ocean. <i>Geophys. Res. Lett.</i> , <b>24</b> (13), 1603-1606. -----	63
Scott, R., D. Entekhabi, <b>R. Koster</b> , M. Suarez, 1997: Timescales of land surface evapotranspiration response. <i>J. Climate</i> , <b>10</b> (4), 559-566. -----	65
Teng, W.L., <b>B.J. Choudhury</b> , and <b>J.R. Wang</b> , 1997: The effects of laterite and associated terrain components on PBMR response in HAPEX-Sahel. <i>J. Hydrol.</i> , <b>188-189</b> , 310-329. -----	67
Vukovich, F.M., R. Wayland, and <b>D. Toll</b> , 1997: The surface heat flux as a function of ground cover for climate models. <i>Mon. Wea. Rev.</i> , <b>125</b> (4), 572-586. -----	69
<b>Wang, L.</b> and <b>C. Koblinsky</b> , 1997: Can the Topex/Poseidon altimetry data be used to estimate air-sea heat flux in the North Atlantic? <i>Geophys. Res. Lett.</i> , <b>24</b> (2), 139-142. -----	71

## NATURAL HAZARDS SUMMARY ----- 73

<b>Abdalati, W.</b> , and K. Steffen, 1997: The apparent effects of the Mt. Pinatubo eruption on the Greenland ice sheet melt extent. <i>Geophys. Res. Lett.</i> , <b>24</b> (14), 1795-1797. -----	75
<b>Chang, A.T.C.</b> , <b>L.S. Chiu</b> , G.R. Liu, and K.H. Wang, 1997: Analyses of 1994 typhoons in the Taiwan region using satellite data. In: <i>Space Remote Sensing of Subtropical Oceans (SRSSO)</i> , C.T. Liu, Ed., Elsevier Science, New York, New York, 89-96. -----	77

## LONG-TERM CLIMATE VARIABILITY SUMMARY ----- 79

<b>Abdalati, W.</b> , and K. Steffen, 1997: Snowmelt on the Greenland ice sheet as derived from passive microwave satellite data. <i>J. Climate</i> , <b>10</b> (2), 165-175. -----	81
Alley, R.B., <b>C.A. Shuman</b> , D.A. Meese, A.J. Gow, K.C. Taylor, K.M. Cuffey, J.J. Fitzpatrick, P.M. Grootes, G.A. Zielinski, M. Ram, G. Spinelli, and B. Elder, 1997: Visual-stratigraphic dating of the GISP2 ice core: Basis, reproducibility, and application. <i>J. Geophys. Res.</i> , <b>102</b> (C12), 26,367-26,381. -----	83
Cane, M.A., A.C. Clement, A. Kaplan, Y. Kushnir, D. Pozdnyakov, R. Seager, S.E. Zebiak, and <b>R. Murtugudde</b> , 1997: Twentieth-century sea surface temperature trends. <i>Science</i> , <b>275</b> , 957-960. -----	85



<b>Chang, A.T.C., D.K. Hall, and J.L. Foster</b> , 1997: Multiangle observations of directional reflectances of snow fields. <i>Chinese J. Remote Sens.</i> , <b>1</b> (Suppl.) 11-17. -----	87
<b>Joughin, I., M. Fahnestock</b> , S. Ekholm, R. Kwok, 1997: Balance velocities of the Greenland ice sheet. <i>Geophys. Res. Lett.</i> , <b>24</b> (23), 3045-3048. -----	89
<b>Mauritzen, C., and S. Häkkinen</b> , 1997: Influence of sea ice on the thermohaline circulation in the Arctic-North Atlantic Ocean. <i>Geophys. Res. Lett.</i> , <b>24</b> (24), 3257-3260. -----	91
<b>Rignot, E.J., S.P. Gogineni, W.B. Krabill</b> , and S. Ekholm, 1997: North and northeast Greenland ice discharge from satellite radar interferometry. <i>Science</i> , <b>276</b> , 934-937. -----	93
<b>Rind, D., R. Healy, C. Parkinson</b> , and D. Martinson, 1997: The role of sea ice in 2xCO <sub>2</sub> climate model sensitivity: Part II: Hemispheric dependencies. <i>Geophys. Res. Lett.</i> , <b>24</b> (12), 1491-1494. -----	95
<b>Seager, R., and R. Murtugudde</b> , 1997: Ocean dynamics, thermocline adjustment, and regulation of tropical SST. <i>J. Climate</i> , <b>10</b> (3), 521-534. -----	97
<b>Shuman, C.A., R.B. Alley, M.A. Fahnestock, P.J. Fawcett, R.A. Bindshadler, J.W.C. White, P.M. Grootes, S. Anandakrishnan, and C.R. Stearns</b> , 1997: Detection and monitoring of stratigraphic markers and temperature trends at the Greenland Ice Sheet Project 2 using passive-microwave remote-sensing data. <i>J. Geophys. Res.</i> , <b>102</b> (C12), 26,877-26,886. -----	99
<b>Williams, Jr., R.S., D.K. Hall, O. Sigurdsson, and J.Y.L. Chien</b> , 1997: Comparison of satellite-derived with ground-based measurements of the fluctuations of the margins of Vatnajökull, Iceland, 1973-92. <i>Ann. Glaciol.</i> , <b>24</b> , 72-80. ....	101
<b>Zwally, H.J., and M.B. Giovinetto</b> , 1997: Annual sea level variability induced by changes in sea ice extent and accumulation on ice sheets: An assessment based on remotely sensed data. <i>Surveys in Geophys.</i> , <b>18</b> , 327-340. -----	103
<b>Zwally, H.J., and M.B. Giovinetto</b> , 1997: Areal distribution of the oxygen-isotope ratio in Greenland. <i>Ann. Glaciol.</i> , <b>25</b> , 208-213. -----	105

## ATMOSPHERIC OZONE SUMMARY ----- 107

<b>Bittner, M., D. Offermann, P. Preusse, M. Riese, H. Claude, and F.J. Schmidlin</b> , 1997: CRISTA ozone measurements/validation. <i>Adv. Space Res.</i> , <b>19</b> , 567-570. -----	109
---	-----

## SENSOR/ALGORITHM DEVELOPMENT SUMMARY ----- 111

<b>Aiken, J., and S.B. Hooker</b> , 1997: The Atlantic Meridional Transect: Spatially extensive calibration and validation of optical properties and remotely-sensed measurements of ocean colour. <i>Backscatter</i> , <b>8</b> (3), 8-11. ----	113
<b>Bilitza, D., S. Bhardwaj, and C. Koblinsky</b> , 1997: Improved IRI predictions for the GEOSAT time period. <i>Adv. Space Res.</i> , <b>20</b> (9), 1755-1760. -----	115

<b>Bliven, L.F., P.W. Sobieski, A. Guissard, and H. Branger, 1997:</b> Friction velocity estimation using dual-frequency altimeter data. In: <i>The Air-Sea Interface, Radio and Acoustic Sensing, Turbulence and Wave Dynamics</i> , M.A. Donelan, W.H. Hiu, and W.J. Plant, Eds., RSMAS University of Miami, Miami, Florida, 755-760. -----	117
<b>Bliven, L.F., J-P. Giovanangeli, H. Branger, and P.W. Sobieski, 1997:</b> A summary of scatterometer returns from water surfaces agitated by rain. In: <i>The Air-Sea Interface, Radio and Acoustic Sensing, Turbulence and Wave Dynamics</i> , M.A. Donelan, W.H. Hiu, and W.J. Plant, Eds., RSMAS University of Miami, Miami, Florida, 761-766. -----	119
<b>Caylor, I.J., G.M. Heymsfield, R. Meneghini, and L.S. Miller, 1997:</b> Correction of sampling errors in ocean surface cross-sectional estimates from nadir-looking weather radar. <i>J. Atmos. Ocean. Technol.</i> , <b>14</b> (1), 203-210. -----	121
<b>Chang, A.T.C., and L.S. Chiu, 1997:</b> Uncertainty in satellite rainfall estimates: Time series comparison. <i>Adv. Space Res.</i> , <b>19</b> (3), 469-472. -----	123
<b>Chang, A.T.C., J.L. Foster, D.K. Hall, B.E. Goodison, A.E. Walker, J.R. Metcalfe, and A. Harby, 1997:</b> Snow parameters derived from microwave measurements during the BOREAS winter field campaign. <i>J. Geophys. Res.</i> , <b>102</b> (D24), 29,663-29,671. -----	125
<b>Chanzy, A., T.J. Schmugge, J.-C. Calvet, Y. Kerr, P. van Oevelen, O. Grosjean, J.R. Wang, 1997:</b> Airborne microwave radiometry on a semi-arid area during HAPEX-Sahel. <i>J. Hydrol.</i> , <b>188-189</b> , 285-309. -----	127
<b>Comiso, J.C., D.J. Cavalieri, C.L. Parkinson, and P. Gloersen, 1997:</b> Passive microwave algorithms for sea ice concentration: A comparison of two techniques. <i>Remote Sens. Environ.</i> , <b>60</b> , 357-384. -----	129
<b>Craeye, C., P.W. Sobieski, and L.F. Bliven, 1997:</b> Scattering by artificial wind and rain roughened water surfaces at oblique incidences. <i>Int. J. Remote Sens.</i> , <b>18</b> (10), 2241-2246. -----	131
<b>Elfouhaily, T., B. Chapron, K. Katsaros, and D. Vandemark, 1997:</b> A unified directional spectrum for long and short wind-driven waves. <i>J. Geophys. Res.</i> , <b>102</b> (C7), 15,781-15,796. -----	133
<b>Foster, J.L., A.T.C. Chang, and D.K. Hall, 1997:</b> Comparison of snow mass estimates from a prototype passive microwave snow algorithm, a revised algorithm and a snow depth climatology. <i>Remote Sens. Environ.</i> , <b>62</b> , 132-142. -----	135
<b>Fraser, R.S., S. Mattoo, E-n. Yeh, and C.R. McClain, 1997:</b> Algorithm for atmospheric and glint corrections of satellite measurements of ocean pigment. <i>J. Geophys. Res.</i> , <b>102</b> (D14), 17,107-17,118. -----	137
<b>Goldberg, R.A., G.A. Lehmacher, F.J. Schmidlin, D.C. Fritts, J.D. Mitchell, C.L. Croskey, M. Friedrich, and W.E. Swartz, 1997:</b> Equatorial dynamics observed by rocket, radar, and satellite during the CADRE/MALTED campaign. 1. Programatics and small-scale fluctuations. <i>J. Geophys. Res.</i> , <b>102</b> (D22), 26,179-26,190. -----	139
<b>Gregg, W.W., F.S. Patt, and R.H. Woodward, 1997:</b> Development of a simulated data set for the SeaWiFS mission. <i>IEEE Trans. Geosci. Remote Sens.</i> , <b>35</b> (2) 421-435. -----	141
<b>Liu, A.K., C.Y. Peng, and S.Y.-S. Chang, 1997:</b> Wavelet analysis of satellite images for coastal watch. <i>IEEE. J. Ocean. Eng.</i> , <b>22</b> (1), 9-17. -----	143
<b>Meneghini, R., H. Kumagai, J.R. Wang, T. Iguchi, and T. Kozu, 1997:</b> Microphysical retrievals over stratiform rain using measurements from an airborne dual-wavelength radar-radiometer. <i>IEEE Trans. Geosci. Remote Sens.</i> , <b>35</b> (3) 487-506. -----	145



<b>Patt, F.S., R.H. Woodward, and W.W. Gregg</b> , 1997: An automated method for navigation assessment for Earth survey sensors using island targets. <i>Int. J. Remote Sens.</i> , <b>18</b> (16), 3311-3336. -----	147
<b>Prabhakara, C., M. Cadeddu, D.A. Short, J.A. Weinman, J.L. Schols, and J. Haferman</b> , 1997: "Stratiform and convective rain discrimination from microwave radiometer observations." In: IRS '96: Current Problems in Atmospheric Radiation. Eds. W.L. Smith and K. Stamnes, <i>Proc. Int. Radiation Symp.</i> , Fairbanks, Alaska, August 19-24, 1996, 498-501. -----	149
<b>Roman, D.R., B. Csatho, K.C. Jezek, R.H. Thomas, W.B. Krabill, R.R.B. von Frese, and R. Forsberg.</b> , 1997: A comparison of geoid undulations for west central Greenland. <i>J. Geophys. Res.</i> , <b>102</b> (B2), 2807-2814. -----	151
<b>Shi, J.C., J. Wang, A.Y. Hsu, P.E. O'Neill, and E.T. Engman</b> , 1997: Estimation of bare surface soil moisture and surface roughness parameter using L-band SAR image data. <i>IEEE Trans. Geosci. Remote Sens.</i> , <b>35</b> (5) 1254-1266. -----	153
<b>St. Germain, K.M., and D.J. Cavalieri</b> , 1997: A microwave technique for mapping ice temperature in the Arctic seasonal sea ice zone. <i>IEEE Trans. Geosci. Remote Sens.</i> , <b>35</b> (2) 946-953. -----	155
<b>Toll, D.L., D. Shirey, and D.S. Kimes</b> , 1997: NOAA AVHRR land surface albedo algorithm development. <i>Int. J. Remote Sens.</i> , <b>18</b> (18), 3761-3796. -----	157
<b>Vandemark, D., J.B. Edson, B. Chapron</b> , 1997: Altimeter estimation of sea surface wind stress for light to moderate winds. <i>J. Atmos. Ocean. Technol.</i> , <b>14</b> (3), 716-722. -----	159
<b>Wang, J.R., A. Hsu, J.C. Shi, P.E. O'Neill, and E.T. Engman</b> , 1997: A comparison of soil moisture retrieval models using SIR-C measurements over the Little Washita River watershed. <i>Remote Sens. Environ.</i> , <b>59</b> , 308-320. -----	161
<b>Wang, J.R., P. Racette, and L.A. Chang</b> , 1997: MIR measurements of atmospheric water vapor profiles. <i>IEEE Trans. Geosci. Remote Sens.</i> , <b>35</b> (2) 212-223. -----	163
<b>Wang, J.R., J.D. Spinhirne, P. Racette, L.A. Chang, and W. Hart</b> , 1997: The effect of clouds on water vapor profiling from the millimeter-wave radiometric measurements. <i>J. Appl. Meteorol.</i> , <b>36</b> (9), 1232-1244. -----	165
<b>Wang, J.R., J. Zhan, and P. Racette</b> , 1997: Storm-associated microwave radiometric signatures in the frequency range of 90-220 GHz. <i>J. Atmos. Ocean. Technol.</i> , <b>14</b> (1), 13-31. -----	167
<b>Wang, M., and M.D. King</b> , 1997: Correction of Rayleigh scattering effects in cloud optical thickness retrievals. <i>J. Geophys. Res.</i> , <b>102</b> (D22), 25,915-25,926. -----	169

## OTHER CONTRIBUTIONS ----- 171

<b>Barnes, R.A., R.E. Eplee, Jr., E-n. Yeh, and W.E. Esaias</b> , 1997: <i>SeaWiFS Calibration Topics, Part 2</i> . SeaWiFS Technical Report Series, TM 104566, Vol. 40, <b>S.B. Hooker and E.R. Firestone</b> , Eds., NASA Goddard Space Flight Center, Greenbelt, Maryland, 67pp., June 1997. -----	173
<b>Barnes, R.A., and W.E. Esaias</b> , 1997: "A nominal top-of-the-atmosphere spectrum for SeaWiFS." In: <i>SeaWiFS Calibration Topics, Part 2</i> . SeaWiFS Technical Report Series, TM 104566, Vol. 40, <b>S.B. Hooker and E.R. Firestone</b> , Eds., NASA Goddard Space Flight Center, Greenbelt, Maryland, 3-11, June 1997. -----	175



- Barnes, R.A., R.E. Eplee, Jr., and E-n. Yeh**, 1997: "SeaWiFS measurements in orbit: Spectral radiances at the nominal center wavelengths." In: *SeaWiFS Calibration Topics, Part 2*. SeaWiFS Technical Report Series, TM 104566, Vol. 40, **S.B. Hooker and E.R. Firestone**, Eds., NASA Goddard Space Flight Center, Greenbelt, Maryland, 12-22, June 1997. ----- 177
- Barnes, R.A.**, 1997: "The effect of atmospheric absorption on the output of SeaWiFS band 7." In: *SeaWiFS Calibration Topics, Part 2*. SeaWiFS Technical Report Series, TM 104566, Vol. 40, **S.B. Hooker and E.R. Firestone**, Eds., NASA Goddard Space Flight Center, Greenbelt, Maryland, 23-38, June 1997. ----- 179
- Barnes, R.A., and R.E. Eplee, Jr.**, 1997: "The 1993 SeaWiFS calibration using band-averaged spectral radiances." In: *SeaWiFS Calibration Topics, Part 2*. SeaWiFS Technical Report Series, TM 104566, Vol. 40, **S.B. Hooker and E.R. Firestone**, Eds., NASA Goddard Space Flight Center, Greenbelt, Maryland, 39-47, June 1997. ----- 181
- Barnes, R.A.**, 1997: "SeaWiFS measurements in orbit: band-averaged spectral radiances." In: *SeaWiFS Calibration Topics, Part 2*. SeaWiFS Technical Report Series, TM 104566, Vol. 40, **S.B. Hooker and E.R. Firestone**, Eds., NASA Goddard Space Flight Center, Greenbelt, Maryland, 48-55, June 1997. ----- 183
- Barnes, W.L., (Ed.)**, 1997: Earth Observing Systems II. *Proc. SPIE 3117*, The Int. Soc. for Opt. Eng., Bellingham, Washington, 334 pp. ----- 185
- Birkett, C., and G. Kite**, 1997: "Derivation of lake areas and elevations for the Mackenzie basin using satellite remote sensing." In: *Applications of Remote Sensing in Hydrology. Proc. 3<sup>rd</sup> Intl. Workshop*, NHRI Symposium No. 17, NASA, Goddard Space Flight Center, Greenbelt, Maryland, October 1996, 19-32. ----- 187
- Chang, A.T.C., and L.S. Chiu**, 1997: Comparison of satellite global rainfall algorithms. Technical Report Series on Global Modeling and Data Assimilation, M.J. Suarez, Ed., , NASA Tech. Memo. 104606, Vol. 12, NASA Goddard Space Flight Center, Greenbelt, Maryland, 96 pp., August 1997. ----- 189
- Comiso, J.C., and H.J. Zwally**, 1997: "Temperature Corrected Bootstrap Algorithm." *Proc. IGARSS '97*, 2, Singapore, August 3-8, 857-861. ----- 191
- Comiso, J.C., and L. Stock**, 1997: "Antarctic surface temperatures using satellite infrared data from 1979 through 1995." *Proc. IGARSS '97*, 3, Singapore, August 3-8, 1300-1304. ----- 193
- Cuddapah, P., M. Cadetdu, R. Meneghini, D.A. Short, J-M. Yoo, G. Dalu, J.L. Schols, and J.A. Weinman**, 1997: Rainfall estimation over tropical oceans: 1) Area average rain rate. In: *Proc. WMO Workshop on Measurements of Cloud Properties for Forecasts of Weather and Climate*. D. Baumgardner and G. Raga, Eds., Mexico City, Mexico, June 23-27, 286-291. ----- 195
- Delcroix, T., L. Gourdeau, P. Rual, and R. Murtugudde**, 1997: Zonal and meridional mass redistribution in the tropical Pacific during El Niño Southern Oscillation events. In: *Proc. Int. Symp., Monitoring the Oceans in the 2000s: An Integrated Approach*. Poster Session 1 – Oceanography and Climate (paper 1-5). TOPEX/POSEIDON Science Team Meeting, Biarritz, France, Centre National D'Etudes Spatiales, October, 1997. ----- 197
- Engman, E.T.**, 1997: "Potential for remotely sensed soil moisture data in hydrologic modeling." *Proc. Earth Surface Remote Sens.*, SPIE 3222, London, United Kingdom, 161-170. ----- 199
- Eplee, R.E., Jr., and R.A. Barnes**, 1997: "The SeaWiFS temperature calibration." In: *SeaWiFS Calibration Topics, Part 2*. SeaWiFS Technical Report Series, TM 104566, Vol. 40, **S.B. Hooker and E.R. Firestone**, Eds., NASA Goddard Space Flight Center, Greenbelt, Maryland, 56-62, June 1997. ----- 201



<b>Foster, J.L., A.T.C. Chang, and D.K. Hall</b> , 1997: "Improved passive microwave algorithms for North America and Eurasia." <i>Applications of Remote Sensing in Hydrology. Proc. 3<sup>rd</sup> Intl. Workshop</i> , NHRI Symposium No. 17, NASA, Goddard Space Flight Center, Greenbelt, Maryland, October 1996, 63-70. -----	203
<b>Foster, J.L., D.K. Hall, A.T.C. Chang, A. Rango, W. Wergin, and E. Erbe</b> , 1997: "Snow Crystal Shape and Microwave Scattering." <i>Proc. IGARSS '97</i> , 2, Singapore, August 3-8, 625-627. -----	205
<b>Gasiewski, A.J., J.R. Piepmeier, R.E. McIntosh, C.T. Swift, J.R. Carswell, W.J. Donnelly, E. Knapp, E.R. Westwater, V.I. Irisov, L.S. Fedor, and D.C. Vandemark</b> , 1997: Combined high-resolution active and passive imaging of ocean surface winds from aircraft." <i>Proc. IGARSS '97</i> , 2, Singapore, August 3-8, 1001-1005. -----	207
<b>Geiger, C.A.</b> , 1997: Importance of sea ice for validating global climate models. <i>Workshop on Polar Processes in Global Climate</i> , Cancun, Mexico, American Meteorological Society, Boston, Massachusetts, November 13-15, 122-125. -----	209
<b>Gourdeau, L., J. Verron, R. Murtugudde, and A.J. Busalacchi</b> , 1997: An extended Kalman filter to assimilate altimetric data into a non-linear model of the tropical Pacific. <i>Proc. Int. Symp., Monitoring the Oceans in the 2000s: An Integrated Approach</i> . Poster Session 4 – Dynamic Oceanography (paper 4-34). TOPEX/POSEIDON Science Team Meeting, Biarritz, France, Centre National D'Etudes Spatiales, October, 1997. ....	211
<b>Hackert, E.C., and A.J. Busalacchi</b> , 1997: Comparison of TOPEX/POSEIDON sea level and linear model results forced by various wind products for the tropical Pacific. <i>Proc. Int. Symp., Monitoring the Oceans in the 2000s: An Integrated Approach</i> . Poster Session 1 – Oceanography and Climate (paper 1-11). TOPEX/POSEIDON Science Team Meeting, Biarritz, France, Centre National D'Etudes Spatiales, October, 1997. ....	213
<b>Hancock, III, D.W., G.S. Hayne, R.L. Brooks, J.E. Lee, and D.W. Lockwood</b> , 1997: <i>TOPEX Radar Altimeter Engineering Assessment Report, Update: Launch to January 1, 1997</i> , NASA Goddard Space Flight Center/Wallops Flight Facility, Greenbelt, Maryland, 72 pp. & attachment, March 1997. -----	215
<b>Hilliard, L., D. Jenstrom, D. Chesters, and P. Racette</b> , 1997: Geosynchronous technology infusion studies. <i>Proc. IGARSS '97</i> , 2, Singapore, August 3-8, 984-987. -----	217
<b>Hsu, A.Y., P.E. O'Neill, E.F. Wood, and M. Zion</b> , 1997: "Examination of soil moisture retrieval using SIR-C radar data and a distributed hydrological model." <i>Proc. IGARSS'97</i> , 3, Singapore, August 3-8, 1266-1268. -----	219
<b>Iguchi, T., T. Kozu, R. Meneghini, and K. Okamoto</b> , 1997: Rain profiling algorithm for the TRMM precipitation radar." <i>Proc. IGARSS '97</i> , 4, Singapore, August 3-8, 1636-1638. -----	221
<b>Jackson, T.J., T.J. Schmugge, W.J. Rawls, P.E. O'Neill, and M.B. Parlange</b> , 1997: Passive microwave observation of soil water infiltration. <i>Proc. IGARSS '97</i> , 3, Singapore, August 3-8, 1099-1101. -----	223
<b>Jones, J.A., R. Meneghini, T. Iguchi, W.-K. Tao</b> , 1997: Synthetic data for testing TRMM radar algorithms. Amer. Meteorol. Soc. 28 <sup>th</sup> Conf. Radar Meteorol., Austin, Texas, September 1997, 196-197. -----	225
<b>Klein, A.G., D.K. Hall, and G.A. Riggs</b> , 1997: Improving the MODIS global snow-mapping algorithm. <i>Proc. IGARSS '97</i> , 2, Singapore, August 3-8, 619-621. -----	227
<b>Le Vine, D.M., and M. Kao</b> , 1997: "Effects of Faraday rotation on microwave remote sensing from space at L-band. <i>Proc. IGARSS '97</i> , 1, Singapore, August 3-8, 377-379. -----	229



- Liao, L., R. Meneghini, T. Iguchi, and A. Detwiler**, 1997: Estimation of snow parameters from dual-wavelength airborne radar. *Amer. Meteorol. Soc. 28<sup>th</sup> Conf. Radar Meteorol.*, Austin, Texas, September 1997, 510-511. -----231
- Liu, A.K., M-K. Hsu, N.K. Liang**, 1997: Evolution of nonlinear internal waves in China seas. *Proc. 3<sup>rd</sup> ERS Symp. on Space at the service of our Environment*, Florence, Italy, 17-21 March, (ESA SP-414, 3 Vols., May 1997). -----233
- Mattikalli, N.M., E.T. Engman, and T.J. Jackson**, 1997: Microwave remote sensing of soil moisture for estimation of soil properties. *Proc. IGARSS '97*, 3, Singapore, August 3-8, 1093-1095. -----235
- Mattikalli, N.M., E.T. Engman, T.J. Jackson, and L. R. Ahuja**, 1997: Application of multitemporal remotely sensed soil moisture for the estimation of soil physical properties. *Applications of Remote Sensing in Hydrology. Proc. 3<sup>rd</sup> Intl. Workshop*, NHRI Symposium No. 17, NASA, Goddard Space Flight Center, Greenbelt, Maryland, October 1996, 183-197. -----237
- McLean S., B. Schofield, G. Zibordi, M. Lewis, S. Hooker, and A. Weidemann**, 1997: Field evaluation of anti-biofouling compounds on optical instrumentation. *Proc. Ocean Optics XIII*, SPIE 2963, Halifax, Nova Scotia, Canada, 708-713. -----239
- Meneghini, R., and J.A. Jones**, 1997: Application of a threshold method to the TRMM radar for the estimation of space-time rain rate statistics. *Amer. Meteorol. Soc. 28<sup>th</sup> Conf. Radar Meteorol.*, Austin, Texas, September 1997, 280-281. -----241
- Murtugudde, R., A.J. Busalacchi, and J. Beauchamp**, 1997: Can TOPEX/POSEIDON data be used for monitoring the Indonesian throughflow? *Proc. Int. Symp., Monitoring the Oceans in the 2000s: An Integrated Approach*. Poster Session 1 – Oceanography and Climate (paper 1-12). TOPEX/POSEIDON Science Team Meeting, Biarritz, France, Centre National D'Etudes Spatiales, October, 1997. -----243
- O'Neill, P.E., A.Y. Hsu, T.J. Jackson, E.F. Wood, and M. Zion**, 1997: The impact of microwave-derived surface soil moisture on watershed hydrological modeling. *Applications of Remote Sensing in Hydrology. Proc. 3<sup>rd</sup> Intl. Workshop*, NHRI Symposium No. 17, NASA, Goddard Space Flight Center, Greenbelt, Maryland, October 1996, 211-226. -----245
- Owe, M., J. de Ruiter, B. Gouweleeuw, and A. van de Griend**, 1997: Ground-based microwave radiometer measurements over various surface covers. *Applications of Remote Sensing in Hydrology. Proc. 3<sup>rd</sup> Intl. Workshop*, NHRI Symposium No. 17, NASA, Goddard Space Flight Center, Greenbelt, Maryland, October 1996, 227-236. -----247
- Parkinson, C.L.**, 1997: PM Science Working Group meeting on spacecraft maneuvers. *The Earth Observer*, 9(3), 3-6. -----249
- Picaut, J.**, 1997: ENSO Mechanisms. *Proc. Int. Symp., Monitoring the Oceans in the 2000s: An Integrated Approach*. Plenary Session 1 - Oceanography and Climate (paper 1). TOPEX/POSEIDON Science Team Meeting, Biarritz, France, Centre National D'Etudes Spatiales, October, 1997. -----251
- Scharfen, G.R., D.K. Hall, and G.A. Riggs**, 1997: MODIS snow and ice products from the NSIDC DAAC. *Proc. Earth Observing Systems II*, SPIE 3117, San Diego, California, 143-147. -----253
- Schmidlin, F.J., S. McCarthy, W. Michel, and E.D. Ross**, 1997: Vertical ozone profile comparisons between ozonesondes and remote instrumentation. *Proc. 13<sup>th</sup> ESA Symposium on European Rocket and Balloon Programmes and Related Research*, Oland, Sweden, May 26-29, 1997, ESA SP-397, 169-173. -----255



Shaw, P.-S. , B.C. Johnson, <b>S.B. Hooker</b> , and D. Lynch, 1997: The SeaWiFS Quality Monitor – a portable field calibration light source. <i>Proc. Ocean Optics XIII</i> , SPIE 2963, Halifax, Nova Scotia, Canada, 772-776. ----	257
Shi, J.C., <b>J. Wang</b> , <b>A. Hsu</b> , <b>P. O'Neill</b> , and <b>E.T. Engman</b> , 1997: Estimation of bare surface soil moisture and surface roughness parameter using L-band SAR image data. <i>Applications of Remote Sensing in Hydrology. Proc. 3<sup>rd</sup> Intl. Workshop</i> , NHRI Symposium No. 17, NASA, Goddard Space Flight Center, Greenbelt, Maryland, October 1996, 323-335. -----	259
Shi, J.C., G. Sun, <b>A. Hsu</b> , <b>J. Wang</b> , <b>P. O'Neill</b> , J. Ranson, and <b>E.T. Engman</b> , 1997: Estimation of soil moisture for vegetated surfaces using multi-temporal L-band SAR measurements. <i>Proc. IGARSS '97</i> , 3, Singapore, August 3-8, 1269-1271. -----	261
St. Germain, K., <b>D.J. Cavalieri</b> , and <b>T. Markus</b> , 1997: A comparison of sea ice type, sea ice temperature, and snow thickness distributions in the Arctic seasonal ice zones with the DMSP SSM/I. <i>Proc. IGARSS '97</i> , 3, Singapore, August 3-8, 1291-1293. -----	263
<b>Takahashi</b> , N., H. Horie, and <b>R. Meneghini</b> , 1997: "Rainfall measurement with a ground based dual frequency radar. Amer. Meteorol. Soc. 28 <sup>th</sup> Conf. on Radar Meteorol., Austin, Texas, September 1997, 206-207. -----	265
<b>Toll</b> , <b>D.L.</b> , F.M. Vukovich, and E.G. Pontikes, 1997: Surface energy heat fluxes using remotely sensed parameters. <i>Applications of Remote Sensing in Hydrology. Proc. 3<sup>rd</sup> Intl. Workshop</i> , NHRI Symposium No. 17, NASA, Goddard Space Flight Center, Greenbelt, Maryland, October 1996, 337-344. -----	267
<b>Wang</b> , <b>J.R.</b> , and <b>P. Racette</b> , 1997: Airborne millimeter-wave radiometric observations of cirrus clouds. <i>Proc. IGARSS '97</i> , 4, Singapore, August 3-8, 1737-1739. -----	269
<b>Wang</b> , <b>J.R.</b> , <b>P. Racette</b> , <b>M.E. Triesky</b> , E.V. Browell, S. Ismail, and <b>L.A. Chang</b> , 1997: Simultaneous measurements of water vapor profiles from airborne MIR and LASE. <i>Proc. IGARSS '97</i> , 4, Singapore, August 3-8, 1969-1971. -----	271
Yeh, E-n., and <b>R.A. Barnes</b> , 1997: A simplified out-of-band correction algorithm for SeaWiFS. <i>Case Studies for SeaWiFS Calibration and Validation, Part 4</i> . SeaWiFS Technical Report Series, TM 104566, Vol. 41, <b>S.B. Hooker</b> and <b>E.R. Firestone</b> , Eds., NASA Goddard Space Flight Center, Greenbelt, Maryland, 22-23, June 1997. -----	273
Yeh, E-n., <b>R.A. Barnes</b> , M. Darzi, <b>L. Kumar</b> , E.A. Early, B.C. Johnson, J.L. Mueller, and C.C. Trees, 1997: <i>Case Studies for SeaWiFS Calibration and Validation, Part 4</i> , SeaWiFS Technical Report Series, NASA Technical Memorandum 104566, Vol. 41, <b>S.B. Hooker</b> and <b>E.R. Firestone</b> , Eds., NASA Goddard Space Flight Center, Greenbelt, Maryland, 35pp., August 1997. -----	275
Yeh, E-n., M. Darzi, and <b>L. Kumar</b> , 1997: SeaWiFS stray light correction algorithm. <i>Case Studies for SeaWiFS Calibration and Validation, Part 4</i> . SeaWiFS Technical Report Series, TM 104566, Vol. 41, <b>S.B. Hooker</b> and <b>E.R. Firestone</b> , Eds., NASA Goddard Space Flight Center, Greenbelt, Maryland, 24-30, June 1997. -----	277
Author Index -----	279

**Laboratory for Hydrospheric Processes Personnel  
NASA Civil Service Scientists**

Name/Code*	Phone Number
Waleed Abdalati/971	301-286-4717
David Adamec/971	301-286-1442
Kevin Arrigo/971	301-286-9634
Steven Bailey/972/565	757-824-1429
William Barnes/970	301-286-8670
Steven Bidwell/975/555	301-286-6720
Robert Bindschadler/971	301-286-7611
Geoffrey Bland/972	757-824-1267
Larry Bliven/972	757-824-1057
Antonio Busalacchi/970	301-286-6171
Robert Caffrey/970.2	301-286-0846
Donald Cavalieri/971	301-286-2444
Alfred Chang/974	301-286-8997
Bhaskar Choudhury/974	301-286-5155
Thomas Clem/972	757-824-1405
Josefino Comiso/971	301-286-9135
Daniel Endres/970.2	301-286-3434
Edwin Engman/974	301-286-5480
Wayne Esaias/971	301-286-5465
James Foster/974	301-286-7096
John Gerlach/972	757-824-1515
Per Gloersen/971	301-286-6362
Watson Gregg/971	301-286-3464
Sirpa Hakkinen/971	301-286-8513
Dorothy Hall/974	301-286-6892
Dave Hancock/972	757-824-1238
George Hayne/972	757-824-1294
Donald Hines/972/565	757-824-1594
Frank Hoge/972	757-824-1567
Stanford Hooker/971	301-286-9503
Paul Houser/974	301-286-7702
Norden Huang/971	301-286-8879
Michael Jasinski/974	301-286-7099
Rosa Kao/970	301-286-8302
Robert Kirk/970	301-286-7895
Chester Koblinsky/971	301-286-4718
Randal Koster/974	301-286-7061
William Krabill/972	757-824-1417
David Le Vine/975	301-286-8059
Anthony Liu/971	301-286-8534
Steven Long/972	757-824-1034
Charles McClain/970.2	301-286-5377
Robert Meneghini/975	301-286-9128
Peggy O'Neill/974	301-286-8273
James Ormsby/970	301-286-9869
Manfred Owe/974	301-286-5173
Claire Parkinson/971	301-286-6507
Paul Racette/975	301-286-9114
Michele Rienecker/971	301-286-6178
T. John Riley/970.2/730	301-286-0712
Laurence Rossi/972	757-824-1590
Frank Schmidlin/972	757-824-1618
James Shiue/975	301-286-6716
Robert Tittle/972	757-824-1244
David Toll/974	301-286-9256

Name/Code*	Phone Number
Michael Triesky/975/555	301-286-9091
Douglas Vandemark/972	757-824-2038
Edward Walsh/972	303-497-6357
James Wang/975	301-286-8949
John Ward/972/571	757-824-1010
James Weinman/975	301-286-3175
Wayne Wright/972	757-824-1698
H. Jay Zwally/971	301-286-8239

**NASA Civil Service Support**

Sandra Banks/972	757-824-2526
Cheryl-Ann Barrington/903	301-286-8530
Debbie Boyer/903	301-286-4104
Patricia Brasure/970	301-286-8670
Michele Gover/970	301-286-6171
Nadia Kines/971	301-286-4718
Omega Williams/970.2	301-286-9676
Lynn Hoppel/219	301-286-3035
Ann McDowell/903	757-824-1037
Jolyn Nace/975	301-286-9831
India Robinson/970.2	301-286-6800

**Resident Research Associates, Visiting Faculty,  
and Post Doctoral Scientists**

Charon Birkett/971	301-286-6056
Anna Borovikov/971	301-286-2477
Kenneth Casey/971	301-286-3169
Jim Christian/970.2	301-286-9911
Victoria Coles/971	301-286-4001
Agnes Ducharme/974	301-286-5986
Mark Fahnstock/971	301-286-2142
Cathleen Gieger/971	301-286-5921
Steve Howden/971	301-286-2141
Gail Jackson/975	301-286-3196
Alban Lazar/970	301-286-2036
Stephen Maritorena/970.2	301-286-9975
Thorsten Markus/971	301-286-6808
Ragu Murtugudde/970	301-286-2071
Joel Picaut/970	301-286-2108
Dale Robinson/971	301-286-9320
Chris Shuman/971	301-286-8725
Kostas Stefanidis/971	301-286-4151
Andrew Tait/974	301-286-7095
Nobuhiro Takahashi/975	301-286-8329
Les Thompson/975	301-286-8382
Maria Varnet/972	757-824-1896
Mark Verschell/970	301-286-2027
Liping Wang/971	301-286-5105
Menghua Wang/970.2	301-286-6421
Jerry Wiggert/971	301-286-0946
Sunny Wu/971	301-286-9835
Jiayan Yang/971	301-286-9159
Lisan Yu/971	301-286-7428

\*970 Laboratory for Hydrospheric Processes  
 970.2 SeaWiFS Project  
 971 Oceans and Ice Branch  
 972 Observational Science Branch

974 Hydrological Sciences Branch  
 975 Microwave Sensors Branch  
 903 Administration and Resources Management Office  
 903.2 Business Management Branch



## Support Service Contractors

### Caelum Research Corp.

Name/Code*	Phone Number
Michael Kao/975	301-286-5239
Liang Liao/975	301-286-2293
Lawrence Stock/971	301-286-3179
Yunhe Zhao/971	301-286-3548

### Computer Sciences Corporation

Lisa Brett/972	757-842-2292
Ronald Brooks/972	757-824-1041
Peggy Jester/972	757-824-2093
Jeffrey Lee/972	757-824-1853
Dennis Lockwood/972	757-824-2252
Gerry McIntire/972	757-824-1889
James McMillan/972	757-824-1032
Thomas Northam/972	757-824-1286
Carol Purdy/972	757-824-1596
Donald Shirk/972	757-824-1312

### EG&G, Inc

Alex Chekalyuk/972	757-824-2401
Earl Frederick/972	757-824-1018
Serdar Manizade/972	757-824-1025
Richard Mitchell/972	757-824-1026
Carl Schirtzinger/972	757-824-1021
John Scott/972	757-824-1019
Robert Swift/972	757-824-1432
Alan Waller/972	757-824-2029
Mark Williams/972	757-824-1744
James Yungel/972	757-824-1026

### Future Technology Corp.

Sean Bailey/970.2	301-286-3931
Aaron Chang/975	301-286-3542
Linwood Smith/970.2	301-286-3261
Julie Thomas/970.2	301-286-1403
William Woodford/970.2	301-286-8910

### General Sciences Corp.

Karen Baith/970.2	301-286-4759
Mark Baith/970	301-286-5146
Robert Barnes/970.2	301-286-0501
Jonathon Barton/974	301-286-4738
Judy Chen/970.2	301-286-9494
Yu-Ping Chen/971	301-286-6614
Janet Chien/974	301-286-7021
Long Chiu/974	301-286-0536
Angela Converse/971	301-286-1501
Robert Eplee/970.2	301-286-0953
Elaine Firestone/970.2	301-286-4553
Bryan Franz/970.2	301-286-5429
Gary Fu/970.2	301-286-7107
Sudhakar Gududuri/970.2	301-286-9976
Mark Heiser/974	301-286-1447
Barry Herchenroder/971	301-286-5990
Josephine Humphrey/971	301-286-2128
Alice Isaacman/970.2	301-286-7108
Christian Keppenne/971	301-286-4572
Andrew Klein/974	301-286-3314

\*970 Laboratory for Hydrospheric Processes  
 970.2 SeaWiFS Project  
 971 Oceans and Ice Branch

### General Sciences Corp. (Con't)

Name/Code*	Phone Number
Dan Knowles/970.2	301-286-0563
Catherine Larko/974	301-286-5084
Sung Lee/970	301-286-9013
Lena Marshak/971	301-286-1436
Jie Meng/974	301-286-7095
Mila Mitra/970.2	301-286-7109
Frederick Patt/970.2	301-286-5723
Christophe Pietras/970.2	301-286-9892
Hugh Powell/974	301-286-2310
Indira Rao/970.2	301-286-9531
Wayne Robinson/970.2	301-286-3883
Kellie Ruebens/970.2	301-286-4072
Brian Schieber/970.2	301-286-1440
Paul Schoenly/971	301-286-5899
Daniel Shaffer/971	301-286-3133
Paul Smith/970.2	301-286-2852
Kevin Turpie/971	301-286-3137
M. Grey Valenti/970.2	301-286-3288
Patricia Vornberger/971	301-286-5687
John Wilding/970.2	301-286-4569
Robert Woodward/971	301-286-1441
Denise Worthen/971	301-286-2339

### Mantech

Dave Ross/972	757-824-1156
---------------	--------------

### NYMA

Richard Aldridge/975	301-286-2955
Maurice Butler/970	301-286-9677

### Raytheon STX

Saji Abraham/975	301-441-4018
James Beauchamp/970	301-286-3291
Brian Beckley/971	301-441-4413
Anita Brenner/971	301-441-4132
Scott Bringen/971	301-441-4019
Helen Cornejo/971	301-441-4070
Narinder Chauhan/975	301-286-5072
John DiMarzio/971	301-441-4122
Michael Dinniman/971	301-286-3690
Steven Fiegles/971	301-286-6805
Robert Gersten/971	301-441-0476
Daya Gilra/971	301-441-4022
Eric Hackert/970	301-286-3334
Michael Haken/975	301-286-2807
Mahabaleshwara Hegde/971	301-286-3581
Joseph Lyu/975	301-286-5855
N. William Manning/971	301-286-9246
Michael Martino/971	301-286-3180
Abraham Ramsey/970	301-286-3050
Jamila Saleh/971	301-286-4946
John Shepperd/971	301-441-4099

### Research Data Corp.

George Riggs/974	301-286-6811
Angela Li/970.2	301-286-5253

972 Observational Science Branch  
 974 Hydrological Sciences Branch  
 975 Microwave Sensors Branch

# Support Service Contractors (con't.)

## Science & Engineering Services, Inc.

<u>Name/Code*</u>	<u>Phone Number</u>
Alfred Beebe/972	757-824-1564
Dawn Holdren/972	757-824-1761
Robert Olsen/972	757-824-2175

## Systems Engineering and Security, Inc.

Donna Geiman/974	301-286-5347
Claire Macaulay/971	301-286-4716
Jennifer Jackson/974	301-286-5480
Janice Phipps-Harmon/971	301-286-5380

## Science Systems & Applications, Inc.

<u>Name/Code*</u>	<u>Phone Number</u>
Nick Digirolamo/974	301-286-9784
Charles Hoisington/970.2	301-286-8910
Ann Hsu/974	301-286-8909
Lun Li/971	301-286-2128
Rafael Rincon/975	301-286-2910

## University of Maryland

Carlos Morales/975	301-286-9112
--------------------	--------------

\*970 Laboratory for Hydrospheric Processes  
970.2 SeaWiFS Project  
971 Oceans and Ice Branch

972 Observational Science Branch  
974 Hydrological Sciences Branch  
975 Microwave Sensors Branch



## Journal Papers and Book Chapters

**Page intentionally left blank**



## LAND COVER CHANGE and GLOBAL PRODUCTIVITY

The papers in this section provide observations and modeling to quantify land cover change and global productivity, and this quantification is required to understand key aspects of global carbon, water, and energy cycles. Determination of carbon production in the Antarctic has been a challenging problem because of high spatial and temporal variabilities of the rate of production and significant seasonal variation of the extent of sea ice surrounding the Antarctic continent. Arrigo, et al. present modeling results for annual carbon production in the Antarctic sea ice. The model used is one dimensional, in which algae grow within an infiltration layer located at the sea ice/snow interface and within an internal freeboard layer near sea level. Nutrient exchange is a function of surface flooding and sea ice porosity. The model was validated using *in situ* measurements in the Weddell Sea. They estimate that 40 teragrams of carbon are annually produced in the Antarctic ice pack, of which 70 per cent is associated with first-year ice. They also find that production in the Weddell Sea constitutes about 50 per cent of the total production.

Monger, et al. used observations by the Coastal Zone Color Scanner (CZCS) onboard the Nimbus-7 satellite to estimate phytoplankton production to be 2.3 Gt carbon in the surface waters of the eastern tropical Atlantic ( $5^{\circ}\text{N}$ - $10^{\circ}\text{S}$ ,  $25^{\circ}\text{W}$ - $10^{\circ}\text{E}$ ) during March 1979 to February 1980, with a 3.5 fold seasonal variation in the rate of production. While describing the principal physical mechanisms controlling seasonal production they propose that in addition to seasonal changes in the thermocline depth, one must also consider changes in the depth of the equatorial undercurrent. Furthermore, they find that standard CZCS global products of the pigment concentration are highly underestimated due to errors in the aerosol correction and significant reduction in the concentration of dissolved organic matter as a result of strong equatorial upwelling.

A highly significant characteristic of the Earth's climate, in general and specifically of El Nino Southern Oscillation (ENSO), is the occurrence and spatial shift of the warm pool of surface water in the western equatorial Pacific. While Skipjack tuna are distributed in the surface mixed layer throughout the equatorial and subtropical Pacific, catches are highest in the western equatorial Pacific warm pool. Lehodey, et al. show that displacement of the warm pool associated with ENSO events strongly correlate with the displacement of the fishing ground as indicated by catch per unit effort. This correlation can be used to predict the region of highest tuna abundance several months in advance.

Changes in land cover have numerous direct and indirect effects on carbon, water, and energy cycles, and several of these effects can be due to changes in soil moisture. Active and passive microwave measurements can be used to monitor surface layer soil moisture, which is a significantly more dynamic and spatially variable characteristic than root-zone soil moisture. Chen, et al. present an analysis of aircraft observations of infrared surface temperature and microwave brightness temperature over a 20x20 km grassland area. Temporal variation of brightness temperature was highly correlated with *in situ* gravimetric soil moisture. They also found that cross-correlation between surface temperature, brightness temperature, and vegetation index to be rather low, suggesting that different time scales are involved in different processes of vegetation growth, and near surface soil moisture and energy balance. Jackson, et al. demonstrate that passive microwave observations at 2.65 and 1.4 GHz provide soil moisture information, respectively, for the 10mm and 30-50 mm layer. Engman shows that microwave remote sensing can detect unique signatures associated with many hydrologic processes. Specifically, spatial and temporal distributions of surface soil moisture can provide information about such hydrologic processes as areas of potential and less potential evaporation, ground water recharge and discharge zones, and contributing areas of storm runoff.

**Page intentionally left blank**



# Primary Production in Antarctic Sea Ice

Kevin R. Arrigo,\* Denise L. Worthen, Michael P. Lizotte,  
Paul Dixon, Gerhard Dieckmann

A numerical model shows that in Antarctic sea ice, increased flooding in regions with thick snow cover enhances primary production in the infiltration (surface) layer. Productivity in the freeboard (sea level) layer is also determined by sea ice porosity, which varies with temperature. Spatial and temporal variation in snow thickness and the proportion of first-year ice thus determine regional differences in sea ice primary production. Model results show that of the 40 teragrams of carbon produced annually in the Antarctic ice pack, 75 percent was associated with first-year ice and nearly 50 percent was produced in the Weddell Sea.

Sea ice surrounding the Antarctic continent varies in extent from  $4 \times 10^6$  km<sup>2</sup> in summer to  $20 \times 10^6$  km<sup>2</sup> in winter (1) and represents one of the largest and most dynamic ecosystems on Earth. Algae associated with ice may attain standing crops with amounts of chlorophyll *a* in excess of 400 mg m<sup>-2</sup> and rates of primary production of  $>1$  g C m<sup>-2</sup> day<sup>-1</sup>, comparable to productive oceanic regions (2, 3). Because sea ice microalgal production is spatially and temporally variable, its contribution to the carbon cycle of the Southern Ocean and its importance as a food source for higher trophic levels [such as overwintering juvenile krill (4)] have been difficult to determine.

We used an expanded version of a one-dimensional numerical model (5-7) to investigate the dynamics of primary production in Antarctic pack ice between 1 October 1989 and 30 April 1990. This approach allowed us to resolve regional differences in the size of the sea ice algal standing crop and in the rate of carbon fixation as a function of sea ice type (first-year and multiyear ice), sea ice habitat (infiltration and internal freeboard layers), and environmental conditions. In the

model, algae grow within an infiltration layer located at the sea ice-snow interface and within an internal freeboard layer near sea level. Nutrient exchange is a function of surface flooding and sea ice porosity (8). Algal growth in the bottom ice layer is neglected because this community is generally absent in pack ice (9). As input, the model uses measurements collected remotely (sea ice extent and snow thickness) and in situ (cloud cover and air temperature) (10). Simulations of sea ice in the Weddell Sea produced algal standing crops that compare favorably with in situ observations (Fig. 1); consequently, the model was extended to the entire Antarctic ice pack.

In the model, regional differences in primary production (Fig. 2) were largely determined by variations in the proportion of first-year ice. Although production within the freeboard layer of both ice types was similar and showed little spatial variation (11), annual production in the first-year infiltration layer was 27 times that in multiyear ice (Table 1). The highest rates of production were associated with those regions that had the highest proportion of first-year ice, such as the Weddell Sea ( $0.95$  g C m<sup>-2</sup> month<sup>-1</sup>) and the southern Indian Ocean ( $1.02$  g C m<sup>-2</sup> month<sup>-1</sup>). Productivity in these regions also was enhanced by thick mean snow cover (0.17 m) and high seawater nitrate concentration (23  $\mu$ M). In contrast, in the southwestern Pacific, the transience of first-year ice and high proportion of multiyear ice (40 to 65%), thinner mean snow cover (0.13 m), and lower seawater nitrate concentration (18  $\mu$ M) resulted in the

K. R. Arrigo, NASA Oceans and Ice Branch, Goddard Space Flight Center, Code 971.0, Greenbelt, MD 20771, USA.

D. L. Worthen, Science Systems and Applications Inc., Lanham, MD 20706, USA.

M. P. Lizotte, Department of Biology and Microbiology, University of Wisconsin-Oshkosh, Oshkosh, WI 54901, USA.

P. Dixon, Scripps Institution of Oceanography, University of California, San Diego, La Jolla, CA 92093, USA.

G. Dieckmann, Alfred-Wegener Institut für Polar- und Meeresforschung, Columbusstrasse, D-27570 Bremerhaven, Germany.

\*To whom correspondence should be addressed.

lowest mean rate of production ( $0.59 \text{ g C m}^{-2} \text{ month}^{-1}$ ) of any Antarctic region (Table 1).

The relative importance of light and nutrients for algal productivity throughout the Antarctic ice pack varied markedly with season and habitat. In the freeboard layer during the spring, algal biomass, productivity (Fig. 3A), and nutrient uptake were low, and algal growth was controlled by light availability (Fig. 3B). Increased amounts of light in November led to a marked rise in productivity; however, the concomitant increase in nutrient demand and reduction in nutrient concentrations limited algal growth during the austral summer. As temperatures cooled in late February (Fig. 3C), sea ice porosity decreased below the threshold required for nutrient exchange (8), resulting in a rapid decline in production within the freeboard layer (Fig. 3A). The timing of this decline varied spatially by more than 1 month (Fig. 3A) because of temperature differences. Because of its more restricted nutrient supply, the infiltration layer exhibited rates of primary production that peaked 1 to 2 months later than in the freeboard layer (Fig. 3D) (8). In the infiltration layer, light availability exceeded de-

mand until early February (Fig. 3E). Consequently, primary production was restricted to locations that were submerged and suffused with nutrients, which amounted to 15 to 25% of the total ice area (12). The infiltration layer became light-limited after February as sun elevation decreased and the nutrient demand of the diminishing algal community declined.

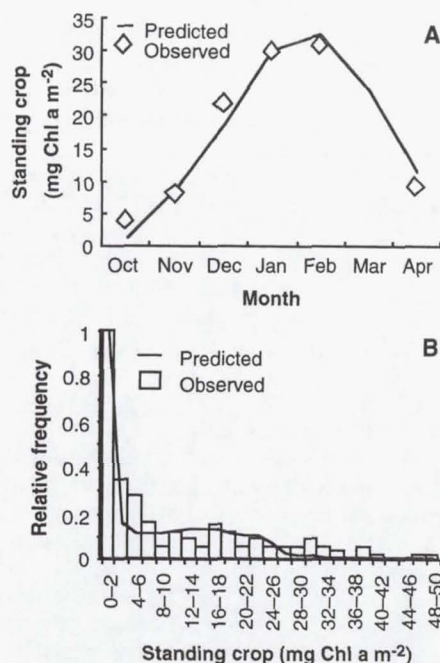


**Fig. 1.** (A) Mean monthly ice algal standing crop for the Weddell Sea predicted by the model and measured in sea ice cores ( $n = 257$ ). In both cases the SDs were similar in magnitude and were approximately equal to the monthly means. (B) Frequency histograms for data used to generate (A). Chl *a*, chlorophyll *a*.

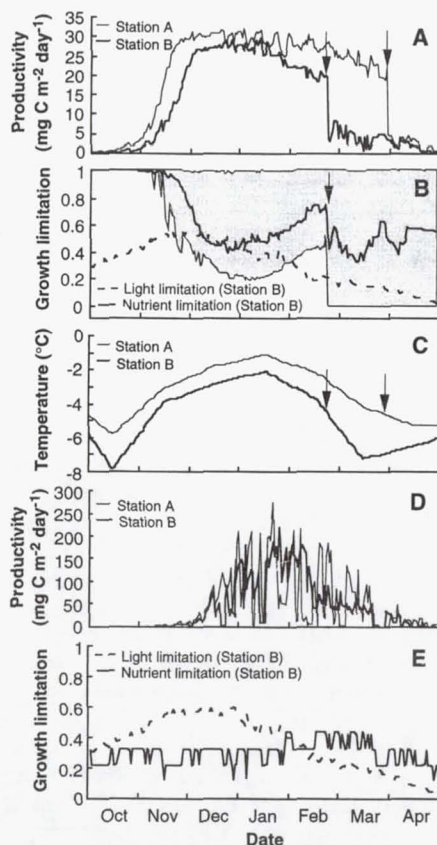


**Fig. 3.** (A) Modeled primary production in the freeboard layer at station A ( $71.4^{\circ}\text{S}$ ,  $41^{\circ}\text{W}$ ) and station B ( $74.1^{\circ}\text{S}$ ,  $42^{\circ}\text{W}$ ) in the first-year ice of the Weddell Sea. Arrows indicate when air temperature dropped below  $-4.7^{\circ}\text{C}$  [see (C)], the temperature at which brine volume decreases below the threshold necessary for nutrient exchange within the ice sheet. (B) Magnitude of growth limitation induced by both light and nutrients (the lowest value determines the most limiting resource) in the freeboard layer at station B. The gray area denotes the range of values and the thick line denotes the mean for the nutrient limitation term at the nine grid points comprising station B. The steep decline in primary productivity shown in (A) at station B in late February resulted from the drop in the nutrient limitation term to zero in many of the grid points (the mean value was 0.42). A similar decline in primary productivity was not observed in late December, when the mean nutrient limitation term was similarly low (0.41), because the nutrient limitation term in all subsectors of station B exhibited values greater than zero. (C) Surface air temperatures at stations A and B. (D) Primary production in the infiltration layer at stations A and B. (E) Magnitude of growth limitation induced by light and nutrients in the infiltration layer at station B.



# Spatial Distribution and Pattern Persistence of Surface Soil Moisture and Temperature over Prairie from Remote Sensing

Daoyi Chen,<sup>\*1</sup> Edwin T. Engman,<sup>†</sup> and Wilfried Brutsaert<sup>‡</sup>

*Images remotely sensed aboard aircraft during FIFE, namely, PBMR (microwave) soil moisture and NS001 thermal infrared surface temperature, were mapped on the same coordinate system covering the 20 km×20 km experimental site. For both kinds of image data, the frequency distributions were close to symmetric, and the area averages compared reasonably well with the ground based measurements. For any image on any given day, the correlation between the remotely sensed values and collocated ground based measurements over the area was usually high in the case of NS001 surface temperature but low in the case of PBMR soil moisture. On the other hand, at any given flux station the correlation between the PBMR and gravimetric soil moisture over all available days was usually high. The correlation pixel by pixel between images of PBMR on different days was generally high. The preservation of the spatial patterns of soil moisture was also evaluated by considering the correlation station by station between ground-based soil moisture measurements on different days; no persistence of spatial pattern was apparent during wet periods, but a definite pattern gradually established itself toward the end of each drying episode. The spatial patterns of surface temperature revealed by NS001 were not preserved*

*even within a single day. The cross-correlations among the two kinds of images and the vegetation index NDVI were normally poor. This suggests that different time scales were involved in the different processes of vegetation growth, and of the near-surface soil water and energy budgets. ©Elsevier Science Inc., 1997*

## INTRODUCTION

The spatial variation of landsurface characteristics and their impact on regional hydrologic processes have become the focus in a number of issues such as subgrid variation of GCM models and catchment hydrology. During FIFE [First ISLSCP (International Satellite Land Surface Climatology Project) Field Experiment], ground measurements and satellite and airborne observations have been made over a tall grass prairie in northeastern Kansas.

Various aspects of the spatial variation of water vapor flux, soil moisture, vegetation, and surface temperature have been analyzed by, among others, Shuttleworth et al. (1989), Charpentier and Groffman (1992), and Chen and Brutsaert (1995) with ground-measured data, and by Desjardins et al. (1992) and Holwill and Stewart (1992) with aircraft-based measurements. More recently, Chen and Brutsaert (1997) have looked at the spatial variation of vegetation density, mainly on the basis of satellite measurements of the normalized difference vegetation index (NDVI).

In a continuing effort to shed more light on landsurface spatial variability of natural grassland, the present article focuses on soil moisture and surface temperature. For the former use is made of PBMR (Pushbroom Microwave Radiometer) data and for the latter NS001 data,

<sup>\*</sup>School of Engineering, University of Manchester, Manchester, United Kingdom

<sup>†</sup>Hydrologic Sciences Branch, Goddard Space Flight Center, NASA, Greenbelt, Maryland

<sup>‡</sup>School of Civil and Environmental Engineering, Cornell University, Ithaca, New York

<sup>1</sup>Previously at Cornell University.

Address correspondence to D. Chen, Univ. of Manchester, School of Engineering, Oxford Rd., Manchester M13 9PL, UK.

Received 23 August 1995; accepted 20 January 1997.



tion between NS001 and PAM surface temperature as shown in Figure 11 was improved to  $r=0.948$ , and the other parameters became  $m_d=1.09^\circ\text{C}$  and  $\delta=2.44^\circ\text{C}$  for all data points. For the mean values shown in Figure 12, these are  $r=0.969$ ,  $m_d=1.17^\circ\text{C}$ , and  $\delta=1.43^\circ\text{C}$ . The results presented here are comparable to those obtained by Sugita and Brutsaert (1993) with  $\delta$  on the order of  $1\text{--}3^\circ\text{C}$ .

In addition, correlations between the NS001 (retrieved at ground stations) and the PAM (collocated) surface temperature on each of the 13 images are shown in Table 7.  $r$  was quite high, namely between 0.57 and 0.89, on six (out of 13) images. The correlations for the rest of the images were relatively weak. This inconsistency may be due, in part, to the different coverage of the FIFE area by each image.

### Persistence of Spatial Patterns

Correlations between NS001 images at different times of those three days are used to evaluate the persistence of spatial patterns of surface temperature. It is found that all the correlation coefficient  $r_{img}$  are low below 0.29, mostly around 0.1. Although one minor reason may be the incomplete overlap between images, the main reason is probably that the surface temperature responds rather quickly to such highly unsteady variables as net radiation and wind. Therefore, their low correlation are not surprising.

### CROSS CORRELATION BETWEEN DIFFERENT IMAGES

Chen and Brutsaert (1997) and previous sections describe the individual characteristics of several remotely sensed images, namely, vegetation index NDVI (both SPOT and TM), PBMR soil moisture, and NS001 surface temperature. The relationships between these different images were also investigated. The detailed results are not presented but are now briefly summarized in what follows. Considering the physical and biological processes, one would expect vegetation and soil moisture to be relatively independent. However, the surface temperature is likely to be affected by soil moisture and vegetation for given radiative and atmospheric conditions.

The values of the correlation coefficient  $r_{img}$  between NDVI and PBMR soil moisture were indeed found to be very low, mostly below 0.1. This means that the growth of vegetation and the wetting of soil are two relatively independent processes. This is consistent with our earlier findings regarding the ground measurements of gravimetric soil moisture and the vegetation parameter LAI (Chen and Brutsaert, 1995).

The maximal values of  $r_{img}$  between NDVI and NS001 surface temperature were found to be about  $-0.3$ . Negative  $r_{img}$  values are reasonable because a denser vegeta-

tion should tend to cool the surface and lower the surface temperature. Because soil moisture is one of the primary factors in controlling evaporation and surface temperature, these weak correlations were as expected.

The  $r_{img}$  values between PBMR soil moisture and NS001 surface temperature were found to be quite low. Common sense suggests that wet areas should be cooler. Thus, while negative  $r_{img}$  values were expected, the small values might somehow be considered disappointing. On the other hand, PBMR soil moisture and thermal infrared surface temperature really respond to processes at different depths; moreover, in 1987 conditions were fairly moist, with very little stress for the vegetation. Clearly, more work will be necessary to improve present understanding of PBMR soil moisture.

### CONCLUSION

From the mechanistic point of view, the preservation of spatial patterns has provided some insight into the gradual evolution of certain physical and biological processes. From the applications point of view, a persistence of spatial patterns indicates that simplification can be made by assuming some degree of similarity. This means that interpolations can be made between available measurements, and that observed spatial patterns can be integrated in modeling at the hydrologic catchment and GCM grid scale.

Area averaged PBMR soil moisture was about 4.16% lower than the site average of gravimetric soil moisture and the root mean square difference  $\delta$  was 6.04% soil moisture. The correlations at any station between PBMR and gravimetric soil moisture for all days were also good. The strength of the correlations cannot be explained by the burning treatment alone. Unfortunately, there were only five to nine ground stations on the images, and the correlations with the measurements at these stations (indicating spatial variation) were poor for all days. This indicated that the accuracy of PBMR soil moisture was somehow affected by a number of factors, such as vegetation, thatch layer, and surface slope, which will need more work to improve understanding. The persistence of the soil moisture spatial patterns was revealed by correlation between data (both PBMR and gravimetric) on different days. It preserved well during the dry season but poor for the wet season.

The NS001 surface temperatures were also in good agreement with the ground measurements, although there was a systematic bias of  $m_d=2.54^\circ\text{C}$ . The correlations with ground measured surface temperature were good for most images. However, their spatial patterns did not persist at all even in the same day. The fast response of surface temperature to a number of highly unsteady factors may be the main reason. Furthermore, the incomplete overlap of different images (four to nine stations only) may also be responsible for weaker persistence.



## **Soil moisture, the hydrologic interface between surface and ground waters**

**EDWIN T. ENGMAN**

*Hydrological Sciences Branch, Code 974, Laboratory for Hydrospheric Processes, NASA, Goddard Space Flight Center, Greenbelt, Maryland 20771, USA*

**Abstract** A hypothesis is presented that many hydrologic processes display a unique signature that is detectable with microwave remote sensing. These signatures are in the form of the spatial and temporal distributions of surface soil moisture. The specific hydrologic processes that may be detected include groundwater recharge and discharge zones, storm runoff contributing areas, regions of potential and less than potential evapotranspiration (ET), and information about the hydrologic properties of soils. In basin and hillslope hydrology, soil moisture is the interface between surface and ground waters.

### **INTRODUCTION**

The hydrologic cycle's interaction with the Earth's land surface occurs within a thin reservoir that stores and distributes (spatially and temporally) water that falls on the surface in the form of rain or melting snow. This reservoir is commonly referred to as *soil moisture*. Soil moisture integrates much of the land surface hydrology, acts as the interface between the land surface and the atmosphere, the land surface and the groundwater reservoir, and controls the infiltration and surface runoff processes. The production of surface water through the runoff process is to a large degree controlled by the antecedent soil moisture and groundwater recharge is also controlled by soil moisture.

Although soil moisture physically represents only the surface layer of soil, much of the time it is highly correlated with the total water in the soil profile and is an indicator of total water availability. Unfortunately, soil moisture is not a uniform variable in either a spatial or temporal sense. The very large spatial variability of soil moisture is the result of variable inputs (rain or snowmelt), land cover, highly variable soil properties and topography. The temporal patterns of soil moisture respond to the spatial distribution and variable atmospheric forcing. The net result of this is that soil moisture is a difficult variable to measure, not necessarily at one point in time, but in a temporally consistent and spatially comprehensive basis. Because it exhibits such large spatial and temporal variability; a snap shot or point measurements have had very little meaning in a hydrologic sense.

This paper reviews the current interest in soil moisture which is primarily driven by the science interests in the land-atmosphere interactions, both at the General Circulation Model (GCM) scale and at the mesoscale. Although these interests have driven the development of remote sensing of soil moisture, there are other potential applications for soil moisture in hydrology. The paper makes the case for interpreting remotely sensed soil moisture as a hydrologic signature. A hydrologic signature that can be used to identify runoff areas, recharge areas, and the general



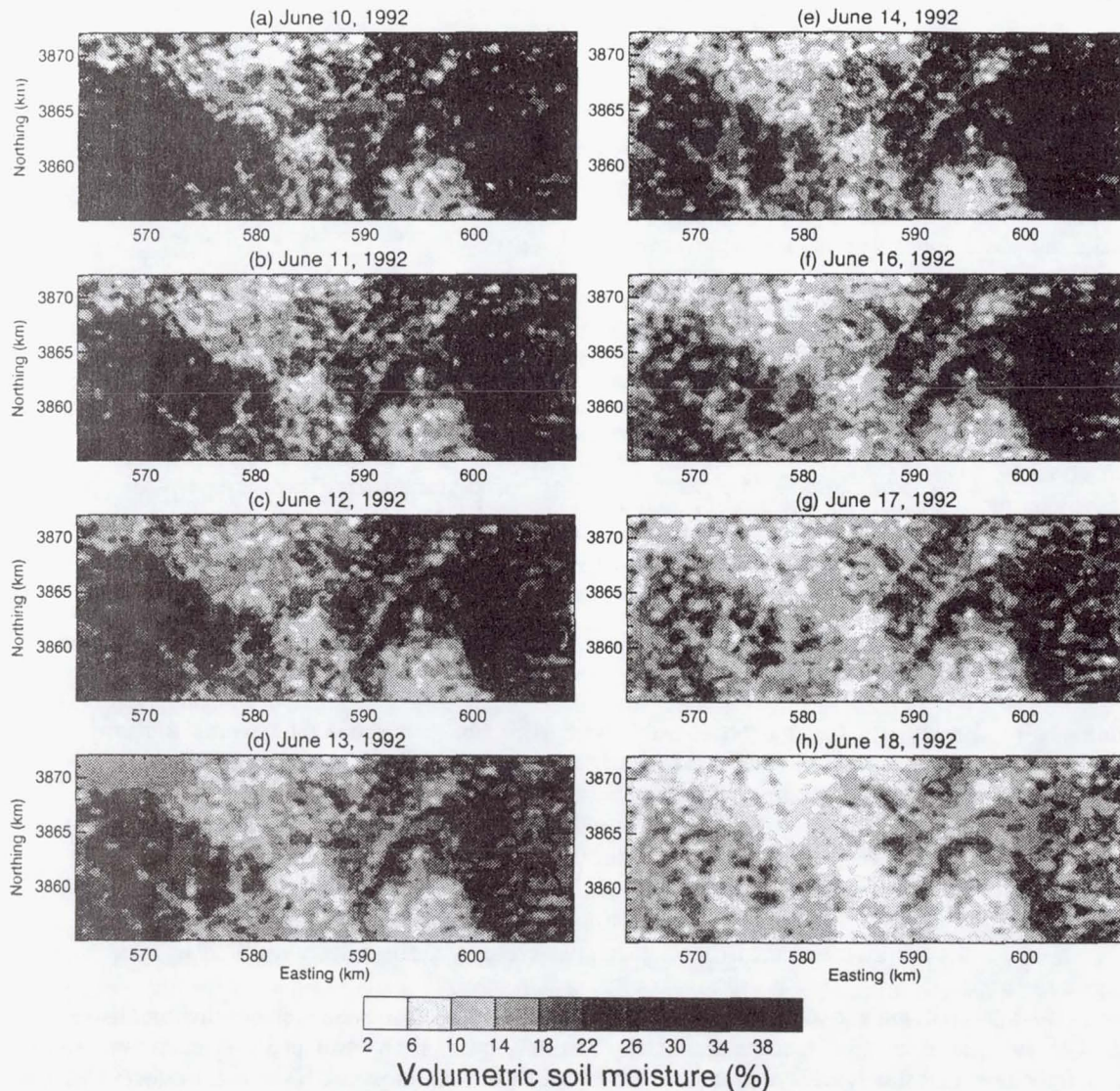


**Fig. 7** Time sequence of passive microwave produced soil moisture maps from the Little Washita Watershed near Chickasha, Oklahoma. The developing light grey (dry) from black (wet) illustrates sequential and nonuniform drying of soil moisture. This new spatial data provides a hydrologic signature of the drainage basin.

## CONCLUSION

In this paper, I have tried to make the case that many hydrologic processes have a signature that is detectable with remote sensing in the form of the spatial and temporal signatures of soil moisture. The level (wetness) of the signature, its location in the landscape, its rate of change can all provide information to the hydrologist about the spatial distribution of processes in a basin. The types of information that may be detected include groundwater recharge and discharge zones, storm runoff contributing areas, regions of potential and less than potential ET, and information about the hydrologic properties of soils. Microwave remote sensing has the potential to detect these signatures within a basin. These signatures should also be the key on how and where to apply soil physical parameters in distributed models.



# Passive Microwave Observation of Diurnal Surface Soil Moisture

Thomas J. Jackson, *Senior Member, IEEE*, Peggy E. O'Neill, and Calvin T. Swift, *Fellow, IEEE*

**Abstract**—Microwave radiometers operating at low frequencies are sensitive to surface soil moisture changes. Few studies have been conducted that have involved multifrequency observations at frequencies low enough to measure a significant soil depth and not be attenuated by the vegetation cover. Another unexplored aspect of microwave observations at low frequencies has been the impact of diurnal variations of the soil moisture and temperature on brightness temperature. In this investigation, observations were made using a dual frequency radiometer (1.4 and 2.65 GHz) over bare soil and corn for extended periods in 1994. Comparisons of emissivity and volumetric soil moisture at four depths for bare soils showed that there was a clear correspondence between the 1 cm soil moisture and the 2.65-GHz emissivity and between the 3–5 cm soil moisture and the 1.4-GHz emissivity, which confirms previous studies. Observations during drying and rainfall demonstrate that new and unique information for hydrologic and energy balance studies can be extracted from these data.

## I. INTRODUCTION

PASSIVE microwave sensors operating at low frequencies ( $<5$  GHz) are sensitive to surface soil moisture changes. Reliable algorithms have been developed that can be applied even with vegetation cover, subject to limitations [1]. Observation of the surface soil moisture status is of value primarily in land-atmosphere interaction studies, serving as a source of calibration, verification or input data in large scale modeling. A broader range of hydrologic applications could be addressed if it was possible to measure the depth distribution of soil moisture. Furthermore, if changes in the state of the soil moisture could be observed, it might be possible to quantify fluxes such as evaporation and infiltration.

Traditional passive microwave radiometry experiments have typically employed a single daily observation of the land surface, often at a single wavelength. There exists the potential for new information to address the hydrologic issues described above by enhancing the temporal coverage and by using multifrequency sensor packages. To explore these new directions, a truck-based observing system was developed consisting of two low frequency passive microwave sensors, at L and S band, as well as ancillary instrumentation. An experimental design

was then created which effectively utilized the multifrequency information provided by this system to study the temporal and diurnal aspects of soil moisture.

A critical issue in the interpretation of microwave observations for hydrologic studies is the inversion of brightness temperature to estimate surface soil moisture. Theory describes the passive microwave measurement as a function of the dielectric and temperature profiles of the soil [2]. A single microwave observation cannot be used to invert these models. Based on general characteristics and field observations, generalizations on the contributing depth of the soil are often made to allow the application of models such as the Fresnel equations that can be inverted to extract soil moisture. The validity of the uniform contributing depth assumption that allows this application and the definition of the depth as a function of frequency have not been adequately verified.

Another previously ignored aspect of passive microwave observations at low frequencies has been the diurnal variations of the soil moisture and soil temperature and the impact of these on the brightness temperature [3]. Important information on hydrologic processes such as evaporation and infiltration could be related to patterns of variation in the brightness temperature.

This paper describes results of field experiments which were conducted during 1994 at the USDA Beltsville Agricultural Research Center using the L and S band truck-based system to address the issues described above through extended diurnal observations over bare soil and corn.

## II. DIURNAL VARIATIONS OF SOIL MOISTURE

The temporal regime of surface soil moisture and microwave brightness temperature contain important information that can be used for system design as well as extracting estimates of profile moisture and water flux. Rose [4] and [5] was first to report on the diurnal variations of the surface layer. Using several measurements of the 0–15 cm layer over the course of the day, he demonstrated the nature of water and temperature profiles. Jackson [6] significantly expanded on this with comprehensive field experiments in Arizona in which bare soil plots were irrigated and monitored during extended periods of drying. Hourly observations were made of water content for eight separate layers to a depth of 9 cm in conjunction with temperature measurements at selected depths in two separate experiments (seven days in 1970 and 37 days in 1971). The data from these experiments have served

Manuscript received May 10, 1996; revised February 26, 1997.

T. J. Jackson is with the USDA-ARS Hydrology Lab, Beltsville, MD 20705 USA.

P. E. O'Neill is with the NASA Goddard Space Flight Center, Hydrological Sciences Branch, Laboratory for Hydrospheric Processes, Greenbelt, MD 20771 USA.

C. T. Swift is with the Department of Electrical and Computer Engineering, University of Massachusetts, Amherst, MA 01003 USA.

Publisher Item Identifier S 0196-2892(97)05505-8.



modified over time. For this study, an attempt was made to prepare an area that was large enough and homogeneous to allow sampling outside the SLMR footprint. However, some variability within this area became obvious over time based on visual observation. Soil moisture samples were collected at 0–1, 0–3, 0–5, and 0–15 cm soil layers from an area adjacent to the sensor footprint each time we obtained microwave data in the first portion of the experiments. In general, three samples were collected each time at each depth. Bulk density was sampled independently for use with the gravimetric data to compute volumetric soil moisture.

The test plots utilized in these experiments are quite sandy. Soil texture analyzes of the surface 5 cm indicated a sand fraction of 76% and a clay fraction of 4%, which is classified as a loamy sand. Soil surface roughness was determined by photographing a grid board that was pushed into the soil and then digitizing the image. Conditions were characteristic of a very smooth surface. Daily characterization of the entire soil moisture profile (one or more meters in depth) was performed using a commercially available capacitance-based probe. The shallowest depth that this instrument measures is a layer at 15 cm.

Meteorological and energy balance information was also collected. Basic meteorological observations were obtained for the entire study period. Variables measured include air temperature, humidity, solar radiation, wind speed and wind direction, net radiation, soil heat flux, and soil temperature at depths of 1.5, 3, 5, 10, and 15 cm and at the surface. The surface energy balance was estimated using the Bowen Ratio technique; however, this system was not operating until the latter portion of the experiment period. Averages of the meteorological and Bowen Ratio station data were recorded every 15 min.

## V. EXPERIMENT DESCRIPTION

Sites used in these studies were located on the North Farm area of the USDA Beltsville Agricultural Research Center and were used in previous truck-based microwave experiments. Two approaches were used for data collection. The original procedure involved observing one or more plots and moving the boom to recenter the L and S band footprints. Truck and ground data were collected about every hour for most of the day. This procedure was valuable in establishing basic patterns and relationships. This approach was used in Series 1 (days 157–167 bare soil) and Series 2 (days 199–206 bare soil and corn). However, experiments designed to study temporal dynamics of the variables and fluxes required some modification of this procedure. In these experiments, the radiometers were set and left in a fixed position and operated in a near continuous mode 24 h a day. Soil moisture sampling was limited to occasional observations. This approach was used in Series 3 (days 259–264) and several short term infiltration experiments.

Observations of the plot with corn were primarily limited to an intensive period between days 199 and 206. This corresponded to a condition of near-peak vegetation water content. The original canopy was modified by removing approximately 50% of the plants (observed density  $\sim 3.22$  plants/m<sup>2</sup>).

## VI. RESULTS

### A. Verification of the Fresnel Model Assumptions

As noted previously, the emission from a soil with known dielectric and temperature properties with depth can be modeled using radiative transfer theory [2], [14], [15]. The complex nature of the depth weighting function and the details on the profile characteristics make it virtually impossible to invert the model to determine profile conditions from a single surface observation of emissivity.

If the profile of dielectric properties and temperature is uniform, the situation simplifies to the Fresnel reflection equations that provide a direct linkage between the soil complex dielectric constant ( $k_s$ ) and the emissivity ( $E$ ). For horizontal ( $H$ ) polarization and look angle  $\theta$  this equation is

$$E(H, \Theta) = 1 - \left( \frac{(\cos \Theta - \sqrt{k_s - \sin^2 \Theta})}{(\cos \Theta + \sqrt{k_s - \sin^2 \Theta})} \right)^2 \quad (1)$$

Application of (1) requires a knowledge and verification of the soil depth that is representative of the energy being measured by the radiometer.

The depth through which energy is emitted and sensed by microwave instruments has been the subject of research and discussion for many years. Some of the discrepancies reported are related to the definition of sampling depth. Another issue is that the depth contributing to the measurement does not come from a fixed single depth; however, the measurement is dominated for most conditions by a depth varying by a small amount. This dominant depth will depend upon many factors such as soil type, general climate and system observation variables such as the time of day. Finally, part of the reason for different conclusions may be related to the fact that some conclusions were based on modeling while others were based on field observation.

Wilheit [14] noted in assessing the composite properties of profiles that the effective (or significant) depth of soil dielectric properties that influences the brightness temperature is much shallower than the depth of the effective soil temperature. Choudhury *et al.* [16] evaluated the temperature profile aspects of this problem and found that an adequate approximation of nonuniform temperature profiles could be obtained using temperatures for a near surface and a deeper depth ( $\sim 15$  cm) with the effect of the near surface weighted by a frequency-specific coefficient. Raju *et al.* [17] verified that this is an adequate representation, which introduces only minimal error into the analysis.

One of the basic concepts in electromagnetic remote sensing is the penetration depth. This is also referred to as the skin depth, however, as noted in Ulaby *et al.* [18], they are related but not identical. The penetration depth is the distance over which an electric field is attenuated to  $1/e$  or 37% of its initial strength as it passes through a media. When  $k''/k' < 0.1$ , the penetration depth can be approximated as [18]

$$d = \frac{\lambda \sqrt{k'}}{2\pi k''} \quad (2)$$



# El Niño Southern Oscillation and tuna in the western Pacific

P. Lehodey\*, M. Bertignac\*, J. Hampton\*, A. Lewis\* & J. Picaut†

\* Oceanic Fisheries Programme, South Pacific Commission, BP D5, 98848 Noumea, New Caledonia

† Groupe SURTROPAC, ORSTOM, BP A5, 98848 Noumea, New Caledonia

Nearly 70% of the world's annual tuna harvest, currently 3.2 million tonnes, comes from the Pacific Ocean. Skipjack tuna (*Katsuwonus pelamis*) dominate the catch. Although skipjack are distributed in the surface mixed layer throughout the equatorial and subtropical Pacific, catches are highest in the western equatorial Pacific warm pool, a region characterized by low primary productivity rates<sup>1</sup> that has the warmest surface waters of the world's oceans (Fig. 1). Assessments of tuna stocks indicate that recent western Pacific skipjack catches approaching one million tonnes annually are sustainable<sup>2</sup>. The warm pool, which is fundamental to the El Niño Southern Oscillation (ENSO) and the Earth's climate in general<sup>3–5</sup>, must therefore also provide a habitat capable of supporting this highly productive tuna population. Here we show that apparent spatial shifts in the skipjack population are linked to large zonal displacements of the warm pool that occur during ENSO events<sup>5,6</sup>. This relationship can be used to predict (several months in advance) the region of highest skipjack abundance, within a fishing ground extending over 6,000 km along the Equator.

There is a permanent convergence of surface-layer water masses on the eastern edge of the western Pacific warm pool<sup>5</sup>. The convergence zone is identified by a well-marked salinity front<sup>5</sup>, *in situ* observations of currents<sup>7</sup> and nutrients<sup>8</sup>, and simulated trajectories of drifters<sup>5</sup>. It is induced by westward advection of cold, saline water from the central-eastern equatorial Pacific encountering a sporadic eastward advection of warm, low-salinity water from the western equatorial Pacific, generated by westerly wind bursts. Spectacular zonal displacements of the convergence zone over 50° of longitude occur in phase with the warm and cold phases of the ENSO cycle, with eastward displacement occurring during El Niño episodes and westward displacement occurring during La Niña episodes. Convergence zones and fronts are important aggregating mechanisms of plankton and micronekton<sup>9–13</sup>, and therefore also of larger predators such as tuna<sup>14,15</sup>. We would expect, therefore, that the distribution of skipjack tuna would respond to displacement of the convergence zone, and that this might provide a basis for the prediction of good fishing grounds. We tested this hypothesis by correlating observations of skipjack relative abundance with a proxy for location of the convergence zone, the 29°C sea surface temperature (SST) isotherm, and with the southern oscillation index (SOI). A proxy variable for the location of the convergence was required because the spatio-temporal coverage of salinity, nutrient and surface current observations was insufficient to map the convergence location in a continuous time series suitable for study. Movement of the 29°C-SST isotherm is highly correlated with both the movement of the salinity front and movement of the convergence zone determined by drifter trajectories<sup>5</sup>. This isotherm therefore seems to be a reasonable proxy for the convergence.

Catch per unit effort (CPUE) data from commercial fisheries are often used to measure the relative abundance of fish stocks<sup>16</sup>. Average global CPUE for the United States purse seine fleet (see Methods) shows that the skipjack fishing ground extends across 60° of longitude (Fig. 2a), with strong interannual variations in location (Fig. 2b). The purse seine fleet was concentrated west of 160°E during the well-defined La Niña period of 1988 to 1989, the short

intermediate period in late 1990 to early 1991, and the 1995 La Niña. During El Niño years (1992–1994), the fleet extended its activities as far east as 160°W. To calculate the correlation between CPUE and environmental indices, we computed *G*, a longitudinal gravity centre of CPUE. *G* is correlated ( $R = 0.75$ , zero lag) with the 29°C SST isotherm (Fig. 2b), and the amplitude of the variables is very similar (standard deviation ratio of 0.8). Despite a generally good relationship, at times (early 1991, early 1992, early 1995) *G* is located a long way to the west of the 29°C isotherm. Such departures from the relationship could suggest some inconsistency in the identification of the convergence by the 29°C isotherm, variability in the response of the skipjack population to movement of the convergence, imperfect location of highest skipjack abundance by the purse seine fleet, or a combination of these factors. Nevertheless, it seems that a strong relationship exists between the location of the convergence and skipjack relative abundance.

Shifts in *G* of up to 40° of longitude (nearly 4,000 km) during periods as brief as six months occurred on several occasions (Fig. 2b). The magnitude and speed of these shifts are not inconsistent with the mobility of individual skipjack. The South Pacific Commission's skipjack-tagging database has numerous records of tagged skipjack showing displacements of this order (South Pacific Commission, unpublished data). Also, during several periods of rapidly changing *G*, shown in Fig. 2b, the magnitude and direction of observed movements of tagged skipjack are consistent with the changes in *G*. During mid 1991 to early 1992, observed long-distance (>10° longitude) movements of tagged skipjack were predominantly towards the east (Fig. 3a, b), consistent with the shifts in CPUE and the 29°C isotherm (Fig. 2b). In contrast, during March to October 1992, westerly movement of tagged skipjack predominated (Fig. 3c), again consistent with CPUE and 29°C isotherm shifts (Fig. 2b). These data suggest that changes in skipjack CPUE occurring in phase with changes in the location of the

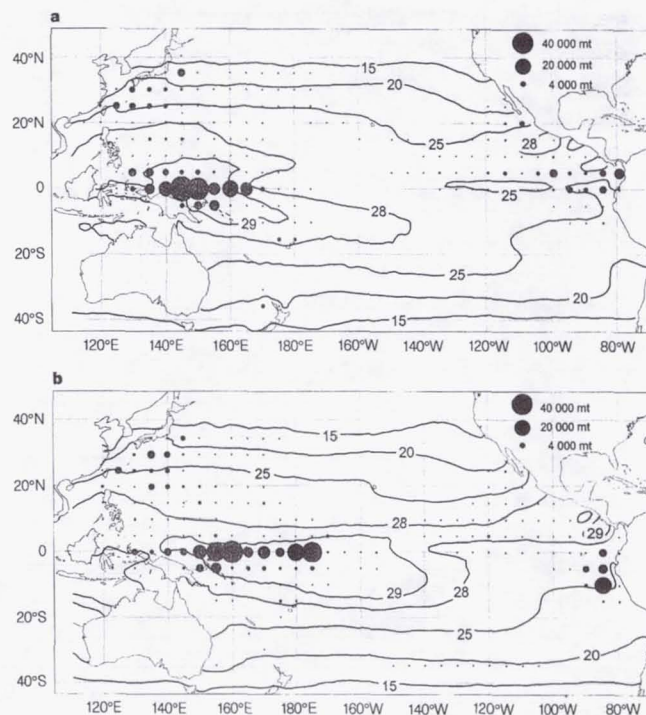


**Figure 1** Distribution of skipjack tuna catch (tonnes) and mean sea surface temperature (SST, in °C) in the Pacific Ocean. **a**, In the first half of 1989 (La Niña period). **b**, In the first half of 1992 (El Niño period). The effect of ENSO on the location of the warm pool (SST > 28–29°C) and the distribution of skipjack catch is clearly evident.



warm pool with good accuracy<sup>5</sup>, and could improve the forecast in the location of the convergence. The lead time of prediction of favourable fishing grounds could therefore probably be increased by the use of these models. Such forecasts could result in improved catches and considerable reductions in searching time and costs for the fishing fleet.

The warm pool is characterized by low primary productivity (coastal waters excepted), which contrasts strongly with the enriched water masses of the adjacent central and eastern Pacific equatorial upwelling<sup>1,21</sup>. Given the very high energetic requirements of skipjack<sup>22</sup>, and the short trophic linkage between their diet of epipelagic zooplankton and micronekton<sup>23–25</sup> and the primary productivity of the surface layer, it is initially counter-intuitive that the world's largest tuna stock occurs in the oligotrophic western Pacific warm pool. Our results indicate that the presence of a large front of oceanic convergence is probably important for maintaining the skipjack stock in the warm pool. However, mechanisms that provide the necessary biomass of forage for the skipjack tuna stock have not yet been identified. A plausible explanation could involve the zonal transport of planktonic communities originating in the Pacific equatorial upwelling by the westwards-flowing south equatorial current. Such zonal equatorial advection can produce westward displacement of planktonic communities of 1,800–2,500 km (refs 26, 27). During this westward transport, the planktonic community would mature for up to several months, consistent with the residence time of 3–4 months of drifting buoys in the 5° N–5° S equatorial divergence zone<sup>27</sup>. Westward transport would terminate on exiting the westward flow, through lateral drift or encoun-

tering the convergence zone at the eastern edge of the warm pool. The increasing mobility of the organisms through the upper trophic levels<sup>28</sup> and the large ENSO-related zonal movements of the convergence zone are likely to increase the patchiness of the spatial distribution of the secondary and tertiary production in a large zonal band associated with the physical front. The location of high abundance of skipjack tuna, centred on the longitudinal gravity centre of CPUE and extending about 14° in longitude ( $\pm$  one standard deviation), may reflect this zone of enrichment in secondary and tertiary production. Unfortunately, direct observation of zooplankton and micronekton distributions on a spatial and temporal scale that would be required to test the mechanism described above remains problematic. Recently developed physical-biological coupled models<sup>29</sup> (P.L., unpublished data) are a promising means of investigating potential causal mechanisms associated with the strong relationship we have observed between skipjack tuna abundance, the water mass convergence at the eastern edge of the warm pool, and their drastic zonal displacements associated with ENSO. Because the signal is strong and the correlation high, the relationship could be a useful test of these models. The prediction of ENSO and, as a consequence, the location of the highest abundance of skipjack tuna, has important implications for the commercial tuna fishing industry. It may also allow fisheries management authorities to distinguish between changes in local fish abundance caused by movement to other areas, and changes resulting from the impacts of fishing. □

#### Methods

**Gravity centre of CPUE.** CPUE as an index of fish stock abundance will be most reliable when the sampling units (fishing vessels) are as homogeneous in their characteristics and operating behaviour as possible<sup>16</sup>. We used only United States purse seine CPUE data because: this highly mobile fleet consists of similar vessels using similar fishing techniques; unlike other purse seine fleets, this fleet has had virtually unrestricted access since 1988 to the exclusive economic zones of Pacific Island countries under the South Pacific Tuna Treaty, as well as adjacent high seas; and catch and effort data quality and coverage for log books submitted by the fleet is high. The time-longitude section of monthly skipjack catch (in tonnes) and effort (in days fishing) was produced by aggregating the data in the area 5° N–5° S, 120° E–120° W by months and 1° of longitude. The longitudinal gravity centre of CPUE in month  $j$  ( $G_j$ ) is then defined as:  $G_j = \sum_i L_i (C_{ij}/E_{ij}) / \sum_i (C_{ij}/E_{ij})$ , where  $L_i$  denotes the longitudinal mid-point of the  $i$ th area of 1° longitude width between 5° N and 5° S,  $C_{ij}$  is the skipjack catch in area  $i$  in month  $j$ , and  $E_{ij}$  is the number of fishing days in area  $i$  in month  $j$ .

Received 3 June; accepted 14 August 1997.

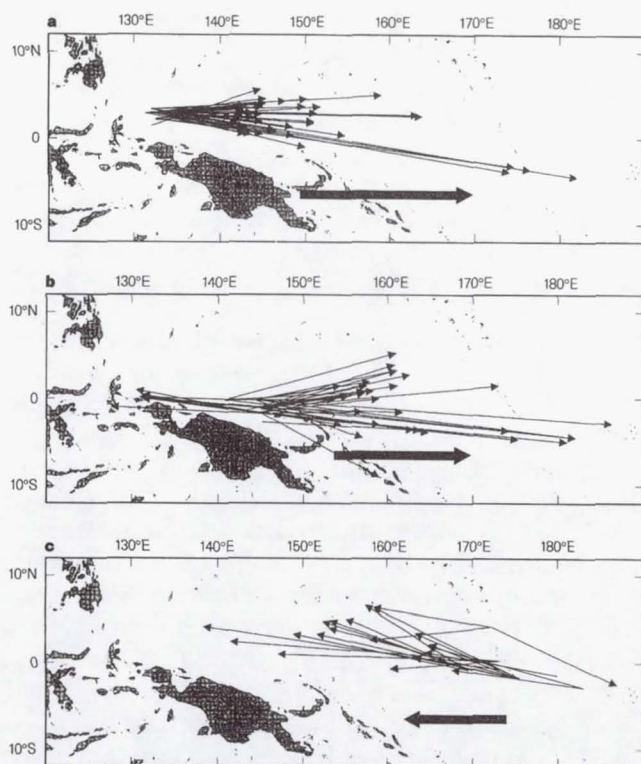


**Figure 3** Displacements of tagged skipjack tuna. **a**, Tuna released April 1991, recaptured before February 1992. **b**, Tuna released May 1991, recaptured before February 1992. **c**, Tuna released March 1992, recaptured before October 1992. For clarity, only tagged fish recaptured in the zone 10° N–10° S and more than 10° of longitude east or west of their release location are plotted. Tagging data were compiled from records of a large-scale tagging programme carried out by the South Pacific Commission during 1990 to 1992 (ref. 30). Thick arrows indicate the direction and magnitude of displacement of the skipjack CPUE gravity centre (see Methods) during the tag recapture periods.



# Seasonal phytoplankton dynamics in the eastern tropical Atlantic

Bruce Monger<sup>1</sup>

Universities Space Research Association, NASA Goddard Space Flight Center, Greenbelt, Maryland

Charles McClain

Oceans and Ice Branch, NASA Goddard Space Flight Center, Greenbelt, Maryland

Ragu Murtugudde

Joint Center for Earth Sciences, University of Maryland, College Park

**Abstract.** The coastal zone color scanner (CZCS) that operated aboard the Nimbus 7 satellite provided extensive coverage of phytoplankton pigment concentrations in the surface waters of the eastern tropical Atlantic (ETA) from March 1979 to February 1980 and coincided with four major research cruises to this region. Total primary production within the ETA (5°N–10°S, 25°W–10°E) was determined from CZCS pigment estimates and an empirical algorithm derived from concurrent in situ data taken along 4°W that relates near-surface chlorophyll concentration and integrated primary production. We estimated an average annual production for the ETA of 2.3 Gt C yr<sup>-1</sup> with an associated 3.5-fold seasonal variation in the magnitude of this production. We describe the principal physical mechanisms controlling seasonal phytoplankton dynamics within the ETA and propose that in addition to seasonal change in the thermocline depth, one must also consider changes in the depth of the equatorial undercurrent. An extensive validation effort indicates that the standard CZCS global products are a conservative estimate of pigment concentrations in ETA surface waters. Significant underestimates by the CZCS global products were observed in June and July which we attributed, in part, to aerosol correction errors and, more importantly, to errors caused by a significant reduction in the concentration of near-surface dissolved organic matter that resulted from strong equatorial upwelling.

## 1. Introduction

Biological processes within tropical oceans have recently gained strong recognition for the important role they play in global carbon cycling [Longhurst, 1993; Murray *et al.*, 1994]. Tropical Pacific processes have received a great deal of attention in recent years because of interest in El Niño–Southern Oscillation (ENSO) events and because the shear size of the equatorial Pacific dictates that it have a significant influence on global-scale biogeochemical processes. Considerably less study has been devoted to understanding biological processes within the tropical Atlantic; however, new long-term studies aimed at dramatically increasing our understanding of the biology and physics in this region are currently being planned. With much of the anticipated tropical Atlantic research still being formulated, we feel it is timely to present a detailed description of the biological-physical interactions occurring within this region.

Much of our understanding of the biological processes within the tropical Atlantic is derived from shipboard observations that were made during the Equalant I and II program in 1963–1964, the CIPREA program in 1978–1979, the First Global Atmospheric Research Program Global Experiment

(FGGE) study in 1979, and the Seasonal Equatorial Atlantic Experiment–Français Océan-Climat en Atlantique Equatorial (SEQUAL–FOCAL) program in 1983–1984. The more recent application of coastal zone color scanner (CZCS) imagery of near-surface phytoplankton pigments (chlorophyll + phaeopigments) in the tropical Atlantic has greatly enhanced our understanding of the biological processes in this region. Platt *et al.* [1991] combined CZCS imagery and a semi-analytical primary production model to examine regional differences in Atlantic primary production and concluded that annual primary production in the tropical Atlantic exceeds that of the entire North Atlantic bloom region (temperate and Subarctic oceans). Longhurst [1993] determined a possible mechanism controlling the timing and spatial extent of phytoplankton blooms in the eastern tropical Atlantic (ETA) by combining regional CZCS imagery and recent advances in our understanding of equatorial dynamics that have been brought about by improved general circulation models (GCMs) [e.g., Busalacchi and Picaut, 1983; Philander and Pacanowski, 1986]. Longhurst noted that the thermocline shoals dramatically in the ETA in response to seasonal intensification of the trade winds in the western tropical Atlantic. He proposed that the dynamic uplift of the thermocline combined with mixing by local winds may be the principal mechanism controlling vertical nutrient fluxes and therefore phytoplankton blooms in the ETA.

Some important issues concerning blooms in the ETA remain unresolved. Results of Platt *et al.* [1991] suggested that the tropical Atlantic exhibits significant seasonal variation in

<sup>1</sup>Now at Center for the Environment, Cornell University, Ithaca, New York.



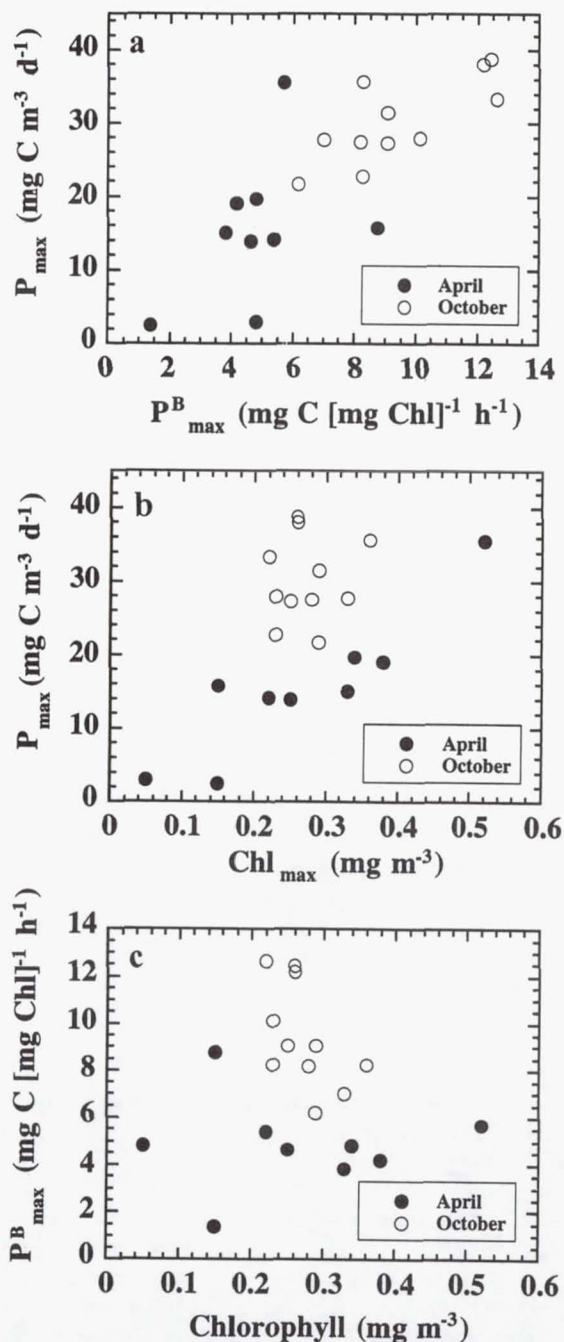


**Figure 9.** Relationship between primary production, chlorophyll-specific production, and chlorophyll concentration at the depth of the production maximum ( $P_{\max}$ ,  $P_{\max}^B$ ,  $\text{Chl}_{\max}$ , respectively). All data collected between 12°S and 2°N along 4°W.

Model results presented in this paper reveal a monthly averaged primary production in the ETA that ranged from 0.356 to 1.24  $\text{g C m}^{-2} \text{ d}^{-1}$  and had an annual average of 980  $\text{mg C m}^{-2} \text{ d}^{-1}$ . With regard to factors contributing to changes in primary production within the ETA, we make the following observations. The magnitude of the subsurface primary production maximum ( $P_{\max}$ ) is closely correlated with the corresponding assimilation number ( $P_{\max}^B$ ) and to a somewhat lesser extent with chlorophyll concentration ( $\text{Chl}_{\max}$ ) at this depth (Pearson correlation coefficient = 0.79 and 0.52, respectively). Meanwhile,  $P_{\max}^B$  and  $\text{Chl}_{\max}$  are not obviously correlated with each other (Figures 9a, 9b, and 9c). These observations suggest

that like the central equatorial Pacific, natural variations in  $P^B$  due to changes in optimal growth conditions, and changes in chlorophyll concentration due to temporary loss of tight grazer control jointly contribute to the variation in the magnitude of primary production in the ETA. Given the high  $P_{\max}^B$  values (average: 7.2  $\text{mg C (mg Chl)}^{-1} \text{ h}^{-1}$ ) in the ETA, it can be assumed that the phytoplankton community on a whole is probably growing at near-maximal rates in a manner similar to the situation in the central equatorial Pacific. During strong ETA upwelling, nitrate concentrations in the surface waters increase and the relative amounts of chlorophyll in the 0.0- to 1.0- and the 1.0- to 3.0- $\mu\text{m}$  diameter size fractions shift toward the larger fraction [Herbland *et al.*, 1985]. Although there was no taxonomic distinction made by Herbland *et al.* [1985], it can be presumed that the relative increase in chlorophyll concentration in the 1.0- to 3.0- $\mu\text{m}$  size fraction represented a diatom increase similar to that measured directly during the EqPac study. We propose that, in general, the factors contributing to variation in the magnitude of primary production in the ETA closely resemble those in the central equatorial Pacific except that nitrate in the case of the ETA replaces iron in the case of the central equatorial Pacific as the growth-limiting nutrient. We stress, however, that this area of research needs much further study before anything very definite can be said about these similarities.

## 5. Conclusion

An empirical primary production model derived from spatially and temporally sparse in situ data was combined with the spatially and temporally rich CZCS coverage to obtain an ETA production estimate of 2.3  $\text{Gt C yr}^{-1}$ , which is higher than previous production estimates for this region. Results from this study also suggested that there is a 3.5-fold seasonal variation in ETA production. This later result is in conflict with prior studies, and we offered evidence which suggested that sampling bias due to limited spatial and temporal ship coverage may explain why these previous studies did not measure a significant seasonal variation in primary production.

Extensive validation efforts revealed fairly good agreement between satellite-derived and directly measured pigment concentrations within the ETA over most of the year (Appendix). However, significant underestimates by the standard CZCS products were observed in June and July which could be attributed to errors in aerosol correction and a reduction in near-surface dissolved organic matter (DOM) occurring during strong upwelling. When scene-specific aerosol corrections are used and the DOM-induced bias is accounted for, the RMS error between satellite and direct observations was reduced by roughly 50%. The bias in the regression was reduced by a similar amount with this type of correction. We used the standard CZCS products in our present analysis as a conservative estimate of pigment concentrations within the ETA.

Phytoplankton blooms in the ETA are initiated in late May or early June by thermocline uplift forced, primarily, by winds in the western Atlantic. By August the thermocline has returned to a pre-uplift depth, but ETA blooms continue beyond this period because the EUC is deeper than before the initial thermocline uplift, and, consequently, water is upwelled from a greater depth that is richer in nitrate. By the end of December the EUC has moved above the thermocline core, and, consequently, any remaining upwelling brings only nitrate-depleted waters to the surface.



## SEASONAL-TO-INTERANNUAL VARIABILITY

The manuscripts in this section relate and provide insight to seasonal-to-interannual (S-I) variability in the global climate system. S-I variability is currently the only global climate mode that can be measured during the lifetime of an individual satellite or in-situ sensor. A discussion of some of these sensors can be found in Parkinson, and how these measurements along with in-situ observations are used in conjunction to aid large coordinated multi-agency field programs is addressed in the manuscript by Busalacchi. Wang and Koblinsky discuss the possibility of extracting heat flux from satellite altimeter data; which is an important, but as of yet not directly measurable property for S-I studies. Chen et al. (2) also provide expanded measurements from TOPEX by using the microwave radiometer to retrieve rain rates that compare favorably with other microwave measurements. Ho et al. discuss how rain rates may affect rates of gas transfer to water using laboratory simulations and field measurements. Choudhury provides a study on how global potential evaporation could be used as a proxy for actual evaporation to be used for forcing. Kalnay et al. then go on to ponder the question on how data from the measurement systems are best used in models that include data assimilation components to further elucidate the governing balances of S-I variability.

One of the best known and strongest S-I variation occurs with variability in the equatorial Pacific Ocean associated with the El Nino Southern Oscillation (ENSO). Picaut et al. describe how the advection of warm water and the reflection of equatorial waves off the eastern Pacific boundary play a critical role in the evolution and development of ENSO. Miller et al. demonstrate the utility of GEOSAT altimeter data in an assimilation scheme for reproducing variability in the equatorial Pacific during the late 1980's. Chen et al. (1) used scatterometer wind data in a coupled model to show that the predictability of ENSO events could be extended past the so-called spring barrier by nudging the winds in the coupled simulation itself as opposed to direct forcing of the ocean model only. An interesting study by Pinkel et al. showed that internal waves generated by spring tides could trigger internal waves that could flux as much as  $10\text{--}15 \text{ W/M}^2$  of heat into the equatorial Pacific mixed-layer, thus providing important forcing for variability there.

The ocean maintains a longer term control over weather through its thermal inertia, but the land surface has also been shown to play an important role in seasonal variability. Vukovich et al. describe how it is possible to determine more accurate heat flux estimates from the land to the atmosphere on 100 km scales by partitioning the area into specific types of ground cover. Latent heat release and soil moisture are closely tied in the seasonal variability, three of the studies listed, e.g., Teng et al. and Lakshmi et al. (2,3) discuss how microwave measurements can be used in land surface models (LSM's) to study S-I variability. Koster and Milly, Scott et al., and Chen et al. (3) all discuss improvements and intercomparisons of differing LSM's to show that the important contribution of rainfall on the soil moisture budget on S-I time scales and also the very important effects of vegetative control on the evapotranspiration process. Lakshmi et al. (1) discuss the importance of including a thin upper layer in an LSM to be able to use surface measurements from satellite sensors.

In the mid latitude region of the north and south Atlantic Hooker et al. use historical satellite-derived sea surface temperature data to study eddies. Using a zebra color palette and a thermal separatrix method for analysis they have determined that many features thought to be monopole ocean eddies are actually dipole eddies and need to be studied in that dynamical context.

Many global warming scenarios suggest that effect is amplified and will first show in the high latitude regions, including effects on sea ice and the ice sheets. Giovenetto et al. discuss how regression can be used to determine stable isotopes of  $\text{O}_{18}$  over complex terrain such as Greenland. However, Jouzel et al. suggest that the differing distributions of the spatial and temporal slopes of the  $\text{O}_{18}$  isotope complicate an

interpretation of using that isotope as a paleothermometer. Two studies suggest that sea-ice is decreasing in the high latitudes. Cavalieri et al. show that sea ice is being reduced faster in the Arctic than it is in the Antarctic which is consistent with some global warming scenarios. Jacobs and Comiso note a reduction in the sea ice extent in the Amundsen and Bellingshauser Seas and find that the reduction correlates well with atmospheric temperatures. Geiger et al. also found that nearby atmospheric temperatures played a role in influencing the seasonal cycle of ice in the Weddell Sea. Both passive microwave and SAR data have been used in sea-ice variability studies. Kwok and Comiso show that passive microwave estimates of sea ice can be up to 30% lower than SAR estimates of sea ice. Liu et al. have determined that SAR can provide superior tracking of sea ice floes using wavelet techniques.



## Oceanic Observations

By Antonio J. Busalacchi

Laboratory for Hydrospheric Processes, NASA/Goddard Space Flight Center,  
Greenbelt, MD, USA

(Manuscript received 3 August 1995, in revised form 4 June 1996)

### Abstract

For many years, merchant ships and the naval fleets of various countries have been the major source of data over and in the open ocean. Oceanographic research experiments and process studies in the field have also contributed to the climatological data bases for the global ocean, but, for the most part, these have been limited in duration and extent. However, over the last 10 years under the auspices of the World Climate Research Program and the International Geosphere Biosphere Program the role of the oceans in global and climate change has taken on increased significance. This has created a need for a considerably improved understanding of the seasonal, interannual, decadal and longer time-scale variability of the physical and biogeochemical attributes of the global ocean. As a result, over the past 10 years several major international field programs have been implemented and have had a tremendous impact on the number of in situ observations obtained for the global ocean. The Tropical Ocean Global Atmosphere (TOGA) program, the World Ocean Circulation Experiment (WOCE), and the Joint Global Ocean Flux Study (JGOFS) were designed with observational, modelling, and process study components aimed at analyzing different aspects of the ocean's role in the coupled climate system. In parallel with the field programs, continuous space-based observations of sea surface temperature, sea surface topography, and sea surface winds spanning nearly a decade or longer have become a reality. During this same time period, numerical ocean models and computational power have advanced to the point where the oceanographic observations, both in situ and remotely sensed, can be assimilated into numerical ocean models in order to provide a four-dimensional (x-y-z-t) depiction of the evolving state of the global ocean.

### 1. Introduction

Our historical knowledge of properties at the ocean surface has come from merchant marine vessels taking routine meteorological observations (Fig. 1) for the world weather services (Rossby *et al.*, 1995). The suite of measurements often includes the sea surface temperature (SST), estimates of the sea state, wind velocity, barometric pressure, wet and dry bulb temperatures, and cloud fraction. From a global perspective, seasonal averages of the observational coverage may appear to be relatively dense, yet careful inspection reveals the sampling coverage is biased toward the major shipping lanes and away from regions of severe weather. This leaves large regions of the world ocean left unsampled. This is best illustrated at the basin scale and for a monthly mean interval (Fig. 2). Even for sea surface quantities such as wind velocity, there is no mistaking the fact that large regions of the world ocean are not sampled on a regular basis.

The situation for observations of the ocean below the surface is considerably worse. Archived measurements of such subsurface properties as temperature, currents, salinity, nutrients, and dissolved gases have been obtained from past research cruises, naval fleets, and volunteer "Ships-of-Opportunity" (Fig. 3). The total number of subsurface observations can be several orders of magnitude less than the surface observations. Thus, the state of the ocean is grossly undersampled to a point that the dominant space and time scales of many oceanic properties remain unknown. Nonetheless, our fundamental understanding of the large-scale four-dimensional structure of the global ocean, as crude as it may be, comes from a number of climatological data bases such as Levitus (1982) and the Comprehensive Ocean-Atmosphere Data Set (COADS) (Woodruff *et al.*, 1987). Compilations of the historical observations, however sparse, are interpolated to fixed horizontal grids to produce smooth fields of hydrographic data of use in process studies, empirical studies, and model initialization. Examples



every three days with approximately a 75 km resolution. When two satellites are in orbit, as is normally the case, global coverage is possible every one and one-half days. Comparisons with in situ wind measurements indicate the mean absolute error of SSM/I wind speeds is typically  $2 \text{ m s}^{-1}$  (Atlas, *et al.*, 1991). These wind speed estimates are not only important for computing the momentum flux, but they are also critical to estimating the latent heat flux. When SSM/I wind speeds are substituted for contemporaneous wind speed distributions from operational weather centers, the latent heat flux can be changed by more than  $30 \text{ W m}^{-2}$ .

After a hiatus of approximately fourteen years, scatterometer estimates of surface wind velocity resumed in 1991 with the radar backscatter measurements from ERS-1. The ERS-1 scatterometer has a 500 km swath width and an effective 50 km resolution within the swath. This makes it possible to obtain approximately 40,000 observations of the wind field every day. Since the vector wind is being measured, derivative quantities such as the wind stress curl can be determined and compared with similar fields estimated from weather center analyses. These vector wind measurements are expected to continue into the future with the launch of ERS-2 and the NASA Scatterometer (NSCAT) onboard the ADEOS. An added advantage of the NSCAT instrument will be a dual set of antennas that will provide a total wind vector swath width of 1200 km with an anticipated accuracy of  $\pm 2 \text{ m s}^{-1}$ . A more detailed discussion of these surface wind data can be found in the companion paper by R. Atlas.

The same SSM/I instrument that measures the surface wind speed, is also capable of providing information on other properties relevant to the sea surface. For example, the microwave signal is attenuated by liquid water in the atmospheric column, *i.e.*, cloud droplets and rainfall. It is therefore possible to begin constructing coarse estimates of the global distribution of precipitation (Fig. 21) with order 50 % accuracy on monthly mean time scales and  $5^\circ$  by  $5^\circ$  resolution. In view of the sampling problem associated with precipitating systems, reduction in the errors of the passive microwave estimates of precipitation will have to wait until the Tropical Rainfall Measurement Mission (TRMM). Nonetheless, together with the estimates of the latent heat flux, it is possible to begin studying the evaporation minus precipitation forcing of the global ocean. At high latitudes, where there is a marked contrast in emissivity between open water and sea ice, the SSM/I measurements are also used to map sea ice concentration (to an accuracy of approximately 6 %) and extent. These observations have been used to extend time series of the sea ice variability in the Arctic and around Antarctica. These time series

began in the 1970's with passive microwave observations from the Nimbus 5 and 7 satellites (Fig. 22). Long-term observations of sea ice variability have important implications for monitoring the heat exchange from the ocean to the atmosphere and possible source regions of bottom water formation.

Just as the altimeter and scatterometer are key instruments for programs such as WOCE and TOGA, the ocean color sensor is critical to JGOFS. The Coastal Zone Color Scanner (CZCS) on board Nimbus 7 was a proof of concept instrument that showed how this class of optical sensor could be used to monitor the biologically (plankton) active regions of the world ocean, from the coastal margins to the open ocean. The CZCS had a limited duty cycle and provided far from global coverage. However, composites of the CZCS imagery indicated it was possible to monitor the seasonal variability of ocean color and hence chlorophyll concentration. The progression from ocean color measurements to estimates of oceanic primary production remains an active area of research. Global measurements of ocean color will be possible on a daily basis following the anticipated launch of the Sea-viewing Wide Field-of-view Sensor (SeaWiFS) in 1997.

## 6. Summary

This paper is intended to provide the students of the WMO Symposium on Assimilation of Observations in Meteorology and Oceanography with a brief introduction to the burgeoning amounts of ocean data available today. The international field programs of TOGA, WOCE, and JGOFS, together with ocean remote sensing, have changed our view of the global ocean over the past decade. Impressive and daunting amounts of data have been obtained and are expected to continue into the future. Ocean observations are now available from a variety of different sources and sensors at a level never achieved previously. The ocean sciences community has a responsibility and obligation to extract the maximum amount of information from these observations. Ocean data assimilation provides a means for incorporating disparate data types from different programs, platforms, and instruments into a coherent four-dimensional depiction of the evolving state of the global ocean. The synthesis that will arise from such an approach will enable process, empirical, monitoring, and prediction studies of the global ocean circulation that in the past have proved impossible. This issue will become increasingly important as the community builds upon the successes of TOGA and WOCE towards new research programs such as studies of Climate Variability and Predictability (CLIVAR), and as it begins to formulate strategies for Global Climate and Global Ocean Observing Systems.



# Observed Hemispheric Asymmetry in Global Sea Ice Changes

D. J. Cavalieri,\* P. Gloersen, C. L. Parkinson, J. C. Comiso, H. J. Zwally

From November 1978 through December 1996, the areal extent of sea ice decreased by  $2.9 \pm 0.4$  percent per decade in the Arctic and increased by  $1.3 \pm 0.2$  percent per decade in the Antarctic. The observed hemispheric asymmetry in these trends is consistent with a modeled response to a carbon dioxide-induced climate warming. The interannual variations, which are 2.3 percent of the annual mean in the Arctic, with a predominant period of about 5 years, and 3.4 percent of the annual mean in the Antarctic, with a predominant period of about 3 years, are uncorrelated.

Model experiments simulating future conditions assuming a gradual increase in atmospheric  $\text{CO}_2$  show various hemispheric asymmetries (1–4); in particular, some suggest that Arctic sea ice will decrease, whereas Antarctic sea ice will decrease substantially less than Arctic sea ice (3) or may even increase (4). Here we report observational evidence of a hemispheric asymmetry in global sea ice changes from late 1978 through 1996.

Analyses of passive microwave satellite observations (5, 6) have suggested that the extent of the Arctic sea ice cover (the total area with ice concentration greater than 15%) shrank at 2.5% per decade from 1978 to 1987, whereas there were only insignificant changes in the Antarctic sea ice cover. A more recent study (7) that extended the analysis to 1994 found that Arctic ice extent continued to decrease and that the Antarctic ice also was decreasing by  $0.7 \pm 0.6\%$  per decade.

We have extended the passive microwave satellite observations through December 1996, using data from the Nimbus 7 Scanning Multichannel Microwave Radiometer (SMMR) (8) and three Defense Meteorological Satellite Program (DMSP) Special Sensor Microwave Imager (SSM/I) (9) sensors. The SMMR was launched in October 1978 and was fully operational until August 1987; data were collected every other day through most of that period. The first of the three SSMIs was launched on the DMSP F8 spacecraft in June 1987, the second was launched on the F11 spacecraft in November 1991, and the third was launched on the F13 spacecraft in March 1995. A period of almost 6 weeks of data overlap in 1987 provides a means of cross-calibrating the SMMR and SSM/I sea ice

data sets. Overlap between the DMSP F8 and F11 spacecraft is only 2 weeks, but the overlap between the F11 and F13 spacecraft is 5 months. Our analyses show that these sensors required intercalibration, because during the overlap periods the residual differences of several percent in sea ice extent and area (the sum of the products of pixel area times ice concentration for ice concentration greater than 15%) would adversely affect the trend analysis (10).

After corrections for residual instrument drift, bad or missing data, and false sea ice signals over ice-free ocean areas (11), comparisons of sea ice concentrations from different sensors (12) during overlap periods still revealed significant differences, particularly in marginal ice zones. Much of the SMMR-SSM/I difference is attributed to the greater sensitivity of SSM/I to atmospheric water vapor (13, 14). The initial uncorrected differences for daily Arctic and Antarctic sea ice extents and areas were 2 to 4% during the overlap periods. To lessen these differences, we developed linear relations between the measured radiances for corresponding channels from each sensor during the overlap periods. These relations were used to adjust the SSM/I algorithm radiance tie points relative to the SMMR tie points. These adjustments reduced the ice extent and area differences to about 1%. Further adjustments of the ice-free ocean tie points

reduced the differences in ice extents and areas to 0.02 and 0.4%, respectively, for the SMMR and SSM/I F8 data, 0.04 and 0.6% for the SSM/I F8 and F11 data, and 0.06 and 0.6% for the SSM/I F11 and F13 data (15).

Accurate determination of long-term sea ice trends depends in large part on accounting for shorter-term fluctuations, the largest of which is the annual cycle of ice growth and decay (Fig. 1). Day-to-day variations, resulting from storms and currents, and annual variations are removed by calculating the monthly deviations (Fig. 2). We used a band-limited regression (BLR) technique (5, 16) to determine the trend in each of the monthly deviation time series shown in Fig. 2 for the period November 1978 through December 1996 (Table 1). This technique suppresses fluctuations having periods less than one-quarter the data record length of 18.2 years, including intra-annual fluctuations not already removed in the process of computing monthly deviations and some interannual fluctuations. The method entails substituting a truncated form of the sinc function matrix for the usual correlation matrix in a weighted least-squares formulation for obtaining a linear fit to the data. The sinc function, described in (5), is a function of the form  $(\sin x)/x$  that is used here as a multiple-window filtering function. This method effectively applies a narrow band-pass filter centered about zero frequency before extracting the trend line.

Superimposed on the monthly deviation time series shown in Fig. 2 are two trend lines for each hemisphere. One corresponds to the BLR result and the other to an ordinary least-squares regression (OLR) fit of the monthly deviation data. The difference in slopes of the Antarctic trend lines is attributed to the BLR filtering of fluctuations with periods shorter than about 4.5 years, including the predominant 3-year fluctuations observed in the curve smoothed with an annual running mean, also shown in Fig. 2B. Thus, the BLR technique may provide a more accurate determination of the long-term trends through its filtering of shorter-term fluctuations. The rate of change per decade for the

**Table 1.** Trends in Arctic and Antarctic sea ice covers during the period 1978–1996 from a BLR analysis. The OLR results are given in parentheses. For all the BLR results, the confidence level exceeds 99% (29).

Parameter	Slope $\pm$ SD ( $10^6 \text{ km}^2 \text{ year}^{-1}$ )	Rate of change (% per decade)
Arctic		
Extent	$-0.0345 \pm 0.0053$	$-2.9 \pm 0.4$ ( $-2.9 \pm 0.3$ )
Area	$-0.0294 \pm 0.0044$	$-2.9 \pm 0.4$ ( $-2.9 \pm 0.4$ )
Antarctic		
Extent	$+0.0143 \pm 0.0026$	$+1.3 \pm 0.2$ ( $+1.0 \pm 0.5$ )
Area	$+0.0138 \pm 0.0025$	$+1.6 \pm 0.3$ ( $+1.3 \pm 0.6$ )

Laboratory for Hydrospheric Processes, NASA Goddard Space Flight Center, Code 971, Greenbelt, MD 20771, USA.

\*To whom correspondence should be addressed.



Arctic ice extents is  $-2.9 \pm 0.4\%$ , whereas the rate for the Antarctic is  $+1.3 \pm 0.2\%$  (Table 1). The fluctuations of sea ice extent observed in the monthly deviation time series in each hemisphere (Fig. 2, A and B) are uncorrelated ( $r = -0.06$ ), but there is a small negative correlation ( $r = -0.44$ ) for the smoothed time series. In contrast to the Arctic, the Antarctic ice extents showed no significant trend from 1978 through 1993. From late 1993 through 1996, the Antarctic ice extent remained above the 18-year mean.

Our study and earlier studies indicate that, overall, the Arctic sea ice cover has been decreasing, although not monotonically, during the past 20 years. Nimbus 5 electrically scanning microwave radiometer (ESMR) data show that Arctic ice extent increased from 1973 through 1976, before the decrease from 1979 through 1986 revealed in the SMMR data (17). For our entire time series (see Fig. 1A), the four lowest summertime extents occurred during the last 7 years, with the two lowest extents occurring in 1990 and 1995. The 1990 minimum has been attributed to a combination

of high springtime temperatures and an anomalous high-latitude circulation pattern that year (18) and may be related to a recent decrease of sea level pressure in the central Arctic (19). Also, variations in Arctic sea ice extent and its overall trend correspond both spatially and temporally to variations in surface air temperatures over the past three decades (20).

Although we lack overlap between the ESMR and SMMR data that would permit precise matching of these two data sets, it appears that the maximum Antarctic sea ice extent since 1972 occurred in 1973. Analysis using ESMR data, combined with NOAA-Navy analyses based in part on passive microwave data, showed that Antarctic

sea ice decreased during the mid-1970s (21) and increased in the late 1970s and early 1980s (22). The increase in Antarctic sea ice during the SMMR and SSIM period (Fig. 2B), although occurring in spite of a warming trend in the Southern Hemisphere (23), conforms with recent results on changes in the length of the sea ice season in the Southern Ocean from 1988 through 1994. The length of the sea ice season decreased in some areas while increasing in others, but overall the area of increases exceeded the area of decreases by about 20% (24).

Although model simulations do not incorporate all the complexities in the climate system, they can provide valuable insights

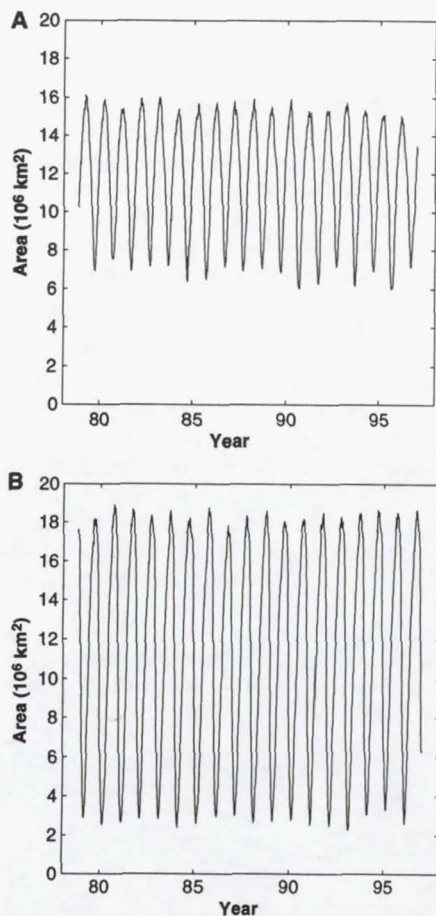


**Fig. 1.** Sea ice extents derived from multisensor single-day records for (A) the Arctic and (B) the Antarctic.

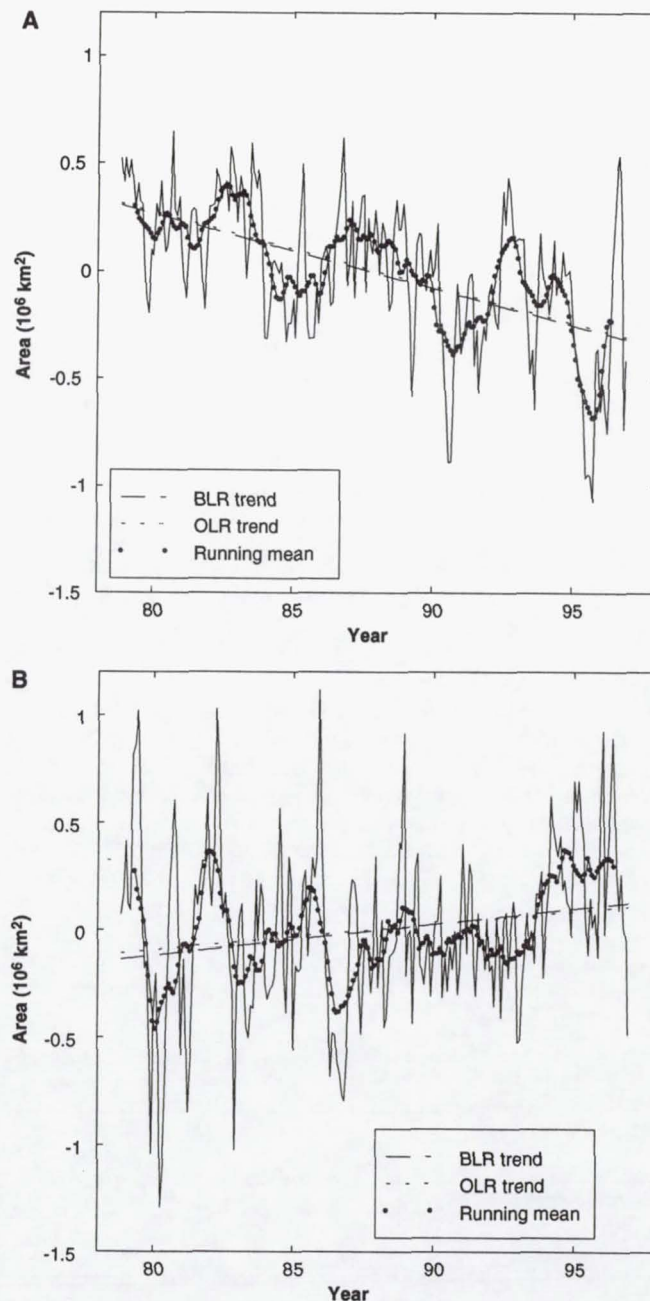


**Fig. 2.** Monthly deviations in sea ice extent (light solid curve) with both BLR (long-dashed) and OLR (short-dashed) trend lines for (A) the Arctic and (B) the Antarctic. A 12-month running mean (curve with dots) is also shown for both.



## Initialization and Predictability of a Coupled ENSO Forecast Model\*

DAKE CHEN, STEPHEN E. ZEBIAK, AND MARK A. CANE

*Lamont-Doherty Earth Observatory, Columbia University, Palisades, New York*

ANTONIO J. BUSALACCHI

*Laboratory for Hydrospheric Processes, NASA/GSFC, Greenbelt, Maryland*

(Manuscript received 19 June 1995, in final form 13 March 1996)

### ABSTRACT

The skill of a coupled ocean-atmosphere model in predicting ENSO has recently been improved using a new initialization procedure in which initial conditions are obtained from the coupled model, nudged toward observations of wind stress. The previous procedure involved direct insertion of wind stress observations, ignoring model feedback from ocean to atmosphere. The success of the new scheme is attributed to its explicit consideration of ocean-atmosphere coupling and the associated reduction of "initialization shock" and random noise. The so-called spring predictability barrier is eliminated, suggesting that such a barrier is not intrinsic to the real climate system. Initial attempts to generalize the nudging procedure to include SST were not successful; possible explanations are offered. In all experiments forecast skill is found to be much higher for the 1980s than for the 1970s and 1990s, suggesting decadal variations in predictability.

### 1. Introduction

A hierarchy of coupled ocean-atmosphere models has been developed during the last decade for predicting El Niño-Southern Oscillation (ENSO), the largest interannual fluctuation in the world's climate system. Among them, the earliest physically based model is the intermediate coupled model designed by Cane and Zebiak (hereafter CZ model) (Cane et al. 1986; Zebiak and Cane 1987). The predictive ability of this model has been demonstrated extensively but has not been significantly improved since the model was first introduced almost a decade ago. Although it has been suggested that incomplete model physics puts a limit on this model's predictability (Goswami and Shukla 1991), the overall skill of more complicated coupled general circulation models presently does not significantly exceed that of the CZ model (Barnston et al. 1994). Since the predictive skill of even the best available models is far from perfect, there appears to be considerable room for improvement in modeling, observation, and forecasting technique. However, it is not yet known how much room there is.

One possible limitation on many of the forecast systems is the initialization procedure (Cane et al. 1986; Latif et al. 1993). Errors in initial conditions are due to inaccuracies in the observations and deficiencies in the models using the observations. These errors may be

TABLE 1. Forecast-observation correlation for the periods from 1972 to 1985 and from 1986 to 1992.

Nudging parameter		Lead time in months							
<i>a</i>	<i>b</i>	0	3	6	9	12	15	18	
1972–85									
1.00	1.00	0.77	0.71	0.63	0.57	0.51	0.35	0.24	
0.25	0.45	0.80	0.77	0.72	0.62	0.58	0.46	0.34	
0.25	0.55	0.83	0.82	0.75	0.65	0.64	0.56	0.52	
0.25	0.65	0.80	0.77	0.72	0.63	0.60	0.46	0.36	
0.25	0.75	0.87	0.84	0.74	0.59	0.50	0.31	0.29	
0.25	0.95	0.87	0.84	0.75	0.60	0.50	0.33	0.30	
0.20	0.60	0.79	0.77	0.72	0.63	0.58	0.45	0.29	
0.30	0.50	0.80	0.78	0.72	0.63	0.58	0.45	0.32	
0.30	0.60	0.83	0.81	0.74	0.64	0.61	0.47	0.35	
0.30	0.80	0.83	0.80	0.68	0.53	0.47	0.29	0.25	
0.32	0.32	0.78	0.72	0.64	0.51	0.34	0.08	−0.06	
0.50	0.50	0.83	0.80	0.71	0.54	0.38	0.07	−0.10	
0.60	0.60	0.81	0.80	0.72	0.62	0.53	0.27	−0.15	
1986–92									
1.00	1.00	0.67	0.69	0.76	0.74	0.62	0.52	0.50	
0.25	0.55	0.83	0.85	0.82	0.79	0.80	0.79	0.80	
0.25	0.75	0.79	0.81	0.74	0.66	0.63	0.47	0.35	
0.25	0.95	0.76	0.75	0.71	0.66	0.65	0.62	0.45	
0.30	0.60	0.80	0.83	0.74	0.63	0.60	0.50	0.33	
0.32	0.32	0.81	0.85	0.80	0.75	0.73	0.71	0.59	

\* Lamont-Doherty Earth Observatory Contribution Number 5592.

Corresponding author address: Dr. Dake Chen, Lamont-Doherty Earth Observatory, Columbia University, P.O. Box 1000, RT 9W, Palisades, NY 10964-8000.  
E-mail: dchen@ldeo.columbia.edu



#### 4. Discussion and summary

Considering that the new initialization scheme is so simple and does not require any more observational data than the wind stress used in the original scheme, it may seem quite surprising that such a dramatic improvement of predictive skill can be achieved over a rather large ensemble of forecasts. In fact, improvement of this magnitude has not been achieved with any other forecast system to date. From Fig. 1, it is clear that including the coupled model in initialization has the effect of filtering out high-frequency signals present in the standard initial conditions. This occurs because the dominant mode of variability in the coupled model is ENSO-like, that is, large scale and low frequency. The high-frequency components of the initial conditions, which act as noise to the coupled model, degrade the forecast performance. By filtering these components, the new initialization procedure effectively reduces the mismatch between initial conditions and the model's intrinsic variability, while retaining the essential large-scale, low-frequency information.

The nudging procedure affects more than just "noise" in the system—it also affects the signal. For instance, if there are systematic differences in the spatial structure of observed and (unassimilated) model variables, the nudging procedure will lessen this mismatch and may improve forecast performance (relative to straight insertion or no assimilation). Whether this will be true in practice depends on the nature and magnitude of the model errors. In our experiments, wind nudging reduced the systematic difference between observed and model winds, leading to improved forecast skill. However, combined SST–wind nudging did not improve performance over just wind nudging, although the result might change with a more careful tuning of assimilation parameters. In general one can expect a trade-off between the degree of realism of initial conditions and the degree of conformity to model physics that can be balanced optimally only with a comprehensive assimilation scheme. One of the most important aspects of this balancing is the reduction of "initialization shock"—the transition from hindcast to forecast mode. For all coupled forecast models one expects smaller initialization shock to lead to improved forecasts.

Though other coupled models differ significantly from this one (e.g., in containing internal high-frequency variance), they all exhibit modes of variability that differ in some way from nature. In all such situations, a nudging or more elaborate assimilation procedure that invokes the *coupled* model offers the potential for improvement. Of course, a prerequisite for the potential to be realized in predicting ENSO is that the coupled model exhibits realistic ENSO-like natural variability.

The new forecasts are certainly improved but are not without shortcomings. They do a poor job of distinguishing the amplitude of different ENSO extremes (Fig. 2). For example, the 1976–77 event is largely over-predicted. Though the gradual warming from 1988 to 1992 and the present cold phase are well captured, the short warm episodes in 1993 and late 1994 are missed. The shorter-lead standard forecasts do better with these (as do a number of other forecast procedures). The skill of the forecasts increased dramatically in the 1980s, especially for the transitions from warm to cold events, but was not much improved for the 1970s. Perhaps the assimilation of additional data (sea level, subsurface thermal structure) will be a remedy. However, decadal variations in prediction skill appear to be common among all forecast schemes. Further research will tell us whether these decadal variations in forecast skill result from processes poorly treated by present models, or whether they reflect changes in the predictability of the real climate system.

In summary, the experimental ENSO forecasts made by the CZ model for a period of more than two decades are significantly improved without using additional observational data for model initialization. The key to the success is a simple procedure to generate self-consistent initial conditions using the coupled model and observed wind stress anomalies. In essence, the coupled model itself is used to dynamically filter the initial conditions for the forecast. There are a number of implications. First, the performance of a coupled ENSO forecast model depends crucially on initialization; a good initial state for this model is one that contains principally the low-frequency signal relevant to ENSO. The character of the initial conditions is at least as important as model deficiencies in limiting the predictive skill of the original CZ forecast system. Second, the predictability of ENSO in a coupled model is likely to be affected by high-frequency fluctuations forced by the initialization procedure. Careful attention to this issue will likely be important for coupled models at all levels of complexity. Third, the seemingly inevitable "spring barrier" in ENSO prediction is largely eliminated by improving initial conditions. This suggests that the spring barrier is not intrinsic to the tropical Pacific climate system and may be overcome without modeling the Asian monsoon or other processes outside of the tropical Pacific Ocean. Fourth, although the simple nudging scheme used in this study may not be directly applicable to other models, the approach of using both coupled model and observational data for initialization should be generally useful, as all schemes are limited by model/data mismatches in some form. A trade-off scheme will always be necessary since neither data nor models will ever be perfect.



# Global oceanic precipitation: A joint view by TOPEX and the TOPEX microwave radiometer

Ge Chen<sup>1</sup>

Ocean Remote Sensing Institute, Ocean University of Qingdao, Qingdao, China

Bertrand Chapron, Jean Tournadre, and Kristina Katsaros

Département d'Océanographie Spatiale, Centre de Brest, IFREMER, Plouzané, France

Douglas Vandemark

Wallops Flight Facility, NASA Goddard Space Flight Center, Wallops Island, Virginia

**Abstract.** The TOPEX/POSEIDON mission offers the first opportunity to observe rain cells over the ocean by a dual-frequency radar altimeter (TOPEX) and simultaneously observe their natural radiative properties by a three-frequency radiometer (TOPEX microwave radiometer (TMR)). This work is a feasibility study aimed at understanding the capability and potential of the active/passive TOPEX/TMR system for oceanic rainfall detection. On the basis of past experiences in rain flagging, a joint TOPEX/TMR rain probability index is proposed. This index integrates several advantages of the two sensors and provides a more reliable rain estimate than the radiometer alone. One year's TOPEX/TMR data are used to test the performance of the index. The resulting rain frequency statistics show quantitative agreement with those obtained from the Comprehensive Ocean-Atmosphere Data Set (COADS) in the Intertropical Convergence Zone (ITCZ), while qualitative agreement is found for other regions of the world ocean. A recent finding that the latitudinal frequency of precipitation over the Southern Ocean increases steadily toward the Antarctic continent is confirmed by our result. Annual and seasonal precipitation maps are derived from the index. Notable features revealed include an overall similarity in rainfall pattern from the Pacific, the Atlantic, and the Indian Oceans and a general phase reversal between the two hemispheres, as well as a number of regional anomalies in terms of rain intensity. Comparisons with simultaneous Global Precipitation Climatology Project (GPCP) multisatellite precipitation rate and COADS rain climatology suggest that systematic differences also exist. One example is that the maximum rainfall in the ITCZ of the Indian Ocean appears to be more intensive and concentrated in our result compared to that of the GPCP. Another example is that the annual precipitation produced by TOPEX/TMR is constantly higher than those from GPCP and COADS in the extratropical regions of the northern hemisphere, especially in the northwest Pacific Ocean. Analyses of the seasonal variations of prominent rainy and dry zones in the tropics and subtropics show various behaviors such as systematic migration, expansion and contraction, merging and breakup, and pure intensity variations. The seasonality of regional features is largely influenced by local atmospheric events such as monsoon, storm, or snow activities. The results of this study suggest that TOPEX and its follow-on may serve as a complementary sensor to the special sensor microwave/imager in observing global oceanic precipitation.

## 1. Introduction

Global oceanic precipitation is one of the most needed but least known geophysical parameters. Oceanic rainfall plays a key role in defining regional and global climate, being responsible for most of the freshwater flux to the sea and serving as a link in the global hydrological and geochemical cycles. The associated latent heat release is of great importance for the

general circulation of the atmosphere. Further progress in understanding the El Niño–Southern Oscillation (ENSO) could also be made with more reliable data on tropical rainfall. However, continuous and accurate measurement of rain over the global ocean is extremely difficult, owing to its intermittent nature and highly variable intensity, as well as the well-known limitations of the conventional ship observations.

In view of its geophysical importance and the observational difficulties, tremendous efforts have been expended in the past 2 decades to extract rain signatures and to derive rain parameters from spaceborne sensors ranging from visible and infrared radiometers (e.g., GOES [Barrett and Martin, 1981; Janowiak and Arkin, 1991], Meteosat [Cheng and Brown, 1995]), passive microwave radiometers (e.g., scanning multichannel

<sup>1</sup>Also at Département d'Océanographie Spatiale, Centre de Brest, IFREMER, Plouzané, France.



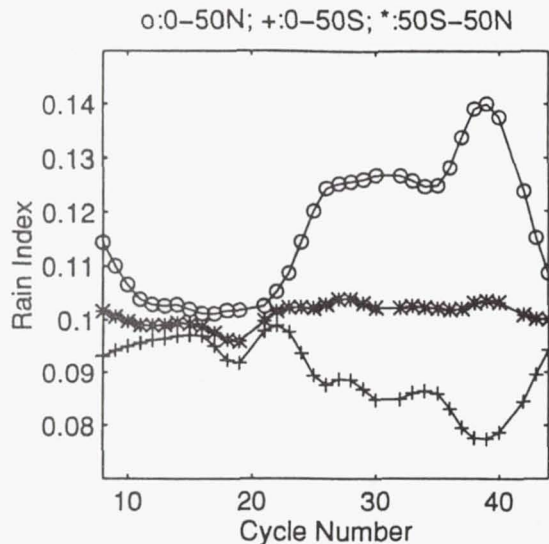


Figure 6. Temporal variations of the TOPEX/TMR rain index ( $P_{i,j}$ ) averaged over 0–50°N (circles), 0–50°S (pluses), and 50°S–50°N (stars) for cycles 8–44.

desert undergoes an annual cycle of expansion and contraction, increasing to a maximum size in autumn (Plate 4d) and shrinking to a minimum size in spring (Plate 4b). The North Atlantic and South Indian Ocean deserts are characterized by a process of merging and breakup: The former merges in summer and breaks in other seasons, while the latter merges in winter and breaks during the rest of the year. The South Atlantic desert has little change in position and pattern throughout the year, except a weaker intensity in spring (Plate 4b). The North Indian Ocean desert is somewhat different from others due to its special geographical location and climatic condition. It is the smallest one among the six deserts, oscillating slightly with seasons along the coast of the Arabian Sea.

5. A number of local precipitation anomalies along the world coasts have been noted in Plate 3a. Following these features in the seasonal maps (Plates 4a–4d), one finds that most of them are time dependent rather than persistent. For instance, intensified rainfall in the Mozambique Channel is only seen in winter (Plate 4a). The enhanced maxima related to the western Pacific storm track start to form in the East China Sea during spring and extend to the surrounding waters of Japan in summer (Plates 4b and 4c). They almost vanish during the other half of the year (Plates 4a and 4d) and consequently become less visible in the annual map (Plate 3a) as a result of seasonal averaging. The rainfall around Florida peaks in autumn, leading to a subsequent narrowing of the dry zone in the Gulf of Mexico (Plate 4d). The local minimum in the Bay of Bengal is nudged off the coast in summer when the Indian monsoon and its associated heavy precipitation prevail (Plate 4c). As a result the summer rainfall pattern in this area is characterized by the coexistence of a prominent maximum in the northeast and a weakened minimum in the southwest.

From the preliminary analysis presented above, it is evident that 1 year's TOPEX and TMR data have allowed us to capture and delineate the major seasonal characteristics of global oceanic precipitation. It is hopeful that the expected 5-year TOPEX/TMR data will enable us to confirm these results, particularly those previously unknown features, and eventually to investigate the interannual variability of rainfall and its

relation with ENSO which has a 2- to 4-year cycle and a strong dependence as well as influence on global and regional climate.

## 5. Summary and Final Remarks

The work presented here is primarily a feasibility study on the observation of global oceanic precipitation by TOPEX and TMR. The results obtained have clearly demonstrated the effectiveness and potential of the proposed methodology. Key contributions to its success include the following. First, the introduction of a rain probability index, which is an outgrowth of various thresholds used earlier, has enabled us to quantify rain effects on altimeter and radiometer measurements and relate them to rain frequency and intensity. The second contribution is the unique role of TOPEX, which results from the fact that TOPEX is the first dual-frequency altimeter and is perhaps also the first active spaceborne sensor used to derive precipitation maps over the ocean. An important advantage of an active microwave system is that it allows the two-way attenuation to be measured, leading to an improved efficiency in rain detection compared to a passive system. Third, the joint use of TOPEX and TMR has shown that the complementarity of the two sensors in rain detection is largely latitude dependent. In the tropics the two measurements usually differ by a factor of 2. In midlatitude areas the TOPEX altimeter tends to underestimate the rainfall due to possible wave damping, while the TMR is hardly affected by this effect. In subpolar regions where the radiometer is almost ineffective, the altimeter is seen to have a better performance. Despite the above-mentioned strengths the weaknesses of the present methodology should also be pointed out. For instance, the proposed rain probability index cannot, at this stage, provide a direct and quantitative estimate of rain rate. An attempt to establish an empirical relation between them is currently underway. In addition, the TOPEX altimeter can only detect rain events at nadir points along fixed ground tracks. This is obviously a disadvantage compared to the wide swath radiometer like SSM/I.

This work is also a step toward constructing a TOPEX/TMR precipitation climatology. Attempts have been made to compare our results with those from the GPCP and COADS rain climatologies. In terms of rain frequency, TOPEX/TMR and COADS show quantitative agreement in the ITCZ and qualitative agreement in other regions. Recalling that more than two thirds of the global precipitation falls in the tropics and subtropics, such an agreement is encouraging. On the basis of a rain index combining TOPEX and TMR, annual and seasonal precipitation maps are constructed which, to our knowledge, are the first of their kind. On global scale the three basins bear a number of similarities such as a prominent rain belt in the ITCZ, a dry zone in the subtropics of each hemisphere, and a northwest-southeast oriented rain belt in the southwestern part of each basin (Plate 3a). Comparisons with simultaneous GPCP multisatellite precipitation rate and COADS rain climatology suggest that systematic differences also exist. One example is that the maximum rainfall in the ITCZ of the Indian Ocean appears to be more intensive and much concentrated in our result (Plate 3a) compared to that of the GPCP (Plate 3b). Another example is that the annual precipitation produced by TOPEX/TMR is constantly higher than those from GPCP and COADS in most of the extratropical regions of the northern hemisphere, especially along the northwest coasts of the Pacific and Atlantic Oceans (Plates 2 and 3). On regional scale, notable features are several local maxima and minima of rain



## Cabauw Experimental Results from the Project for Intercomparison of Land-Surface Parameterization Schemes

T. H. CHEN,<sup>a</sup> A. HENDERSON-SELLERS,<sup>a</sup> P. C. D. MILLY,<sup>b</sup> A. J. PITMAN,<sup>a</sup> A. C. M. BELJAARS,<sup>c</sup> J. POLCHER,<sup>d</sup>  
 F. ABRAMOPOULOS,<sup>e</sup> A. BOONE,<sup>f</sup> S. CHANG,<sup>g</sup> F. CHEN,<sup>h</sup> Y. DAI,<sup>i</sup> C. E. DESBOROUGH,<sup>a</sup> R. E. DICKINSON,<sup>j</sup>  
 L. DUMENIL,<sup>k</sup> M. EK,<sup>c</sup> J. R. GARRATT,<sup>l</sup> N. GEDNEY,<sup>m</sup> Y. M. GUSEV,<sup>n</sup> J. KIM,<sup>o</sup> R. KOSTER,<sup>p</sup> E. A. KOWALCZYK,<sup>1</sup>  
 K. LAVAL,<sup>d</sup> J. LEAN,<sup>q</sup> D. LETTENMAIER,<sup>r</sup> X. LIANG,<sup>s</sup> J.-F. MAHFOUF,<sup>t</sup> H.-T. MENGELKAMP,<sup>u</sup> K. MITCHELL,<sup>h</sup>  
 O. N. NASONOVA,<sup>n</sup> J. NOILHAN,<sup>v</sup> A. ROBOCK,<sup>w</sup> C. ROSENZWEIG,<sup>c</sup> J. SCHAAKE,<sup>x</sup> C. A. SCHLOSSER,<sup>w</sup>  
 J.-P. SCHULZ,<sup>k</sup> Y. SHAO,<sup>y</sup> A. B. SHMAKIN,<sup>z</sup> D. L. VERSEGHY,<sup>aa</sup> P. WETZEL,<sup>f</sup> E. F. WOOD,<sup>s</sup> Y. XUE,<sup>bb</sup>  
 Z.-L. YANG,<sup>j</sup> AND Q. ZENG<sup>1</sup>

<sup>a</sup>Climatic Impacts Centre, Macquarie University, Sydney, Australia

<sup>b</sup>U.S. Geological Survey and Geophysical Fluid Dynamics Laboratory/NOAA, Princeton, New Jersey

<sup>c</sup>Royal Netherlands Meteorological Institute, De Bilt, the Netherlands

<sup>d</sup>Laboratoire de Météorologie Dynamique du CNRS, Paris, France

<sup>e</sup>Science Systems and Applications Incorporated, New York City, New York

<sup>f</sup>Mesoscale Dynamics and Precipitation Branch, NASA/Goddard Space Flight Center, Greenbelt, Maryland

<sup>g</sup>Phillips Laboratory (PL/GPAB), Hanscom AFB, Massachusetts

<sup>h</sup>Development Division, National Centers for Environmental Prediction, NOAA, Camp Springs, Maryland

<sup>i</sup>Institute of Atmospheric Physics, Academy of Science, Beijing, People's Republic of China

<sup>j</sup>Institute of Atmospheric Physics, The University of Arizona, Tucson, Arizona

<sup>k</sup>Max-Planck-Institut für Meteorologie, Hamburg, Germany

<sup>l</sup>Division of Atmospheric Research, CSIRO, Aspendale, Victoria, Australia

<sup>m</sup>Meteorology Department, Reading University, Reading, United Kingdom

<sup>n</sup>Institute of Water Problems, Moscow, Russia

<sup>o</sup>Lawrence Livermore National Laboratory, Livermore, California

<sup>p</sup>Hydrological Sciences Branch, NASA/GSFC, Greenbelt, Maryland

<sup>q</sup>Hadley Centre for Climate Prediction and Research, Meteorological Office, Berkshire, United Kingdom

<sup>r</sup>Department of Civil Engineering, University of Washington, Seattle, Washington

<sup>s</sup>Department of Civil Engineering and Operations Research, Princeton University, Princeton, New Jersey

<sup>t</sup>ECMWF, Reading, United Kingdom

<sup>u</sup>Institute for Atmospheric Physics, GKSS—Research Center, Max-Planck-Strasse, Geesthacht, Germany

<sup>v</sup>Météo-France/CNRM, Toulouse, France

<sup>w</sup>Department of Meteorology, University of Maryland at College Park, College Park, Maryland

<sup>x</sup>Office of Hydrology, NWS/NOAA, Silver Spring, Maryland

<sup>y</sup>Centre for Advanced Numerical Computation in Engineering and Science, University of New South Wales, Sydney, Australia

<sup>z</sup>Institute of Geography, Moscow, Russia

<sup>aa</sup>Climate Research Branch, Atmospheric Environment Service, Downsview, Ontario, Canada

<sup>bb</sup>Centre for Ocean—Land—Atmosphere Studies, Calverton, Maryland

(Manuscript received 18 December 1995, in final form 2 May 1996)

### ABSTRACT

In the Project for Intercomparison of Land-Surface Parameterization Schemes phase 2a experiment, meteorological data for the year 1987 from Cabauw, the Netherlands, were used as inputs to 23 land-surface flux schemes designed for use in climate and weather models. Schemes were evaluated by comparing their outputs with long-term measurements of surface sensible heat fluxes into the atmosphere and the ground, and of upward longwave radiation and total net radiative fluxes, and also comparing them with latent heat fluxes derived from a surface energy balance. Tuning of schemes by use of the observed flux data was not permitted. On an annual basis, the predicted surface radiative temperature exhibits a range of 2 K across schemes, consistent with the range of about 10 W m<sup>-2</sup> in predicted surface net radiation. Most modeled values of monthly net radiation differ from the observations by less than the estimated maximum monthly observational error ( $\pm 10$  W m<sup>-2</sup>). However, modeled radiative surface temperature appears to have a systematic positive bias in most schemes; this might be explained by an error in assumed emissivity and by models' neglect of canopy thermal heterogeneity. Annual means of sensible and latent heat fluxes, into which net radiation is partitioned, have ranges across schemes of 30 W m<sup>-2</sup> and 25 W m<sup>-2</sup>, respectively. Annual totals of evapotranspiration and runoff, into which the precipitation is partitioned, both have ranges of 315 mm. These ranges in annual heat and water fluxes were approximately halved upon exclusion of the three schemes that have no stomatal resistance under non-water-stressed conditions. Many schemes tend to underestimate latent heat flux and overestimate sensible heat flux in summer, with a reverse tendency in winter. For six schemes, root-mean-square deviations of predictions from monthly observations are less than the estimated upper bounds on observation errors (5 W m<sup>-2</sup> for sensible heat flux and 10 W m<sup>-2</sup> for latent heat flux). Actual runoff at the site is believed to be dominated by vertical drainage to groundwater, but several schemes produced significant amounts of runoff as overland flow or interflow. There is a range across schemes of 184 mm (40% of total pore volume) in the simulated annual mean root-zone soil moisture. Unfortunately, no measurements of soil moisture were available for model evaluation. A theoretical analysis suggested that differences in boundary conditions used in various schemes are not sufficient to explain the large variance in soil moisture. However, many of the extreme values of soil moisture could be explained in terms of the particulars of experimental setup or excessive evapotranspiration.

Corresponding author address: Dr. Tian Hong Chen, Australian Oceanographic Data Centre, Maritime Headquarters, Potts Point, NSW 2001, Australia.

E-mail: tian@aodc.gov.au



earlier in the explanation of runoff, maintained the root zone at a moisture content near saturation. The strong water-table influence in SEWAB and SPONSOR had a similar effect. The high evaporation in BUCK and SWB, in the absence of water-table support, caused those schemes to have the lowest water contents of all schemes; a similar argument may also explain the moderately low soil moisture in CAPS and CAPSNMC. Relatively low water content in MOSAIC is associated with the subgrid production of surface runoff, as already discussed.

Unfortunately, no measurements of soil moisture were available for evaluating the various model outputs in this project. But lacking such data, one can at least make some comparisons with theoretical limiting cases that would be consistent with the specified soil properties. Assuming that runoff, as observed (Beljaars and Bosveld 1997), is by soil drainage, the modeled winter runoff rate of about  $1 \text{ mm day}^{-1}$  can be equated to an unsaturated hydraulic conductivity to estimate an expected winter water content in those models assuming free drainage. This implies a root-zone water content of about 370 mm. If the summer value is 40 mm lower (Fig. 11), then the annual average would be about 350 mm. For a water table at 1-m depth, on the other hand, a hydrostatic soil-moisture profile can be shown to contain 390 mm of water in the root zone; for a shallow water table, the mean storage will not differ much from the equilibrium storage (Salvucci and Entekhabi 1994). The difference in water storage associated with different boundary conditions (40 mm) is much smaller than the range of values found in this project (184 mm). This may explain why no significant relation was found between annual soil moisture and the type of boundary condition applied.

On the basis of these theoretical analyses, and allowing for some errors in them, it is expected that annual mean values of root-zone soil moisture will be between 330 and 410 mm. It is interesting that the center of this range agrees quite well with the central cluster of schemes in Fig. 15. As already noted, many of the higher and lower values can be explained in terms of experimental setups or anomalous evaporation rates. In some cases, it appears that other significant departures from the expected range may be explained by use of soil properties different from those specified for the experiment.

## 5. Concluding remarks

The PILPS phase 2a experiment, described in this paper, was conducted using observed data (downward shortwave and longwave radiation, precipitation, and near-surface air humidity, temperature, and wind speed) for the year 1987 from Cabauw as inputs to a variety of land-surface schemes. Schemes were evaluated by comparing their outputs with long-term measurements of surface sensible heat fluxes into the atmosphere and

the ground, and of upward longwave radiation and total net radiative fluxes, and with latent heat fluxes derived from a surface energy balance. The observation that no overland flow occurs at the site also served as a data point to check model performance. Tuning of schemes by use of the observed flux data was not permitted.

Twenty-three land-surface schemes have participated in the experiment. Analyses of the experimental results were focused on the energy budget, the water budget, and their linkage. Although all schemes used identical atmospheric forcing data and the land-surface parameters were specified with great care, the differences in experimental results among the land-surface schemes and observations were found to be significant. The magnitudes of differences for some recognized key variables are qualified and discussed below.

- 1) On an annual mean basis, there is a range across schemes of about  $10 \text{ W m}^{-2}$  in simulated net radiation, which is associated with the range of 2 K in the surface radiative temperature. Annual means of sensible and latent heat fluxes, into which net radiation is partitioned, have ranges across schemes of  $30 \text{ W m}^{-2}$  and  $25 \text{ W m}^{-2}$ , respectively. Annual totals of evapotranspiration and runoff, into which the precipitation is partitioned, both have ranges of 315 mm. These ranges of energy- and water-flux partitioning are, of course, related directly through the latent heat of vaporization of water. Three schemes do not include any explicit stomatal resistance under non-water-stressed conditions; these produce the three highest latent heat flux (evaporation) values. When these schemes are excluded, the ranges of annual heat and water fluxes are approximately halved.
- 2) The STD of simulated monthly net radiation has an average over the year of  $3 \text{ W m}^{-2}$ . This difference is mainly attributed to the simulated surface radiative temperatures, which have an average STD of 0.6 K. The predicted net radiation from each scheme does not differ from the observation by more than the estimated observation error ( $\pm 10 \text{ W m}^{-2}$ ) through most of the year. Models appear to systematically overestimate the observed radiative surface temperature. This discrepancy may be associated with erroneous assumptions about surface emissivity in the experiment and with the models' neglect of canopy thermal heterogeneity.
- 3) The STDs of both monthly latent and sensible heat fluxes average  $8 \text{ W m}^{-2}$  over the course of the year. The most significant deviations from monthly observations are associated with the three schemes that neglect non-water-stressed stomatal resistance. Relative to the observations, there is a tendency for many schemes to underestimate latent heat flux and overestimate sensible heat flux during summer months, while the reverse holds true during the winter months. The monthly ground heat flux at the surface has an average STD of  $5 \text{ W m}^{-2}$ . The mean



# Global Pattern of Potential Evaporation Calculated from the Penman–Monteith Equation Using Satellite and Assimilated Data

Bhaskar J. Choudhury\*

*P*otential evaporation has been used to provide a reference level for actual evaporation in many studies of land surface heat and water balance. While Thornthwaite's formula has been used in many regional and global studies, the Penman–Monteith equation has been shown to provide an accurate estimate of this evaporation. Thus, global pattern of potential evaporation has been calculated from the Penman–Monteith equation using satellite and assimilated data for a 24-month period, January 1987 to December 1988. The albedo and surface resistance have been taken to be, respectively, 0.23 and  $70 \text{ s m}^{-1}$ , which are considered to be representative values for actively growing well-watered grass covering the ground. Satellite observations have been used to obtain spatially representative monthly values of solar radiation, fractional cloud cover, air temperature, and vapor pressure, while aerodynamic resistance has been calculated using four-dimensional data assimilation results. Meteorologic data derived from satellite observations are compared with the surface (station) measurements. The calculated potential evaporation values are compared with lysimeter observations for evaporation from well-watered grass at 35 widely distributed locations in different climatic regimes to quantify the accuracy of the calculated values. The evaporation values have been archived for distribution. <http://hydro4.gsfc.nasa.gov/STAFF/choudhuryBJ/pmpotevap.html> Published by Elsevier Science Inc.

## INTRODUCTION

The concept of potential evaporation ( $E_0$ ), popularized by Thornthwaite (1948), has provided a useful avenue for

setting a reference level for actual evaporation in practical applications (Doorenbos and Pruitt, 1977; Jensen et al., 1990), in research (Villalobos and Fereres, 1990; Choudhury et al., 1994), as well as in regional and global analyses of evaporation (Budyko, 1974; Willmott et al., 1985; Mintz and Walker, 1993). A physically based equation for  $E_0$  was derived by Penman (1948) by combining energy balance equation with the aerodynamic equation for vapor transfer, which was subsequently modified by Monteith (1965) to include a canopy resistance for vapor diffusion out of stomata. The Penman–Monteith equation can be used to estimate evaporation from well-watered and stressed canopies, depending upon the surface resistance. Apart from Thornthwaite and Penman–Monteith equations, there are many other equations which have been proposed for estimating  $E_0$  (Jensen et al., 1990; Monteith, 1994). By comparing 20 different methods of estimating  $E_0$ , Jensen et al. (1990) showed that the Penman–Monteith equation provides the most accurate estimate of monthly evaporation from well-watered grass or alfalfa (called the reference crop evaporation) under varied climatic conditions, while Thornthwaite's formula ranked 13th and 20th, respectively, for humid and arid regions. Milly (1994) found that  $E_0$  computed from Thornthwaite's formula was lower than actual evaporation over a large part of the eastern United States, and similar large scale discrepancies have been noted by others (Ramdas, 1957). Nevertheless, Thornthwaite's formula has been widely used in regional and global studies (cf. Rosenzweig, 1968; Willmott et al., 1985; Mintz and Walker, 1993; Lo Seen Chong et al., 1993; Potter et al., 1993) because of the advantage that the only data required is air temperature. Monteith (1994) wrote, "For regional and global use, the main disadvantage of Penman's formula is the number of climatic measurements needed—temperature, humidity, wind and net radiation

\*Laboratory for Hydrospheric Processes, Hydrological Sciences Branch, NASA Goddard Space Flight Center, Greenbelt

Address correspondence to Bhaskar J. Choudhury, Code 974, NASA/GSFC, Hydrological Sciences Br., Greenbelt, MD 20771.

Received 15 July 1996; revised 5 November 1996.



gions in the present calculations are about 50 mm yr<sup>-1</sup> lower than Thornthwaite's, while in the humid tropical region, the present values are c. 150 mm yr<sup>-1</sup> higher. However, the present calculations agree with Thornthwaite's results in finding that  $E_0$  values over the Southeast Asia are generally higher than those over the equatorial humid regions of South America and Africa. Jensen et al. (1990) had found that Thornthwaite's equation underestimates potential evaporation, when compared with observations for well-watered grass or alfalfa, in both arid and humid environments.

Figure 13 shows the zonal variation of annual potential evaporation values averaged over 5° latitude bands (area weighted), together with actual evaporation derived by Baumgartner and Reichel (1975) based on water balance of major river basins. The zonal variations of these two evaporation show some mirror image type of characteristics. [Note that while actual evaporation derived by Baumgartner and Reichel has been plotted in Fig. 13, the essential aspects of the zonal variation of actual evaporation seen in this figure also appear in Budyko (1978), Henning (1989) and other, although magnitudes are somewhat different.] Maximum actual evaporation (ca. 1214 mm yr<sup>-1</sup>) occurs in 0–5°S latitude band, where potential evaporation has a local minimum (ca. 1230 mm yr<sup>-1</sup>). Maximum potential evaporation (ca. 1955 mm yr<sup>-1</sup>) occurs in 15–20°N, with a secondary peak (ca. 1538 mm yr<sup>-1</sup>) in 20–25°S. Actual evaporation show local minimum in 25–30°N (342 mm yr<sup>-1</sup>), 25–30°S (434 mm yr<sup>-1</sup>) and 45–50°S (340 mm yr<sup>-1</sup>) latitude bands.

The complementarity hypothesis of Bouchet (1963) was expressed mathematically as

$$E_0 = 2E_{00} - E, \quad (7)$$

where  $E$  is actual evaporation and  $E_{00}$  is the evaporation from an extensive saturated area which would occur when the atmospheric conditions have adjusted to this evaporation rate (Brutsaert, 1984; Nash, 1989). The Priestley and Taylor (1972) equation could provide an estimate of  $E_{00}$  (McNaughton and Spriggs, 1989; Culf, 1994). Theoretical analyses of the hypothesis have been presented by Sequin (1975) and McNaughton and Spriggs (1989), while several studies have evaluated field observations according to this hypothesis (Fortin and Seguin, 1975; Brutsaert and Stricker, 1979; Morton, 1983; Byrne et al., 1988; Lemeur and Zhang, 1990).

It follows from Eq. (7) that, for a given  $E_{00}$ , a decrease in  $E$  would correspond to an increase in  $E_0$ . Thus, over the humid tropics,  $E$  and  $E_0$  could have similar values (since  $E_{00}$  and  $E_0$  are approximately equal), but with the appearance of deserts, as  $E$  decreases,  $E_0$  will increase. Thus, possible relation between actual and  $E_0$  suggested by Eq. (7) appears, to some degree, in Figure 13. Further evaluation of this relationship will be presented in the future.

## SUMMARY

Potential evaporation ( $E_0$ ) has been found to be useful in many practical applications and in research for setting a reference level for actual evaporation. All previous estimates of regional or global  $E_0$  are based upon empirical formulae using climatologic meteorologic measurements at isolated stations (i.e., point data). However, the Penman–Monteith equation provides a physically based approach for computing  $E_0$ , and by comparing 20 different methods of estimating  $E_0$ , Jensen et al. (1990) showed that the Penman–Monteith equation provides the most accurate estimate of monthly  $E_0$  from well-watered grass or alfalfa.

In the present study, monthly total  $E_0$  for 24 months (January 1987 to December 1988) was calculated from the Penman–Monteith equation, with prescribed albedo of 0.23 and surface resistance of 70 s m<sup>-1</sup>, which are considered to be representative of actively growing well-watered grass covering the ground. These calculations have been done using spatially representative data derived from satellite observations and data assimilation results. Satellite observations were used to obtain solar radiation, fractional cloud cover, air temperature, and vapor pressure, while four-dimensional data assimilation results were used to calculate the aerodynamic resistance. Meteorologic data derived from satellite observations were compared with the surface measurements to provide a measure of accuracy. The accuracy of the calculated  $E_0$  values was assessed by comparing with lysimeter observations for evaporation from well-watered grass at 35 widely distributed locations, while recognizing that the period of present calculations was not concurrent with the lysimeter measurements and the spatial scales of these measurements and calculations are vastly different. These comparisons suggest that the error in the calculated  $E_0$  values may not be exceeded, on average, 20% for any month or location, but are more likely to be about 15%. These uncertainties are difficult to quantify for mountainous areas or locations close to extensive water bodies. The difference between the calculated and observed  $E_0$  is about 5% when all month and locations were considered. Errors are expected to be less than 15% for averages of  $E_0$  over large areas or several months. Further comparisons with lysimeter observations could provide a better appraisal of the calculated values. Global pattern of  $E_0$  was presented, together with zonal average values.

## DATA AVAILABILITY

The evaporation values have been archived for distribution (via ftp from the World Wide Web) or can be obtained by contacting the author. <http://hydro4.gsfc.nasa.gov/STAFF/choudhuryBJ/pmpotevap.html>



# Year-round pack ice in the Weddell Sea, Antarctica: response and sensitivity to atmospheric and oceanic forcing

CATHLEEN A. GEIGER,<sup>1</sup> STEPHEN F. ACKLEY,<sup>2</sup> WILLIAM D. HIBLER, III<sup>1</sup>

<sup>1</sup>*Thayer School of Engineering, Dartmouth College, Hanover, NH 03755, U.S.A.*

<sup>2</sup>*U. S. Army Cold Regions Research and Engineering Laboratory, 72 Lyme Road, Hanover, NH 03755, U.S.A.*

**ABSTRACT.** Using a dynamic-thermodynamic numerical sea-ice model, external oceanic and atmospheric forcings on sea ice in the Weddell Sea are examined to identify physical processes associated with the seasonal cycle of pack ice, and to identify further the parameters that coupled models need to consider in predicting the response of the pack ice to climate and ocean-circulation changes. In agreement with earlier studies, the primary influence on the winter ice-edge maximum extent is air temperature. Ocean heat flux has more impact on the minimum ice-edge extent and in reducing pack-ice thickness, especially in the eastern Weddell Sea. Low relative humidity enhances ice growth in thin ice and open-water regions, producing a more realistic ice edge along the coastal areas of the western Weddell Sea where dry continental air has an impact. The modeled extent of the Weddell summer pack is equally sensitive to ocean heat flux and atmospheric relative humidity variations with the more dynamic responses being from the atmosphere. Since the atmospheric regime in the eastern Weddell is dominated by marine intrusions from lower latitudes, with high humidity already, it is unlikely that either the moisture transport could be further raised or that it could be significantly lowered because of its distance from the continent (the lower humidity source). Ocean heat-transport variability is shown to lead to overall ice thinning in the model response and is a known feature of the actual system, as evidenced by the occurrence of the Weddell Polynya in the mid 1970s.

## INTRODUCTION

Sea ice in the Weddell Sea undergoes a large seasonal cycle, varying from about  $2 \times 10^6 \text{ km}^2$  area for the summer minimum to about  $8 \times 10^6 \text{ km}^2$  for the winter maximum (Zwally and others, 1983). The summer minimum of the Weddell Sea ice represents about half the area of the pack ice in Antarctica at that time. The Weddell Sea pack ice as a whole is a climatic feature of some importance. Its northern limit ( $55^\circ \text{S}$  latitude) extends well into sub-Antarctic regions and consequently has an influence on the climate, ocean and ecosystems of the South Atlantic region.

Sea-ice cover in the Southern Ocean has been modeled by Parkinson and Washington (1979) using comprehensive atmospheric and oceanic heat flux inputs and ice thermodynamics together with ad hoc sea-ice dynamics. Using more realistic sea-ice dynamics, Hibler and Ackley (1983) examined the dynamic-thermodynamic response of a Weddell Sea sea-ice model focusing on the role of sea-ice processes on the advance and retreat of the ice margin. An important conclusion of that study was that the inclusion of sea-ice dynamics produces a realistic seasonal cycle of sea-ice extent. Following these, a series of ice-ocean coupled models (e.g. van Ypersele, 1986; Lemke and others, 1990; Owens and Lemke, 1990; Stössel and others, 1990), and an atmospheric-ice coupled model (Koch, 1988) have also been developed.

Expanding from the results of Hibler and Ackley (1983), we pose the following question: how do specific external (air and ocean) forcings affect the ice expansion and decay cycle in the Weddell Sea region? To address this question, we con-

sider sensitivity studies of a sea-ice model to the external thermal forcing terms of air temperature, ocean heat flux and relative humidity variations. These three variables, plus solar radiation and cloud cover, comprise the thermal inputs for sea ice. Solar radiation is well defined, has a invariable annual cycle and is included in the model at 6 hour interval averages. Cloud cover can vary widely, is estimated poorly and understood very little.

The three variables examined here fall between being constant (and well defined) and wildly variable (and not understood); they are examined in this paper as a collective. Based on results from a more comprehensive model study (Geiger, 1996), increasing the temporal resolution of the input fields from daily to 6 hour time intervals has a far greater impact on the response of the seasonal cycle of sea ice than does an increase in spatial resolution from 200 to 50 km. This result allows for a considerable reduction in computational time, and enables an efficient series of sensitivity studies. For this reason a relatively low spatial-resolution (200 km) model with high temporal-input field resolution (4 times a day) is used in the simulations presented here. The sensitivity responses of sea ice to sub-daily atmospheric and radiation forcing conditions presented here have not been well investigated previously. The emphasis of this study is to identify in relative terms how external factors affect sea-ice growth and decay processes. By looking specifically at the response of sea ice to each imposed condition, the intent is to identify the response of the ice prior to the onset of feedback processes to get a first order look at how sea ice reacts to these imposed conditions.



impacted by the relative humidity in the annual cycle.

Along the dry continent of Antarctica relative humidity is low, while moist air of marine origin is located closer to the ice edge. Because of the presence of a dry central continent in the Antarctic region, the seasonal sea-ice cycle is subjected to a greater range of humidity than the Arctic, which is typically close to 90% relative humidity year round. The presence of melt ponds in the summer in the Arctic vs a lack of melt ponds in the Antarctic (Andreas and Ackley, 1982) further substantiates the lower humidity seen in the western Weddell Sea relative to the Arctic. Hence the need for high-quality humidity data in input fields is more critical for sea-ice modeling in the Antarctic than in the Arctic.

A test to illustrate this effect is shown in Figure 5 using the standard model. Climatological monthly average relative humidity at the tip of the Antarctic Peninsula ranges from 80% to > 90%. Also in this region, the standard model poorly predicts the northward ice margin near the Peninsula coast during the summer months (Fig. 2, right

panel), a difficulty not atypical of ice models in the Weddell Sea (Hibler and Ackley, 1983). By reducing the humidity near the continent to 40% (boxed area in Fig. 5) we obtain an increase in ice growth in summer along the Peninsula compared to the standard run (Fig. 2), producing an ice edge closer to the observed. Increasing the local northward ocean current along the Antarctic Peninsula (by  $7 \text{ cm s}^{-1}$ ) is also capable of increasing the northern extent of the ice growth there (Geiger, 1996). While the humidity may not be the only reason for the lack of good correlation in summer months between models and observed ice at the northern tip of the Peninsula, it is a likely candidate to explain the discrepancy.

## DISCUSSION AND SUMMARY

Ice-edge and ice-thickness distribution were used to determine responses and relative differences caused by the specific thermal input variables of air temperature, ocean heat flux and relative humidity. Air temperature dominates ice-edge extent during the winter months. The difference in ocean heat flux values between the eastern and western areas of the Weddell Sea indicate that minimum ice extent and overall thickness were both reduced by increased ocean heat flux with responses in the eastern Weddell Sea being particularly sensitive to the high heat fluxes currently observed there. Later stages of ice-edge retreat and earlier stages of expansion (summer months) are sensitive to relative humidity, which affects the latent heat flux. Because of the presence or absence of the cold dry air along the Antarctic Peninsula, relative humidity sensitivity was most noticeable there, such that the case with an imposed  $RH = 40\%$  along the coast produced the best results compared to observed ice-edge composites.

In terms of sea-ice response to climate changes, increases and decreases in mean air temperature can significantly affect the ice-edge extent. In this respect, air temperature acts as an activator for the seasonal meltback by preconditioning the system such that albedo feedback, radiative heat transfer and dynamic processes begin once significant amounts of open water form. Events that increase ocean heat flux will reduce the overall ice-thickness distribution, but have little effect on the maximum ice-edge extent during the winter months. It will, however, be very difficult to detect these ice-thickness changes using remote sensing unless the ice becomes critically thin, and an overall catastrophic melt-back occurs. On the other hand, if increased atmospheric temperatures also lead to an overall increase in atmospheric moisture, the latent heat transfer from air to ice, as well as the sensible heat, will be altered. In this scenario ice-edge extent would be changed considerably, and would probably be readily detectable by current satellite monitoring methods. These findings emphasize the need for comparison of both ice-edge location and interior ice-thickness distribution in model validation. The ice-thickness distribution is the more critical and sensitive variable to variations in oceanic forcing, while ice extent responds more directly to atmospheric forcing changes.

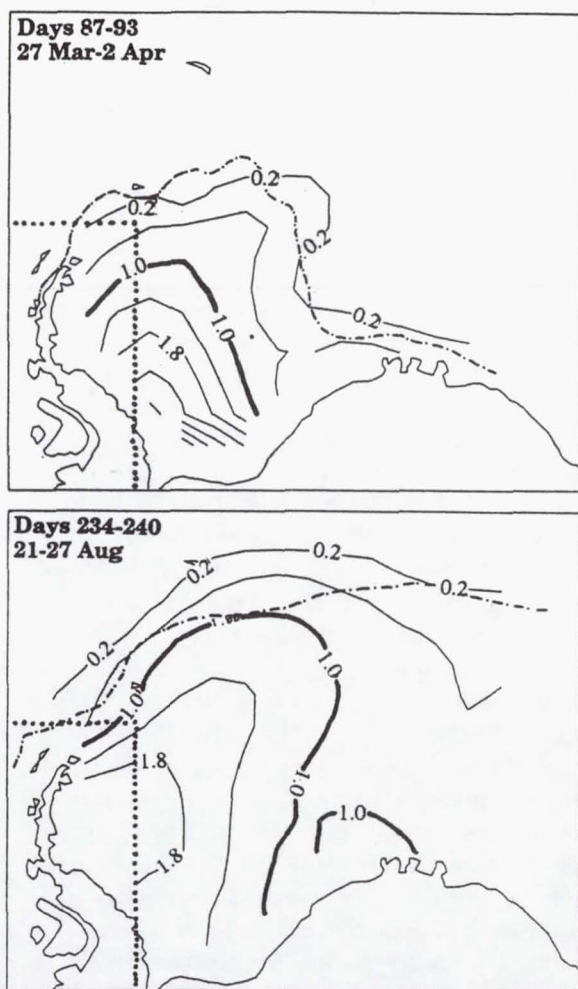


Fig. 5. The 2-D model sensitivity to low relative humidity along the Antarctic Peninsula. Model inputs are the same as the standard case except for constant low humidity ( $RH = 40\%$ ) in the dotted box area. The solid contours are m of ice thickness; dash-dot line is the NSIDC observed 7 day composite ice edge.



# An assessment of the regional distribution of the oxygen-isotope ratio in northeastern Canada

MARIO B. GIOVINETTO,<sup>1</sup> GERALD HOLDSWORTH,<sup>2</sup> DAVID A. FISHER,<sup>3</sup> NIGEL M. WATERS,<sup>4</sup> H. JAY ZWALLY<sup>5</sup>

<sup>1</sup>Earth Sciences 356, University of Calgary, Calgary, Alberta T2N 1N4, Canada

<sup>2</sup>Arctic Institute of North America, ML T 11th floor, Calgary, Alberta T2N 1N4, Canada

<sup>3</sup>Terrain Sciences Division, Geological Survey of Canada, 601 Booth Street, Ottawa, Ontario K1A 0E8, Canada

<sup>4</sup>Department of Geography, University of Calgary, Calgary, Alberta T2N 1N4, Canada

<sup>5</sup>Code 971, NASA/Goddard Space Flight Center, Greenbelt, MD 20771, U.S.A.

**ABSTRACT.** A compilation of mean values of the oxygen-isotope ratio relative to standard mean ocean water ( $\delta^{18}\text{O}$ , in ‰) for 22 sites representative of conditions in northeastern Canada is complemented with data on mean annual surface temperature, latitude, surface elevation, and mean annual shortest distance to open ocean denoted by the 10% sea-ice concentration boundary. Stepwise regression analysis is used to develop a multivariate model suitable to infer the distribution of  $\delta^{18}\text{O}$  in an area of complex topography and possibly mixed sourcing of advected water vapor. The best model is produced by a run in the backward mode at the 95% confidence level in which only temperature, latitude and distance to the open ocean remain in the model (the correlation coefficient is 0.915, the adjusted coefficient of determination is 0.809, the root mean square residual is 1.62). This model is similar to the best  $\delta^{18}\text{O}$  predictive model derived elsewhere for Greenland, suggesting a common principal source of advected moisture.

## INTRODUCTION

Earlier studies of the areal distribution of  $^{18}\text{O}/^{16}\text{O}$  values relative to standard mean ocean water (SMOW) ( $\delta^{18}\text{O}$  in ‰) in northeastern Canada and northwest Greenland (e.g. Koerner, 1979) have focused on bivariate relationships between  $\delta^{18}\text{O}$  and independent variables such as mean annual surface temperature, surface elevation, and distance to the coastline. In this study we assess the areal distribution of  $\delta^{18}\text{O}$  and covariation of the independent variables using stepwise regression analysis.

Our compilation of  $\delta^{18}\text{O}$  values determined from firn samples collected in ice caps and snow fields in northeastern Canada lists 23 sites (Fig. 1 and Table 1; site 1 on the North Ice Cap, Greenland, is included because it shares the same lower troposphere flow with at least nine other sites to the west). Data for one other site on the Devon Ice Cap (at about 115 km on the traverse route, 75.60° N, 83.3° W, 500 m (Koerner and Russell, 1979)), and from two other ice caps (Meighen Ice Cap, 79.95° N, 99.4° W, 270 m (Koerner and Paterson, 1974); Barnes Ice Cap (five sites centered at about 69.75° N, 72.0° W at elevations between 500 and 870 m (Hooke and Clausen, 1982)) were excluded from the compilation because the samples were collected from areas either of net ablation, or of intense summer melt and percolation. On some of the ice caps, ice shelves, and snow fields listed in Table 1 there are many more sites for which  $\delta^{18}\text{O}$  values have been determined. We selected relatively few sites from each in an attempt to attain a regionally representative (un-biased) database.

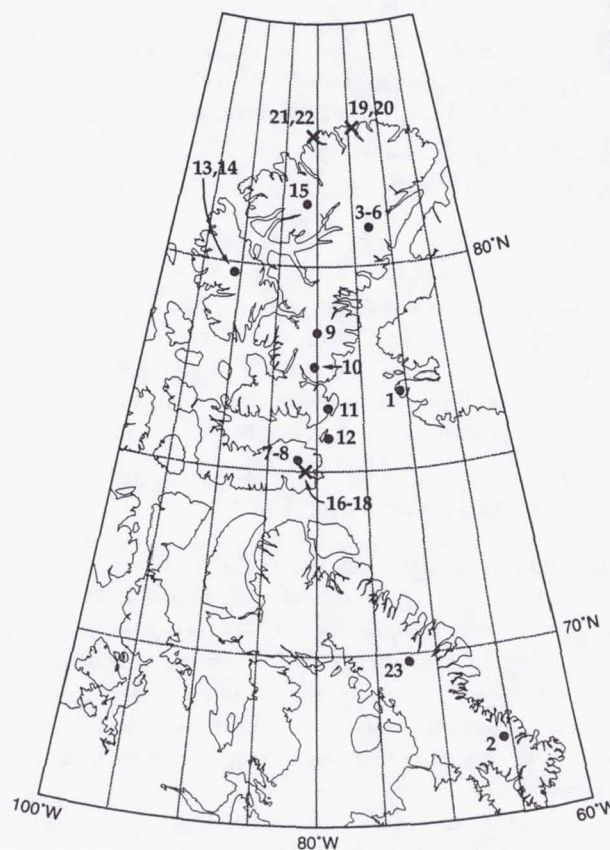


Fig. 1. Location of sites listed in Table 1. Full circles indicate sites for which mean annual surface temperature could be determined from surface data ( $T_s$ ). Crosses indicate sites for which mean annual surface temperature was determined exclusively from remotely sensed data ( $T_r$ ).



Table 6. Summary of stepwise regression analyses ( $N_{22}$ ;  $\delta^{18}\text{O}$  as the dependent variable)

Confidence level	Step F/B	Independent variables		$R$ (model)	$R_a^2$ (model)	Partial correlations ( $R_p$ )				rms (model)
		Inc.	Exc.			$L$	$H$	$T_a$	$D$	
>99%	F0	—	—	—	—	−0.611	0.014	0.858	−0.195	3.71
	F1*	$T_a$	$L, D, H$	0.858	0.722	−0.386	0.408	—	0.218	1.95
95%	F0	—	—	—	—	−0.611	0.014	0.858	−0.195	3.71
	F1	$T_a$	—	0.858	0.722	−0.386	0.408	—	0.218	1.95
	F2†	$T_a, H$	$L, D$	0.883	0.756	−0.233	—	—	0.165	1.83
95%	B0	all	—	0.915	0.798	—	—	—	—	1.67
	B1‡	$L, T_a, D$	$H$	0.915	0.809	—	−0.031	—	—	1.65

\* Same results as a run in the backward mode at a confidence level >99%, step B3: i.e.  $T_a$  remains in the model,  $H, D$ , and  $L$  are removed in that order.

† Same results as a run in the forward mode at the 90% confidence level.

‡ Best model. Same results as a run in the backward mode at the 90% confidence level.

95% confidence level,  $T_a$  enters the model first,  $H$  second while  $L$  and  $D$  do not enter ( $R$  is 0.883,  $R_a^2$  is 0.809, rms is 1.65). Runs at the 90% confidence level in either the forward or backward mode did not show any changes.

The best model produced using the  $N_{22}$  set in the backward mode at the 95% confidence level is:

$$\delta^{18}\text{O} = -203.501 + 0.782T_a + (-0.354L) + 3.814E - 3D. \quad (5)$$

This model is similar to that obtained from Greenland data for 46 sites (Zwally and Giovinetto, 1997), also at the 95% confidence level in the backward mode ( $R$  is 0.987,  $R_a^2$  is 0.973, rms is 0.53):

$$\delta^{18}\text{O} = -211.082 + 0.700T_s + 0.104L + (-1.085E - 3D) \quad (6)$$

where  $T_s$ ,  $L$  and  $D$ , have the same units and were obtained on the same basis described in this study. It is remarkable that the intercept and temperature coefficient values in Equations (5) and (6) are close, although the Greenland data are, for the most part, representative of central and southern regions, rather than northwestern part.

## DISCUSSION AND CONCLUSIONS

Our findings indicate that despite the relatively small dataset available to study the areal distribution of  $\delta^{18}\text{O}$  in north-eastern Canada, it is possible to define a multivariate model at an acceptable confidence level. Moreover, the model may be used to produce a contoured pattern based on mean annual surface temperature, latitude and mean annual shortest distance to open ocean, ignoring the effects of surface elevation.

Inversion of Equation (5) produces ratio values  $(\delta^{18}\text{O})_i$ , Table 1) that illustrate local differences between observation and model  $[(\delta^{18}\text{O}) - (\delta^{18}\text{O})_i]$ . The difference is largest, as expected, for the location on Axel Heiberg Island that was excluded from most analyses (site 13, −5.98‰). For the 22 sites used in the final analysis, the mean difference and std dev. are  $-0.11 \pm 1.50\text{‰}$ , with a

range −3.60–3.05‰ (sites 16 and 18, respectively, both on Devon Island). The difference is smallest for the location on the Penny Ice Cap (site 2, −0.08‰). This is of interest because, together with the difference for the location on the Barnes Ice Cap (site 23, 1.00‰), the two sites lie farthest south and away from the cluster to the north, indicating that the model is valid for a large area.

Our data compilation is not suitable to examine the variation of  $\delta^{18}\text{O}$  relative to elevation (e.g. over the area of a single ice cap). Nevertheless, it provides the basis to assess why elevation does not contribute to particular stepwise models. As listed in Table 1, the  $\delta^{18}\text{O}$  and  $H$  values show no correlation ( $N_{22}$ ;  $R < 0.1$ ,  $P > 0.9$ ). Exclusion of the data for ice shelves (sites 19–22) improves the correlation ( $N_{18}$ ;  $R$  is 0.758,  $P$  is 0.0003). However, the variation over a relatively small area requires using residual  $\delta^{18}\text{O}$  values produced in three steps, at each one removing the partial variation explained by  $L$ ,  $D$  and  $T_a$ , respectively. There is no correlation between the  $\delta^{18}\text{O}$  residuals produced at the third step and  $H$  ( $N_{18}$ ;  $R < 0.3$ ,  $P > 0.2$ ).

The best  $\delta^{18}\text{O}$  predictive model described for northeastern Canada (Equation (5)) is similar to the best predictive model described for Greenland (Equation (6)), the latter based largely on data from its central and southern regions for which the principal sources of advected moisture are the North Atlantic sector extending from the Labrador Sea to the Norwegian Sea and waters to the south. This suggests that the bulk of the precipitation in Canada sampled by the sites compiled for this study may share moisture advected from that sector.

The description of the sector must be qualified in that it is based on the mean annual position of the 10% sea-ice concentration boundary. If shortest distance to open ocean is measured using the mean annual position of the 50% concentration boundary, the description of the sector could be stated as extending from Baffin Bay to the Greenland Sea and waters to the south and east. In any event, the suggestion fits the findings of a detailed study on the origin of Arctic precipitation (Johnsen and others, 1989).



# The effect of rain on air-water gas exchange

By DAVID T. HO<sup>1</sup>\*, LARRY F. BLIVEN<sup>2</sup>, RIK WANNINKHOF<sup>3</sup> and PETER SCHLOSSER<sup>1</sup>,

<sup>1</sup>Lamont-Doherty Earth Observatory and Department of Earth and Environmental Sciences, Columbia University, Palisades, NY 10964, USA; <sup>2</sup>NASA/GSFC, Laboratory for Hydrospheric Processes, Wallops Island, VA 23337, USA; <sup>3</sup>NOAA/AOML, Ocean Chemistry Division, Miami, FL 33149, USA

(Manuscript received 23 September 1996; in final form 9 December 1996)

## ABSTRACT

The relationship between gas transfer velocity and rain rate was investigated at NASA's Rain-Sea Interaction Facility (RSIF) using several SF<sub>6</sub> evasion experiments. During each experiment, a water tank below the rain simulator was supersaturated with SF<sub>6</sub>, a synthetic gas, and the gas transfer velocities were calculated from the measured decrease in SF<sub>6</sub> concentration with time. The results from experiments with 18 different rain rates (7 to 110 mm h<sup>-1</sup>) and 1 of 2 dropsizes (2.8 or 4.2 mm diameter) confirm a significant and systematic enhancement of air-water gas exchange by rainfall. The gas transfer velocities derived from our experiment were related to the kinetic energy flux calculated from the rain rate and dropsize. The relationship obtained for mono-dropsizes rain at the RSIF was extrapolated to natural rain using the kinetic energy flux of natural rain calculated from the Marshall-Palmer raindrop size distribution. Results of laboratory experiments at RSIF were compared to field observations made during a tropical rainstorm in Miami, Florida and show good agreement between laboratory and field data.

## 1. Introduction

Exchange of gases across the air-water interface influences many properties of natural waters. Knowledge of this parameter is critical for evaluating indicators of water quality (e.g., dissolved oxygen=DO) (Odum, 1956; O'Connor, 1962; Clark et al., 1995b), understanding cycling of biogeochemically important trace gases (e.g., CO<sub>2</sub>, CH<sub>4</sub>, DMS, N<sub>2</sub>O, CH<sub>3</sub>Br) (Broecker et al., 1985; Bates et al., 1993; Yvon and Butler, 1996), and predicting evasion rates of volatile pollutants (e.g., toxic halogenated compounds) (Bopp, 1983; Dyrssen et al., 1990; Thomann et al., 1991; McConnell et al., 1993).

Over large water bodies such as oceans or large lakes, gas exchange is governed primarily by wind

driven turbulence on the water surface and, to a lesser extent, by air bubble entrainment (Merlivat and Memery, 1983; Jähne et al., 1987). However, on the local scale of rivers, small lakes, estuaries, and wetlands, other factors contribute significantly to the turbulence regime, especially at low wind speeds (Livingstone and Imboden, 1993; Clark et al., 1995a). One of these factors is rain falling onto the water surface.

Relatively little experimental work has been directed at quantifying the influence of rainfall on air-water gas exchange. Bopp et al. (1981) speculated that rain might have been responsible for rapid gas exchange observed during a gas-exchange experiment in a model estuarine ecosystem. For light rains (<25 mm h<sup>-1</sup>), some exploratory laboratory (Banks et al., 1984) and field experiments (Belanger and Korzun, 1991) suggest a power law and linear relationship,

\* Corresponding author.



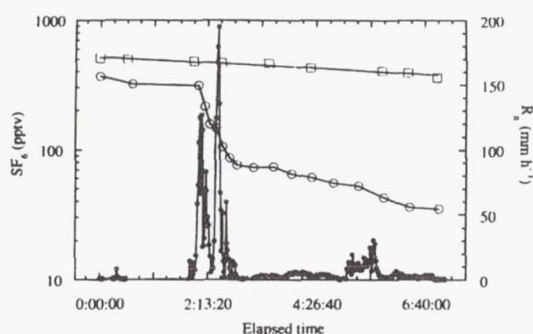


Fig. 4.  $\text{SF}_6$  concentration decrease in the two pools with time (log scale) along with the rain rate during the Miami field experiment. Open squares = control; open circles =  $\text{SF}_6$  evasion experiment; filled circles = rain rate (1-min averages).

ant. Therefore, future work should pay attention to the contribution of rain to density-driven convection in the water boundary layer. Furthermore, since surfactants tend to impede gas exchange, the effect of rain on dispersing surfactants should be examined. The effect of rain falling on salt water should be considered. For salt water, the enhancement of gas exchange due to rainfall on the water surface could be suppressed by the density stratification created by the rain. Finally, the interaction between rain and wind should be considered. Because of the effect of rain on air-water gas exchange shown here and the fact that rain can enhance the wind stress acting on the water surface (Caldwell and Elliott, 1972), rain will almost certainly have an effect on wind-induced gas exchange. Yet, the combined effect is probably not a simple addition of the two individual processes. Further studies should examine the combined effect of rain and wind on air-water gas exchange.

#### 5.4. Comparison to field data

During a tropical rainstorm in Miami, Florida, an  $\text{SF}_6$  evasion experiment was performed in a similar fashion as those described above. Two round water pools (diameter = 136 cm; height = 30 cm) were placed next to each other. One of them was sheltered from the rain by a canopy suspended at a height of 3 m to provide the control experiment. Fig. 4 shows the  $\text{SF}_6$  concentration decrease in the two pools with time along with

the rain rate. The rain rate was measured with a capacitance rain gauge, and RSD was obtained on a Joss-Waldvogel disdrometer (Nystuen et al., 1994).

The kinetic energy flux of the Miami rain was calculated from the measured RSD and related to  $k(600)$ . Most of the rain events during this storm exhibited the MP RSD. The comparison of field data from Miami with the laboratory data from RSIF shows good agreement between controlled laboratory experiments and field observations (Fig. 5a). To determine the robustness of the transformation using KEF from MP RSD, we plot, in Fig. 5b, the rain rate versus gas exchange for the Miami experiment along with the relationship calculated from eq. (20). Again, there is good agreement between the laboratory data from RSIF and the field data from Miami. Both data sets show a significant increase in  $k(600)$  with either increasing KEF or  $R_n$ .

## 6. Conclusions

The gas exchange study conducted at RSIF using  $\text{SF}_6$  in gas evasion experiments clearly shows that rain enhances gas exchange. The gas exchange rate can be related to rain rate and dropsizes by a single parameter, the kinetic energy supplied to the water surface by the raindrops (kinetic energy flux). Additionally, the relationship between mono-dropsizes laboratory rain and gas exchange could be extended to natural rain using the Marshall-Palmer raindrop size distribution (MP RSD). This relationship should hold for most natural rain events as the MP RSD is well established. In cases where the RSD differs dramatically from the MP distribution, other parameterizations could be used instead to estimate the RSD and the KEF could then be calculated accordingly.

The effect of rain on air-water gas exchange is probably most pronounced at sites where wind-driven turbulence is not the dominant contributor to gas exchange. Such sites include wetlands, particularly because most wetlands are sheltered and located in high-precipitation regions. In view of the results presented here and the preliminary studies done in the field showing the dramatic effect that rain can have on air-water gas exchange, more extensive investigations should be consid-



# Remote Sensing of Dipole Rings

Stanford B. Hooker, Richard P. Mied, James W. Brown, and A. D. Kirwan, Jr.

**Abstract**—Historical satellite-derived sea surface temperature (SST) data are reanalyzed with a *zebra* color palette and a thermal *separatrix* method. The new results from this reanalysis are as follows: a) Thirteen observational sequences of six rings from the Gulf Stream and the Brazil Current, which have historically been interpreted as solitary vortices or monopoles are shown to have a dipolar character; b) some of these dipole rings have been observed in the open ocean, thereby eliminating the possibility that they are sustained by topographic interactions with the continental slope; c) whether interacting with other features or evolving as isolated circulations, dipoles are seen to rotate within a relatively narrow range of approximately  $4\text{--}8^\circ \text{ day}^{-1}$  (interacting) and  $10\text{--}15^\circ \text{ day}^{-1}$  (isolated); and d) feature tracking delineates energetic fluid in both vortices and eliminates the possibility of interpreting dipole rings as transient features produced by active monopoles and patches of entrained fluid.

## I. INTRODUCTION

GULF Stream rings [7] form or *pinch off* from the meandering of the jet if the meander amplitude is sufficiently large. A warm core ring (WCR) consists of a core of relatively warm Sargasso Sea water encircled by an anticyclonically rotating current of Gulf Stream water, while a cold core ring (CCR) consists of relatively cold Slope Water surrounded by cyclonically rotating Gulf Stream fluid [22]. In this generally accepted definition of a ring, no other circulation other than the rotating annulus of Gulf Stream water is a part of the eddy. A WCR consistent with this solitary vortex or *monopole* description is depicted in Fig. 1(a).

Because they can transport fluid and stir their surroundings while they translate, mesoscale eddies are an important mechanism for the redistribution of energy and biogeochemical properties in the world ocean. Consequently, analytical and numerical models of isolated oceanic and atmospheric vortices have been intensively investigated since the pioneering work of Rossby [23]. While the existence of isolated rings on a  $\beta$ -plane determines their basic westward propagation, their evolution is also influenced by mean flows [13], eddy size [18] and shape [17], vertical modal coupling [19], bottom

topography [24], and the interaction of the eddy with its dispersion field [4], [27]. These studies are representative of the many efforts that have expanded the understanding of isolated rings.

During the era of the investigations cited above, neither *in situ* nor remote-sensing data provided any compelling reasons to view Gulf Stream rings as anything but monopoles. A new image display procedure using a so-called *zebra* palette [9] and a new data analysis technique based on the time evolution of the flow field *separatrix* [11], however, have recently provided highly detailed views of the oceanic mesoscale, particularly of rings. A *zebra* palette consists of one or more *slow* (color) gradients superimposed upon a more rapidly varying or *fast* (grey-scale) sinusoid; it is the latter that gives the palette the distinctive stripes and introduces the clarifying edges into the imagery (Fig. 1). A *separatrix* is the dividing line between two vortical flows which, although visible in standard gradient or *rainbow* palettes, is better delineated by the *zebra* palette (see [11] for a comparison).

In satellite-derived SST data, the *separatrix* is usually evident as a narrow region of increased thermal contrast. For a pair of oppositely signed vortices or *dipole*, the *separatrix* is a line of convergence between the eddies that flattens the local curvature of the eddies where they join, and which rotates necessarily at the same rate as the whole system. The changing angular position of the *separatrix* is an estimate of the dipole's rotation. Monitoring this rotation rate is the basis of the *separatrix* method. A pair of eddies labeled as "Two Vortices" are shown in Fig. 1. The dipole terminology is used here because this particular WCR, called 82-B (since it was the second WCR to form in 1982), has long been identified as a monopole (see, e.g., Olson *et al.* [21]). As is evident from Fig. 1(b), however, WCR 82-B is vortically more complicated than a monopole model permits—it is paired with a smaller vortex having an opposing circulation that is advecting filaments of (dark blue) Slope Water around its periphery. The *separatrix* for the WCR dipole lies along a northeast-to-southwest line and separates the warm (green) water of the primary anticyclone from the cool (blue) water of the secondary cyclone. Note how the convergence along the *separatrix* flattens the isotherms and produces a D-shaped primary vortex.

The reason for this study is twofold. First, new rotation rate data extracted from SST images of dipoles are presented. Combined with previous estimates of dipole rotation, all of the data are seen to fall into two groups, depending upon whether they are isolated circulations, or interacting with an adjacent feature. Second, an image sequence of a Gulf Stream CCR dipole is presented. The latter is a significant new result,

Manuscript received May 21, 1996; revised March 12, 1997. The work of A. D. Kirwan, Jr., was supported by the Office of Naval Research and the Samuel L. and Fay M. Slover endowment to Old Dominion University. R. Mied was supported by the Shelf Break Exchange Processes Project at the Naval Research Laboratory.

S. B. Hooker is with the Laboratory for Hydrospheric Processes, NASA Goddard Space Flight Center, Code 971, Greenbelt, MD 20771 USA (e-mail: stan@ardebeg.gsfc.nasa.gov).

R. P. Mied is with the Remote Sensing Division, Naval Research Laboratory, Code 7250, Washington, DC 20375 USA.

J. W. Brown is with the MPO/RSMAS, University of Miami, Miami, FL 33149 USA.

A. D. Kirwan, Jr. is with CCPO, Old Dominion University, Norfolk, VA 23508 USA.



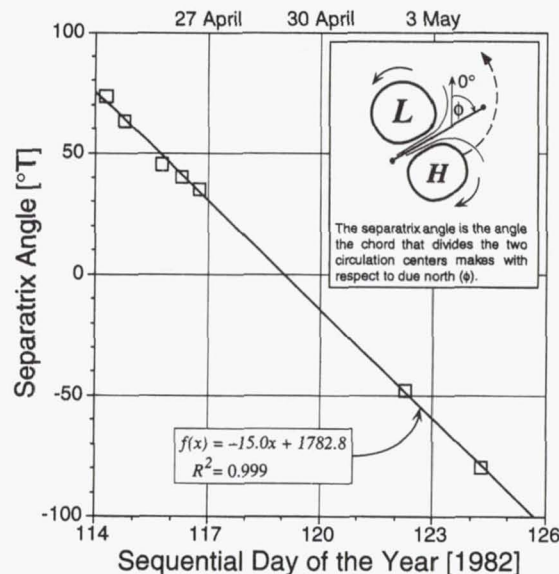


Fig. 3. A compilation of all the satellite-derived separatrix positions for the CCR dipole shown in Fig. 2. The rotation of the dipole is simply the slope of the (least squares) fitted line, or about  $15.0^\circ \text{ day}^{-1}$ . (The negative slope of the line indicates CCW rotation.)

motion of apparently unique small-scale features over short periods of time) is used to determine the rotation sense and maximum surface velocities of each eddy. As expected, the primary cyclone displays an energetic speed (approximately  $83 \text{ cm/s}^{-1}$ ), but the secondary anticyclone has a vigorous circulation (about  $57 \text{ cm/s}^{-1}$ ) as well.

Although the swirling motion of the eddies in Fig. 2 is best seen in a movie loop presentation of the data, the intervening separatrix between the eddies is clearly visible in each subpanel. Over the time period covered in the figure, the separatrix and the anticyclone rotate counterclockwise (CCW) around the cyclone at approximately  $15.0^\circ \text{ day}^{-1}$  (Fig. 3), corresponding to a 24-day rotation period. The energetic velocities and phase-locked rotation of the eddy pair establish this CCR as a dipole during this time period. The presence of dipole CCR's establishes the applicability of the dipole model to explain the observed vortical complexity of some Gulf Stream rings, so it is natural to question whether this implies a wider relevance to other current systems that produce rings.

Hooker and Brown [10] investigated whether Brazil Current rings exhibit dipole signatures and showed several examples of WCR and CCR dipoles from this current system. They studied a particular WCR in great detail and discovered it existed as a dipole for approximately 60 days, during which it encountered a solitary cold eddy. The result of the interaction of these two vortices appeared to be coalescence and not simple pairing. They cite coalescence as further evidence the WCR was a dipole: since the cold eddy has vorticity opposite that of the primary vorticity of the WCR, the only way the two features could coalesce is if the WCR were a dipole having a vorticity pole of the same sign as the cold eddy. If the ring was not a dipole—the two features could not coalesce—they could only pair up.

Fig. 4 is a compilation of the magnitudes of the separatrix rotation rates for a variety of Gulf Stream and Brazil Cur-

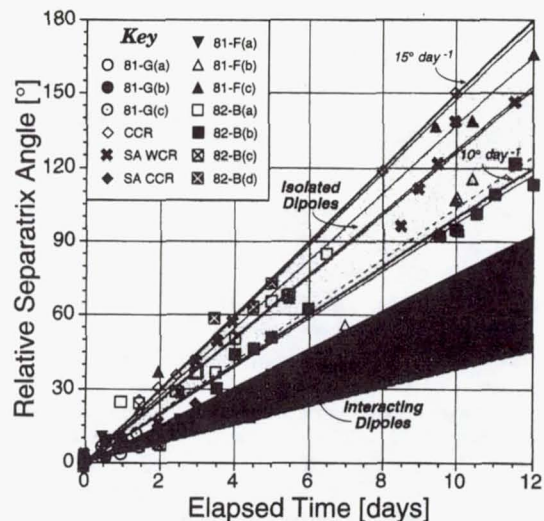


Fig. 4. A compilation of dipole separatrix positions for Gulf Stream and Brazil Current (denoted SA for South Atlantic) rings with the values for CCW rotation adjusted to give positive slopes. Elapsed times from the first satellite-derived position are used, so all the data can be presented in a summary fashion. The Gulf Stream WCR's are indicated by decadal numbers and letters. The parenthetical letters indicate a separate rotational period for the rings so denoted. Rotation rates for isolated dipole rings are shown as thin solid lines (and light stipling), while those interacting with the jet, topography, or another eddy are shown as thin dashed lines (and dark stipling).

rent rings which fall naturally into two groups: isolated and interacting. There is, admittedly, some subjectivity associated with these definitions, since universally applicable definitions do not exist. For example, at what point is a dipole no longer demonstrably influenced by topography? In the case of 81-G, its rotation rate doubled from  $3.8^\circ \text{ day}^{-1}$  to  $7.7^\circ \text{ day}^{-1}$  as it moved through the New England Seamount chain, but the latter estimate might still be representative of a dipole influenced by topography. Similarly, at what point is a dipole no longer influenced by another dipole? The rotation rate of 81-F increased slightly from  $10.3^\circ \text{ day}^{-1}$  to  $13.7^\circ \text{ day}^{-1}$  as it moved farther from 82-B, which underscores that the question of proximity in vortex features is a matter of degree. These two cases are the only ones that do not fall unambiguously into either the isolated or interacting regimes, and appear in Fig. 4 as opposing entries for the categories involved.

The more rapid rotation of the isolated dipoles,  $10^\circ$ – $15^\circ \text{ day}^{-1}$ , versus  $4^\circ$ – $8^\circ \text{ day}^{-1}$  for the interacting dipoles, is qualitatively consistent with the numerical modeling results presented in [9], which showed dipoles far from a boundary rotate more rapidly than those close to it. Although interacting dipoles generally rotate more slowly, rotation rates for all the vortex pairs fall within a relatively narrow range,  $4^\circ$ – $15^\circ \text{ day}^{-1}$ .

### III. DISCUSSION

Images of the type used to produce Fig. 4 raise two deeper questions: how are dipoles generated, and do viable models exist to describe their behavior? While complete answers are outside the scope of this study, brief comments are appropriate. Although rings are formed under similar circumstances from all of the western boundary currents, these results suggest



## Climate Variability in the Amundsen and Bellingshausen Seas\*

STANLEY S. JACOBS

*Lamont-Doherty Earth Observatory, Palisades, New York*

JOSEFINO C. COMISO

*NASA/Goddard Space Flight Center, Greenbelt, Maryland*

(Manuscript received 17 January 1996, in final form 18 July 1996)

### ABSTRACT

Satellite data reveal a 20% decline in sea ice extent in the Amundsen and Bellingshausen Seas in the two decades following 1973. This change is negatively correlated with surface air temperatures on the west side of the Antarctic Peninsula, which have increased  $\sim 0.5^{\circ}\text{C decade}^{-1}$  since the mid-1940s. The recession was strongest during summer, when monthly average minima in 1991–92 removed much of the incipient multiyear ice over the continental shelf. This would have lowered the regional-mean ice thickness, impacting snow ice formation, brine production, and vertical heat flux. The northern ice edge contracted by  $\sim 1^{\circ}$  of latitude in all seasons from 1973–79 to 1987–93, returning toward mean conditions in 1993–95. The decline included multiyear cycles of several years in length, superimposed on high interannual variability. A review of atmospheric forcing shows winds consistent with mean and extreme ice extents, and suggests links to larger-scale circulation changes in the South Pacific. Historical ocean measurements are sparse in this sector, but mixed-layer depths and upper pycnoclines beneath the sea ice resemble those in the Weddell Sea. Weaker surface currents or changes in the upwelling of Circumpolar Deep Water on the continental shelf could have contributed to the anomaly persistence.

### 1. Introduction

On 30 January 1774, in what we now call the Amundsen Sea (Fig. 1), heavy sea ice near  $71^{\circ}\text{S}$ ,  $107^{\circ}\text{W}$  forced Captain James Cook to abandon his attempt to reach the fabled southern continent. In 1820, Admiral Thaddeus von Bellingshausen was able to reach far enough south to discover Peter I Island and sight what is now Alexander Island. The first expedition to the south and west of those islands, in 1898–99 on the *Belgica*, was beset for more than a year in sea ice (Cook 1900). Sealers had earlier wintered over on the Antarctic Peninsula (Campbell 1992), but the *Belgica* crew, sustained in its ordeal by the fledgling polar explorers Roald Amundsen and Fred Cook, were probably the first to winter south of the Antarctic Circle. Since that time, the sea ice of the southeastern Pacific has enjoyed a reputation of being of “much greater age and thickness than usual, [making] the con-

tinental coasts between Alexander Island and the Ross Sea the most inaccessible” (Heap 1964).

Routine satellite monitoring of sea ice in the polar regions began in 1973. In 1993 we reported that a major decrease in sea ice extent had occurred in the Bellingshausen Sea from mid-1988 through early 1991. That retreat was strongly correlated with surface air temperatures on the west coast of the Antarctic Peninsula (AP), which reached a historic high in 1989 (Morrison 1990). The sea ice decline coincided with more northerly surface winds and greater cyclonic activity, and was particularly evident during the austral summer, extending during 1992 into the adjacent Amundsen Sea. The timing of the record Bellingshausen Sea ice recession corresponded with the low-ice phase of a double wave that propagates eastward around Antarctica every 7–10 yr, with regional ice edge expansion and contraction every 3–5 yr (Murphy et al. 1995; White and Peterson 1996).

In this paper we describe a longer-term sea ice recession over the larger Amundsen and Bellingshausen Seas (Fig. 1). We note that errors in quantification of the ice cover due to gridding, moisture effects and precipitation are small compared with the interannual variability. A discussion of the spatial and temporal extent of the regional temperature anomaly is followed by an evaluation of probable atmospheric and

\* Lamont-Doherty Earth Observatory Contribution Number 5597.

Corresponding author address: Stanley Jacobs, Lamont-Doherty Earth Observatory, P.O. Box 1000, Palisades, NY 10964.  
E-mail: sjacobs@lamont.columbia.edu



archived data (Swift 1995), and consistent with a retreat of the northern ice edge. The evidence is thus mixed, and the limited historical data make it difficult to separate any possible trend from natural variability in the A and B deep water.

There are indications that a recent change may have occurred in the rate of upwelling of CDW onto the continental shelf. Deep water floods the deeper regions of the southeastern Pacific continental shelves and is only slightly cooled and freshened in the process (Jacobs et al. 1996). At depths below 200 m near Alexander Island (Fig. 1), CDW was up to several tenths of a degree warmer in 1994 than in the early 1980s data of Potter et al. (1988). Warmer CDW would enhance melt-driven upwelling near the coastline, but better time series data and models are needed to evaluate the potential impacts of such changes on mixed-layer temperatures and sea ice extent.

## 6. Discussion

### a. Modeling implications

Coupled air-sea general circulation models (GCMs) incorporate feedback mechanisms, such as variable surface albedo, and project decreasing sea ice extents as atmospheric temperature rises. These results agree with the generally negative correlations found between ice extent and surface air temperature (Jacka and Budd 1991; Weatherly et al. 1991). Early model simulations with enhanced greenhouse gases did not include ice dynamics, leads, or salinity effects, compromising quantitative projections of sea ice extent and thickness (Mitchell et al. 1990). Some GCMs now incorporate sea ice dynamics (e.g., Pollard and Thompson 1994), and future models may benefit from the inclusion of variable snow cover and surface mixed layers. Zonally variable warming over the Antarctic sea ice in a model that includes the response to aerosols (Taylor and Penner 1994) is consistent with recent warming near the AP.

A few models emphasize the tendency for warming and freshening to stabilize the ice-ocean system with a deeper pycnocline and weaker ice divergence (Martinson 1990; Manabe et al. 1991). The latter project thicker sea ice on the Southern Ocean in a warmer climate as a cap of lower-salinity surface water caused by higher P - E and continental runoff strengthens the pycnocline and damps the vertical ocean circulation and heat flux. However, with a surface water residence time of  $\sim 2$  yr (Gordon and Huber 1990), an improbable  $5 \text{ m yr}^{-1}$  of freshwater would be needed to produce mixed-layer salinities as low as those in the Arctic (Fig. 13)—that is, sufficient to greatly decrease heat flux from the CDW. Manabe et al. (1991) modeled an air temperature increase of  $\sim 0.05^\circ\text{C yr}^{-1}$ , similar to that observed in the A and B, and obtained a high runoff by transferring to the ocean any  $P - E > 20 \text{ cm yr}^{-1}$  on Antarctica. They noted that precipitation may be overestimated at high

southern latitudes, a typical problem in current GCMs (Chen et al. 1995). A lower ice extent and a reduction of multiyear ice seems incompatible with greater ice thickness, and would imply that the observed warming and any related freshening in the A and B did not markedly increase the regional stability of the upper ocean.

### b. Circumpolar ice extent

Satellite observations of sea ice extent now extend over more than two decades, revealing interannual changes and a declining sea ice cover in the A and B. While decadal and longer trends are common in regional records (e.g., Fletcher 1972), this retreat probably exceeded that at any other time this century and diminished the regional-mean sea ice thickness. In the full Southern Ocean, decreases in sea ice extent in one area are typically balanced by increases elsewhere (Ackley 1981; Zwally et al. 1983b; Parkinson 1994). Over the 1979–87 period, Gloersen and Campbell (1991) did not find a significant change in Antarctic sea ice extent, but Johannessen et al. (1995) reported a net decline of  $0.13 \text{ Mkm}^2$  from 1978 to 1994. That would correspond to a warming of  $\sim 0.14^\circ\text{C}$  over the full sea ice region if the air temperature-ice extent relationship in Fig. 8 were extrapolated to the circumpolar ice edge. In addition, the A and B ice edge recession of  $\sim 1^\circ$  of latitude (Fig. 2), or  $0.29 \text{ Mkm}^2$ , implies sufficient net growth in other sectors to compensate about half of this regional decline. The retreat depicted in Fig. 4 may be reversed over the next several years, but continued warming in high southern latitudes (Jones 1990; Jacka and Budd 1991) will eventually register as a significant loss of circumpolar sea ice cover.

### c. Future work

The significance of the recent southeastern Pacific sea ice retreat has been its duration and association with a lengthy regional warming trend. The forcing is not yet clear, but probably lies external to the region, associated with large-scale changes in the state and circulation of the atmosphere and ocean. The high variability of sea level pressure and increased open water in the southeastern Pacific sector probably enhanced air-sea interactions, heat and moisture fluxes, and divergence of the mixed layer. In situ ocean data are as yet inadequate to define reliable time series, but evidence of A and B surface water alterations might be found downstream in the ACC or in the Antarctic Intermediate Water. Sea ice time series should be lengthened by continued satellite monitoring, and by the use of ice core and tree ring proxies (e.g., Cook et al. 1992; Thompson et al. 1994). Understanding the cause and course of this kind of climate variability would benefit from the identification and monitoring of key indices of the subsurface ocean circulation, application of regional coupled circulation models, and more regular field measurements.



## Validity of the temperature reconstruction from water isotopes in ice cores

J. Jouzel,<sup>1</sup> R. B. Alley,<sup>2</sup> K. M. Cuffey,<sup>3</sup> W. Dansgaard,<sup>4</sup> P. Grootes,<sup>3,5</sup> G. Hoffmann,<sup>6</sup> S. J. Johnsen,<sup>4,7</sup> R. D. Koster,<sup>8</sup> D. Peel,<sup>9</sup> C. A. Shuman,<sup>10</sup> M. Stievenard,<sup>1</sup> M. Stuiver,<sup>3</sup> and J. White<sup>11</sup>

**Abstract.** Well-documented present-day distributions of stable water isotopes (HDO and  $\text{H}_2^{18}\text{O}$ ) show the existence, in middle and high latitudes, of a linear relationship between the mean annual isotope content of precipitation ( $\delta\text{D}$  and  $\delta^{18}\text{O}$ ) and the mean annual temperature at the precipitation site. Paleoclimatologists have used this relationship, which is particularly well obeyed over Greenland and Antarctica, to infer paleotemperatures from ice core data. There is, however, growing evidence that spatial and temporal isotope/surface temperature slopes differ, thus complicating the use of stable water isotopes as paleothermometers. In this paper we review empirical estimates of temporal slopes in polar regions and relevant information that can be inferred from isotope models: simple, Rayleigh-type distillation models and (particularly over Greenland) general circulation models (GCMs) fitted with isotope tracer diagnostics. Empirical estimates of temporal slopes appear consistently lower than present-day spatial slopes and are dependent on the timescale considered. This difference is most probably due to changes in the evaporative origins of moisture, changes in the seasonality of the precipitation, changes in the strength of the inversion layer, or some combination of these changes. Isotope models have not yet been used to evaluate the relative influences of these different factors. The apparent disagreement in the temporal and spatial slopes clearly makes calibrating the isotope paleothermometer difficult. Nevertheless, the use of a (calibrated) isotope paleothermometer appears justified; empirical estimates and most (though not all) GCM results support the practice of interpreting ice core isotope records in terms of local temperature changes.

### 1. Introduction

Important relationships have been uncovered between the global distributions of  $\delta\text{D}$  and  $\delta^{18}\text{O}$  in modern precipitation and certain climatic variables [Craig, 1961; Dansgaard, 1964]. (The concentrations of HDO and  $\text{H}_2^{18}\text{O}$ , the two stable isotopic forms of water, are expressed in per mil units with respect to standard mean ocean water (SMOW) as  $\delta\text{D}$  or  $\delta^{18}\text{O}$ .) Of primary interest to the paleoclimatologist is the linear relationship between annual values of  $\delta\text{D}$  and  $\delta^{18}\text{O}$  and mean annual

temperature at the precipitation site that is observed at middle and high latitudes. In order to use the isotope signal as a paleothermometer, the present-day spatial isotope/surface temperature relationship  $\delta = aT_s + b$  defined over a certain region ( $\delta$  stands for either  $\delta\text{D}$  or  $\delta^{18}\text{O}$  of the precipitation and  $T_s$  for the surface temperature; the isotope/surface temperature slope is  $a = d\delta/dT_s$ ) is generally assumed to hold in time throughout the region, i.e., it is assumed that the spatial and temporal slopes are similar (hereafter “temporal” applies to the relationship describing the variation of isotopic contents with temperature through different climates over time, at a single geographic location). A so-called “modern analogue method” is thus used, similar to that adopted in most other approaches for reconstructing paleoclimates. Of course, the fact that present-day isotope concentrations and local temperature are strongly correlated, as illustrated in Figure 1 for Greenland and Antarctica, does not validate this critical assumption. Such factors as the evaporative origin and the seasonality of precipitation can also affect  $\delta\text{D}$  and  $\delta^{18}\text{O}$ , and if these factors change markedly under different climates, the accuracy of the isotope paleothermometer is reduced. The possibility of a difference between the temporal and spatial  $\delta/T_s$  relationships must therefore be seriously examined. There is, indeed, growing evidence that a difference between temporal and spatial  $\delta/T_s$  relationships does exist and appears to be time dependent, thus complicating the use of water stable isotopes as a paleothermometer.

The temporal  $\delta/T_s$  relationships can be tested in several ways. An empirical calibration can be inferred by direct comparison of the stable isotope composition of the upper snow

<sup>1</sup>Laboratoire de Modélisation du Climat et de l'Environnement, Gif sur Yvette, France.

<sup>2</sup>Department of Geosciences and Earth System Science Center, Pennsylvania State University, University Park.

<sup>3</sup>Department of Geological Sciences and Quaternary Research Center, University of Washington, Seattle.

<sup>4</sup>Department of Geophysics, University of Copenhagen, Copenhagen.

<sup>5</sup>Now at Leibnitz Laboratory, Christian Albrechts University, Kiel, Germany.

<sup>6</sup>Max-Planck-Institut für Meteorologie, Hamburg, Germany.

<sup>7</sup>Science Institute, University of Reykjavik, Reykjavik, Iceland.

<sup>8</sup>Hydrological Sciences Branch, NASA Goddard Space Flight Center, Greenbelt, Maryland.

<sup>9</sup>British Antarctic Survey, Cambridge, England.

<sup>10</sup>Oceans and Ice Branch, NASA Goddard Space Flight Center, Greenbelt, Maryland.

<sup>11</sup>Institute of Arctic and Alpine Research Institute and Department of Geological Sciences, University of Colorado, Boulder.



## 5. Discussion and Conclusion

In the light of simple model results (Figure 5), it is tempting to explain the fact that the temporal slope is lower than the spatial slope, as inferred from paleothermometry in central Greenland, at least in part, by a cooler source of Greenland precipitation for glacial than for present-day climate. Presently available GCM experiments do not, however, allow direct testing of this intuitively reasonable assumption as the experiment in which precipitation origin is tagged with respect to the source temperature has not yet been run for glacial conditions. The relatively good agreement between GISS model and paleothermometry results noted by Cuffey *et al.* [1995] provided strong encouragement for further exploring this assumption. Preliminary analyses of the GISS  $4 \times 5$  simulation data suggest, however, that this agreement may depend on model resolution. We need to verify this resolution dependence and, if it truly exists, understand it; only then can we use the models to assess the possible influence of glacial-interglacial changes in moisture source on temporal slopes in Greenland. A complementary way to assess the role of the origin of the precipitation is to exploit the deuterium excess signal, which is clearly influenced by the characteristics (temperature and humidity) in the moisture source regions [Jouzel *et al.*, 1982; Johnsen *et al.*, 1989; Dansgaard *et al.*, 1989]. The excess profiles will be available soon along the full length of the GRIP and GISP2 cores, and they should tell us if, as we can expect, the average source temperature was colder during glacial than during interglacial periods (to the extent that the influence of other factors potentially influencing the deuterium excess of polar snow, such as changes in cloud microphysical processes, could be evaluated).

Among the processes that we have invoked when pointing out that the temperature recorded by isotopes may differ from the mean annual surface temperature, our scientific community focuses on the changes in seasonal timing of the precipitation. This should be explored further both in examining new data sets and through a modeling approach [Charles *et al.*, 1995]. In this context it would also be important to examine thoroughly the capacity of models to correctly reproduce both the seasonal timing of precipitation fallout and its isotopic content. Note that as for seasonality, the bias linked with precipitation intermittency could be easily evaluated in a GCM (in comparing the weighted average temperature during precipitation events with the annual average). This has not been done yet but could help in testing the suggestion of White *et al.* [1995] that a drastic change in frequency distribution may affect the temporal slope. We have drawn attention, here, to the possible changes in the strength of the inversion layer and would like to put some emphasis on this assumption because of the difference in atmospheric circulation associated with the presence of the Laurentide Ice Sheet. Also, temperatures above the inversion layer are, for polar areas, probably of larger geographical significance than surface temperature, and the former is probably a more significant parameter for study of past climates.

To sum up, several explanations may be offered to explain why temporal slopes are lower than spatial slopes over Greenland and why this discrepancy was apparently much greater during the last glacial. Most probably, this difference is due to changes either in the moisture origin or seasonality of the precipitation, or in the strength of the inversion layer (or obviously to a combination of these changes). Unfortunately, we are not yet able (even in a model world) to assess the influence of each of these factors taken individually.

However, we have strong evidence that taken together, the influence of these various factors does not mask the local temperature signal in the isotopic record. To illustrate this, Jouzel *et al.* [1994] examined, with the  $8 \times 10$  GISS model, the relative influences of local temperature and other parameters on the glacial-interglacial isotope shifts by plotting the change in  $\delta^{18}\text{O}$  against the concurrent change in local temperature over the Laurentide Ice Sheet region. The same plot is given for the grid squares comprising the combined Laurentide and Greenland Ice Sheets by Jouzel *et al.* [1996]. This shows a strong correlation ( $r^2 = 0.72$ ) between  $\Delta\delta^{18}\text{O}$  and  $\Delta T_s$ , which indicates that over 70% of the simulated  $\Delta\delta^{18}\text{O}$  changes are accounted for by local temperature changes alone (note that the strength of the correlation gives an indication of the capacity to extract temperature changes from isotopic series but contains, by itself, no information on the value of the temporal slope). This suggests that climatic changes in other parameters, such as evaporative source, precipitation seasonality, and inversion strength (but the model also accounts for the intermittency of precipitation events and for the large changes in topography and atmospheric circulation) may explain less than 30% of the isotope signal. We give (Figure 8) the regression analysis of the  $4 \times 5$  GISS model results over Greenland alone. It is even more significant ( $r^2 = 0.76$ ), despite the smaller range of temperature differences.

As paleoclimatologists, we consider this result as extremely satisfying in that the GCM modeling approach confirms one important conclusion drawn from empirical estimates of the temporal slope [Cuffey *et al.*, 1995; Johnsen *et al.*, 1995], i.e., that the Greenland ice  $\delta^{18}\text{O}$  record is a faithful "thermometer" for the long-term temperature changes we have examined in these GCM experiments. We cannot, however, be as optimistic when examining the ECHAM model in the same way because the correlation coefficient, and thus the part explained by the temperature alone, is low there ( $r^2 = 0.22$ ). Whether this difference between the GISS and ECHAM models results from differing model physics [CLIMAP, 1981], from the use of a different ice sheet topography [Peltier, 1994], from too short integration times, or from other reasons has not yet been established. Also, experiments were run by Cole *et al.* [1993] using the GISS isotopic model to examine the relationship between isotope variability and interannual climate change which is relevant to smaller isotopic changes that characterized the recent period. These authors inferred that isotope response is less predictable between relatively similar climates than between glacial and interglacial climates.

As modelers, we are disappointed not to have been able to predict that temporal and spatial slopes differ for glacial-interglacial changes on which model experiments have focused, and not even to be, now, in a position to clearly assess why they differ. This is largely because beyond the fairly strong link between precipitation isotopic content and local temperature that they have in common, the various isotopic models show differences as far as temporal slopes are concerned. These inconsistencies between isotopic models must be resolved (or at least understood). With this in mind, the isotope GCM groups are now promoting an intercomparison of their models. Ten-year simulations of several different climates (present-day, glacial, Little Ice Age, Climatic Optimum, 6 kyr B. P. and  $2\text{CO}_2$  climates) will be compared. In addition to the three models presently available (LMD-Paris, NASA/ GISS-New York and ECHAM-Hamburg with, in each case, coarse and fine grid versions), isotopes are now being incorporated into



## Data Assimilation in the Ocean and in the Atmosphere: What Should be Next?

By Eugenia Kalnay (Chair)

*National Centers for Environmental Prediction, Washington DC*

David L.T. Anderson

*Oxford University*

Andrew F. Bennett

*Oregon State University*

Antonio J. Busalacchi, Stephen E. Cohn

*NASA/Goddard Space Flight Center*

Philippe Courtier

*European Centre for Medium-range Weather Forecasts*

John Derber

*National Centers for Environmental Prediction, Washington DC*

Andrew C. Lorenc

*United Kingdom Meteorological Office*

David Parrish, James Purser

*National Centers for Environmental Prediction, Washington DC*

Nobuo Sato

*Japan Meteorological Agency*

and

Thomas Schlatter

*NOAA/Forecast Systems Laboratory*

*(Manuscript received 8 May 1995, in revised form 14 November 1996)*

As part of the International Symposium on Assimilation of Observations in Meteorology and Oceanography, a panel discussion was held on the

evening of 15 March 1995. The purpose of this panel discussion was to focus on what the next major areas of research in data assimilation should be. The panelists had five minutes each for short presentations and this was followed by an open discussion. The



Kalman filters, representers, *etc.* This preprocessing will require a good understanding of the fine-scale phenomena.

3. Least-squares methods such as Kalman filters and variational schemes are inefficient estimators of non-Gaussian fields such as chemical tracers. Regardless of the modeling technique employed (Lagrangian methods seem best), a least-squares assimilation scheme will smear fine structure. The estimator of maximum likelihood must be sought, by examination of tracer probability distributions.

*Antonio J. Busalacchi*

Questions on ocean data assimilation at the end of the Tropical Ocean and Global Atmosphere (TOGA) program, and start of the Global Ocean-Atmosphere-Land System (GOALS) Program:

How routine, if not operational, short-term climate prediction will generate the need/demand for operational ocean data assimilation? This might also point to a possible distinction between ocean data assimilation for monitoring versus that for prediction.

How the skill of short-term climate prediction can be a very powerful metric for assessing the impact of various ocean data sets and types?

Need for assessing the total ocean observing system: not just *in situ* observations by themselves, and not just remotely sensed observations in isolation, but the need to consider the two types together.

What does it mean to be doing data assimilation into a coupled forecast model?

"... Characterization of the errors in the forcing, errors in the observations, and errors in the models are all at a rather rudimentary level. Numerous assumptions and simplifications are made when constructing present error covariance structures. If the merging of models with data is to be truly optimal, there will be an ever increased need for improved error estimates as more and more data from the observing systems in the tropics become assimilated. This will include a closer examination of what constitutes noise as opposed to real small-scale structure supported by observations. Access to more data should also permit data to be withheld in support of more rigorous evaluations of the impact of assimilated data. A case in point are the theoretical estimates of analysis errors provided by the Kalman filter, and the need to verify these estimates against actual data.

With a few exceptions, most of the data assimilation efforts for the tropical oceans have demonstrated the potential of a particular assimilation method. However, the relative importance of one scheme versus another for practical applications has not been addressed. For example, do the benefits

of implementing a Kalman filter or adjoint method outweigh the computational expense involved? In other words, for the present implementation of these methods in reduced-gravity models, what improvements are made to the height fields above and beyond those with a straightforward use of optimal interpolation? Do the finite degrees of freedom contained in today's limited ocean data sets justify the vast state spaces required to solve the Kalman filter or the adjoint? Is it practical and advisable to implement versions of the Kalman filter and the adjoint in tropical ocean models more complex than linear shallow-water models? Alternatively, can more information be extracted when assimilating today's ocean data into a GCM if assimilation techniques other than optimal interpolation or successive corrections are used? As more of these questions are answered, data assimilation will become less of an end in itself and more of a tool in support of larger process and phenomenological studies. A unique advantage of tropical ocean data assimilation is that some of these questions will be answered in the context of the impact on the initial conditions for coupled ocean-atmosphere model forecasts. Prediction skill will be a very powerful metric. Routine short-term climate predictions will create a sustained demand for the data and provide a means to quantify the impact of a particular data type and assimilation methodology" (Busalacchi, 1996).

*Stephen E. Cohn*

While the last few years have witnessed great progress in the field of data assimilation, there remain far more open questions than solved ones. Some of the open questions are categorized here into three general areas.

#### *Area 1. New Types of Data Assimilation Problems*

For many years, the primary purpose of data assimilation was to provide initial conditions for numerical weather forecasts. In estimation theory terminology, this corresponds to the filtering problem. The analysis is based on data observed up to and including the analysis time. The traditional measure of success is the accuracy of forecasts issued from the analyses.

Reanalysis projects are now underway at various institutions. Since reanalyses are produced off-line, in delayed time, one can in principle use data observed well past each analysis time to produce each analysis, in effect doubling the amount of data incorporated into each analysis. This sort of data assimilation problem can be considered to be a fixed-lag smoothing problem. Is there a way to carry out fixed-lag smoothing in a computationally efficient manner? In reanalysis projects the measure of success should be the quality of the analyses, rather than that of forecasts. The most accurate analysis does not necessarily lead to the most accurate fore-



## The Interplay between Transpiration and Runoff Formulations in Land Surface Schemes Used with Atmospheric Models

RANDAL D. KOSTER

*Hydrological Sciences Branch, Laboratory for Hydrospheric Processes, NASA/Goddard Space Flight Center, Greenbelt, Maryland*

P. C. D. MILLY

*U.S. Geological Survey, Geophysical Fluid Dynamics Laboratory/NOAA, Princeton, New Jersey*

(Manuscript received 1 July 1996, in final form 20 November 1996)

### ABSTRACT

The Project for Intercomparison of Land-surface Parameterization Schemes (PILPS) has shown that different land surface models (LSMs) driven by the same meteorological forcing can produce markedly different surface energy and water budgets, even when certain critical aspects of the LSMs (vegetation cover, albedo, turbulent drag coefficient, and snowcover) are carefully controlled. To help explain these differences, the authors devised a monthly water balance model that successfully reproduces the annual and seasonal water balances of the different PILPS schemes. Analysis of this model leads to the identification of two quantities that characterize an LSM's formulation of soil water balance dynamics: 1) the efficiency of the soil's evaporation sink integrated over the active soil moisture range, and 2) the fraction of this range over which runoff is generated. Regardless of the LSM's complexity, the combination of these two derived parameters with rates of interception loss, potential evaporation, and precipitation provides a reasonable estimate for the LSM's simulated annual water balance. The two derived parameters shed light on how evaporation and runoff formulations interact in an LSM, and the analysis as a whole underscores the need for compatibility in these formulations.

### 1. Background

The overall goal of the Project for Intercomparison of Land-surface Parameterization Schemes (PILPS) is to compare the numerous land surface models (LSMs) that are currently used with atmospheric general circulation models (GCMs) and mesoscale models (Henderson-Sellers et al. 1993) and to understand any differences found in their behavior. In the initial phase of PILPS, land surface modelers were provided with a common set of soil and vegetation physical characteristics and a full year of GCM-generated meteorological forcing for two land surface biomes (tropical forest and a grassland) and were asked to generate surface energy and water balances for each. The salient result was the wide disparity in the balances generated by the different schemes (Pitman et al. 1993).

This disparity is not surprising given the numerous model-specific parameterizations that comprise a typical LSM. In fact, the interactions among the components of an LSM are so complex that isolating and quantifying a given component's contribution to the disparity is very

difficult. Partly for this reason, PILPS participants were asked to perform some supplemental simulations that imposed further controls on certain processes. In the most tightly controlled of these simulations, the LSMs used common, prescribed values of vegetation coverage, albedo, and surface-to-air bulk transfer coefficients for heat and vapor. In effect, further controls were imposed in the tropical forest version of this experiment relative to the grassland version because the former avoided intermodel differences in snow formulation and in the seasonal variation of surface characteristics, such as leaf-area index.

The tropical forest version of this tightly controlled experiment has been referred to in PILPS documentation as "TRF-HAR" (with "TRF" denoting tropical forest, "H" denoting homogeneous vegetation, "A" denoting fixed albedo, and "R" denoting fixed transfer coefficients). Figure 1 shows the annual evaporation produced for TRF-HAR by the different PILPS participants (Table 1). In spite of the added controls, the evaporation, which is a key term in both the water and energy balances, still varies significantly among the LSMs. The annual evaporation has a standard deviation of  $0.79 \text{ mm day}^{-1}$ , equivalent to  $22 \text{ W m}^{-2}$ .

This degree of intermodel variability has persisted into more recent phases of PILPS, which focus on testing LSM outputs against observations (e.g., Chen et al.

---

Corresponding author address: Dr. Randal D. Koster, Hydrological Sciences Branch, NASA/GSFC, Code 974, Greenbelt, MD 20771.  
E-mail: randal.koster@gsfc.nasa.gov



## 5. Summary

We emphasize that the monthly water balance model (MWBM) is not being introduced here as a potential substitute for more complex land surface models (LSMs) in climate studies. The functional relationships fitted for the MWBM are the net, effective result of more physically based parameterizations, and the examination of the same vegetation type under different conditions would lead to changes in these relationships that cannot be predicted *a priori*. (Indeed, the fitted MWBM parameters presented in Table 1 are consistent with the LSMs' response to imperfect GCM forcing over the Amazon and might not describe the LSMs' behavior under less extreme conditions. These particular values are in any case subject to error given their derivation from monthly diagnostics.) Operational use of the MWBM is further limited by the prescription, rather than prediction, of interception loss and potential evaporation and by complications associated with snowfall and seasonally varying vegetation characteristics.

We instead introduce the MWBM as a tool for understanding the differences in evaporation rates shown in Fig. 1 and, in particular, for understanding how the interplay between evaporation and runoff formulations affects simulated soil water dynamics. The MWBM successfully reproduces the evaporation rates of each of the sixteen PILPS LSMs (Figs. 3 and 4). This implies that we can relate much, if not most, of the evaporation differences in Fig. 1 differences in MWBM parameter values—that is, to different interception loss rates and different functional relationships between root zone soil moisture and (a) transpiration efficiency ( $\beta_T$ ), (b) surface runoff generation, and (c) root-zone drainage generation.

These different functional relationships can in turn be represented very simply by two derived parameters: (a) the average of the  $\beta_T$  function across the active soil moisture range,  $\langle\beta_T\rangle$ , and (b) the fraction of this range over which runoff can form,  $f_R$ . We have, in fact, shown that the intermodel variability in Fig. 1 for the PILPS TRF-HAR experiment can be discussed in terms of intermodel variations in interception loss and in these two parameters. If we know  $\langle\beta_T\rangle$  and  $f_R$  for a given LSM, and if we can characterize the climate in terms of an index of dryness (as modified by known interception loss rates), we can predict the annual ratio of soil water evaporation to applied throughfall using (18) alone—that is, without detailed knowledge of the LSM's formulations, which may be very complex.

The values of  $\langle\beta_T\rangle$  and  $f_R$  in an LSM are determined by the shapes and relative positions of the LSM's effective  $\beta_T$ ,  $R$ , and  $G$  functions, that is, by the nature of soil moisture's simultaneous control over evaporation and runoff. We infer that one requirement for an accurate simulation of a region's water budget (and thus energy budget) is compatibility between the LSM's evaporation and runoff formulations. The simple sensitivity exper-

iments in Fig. 9 demonstrate that even a "perfect" description of canopy structure and stomatal behavior, toward which many LSMs strive, does not ensure realistic evaporation rates if the runoff formulation remains relatively crude or incompatible with the evaporation formulation. Understanding the interaction between evaporation and runoff processes in an LSM—understanding, for example, how runoff processes affect soil moisture and thereby the active part of the effective  $\beta_T$  curve—is critical to a full understanding of the LSM's behavior.



# The perennial ice cover of the Beaufort Sea from active- and passive-microwave observations

R. KWOK,<sup>1</sup> J. C. COMISO<sup>2</sup>

<sup>1</sup>*Jet Propulsion Laboratory, California Institute of Technology, 4800 Oak Grove Drive, Pasadena, CA 91109, U.S.A.*

<sup>2</sup>*Laboratory for Hydrospheric Processes, Goddard Space Flight Center, Greenbelt, MD 20771, U.S.A.*

**ABSTRACT.** The perennial ice concentration in the Beaufort Sea was examined using active- and passive-microwave observations. We compared the ice type and concentration estimates from SSM/I and ERS-1 SAR data over a seasonal cycle from January 1992 to January 1993. It was found the multi-year (MY) ice-concentration estimates from the SAR data were very stable and were nearly equivalent to the ice concentration estimated at the end of the previous summer. We contrast this with the variability of the MY ice-concentration and ice-fraction estimates obtained using the NASA Team algorithm. The passive- and active-microwave algorithms provide total ice concentrations that are comparable during the winter, but the passive estimates are significantly lower during the summer. Passive-microwave estimates of multi-year-ice concentrations are consistently lower (up to 30%) than those from the SAR data. We discuss reasons for these discrepancies and the possible biases introduced by the active and passive algorithms.

## INTRODUCTION

The radar imagery from the ERS-1 Synthetic Aperture Radar (SAR) provides an alternate view of the sea-ice cover in addition to the relatively long record provided by the SSM/I multichannel radiometer. The NASA sea-ice algorithm, or "Team" algorithm (Cavalieri and others, 1984), routinely estimates ice type and ice concentrations from passive-microwave observations. However, the procedures used to estimate these same parameters from active-microwave observations (Kwok and others, 1992; Comiso and Kwok, 1996) are still relatively new. Large-scale (temporal and spatial) comparative studies between the estimates from the active and passive datasets are limited by the coverage, and hampered by the volume of high-resolution ERS-1 SAR data. Here, we present a regional scale comparative study of the ice-cover parameters inferred from the active- and passive-microwave datasets. The objectives of this study are: to compare the retrieval results obtained using the active and passive procedures, and to understand the physical meaning of these differences and what they imply about the state of the ice cover.

If records of the Team algorithm results are examined, one finds that the estimates of multi-year (MY) ice concentration in the winter are much lower (by up to 30%) than those of the summer total-ice concentration. From a mass-balance perspective, such large discrepancies need to be resolved. If ice that survives the summer is classified as MY ice, then the MY-ice concentration during the winter should be nearly equivalent to the ice concentration during the previous summer's minima, differing by an amount due to melt, ridging, new/young ice formation and export of ice from the Arctic. This mismatch was noted by a number of investigators in terms of the variability of the multichannel microwave signatures of sea ice on regional studies (Thomas, 1993), from comparison with surface measurements (Gren-

fell and Lohanick, 1985; Grenfell, 1992), and from a mass-balance perspective (Comiso, 1990; Rothrock and Thomas, 1990; Gloersen and others, 1992; Thomas and Rothrock, 1993).

## DATA DESCRIPTION

The comparative analysis of the active and passive ice type and concentration estimates was conducted in the region shown in Figure 1. This covers an area of approximately  $1.35 \times 10^6 \text{ km}^2$ . The selection of this region was based on the dataset available to us at the time of the study, through

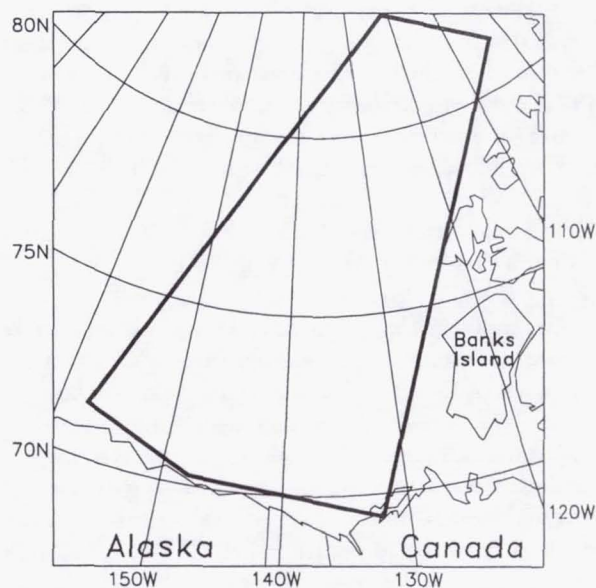


Fig. 1. The comparative analysis uses ERS-1 SAR and SSM/I data from the region defined by these boundaries.



properly accounted for.

There is also a large difference between MY ice-concentration estimates from the SAR and the Team algorithms. The differences are likely to be due to the spatial variations in the emissivity of sea ice in the Arctic region (Carsey, 1982; Comiso, 1983). One factor that causes such spatial changes in the emissivity (as high as that of FY ice) is melt ponding, since frozen melt ponds are known to have emissivities of first-year ice (Grenfell, 1992). This can be a substantial effect, since 20–30% of the summer ice has been observed to be ponded (personal communication from W. B. Tucker, 1994). Another factor could be unusually thick snow cover in some areas that can cause flooding (and subsequent refreezing) at the snow–ice interface. Such effects cause the snow–ice interface to be saline and the emissivity of the ice floe to be similar to that of FY ice. We also note that the depth of the snow cover tends to decrease the gradient ratio that would lead to a positive bias in the MY concentration.

Do the SAR algorithms overestimate MY-ice concentration? It has been reported (Rignot and Drinkwater, 1994) that deformed FY ice has backscatter characteristics similar to that of MY ice in single polarization C-band datasets like ERS-1. This would cause the SAR winter algorithm to overestimate the MY-ice concentration. Due to deformation of the ice cover, the amount of deformed ice should increase as the winter wears on, resulting in a gradual increase in the estimated MY-ice concentration. Such a trend was not observed in the data, at least not within the level of uncertainty of the estimates. The effect of the ridging process is discussed, with an example: if there is a 15% convergence of the ice cover, and this FY-ice area is converted into deformed ice, what is the expected bias in the MY-ice concentration if the signature of deformed ice is identical to that of FY ice? When FY ice ridges, and here it is assumed that we only ridge the very thin ice from closing of leads, the area is not conserved. The mechanical thickness redistribution takes the volume of ice participating in a ridging event, and creates an approximately equivalent volume of ice occupying a smaller area. As a crude estimate, if the assumption is made that all ridged ice is five times its original thickness before ridging (a parameter used by Thorndike and others, 1975) then the contribution of the FY ice area after convergence is much smaller. The 15% undeformed-ice area now occupies an area of 3%.

This leads to a very significant question. If large volumes of FY ice are piled onto MY ice, is this area labelled as MY ice or FY ice? The SAR algorithms described here would label the area as MY. The passive algorithms might label that area differently, depending on the emissivity of that ice. It does not seem to be important from the heat-flux point-of-view, because thick ice makes a relatively small contribution to the total flux, but it is certainly important from the mass-balance point-of-view. It is possible that deformed FY ice is piled onto the MY ice, and therefore does not increase the concentration of MY ice, even though the polarimetric radar senses a surface type (Rignot and Drinkwater, 1994) which seems to be different than that of MY ice. The areal contribution of this deformed FY/MY

ice type is not known. If the areal fraction of this surface type is significant, it would affect the passive-microwave retrieval algorithms as well.

## SUMMARY/DISCUSSION

Over the annual cycle, the total-ice concentration remained fairly high in the region of study. From the Team-algorithm estimates, a significant decrease was observed in the amount of MY ice (almost 40%) between January and prior to spring melt, and a slow increase in the amount of MY ice between September and December. The MY-ice concentration at freeze up (October) is much lower than the ice concentration at the end of summer (August), an inconsistency in the analysis that suggests an underestimation of MY ice in the winter time.

The SAR analyses suggest an ice cover in the Beaufort Sea that is stable away from the seasonal ice zone, throughout a season, in terms of MY-ice concentration. The amount of MY ice remained approximately constant, within the level of uncertainty of the analysis. The average MY-ice concentration in this part of the Arctic Ocean is approximately 80%. The MY-ice concentration is approximately equivalent to the ice concentration at the end of the summer. These analyses seem to provide a consistent view of the annual cycle from an ice-balance perspective. The C-band radar, to first-order, is not affected by snow cover when the temperature is below freezing, and is much less sensitive to weather effects than the higher frequency radiometer channels. The equivalence between summer ice minima and winter MY-ice concentration, and the small fluctuations in the SAR estimates in the winter, suggest that these estimates are at least consistent. At this point, the analysis of the SAR data offers another estimate of the MY ice, which seems to be consistent with the summer ice concentration.

Because melt ponds have signatures of open water and the Team algorithm does not discriminate between the two surface types, the Team algorithm underestimates the ice concentrations in the summer. If the melt-pond concentration is 30%, then the ice concentration would be underestimated by a similar amount. This is consistent with the differences between the SAR analysis and the Team algorithm analysis: the SAR estimates of total-ice concentration is always higher than that of the Team algorithm estimates in the summer. If the Team algorithm underestimates the total-ice concentration due to melt ponds, especially in the ice margin in the summer, then computed total-ice area would also be underestimated.

The estimates from the SAR and Team algorithms provided two fairly different views of the Beaufort Sea ice cover. The limitations of both algorithms were discussed. The differences explain some of the possible biases of these algorithms due to variability in signature as functions of wavelength and environmental conditions. Future investigations using these datasets should exercise caution in terms of the possible biases introduced by these analysis algorithms.



## A soil-canopy-atmosphere model for use in satellite microwave remote sensing

Venkataraman Lakshmi,<sup>1</sup> Eric F. Wood, and Bhaskar J. Choudhury<sup>2</sup>

Water Resources Program, Department of Civil Engineering and Operations Research, Princeton University, Princeton, New Jersey

**Abstract.** Regional and global scale studies of land-surface-atmosphere interactions require the use of observations for calibration and validation. In situ field observations are not representative of the distributed nature of land surface characteristics, and large-scale field experiments are expensive undertakings. In light of these requirements and shortcomings, satellite observations serve our purposes adequately. The use of satellite data in land surface modeling requires developing a hydrological model with a thin upper layer to be compatible with the nature of the satellite observations and that would evaluate the soil moisture and soil temperature of a thin layer close to the surface. This paper outlines the formulation of a thin layer hydrological model for use in simulating the soil moistures and soil temperatures. This thin layer hydrological model is the first step in our attempt to use microwave brightness temperature data for regional soil moisture estimation. The hydrological model presented here has been calibrated using five years (1980–1984) of daily streamflow data for the Kings Creek catchment. The calibrated parameters are used to validate the daily streamflows for the next 5 year period (1985–1989). The comparison of surface soil moistures and surface temperatures for the period of the Intensive Field Campaigns (IFCs) during the First ISLSCP (International Satellite Land Surface Climatology Project) Field Experiment (FIFE) in 1987 is carried out and yields good results. The thin layer hydrological model is coupled with a canopy radiative transfer model and an atmospheric attenuation model to create a coupled soil-canopy-atmosphere model in order to study the effect of the vegetation and the soil characteristics on the Special Sensor Microwave Imager (SSM/I) brightness temperatures. The sensitivities of the brightness temperatures to the soil and vegetation is examined in detail. The studies show that increasing leaf area index masks the polarization difference signal originating at the soil surface.

### 1. Introduction

Surface soil moisture is perhaps the most important indicator of land surface response to atmospheric forcing and provides feedback to the atmosphere. The proper estimation of soil moisture would greatly enhance our understanding of land-surface-atmosphere interactions. Surface soil moisture plays an important role in partitioning rainfall into infiltration and runoff. The land surface evaporation and transpiration depend on the amount of soil moisture available. Together, surface temperature and soil moisture determine the land surface heat and water balance. In large-scale modeling, the soil moisture and temperature are important in deciding the depth of the planetary boundary layer, circulation/wind patterns [Mahfouf *et al.*, 1987; Lanicci *et al.*, 1987; Zhang *et al.*, 1982] and regional water and energy budgets. It is therefore important for improved modeling of these quantities and the use of observational data on scales comparable to the modeling scales. Satellite data are useful in this regard. Research in and

utilization of remotely sensed data is important for the purposes of understanding spatial variability and regional scales and in verifying land surface parameterizations [Wood, 1991].

Projects like the Global Energy and Water Experiment (GEWEX) Continental Scale International Project (GEWEX) involve the development and testing of hydrological models on a continental scale over the southern plains of the United States. The availability of data sets for the validation of continental scale soil moisture simulations would be very useful. There are many advantages to remote sensing as a method of soil moisture determination as compared to field sampling. Field sampling is point based and does not give a clear picture of the variation of the soil moisture over an area. Accuracy (difference between the actual soil moisture pattern and the interpolated soil moisture pattern) of interpolation schemes depends on the closeness of the sampled soil moisture data points and the heterogeneity of the soil moisture distribution. In the case where the correlation lengths of soil moisture are smaller than the measurement spatial interval, ground-based data collection may result in the biased sampling of the soil moisture.

Satellite remote sensing offers spatial coverage and a certain temporal frequency in monitoring soil moisture from space. The microwave frequencies of the electromagnetic spectrum are the most sensitive to the variations of soil moisture [Schmugge, 1985] due to the polar nature of water. This change in dielectric constant of the soil (caused by changes in soil moisture) is recorded as changes in the radiation emitted by

<sup>1</sup>Now at General Sciences Corporation, Laboratory for Atmospheres, NASA Goddard Space Flight Center, Greenbelt, Maryland.

<sup>2</sup>Now at Hydrological Sciences Branch, NASA Goddard Space Flight Center, Greenbelt, Maryland.



case is not shown here because the results for 37 GHz qualitatively resemble that for 19 GHz and has no new features.

## 7. Conclusions

A thin layer model of hydrology with complete water and energy budgets has been presented here. The model is built on the framework of *Mahrt et al.* [1984] for inclusion of a thin upper layer. The parameterizations include the moisture gradient driven flux for diffusion of water from the lower layer to the upper layer to replenish the moisture lost during evaporation. It should be pointed out that in application of the *Mahrt and Pan* [1984] scheme, the conclusions of *Mahrt and Pan* [1984] hold good for clay type of soils and will not work for sand. The soil type in our application is silt loam whose properties are closer to clay than to sand, hence the appropriateness of this approach.

The hydrological model is applied over a 10 year period. The observed daily streamflows from 1980 to 1984 are used to calibrate the model parameters. The simulated streamflows are validated over the 1985–1989 period. The comparisons between observed and simulated streamflows have been good given the fact that the rain gage used for rainfall input was about 16 km away from the catchment. The aim of this paper was not to develop a model for accurate streamflow prediction. The aim of this paper is to develop a scheme to predict the surface temperature and soil moisture with a sufficient degree of accuracy for the 1 cm surface layer. The streamflow is compared to determine that the hydrological model behaves properly with the rainfall process. The model-simulated soil moistures and surface temperatures are compared for the time periods during the four IFCs in FIFE. This model produces values of the 1 cm layer soil moistures which agree with our understanding of hydrology. This hydrological model shows a definite promise in estimating soil moisture and can be used along with microwave satellite data.

The 19 and 37 GHz polarization difference indices have a greater range between the residual and the saturated soil moisture levels, showing greater sensitivity to soil moisture variations. The sensitivity of the polarization difference index to the soil moisture is affected by the leaf area index; an increase in leaf area index decreases this sensitivity; an increase in soil moisture results in increased sensitivity followed by a decrease in sensitivity at high soil moistures. Among the vegetation parameters, the stem area index and the canopy moisture content affect the polarization difference the greatest. An increase in the stem area index and/or the canopy moisture content results in a masking of the polarization difference signal originating at the soil surface. We wish to caution the reader(s) that a straight forward regression type of analysis (between soil moisture and polarization difference index) may not work without due attention to the sensitivities and uncertainties that are studied in this paper. Ignoring these may result in incorrect results.

It is proposed that this model can be used in conjunction with passive microwave satellite data for soil moisture estimation. The 19 and 37 GHz Special Sensor Microwave Imager (SSM/I) brightness temperature data are proposed to be used for the study. This does not imply that the microwave brightness temperature data are the only way to estimate soil moistures. We would emphasize at this point that the use of satellite data is useful given its spatial and temporal coverage, and it can be used in conjunction with hydrological modeling to achieve better estimates of soil moisture. Microwave satellite

data at lower frequency (6.6 GHz) has been used in the past to infer soil moisture [*Owe et al.*, 1992] and soil wetness [*Choudhury and Monteith*, 1988]. These, however, use simple regression-based relations between soil moisture (or antecedent precipitation index API) and brightness temperature. In the case of higher frequencies (such as the 19 and 37 GHz frequencies that we propose to use), a simple inversion may not be very effective. It is desired that a complete model of soil hydrology providing the surface temperature and soil moisture along with a radiative transfer model for the plant canopy and an attenuation model for the atmosphere would be used to simulate the SSM/I brightness temperature and subsequently help in retrieving soil moistures from observed brightness temperatures. The model of thin layer soil hydrology will help in this regard.



## Investigation of effect of heterogeneities in vegetation and rainfall on simulated SSM/I brightness temperatures

V. LAKSHMI†, E. F. WOOD and B. J. CHOUDHURY‡

Water Resources Program, Department of Civil Engineering and Operations Research, Princeton University, Princeton, NJ 08544, U.S.A.

(Received 24 July 1996; in final form 26 November 1996)

**Abstract.** Land surface characteristics: soil and vegetation and rainfall inputs are distributed in nature. Representation of land surface characteristics and inputs in models is lumped at spatial scales corresponding to the grid size or observation density. Complete distributed representation of these characteristics or inputs is infeasible due to excessive computational costs or costs associated with maintaining dense observational networks. The measurements of microwave brightness temperatures by the SSM/I (Special Sensor Microwave Imager) are at resolutions of the order of  $56\text{ km} \times 56\text{ km}$  for 19 GHz and  $33\text{ km} \times 33\text{ km}$  for 37 GHz. At these resolutions, soil moisture and vegetation are not homogeneous over the measurement area. The experiments carried out in this study determine the effect of heterogeneities in vegetation (leaf area index) and input rainfall on simulated soil moisture and brightness temperatures and the inversion of brightness temperatures to obtain soil moisture estimates. This study would help us to understand the implications of using the SSM/I microwave brightness temperatures for soil moisture estimation. The consequences of treating rainfall inputs and vegetation over large land surface areas in a lumped fashion is examined. Simpler methods based on dividing the leaf area index or input rainfall into classes rather than explicit representation for representing heterogeneities in leaf area index and spatial distribution of rainfall is tested. It is seen that soil moisture is affected by the representation (lumped vs distributed) of rainfall and not leaf area index. The effect of spatially distributed soil moisture on the inversion of observed SSM/I brightness temperatures to obtain soil moisture estimates is investigated. The inversion process does not exhibit biases in the retrieval of soil moisture. The methodology presented in this paper can be used for any satellite sensor for purposes of analysis and evaluation.

### 1. Introduction

Regional soil moisture is a very important variable in continental scale water and energy budgets. Soil moisture is an integrated response of the soil-vegetation system to the atmospheric forcing. The Special Sensor Microwave Imager (SSM/I) has a resolution of about  $56\text{ km}$  at 19 GHz and  $33\text{ km}$  at 37 GHz (Hollinger *et al.* 1990). At this spatial coverage, there are bound to be heterogeneities in leaf area index and variability in soil moisture caused by spatial variations in rainfall input, among other factors. The microwave brightness temperature reported at these

† V. Lakshmi is with General Sciences Corporation, Laboratory for Atmospheres, Code 910.4, NASA/Goddard Space Flight Center, Greenbelt, MD 20771, U.S.A.

‡ B. J. Choudhury is with Hydrological Sciences Branch, Code 974, NASA/Goddard Space Flight Center, Greenbelt, MD 20771, U.S.A.



## **7. Conclusions**

In the above discussions of the effects of heterogeneity on the simulated soil moisture and polarization difference index, no reference has been made to the actual variations of leaf area index or spatial distribution and coverage of rainfall in the SSM/I field of view. The SSM/I field of view is  $56 \times 56$  km for the 19 GHz frequency and  $33 \times 33$  km for the 37 GHz frequency. There are variations in leaf area index and rainfall at these scales. However, instead of explicitly investigating for a particular set of variations, an entire spectrum of variations were investigated in this paper. The coefficient of variation for the leaf area index of 0.655 (corresponding to the FIFE site), 1.0 and 2.0 results in a range of standard deviations up to 2.2. The mean leaf area index in this study varies between 0.02 and 1.5. This is a range of variation for the midwestern United States, corresponding to Kansas. This does not mean that this study is relevant only to Kansas but holds good for the presented range of leaf area index data, rainfall and its variability.

Polarization difference index is a measure of the soil moisture. The sensitivity of the polarization difference index to the soil moisture is affected by the leaf area index; an increase in leaf area index decreases this sensitivity. The effect of heterogeneity of leaf area index and the spatial variability of rainfall on the surface soil moisture and the SSM/I observations through the use of the polarization difference index is examined. The results show that lumped representation of vegetation variability (variability of leaf area index) does not result in a bias for soil moisture or polarization difference index. An average value of leaf area index would be a sufficient representation. On the other hand soil moisture and polarization difference index show sensitivity to the distributed rainfall representation. An increase in the coefficient of variation of the leaf area index does not affect the soil moisture and the polarization difference index whereas increase in fractional coverage of rainfall reduces the bias and the root mean squared differences between the lumped and the spatially distributed representation of rainfall. The surface temperature is a very stable variable and shows almost no change for the different cases of heterogeneity. The differences between the surface temperature and the corresponding air temperatures are very small, and the air temperatures are used in place of surface temperatures in the soil moisture estimation from SSM/I brightness temperature data. In the case of using the SSM/I observations for soil moisture estimation, the heterogeneity in vegetation and spatial distribution and coverage of rainfall (hence distributed soil moisture) is seen not to introduce a bias. Therefore, it is concluded that for this case study, the relationship between the SSM/I brightness temperature and the soil moisture and vegetation leaf area index is only weakly nonlinear for the given range of leaf area index variations. This weak nonlinearity does not introduce a bias in the soil moisture estimation using the SSM/I brightness temperature data. This is very encouraging for the use of the SSM/I sensor for the estimation of soil moisture.

EOS platforms will carry various sensors like the AIRS-AMSU, MISR, MODIS etc. All these sensors have a field of view which would contain heterogeneity in the sampled geophysical variables. The use of analysis like the one presented in this paper would give a greater understanding on the interpretation of a single brightness temperature (or radiance) corresponding to the field of view as well as the retrieved geophysical variable using this brightness temperature (or radiance). It is possible that the brightness temperature from some channels may result in biased retrievals. Simulation studies will help in detecting such situations and corrections can be prescribed.



## Evaluation of Special Sensor Microwave/Imager Satellite Data for Regional Soil Moisture Estimation over the Red River Basin

VENKATARAMAN LAKSHMI,\* ERIC F. WOOD, AND BHASKAR J. CHOUDHURY†

*Water Resources Program Department of Civil Engineering and Operations Research,  
Princeton University, Princeton, New Jersey*

(Manuscript received 14 August 1996, in final form 8 January 1997)

### ABSTRACT

Regional-scale estimation of soil moisture using in situ field observations is not possible due to problems with the representativeness of the sampling and costs. Remotely sensed satellite data are helpful in this regard. Here, the simulations of 19- and 37-GHz vertical and horizontal polarization brightness temperatures and estimation of soil moistures using data from the Special Sensor Microwave/Imager (SSM/I) for  $798\ 0.25^\circ \times 0.25^\circ$  boxes in the southwestern plains region of the United States for the time period between 1 August 1987 and 31 July 1988 are presented. A coupled land-canopy-atmosphere model is used for simulating the brightness temperatures. The land-surface hydrology is modeled using a thin-layer hydrologic model. The canopy scattering is modeled using a radiative transfer model, and the atmospheric attenuation is characterized using an empirical model. The simulated brightness temperatures are compared with those observed by the SSM/I sensor aboard the Defense Meteorological Satellite Program satellite. The observed brightness temperatures are used to derive the soil moistures using the canopy radiative transfer and atmospheric attenuation model. The discrepancies between the SSM/I-based estimates and the simulated soil moisture are discussed. The mean monthly soil moistures estimated using the 19-GHz SSM/I brightness temperature data are interpreted along with the mean monthly leaf area index and accumulated rainfall. The soil moistures estimated using the 19-GHz SSM/I data are used in conjunction with the hydrologic model to estimate cumulative monthly evaporation. The results of the simulations hold promise for the utilization of microwave brightness temperatures in hydrologic modeling for soil moisture estimation.

### 1. Introduction

Soil moisture is an important hydrologic variable in a variety of land-surface-atmosphere interactions. It is the response of the land surface to atmospheric forcing and controls the partitioning of rainfall into runoff and infiltration. Soil moisture affects (along with the surface temperature) the depth of the planetary boundary layer, circulation-wind patterns (Mahfouf et al. 1987; Lanicci et al. 1987; Zhang et al. 1982), and regional water and energy budgets. The study of global climate using global climate models (GCMs) has shown that soil moisture is a very important factor (Walker et al. 1977; Rowntree et al. 1983; Rind 1982; Mintz 1984). Evapotranspiration plays an im-

portant role in determining surface temperatures, surface pressure, rainfall, and motion (Shukla et al. 1982). Evapotranspiration in turn depends on soil moisture (together with incoming radiation and a host of other meteorological factors). Soil moisture is very closely connected to hydrology and climate (Yeh et al. 1984) and is important in agricultural applications. Simulated soil moisture can be compared to observations to determine the validity of the parameterizations used in modeling.

Projects like the Global Energy and Water Experiment Continental Scale International Project involve the development and testing of hydrologic models on a continental scale over the southern plains of the United States. The availability of datasets for the validation of continental-scale soil moisture would be very useful. Remote sensing methods have an advantage over in situ observations because they sample the variability and offer repeated temporal coverage. In addition, in situ observations are expensive and may result in biases depending on the heterogeneity of variations and the spatial sampling interval.

The microwave frequencies of the electromagnetic spectrum are the most sensitive to the variations of soil moisture (Schmugge 1985) due to the polar nature of water. Here, the choice of which passive microwave remote sensing system to use was dictated by the availability of only

\* Current affiliation: General Sciences Corporation, Laboratory for Atmospheres, NASA/Goddard Space Flight Center, Greenbelt, Maryland.

† Current affiliation: Hydrological Sciences Branch, NASA/Goddard Space Flight Center, Greenbelt, Maryland.

Corresponding author address: Dr. Venkataraman Lakshmi, General Sciences Corporation, Laboratory for Atmospheres, NASA/Goddard Space Flight Center, Greenbelt, MD 20771.  
E-mail: venkat@spectra.gsfc.nasa.gov



errors in assimilating the soil moistures into the hydrologic model using the results of the present work.

### 5. Conclusions and implications for future work

The coupled soil-canopy-atmosphere model has been used to simulate soil moisture and brightness temperatures for a region in the Red River basin of the southern United States. The 19- and 37-GHz simulations and comparisons with observed values were carried out on a  $0.25^\circ \times 0.25^\circ$  grid for a period of 1 yr between 1 August 1987 and 31 July 1988. The simulated brightness temperatures at 19 and 37 GHz were compared against the SSM/I-observed brightness temperatures. The root-mean-squared difference between the simulated and the observed average and the polarization difference brightness temperatures decreases as the comparison period for which the averaging is done is increased—that is, the monthly average brightness temperatures show a lower root-mean-squared difference than the weekly values, and the weekly values exhibit a lower error than the daily values. The simulated surface temperatures were compared with the observed surface temperatures derived from air temperature measurements. These results showed that the root-mean-squared error of the surface temperature at the time of the SSM/I overpass ranged between 1 and 4 K. The comparisons between the simulated and the 19-GHz SSM/I-estimated soil moistures show reasonable correlations. The range of the correlation coefficient increases as the time period of averaging for the soil moisture comparison decreases. The monthly average estimates of surface soil moisture derived from the SSM/I are interpreted in context with the monthly rainfall and the monthly averaged LAI. The SSM/I-derived monthly average surface soil moisture shows a very strong relationship with the cumulative monthly rainfall. The root-mean-squared differences between the SSM/I-derived and the hydrologic model estimates of soil moisture depend on the amount of vegetation. Higher values of LAI in the growing season mask the soil moisture signal and result in larger root-mean-squared differences. The cumulative monthly estimates of evapotranspiration computed using the SSM/I estimates of soil moisture in conjunction with the hydrologic model yielded good comparisons with the monthly estimates obtained via the atmospheric budget analysis.

The study described in this paper can be extended in time and space to achieve better understanding of more diverse situations. Extension of this study to a time period of 5 yr would help to explain some of the interannual variations observed by the SSM/I. This is very relevant in the discussions of SSM/I monthly climatology for the calculation of the mean monthly SSM/I-estimated soil moisture and the cumulative monthly evapotranspiration computed using the SSM/I and the hydrologic model. Extension of this analysis to a larger area (the Mississippi River basin or the Red-Arkansas

River basin) would definitely help to interpret the results in the context of varying geographic regions. The use of SSM/I data in conjunction with AVHRR NDVI data can help to monitor crop development and detect early stages of drought (Teng et al. 1995). Studies have shown that vegetation indexes like NDVI are good indicators of the onset of drought (Tucker 1989). The use of surface soil moisture information estimated using SSM/I in conjunction with the NDVI estimates from AVHRR may provide a better indicator of the vegetation information. The spatial resolutions of the SSM/I at 19 and 37 GHz are about 56 and 33 km, respectively. It is very difficult to plan field experiments at such large scales. However, if homogeneous areas (with respect to vegetation type) are chosen and a field experiment carried out to measure soil moisture, a valuable dataset will be provided with which the results of modeling and the estimation of soil moisture can be compared. Field experiments on large scales, such as the SSM/I resolution scale, will help bridge the gap that exists between small-scale field experiments and large-scale modeling.

We lack field observations of soil moisture over large scales. This makes it very difficult to quantify the errors in simulation and estimation. We therefore did the next best thing—made comparisons of SSM/I estimations and hydrologic simulations. This does not mean that the hydrologic simulations are the truth. It is our hope that large-scale field experiments will help us to create databases for the future and that SSM/I data can be used to estimate soil moisture, as well as the errors in estimation. These estimates can be used in a data-assimilation mode, which is one of our goals for land surface modeling efforts in the Earth Observing System context.

The importance of large-scale datasets of soil moisture cannot be emphasized enough. In situ field observations are expensive and may not be representative of the actual variations. The use of satellite microwave brightness temperatures will help us in the estimation of soil moistures and will, in conjunction with a hydrologic model, provide measures of evapotranspiration. These quantities (soil moisture and evapotranspiration) are useful for large-scale water and energy balances studies.



## Tracking of Ice Edges and Ice Floes by Wavelet Analysis of SAR Images

ANTONY K. LIU

*Oceans and Ice Branch, NASA/Goddard Space Flight Center, Greenbelt, Maryland*

SEELYE MARTIN

*University of Washington, School of Oceanography, Seattle, Washington*

RONALD KWOK

*Jet Propulsion Laboratory, California Institute of Technology, Pasadena, California*

(Manuscript received 27 December 1995, in final form 31 January 1997)

### ABSTRACT

This paper demonstrates the use of wavelet transforms in the tracking of sequential ice features in the *ERS-1* synthetic aperture radar (SAR) imagery, especially in situations where feature correlation techniques fail to yield reasonable results. Examples include the evolution of the St. Lawrence polynya and summer sea ice change in the Beaufort Sea. For the polynya, the evolution of the region of young ice growth surrounding a polynya can be easily tracked by wavelet analysis due to the large backscatter difference between the young and old ice. Also within the polynya, a 2D fast Fourier transform (FFT) is used to identify the extent of the Langmuir circulation region, which is coincident with the wave-agitated frazil ice growth region, where the sea ice experiences its fastest growth. Therefore, the combination of wavelet and FFT analysis of SAR images provides for the large-scale monitoring of different polynya features. For summer ice, previous work shows that this is the most difficult period for ice trackers due to the lack of features on the sea ice cover. The multiscale wavelet analysis shows that this method delineates the detailed floe shapes during this period, so that between consecutive images, the floe translation and rotation can be estimated.

### 1. Introduction

Because sea ice serves as an insulator between the ocean and atmosphere, calculation of the heat transfer between the two depends on an accurate determination of floe convergence and divergence, where the divergence generates open water areas within the pack. Specifically, in the pack ice interior and adjacent to coastlines, ice divergence generates quasi-permanent, large openings in the pack called polynyas. Because open water is exposed directly to the atmosphere in polynyas, they are regions of large heat flux and ice growth. This means that the polynyas are also regions of large brine production (Cavalieri and Martin 1994). Given the importance of the polynya heat loss, ice growth, and brine production, we would like to determine the ice divergence rates that generate the polynyas and the resultant polynya areas.

The European *ERS-1* synthetic aperture radar (SAR)

data used in this study were received and processed at the Alaska SAR Facility (ASF). In support of ice studies at ASF, the Geophysical Processors System (GPS) has been developed to manipulate and analyze the SAR data as well as provide routine generation of geophysical products. Within the GPS, the ice motion field is generated by first selecting an image pair, then performing an area-based matching predicated on a 2D correlation of the image intensity. This motion tracker has been successful in the Arctic winter (Kwok et al. 1990), but has difficulties with summer ice, coastal polynyas, and the marginal ice zone (MIZ). An alternate tracking method is described by McConnell et al. (1991), who use feature tracking to match floe boundaries in pairs of SAR images. If the ice contrast is reduced so that the boundaries between floes are no longer clear, as occurs in summer, this tracking scheme fails.

Our objective in this paper is to demonstrate the use of a 2D wavelet transform for feature tracking and identification in the SAR imagery, in particular in situations where the feature correlation techniques fail to yield reasonable results. The 2D wavelet transform that we employ is an efficient bandpass filter, which can be used to separate various scale processes and show their relative phase/location information, as shown for SAR im-

---

Corresponding author address: Antony K. Liu, Oceans and Ice Branch, NASA/Goddard Space Flight Center, Code 971, Greenbelt, MD 20771.

E-mail: liu@neptune.gsfc.nasa.gov



$f$ , namely, the window enclosing the closed contour for the template. A small value of  $m$  indicates that two patterns are similar; a large value indicates that they are different. Because  $f$  and  $g$  consist of binary digits, Eq. (4) can be further simplified by

$$m = \sum_R \text{XOR}(f, g). \quad (5)$$

This follows simply from the fact that the method of exclusive-or, XOR, of two binary digits always gives 0 when they are of the same value, otherwise 1. Thus, we only need to perform a logical XOR operation on the pairs of pixel values for each closed contour. The pair of binary images with the minimum  $m$  are those whose shapes have the best match. Figure 7c shows the sum of the differences  $m$  for comparison of all closed contours on 24 February to contour number 16 on 21 February. On 24 February, the contour number 80 has the lowest value of  $m$ , and we select it as the matched ice floe. The matched ice floe is then used in turn as a template to be correlated with the ice floes at a later time by repeating the above procedures so that ice floes can be tracked sequentially. Figure 8 shows the summary of our floe tracking results for 21, 24, and 27 February.

After the ice floe has been matched and tracked, a refined boundary can be obtained again by the method of proximity of approximation, discussed above for the ice edge tracking. First, we assemble edge elements obtained by wavelet transform using a small scale ( $a = 2$  units of pixel spacing) within the neighborhood of the approximate boundary, and then we link the center of mass of these edge elements consecutively, as shown in Fig. 9. The summary of floe tracking is also shown in Fig. 4. Notice that the detailed shape of the ice floe with sharp edges and corners is well delineated by this method. Based on these detailed floe shapes, the floe translation and rotation can be estimated. The floe speeds are approximately  $0.32 \text{ m s}^{-1}$  from 21 to 24 February, and then  $0.26 \text{ m s}^{-1}$  to 27 February. The rotations of floe due to the shear through the opening of polynya are approximately  $50^\circ$  and  $40^\circ$  from 21 to 24 February and to 27 February. Within 6 days, the floe has moved approximately 150 km and rotated about  $90^\circ$ .

In our second case study of ice floe tracking, we use two sequential SAR images in the Beaufort Sea during the summer of 1992 on 23 and 26 August. During summer, there is relatively little contrast between ice types due to the presence of liquid water on top of the ice surface that removes the contribution of the sea ice to the observed backscatter.

Figure 10 shows the contours of wavelet transform of a medium scale ( $a = 16$ ) with an above-zero threshold as a bandpass filter and labeled by index numbers for two SAR images separated by three days. By translation of these two contour maps, the contours from each map are found to match very well, as shown in Fig. 11. Most of contours can be identified after three days, and the degree of change/distortion can be estimated by mea-

suring the difference. The prominent ice floe with lesser change is used to construct its detailed shape using the same method of proximity of approximation. A small scale,  $a = 2$ , is chosen for wavelet transform to assemble edge elements within the neighborhood of the approximate boundary. The detailed shape of an ice floe can be constructed by linking the center of mass of these edge elements. Figure 12 summarizes the ice floe tracking results and the ice motion vector. Again, based on these detailed floe shapes, the floe motion of both translation and rotation can be estimated. In this case the ice floe speed is approximately  $0.12 \text{ m s}^{-1}$  with almost no rotation.

## 5. Discussion

In this paper, the 2D Gaussian wavelet transform is used at several scales to separate texture and features in SAR images of sea ice. The technique is applied to the specific problems of polynya evolution and the determination of the displacement and drift of ice floes in the summer Beaufort Sea. For the specific case of the St. Lawrence Island polynya, our analysis shows that this wavelet procedure can systematically extract geophysically relevant parameters from SAR imagery of polynyas. For the summer case, the presence of liquid water on the ice surface greatly reduces the backscatter contribution from the sea ice. Due to the lack of features on the ice, this is one of the most difficult period for ice trackers. In spite of the lack of features, our multi-scale wavelet analysis seems to work well in this case, and the detailed shape of ice floes are well delineated. Based on these detailed floe shapes, both the translation and rotation of the floes can be estimated from consecutive SAR images. In this technique, the wavelet analysis is concentrated on feature or pattern recognition and is fairly insensitive to the absolute calibration of the SAR data. The current method of template matching of ice floe shapes by use of a binary window obtained after manipulating the results of wavelet transform is very efficient computationally. This is mainly due to the fact that the only computation operations involved are bitwise logical operation and addition, while the classical template matching involves the operation of addition, square, and multiplication. Furthermore, it is only necessary to match the template pattern to a limited number of target patterns generated by the results of wavelet transform, not to every location in the images as with classical template matching.

In summary, the processing of SAR imagery with wavelet transforms is a rapid, efficient computational process. Therefore, the transforms can be used as a near-real-time "quick look" for feature detection in SAR images, and the assimilation of SAR data with the mesoscale ocean-ice interaction model (Liu et al. 1993) can provide a cost-effective monitoring program to keep track of changes in important elements such as open leads, ice edges, and ice floes.



## Applications of Data Assimilation to Analysis of the Ocean on Large Scales<sup>1</sup>

By Robert N. Miller

*College of Oceanography and Atmospheric Sciences,  
Oregon State University, Corvallis, Oregon 97331.*

Antonio J. Busalacchi

*Laboratory for Hydrospheric Processes,  
NASA Goddard Space Flight Center, Greenbelt, Maryland 20771.*

and

Eric C. Hackert

*Hughes STX Corporation and Laboratory for Hydrospheric Processes,  
NASA Goddard Space Flight Center, Greenbelt, Maryland 20771.*

*(Manuscript received 16 October 1995, in revised form 20 February 1997)*

### Abstract

It is commonplace to begin talks on this topic by noting that oceanographic data are too scarce and sparse to provide complete initial and boundary conditions for large-scale ocean models. Even considering the availability of remotely-sensed data such as radar altimetry from the TOPEX and ERS-1 satellites, a glance at a map of available subsurface data should convince most observers that this is still the case. Data are still too sparse for comprehensive treatment of interannual to interdecadal climate change through the use of models, since the new data sets have not been around for very long.

In view of the dearth of data, we must note that the overall picture is changing rapidly. Recently, there have been a number of large scale ocean analysis and prediction efforts, some of which now run on an operational or at least quasi-operational basis, most notably the model based analyses of the tropical oceans. These programs are modeled on numerical weather prediction.

Aside from the success of the global tide models, assimilation of data in the tropics, in support of prediction and analysis of seasonal to interannual climate change, is probably the area of large scale ocean modeling and data assimilation in which the most progress has been made. Climate change is a problem which is particularly suited to advanced data assimilation methods. Linear models are useful, and the linear theory can be exploited. For the most part, the data are sufficiently sparse that implementation of advanced methods is worthwhile.

As an example of a large scale data assimilation experiment with a recent extensive data set, we present results of a tropical ocean experiment in which the Kalman filter was used to assimilate three years of altimetric data from Geosat into a coarsely resolved linearized long wave shallow water model.

Since nonlinear processes dominate the local dynamic signal outside the tropics, subsurface dynamical quantities cannot be reliably inferred from surface height anomalies. Because of its potential for large scale synoptic coverage of the deep ocean, acoustic travel time data should be a natural complement to satellite altimetry. Satellite data give us vertical integrals associated with thermodynamic and dynamic processes,

<sup>1</sup> Some of this material was first presented as an invited lecture at the Second International Symposium on Assimilation of Observations in Meteorology and Oceanography, 13-17 March, 1995, Tokyo, Japan. Much of this material is based on research supported in part by NOAA Office of Global Programs Grant NA-36-GP0123-01, Office of Naval Research Contract N00014-92J1595 and NASA RTOP 578-21-03.



5°S, 140°W during the Geosat period.

Comparison of *in situ* data, viz. tide gauge data and dynamic height derived from TOGA-TAO moorings, with assimilation of raw Geosat data (see Tables 1 and 2) shows that in most cases the assimilation agrees at least as well with ground truth as the gridded product does. Correlation between tide gauge data and the processed Geosat data (column 2, Table 2) are comparable to the model results from the raw Geosat assimilation (column 6, Table 2).

The big advantage of data assimilation is shown at Callao and Rabaul. Data assimilation provides values at these stations whereas the gridded product does not due to orbit error constraints of the Geosat data. Almost uniformly, the data assimilation product which uses the raw Geosat product has higher correlation relative to the TOGA-TAO dynamic height than the gridded Geosat product with benefit of data assimilation (see Table 2).

Expected errors in the data make for difficulty in the interpretation of RMS differences between the *in situ* data and the Geosat data and between the *in situ* data and the output from the various model runs. If the errors in the Geosat data were independent of the errors in the *in situ* data, and the two instruments were measuring exactly the same quantity, we would expect RMS differences of 5 cm between the tide gauge data and the Geosat data, based on estimates of 3 cm RMS errors in the tide gauge data and 4 cm RMS errors in the Geosat data. Most of the RMS differences between the *in situ* data, the Geosat data and the output from the model runs are between 4 and 7 cm, which makes precise quantitative conclusions difficult to draw. Some exceptions are found at the TOGA-TAO mooring on the equator at 140°W, where the RMS difference between the dynamic height and the subjectively processed Geosat data is 9 cm, at the TOGA-TAO mooring on the equator at 165°E, where the RMS difference between the output of the model with tide gauge data assimilated and the observed dynamic height anomaly is 3 cm, and at Yap, where the RMS differences between the observed surface height anomaly and all of our estimates are greater than 8 cm.

Use of advanced data assimilation techniques with satellite altimetric data and reasonably detailed models is a practical reality. The present version of the Kalman filter does not perform in a truly optimal fashion. This dynamical model has been observed to perform better in the Kalman filter with tide gauge data and a similar system noise model. The major defect is probably the model of the observation noise covariance.

Even in its present suboptimal state, comparisons of model output with raw Geosat data alone compare as well with tide gauge data (which were withheld from the assimilation) as the gridded product

does. There is no reason to prefer the subjective analysis to the analysis based on data assimilation. The data assimilation analysis has the advantages of being based on explicit quantitative assumptions and of saving the considerable labor involved in the gridding process.

#### 4. Discussion

Most reviews of data assimilation begin with the assertion that ocean data assimilation is in its infancy, but infants grow quickly, and a complete review of the subject of application of data assimilation to analysis of the ocean on large scales is no longer possible in this format. Here we have concentrated on the emerging observing technologies of acoustic tomography and satellite altimetry. These techniques were at the point of feasibility study at the time the review article by Munk and Wunsch (1982) was written. There is now a large body of data from both types of systems, and we are just now learning how to extract the information contained in these data sets.

Direct inversion of tomographic data to recover complete ocean fields without regard to dynamics is an inefficient process. We have seen that this inversion amounts to a quadrature in two space dimensions which is bound to be inaccurate. We know from results of model experiments and theoretical calculations that tomographic data sets from relatively sparse arrays, when assimilated into models, will produce better analyses than those produced from relatively dense arrays without regard to dynamics. Data assimilation is necessary if acoustic tomography is to fulfill its potential.

We have made more progress in the direction of assimilation of satellite altimetric data. We have seen from our own analysis of the Geosat data that altimetric data can have great impact on analyses of the ocean on large scales. Our analysis, which is close to optimality with *in situ* data, (see Miller *et al.*, 1995) is far from optimal in treatment of satellite altimetry. The key to progress in this area lies in better estimates of error statistics.

As of this writing, we know of no assimilation experiment in which both satellite altimetry and acoustic tomography were assimilated. There are few simultaneous sets of tomographic and altimetric data. It is unfortunate that no altimeter was in place during the recently completed Acoustic Mid-Ocean Dynamics Experiment. The real promise of altimetry and tomography is that together they will yield a four-dimensional picture of the ocean on large scales. Many technical obstacles must be overcome before this promise can be fulfilled, so we cannot know the details of the construction of this much desired analysis, but it seems all but certain that the final product will be the result of data assimilation in a large-scale model.



---

# Earth from Above

USING COLOR-CODED SATELLITE IMAGES  
TO EXAMINE THE GLOBAL ENVIRONMENT

Claire L. Parkinson

LABORATORY FOR HYDROSPHERIC PROCESSES  
NASA GODDARD SPACE FLIGHT CENTER



University Science Books  
Sausalito, California



## Preface

---

The advent of satellite technology in the second half of the twentieth century has provided mankind with an amazing new ability to see the Earth-atmosphere system in a way never before possible. With satellites, the most remote regions of the oceanic and continental surfaces can be viewed as readily as the least remote. Data can be obtained from the entire Earth surface and, from some satellites, this can be done every day or at least every few days. Additionally, atmospheric data can be obtained from all levels of the atmosphere, over any geographic location, and with updates possible on a frequent basis. Satellite data can thus reveal the state of the Earth-atmosphere system and many of the changes occurring within it.

Of course, for the satellite data to reveal anything, the user or reader of those data must be able to understand them. For many of the satellite data, scientists and computers greatly aid this process by converting the streams of raw data into color-coded maps of geophysical quantities of interest. The central objectives of this book all relate to increasing the understanding of satellite data and the maps or images created from them. These objectives are: to familiarize the uninitiated with satellite data and with the reading of color-coded satellite images of the Earth; to instill a sense of how the raw data are converted into information about the Earth and the atmosphere; to instill a sense of the range of information being collected about the Earth through satellites and a sense of the imperfections and cautions of which the users of satellite data should be aware; and to instruct on six of the important variables in Earth-atmosphere studies that are now being examined with data from satellites—atmospheric ozone, polar sea ice, continental snow cover, sea surface temperature, land vegetation, and volcanoes. These six variables come nowhere near to covering the full range of important topics being examined with satellite data, but they illustrate the types of information that such data are revealing about the Earth-atmosphere system. Furthermore, for each variable, one type of satellite data is highlighted, and this choice also is illustrative only, as each variable can be examined from several different satellite instruments. However, by learning to read the illustrative exam-



## An Advective-Reflective Conceptual Model for the Oscillatory Nature of the ENSO

J. Picaut,\* F. Masia, Y. du Penhoat†

Recent findings about zonal displacements of the Pacific warm pool required a notable modification of the delayed action oscillator theory, the current leading theory for the El Niño–Southern Oscillation (ENSO). Simulations with a linearized coupled ocean-atmosphere model resulted in 3- to 6-year ENSO-like oscillations, with many of the variable model parameters found to be very close to their observed values. This simple model suggests that ocean processes that are ignored or underestimated in the delayed action oscillator theory, such as zonal current convergence, zonal advection of sea surface temperature, and equatorial wave reflection from the eastern ocean boundary, are fundamental to the development of the ENSO, in particular to its manifestations in the central equatorial Pacific.

Earth climate variations on interannual time scales are dominated by a coupled ocean-atmosphere interaction in the Pacific. This interaction connects a large-scale oceanic sea surface temperature (SST) anomaly of the tropical Pacific (El Niño) to the large-scale atmospheric Southern Oscillation, which is characterized by a sea-level pressure seesaw between French Polynesia and north Australia [defined by the Southern Oscillation Index (SOI)]. This coupled phenomenon, named the ENSO, oscillates irregularly

(roughly every 4 years) into a warm phase and a cold phase (Fig. 1). The warm phase, El Niño, is characterized by warm SST and weak easterly winds in the central and eastern equatorial Pacific, energetic westerly winds in the western Pacific, and negative SOI; whereas the cold phase, La Niña, is characterized by cold SST and strong easterly winds in the central and eastern equatorial Pacific, weak westerly winds in the western Pacific, and positive SOI. The gross features of the ENSO, and some of its dramatic climatic impacts, can be predicted 6 months to a year in advance by dynamical coupled ocean-atmosphere models (1–3). However, the prediction skills of these models are still limited by our insufficient understanding of the intrinsic mechanism that is responsible for the ENSO.

Bjerknes (4) proposed that the ENSO

is a self-sustained system in which SST variations in the eastern and central equatorial Pacific produce wind variations, which in turn produce SST changes. However, this scenario leads to a never ending warm or cold state. A mechanism for the oscillatory nature of the ENSO was originally proposed by McCreary (5), based on the reflection of a subtropical oceanic upwelling Rossby wave against the western ocean boundary. Battisti, Hirst, Schopf, and Suarez (6–8) proposed a concept that was similar to McCreary's (but was better supported by observations and equatorial wave theory), known as the delayed action oscillator, in which equatorial Rossby waves reflected as upwelling equatorial Kelvin waves are essential (9). Given the 9-month total travel time of the equatorial upwelling Rossby and reflected Kelvin waves, this concept asserts that it is the continuous arrival of upwelling Kelvin waves that slowly erodes the growing SST-wind interaction in the eastern equatorial Pacific, finally stops it after 1 or 2 years, and eventually turns the El Niño event into a La Niña event.

The delayed action oscillator theory is currently the leading theory for the ENSO, although it has several flaws. First, the maxima in the coupled SST–wind stress fields, simulated by the different models that led to this theory, are located 20° to 40° too far into the eastern equatorial Pacific as compared with observations (Fig. 1) (10). Second, on the basis of mooring data all along the equatorial Pacific and satellite altimetry data, several authors have questioned the effectiveness of the western ocean boundary as an equatorial wave reflector (11–14). In contrast, it seems that equatorial Kelvin waves reflect quite well on the eastern boundary as equatorial Rossby waves (14). Third, the models that have led to this theory of the ENSO are based on the dominant role of thermocline displacements on SST in the eastern equatorial Pacific, and they underestimate or misinterpret the effects of zonal advection (15). As a result, these models consider the eastern equatorial Pacific (where ENSO-related SST variations are the strongest) to be the source of the ENSO air-sea interaction, instead of the central equatorial Pacific (Fig. 1) (10).

The central equatorial Pacific has been confirmed as the source of the ENSO in recent studies (16–19), which indicated that the central equatorial Pacific SST varies between 26° and 30°C, predominantly on the ENSO time scale, as a result of the strong eastward and westward displacements of the eastern edge of the western Pacific warm pool. Because the SST varies around the approximate 28°C

Groupe SURTROPAC, L'Institut Français de Recherche Scientifique pour le Développement en Coopération—ORSTOM, BP A5, 98848, Nouméa, New Caledonia.

\*To whom correspondence should be addressed. E-mail: picaut@noumea.orstom.nc

†Present address: Groupe de Recherche en Géodésie Spatiale, 14 avenue Edouard Belin, 31401, Toulouse, France.



In this model (Fig. 2A), at initial time ( $t = 0$  month), a westerly wind patch is applied (28), and it induces local zonal currents that advect the OCEE toward the east against the weaker mean zonal current. At the same time, downwelling Kelvin waves and upwelling Rossby waves, on each side of the wind patch, propagate eastward

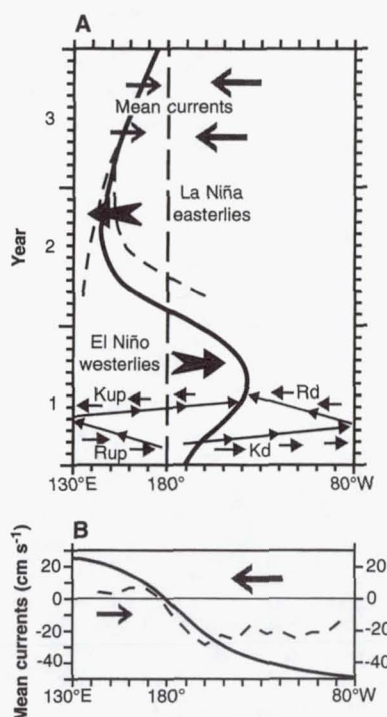


**Fig. 2.** Concept of the reflective-advective coupled system: (A) Longitude-time distribution within 2°N to 2°S of the common OCEE of the warm pool (thick line). Superimposed are the schematic representations of the equatorial Kelvin (Kup and Kd for upwelling and downwelling, respectively) and first meridional mode Rossby wave (Rup and Rd for upwelling and downwelling, respectively) propagating paths (lines with small dark arrows) and their associated zonal currents (small gray arrows), the mean zonal converging currents, and the westerly and easterly winds. Also shown is an example of two drifters converging into the OCEE of the warm pool (19). (B) Longitude distribution of the mean zonal currents (in centimeters per second) averaged within 2°N to 2°S deduced from observations (dashed line) and schematized for this model (thick line).

and westward, respectively. The wind patch expands eastward simultaneously with the displacement of the OCEE and generates local currents and equatorial waves of greater amplitude. As a consequence, the displacement of the OCEE accelerates and El Niño enters into a growth phase. It is the combination of two sets of zonal currents, in opposite direction to the original wind-forced currents, that gradually reduces the acceleration of the eastward progression of

the OCEE. One set is produced by the delayed arrival of the reflected equatorial waves from both ocean boundaries (Fig. 2A); the other corresponds to the mean zonal current that, as shown on Fig. 2B, increases in strength concurrently with the eastward displacement of the OCEE. Eventually, this combination stops the OCEE displacement toward the east ( $t \sim 8$  months) and finally pushes it back toward the midpoint. Once the midpoint is crossed, the wind shifts from westerly to easterly (27) and El Niño turns into La Niña ( $t \sim 13$  months); then La Niña turns into El Niño ( $t \sim 39$  months) and the ENSO phases repeat indefinitely.

The model includes several parameters, and numerous sensitivity calculations were done to determine the ranges of parameters that result in an ENSO-like oscillation of the model. We defined a "standard case," in which all parameters were set very close to their mean values (29). It resulted (Fig. 3, curve b) in a lopsided oscillation (that is, a longer time to go into an El Niño than into a La Niña) with a 4-year period and an amplitude of 25° (defined as half the distance from the crest to the trough). The simulation resembled the observed ENSO (Fig. 1), which has on average a 3.8-year period (30) and a lopsided pattern. The sensitivity calculations are summarized on Fig. 4, where one parameter at a time was changed, while the others were kept fixed at their standard case values. The equatorial Kelvin wave-speed range corresponded to the first baroclinic mode and was found to be very close to the one determined from in situ and satellite observations (Fig. 4A) (13, 31). The location of the midpoint (mean OCEE) ranged around the observed value of 180° (Figs. 1 and 4B). The latitudinal trapping remained close to the observed value of 7° (Figs. 1D and 4C). A close look at Fig. 1 suggests a 5° to 15° longitudinal shift between the eastern edge of the warm pool and that of the wind patch (Fig. 4D). The amplitude of the wind stress had a narrow range around 0.33 dynes cm<sup>-2</sup> which fell into the 0.20 to 0.40 dynes cm<sup>-2</sup> range of observed ENSO wind stress anomalies (Fig. 4E) (15). Many ocean modelers use 2.5 year<sup>-1</sup> for the Rayleigh friction. Comparisons with observations (32) suggest a friction of 6 month<sup>-1</sup> for the first baroclinic mode, and the present sensitivity experiment implied the use of friction smaller than 1.5 year<sup>-1</sup> (Fig. 4F). A series of tests (33) indicated a rather limited north-south extension for the width of the equatorial band over which the zonal currents are averaged to displace the OCEE (within 1.75°N to 1.75°S and 2.25°N to 2.25°S). A previous study (18) based on observa-

tions did not find a substantial change in OCEE displacements when the zonal currents were averaged within 2°N to 2°S and 6°N to 6°S. The final test considered different values for the mean zonal current near the western and eastern ocean boundaries (Fig. 2B). It appears to be difficult to get the model to oscillate for values below 15 cm s<sup>-1</sup> near the western boundary and above -35 cm s<sup>-1</sup> near the eastern boundary. These numbers are still too large compared with those of the observations (34).

As discussed above, an important and controversial question about the delayed action oscillator theory compared with the present approach is the effectiveness of the western and eastern ocean boundaries as equatorial wave reflectors. Several simulations were done with our model, with the addition of reflection coefficients on both boundaries. It is possible to get ENSO-like oscillations with no or very little (<10%) western boundary reflection, through a reduction of the wind stress amplitude (Fig. 3, curve a). In contrast, it is impossible to obtain ENSO-like oscillations with a reflection coefficient on the eastern boundary that is smaller than 85% (Fig. 3, curve c).

Despite its simplicity, the proposed coupled model is adequate to illustrate the advective-reflective concept for the oscillatory nature of the ENSO. Many of the parameters that yielded realistic simulations of the ENSO were found to be surprisingly close to their observed values. The concept is based on the discovery of the OCEE that is advected in phase with the SOI (19); as a consequence, the ENSO time scale can be accurately determined by the duration of advection of the eastern edge of the warm pool by surface zonal currents in the equatorial band. This is more direct than the estimation proposed by recent ENSO theories, based on the time taken by some negative feedback to stop the unstable growth of the coupled system. However, our model results in regular oscillations, and as seen on Figs. 1 and 3, curve b, the ENSO is subject to strong irregularities. This could be due to the fact that several parameters that were treated as constants in the model are not really constant in nature (such as Kelvin wave speed and wind amplitude). These irregularities are beyond the scope of the present study.

The present model requires stronger than observed mean zonal converging currents (Fig. 2B), very likely to compensate for the simplified model physics, such as the exclusion of nonlinear terms and of vertical advection for changing SST. During the fully developed El Niño, when warm waters stretch well into the eastern



# Solitary waves in the western Equatorial Pacific Ocean

R. Pinkel,<sup>1</sup> M. Merrifield,<sup>2</sup> M. McPhaden,<sup>3</sup> J. Picaut,<sup>4</sup> S. Rutledge,<sup>5</sup> D. Siegel,<sup>6</sup> and L. Washburn<sup>6</sup>

**Abstract.** During the spring tides of early January and February 1993, groups of solitary internal waves were observed propagating through the Intensive Flux Array of the TOGA COARE experiment. The waves appear to originate near the islands of Nugarba (3°S 30°E - 154° 30°E). They travel north-eastward at 2.5-3 m/s, closely coupled with the semi-diurnal baroclinic tide. Peak amplitudes exceed 60 m. Velocities are in excess of .8 m/s. Sea-surface vertical displacements of order .3 m can be inferred directly from the lateral acceleration of surface waters. The Equatorial Undercurrent is displaced by soliton passage but apparently is unaffected otherwise. The intrinsic shear of the solitary crests is small compared to ambient equatorial shears. The crests, while not themselves unstable, are effective at triggering instabilities on the background flow. The motions potentially contribute 10-15 Watts/m<sup>2</sup> to the flux of heat into the mixed layer.

## 1. Introduction

From November 1992 through February 1993 a multi-national air-sea interaction experiment was conducted in the Western Equatorial Pacific. Termed the Intensive Observation Period (IOP) of TOGA COARE (Webster and Lukas, 1992), the experiment involved ship, aircraft and land-based observations. The COARE intensive Flux Array (IFA) was centered at 2°S, 156°E over the 2 km deep Ontong Java Plateau (Fig. 1a,b). The surface waters of this region are among the warmest on the planet. Fluctuations in the state of the so-called "Warm Pool" and the overlying atmosphere are linked to subsequent climatic fluctuations eastward along the equator and at higher latitudes. Numerous oceanographic sensors were deployed in COARE to investigate processes which regulate the heat exchange between the warm surface waters and the cooler waters below.

A major surprise was the discovery of large (60 m) amplitude internal solitary waves propagating toward the northeast through the COARE IFA during periods of spring tide. Such waves are often seen on continental shelves, generated by tidal flow around coastal topography (Haury et al., 1979, Holloway, 1987, Sandstrom and Elliot, 1984. Fewer observations of deep sea solitary waves exist (Osborne and Burch, 1980, Apel et al., 1985,

New and Pingree, 1990). Deep-ocean solitons propagate faster than their coastal counterparts and can be an order of magnitude more energetic. Their generation mechanism, interaction with the ambient environment, and ultimate fate are the subjects of present conjecture.

The COARE observations are of particular interest in that the solitons pass through an oceanographic region of extreme complexity. The South Equatorial Current (0-80 m depth, westward flow) and the Equatorial Undercurrent (160-250 m depth, eastward flow) dominate the large-scale background. The observations provide an ideal opportunity to investigate the interaction between the solitons and the ambient environment. Indeed, as distinct and significant perturbations, the solitons can provide insight into the stability of the pre-existing flows. Here we present data representative of the observed encounters.

## 2. Observations

The first observation of a well defined soliton was on 28 November, 1992. The Doppler sonar on the R/V Vickers (2°S, 156°15' E) detected passage of a single 40 m downward pointing "crest" at 1400 UTC. During the spring tides of 7-9 January and 8-11 February 1993, numerous solitary waves transited the COARE domain. A clear signature of event passage can be seen in ship's navigational records (Fig. 1c). For example, on 11 January 1993, the predominately southwestward drift of the R/V Vickers was interrupted by successive 1000 m displacements toward the northeast as the ship was advected by passing wave crests.

In conditions of moderate wind, the solitary waves strain the sea-surface sufficiently to modify the propagation of short gravity waves. The disturbance is often adequate to produce a pattern visible to the eye, to ship's radar, and to the advanced meteorological radars fielded in COARE (Fig. 1d). The propagation speed of the events, ~2.5 m s<sup>-1</sup>, can be inferred from the time evolution of these radar images. Wavefronts can extend 50 km.

A consistent record of wave passage is obtained from the Vickers Doppler sonar, which operated throughout the COARE IOP. The sonar, designed and constructed at SIO, transmits repeat sequence coded pulses (Pinkel and Smith, 1992) every .6 sec. at 161 kHz. Profiles of ocean velocity and acoustic scattering strength are obtained with a resolution of 2.5 m in depth, 2 min. in time to depths in excess of 200 m. An inertial reference sensor is interfaced to the sonar processor, such that data are averaged in constant depth bins, independent of the instantaneous roll of the ship. To convert to absolute velocity, sonar data are combined with ship velocity estimates obtained from a Magnavox 4200 C/A code GPS receiver.

Six packets of solitons traversed the COARE domain between 23:00 UTC on 9 January and 22:00 UTC on 11 January. The subsequent baroclinic tidal waveform was significantly non-sinusoidal, although neither solitary wave nor bore-like behavior was observed. The January packets consisted of 2,2,2,3,3 and 2 distinct crests, respectively, occurring at 12.4 hr intervals. In

<sup>1</sup> Robert Pinkel, Scripps Inst. of Oceanography, code 0213, La Jolla, CA 92093-0213

<sup>2</sup> M. Merrifield  
University of Hawaii, Honolulu, Hawaii

<sup>3</sup> M. McPhaden  
Pacific Marine Environmental Laboratory, NOAA, Seattle, WA

<sup>4</sup> J. Picaut  
Groupe SURTROPAC, ORSTOM, Noumea, New Caledonia

<sup>5</sup> S. Rutledge  
Colorado State University, Fort Collins, Colorado

<sup>6</sup> D. Siegel and L. Washburn  
University of California Santa Barbara, Santa Barbara, CA



in acoustic return (Thorpe and Brubaker, 1983, Goodman, 1990, Seim and Gregg, 1995). The increased structure in the associated temperature and salinity fields is a consequence of local turbulent events which follow passage of the solitons. This interpretation is supported by the relative uniformity of scattering in the surface mixed layer. In such an isothermal, isohaline region, turbulent motion does not produce the fine-scale fluctuations required for increased Bragg scattering (Thorpe and Brubaker, 1983).

The "turbulence" fails to decay in the hours following soliton passage. We note that salinity structures at the Bragg scale can be responsible for much of the scattering increase (Seim and Gregg, 1995). A characteristic diffusive decay time for salinity structure is of order  $\lambda_b^2/\nu_s \approx 5$  hrs, where  $\lambda_b$  is the Bragg length scale, and  $\nu_s$  is the molecular diffusivity of salt. Long after active turbulence ceases, elevated scattering levels should persist. The salinity fine structure acts as a nearly passive tracer, providing an "acoustic dye" which marks the advective stirring following event passage.

Profiles of density, temperature and salinity have been obtained at 20 minute intervals to a depth of 180 m throughout the passage of the January solitons. The purple rectangles in Fig. 2b represent regions where unstable density gradients are encountered. The gradient is here determined as a 5 meter first difference. Persistent overturning is seen at the base of the surface layer (45-60 m), and in a layer centered at 110 m. The overturning in these layers precedes the arrival of the solitons, emphasizing the marginal dynamic stability (Miles, 1963) of the equatorial currents. The 11:30 profile coincides with the passage of the second crest. Multiple overturns are observed between 120 m and 180 m, as well as in the weakly stratified layer.

### 3. Event Evolution

Liu et al., 1985, demonstrated numerically that under appropriate conditions, a fairly arbitrary upper layer current jet (in a two layer fluid) would evolve into a train of deep water solitary waves. They suggested that barotropic (surface) tidal flow near the Pearl Bank produced the surface jet which was responsible for the Sulu Sea solitary waves. Observations in the Bay of Biscay prompted New and Pingree, 1990, to suggest that the solitary wave trains evolve as an instability, not on an arbitrary disturbance, but on the internal tide itself. Recent modeling studies (Gerkema and Zimmerman, 1995) explore this conjecture.

The downward cresting solitons appear at the Vickers site several hours after the observed upward crest of the semi-diurnal baroclinic tide. Is this co-occurrence coincidental, or are the two phenomena closely coupled? A long-term perspective can be obtained from moored time series data collected at 2S, 156E. The mooring, deployed as part of the Tropical Atmosphere Ocean (TAO) Array (McPhaden, 1993), was specially instrumented with a dense vertical array of temperature and salinity sensors for deep ocean validation of the TOPEX/POSEIDON satellite altimeter mission. The time series provide estimates of the volumetric variations in water masses with 5-minute temporal resolution. From these, changes in sea-surface height can be inferred to an accuracy of 1-2 cm (Picaut et al., 1995).

Fig. 3a shows a three-day estimate of this "dynamic height", relative to 1692 m, obtained in September 1992. A clear relationship between the "solitary" waves and the underlying tide is seen. During January 1993, dynamic height estimates from the TAO mooring also show the passage of non-linear waves. However, the variability from tide to tide is greater in January than in September.

When dynamic height calculations are repeated for the January 11 event using the Vickers density data, estimates of .1 m relative to 170 m depth (the maximum depth of the density profile) are obtained. However, if the observed fluid acceleration at 170 m is ascribed to a pressure gradient resulting from variable sea-surface elevation, a height estimate comparable to the TAO observations is obtained (Fig. 3b). Coupled with the 1 km approximate horizontal length scale of the crests, sea-surface slopes of  $5 \times 10^{-4}$  are implied. Isopycnal slopes of  $5 \times 10^{-2}$  are seen in the thermocline.

### 4. Energetics

Central to the issue of wave energetics is the definition of an appropriate unperturbed background state. For a potential energy calculation it suffices to use the calculated flow streamlines as surrogate isopycnal surfaces. In determining kinetic energy, we consider only the component of absolute water velocity in the direction of propagation, making no attempt to separate the soliton/bore motion field from the underlying tide.

Estimates of kinetic and potential energy are presented in Fig. 3c. These are based on integrations over the top 170 m, the region sampled by the CTD.

The contribution to soliton energy from depths greater than 170 m can be inferred using theoretical mode-one waveforms for vertical displacement and horizontal velocity, (Gill, 1982, eqns. 6.9.19, 6.10.2). The energy per unit area of the full-depth flow is a factor of 1.1 (kinetic) and 2.2 (potential) greater than the values given in Fig. 3c. The total energy found in the three-wave solitary group is approximately 10% of that in the underlying baroclinic tide. Solitary wave formation represents an efficient means of energy transfer from the tidal band to higher frequency motions.

### 5. Summary

We observe a series of extremely energetic deep-sea solitary waves propagating north-eastward through the Warm Pool of the Western Tropical Pacific. The apparent generation site is in the vicinity of the Nugarba Islands,  $3^\circ 30'S$ ,  $154^\circ 30'E$ . The waves are phase locked to the underlying baroclinic tide, which itself is extremely non-sinusoidal.

The solitons appear to interact minimally with the larger scale Equatorial Current System. The Equatorial Undercurrent is simply displaced vertically by their passage. This "advective displacement" contrasts with the more common principle of "linear superposition" which is generally applicable to lower energy fluid phenomena.

The intrinsic shear and strain of the solitary wave is sufficient to trigger shear instability in the weakly stratified region 40-80 m depth. (However, observations of critical Richardson number are wide-spread, associated with the strong pre-existing shears). Distinct increases in acoustic scattering strength are observed following passage of all of the solitons, suggesting the creation of fine-scale sound-speed (salinity) fluctuations.

It is unclear whether the energy which creates this microstructure is extracted from the solitons, the underlying baroclinic tide, or the pre-existing flows. Even a modest energy loss from the solitons (10% per 100 km) is sufficient to support vertical heat fluxes of order 16 Watts/m<sup>2</sup> in this region of the Warm Pool during periods of spring tide. Such fluxes can introduce significant temporal and spatial inhomogeneity in the larger scale oceanography of the region.



## Timescales of Land Surface Evapotranspiration Response

RUSSELL SCOTT

*USDA Agricultural Research Service, Tucson, Arizona*

DARA ENTEKHABI

*Ralph M. Parsons Laboratory, Massachusetts Institute of Technology, Cambridge, Massachusetts*

RANDAL KOSTER

*Hydrologic Sciences Branch, Laboratory for Hydrospheric Processes, NASA/Goddard Space Flight Center, Greenbelt, Maryland*

MAX SUAREZ

*Climate and Radiation Branch, Laboratory for Atmospheres, NASA/Goddard Space Flight Center, Greenbelt, Maryland*

(Manuscript received 18 September 1995, in final form 13 June 1996)

### ABSTRACT

Soil and vegetation exert strong control over the evapotranspiration rate, which couples the land surface water and energy balances. A method is presented to quantify the timescale of this surface control using daily general circulation model (GCM) simulation values of evapotranspiration and precipitation. By equating the time history of evaporation efficiency (ratio of actual to potential evapotranspiration) to the convolution of precipitation and a unit kernel (temporal weighting function), response functions are generated that can be used to characterize the timescales of evapotranspiration response for the land surface model (LSM) component of GCMs. The technique is applied to the output of two multiyear simulations of a GCM, one using a Surface-Vegetation-Atmosphere-Transfer (SVAT) scheme and the other a Bucket LSM. The derived response functions show that the Bucket LSM's response is significantly slower than that of the SVAT across the globe. The analysis also shows how the timescales of interception reservoir evaporation, bare soil evaporation, and vegetation transpiration differ within the SVAT LSM.

### 1. Introduction

Numerical studies have highlighted the sensitivity of atmospheric general circulation models (GCMs) to the parameterization of the land surface hydrology. In some of these studies, the investigators examine the climatic state that results from a perturbed wet or dry surface moisture at the continental or global scale (Walker and Rowntree 1977; Shukla and Mintz 1982). These experiments collectively illustrate the importance of the land surface, among the many parameterized physical processes in GCMs, in establishing mean model climate.

It is still unknown, however, to what extent moisture anomalies are self-sustaining and what role they play in determining climatic variability. The answer to these questions one must depend in part on the timescales of surface moisture retention, which describe how quickly

the deposited precipitation is returned to the atmosphere. The timescale of moisture storage in the soil determines the timescale of evapotranspiration persistence and thus the timescale of humidity persistence in the near-surface atmosphere. The anomalous soil moisture also affects the partitioning of available energy into latent and sensible heat flux, thereby affecting the temperature persistence.

The question of surface hydrology timescales has been addressed in previous studies. Serafini and Sud (1987) use a simple water budget model to derive a timescale of soil hydrology, which they define as the timescale for the onset of agricultural droughts. An average evapotranspiration is taken as the rate at which the soil dries if there is no precipitation. They model evapotranspiration using the classic Bucket formulation, which equates evapotranspiration to the product of a moisture availability factor and a potential evaporation. The resultant drying timescale in the absence of rain is inversely proportional to the potential evaporation. For typical moisture conditions, it ranges from a few days at low latitudes to several months in higher latitudes.

---

Corresponding author address: Dara Entekhabi, Ralph M. Parsons Laboratory, Massachusetts Institute of Technology, Dept. of Civil and Environ. Eng. (48-331), Cambridge, MA 02139.  
E-mail: darae@MIT.edu



The values are generally high ( $\geq 0.6$ ) except over higher latitudes where snow cover is present during the period analyzed and desert regions where there are extended periods with no precipitation. Conceptualization of the evapotranspiration efficiency  $\beta$  as dependent only on the history of daily precipitation in these regions is thus invalid, and estimates of  $\lambda$  over these regions are unreliable. The correlation values in Fig. 6 are correspondingly small where the single-parameter response function is an incomplete representation of the multiple timescale evapotranspiration efficiency dynamics. When the actual kernel response function is used—that is, without assumptions regarding fits to a general (exponential) function—the correlation coefficient is similarly high.

We can expand the use of the convolution method to analyze each component of evapotranspiration within the SVAT simulation. Since total evapotranspiration in the SVAT is composed of transpiration, interception evaporation, and bare soil evaporation, each one of the components has a separate response and characteristic timescale. The efficiency of each evapotranspiration process is given here by the diagnostics:

$$\begin{aligned}\beta_{tran}(t) &= \frac{e_{tran}(t)}{e_p(t)} & \beta_{intercept}(t) &= \frac{e_{intercept}(t)}{e_p(t)} \\ \beta_{soil}(t) &= \frac{e_{soil}(t)}{e_p(t)},\end{aligned}\quad (11)$$

where subscripts  $_{tran}$ ,  $_{intercept}$ , and  $_{soil}$  refer to transpiration, interception reservoir evaporation, and bare soil evaporation. Equation (6) is used by changing the evaporation efficiency term,  $\beta$ , to any one of the above efficiencies. Figures 7a–c show the results of this analysis.

The timescales of interception reservoir evaporation, Fig. 7a, are the shortest, around one day. Figures 7b and 7c show the expected, longer response times associated with transpiration and bare soil evaporation of soil water in subsurface storage. The percentage contribution to the total evapotranspiration from each component should be considered when looking at the normalized response of the evapotranspiration components. The percentage of contribution determines how influential a component's behavior is to the total evapotranspiration response seen in Fig. 5a. For example, regions in which interception reservoir evaporation is especially important (Scott et al. 1995) should have correspondingly shorter timescales for total evapotranspiration. For the SVAT, the unit response kernel  $h(t)$  represents the combination of influences from interception evaporation, transpiration, and bare soil evaporation, each with a different timescale.

## 5. Summary

In this investigation we present a measure of land surface evapotranspiration timescale that reflects how the GCM simulated land responds over time to inter-

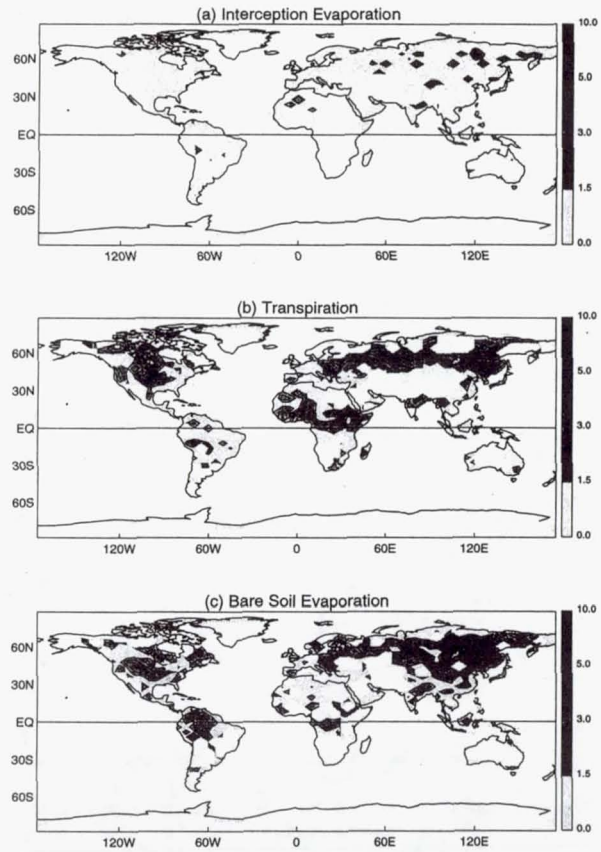


FIG. 7. Characteristic response timescales for the components of the SVAT model evaporation: global plots of  $\lambda^{-1}$  for the SVAT interception reservoir evaporation, transpiration, and bare soil evaporation.

mittent surface wetting. This response is linked with the magnitude of land–atmosphere moisture and energy exchanges, and hence, the ability of the surface to influence climate. The method relates land surface's evaporation efficiency at a certain time to the convolution of past precipitation through a unit response function.

The representation of surface control on the evapotranspiration process as a convolution of precipitation history allows the estimation of timescales associated with the inclusion of interactive soil hydrology and vegetation canopy processes in GCM LSMs. Using the conceptualization and estimation techniques introduced in this paper, the convolution kernel response functions and their associated timescales may be derived from time series of simulated evapotranspiration, potential evapotranspiration, and precipitation. Through this convolution, the unit response provides the intertemporal link that determines how a given land surface responds to forcing. Characteristic behaviors vary due to heterogeneous surface types across the globe (e.g., soil type, soil depth, vegetation.) These diagnostics may be used in validating GCM LSMs as well as in analyzing the role of land surface processes in modulating the temporal variability in model climates. Furthermore, the



## The effects of laterite and associated terrain components on PBMR response in HAPEX-Sahel

William L. Teng<sup>a,\*</sup>, Bhaskar J. Choudhury<sup>b</sup>, James R. Wang<sup>c</sup>

<sup>a</sup>*Hughes STX Corporation, NASA Goddard Space Flight Center, Greenbelt, MD 20771, USA*

<sup>b</sup>*Hydrological Sciences Branch, NASA Goddard Space Flight Center, Greenbelt, MD 20771, USA*

<sup>c</sup>*Microwave Sensors and Data Communication Branch, NASA Goddard Space Flight Center, Greenbelt, MD 20771, USA*

---

### Abstract

Terrain characteristics such as roughness and vegetation have been shown to significantly affect the interpretation of microwave brightness temperatures ( $T_B$ s) for mapping soil moisture. This study, a part of the 1992 HAPEX-Sahel experiment (Hydrologic Atmospheric Pilot Experiment in the Sahel), aimed to determine the effects of laterite and associated terrain components (i.e. vegetation, soil, and exposed water bodies) on the  $T_B$  response of the Pushbroom Microwave Radiometer (PBMR, L-band, 21 cm wavelength), using the NS001 Thematic Mapper Simulator data as a surrogate for ground data. Coincident PBMR and NS001 data acquired from the high altitude (about 1500 m) long transect flights were processed to obtain  $T_B$ s and radiances, respectively. The transects covered a range of moisture conditions. For this preliminary evaluation, no atmospheric corrections were applied, and the data sets were aligned by matching the acquisition times of the data records. NS001 pixels (about 4 m) were averaged to approximate the resolution of the PBMR (about 450 m), before their flight line data were compared. The laterite plateaux were found to have a surprisingly strong effect on the PBMR  $T_B$  response.  $T_B$  variations along the flight line could largely be explained by a combination of density and dielectric properties of laterite. The effect of surface moisture was distinguishable from the laterite effect, with the distinction apparently related to the occurrence of ephemeral pools of water after rainfall. Model simulated  $T_B$ s agreed reasonably well with the observed  $T_B$ s.

---

### 1. Introduction

Terrain components, such as vegetation, surface roughness, and soil properties, have been shown to significantly affect the interpretation of passive microwave data for

---

\* Corresponding author.



The above  $T_B$  calculations were based on the laterite mineral composition (i.e.  $\epsilon'$  of the minerals). If, instead,  $\epsilon'$  was derived from the laterite density, using the relationship from Ulaby et al. (1990), then  $\epsilon'$  would be about 12. The calculated  $T_{BS}$  for the 'dry' and 'wet' cases would then be a few degrees higher than the above calculated  $T_{BS}$ , but still fairly close to the observed  $T_{BS}$ .

## 6. Uncertainties

There are some uncertainties in the data used in this study; however, considering the magnitude of the laterite effect, they should not affect the main results of this study. First, the long transect flight lines were not exactly registered spatially. However, the ground coverages mostly overlapped, as shown by their similar  $T_B$  profiles (Fig. 5(a)–(b)). Second, the long transect flight times were not identical. The August 29 and September 6 long transects were flown about an half hour apart (around mid-morning); the August 24 long transect was flown about 1.5 h later (around noon); the September 17 long transect was flown about 2.5 h later (around mid-afternoon). The effect would be on the surface temperature. However, the two flights analyzed the most in this study, the August 29 'wet' date and the September 6 'dry' date, occurred essentially during the same time of the day. Third, the time between a rain event and the acquisition of the PBMR data varied among the four long transect flights. The actual time lapses are unknown because the 6 a.m. rain gauge sampling provided information for the previous 24 h as a whole. It was thus assumed that, for overall patterns, these time lapses were not significant. Fourth, there was a large variability of sunshine due to rain events and clouds, which resulted in variations of the surface temperatures from day to day and during a given day. Thus, it is possible that part of the decrease in  $T_{BS}$  for the August 29 'wet' day was due to a decrease in surface temperature. Again, the August 29 NS001 Band 8 infrared temperature data could not be used because of the cloudy condition. Finally, terrain features and rain gauge sites do not coincide on the ground, thus, only general trends can be concluded.

## 7. Conclusions

The laterite plateaux within the HAPEX-Sahel experiment area were found to strongly affect the PBMR  $T_B$  response. As small a change as 5% in the laterite area within the PBMR beam area was observed to affect the PBMR  $T_B$  response. The dielectric properties of laterite, related to its high density and mineral composition, could largely explain the variations in the PBMR brightness temperature ( $T_B$ ) profile along the flight line. Calculated  $T_{BS}$  agreed reasonably well with the observed pattern.

The effect of surface moisture on the PBMR  $T_B$  response was distinguishable from the laterite effect. Temporally,  $T_{BS}$  for the entire flight line profiles of the four long transect days generally decreased with increases in rainfall as measured by the EPSAT network of rain gauges. For the entire flight line, there was an average difference of about 40 K between the 'wet' and 'dry' days. Spatially, the  $T_{BS}$  for the 'wet' day decreased from south to north, corresponding to a general increase in rainfall in the same direction. In contrast,  $T_{BS}$  for the 'dry' day remained essentially the same. The averaged NDVI values for the south and north were about the same; thus, the  $T_B$  difference between the south and north was most likely related to rainfall, and not to vegetation. The  $T_B$  difference between adjacent terrain features also increased with an increase in rainfall, for the entire flight line. This difference could be related to the occurrence of ephemeral pools common during the rainy season in the HAPEX-Sahel area.



## The Surface Heat Flux as a Function of Ground Cover for Climate Models

FRED M. VUKOVICH AND ROBERT WAYLAND

*Science Applications International Corporation, Raleigh, North Carolina*

DAVID TOLL

*National Aeronautics and Space Administration, Goddard Space Flight Center, Greenbelt, Maryland*

(Manuscript received 26 September 1995, in final form 9 August 1996)

### ABSTRACT

Surface heat fluxes were examined as a function of surface properties and meteorological conditions in a 100 km  $\times$  100 km grid square at 1-km spatial resolution centered at the location of the First ISLSCP (International Satellite Land Surface Climatology Project) Field Experiment (FIFE), the Forest Ecosystem Dynamics site in central Maine, and a semiarid rangeland site around Walnut Gulch, Arizona. This investigation treats the surface heat flux variability within a GCM grid box to provide insight into methods for treating that variability in climate models. The heat fluxes were calculated using NOAA AVHRR and available meteorological data. The average heat fluxes that were estimated using the various area ground-cover representations were compared with the ensemble average heat fluxes for the entire area, which were assumed to be the best representation of the heat fluxes for the areas. Average heat fluxes were estimated for the entire 100 km  $\times$  100 km area based on a single ground-cover representation, and the mean error for the area sensible heat flux was about 10% and for the area latent heat flux, 21%. The estimation error was reduced, and in some cases significantly reduced, when the area heat fluxes were estimated by partitioning the area according to significant ground cover. The most significant effect of the partitioning was on the latent heat flux estimates.

### 1. Introduction

The atmospheric boundary layer (ABL) provides the physical link between the atmosphere and the earth's surface for exchanges of heat, moisture, and momentum. Since more than half of the incoming solar energy is absorbed at the surface and is then transmitted to the atmosphere by longwave radiation and both sensible and latent heat fluxes, the primary energy sources for driving the atmospheric circulation are at the earth's surface. Clearly then, realistic estimates of radiation parameters (albedo, ground temperature, emissivity, etc.) and surface heat fluxes are paramount to satisfactory performance of a general circulation model (GCM).

One of the primary goals of boundary layer research is to provide atmospheric models with a physically based parameterization of the ABL, surface radiation properties, and heat fluxes, so that these models can ultimately perform better. However, a fundamental problem exists between formulations of ABL processes and the needs of a GCM; that is, the ABL has much smaller

spatial and temporal scales than a GCM. A GCM that uses spatial scales of 1000 km or more requires a physical adjustment time step of 30–60 min, which, under most circumstances, is significantly larger than the adjustment timescale for ABL processes. However, spatial scales of some GCMs are as small as 100 km, which have a corresponding physical adjustment time step of about 5 min. Often, grid-average values or similar parameterization procedures are used to characterize surface properties and processes, bridging the gap between the physics of subgrid-scale processes and the overall influence of the space and timescales of the model. This has been stated more simply with how well the ensemble average of processes over a grid square can be represented by a process at the grid square estimated using average terms.

The physical characteristics and properties of vegetation, and of the underlying substrate associated with a surface, are factors that will markedly influence the surface albedo, ground temperature, surface emissivity, thermal inertia, and atmospheric turbulence (Vukovich et al. 1987; Sud et al. 1993; Bonan 1995; Koster and Suarez 1992a), as well as the surface heat flux within a GCM grid square (Smith et al. 1992; Koster and Suarez 1992b; Sellers et al. 1995). For example, a GCM grid square, which generally covers an area ranging in

---

Corresponding author address: Dr. Fred M. Vukovich, Science Applications International Corporation, 615 Oberlin Road, Suite 300, Raleigh, NC 27605.  
E-mail: f.m.vukovich@larc.nasa.gov



#### 4. Summary and discussion

Surface heat fluxes were examined as a function of surface properties and meteorological forcing in a 100 km  $\times$  100 km area centered at the location of the FIFE site in central Kansas, the FED site in central Maine, and a semiarid rangeland site around the Walnut Gulch catchment in Arizona to provide insight into methods of treating the subgrid-scale variability of the surface heat fluxes in a GCM to improve climate simulations. The heat fluxes over the 100 km  $\times$  100 km area at 1-km spatial resolution were estimated using 1D models similar to those commonly used in many GCMs. The fluxes were computed as the potential difference across the surface multiplied by an exchange coefficient. For the sensible heat flux, the potential difference was expressed by the difference between the ground temperature, provided by NOAA AVHRR data, and the air temperature near the surface, obtained from available meteorological data. For the latent heat flux, the difference between the ground saturation specific humidity adjusted for moisture availability and the specific humidity of the air near the surface was used. The heat fluxes were calibrated by comparisons between the average measured and the averaged derived heat fluxes in a 15 km  $\times$  15 km area centered over the field program sites.

After the calibration procedure was accomplished, area heat fluxes were estimated either based on a single ground-cover representation for each region, or by partitioning the region according to the most significant ground cover. For the FIFE region, the dominant ground cover was prairie grassland and farmland; for the FED region, forested area; and for the Walnut Gulch region, the semiarid rangeland. The results were compared to the ensemble average heat fluxes for the entire area, which were assumed to be the best representation of the area heat fluxes. The areal partitioning was presented in Table 1.

For a single ground-cover representation, the sensible heat flux was consistently overestimated, and the latent heat flux was usually underestimated. This was primarily because the single ground-cover representation does not account for the water surfaces in the FIFE and FED case studies and for the forests in the Walnut Gulch case studies. There were exceptions to this result, notably the latent heat flux for the 7 October 1987 FIFE and the 8 September 1990 FED case studies, which were influenced by lower air and dewpoint temperatures. The area latent heat flux was the most difficult area heat flux to estimate using a single ground-cover representation (i.e., an average estimation error of 21%). This is mainly attributed to the inability to provide representative values of the surface specific humidity for the grid area in a consistent manner. The estimation errors for the area latent heat fluxes were as small as 1% and as large as 78% over the case studies. The average estimation error for the area sensible heat flux using a single ground-cover representation was a factor of two smaller (i.e., the average estimation error was 10%). The differences between the ensemble heat flux and the area heat flux derived using a single ground-cover representation in-

dicate the degree of nonlinearity of the meteorological forcing and land-surface parameters that occurs when deriving GCM grid area surface heat fluxes.

When the area heat fluxes were estimated by partitioning the area according to significant ground cover, the estimation error was reduced in all cases compared to the single ground-cover representation case. This is because the secondary ground-cover representations (i.e., the water surface for the FIFE and FED case studies and the forests for the Walnut Gulch case studies) significantly influenced the area heat fluxes. The most significant reduction in error was for the latent heat fluxes. For the latent heat flux, the error was reduced by as much as a factor of 10 and the range in the error by as much as a factor of 8 compared to the latent heat flux estimates using a single surface-cover representation. For the sensible heat flux, the error was reduced by as much as a factor of 3 and the error range by as much as a factor of 2.

The lowest overall error obtained by any one procedure to estimate both heat fluxes occurred for approach E in which the subarea heat fluxes were calculated using the average meteorological parameters for the entire 100 km  $\times$  100 km area and the ground parameters were averages for each subarea. This procedure simulates using the gridpoint values for the meteorological parameters in a GCM, since the gridpoint value is considered an average over the grid area. The procedure also simulates the application of ground parameters that represent subgrid-scale values that result from partitioning the grid area according to significant ground cover.

Almost identical results were obtained when the heat fluxes for each subarea were calculated using the average meteorological parameters and ground parameters for each subarea (i.e., approach G). The meteorological forcing used for each case study was an interpolated field that did not have a strong association with the local ground cover (e.g., the lakes in the FIFE and FED regions). For this reason, approach G did not make a stronger impact. Approach G requires subgrid-scale meteorology to estimate the subgrid-scale heat flux, and that requirement adds a significant degree of complexity in a GCM.

The area heat fluxes estimated using weighted averages of the meteorological forcing and ground parameters from the partitioned areas (approach D), are identical to the heat fluxes that would be estimated using averages of these parameters over the entire 100 km  $\times$  100 km area. As a result of applying this method for estimating the area heat fluxes, there was a reasonable reduction in the estimation error for the area sensible heat fluxes compared to that using a single surface-cover representation. The estimation errors for the area latent heat flux, though lower than those for the single ground-cover representation, were the largest noted for the partitioning results. These results support the axiom that the average of processes generally is different (sometimes significantly different) from the process determined from the average of the terms, and they indicate



# Can the Topex/Poseidon altimetry data be used to estimate air-sea heat flux in the North Atlantic?

Liping Wang

NASA-UMD JCESS, NASA/GSFC, Greenbelt, Maryland

Chester Koblinsky

NASA/GSFC, Greenbelt, Maryland

## Abstract.

We propose a novel approach to directly invert large-scale anomalous annual net air-sea heat flux from the Topex/Poseidon altimetry data in the North Atlantic. The major advantage of this new approach over the conventional bulk formula approach is that it does not need those climate parameters used in the conventional bulk formula calculation in estimating the large-scale anomalous annual net air-sea heat flux. Comparison with expendable bathythermograph data demonstrates that it is a feasible approach.

## Introduction

The large-scale, mean and fluctuating, ocean circulation, is strongly forced by wind stress, air-sea heat flux, and fresh water flux. To accurately estimate these three forcing fields is of great importance to our understanding of the dynamics of large-scale ocean circulation and climate. Most of the available air-sea heat flux data sets are computed using bulk formulas [Moisan and Niiler, 1996] (MN96). Others are obtained through numerical weather prediction reanalysis, such as the European Center for Medium-range Weather Forecast (ECMWF) data set. Large differences exist among major different heat flux data sets, which presumably indicates the uncertainty in our knowledge of the air-sea net heat exchange. In this study, we propose an alternative and novel approach to directly estimate the large-scale, annual heat flux anomaly from the Topex/Poseidon (T/P) altimetry data in a inverse sense. This approach avoids most of the difficulties inherent in the bulk-formula-based estimation of the heat flux.

## Background

According to Gill and Niiler's [1973] (GN73) study, annual sea level height variability can be written as

$$\eta'_a = \eta'_{ba} + \eta'_{sa}, \quad (1)$$

where prime denotes variability, subscript  $a$  denotes an annual component,  $\eta'$  is the sea level height variability,  $\eta'_b$  is the barotropic component, and  $\eta'_s$  is the steric height variability.  $\eta'_a$  can be readily estimated from the T/P data. Greatbatch and Goulding's [1989] study suggests that in our study domain (shown in Fig. 1 as the lightly shaded region),  $\eta'_{ba}$ , driven primarily by the anomalous annual wind stress [GN73], is less than 0.5 cm. According to Tsaoussi and Koblinsky's [1994] estimate, the measurement error of large-scale sea level height variability, the focus of this study, is about 3 cm in our study region. For the present study, 2-year T/P data are used to estimate  $\eta'_a$ . So the measurement error of the annual sea level height variability is about 0.5 cm, assuming that the measurement errors between different cycles are uncorrelated. Considering that  $\eta'_{ba}$  is no bigger than the measurement error, we will take  $\eta'_a$  measured by the T/P altimeter as the annual steric height variability and include  $\eta'_{ba}$  as part of the overall measurement error of the annual steric height variability. That would increase the measurement error of  $\eta'_{sa}$  to about 0.7 cm, which is still much less than the T/P-observed annual variability in the North Atlantic ( $\sim 5$  cm) [Nerem et al., 1994].

From Huang's [1993] upper boundary condition for salinity (using the conventional notation), the buoyancy budget of the annual steric height variability can be written as [Wang and Koblinsky, 1996a] (WK96a)

$$\begin{aligned} \frac{\partial \eta'_{sa}}{\partial t} = & -\frac{\alpha}{\rho_0^2 C_p} Q'_a + \nabla \cdot \int_{-H}^0 dz \frac{1}{\rho_0} (\bar{u} \rho'_a, \bar{v} \rho'_a) \\ & + \nabla \cdot \int_{-H}^0 dz \frac{1}{\rho_0} (u'_a \bar{\rho}, v'_a \bar{\rho}) + \\ & \nabla \cdot \int_{-H}^0 dz \frac{1}{\rho_0} (u' \rho' - \bar{u} \bar{\rho}', v' \rho' - \bar{v} \bar{\rho}')_a, \end{aligned} \quad (2)$$

where  $H$  is the depth of the ocean,  $\rho_0$  is the reference density, bar represents mean state,  $C_p$  is the specific heat, and  $\alpha$  ( $= -\partial \rho / \partial T$ ) is the thermal expansion coefficient with  $T$  as the temperature. Since the focus of our study is the large-scale annual variability away from the western boundary and subtropical recirculation region, lateral mixing processes are ignored in the buoyancy budget equation (2). As we can see from equa-



heat content variability represented by the left-hand-side term of equation (5). XBT data is used to obtain an independent estimate of the annual heat content variability. Through the heat balance (5), we can then assess the accuracy of the annual heat flux anomaly estimated from the T/P data, i.e., assess the feasibility of directly estimating the large-scale, annual air-sea heat flux anomaly from the T/P data.

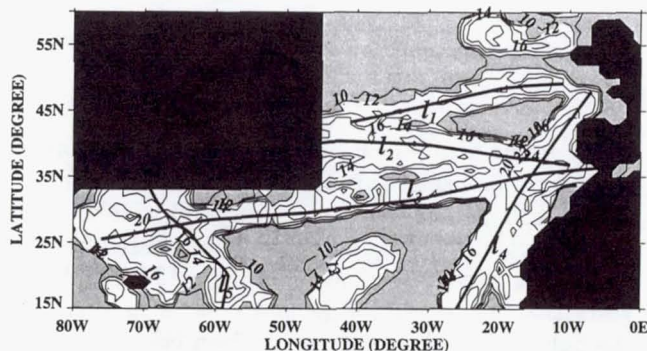


**Figure 2.** Number of monthly observations in the 2-year period from December of 1992 to December of 1994 in the North Atlantic. Regions with fewer than 12 monthly observations are lightly shaded. The 5 XBT lines,  $l_1$ ,  $l_2$ ,  $l_3$ ,  $l_4$ ,  $l_5$ , that go through the most frequently surveyed regions are also shown as the 5 solid lines.

XBT casts of at least 300 m deep, taken in our study region during the same 2-year period as the T/P observations (from December of 1992 to December of 1994), were used to estimate the annual heat content variability. In the region south of about 50°N, the mixed-layer depth is mostly shallower than 300 m [Huang, 1989]. According to Stommel's [1979] discussion, large-scale seasonal variability in the midlatitude is primarily confined within the mixed layer. So, 300 m is deep enough to allow us to capture the large-scale annual variability in our study region. We binned the XBT data into a monthly  $1^\circ \times 1^\circ$  grid with a bin radius of  $2^\circ$  in both longitude and latitude. The observation density of the monthly data is shown in Fig. 2. The figure shows that, except for small regions such as those around the 5 XBT lines ( $l_1$ ,  $l_2$ ,  $l_3$ ,  $l_4$ , and  $l_5$ ), the majority of our study region is not well sampled. Along the 5 XBT lines, there are at least 12 monthly observations in each grid in the 2-year period. To mitigate the undersampling of the annual variability by the XBT data, we will consider only the heat content balance represented by equation (5) along the 5 XBT lines.

According to Wyrski and Uhrich's [1982] estimate, the uncertainty of the left-hand side in eq. (5) estimated from the XBT casts is about  $15 \text{ W/m}^2$ . Both the amplitude and phase of the annual heat content change along each of the 5 XBT lines are filtered by a Gaussian filter with a radius of  $6^\circ$  to remove any sub-basin-scale variability, the results are shown in Fig. 3.

As Fig. 3 (a), (b), (c), (d), (e), and (f) show, along the 3 zonally oriented XBT lines, both the amplitudes and phases of the anomalous annual heat flux estimated from the T/P data agree well within the uncertainty range with those estimated from the XBT data, except for very small segments along XBT lines  $l_2$  and  $l_3$ . Considering that our objective is large-scale annual variability, the disagreement in small segments along  $l_2$  and  $l_3$  is unimportant. Similarly, along XBT lines  $l_4$  and  $l_5$ , both the amplitudes and phases of the anomalous annual heat flux estimated from the T/P data agree well within the uncertainty range with those estimated from the XBT data, except for a small segment south of  $20^\circ\text{N}$  along  $l_4$ . A plausible explanation for the disagreement is that XBT line  $l_4$  is close to the eastern boundary where Rossby wave radiation from the eastern boundary and its attendant buoyancy and heat advection tends to be stronger than in the area farther to the west, especially at low latitude.

For comparison, the ECMWF heat flux (chosen as a representative of available heat flux data sets, either bulk-formula based or numerical model based heat flux data sets) is also shown in Fig. 3 as the thin black lines. Overall, the 10 panels shown in Fig. 3 indicate that in our study region, the anomalous annual net air-sea heat flux from the T/P data is a better representation of the true annual heat flux anomaly than that estimated from the ECMWF data set.

## Conclusion

In this paper we propose to estimate directly the large-scale, annual air-sea heat flux anomaly from the T/P data as an alternative to the bulk-formula based or numerical model based heat flux estimates in the North Atlantic away from the western boundary and subtropical recirculation regions. The major advantages of this new approach over the conventional bulk formula approach are that it does not need those parameters used in the conventional bulk formula calculation in estimating the large-scale, anomalous annual heat flux, and it readily gives error estimates. Comparison with heat content change estimated from simultaneous XBT data suggests that it is a feasible approach.

As pointed out by Fu et al. [1996], the T/P satellite will continue to measure the sea level height for another 2 years, and a follow-on mission to T/P, JASON, is currently being developed by France and the United States, with a launch planned for 1999. A longer observation of the sea level height variability will enable us to make a better estimate of the anomalous, annual (seasonal) heat flux. The main limitation of our simple approach is that it can be used to estimate only the large-scale annual (seasonal) anomalous heat flux in regions that are outside the equatorial band and away from strong boundary current regions. A more systematic study using longer T/P data and comparison with more available heat flux data sets, such as that recently compiled by MN96, will be carried out in the future.



## NATURAL HAZARDS

Technological developments, such as multifrequency and multipolarization sensors, designed to observe Earth science parameters can help understand, characterize, and/or monitor surface and atmospheric conditions that may lead to natural disasters. Microwaves can image the Earth through clouds and darkness to detect flooding beneath a variety of herbaceous and woody vegetation and provide information on snow and ice conditions in the polar regions. Microwaves penetrate the surface of many materials to permit analysis of subsurface properties. The energy received by the sensor is dependent on the dielectric properties of the substance and is generally dependent on the amount of liquid water in the material. There is a distinct melt signal in the microwave emission from an ice sheet due to the transition from volume scattering in the dry snow cover, where losses are high, to surface scattering at the onset of melt where losses are low. As a result, melting snow has a much higher microwave emissivity than dry snow. It is this phenomena that Abdalati and Steffens used to study the melt conditions of the Greenland ice sheet before and after the eruption of Mt. Pinatubo. Using Special Sensor Microwave/Imager (SSM/I) and Scanning Multichannel Microwave Radiometer (SMMR) 19 and 37 GHz brightness temperatures it was shown that Mt. Pinatubo had a significant effect on the melt conditions on the Greenland ice sheet. It can then be assumed that similar changes occurred in other ice covered regions of the Earth.

Chang et al. estimated surface wind speed, water vapor, cloud liquid water, and rainfall rate over the sea for typhoons in the Taiwan region. They used the passive multifrequency (19.4, 22.2, 37, and 85.5 GHz) radiation data from the (SSM/I) on board of the Defense Meteorological Satellite Program (DMSP) satellites. In 1994, five typhoons hit the island of Taiwan in two months. Chang et al. were able to make an assessment of the relative strength of the typhoons with the analyzed data.

In sharp contrast to the satellite remote sensing performed by Chang et al. is the airborne remote sensing application of the Goddard Space Flight Center Scanning Radar Altimeter (SRA) to be used during the 1998 hurricane season. Flying through hurricanes at 1.5 km altitude, the SRA will provide, for the first time, a complete spatial/temporal record of the storm surge as well as the variation of the height and steepness of the waves that ride on top of the storm surge and cause the structural damage.







# The apparent effects of the Mt. Pinatubo eruption on the Greenland ice sheet melt extent

Waleed Abdalati

Universities Space Research Association, Seabrook, Maryland

Konrad Steffen

Cooperative Institute for Research in Environmental Sciences, University of Colorado, Boulder Colorado

**Abstract.** The indirect climatological effects of major volcanic eruptions can be of great importance because of the complex feedbacks that exist in the global climate system. One such effect is the melt area reduction on the Greenland ice sheet. Using passive microwave satellite data for the period 1979-1995, the melt conditions of the ice sheet before and after the 1991 Mt. Pinatubo eruptions are examined. Statistical tests indicate that an observed drop following the eruptions has a 97% to 99% probability of being outside the limits of undisturbed variability. Furthermore, this anomaly diminishes as the time from the eruption increases. These characteristics, in conjunction with an observed increasing melt trend prior to the eruptions indicate that Mt. Pinatubo has had a significant effect on the melt conditions, and consequently the energy balance characteristics of the Greenland ice sheet.

## Introduction

In June of 1991, Mt. Pinatubo erupted spewing massive amounts of debris and an estimated 20 Mt of sulfur dioxide gas into the stratosphere (Bluth et al., 1992). This additional stratospheric loading and the associated increase in atmospheric optical thickness had worldwide implications ranging from reddened sunsets to reduced tropospheric temperatures. Often overlooked, however, are the indirect effects of such an eruption that arise from the Earth's complex feedback mechanisms. One such effect is the surface melt variations of the Greenland ice sheet and other ice caps, and their role in the regional and global energy budgets. The Greenland ice sheet (Fig. 1) is of particular interest due to its great expanse of melt area, its topography, and its situation in the synoptically dynamic northern hemisphere.

The Greenland ice sheet has an area of  $1.75 \times 10^6 \text{ km}^2$  and a volume of  $2.65 \times 10^6 \text{ km}^3$  (Thomas, 1993), sufficient to raise the current level of the world's oceans by 7 m (Warrick and Oerlemans, 1990). In addition to its potential impact on sea level, this vast ice sheet reflects nearly 80% of its incident solar radiation (Stroeve, 1996), and thus helps maintain low temperatures in the Arctic. However, when snow begins to melt, its albedo decreases considerably from about 0.9 for dry snow (Oke, 1987) to approximately 0.7 for wet snow (Konzelmann and Ohmura, 1995). As a result, the occurrence of melt on the ice sheet can as much as triple the heat absorption by the snow pack, which in turn leads to enhanced melt and warming of the firm layer. Thus the snow-albedo reduction due to melt on the ice sheet is a positive feedback mechanism which amplifies changes in climate. For this reason, the Greenland ice sheet, along with the other ice covered regions of the

Earth, is believed to be a sensitive indicator of global change (Mitchell et al., 1990).

An understanding of the behavior of the ice sheet in response to short-term climate perturbations, such as the eruption of Mt. Pinatubo, is important to the understanding of its potential role in long term climate change. In this investigation, we examine the melt of the Greenland ice sheet for the time period 1979-1995. By comparing the pre-Pinatubo melt conditions (1979-1991), with the post-Pinatubo melt conditions (1992-1996), the impact of the eruptions is studied. It should be noted that despite the fact the Mt. Pinatubo erupted in June of 1991, the effects would not be expected to reach the Arctic during the 1991 melt season because of the time needed for aerosol transport. Therefore, in this study, the "pre-Pinatubo" period is taken to include 1991, while the "post-Pinatubo" period begins in 1992.

## Approach

Satellite observations provide some of the best data for climate studies of the remote, high-latitude regions of the earth because of their large spatial coverage and high temporal resolution. Passive microwave data are particularly useful because of microwaves' cloud-penetration capabilities, and the availability of data during the polar night. Furthermore, there is a distinct melt signal in the microwave emission of the ice sheet due to the transition from volume scattering in the dry snow cover, where losses are high, to surface scattering at the onset of melt where losses are low. As a result, melting snow has a much higher microwave emissivity than dry snow (Mätzler and Hüppi, 1989). This melt signal enables the classification of wet and dry snow regions of the ice sheet (e.g. Mote et al., 1993; Ridley, 1993; Zwally and Fiegles, 1994; Mote and Anderson, 1995; Abdalati and Steffen, 1995; Abdalati and Steffen, 1997). For this investigation the melt conditions of the Greenland ice sheet are determined using passive microwave satellite data from the Scanning Multichannel Microwave Radiometer (SMMR, 1978-1987) and the Special Sensor Microwave Imager (SSM/I, 1987- present), both on board polar orbiting satellites.

To assess the melt characteristics, the cross-polarized gradient ratio (XPGR) method (Abdalati and Steffen, 1997) is used. The XPGR is given as:

$$XPGR = \frac{T_b(19h) - T_b(37v)}{T_b(19h) + T_b(37v)} \quad (1)$$

where  $T_b(19h)$  is the 19 GHz horizontally polarized brightness temperature observed by the SSM/I (18 GHz in the case of SMMR), and  $T_b(37v)$  is the 37 GHz vertical polarization brightness temperature for both the SMMR and SSM/I instruments. It has been shown that a threshold can be established in this ratio which



on the Greenland ice sheet, and this anomaly resulted in an abnormally low MME for that year. Assuming a mean summertime solar irradiance of  $286 \text{ W m}^{-2}$  (observed in 1995 at the automatic weather stations shown in Figure 1) the observed shrinkage of melt area that accompanied these anomalies translates to a decrease in absorbed solar power of as much as  $8.6 \times 10^{12}$  watts.

The statistical significance of the 1992 decrease in melt area was first analyzed using the Student *t* test to determine the maximum prediction interval beyond which the observed MME lies. Based on the previous years' melt data, the projected 1992 melt is estimated at  $195,000 \text{ km}^2$  (estimate A in Fig. 2). The 99% prediction interval for this estimate is  $120,400 \text{ km}^2$ , which does not encompass the 1992 observed MME of  $71,000 \text{ km}^2$ . Thus, assuming the trend should have continued as it had in the preceding years, the likelihood of the low 1992 melt extent is less than 1%. The impact of Mt. Pinatubo on temperatures worldwide has been established (Halpert et al., 1994), as well as the relationship between the temperatures and melt on the ice sheet (Abdalati and Steffen, 1997). Therefore, we infer that the exceptionally low melt of 1992 was caused by the enhanced stratospheric loading from the Mt. Pinatubo eruption, and the associated reduction in surface irradiance.

Closer analysis of the trend behavior shows an oscillatory nature with an approximate three-year periodicity. Because of this, one might expect the 1992 MME to be on the low side of the trend regression line (as in 1983, 1986, and 1989). In this case, estimate A in Figure 2 would be too liberal because it does not account for the periodicity of the melt. To assess the relevance of this cycle, its mechanisms must first be understood.

This melt oscillation is not statistically correlated to the El Niño/Southern Oscillation, nor is it significantly correlated with the North Atlantic Oscillation (NAO). Based on the NAO indices of Hurrell (1995), and the Southern Oscillation Index (SOI) values as discussed by Trenberth, (1984), each accounts for less than two percent of the variance of both MME and coastal temperatures (monthly SOI values are available through 1994 from the National

Center for Atmospheric Research in Boulder, Colorado, at [http://www.joss.ucar.edu/publications/southern\\_oscillation.html](http://www.joss.ucar.edu/publications/southern_oscillation.html)). However, two of the three minima in the MME cycle, 1983 and 1989, do coincide with the maxima in the NAO record, suggesting some link between the two in extreme cases. This is consistent with the negative temperature anomalies in Greenland that have historically been associated with positive values of the NAO index (Walker and Bliss, 1932; Van Loon and Rogers, 1978). Therefore, we believe that despite the weak correlation over the limited sample period, the sinusoidal nature is a result of NAO extremes. Since the NAO index of 1992 is approximately half of the 1983 and 1989 values (Hurrell, 1995), the North Atlantic Oscillation is not considered to contribute significantly to the low 1992 MME, and estimate A is valid.

The second test is an analysis of the variance of the pre-Pinatubo detrended values. In this case, the variance about the trend is determined, and the deviation of the 1992 melt area from the pre-Pinatubo MME is calculated as a function of the standard deviation ( $\sigma$ ). This approach assumes that over time, despite the observed trend, the melt will remain constant. With the increase of greenhouse gases and the expected associated warming, this assumption is a very conservative one, and as such will tend to underestimate the significance of Mt. Pinatubo. Using this approach, the standard deviation of the detrended mean melt extent was found to be  $35,700 \text{ km}^2$ . With a pre-Pinatubo average MME of  $147,900 \text{ km}^2$  (estimate B in Fig. 2), the 1992 MME is 2.15 standard deviations from the mean, making it a 97% outlier. Thus, even this modest estimate supports the hypothesis that 1992 was a highly anomalous year, which is most likely attributable to the effects of the Mt. Pinatubo eruption.

Equally as important as the decrease in melt following the eruption, is the rapid increase in the years 1993–1995. The steepness of the curve compared to the pre-Pinatubo years is likely to be a combined result of the disappearance of the additional aerosols and a return toward the pre-Pinatubo trend. The 1995 melt is within nearly 1% of the pre-Pinatubo average MME, which indicates some recovery from the Pinatubo effects. However, considering the estimated time constant (or *e*-folding time) of 500 days (Post et al., 1996), the effects of Pinatubo may still be 11% of their maximum value of May, 1992 (Stone et al., 1993) and are thus still suppressing the melt. If this is the case, then melt in the coming years should continue to rise and resume character of the pre-Pinatubo trend. Additional years of data will verify or refute this.

## Conclusion

It is clear that 1992 was an anomalous melt year on the Greenland ice sheet, with the likelihood of such a low melt amount being between 1/33 and 1/100. Considering the strength of the anomaly and the steep increasing trend in the years that follow, the most likely reason for such an anomaly is the eruption of Mt. Pinatubo. Pinatubo's effects on temperature and other various phenomena have been documented (Halpert et al., 1994), but its impact on the melt characteristics of the Greenland ice sheet have not. Given the role of the Greenland ice sheet in regional and global energy balance, such a significant change in the MME in response to a single atmospheric perturbation underscores the importance of understanding the interactions between the ice sheet and the other components of the global climate system.

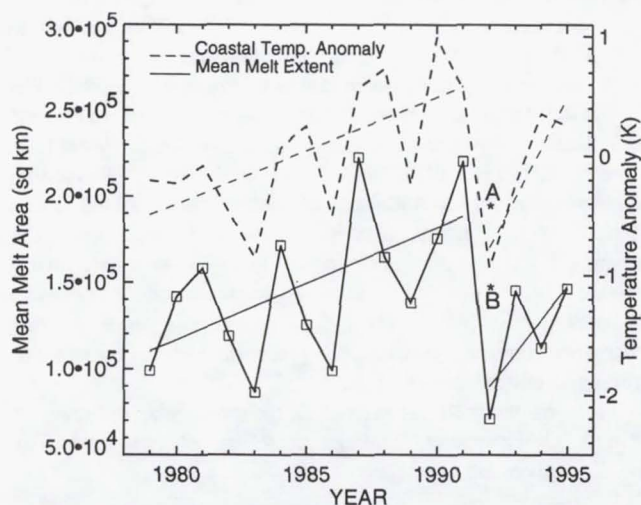


Figure 2. Interannual variations in mean melt extent (MME). The MME is determined by the XPGR classification technique for the years 1979–1995. Also shown are the average temperatures from six coastal stations (shown in Figure 1). Superimposed on the curves are the regression lines indicating the pre- and post-Pinatubo trends. The years 1978–1991 show a 4.4% increase in areal melt extent (Abdalati and Steffen, 1997), which was abruptly interrupted in 1992. Following 1992, the trend appears to resume. Two different estimates of the 1992 expected melt value are also shown (A and B).



## ANALYSES OF 1994 TYPHOONS IN THE TAIWAN REGION USING SATELLITE DATA

A.T.C. Chang	Hydrological Sciences Branch, Laboratory for Hydrospheric Processes NASA Goddard Space Flight Center, Greenbelt, MD 20771, USA
L.S. Chiu	SAIC/General Science Corporation, Laurel, MD 20707, USA
G.R. Liu and K.H. Wang	Center for Space Research and Remote Sensing National Central University, Chung-Li, Taiwan

### ABSTRACT

Taiwan is situated in the prevalent typhoon track in the northwestern Pacific. On average, about one third of the island total annual precipitation is due to typhoons, with the other two third being contributed by the summer monsoon, or Meiyu, and wintertime large scale frontal rainfall. While the typhoons bring the needed moisture for agricultural consumption and industrial utilization, heavy rainfall associated with typhoons often result in large scale flooding and land slide. The prediction of the typhoon track and its severity is therefore a high priority topic both for operation and research.

The severity of a typhoon can be defined in terms of the wind strength and the moisture content. The Special Sensor Microwave/Imager (SSM/I) on board of the Defense Meteorological Satellite Program (DMSP) satellites measures microwave radiation in 19.4, 22.2, 37 and 85.5 GHz. These measurements provide an opportunity to estimate parameters such as surface wind speed, water vapor and cloud water contents, and rainfall rate over oceans.

In 1994, Taiwan experienced an above normal frequency of typhoon hits, five typhoons hit the island in two months. In this report, estimates of the moisture content of these typhoons are made based on the SSM/I measurements. An assessment of the relative strength of the typhoons are made with analyzed data.

### INTRODUCTION

Geosynchronized visible and infrared data have been used to study typhoon. A technique to analyze and forecast tropical cyclone intensities using satellite pictures has been developed by Dvorak (1975). Three parameters: the central features which define the cloud system center and its relation to dense overcast clouds; the outer banding features which curve around the central features; and the vertical depth of the clouds comprising these features are used to estimate cyclone intensity. Using this method, the Central Weather Bureau (CWB) of Taiwan routinely tracks typhoon positions using GMS (Geostationary Meteorological Satellite) data. Since these observations give only information of the topmost layer of clouds, it is difficult to infer quantitative parameters within the typhoon. Microwave radiation, which penetrates the cloud and rain layers, can provide additional information of the internal structure of typhoons.

Multifrequency microwave data has been used to infer surface wind speed, atmospheric water vapor and cloud liquid water content and rainfall rate over the oceans. The retrieval of surface-wind speed, water vapor and non-precipitating liquid water has been discussed by Wilheit and Chang (1980). Linear regression coefficients were derived from an ensemble of models of the calculated brightness temperatures corresponding to different values of the input parameters.



From the calculated rain rate distribution, LHR can be computed for each SSM/I pass. Samples of the LHR and PIP of each typhoon for the inner and outer core regions are tabulated in Table 1. The correlation between LHR and PIP are 0.98 for the inner and 0.96 for the outer core region. The correlation between the maximum wind speed and inner core LHR and PIP are 0.94 and 0.98, respectively, whereas that between maximum wind speed and the outer core LHR and PIP are 0.68 and 0.48, respectively, which are probably not significant. Hence the severity of the typhoon is highly correlated with the latent heat release in the inner core region. The correlation is slightly higher for the PIP than LHR for the inner core region. These results are very similar to those of Rodgers et al. (1994). Results from these five typhoons suggest that the convective heating could be used as a predictor of typhoon severity.

Table 1: Derived LHR and PIP for five typhoons of 1994

Name	Time of the observation	Maximum wind speed (Kts)	L H R (J/sec) (111 km radius)	PIP (%)	LHR (J/sec) (222 km radius)	PIP (%)
Tim	7/9 0121Z	70	$112 \times 10^6$	0.38	$192 \times 10^6$	0.08
Caitlin	8/2 1307Z	30	$91 \times 10^6$	0.19	$248 \times 10^6$	0.23
Doug	8/6 0135Z	115	$255 \times 10^6$	0.80	$608 \times 10^6$	0.52
Fred	8/18 0851Z	100	$239 \times 10^6$	0.69	$256 \times 10^6$	0.10
Gladys	8/31 0145Z	55	$135 \times 10^6$	0.39	$80 \times 10^6$	0.04

There are other factors that could also affect the intensity of the typhoon, such as sea surface temperature, vertical wind shear, tropospheric moisture distribution, etc. Typically, the intensity of tropical cyclones continuously pulsates due to the growth and decay of these factors. In addition, typhoon intensity seems to be regulated by the solar heating, thus varies with time of day. For typhoon Fred, three of the consecutive SSM/I passes (8/18 0851Z, 8/18 2125Z and 8/19 0200Z) give average rainfall rate of 9.2, 7.6 and 10.3 mm/hr for the inner core. The corresponding LHR values are  $239 \times 10^6$ ,  $197 \times 10^6$ , and  $268 \times 10^6$  J/sec respectively. The PIP values are 0.69, 0.48 and 0.87 for the inner core. The intensity estimated by CWB are 100 Kts over the entire time period.

From the patterns of the retrieved parameters one may be able to obtain some clue to the movement of the typhoons. Due to the non-contiguous coverage accurate determination of the typhoon track becomes difficult. Inspection of the retrieved parameters along the satellite swath show there is little additional information from SSM/I retrieved parameters in delineating the location of the typhoon center. In addition, within the vicinity of the typhoon system, the quality of these retrieved parameters degrade rapidly.

## CONCLUSION

Multichannel SSM/I data have been used to retrieve surface wind speed, water vapor, cloud liquid water and rainfall rate in the typhoon cases. Derived values are comparable to the climatological values. Due to the lack of observation data, no direct comparisons are made. The linear relationships between LHR and typhoon intensity and between PIP and typhoon intensity seem holds well for those five typhoons. This linear relation may be inadequate for inferring the intensity of other typhoons. Further investigations are needed to quantify the relationship between intensity, LHR and PIP.



## LONG TERM CLIMATE VARIABILITY

The papers in this section investigate decadal to centennial and glacial scale climate changes from modeling studies and observations. While the duration of remote sensing data are in most cases shorter than a couple of decades, the remote sensing data can be used to assess the spatial, horizontal, and vertical properties as to how the seasonal signal in different climate regimes is stored in the ice sheets. Remote sensing data can be used to understand secular changes, such as those, arising from recent volcanic eruptions (Mt. Pinatubo) and its influence on snow/ice melt. Radar altimetry data, with its finer resolution, although the time series is even shorter than passive microwave, are used in process studies to determine the drainage of ice sheets which occur in narrow ice streams and to make estimates of mass balance.

The study by Abladati and Steffen shows how snow melt can be derived from passive microwave measurements to construct the seasonal melt cycle at different elevations of the Greenland ice sheet. They estimated a trend of 4.4% in the melt area between 1979 and 1991 which came to a halt in 1992 after the Mt. Pinatubo eruption, but started anew after 1993. Their estimate of the melt area change may also signal changes due to the anthropogenic climate change because the estimated melt area change exceeds one standard deviation of the natural variability of melt area variability.

An example of the use of passive microwave data in the ice core stratigraphy is provided in the works of Alley et al. and Shuman et al. The seasonal layers in snow and ice can be determined from dust layers but also from hoar layers which can be detected by passive microwave.

Snow/ice melt in the summer is a key variable in the growth of ice sheets and it depends on surface albedo. However, albedo measurements are not yet available globally. Chang et al. used the airborne Advanced Solid-State Array Spectrometer (ASAS) instrument to construct albedo over a snow field. These data showed strong angular dependence and tended to confirm the anisotropic nature of snow reflectance.

The papers of Joughin et al. and Rignot et al. discuss Greenland ice sheet mass balance. The former paper shows how ice streams can be identified and their velocities estimated from radar altimetry. Rignot et al. derive an estimate for ice discharge using radar interferometry which is 3.5 times larger than derived from observations based on iceberg calving. Williams et al. study the Vatnajökull ice cap retreat and advance from Landsat images and combine them with local observations to construct the behavior of the ice cap. Zwally and Giovinetto have used various data sources to estimate the annual sea level variability and areal distribution of  $\delta^{18}\text{O}$  using multiple regression analysis.

On the ocean front, Cane et al. discuss the SST trends in the Tropical Pacific during this century. Their study points out the opposing trends between the western (warming) and eastern (cooling) Equatorial Pacific and discuss the dynamical reasons. Seager and Murtugudde provide a modeling study to explain the dynamics of the opposing long term trends and find that equatorial upwelling makes the SST less sensitive to surface heat fluxes. The lack of refined equatorial dynamics in the present day coupled models used to predict  $\text{CO}_2$  influence may lack this negative feedback. In the case of sea ice model studies, Rind et al. showed that given the current climatic characteristics, temperature sensitivity to doubled  $\text{CO}_2$  is affected more by sea ice in the Southern Hemisphere and by sea ice thickness in the Northern Hemisphere.

Considering higher latitude oceanic climate, Mauritzen and Hakkinen show that the sea ice export from the Arctic influences strongly the overturning in the North Atlantic. Considering high and low phases of the North Atlantic Oscillation (NAO), which induces increased or decreased ice export, the overturning difference between the extreme NAO states can reach 20-30%.







## Snowmelt on the Greenland Ice Sheet as Derived from Passive Microwave Satellite Data

WALEED ABDALATI AND KONRAD STEFFEN

*Center for the Study of Earth from Space, Cooperative Institute for Research in Environmental Sciences,  
University of Colorado, Boulder, Colorado*

(Manuscript received 1 December 1995, in final form 29 April 1996)

### ABSTRACT

The melt extent of the snow on the Greenland ice sheet is of considerable importance to the ice sheet's mass and energy balance, as well as Arctic and global climates. By comparing passive microwave satellite data to field observations, variations in melt extent have been detected by establishing melt thresholds in the cross-polarized gradient ratio (XPGR). The XPGR, defined as the normalized difference between the 19-GHz horizontal channel and the 37-GHz vertical channel of the Special Sensor Microwave/Imager (SSM/I), exploits the different effects of snow wetness on different frequencies and polarizations and establishes a distinct melt signal. Using this XPGR melt signal, seasonal and interannual variations in snowmelt extent of the ice sheet are studied. The melt is found to be most extensive on the western side of the ice sheet and peaks in late July. Moreover, there is a notable increasing trend in melt area between the years 1979 and 1991 of 4.4% per year, which came to an abrupt halt in 1992 after the eruption of Mt. Pinatubo. A similar trend is observed in the temperatures at six coastal stations. The relationship between the warming trend and increasing melt trend between 1979 and 1991 suggests that a 1°C temperature rise corresponds to an increase in melt area of 73 000 km<sup>2</sup>, which in general exceeds one standard deviation of the natural melt area variability.

### 1. Introduction

The Greenland ice sheet is one of the major ice sheets of the world and as such plays an important role in the global and regional climates. With a present surface area of  $1.75 \times 10^6$  km<sup>2</sup> and a volume of  $2.65 \times 10^6$  km<sup>3</sup>, which correspond to 11% and 8% of the global glacier surface area and ice volume, respectively (Thomas 1993), it contains enough water to raise the current sea level by 7 m (Warrick and Oerlemans 1990). As a result, it can potentially play a significant role in sea level change.

Of major climatological significance is the areal extent and duration of surface snowmelt on the ice sheet. Because wet snow absorbs significantly more incident solar radiation than dry snow, the ice sheet composes an unstable, positive feedback component of the climate system. That is to say that an increase in snowmelt on the ice sheet will result in the absorption of more of the incident solar energy, which will, in turn, cause further melting and so on. In addition, increased melt can contribute to cloud feed-

back, as melting snow provides a vapor source for cloud formation, which, in turn, will increase the downwelling longwave radiation, which can further increase melt. Thus, the instability of the ice sheet due to snowmelt may be much greater than the simple albedo effect. The assessment of these cloud feedback effects is beyond the scope of this paper; however, they do underscore the importance of understanding ice sheet melt characteristics.

Because of the large size and gentle slope of most of the Greenland ice sheet, small changes in the air temperature will result in large areal changes in the dry and wet snow facies. Assuming an adiabatic lapse rate of 0.6°C/100 m (Orvig 1970), a slope above the equilibrium line of 0.4° (Steffen 1995), and a melt area perimeter of 3300 km, a 1°C temperature rise will increase the melt area by 79 000 km<sup>2</sup>. Therefore, it is evident that the melt conditions are a very sensitive parameter in the Arctic climate and climate changes.

To understand the role of melt in the climate variability, and the impact of the climate on ice sheet melt extent, a means of monitoring the melt characteristics of the ice sheet over large areas and long periods of time is necessary. Because of the remoteness and unfavorable environment on the ice sheet, the in situ data are very limited. For this reason spaceborne in-

---

Corresponding author address: Dr. Waleed Abdalati, Universities Space Research Association, NASA/Goddard Space Flight Center, Mail Code 972.0, Greenbelt, MD 20771.  
E-mail: abdalati@osb.wff.nasa.gov



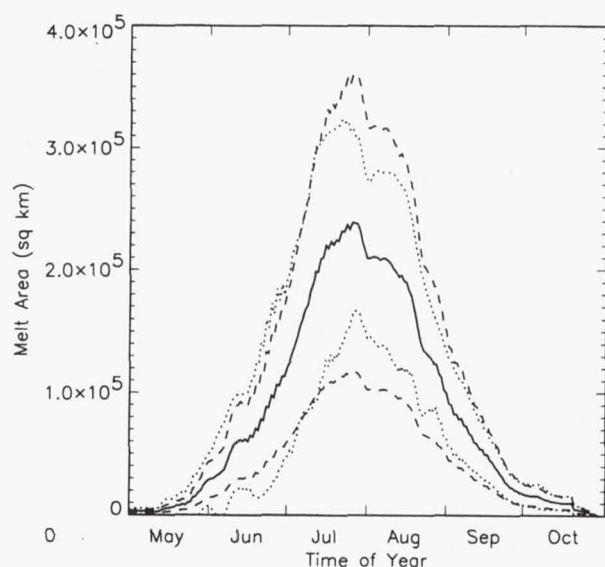


FIG. 3. The average spatial melt extent for the years 1979–94 (solid line), mean melt  $\pm 1$  standard deviation (dotted line), and melt area for  $1^{\circ}\text{C}$  temperature change (dashed line) in  $\text{km}^2$  for the melt months of June, July, and August. The extent was calculated by determining the mean area coverage for these months in each year and then averaging these values over the entire coverage period.

#### g. Effects of bare ice

Bare ice emission on the ice sheet is assumed to be similar to that of thick lake ice and as such is relatively independent of frequency (Ulaby et al. 1986). As a result, the XPGR of a region in which the snow has completely melted is nearly zero, and is classified as melting snow. This assumption is supported by observations of late-season emission in the ablation zone. This phenomena leads to a late estimation of refreeze of exposed ice (until snow has fallen and remained frozen on the surface). However, since melt is considered only between the months of June and August, the assumption that the bare ice is wet is assumed to be of little consequence. Still, it is acknowledged as a limitation of the algorithm for melt assessment purposes.

## 4. Results and discussion

### a. Seasonal melt cycle

The average extent of snowmelt for the years 1979–94 is shown in Fig. 3 along with the range of melt extent within one standard deviation of the average. Also shown are the melt areas associated with a heating or cooling of  $1^{\circ}\text{C}$ , which are discussed in section 4c below. The locations of melt for the primary melt months, June, July, and August, are depicted in Fig. 4. Melt onset begins at a limited number of coastal pixels in April and May and is very slight. In early June, the melt begins to spread, primarily around the region of Sondre Stromfjord and Jakobshavn but is still

limited in areal extent. During mid- to late June, and the early part of July, the melt extent increases rapidly, as is indicated by the steep slope of the curve in Fig. 3. In late July, melt is at its maximum extent covering nearly the entire perimeter of the ice sheet, and most of the southern portion of the ice sheet (south of  $68^{\circ}\text{N}$  lat) with the exception of the high-elevation South Dome. After late July, refreeze begins to occur on the ice sheet and the areal extent of melt begins to drop off steadily until mid- to late September and then more gradually through October.

The area showing the most melt throughout the summer is the region along the west coast beginning at the southern tip of the ice sheet and extending north past Jakobshavn. This region is the first to show melt, the last to show refreeze, and remains wet, farther inland than most other locations (Figs. 4a–c). This may most likely be attributable to the gentle slope on the western side of the ice sheet, the greater radiation intensity at the lower latitudes as compared to the higher ones, and possibly the influence of the warm dry continental air mass approaching from Canada, which dominates the summer circulation (Ohmura and Reeh 1991). Another area of extensive melt is the northeast portion of the ice sheet near Danmarkshavn and Nord. This region also has a very gentle slope and is a low elevation (900 m above sea level). Subsequently, more melt would be expected in this area.

A significant characteristic of Fig. 3 is the skewness, or asymmetry about the peak. This results from a combination of two factors: 1) the differing emission depths for the two frequencies and 2) the fact that melt and refreeze of the snow both occur from the top down (i.e., first near the surface and then progressing deeper into the snow).

For dry snow near its melting point, 19-GHz radiation is emitted primarily in the top 2.5 m of the snowpack and at 37 GHz, most of the emission is from the top 30 cm (Ulaby et al. 1986). When melt begins near the surface, however, the effective emission depth decreases considerably to approximately 10 cm for a 1% liquid water content (Ulaby et al. 1986) for both 19 and 37 GHz. That is to say that more of the signal comes from the snow near the surface when the snow is wet than when the snow is dry. This occurs because in the case of dry snow, the energy can pass through the air between the snow grains with little or no extinction. As the space between the snow grains fills with water, nearly all of the energy that passes between the grains is absorbed by the water. With this increased extinction, the effective emission depth, defined as the inverse of the extinction coefficient, decreases.

During the spring and early summer, the snow is absorbing incident radiation and undergoing heating near the surface. The greater depths, which are primarily heated by conductive heat fluxes from the surface, respond more slowly. Therefore, during this time of year, the deeper snow is colder than the snow closer to the



# Visual-stratigraphic dating of the GISP2 ice core: Basis, reproducibility, and application

R.B. Alley,<sup>1</sup> C.A. Shuman,<sup>2</sup> D.A. Meese<sup>3</sup>, A.J. Gow<sup>3</sup>, K.C. Taylor<sup>4</sup>, K.M. Cuffey<sup>5</sup>, J.J. Fitzpatrick<sup>6</sup>, P.M. Grootes<sup>7</sup>, G.A. Zielinski<sup>8</sup>, M. Ram<sup>9</sup>, G. Spinelli<sup>1</sup>, and B. Elder<sup>3</sup>

**Abstract.** Annual layers are visible in the Greenland Ice Sheet Project 2 ice core from central Greenland, allowing rapid dating of the core. Changes in bubble and grain structure caused by near-surface, primarily summertime formation of hoar complexes provide the main visible annual marker in the Holocene, and changes in "cloudiness" of the ice correlated with dustiness mark Wisconsinan annual cycles; both markers are evident and have been intercalibrated in early Holocene ice. Layer counts are reproducible between different workers and for one worker at different times, with 1% error over century-length times in the Holocene. Reproducibility is typically 5% in Wisconsinan ice-age ice and decreases with increasing age and depth. Cumulative ages from visible stratigraphy are not significantly different from independent ages of prominent events for ice older than the historical record and younger than approximately 50,000 years. Visible observations are not greatly degraded by "brittle ice" or many other core-quality problems, allowing construction of long, consistently sampled time series. High accuracy requires careful study of the core by dedicated observers.

## 1. Introduction

Analyzing visible layers is among the oldest of ice sheet stratigraphic techniques [e.g., *Benson* 1962; *Langway* 1967; *Gow* 1968b]. It is based on the simple observation that summer snow and winter snow look different. This difference in appearance arises from the physical reality that the properties of near-surface snow are affected by atmospheric conditions and radiative fluxes, which change seasonally.

"Correctness" of visible stratigraphy in dating accumulated snow has had a mixed record, ranging from high accuracy to significant errors [e.g., *Clausen* and *Dansgaard*, 1977]. This probably has multiple origins, including variations in visibility of strata, degree of seasonality of strata, accumulation rate, and, we strongly suspect, knowledge/ability of observers. Because visible observation is so easy (almost anyone can look at snow or ice) there may have been a wide diversity in training and experience,

especially in the early traversing days, such that some observers may have lacked the expertise needed for highly accurate observations whereas others certainly were masters of the art. In light of this mixed record, *Hammer et al.*, [1978] estimated that visible stratigraphy is proven to ages of no more than 200 years with accuracy of 10%.

The advantages of visible stratigraphy for ice-core dating include the ease with which it is accomplished, the rapid dating which allows adjustment of sampling schemes in real time during core processing, the adaptability of the method in brittle ice or under other changes in ice quality, and the strong physical basis of the seasonal signal. Before application to the Greenland Ice Sheet Project 2 (GISP2) core, however, it was necessary to demonstrate that visible stratigraphy is sufficiently accurate to be useful and to characterize that accuracy better. We undertook a multicomponent study which included process studies of the origin of visible strata (section 2.1), regional monitoring of the occurrence and timing of visible strata using passive-microwave data (section 2.2), studies of physical processes in the ice that might affect the visible strata (section 2.3), and a variety of comparisons to other annual indicators, to marker events such as volcanic fallout, and to repeat counts by various analysts (section 5). The techniques used are described in sections 3 and 4. We believe visible stratigraphy provides dates for the GISP2 core that are accurate to within roughly 1% in the Holocene and within about 5% in the Wisconsinan ice age to roughly 40-50 kyr B.P. (thousand years before the year 1950).

## 2. Basis of Visible Stratigraphy

### 2.1. Physical Processes of Formation of the Holocene Hoar Signal

One can see many things in an ice core. High concentrations of windblown or basally derived dust or of volcanic ash are easily visible to the eye [e.g., *Gow and Williamson*, 1976]. Melt layers appear in otherwise bubbly ice as glassy-

<sup>1</sup>Earth System Science Center and Department of Geosciences, The Pennsylvania State University, University Park.

<sup>2</sup>Oceans and Ice Branch, NASA Goddard Space Flight Center, Greenbelt, Maryland.

<sup>3</sup>U.S. Army Cold Regions Research and Engineering Laboratory, Hanover, New Hampshire.

<sup>4</sup>Desert Research Institute, University and Community College System of Nevada, Reno.

<sup>5</sup>Department of Geological Sciences, University of Washington, Seattle.

<sup>6</sup>Office of the Central Regional Geologist, U.S. Geological Survey, Denver, Colorado.

<sup>7</sup>Laboratory of the Christian Albrechts University Kiel, Kiel, Germany.

<sup>8</sup>Institute for the Study of the Earth, Oceans and Space, University of New Hampshire, Durham.

<sup>9</sup>Department of Physics, State University of New York at Buffalo.



but they could complicate observations at greater depths in the core. Similarly, other features occasionally are visible in ice cores (e.g., forest-fire-fallout layers, volcanic dust), which complicate the signal. We have demonstrated that visible strata are strongly seasonally controlled, but we do not believe that they are perfectly seasonally controlled.

Fundamentally, in counting any annual marker, we must ask whether it is absolutely unequivocal, or whether nonannual events could mimic or obscure a year. For the visible strata (and, we believe, for any other annual indicator at accumulation rates representative of central Greenland), it is almost certain that variability exists at the subseasonal or storm level, at the annual level, and for various longer periodicities (2-year, sunspot, etc.). We certainly must entertain the possibility of misidentifying the deposit of a large storm or a snow dune as an entire year or missing a weak indication of a summer and thus picking a 2-year interval as 1 year.

Counting of layers in ice cores is often compared to dendrochronology. When properly used, tree-ring dating produces zero-error ages. Notice, however, that "occasionally trees will produce false rings...in extreme years some trees may not produce an annual growth layer at all, or it may be discontinuous" and "two or three cores should be taken from each tree and at least 20-30 trees should be sampled at an individual site" [Bradley, 1985, p. 334-335]. Where similar care has been taken in ice cores with a sufficiently high accumulation rate, zero-error ages also are obtained based on intercomparison and calibration to historical volcanic eruptions [e.g., Hammer *et al.*, 1978; Mosley-Thompson *et al.*, 1993], particularly when the presence of tephra can verify the aerosol signal [Palais *et al.*, 1991].

Perhaps the main practical difference between ice-layer and tree-ring dating is the difficulty of the core recovery and handling in the ice-core case. The GISP2 core, for example, is 3 km long, weighs approximately 40 tons, and required tens of people working over five summers to collect. It is obvious that the ideal tree-ring standard of tens of repetitions to guarantee perfect accuracy is not practicable in the deep-ice-core case, although it is being approached for the most recent centuries [e.g., Hammer *et al.*, 1978; Clausen *et al.*, 1988; White *et al.*, this issue].

We thus must accept that single-core dates, and especially single-core/single-indicator dates, involve some uncertainty. Furthermore, they will involve some "personal" factor, because the way different people deal with the uncertainty in counting years may be different. When faced with a question of whether one is looking at a single long year or two short ones separated by a weak seasonal indicator, some individuals will make one decision and some will make the other ("lumpers" and "splitters"). It is unlikely that such decisions will be random.

We observe this behavior in our intercomparisons. Although we see no statistically significant differences in dating by different visible stratigraphers through the Holocene, we do see small but significant differences in the interannual variability of recorded layer thicknesses between some visible stratigraphers. Careful examination of the data shows that some of the difference in variability is related to placement of the summer maximum within the depth-hoar zones. Because the zones tend to lack sharp, unequivocal onsets and terminations, there is some freedom in choosing the midsummer level, which in turn allows for different observers to obtain slightly different results. In addition, some of the difference in

variability may be related to "splitting" or "lumping" of years in regions of weaker annual signals. (For some time series analyses, the changes in variability in a hybrid time series produced by several observers might introduce spurious results. We thus have prepared a Holocene time series based solely on observations by R.B.A., and we have begun to analyze it statistically; [Alley *et al.*, 1995; Spinelli, 1996].)

## 7. Conclusions

Visible stratigraphy has proven to be a useful dating tool for the GISP2 deep ice core, to roughly 50 kyr B.P., and agrees with independent age assessments within their level of accuracy prior to historical records. The signal of depth-hoar complexes was used in the Holocene. Surface and remote-sensing studies show that the hoar complexes are produced in the upper centimeters of the snow by processes linked to summer sunshine, that they are widespread features of the dry-firm facies of central Greenland that are preserved consistently, and thus that they can be expected to be good annual markers. In the early Holocene/Preboreal, the visible signal was calibrated from depth-hoar layers to visible cloudy bands most probably linked to dust content. Cloudy bands were then counted in the Wisconsinan.

Careful surface preparation and light control are necessary for optimal visible stratigraphy as a dating tool. Failure to do so may degrade the signal to the point that no useful data are obtained. Careful application of technique is essential, with adaptation as needed to adjust for changing signal characteristics.

Comparison of visible-stratigraphic ages to fallout from historical volcanoes over the most recent 2 millennia, to independent ages for the end of the Younger Dryas, to other annual markers in the ice core, and to repeat visible stratigraphy by various observers, indicates accuracy typically at the 1% level over century-length or longer intervals through the Holocene. In the Wisconsinan, comparisons to available absolute time markers and intercomparisons of various layer counts suggest 5% or better accuracy over millennial or longer intervals to perhaps 50 kyr B.P.

Errors may arise from true imperfection of the ice core's climate record, from core-quality problems, or from human error in interpreting the record. Intercomparisons of layer counts show that a human factor does exist, although all counts typically are so close that we cannot choose objectively among different estimates because no significant differences exist. We believe that true climate-record imperfections are scarce or absent for accumulation rates typical of central Greenland and thus that multiparameter counts of multiple cores should allow dating with errors much smaller than 1%; however, the reality of the difficulties in collecting and analyzing such cores probably precludes that level of accuracy over 50 kyr or longer for the foreseeable future.



## Twentieth-Century Sea Surface Temperature Trends

Mark A. Cane,\* Amy C. Clement, Alexey Kaplan,  
Yochanan Kushnir, Dmitri Pozdnyakov, Richard Seager,  
Stephen E. Zebiak, Ragu Murtugudde

An analysis of historical sea surface temperatures provides evidence for global warming since 1900, in line with land-based analyses of global temperature trends, and also shows that over the same period, the eastern equatorial Pacific cooled and the zonal sea surface temperature gradient strengthened. Recent theoretical studies have predicted such a pattern as a response of the coupled ocean-atmosphere system to an exogenous heating of the tropical atmosphere. This pattern, however, is not reproduced by the complex ocean-atmosphere circulation models currently used to simulate the climatic response to increased greenhouse gases. Its presence is likely to lessen the mean 20th-century global temperature change in model simulations.

Amidst the often contentious debate on global warming, there are areas of general consensus. There is agreement that Earth's surface temperature has increased over the last 100 years by between  $\sim 0.3^\circ$  and  $0.6^\circ\text{C}$  (1). There is, however, disagreement as to the causes of this temperature increase. It may be a response to anthropogenic forcing, a part of the climate system's innate natural variability, or a combination of the two. There is also general consensus that the radiative effect of increased atmospheric concentrations of greenhouse gases will cause Earth's temperature to rise. The direct warming effect of these gases is rather small, but there is a potential for amplification by positive feedbacks within the climate system. Understanding of these mechanisms is incomplete, and the strength of the amplification is uncertain, as evidenced

by the fact that, when loaded with twice the modern concentration of atmospheric  $\text{CO}_2$ , state-of-the-art climate models give mean global changes varying from  $1.5^\circ$  to  $4.5^\circ\text{C}$  (1).

Until quite recently, simulations of the climatic response to increasing concentrations of greenhouse gases gave temperature changes that exceeded the observed increase by about a factor of 2 (1, 2). It was then suggested that the discrepancy might result from the neglect of the cooling effect of sulfate aerosols (3). Inclusion of this effect brought simulations into better agreement with observations (1, 2). Unfortunately, the radiative effects of aerosols are poorly understood. It is quite possible that the influence of the values currently used in simulations is considerably larger than the true influence (4) and is substituting for natural moderating mechanisms that are absent or underrepresented in present models.

Here we point out a pattern in the changes of sea surface temperature (SST) over the course of the 20th century—an increase in the zonal gradient across the equatorial Pacific—that has been missed in simulations performed with comprehensive climate models [general circulation models

(GCMs)]. Recent theoretical studies (5–8) have predicted this pattern as a response to exogenous heating of the tropical atmosphere. If the theory is correct, it would provide evidence that the coupled atmosphere-ocean dynamics are delaying, and possibly regulating, global warming. The absence of this mechanism in the GCM simulations may account in part for the discrepancy between the observed and modeled global mean temperature rise.

The theoretical ideas we invoke (5–8) follow the line of argument first proposed by Bjerknes (9), which forms the foundation of our present understanding of the El Niño–Southern Oscillation (ENSO) phenomenon (10). Suppose a uniform external heating is imposed on the tropical Pacific. The SST will tend to rise, leading to increased evaporative cooling until a new, warmer equilibrium is reached. This change would be the only response in the absence of a decisive contribution from ocean dynamics. In the eastern equatorial region, however, vigorous upwelling brings up cold waters from below, counteracting the warming tendency. Thus, initially, the SST increases more in the west than in the east, enhancing the temperature gradient along the equator. The atmosphere responds with increasing trade winds, which in turn will increase the upwelling rate and the thermocline (11) tilt, cooling the surface waters in the east and further enhancing the temperature contrast. As a consequence of this dynamical feedback, the mean temperature will increase less than it would with the purely thermodynamic response.

To test the mechanism, we imposed a uniform forcing on a simplified model of the ocean-atmosphere system in the tropical Pacific, the Lamont model used to forecast El Niño (12). The forcing was chosen so that in the absence of ocean dynamics, SST would increase by  $1^\circ\text{C}$  everywhere. In the model's mean annual response (Fig. 1), not only does the eastern equatorial Pacific cool, consistent with the mechanism described above, but the dynamics of the coupled ocean atmosphere system spreads the influence of the upwelled waters throughout the tropical Pacific, such that the mean increase in temperature is only  $0.5^\circ\text{C}$ .

A number of objections to this theory and model demonstration may be raised. The theory relies on colder upwelled waters balancing some of the imposed heat input, but the simple ocean model used specifies a fixed thermocline temperature. In reality, the waters of the equatorial thermocline originate at the surface at higher latitudes. If these source waters were to warm up, then equatorial thermocline temperatures would eventually increase; the cooling effect would then be reduced on a time scale set by the renewal time for the equatorial thermocline. Some recent

M. A. Cane, A. C. Clement, A. Kaplan, Y. Kushnir, D. Pozdnyakov, R. Seager, S. E. Zebiak, Lamont-Doherty Earth Observatory, Palisades, NY 10964–8000, USA.  
R. Murtugudde, Universities Space Research Association, Laboratory for Hydrospheric Processes, NASA Goddard Space Flight Center, Greenbelt, MD 20771, USA.

\*To whom correspondence should be addressed.



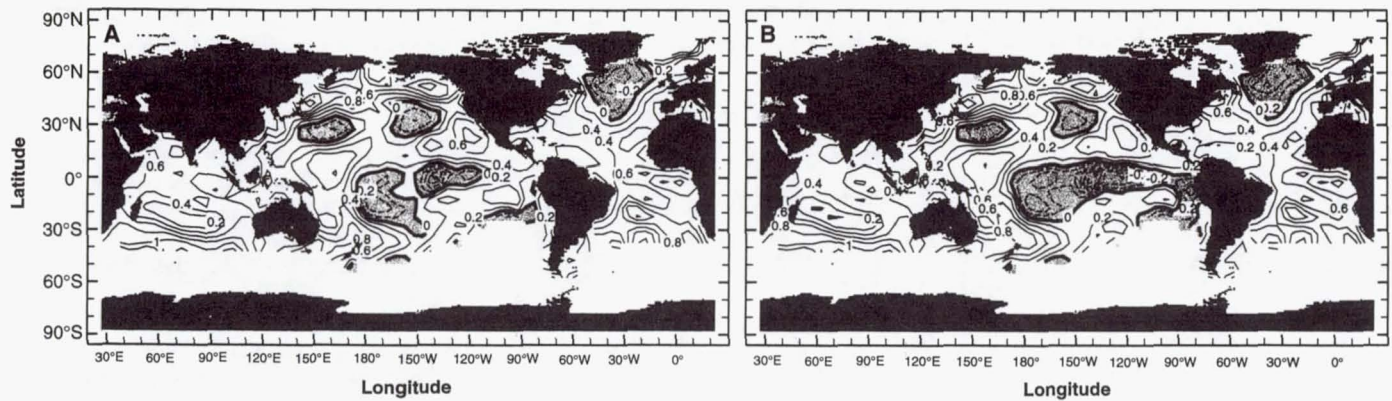


**Fig. 3.** (A) The trend in monthly mean SST anomalies for 1900 to 1991 in degrees Celsius per century. The SST fields are from an optimal smoother analysis (21). (B) As in (A), except that the influence of the large number of ENSO warm events at the end of the record was screened out before the

trend was calculated. This was done by removing the ENSO mode, defined as the leading empirical orthogonal function of the variability in the 2- to 7-year band. The projection of this pattern onto the data was subtracted from the record, and the trend in the remainder was computed.

not. As an index of zonal gradient, we used the difference between climatically important regions in the western (WP) and eastern (NINO3.4) equatorial Pacific. Although trends in the three data sets differ strongly within each region (Fig. 4), the trend in the gradient WP-NINO3.4 is more consistent. All three data sets show a strengthened gradient over the 20th century. In degrees Celsius per century with 95% confidence limits, the trend in the gradient is  $+0.66 \pm 0.14$  for our analysis,  $+0.11 \pm 0.15$  for GOSTA, and  $+0.28 \pm 0.14$  for COADS (29). All three versions of the SST data support the predictions for strong atmospheric coupling (5–8) over the enhanced eastern warming of the greenhouse models (16–18). In addition, the

most relevant previous study (8), which included an analysis of trends since 1949, found an enhanced SST gradient as well as strengthened trade winds in both an atmospheric GCM and observational data.

Equatorial Pacific SST variations have a substantial impact on the global atmospheric circulation (30). The NINO3.4 region is thought to be the area of the tropical Pacific where SST anomalies have the strongest influence on the global atmosphere. Although we do not know how an atmospheric GCM would respond to the equatorial portion of the SST anomaly patterns of Fig. 3, the evidence suggests that atmospheric dynamics and thermodynamics would amplify the coupled negative feedback of the equa-

torial Pacific. First, the patterns have the general features of an ENSO cold event (La Niña), which is accompanied by a reduction of mean global atmospheric temperatures. Second, a recent report (31) examines the climate change associated with doubled atmospheric  $\text{CO}_2$  as simulated by an atmospheric GCM coupled to an ocean mixed layer. In one experiment, the SST was computed everywhere, and in another, the SST was held artificially fixed in the eastern equatorial Pacific. The global surface air temperature change was 22% less in the second experiment.

A scenario consistent with data and theory is that the pattern of 20th-century SST warming combined with eastern equatorial Pacific cooling is a consequence of anthropogenic greenhouse gases. Dynamical coupling between the atmosphere and the tropical Pacific is delaying and regulating global warming. State-of-the-art models, which do not simulate this feedback fully, reproduce the observed temperature rise only if they compensate by assuming a very high value for the poorly known radiative effect of sulfate aerosols. The long-term consequences of the two processes, one an internal feedback and the other a temporary radiative forcing, would be quite different. It is thus important to determine how each contributes to the observed 20th-century temperature rise. Although equatorial Pacific ocean dynamics may delay and reduce global warming, the associated SST changes in the tropical Pacific would engender changes in regional climate and climate variability over much of the Earth that would be likely to have substantial social and economic consequences.

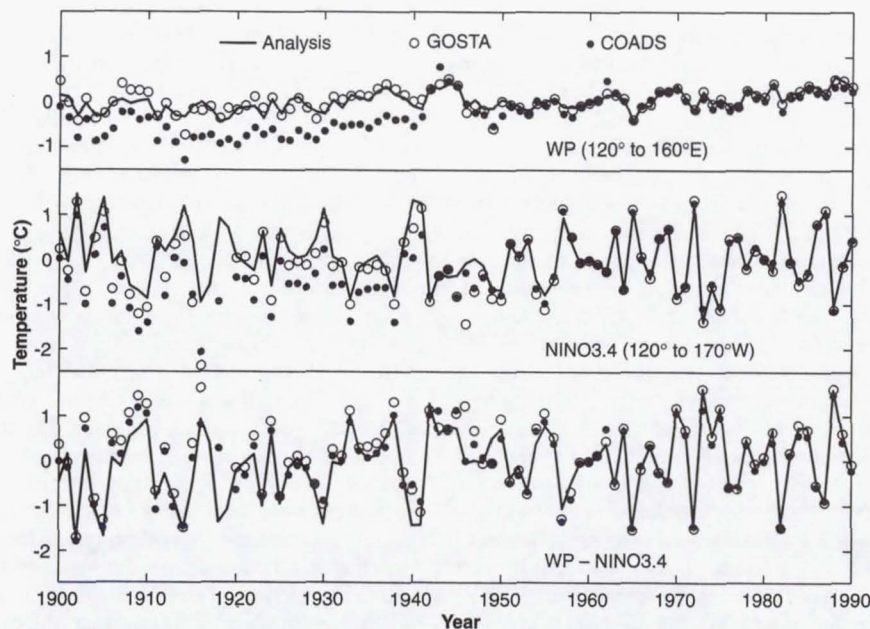


**Fig. 4.** Time series of (top) the average SST anomaly in the WP region ( $120^\circ$  to  $160^\circ\text{E}$ ,  $5^\circ\text{N}$  to  $5^\circ\text{S}$ ), (middle) the average SST anomaly in the NINO3.4 region ( $120^\circ$  to  $170^\circ\text{W}$ ,  $5^\circ\text{N}$  to  $5^\circ\text{S}$ ), and (bottom) the difference, a measure of the anomalous zonal SST gradient. Data from (solid curve) optimal smoother analysis (21), (open circles) GOSTA (27), and (closed circles) COADS (28).



# Multiangule Observations of Directional Reflectances of Snow Fields

A. T. C. Chang, D. K. Hall, J. L. Foster

(Hydrological Sciences Branch, Laboratory for Hydrospheric Processes  
NASA Goddard Space Flight Center, Greenbelt, Maryland 20771, USA)

**Abstract** Accurate measurements of snow areas and surface albedo are crucial to advancing our understanding of the global climate system. This is because of the highly reflective nature of snow combined with its large surface coverage (snow can cover up to 40% of the Earth's land surface during the Northern Hemisphere winter). The reflectance of snow varies with both solar incidence angle and the viewing angle. Visible sensors with different spatial resolutions have been used to infer the snow parameters. Currently, only nadir-viewing directional reflectance data are available from satellite observations. Observations at multiple angles are needed to infer the hemispheric reflectance albedo of snow fields.

We propose to study the directional reflectance of snow fields using POLDER data, which contains information from different viewing angles and polarizations. POLDER was successfully launched on the ADEOS-1 satellite in August, 1996, however, because POLDER data are not yet available, data from ASAS, a pointable, airborne spectroradiometer, were used in this study. Data collected over Glacier National Park of Montana show strong angular dependence. Preliminary results confirm the anisotropic nature of the snow reflectance. Knowledge of the bi-directional reflectance function (BDRF) of snow-covered surfaces is the key to developing a true albedo model in the future.

**Key words** Snowpack, Albedo, BDRF

## 1 INTRODUCTION

The accumulation, distribution, structure and melt characteristics of the snowpack are largely affected by the regional energy balance. In turn, snow on the ground affects weather and climate, and the timing and amount of streamflow runoff. Through modeling, we will be able to improve our understanding of snow accumulation and ablation processes and thus, the snowpack energy budget.

The measurements provided by a remote sensor are primarily a function of the energy flux from the scene which is exiting in the direction of the sensor. This flux is dependent on the spatial, temporal, and angular distribution of energy fluxes entering the scene, and the spatial arrangement and properties of the types of matter within the scene. The critical remote sensing data required for studying the energy balance of a snowpack include snow extent, water e-

quivalent and albedo. Albedo is one of the most important parameters needed to model surface energy interactions. Snow albedo cannot be measured on a global scales, since spaceborne sensors presently only collect energy at narrow spectral bands and angles. However, it should be possible to infer albedo using data from a new breed of satellite sensors beginning in late 1990s.

Albedo is the energy reflected in all directions over the reflective part of the spectrum. Knowledge of the directional distribution of solar radiation reflected from snow surfaces is required to determine albedo because the anisotropic nature of the reflected radiation<sup>[1-3]</sup>. Reflectance of snow is greatest in the forward scattering direction due to specular reflection of snow crystals. Multiple reflections from the numerous ice crystals that comprise a snowpack cause the high reflectance of snow. For fresh snow, reflectance is nearly 100% in the visible region and decreases in the near infrared<sup>[4,5]</sup>. When surface



Fig. 3 and Fig. 4 show the reflectance of snow-covered and grass-covered surfaces with different incidence angles ( $+60^\circ$ ,  $+30^\circ$ ,  $0^\circ$ ,  $-30^\circ$ , and  $-60^\circ$ ) parallel to the principle plane of the sun. A halon target was used as a reference in calculating the surface reflectance. The reflectance factor varied from about 80% to 120% for the snow. For dormant grass, the

reflectance factor varied from 5% to 30%. As reported in the literature, some in-situ measurements using a portable spectrometer showed reflectance factor  $> 100\%$  relative to a barium sulfate or halon reference panel<sup>[9,10]</sup>. The exact reason for this is not well known, but it may be because the snow surface is not a perfect diffuse reflector.

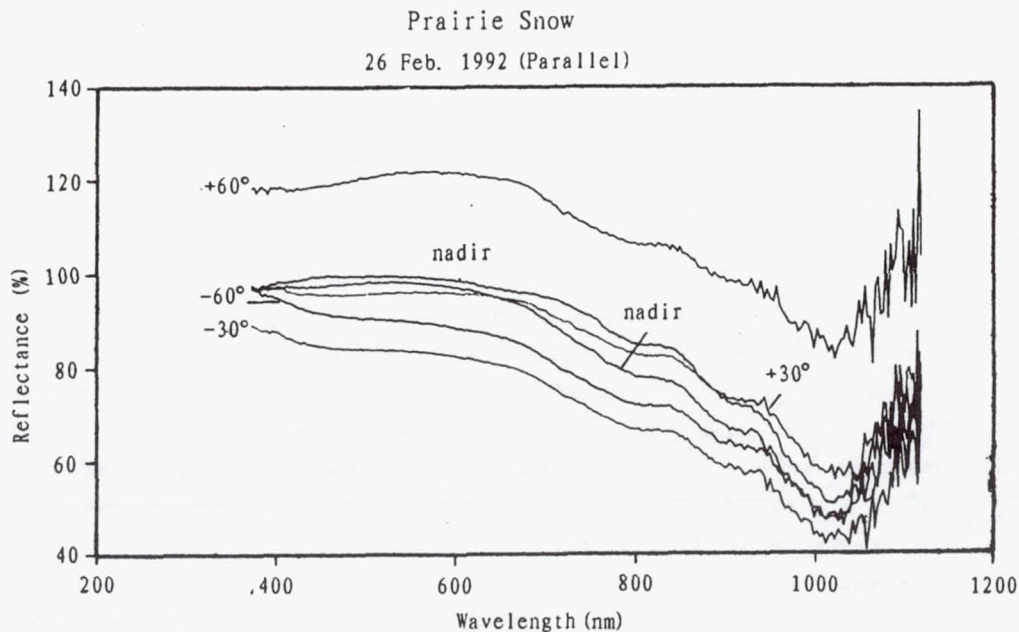


Fig. 3 Show the reflectance of snow-covered surfaces with different incidence angles parallel to the principle plane of the sun

To compare ASAS data derived reflectances with SE-590 observations, a small test area with  $10 \times 10$  ASAS pixels (about  $50\text{m} \times 50\text{m}$ ) was picked for each test site. The 6S model is used to translate the radiance into a reflectance factor. For the SE-590 data, the fractional surface coverage estimated by the ground crew was used to calculate the reflectance factor for a surface having a mixture of snow and dormant grass. Fig. 5 and Fig. 6 show the representative surface reflectance for site 1 and 2. Reflectance factors derived from ASAS are also plotted. At site 1, the match was good. For site 2, ASAS derived reflectance factors were about 10% lower than expected for a surface with 90% snow-cover and 10% dor-

mant grass. This discrepancy could very well be caused by the visual selection of the ASAS sample sites.

#### 4 SUMMARY

ASAS and SE-590 measured reflected solar radiances were used to study the directional reflection characteristics of snow-covered surfaces. A directional snow reflectance factor inferred from these data varied with the solar zenith angle and the surface snow characteristics. Mixtures of different surface types within a footprint will greatly affect the reflectance factor. Based on the knowledge gained in



# Balance velocities of the Greenland ice sheet

Ian Joughin

Jet Propulsion Laboratory, California Institute of Technology, MS 300-235, 4800 Oak Grove Drive, Pasadena, CA 91109, USA.

Mark Fahnestock

JCESS, Dept. of Meteorology, University of Maryland at College Park, College Park, MD 20742, USA.

Simon Ekholm

Kort og Matrikelstyrelsen, Rentemestervej 8, DK-2400 Copenhagen NV, Denmark

Ron Kwok

Jet Propulsion Laboratory, California Institute of Technology, MS 300-235, 4800 Oak Grove Drive, Pasadena, CA 91109, USA.

**Abstract.** We present a map of balance velocities for the Greenland ice sheet. The resolution of the underlying DEM, which was derived primarily from radar altimetry data, yields far greater detail than earlier balance velocity estimates for Greenland. The velocity contours reveal in striking detail the location of an ice stream in northeastern Greenland, which was only recently discovered using satellite imagery. Enhanced flow associated with all of the major outlets is clearly visible, although small errors in the source data result in less accurate estimates of the absolute flow speeds. Nevertheless, the balance map is useful for ice-sheet modelling, mass balance studies, and field planning.

## Introduction

The coverage over the Greenland Ice Sheet by the satellite-borne ERS-1 radar altimeter has dramatically improved our knowledge of the shape of the ice sheet surface. In this paper we will show that this knowledge, when combined with estimates of ice thickness and accumulation, yields a surprising amount of insight into the ice flow in the interior of the ice sheet. While we are only producing an estimate of the vertically averaged velocity required to maintain continuity, the knowledge of the surface from altimetry is detailed enough to show accurately where flow is converging into streams and to show the locations of ice divides and drainage boundaries. This work is in some aspects a repeat of earlier efforts in Greenland by *Budd, et. al* [1982], *Radok et. al* [1982], and *Bindschadler et al* [1989]; it represents an advance because of the greatly improved knowledge of the ice sheet surface.

Interferometric studies of ice motion over limited parts of the ice sheet interior [*Joughin et al*, 1996] required estimates of motion for tiepointing; this in turn led us to the initial calculation of balance velocities using an elevation model derived from ERS and Geosat radar altimetry [*Ekholm*, 1996] [*Ekholm et al.*, 1995]. The rich detail in the velocity fields calculated from this work was unexpected. The detailed patterns of concentrated flow, which are apparent when the

elevation model is used to trace flow lines, are in a number of cases not evident in moderate to high resolution satellite imagery of the ice sheet. We have found the balance velocity map to be useful for understanding ice flow patterns, for working with interferometric data, and for planning locations of field measurements. Because the balance velocity map distinguishes areas of active flow, it may prove useful for siting future ice cores.

Measured velocities on the ice sheet are sparsely distributed. Balance velocities, albeit only estimates, do provide a synoptic view of the motion of an ice sheet in steady state. As such, balance velocities can provide initial conditions for an ice sheet model or for model validation and diagnostics [*Bamber et al.*, 1996].

## Data And Technique

The balance velocity is the depth averaged velocity necessary to maintain the steady-state shape of an ice sheet [*Paterson*, 1994] [*Budd and Warner*, 1996]. Thus, for a gate of width  $L$  oriented normal to the flow direction, balance velocity can be calculated as

$$v_b = \frac{\int_{A_L} b(x, y) dS}{\int_{-\frac{L}{2}}^{\frac{L}{2}} T dl} \quad (1)$$

where  $b(x, y)$  is the mass accumulation field,  $T$  represents ice thickness over the gate (i.e., from  $-\frac{L}{2}$  to  $\frac{L}{2}$ ), and  $A_L$  is the upstream catchment area of the gate. *Radok et al* [1982] used a numerical method for computing the balance velocity along flow lines. Here we adopt a different approach. At each point on a 2-km grid we used a gate of width  $L = 8$  km and plotted the flow lines upstream from both sides of the gate to bound the area  $A_L$ . We then applied Equation (1) to determine the balance velocity for each point. We smoothed the results using a 18-km-by-18-km moving average filter to obtain the final result, which is shown in Plate 1.

Our initial estimates of area were biased by the contributions from flow lines that were spaced less than a pixel apart in divergent areas near the summit. We resolved this problem in two ways. First we used a finer grid (0.5 km) for the flow line and area computation. Second, we weighted the pixels where the flowlines were one pixel apart with an



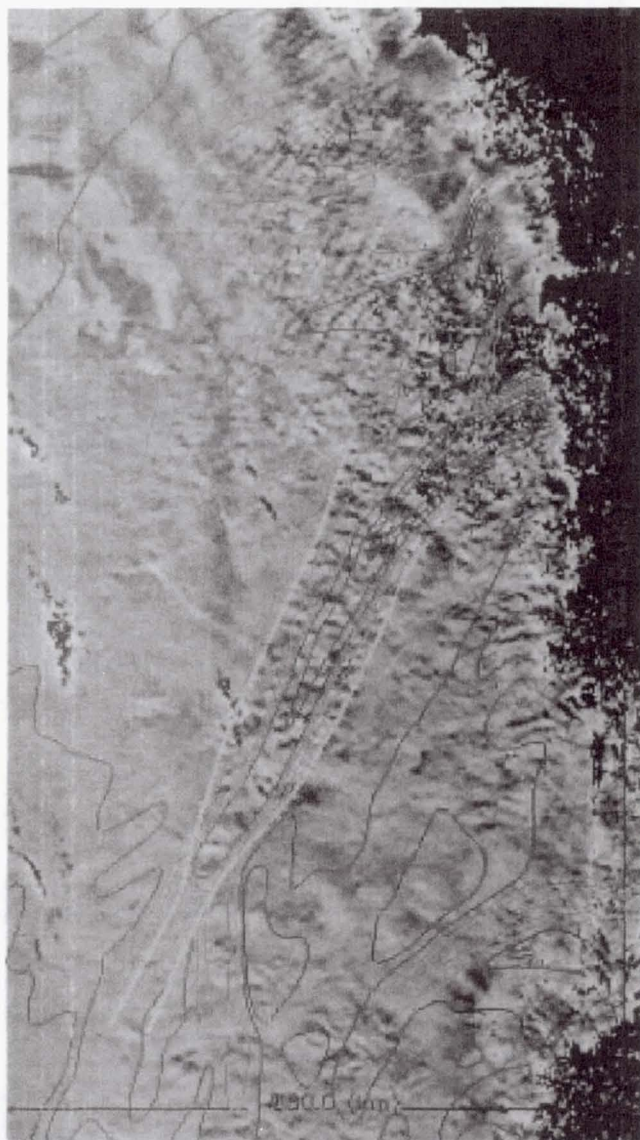


**Plate 2.** Balance velocities for the NE Greenland ice stream plotted over AVHRR visible band data. Contour colors have the same meaning as in Plate 1. The AVHRR data have been high-pass filtered to better illustrate the undulating topography associated with the ice stream. Visible boundaries of the ice stream are highlighted in yellow and high contrast areas near the coast have been blacked out.

near the centerline based on our analysis of preliminary velocity data determined from satellite radar interferometry. Furthermore, the width of the ice stream predicted by the balance velocities is too narrow in comparison with the location of the shear margins, which are visible in the AVHRR imagery (see Plate 2). We attribute the error in the shape of the velocity profile to the smoothing introduced by the altimeter and our processing, which causes our estimates of the flow to be concentrated too near the stream center.

The ice stream shows far more structure in the interior than is evident from visible and SAR imagery of the area. In high resolution imagery it appears to have a single tributary that flows essentially straight along the course of the middle part of the stream; in the balance map it is shown with a sec-

ond tributary of comparable speed flowing in from the south. We have seen preliminary evidence in SAR interferograms that this feature exists as predicted by the balance velocities. Just to the east of this second tributary is another flow feature that reaches well in from the coast, initially flowing northeast and bending around to flow out Waltershausen Glacier.

From this point, as we move south along the east coast, the drainages have large catchment areas and are highly convergent on their outlet glaciers. These glaciers have very steep gradients and flow through large, well established fjords. This produces the branching nature of the drainage divides in this area.

On the west coast, this pattern gives way to a more ordered pattern, where the drainages have nearly parallel sides reaching up to the divide. The Jakobshavns Isbrae drainage breaks from this pattern, with at least three branches converging near the coast. There are several other large glaciers to the north of Jakobshavns Isbrae, including Rinks Isbrae, several drainages to the north of Upernavik, and one just south of Camp Century. These glaciers exhibit rapid flow of several hundred meters per year well into the percolation zone, which shows up as the bright area in SAR imagery shown in Plate 1 [Fahnestock *et al.*, 1993]. These relatively high velocities with respect to the small catchments are needed to balance the high accumulation rates found along the west coast.

The pattern of ice flow changes character again in the north, where Petermann Glacier dominates the drainage, with rapid flow well into the ice sheet; the flow speed in Petermann is substantially greater than what is seen in Humboldt (the 100 km wide glacier just to the south-west). Qualitatively the balance velocity on the Petermann agrees well with the interferometrically measured velocity field [Joughin *et al.*, in preparation], with the areas of rapid flow predicted by the balance velocities in good agreement with the interferometric data. The velocity along the center line of the glacier, however, exceeds the measured velocity. In this area, the disagreement is primarily caused by the low resolution of the bed DEM, which is not sufficient to resolve the channel underlying the Petermann. Because the assumed ice thickness is too thin, continuity dictates that the estimated speed should be greater than the true speed. This phenomenon likely influences our estimates of flow speed on other outlet glaciers that have well developed channels that are missed in the bedrock DEM.

The pattern of ice flow, shown here as balance velocities, reveals a significant amount about the current behavior of the ice sheet. While these velocities assume steady state, and are subject to error from sparse accumulation data and limited ice thickness information, the pattern of ice flow largely is determined by the surface elevations and should be an excellent reflection of reality.

As our understanding of the shape of the ice sheet improves, we learn a substantial amount about the current ice flow. Much of what we see in an elevation model confirms recent observations about discharge; some of what can be learned from the elevation model provides new insight. Each improvement increases the challenge for numerical models of ice sheet behavior; it also improves the boundary conditions needed for this work.



# Influence of sea ice on the thermohaline circulation in the Arctic-North Atlantic Ocean

Cecilie Mauritzen<sup>1</sup> and

National Research Council/NASA Goddard Space Flight Center, Laboratory for Hydrospheric Processes, Greenbelt, MD 20771

Sirpa Häkkinen

NASA Goddard Space Flight Center, Laboratory for Hydrospheric Processes, Code 971, Greenbelt, MD 20771

**Abstract.** A fully prognostic coupled ocean-ice model is used to study the sensitivity of the overturning cell of the Arctic-North-Atlantic system to sea ice forcing. The strength of the thermohaline cell will be shown to depend on the amount of sea ice transported from the Arctic to the Greenland Sea and further to the subpolar gyre. The model produces a 2-3 Sv increase of the meridional circulation cell at 25N (at the simulation year 15) corresponding to a decrease of 800 km<sup>3</sup> in the sea ice export from the Arctic. Previous modeling studies suggest that interannual and decadal variability in sea ice export of this magnitude is realistic, implying that sea ice induced variability in the overturning cell can reach 5-6 Sv from peak to peak.

## 1. Introduction

The objective of this numerical investigation is to explore how interannual variations in the sea ice export from the Arctic influences the meridional overturning cell. Results from a series of observational and modeling studies combine to suggest that there might be a connection between these phenomena. Observations suggest that there are large interannual variations in the sea ice cover in the Polar and Subpolar Seas (Parkinson, 1991). Variations in sea ice cover represents variations in the local ice production as well as variations in the ice transport. The two existing estimates of ice export through the Fram Strait are 2800 km<sup>3</sup>/yr (Aagaard and Carmack, 1989) and 2000 km<sup>3</sup>/yr (Vinje et al., 1996). Modeling studies (Walsh et al., 1985; Häkkinen, 1995) suggest that there are long-term trends of lower and higher ice export at Fram Strait lasting for 5-10 years or more. The period in the late 1960's when fresh water capped the Labrador Sea, the vertical extent of convection, and thus the production of Labrador Sea Water, was limited (Lazier, 1980). This capping of fresh water is considered the largest N. Atlantic oceanic anomaly in this century and is described as a moving fresh water anomaly in the subpolar and polar seas, the "Great Salinity Anomaly", by Dickson et al. (1988). Its cause is still debated, however, modeling studies suggest that excessive Arctic ice export was the cause (Häkkinen, 1993).

Consistent with such a theory, Deser and Blackmon (1993) found that decadal fluctuations in SST east of Newfoundland (which may be taken as an indicator of convection depth) are traced to lag the Labrador Sea ice cover by 2 years.

We thus hypothesize that variations in fresh water input in the form of ice from higher latitudes influences convective overturning and contributes significantly to decadal variability in the North Atlantic Ocean circulation.

The coupled ice-ocean model used here has been previously used to study the seasonal sea ice cover in the Arctic (Häkkinen and Mellor, 1992). The Atlantic version (from 80S to 80N) of the Princeton Ocean Model (POM) has been published by Ezer and Mellor (1997). Our model shares the same ocean code with the inclusion of a sea ice component. The ice and ocean models and their initialization are briefly summarized in section 2. Sea ice export variability is driven by wind stress changes in reality, however to investigate the contribution from sea ice forcing on the overturning cell, we keep the wind stress the same but vary the viscosity of the ice to modulate the ice export. The model results are presented (Section 3) from two experiments which are: EXP1, where the ice export from the Arctic is adjusted to be 2800 km<sup>3</sup> annually; and EXP2 where sea ice is twice as viscous as in EXP1 leading to a considerably reduced sea ice export, about 1900 km<sup>3</sup> annually.

## 2. Model and surface forcing description

The coupled model is previously published in Häkkinen and Mellor (1992; and references thereof). The original POM code uses centered differencing for advection which can develop undesirable effects for scalar variables (such as unrealistic temperatures) when applied at strong frontal regions, e.g. such an intense front occurs over the Iceland Faroe ridge in the near bottom sigma-layers. In our model, we use a modified upstream differencing scheme based on piecewise parabolic method in the form developed by Lin et al. (1994). This scheme is much less diffusive than the regular upstream differencing, however, it still contains numerical diffusion, so we do not apply any explicit horizontal diffusion for T and S.

The coupled ice-ocean model extends from the Bering Strait to 15S with resolution of 7/10 in 'longitude', 9/10 in 'latitude' (in a rotated coordinate system with a equator at 30W and the pole at 120W, 0N). There are 20 sigma-levels in the vertical, with higher resolution near surface. The ocean model was initialized with the annual average hydrographic climatology of Levitus (1982) (Levitus climatology has well known

<sup>1</sup>Now at: EPSHOM CMO, 13, rue du Chatellier, BP 426, 29275 Brest Cedex, France - cecilie@shom.fr



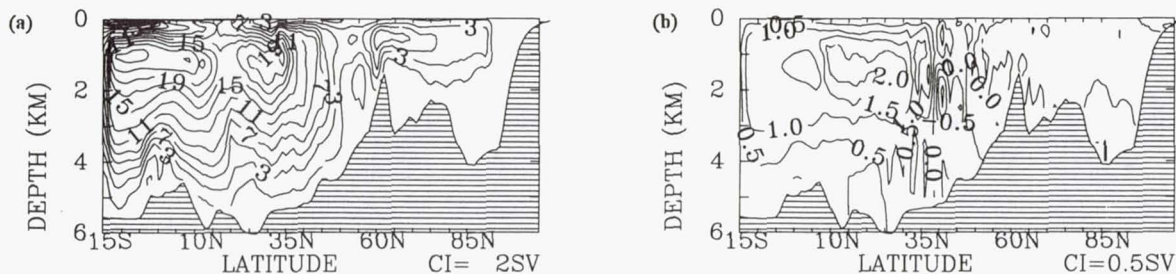


**Figure 4.** Overturning cell (annual average) at year 15 (a) EXP1 and (b) difference EXP2-EXP1. Contour interval is 2 Sv in (a), and 0.5 Sv in (b).

are concentrated in the Gulf Stream and North Atlantic Current area which we attribute to the JEBAR effect (Joint Effect of Baroclinicity and Relief). Its effect derives from deep baroclinic currents which in the North Atlantic are provided by the deep western boundary currents (DWBC) carrying the deep waters, Labrador Sea Water (LSW) and N. Atlantic Deep Water, equatorward (Greatbatch et al., 1991, and references thereof). Greatbatch et al. (1991) show that the subpolar gyre and Northern recirculation gyre are dominated by the bottom pressure torque component of JEBAR. Thus, variability in the thermohaline currents is reflected in mass transports as seen from the model results.

### 3.3. Meridional circulation and heat transport

As a common diagnostic of the model thermohaline circulation, a meridional stream function is computed and shown at year 15 for EXP1 in Fig. 4a and the difference, EXP2-EXP1, in Fig. 4b. The maximum annual overturning rate in EXP1 is 22 Sv which is slower by 2 Sv (as an annual average) than the EXP2 overturning cell. The difference reaches 3 Sv during summer season (not shown). The strengthening of the overturning in EXP2 builds up gradually from the beginning of the simulation and reaches over 1.6 Sv above the EXP1 value (at 25N) by year 6 after the first phase of Rossby adjustment has taken place. The vertical stream function does not necessarily represent how much of the deep water masses are formed: for instance the apparent near discontinuity between the subpolar gyre and GIN Seas is misleading because water masses with different density at the same level are moving in opposing directions. Instead, about 10 Sv of the Atlantic water flows north of the sills to be transformed into heavier deep water masses. Contributions to the overturning cell come from the Nordic sills overflow waters and Labrador Sea Waters. The EXP2 Nordic Seas overflow is 6.7 Sv versus 6.5 Sv in EXP1, i.e. a minimal change, which is expected because the fresh water flux hardly changed north of the sills. Thus, the largest differences originate from the subpolar gyre which receives far less fresh water in this simulation, thus giving an opportunity for more extensive water mass modification through surface heat loss. This increased convection would appear as mixed layer deepening which is the case as shown in Figs. 5 of March mixed layer depth for EXP1 and EXP2. EXP2 shows much deeper mixed layers in the Irminger and Labrador Seas as also evident in Levitus atlas (1982). The Labrador Sea tends to have very deep mixed layers, over 2000 meters, when LSW production is active. Thus, an extensive deep convection in

the Labrador Sea is connected to the strength of the overturning cell and, to the strength of DWBC by inference, as DWBC is an essential part of the thermohaline circulation.

The annual meridional heat transport at year 15 for EXP1 and EXP2 at 25N are 1.2PW and 1.3PW respectively, as one would expect from the difference in the overturning cell. The total heat transport is in a good agreement with the observational estimate of Hall and Bryden (1982). The largest differences between EXP1 and EXP2 occur during summer season, reaching over 0.2 PW, i.e. 10-20% of the annual average.

## 4. Conclusions

We have shown that sea ice export from the Arctic plays a significant role in determining the strength of the overturning cell in the North Atlantic Ocean. For the study we have used a fully prognostic coupled ocean-ice model of the Arctic-North-Atlantic system. The ice export is in reality modulated by the wind stress. However, in order to be able to differentiate processes affecting the circulation we have chosen to consider a pure process study of how ice export alone (i.e. not atmospheric conditions) influences the meridional overturning. Therefore, in order to obtain a reduced ice export we modulated the ice viscosity while keeping the atmospheric forcing constant. Thus, our two experiments share exactly the same initial conditions, and surface and lateral boundary conditions but have a factor of two difference in the sea ice shear viscosity.

In summary, the model produces a 2-3 Sv increase in the meridional circulation cell at 30N (at year 15 of the simulation) corresponding to a decrease of 800km<sup>3</sup> in the sea ice export from the Arctic. This reduction is especially significant in the export through Denmark Strait because it minimizes the role of ice as a fresh water source in the subpolar gyre and thus enhances convection in the Labrador Sea and in subpolar gyre in general. As a result of the reduction in Arctic sea export the thermohaline cell increased by 10-20% with a similar increase the meridional heat transport. Similarly, the annual meridional heat transport changes have a 0.1 to 0.2PW amplitude depending on latitude. In light of previous modeling studies (Walsh et al., 1985; Häkkinen, 1995) interannual and decadal scale changes in sea ice export of the order of +/- 800km<sup>3</sup> are realistic. Since the oceanic adjustment time is of the same timescale (5-10 years) it is not unrealistic to expect that the sea ice induced overturning cell variability can reach 5-6 Sv from low ice export decades to high ice export decades.



## North and Northeast Greenland Ice Discharge from Satellite Radar Interferometry

E. J. Rignot,\* S. P. Gogineni, W. B. Krabill, S. Ekholm

Ice discharge from north and northeast Greenland calculated from satellite radar interferometry data of 14 outlet glaciers is 3.5 times that estimated from iceberg production. The satellite estimates, obtained at the grounding line of the outlet glaciers, differ from those obtained at the glacier front, because basal melting is extensive at the underside of the floating glacier sections. The results suggest that the north and northeast parts of the Greenland ice sheet may be thinning and contributing positively to sea-level rise.

---

The traditional view on the mass balance of the Greenland ice sheet is that accumulation of mass (mostly snow) in the interior regions is released to the ocean through surface ablation (or melting) and calving of icebergs (1). Of all three components of the mass balance, snow accu-

mulation is the best known from measurements of snow pits and ice cores across the ice sheet (2). Observations of surface melt rates are comparatively limited and restricted to the western marginal zone (3). Iceberg calving is the least known of the components (4). Iceberg production has been estimated in the west (5), north, and northeast (6) of Greenland by means of repeated aerial photography. The velocity of the calving front is measured by tracking distinctive patterns of crevasses over time. Ice thickness is deduced from the height of the calving front. Immediately inland of the calving front, ice thickness is not well known (7), surface features are more subdued, and locating the grounding line, which is where a glacier detaches

E. J. Rignot, Jet Propulsion Laboratory, California Institute of Technology, 4800 Oak Grove Drive, Pasadena, CA 91109-8099, USA.

S. P. Gogineni, Radar Systems and Remote Sensing Laboratory, The University of Kansas, 2291 Irving Hill Road, Lawrence, KS 66045-2969, USA.

W. B. Krabill, NASA Goddard Space Flight Center, Wallops Flight Facility, Laboratory for Hydrospheric Processes, Wallops Island, VA 23337, USA.

S. Ekholm, Kort og Matrikelstyrelsen, Geodetic Division, Rentemestervej 8, DK-2400 Copenhagen NV, Denmark

\*To whom correspondence should be addressed. E-mail: eric@adelie.jpl.nasa.gov



that the 14 glaciers discharge  $49.2 \text{ km}^3/\text{year}$  of ice into the ocean (10% uncertainty) (Table 1). This ice volume is 3.5 times that

discharged at the glacier front (6). The largest difference is recorded on Petermann Gletscher, where the grounding line flux is 22 times the glacier-front flux.

If the floating glacier sections are in steady-state conditions, the ice flux decrease implies that they are melting (19). If they are not in steady state, they should be thickening instead, because not enough ice passing the grounding line reaches the glacier front. AOL data collected in 1995 and 1996 on Petermann Gletscher, however, indicate that the glacier tongue did not thicken at detectable levels ( $>1 \text{ m}$ ) over 1 year. Therefore, we assume that the ice tongue is in steady state and the ice flux decrease is due to melting. On Petermann Gletscher, the inferred steady-state melt rate is  $12 \text{ m/year}$ , and peak values exceed  $20 \text{ m/year}$  near the grounding line (10).

The few observations in north and northeast Greenland suggest that surface melt rates are less than  $3 \text{ m/year}$  (20). Thus, the only possible explanation for the ice-flux decrease is that the ice tongues lose mass through extensive melting at the base of the glaciers. If we assume a surface melt rate of  $2 \text{ m/year}$  for the floating tongues (6), basal melting must average  $10 \text{ m/year}$  on Petermann Gletscher,  $8 \text{ m/year}$  on Nioghalvfjærdsbræ Gletscher, and  $6 \text{ m/year}$  on Zachariae Isstrøm to explain the results in Table 1. These values are high compared with the  $1$  to  $2 \text{ m/year}$  average basal melt rate of Antarctic ice shelves (21), but are comparable to the localized high basal melt rates ( $7$  to  $10 \text{ m/year}$ ) measured on several Antarctic tidal outlet glaciers (22).

The outlet glaciers of north and northeast Greenland will maintain a state of balance if the mass discharged at the

grounding line is compensated by an equal amount of mass accumulating in the interior regions, which nourishes them with glacier ice. Over our study area, the predicted balance grounding line discharge for an ice sheet in balance is  $41 \text{ km}^3/\text{year}$  (23), which is less than the discharge of  $49 \text{ km}^3/\text{year}$  measured with the ERS data. If these estimates are correct, this means that north and northeast Greenland glaciers discharge an excess  $8 \text{ km}^3/\text{year}$  of glacier ice into the ocean, which is equivalent to a  $7\text{-Gt/year}$  mass loss (with an ice density of  $0.917$ ), a  $0.02\text{-mm}$  sea-level rise, or a decrease of  $2.5 \text{ cm/year}$  in surface elevation averaged over the total area above the grounding line ( $332,100 \text{ km}^2$ ). The northern sector of the Greenland Ice Sheet is therefore thinning and gives a positive contribution to sea-level rise.

Our results cannot be extrapolated easily to the entire ice sheet because small floating glacier sections exist elsewhere—for example, along the western coast (5, 12). These floating sections may still generate large amounts of basal melt water, because basal melting is often most pronounced near the grounding line, where tidal pumping is most efficient and where the glacier draft reaches the deepest waters (21, 22).

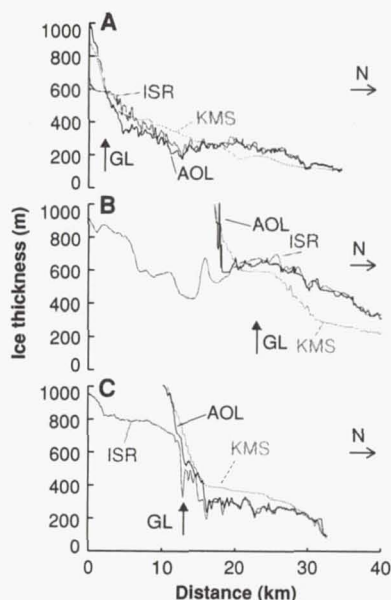


**Fig. 3.** Ice thickness derived from AOL, ISR, and surface elevation (KMS) near the grounding line (GL, indicated by an arrow) of (A) Petermann Gletscher, (B) Nioghalvfjærdsbræ Gletscher, and (C) Zachariae Isstrøm, as a function of the distance along the profile. North (N) is indicated by an arrow. The precision of the KMS elevation, AOL elevation, and ISR thickness is, respectively,  $10$  to  $20 \text{ m}$  (13),  $10 \text{ cm}$  (16), and  $10 \text{ m}$  (15). Georeferencing of the ERS data is accurate to within  $80 \text{ m}$ . The AOL/ISR profile for Nioghalvfjærdsbræ Gletscher is not optimal because it is too close to the ice margin and almost parallel to the grounding line (Fig. 2). The AOL- and KMS-derived thicknesses calculated upstream (south) of the grounding line are in error because the glacier ice is not in hydrostatic equilibrium.

**Table 1.** Glacier width (W), average velocity (V), average thickness (T), grounding line ice flux (GF), and calving flux (CF) from (6) for the outlet glaciers in Fig. 1. W, V, and T for Osterfeld Gletscher and Brikkerne Gletscher are for the main glacier branch only. The last line indicates total ice discharge. Gl., Gletscher; Fj., fjord.

Glacier	W (km)	V (m/year)	T (m)	GF ( $\text{km}^3/\text{year}$ )	CF ( $\text{km}^3/\text{year}$ )
Petermann Gl.	20.5	1139	614	13.20	0.59
Steensby Gl.	3.4	329	547	0.63	0.32
Ryder Gl.	7.9	506	598	2.55	0.70
Osterfeld Gl.	7.6	667	544	2.71	0.54
Harder Gl.	4.5	187	340	0.34	0.03
Brikkerne Gl.	3.8	364	160	0.44	0.37
Jungersen Gl.	1.5	395	340*	0.20	0.10
Naravana Fj. Gl.	1.8	59	200*	0.02	0.01
Henson Gl.	2.2	286	123*	0.08	0.04
Marie Sophie Gl.	3.3	40	136	0.02	0.13
Academy Gl.	7.4	290	120	0.26	0.14
Hagen Bræ Gl.	7.9	111	731	0.64	0.36
Nioghalvfjærdsbræ Gl.	21.5	1022	771	15.74	2.80†
Zachariae Isstrøm	19.8	855	647	12.40	7.40†
Total				49.2	13.5

\*Uncertainties in ice thickness greater than 10%.

†Calving flux from (25).



## The role of sea ice in 2xCO<sub>2</sub> climate model sensitivity: Part II: Hemispheric dependencies

D. Rind<sup>1</sup>, R. Healy<sup>2</sup>, C. Parkinson<sup>3</sup> and D. Martinson<sup>4</sup>

**ABSTRACT.** How sensitive are doubled CO<sub>2</sub> simulations to GCM control-run sea ice thickness and extent? This issue is examined in a series of 10 control-run simulations with different sea ice and corresponding doubled CO<sub>2</sub> simulations. Results show that with increased control-run sea ice coverage in the Southern Hemisphere, temperature sensitivity with climate change is enhanced, while there is little effect on temperature sensitivity of (reasonable) variations in control-run sea ice thickness. In the Northern Hemisphere the situation is reversed: sea ice thickness is the key parameter, while (reasonable) variations in control-run sea ice coverage are of less importance. In both cases, the quantity of sea ice that can be removed in the warmer climate is the determining factor. Overall, the Southern Hemisphere sea ice coverage change had a larger impact on global temperature, because Northern Hemisphere sea ice was sufficiently thick to limit its response to doubled CO<sub>2</sub>, and sea ice changes generally occurred at higher latitudes, reducing the sea ice-albedo feedback. In both these experiments and earlier ones in which sea ice was not allowed to change, the model displayed a sensitivity of  $\sim 0.02^\circ\text{C}$  global warming per percent change in Southern Hemisphere sea ice coverage.

### Introduction

In a recent publication [Rind *et al.*, 1995] we explored the direct and indirect effects of sea ice in doubled CO<sub>2</sub> climate model sensitivity by running doubled CO<sub>2</sub> GCM simulations with and without sea ice change. The results showed that without a sea ice response, the temperature sensitivity of the model to a CO<sub>2</sub> doubling was reduced by 35-40%, indicating the importance of incorporating realistic sea ice formulations in climate models.

In that same publication, we utilized current climate control runs with thicker or more extensive sea ice. The results showed that the global average temperature response in an equilibrium doubled CO<sub>2</sub> simulation was greater if the control-run sea ice cover was either more extensive or thinner. In both cases, the sea ice - albedo feedback was enhanced in the corresponding doubled CO<sub>2</sub> simulations, as more sea ice was removed. With more extensive sea ice cover, there was a greater areal extent to remove as climate warmed, and with thinner sea ice, the ice was easier to remove.

In an attempt to better understand how the distribution of sea ice in control run simulations affects the sensitivity of the modeled climate, a series of experiments was conducted with the Goddard Institute for Space Studies (GISS) General Circulation Model (GCM). The use of this model for doubled CO<sub>2</sub> experiments is described in detail in Hansen *et al.* [1984]; it includes a mixed layer ocean with specified heat transports and thermodynamic sea ice calculations. The results of the following sea ice sensitivity studies highlight some of the different sea ice characteristics which can influence global warming, including hemispheric differences; an additional characteristic, sea ice albedo, has been discussed by Meehl and Washington [1990].

### Experiments

The characteristics of ten control and doubled CO<sub>2</sub> simulations are shown in Table 1. The runs were performed with a mixed layer "q-flux" ocean, in which ocean heat transports are prescribed so as to produce realistic modern day sea surface temperatures and sea ice. In these runs, the primary modification to the standard GISS model was to use remote sensing and in situ observations to better define proper sea ice coverage and sea ice thickness; as indicated in Rind *et al.* [1995, Figure 6], the specified heat transports were increased by  $\sim 10\%$  globally to reduce control-run sea ice thicknesses in both hemispheres and produce more realistic distributions. It is this control run upon which the subsequent perturbations are performed.

Consistent with observations, the modeled sea ice now is thicker in the Northern Hemisphere, and relatively thin in the Southern Hemisphere. In the real world, sea ice in the two hemispheres has very different characteristics: Northern Hemisphere sea ice is often older (multiyear) and thicker, the result of minimal vertical ocean heat flux given strong ocean stability and continental influence. The Southern Ocean has marginal vertical stability, and as sea ice is formed, the

**Table 1.** Global Annual Average Results

Run	Current Climate			2xCO <sub>2</sub>		Difference	
	Area (%)	Thick. (m)	Surf. Temp. (°C)	Area (%)	Thick. (m)	Area (%)	Surf. Temp. (°C)
1	2.5	0.44	13.55	0.60	0.24	-1.9	4.32
2	2.6	0.55	13.98	0.90	0.32	-1.7	4.21
3	2.6	0.78	13.94	1.20	0.56	-1.4	4.23
4	3.1	1.06	13.91	1.60	0.66	-1.5	4.32
5	3.1	1.21	13.60	1.60	0.79	-1.5	4.16
6	3.1	0.67	13.56	1.20	0.51	-1.9	4.38
7	3.2	1.03	13.87	1.60	0.62	-1.6	4.18
8	3.3	0.59	13.10	0.90	0.38	-2.4	4.52
9	3.6	1.75	13.37	2.10	0.97	-1.5	4.20
10	3.7	2.00	13.30	2.10	1.04	-1.6	4.51

<sup>1</sup>Goddard Institute for Space Studies, 2880 Broadway, New York, N.Y. 10025., drind@giss.nasa.gov.

<sup>2</sup>Columbia University, New York, N.Y. and Woods Hole Oceanographic Institution, Woods Hole, Massachusetts

<sup>3</sup>Goddard Space Flight Center, Oceans and Ice Branch, Greenbelt, Md.

<sup>4</sup>Lamont-Doherty Earth Observatory, Palisades, New York..



ice coverage has nearly equal correlation with the change in each hemisphere ( $r=0.72$  with Northern Hemisphere sea ice change,  $r=0.77$  with Southern Hemisphere sea ice change). These conflicting tendencies lower the correlations between global average changes and control-run parameters. A better correlation can be obtained between control-run sea ice coverage in the Southern Hemisphere and global temperature response ( $r=0.56$ , Table 2).

Since both control-run sea ice coverage and sea ice thickness can influence the subsequent surface air temperature change, a multivariate analysis can be used to investigate whether including both variables in any assessment significantly raises the percentage of explained variance. Using the results from Table 1, the following relationship arises:  $\Delta$  global surface air temperature ( $^{\circ}\text{C}$ ) =  $0.23 + 1.35$  (control-run sea ice coverage in %)  $-0.06$  (control-run sea ice thickness in meters). The linear multiple correlation, however, is not significantly changed ( $r=0.31$ ) over the value for control-run sea ice coverage by itself. Again, the hemispheric differences prevent any stronger relationship between the global average changes.

## Discussion and Conclusions

The results shown above suggest that given the current climate characteristics, temperature sensitivity to doubled  $\text{CO}_2$  is affected more by sea ice coverage in the Southern Hemisphere and by sea ice thickness in the Northern Hemisphere. References discussing characteristics of climate model control runs, such as IPCC [1990], do not list the models' sea ice thickness in their validation review; yet ice thickness will obviously affect the climate sensitivity of the models. Future IPCC activities should include this parameter, for both "q-flux" and coupled atmosphere-ocean models.

Where sea ice is changed has a strong influence on the model sensitivity. In these experiments, the global surface air temperature change is more closely related to Southern Hemisphere sea ice coverage changes ( $r=0.68$ ) than to Northern Hemisphere changes ( $r=0.21$ ). Note in Figure 2b that the experiments differ in their sea ice coverage change primarily poleward of  $75^{\circ}\text{N}$ , where there is less sea ice-albedo influence. In addition, there was less change in Northern Hemisphere sea ice overall (1/3 of its ice, compared with 1/2 of the Southern Hemisphere ice). The Arctic ice is sufficiently thick that it can withstand significant warming without losing as much ice coverage. For these reasons, the sea ice differences in the Northern Hemisphere are less important for climate sensitivity in this model.

When sea ice was not allowed to change [Rind et al., 1995], lower latitudes were affected, resulting in a greater impact on climate sensitivity, and reducing simulated global warming from  $4.2^{\circ}\text{C}$  to  $2.8^{\circ}\text{C}$ . This change of  $1.4^{\circ}\text{C}$  in warming was associated with a 60% change in Southern Hemisphere sea ice coverage, or  $-0.02^{\circ}\text{C}$  per percent Southern Hemisphere sea ice coverage loss. In the experiments discussed here, there was a  $65 \pm 7\%$  loss in Southern Hemisphere sea ice coverage, and a  $4.3 \pm 0.13^{\circ}\text{C}$  variation in global warming. Since the difference in Southern Hemisphere sea ice coverage loss among the experiments was relatively small, so was the range in warming:  $0.13^{\circ}\text{C}$  divided by 7% again equals  $-0.02^{\circ}\text{C}$  per

percent Southern Hemisphere sea ice coverage loss. The results in this paper are thus perfectly consistent with the sensitivity derived previously.

Why was the percentage of Southern Hemisphere sea ice lost so similar with the different control runs? Is it a product of the altered q-fluxes which produced the differing control run concentrations, or is it some inherent stability of the system? This question can only be addressed in experiments using more complicated ocean and sea ice models, which will be performed as part of future papers in this series.

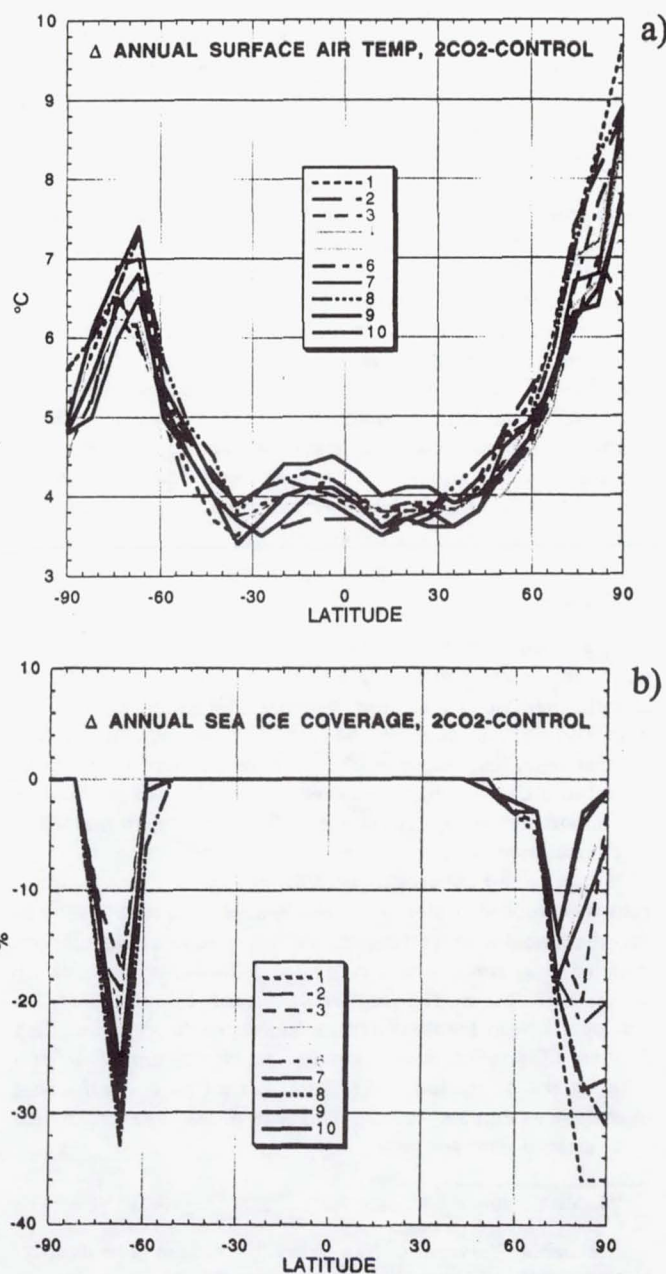


Figure 2. Annual changes due to doubled  $\text{CO}_2$  with different control runs: (a) surface air temperature; (b) percent sea ice coverage.



## Ocean Dynamics, Thermocline Adjustment, and Regulation of Tropical SST

RICHARD SEAGER

*Lamont-Doherty Earth Observatory of Columbia University, Palisades, New York*

RAGU MURTUGUDDE

*Universities Space Research Association, Laboratory for Hydrospheric Processes, NASA/GSFC, Greenbelt, Maryland*

(Manuscript received 11 March 1996, in final form 8 August 1996)

### ABSTRACT

The role of tropical Pacific ocean dynamics in regulating the ocean response to thermodynamic forcing is investigated using an ocean general circulation model (GCM) coupled to a model of the atmospheric mixed layer. It is found that the basin mean sea surface temperature (SST) change is less in the presence of varying ocean heat transport than would be the case if the forcing was everywhere balanced by an equivalent change in the surface heat flux. This occurs because the thermal forcing in the eastern equatorial Pacific is partially compensated by an increase in heat flux divergence associated with the equatorial upwelling. This constitutes a validation of a previously identified "ocean dynamical thermostat."

A simple two-box model of subtropical-equatorial interaction shows that the SST regulation mechanism crucially depends on spatial variation in the sensitivity of the surface fluxes to SST perturbations. In the GCM, this sensitivity increases with latitude, largely a result of the wind speed dependence of the latent heat flux, so that a uniform forcing can be balanced by a smaller SST change in the subtropics than in equatorial latitudes. The tropical ocean circulation moves heat to where the ocean more readily loses it to the atmosphere. Water that subducts in subtropical latitudes and returns to the equatorial thermocline therefore has a smaller temperature perturbation than the surface equatorial waters. The thermocline temperature adjusts on timescales of decades to the imposed forcing, but the adjustment is insufficient to cancel the thermostat mechanism.

The results imply that an increase in the downward heat flux at the ocean surface, as happens with increasing concentrations of greenhouse gases, should be accompanied by a stronger equatorial SST gradient. This contradicts the results of coupled atmosphere-ocean GCMs. Various explanations are offered. None are conclusive, but the possibility that the discrepancy lies in the low resolution of the ocean GCMs typically used in the study of climate change is discussed.

### 1. Introduction

The tropical sea surface temperature (SST) pattern is strongly influenced by ocean dynamics. In some areas of the ocean, the net surface heat flux, and hence the ocean heat transport, is small and the SST is determined by a one-dimensional balance at the surface. This is the case for the west Pacific and west Atlantic warm pools. In contrast, upwelling on the equator and at the eastern boundaries of the Atlantic and Pacific creates a dynamical heat flux divergence that partially balances net surface heating. Oceanic heat flux divergence in the Tropics acts to lower tropical mean SST as is evident in the higher SSTs that result in numerical experiments in which the ocean heat transport is set to zero (e.g., Meehl and Washington 1986; Seager et al. 1988).

The spatial pattern of upwelling and SST is determined through coupled air-sea interaction. In the presence of eastern and western boundaries, mean easterlies cause equatorial upwelling, a thermocline that shoals toward the east and an equatorial cold tongue with a maximum intensity in the east. Warm SSTs induce convective heating in the atmosphere in the west, which forces surface easterlies over the basin. The wind response therefore feeds back positively, and coupled interactions establish the tropical climatology (Bjerknes 1969; Dijkstra and Neelin 1995).

The importance of coupled interactions in establishing the tropical climate suggests they will also play a role in climate change and variability. This is obvious for the case of interannual variability (Zebiak and Cane 1987) but should also be true for longer period variability, including the response to external forcings (e.g., increased greenhouse gases or Milankovitch cycles). However, in the literature on climate change, outside of areas of deep water formation, the ocean is commonly reduced to a passive, dynamically uncoupled, diffusive

---

Corresponding author address: Dr. Richard Seager, Lamont-Doherty Earth Observatory, Columbia University, P.O. Box 1000, Palisades, NY 10964-8000.  
E-mail: rich@seppie.ldeo.columbia.edu



involving surface fluxes to win and lead to a weaker SST gradient. This possibility needs to be explored with fully coupled models in an attempt to explain the contradiction between our results and those of KM.

## 7. Conclusions

The basin mean change of SST due to an imposed uniform heat flux forcing is less in the presence of ocean dynamics than it is in the case of local equilibration by surface heat fluxes. This occurs because changes in vertical transfer of heat by the constant equatorial upwelling partially balance the imposed forcing. If the sensitivity of the surface heat flux to perturbations in SST is spatially uniform, then this effect will wear out as the temperature of upwelled water adjusts. This temperature is given in terms of the SST in the subtropical source regions for the equatorial thermocline water. If, however, the sensitivity of the surface fluxes to SST perturbations varies in space then it is possible that the dynamical SST regulation will persist.

We demonstrated using a simple two-box model that the necessary condition for dynamical regulation of tropical SST is that the ocean move heat from regions of low sensitivity of surface fluxes to SST perturbations to regions of higher sensitivity. In the high sensitivity regions a forcing flux can be balanced by a smaller SST change. The meridional gradient of SST then increases in response to a uniform forcing, which generates increased transport of heat from the equator to the subtropics. The subtropical SST adjusts by as much as is needed to balance the imposed forcing plus the increased dynamical heat flux convergence and is less than the SST adjustment on the equator. In time water subducted in the subtropics makes its way back into the equatorial thermocline and is upwelled but its temperature perturbation is less than that of the SST so the partial compensation of the forcing by a perturbed upwelling flux is not cancelled out.

We verified this mechanism using an ocean GCM thermodynamically coupled to a model of the atmospheric mixed layer. The sensitivity of the fluxes to changes in SST increases with latitude and is dominated by the change in the latent heat caused by increasing mean wind speed. The SST response to a uniform forcing is greatest on the equator but also has a minimum value in the eastern equatorial Pacific. Hence, the equatorial zonal SST gradient increases when a uniform heating is applied. After a few years only the temperature of the near-surface waters has changed, but after a decade the thermocline waters warm up as water subducted in the subtropics makes its way into the Equatorial Undercurrent. With time, the warming makes its way to lower depths. More than half a century is required to reach an equilibrium and, when it does, the altered SST gradient remains.

For comparison we performed an experiment with coupled atmosphere and ocean mixed layers and fixed ocean dynamical heat fluxes to assess how the SST

would change by local heat flux equilibration alone. This case has no minimum SST change in the equatorial east Pacific and has a basin mean SST change 50% larger than the GCM.

Although these experiments use the simplest forcing possible, we believe they are relevant to studies of climatic change. They demonstrate the role that ocean dynamics can play in regulating both the pattern and magnitude of the tropical SST response to atmospheric forcing. In experiments with coupled GCMs subjected to increasing amounts of CO<sub>2</sub>, the zonal SST gradient weakens (KM; Tett 1995), which is the opposite sign of what we would expect from our results. However, the coupled GCMs used have coarse resolution. We demonstrated that this will have little effect on the SST response to a thermodynamic forcing. However, dynamical coupling of the ocean and atmosphere will amplify the initial increase in the zonal SST gradient as in the experiments of Clement et al. (1996). The amplification depends on the sensitivity of eastern equatorial Pacific SST to changes in thermocline depth. The sensitivity is less in low vertical resolution models with diffuse thermoclines. The fact that the latent heat flux is less sensitive to SST changes in the eastern equatorial Pacific than in the west apparently wins out in the low resolution models and reduces the SST gradient.

In the literature on climate change, the ocean is considered to be of importance in two ways. First, the thermohaline circulation is considered to be potentially unstable and changes in the character of its operation are thought to have possible global climatic impacts. Second, the ocean is considered as a diffusive medium that through its large mass acts to delay the response of the climate system to imposed forcing (Hansen et al. 1981; Lindzen 1993). Here we suggest another mechanism, involving tropical ocean dynamics, whereby the ocean can influence climatic change. The mechanism operates on a timescale of decades and involves the thermal adjustment of the thermocline.

Coupled GCMs predict that, in response to increasing CO<sub>2</sub>, temperatures will warm by more in mid and high latitudes than in the Tropics. This will ultimately reduce the strength of the thermocline and, through equatorial upwelling, act to reduce the equatorial SST gradient. In time, this effect could overwhelm the tropical SST regulation mechanism. Even if the SST regulation mechanism ultimately loses out to more powerful feedbacks, it is still relevant to understanding the recent history of the earth's climate and its evolution over the next few decades. If our contention is correct, then attempts to address these issues using models with fixed ocean heat transports (e.g., Mitchell et al. 1995) or low-resolution ocean models risk overlooking a decadal scale mechanism by which the tropical SST equilibrates to an external forcing. The ultimate arbiter of whether an ocean dynamic regulatory mechanism is at work must be a careful analysis of the observational record. This is under way and will be reported on shortly.



## Detection and monitoring of stratigraphic markers and temperature trends at the Greenland Ice Sheet Project 2 using passive-microwave remote-sensing data

C.A. Shuman,<sup>1</sup> R.B. Alley,<sup>2</sup> M.A. Fahnestock,<sup>3</sup> P.J. Fawcett,<sup>2,4</sup> R.A. Bindschadler,<sup>1</sup> J.W.C. White,<sup>5</sup> P.M. Grootes,<sup>6</sup> S. Anandakrishnan,<sup>2</sup> and C.R. Stearns<sup>7</sup>

**Abstract.** Satellite passive-microwave sensors provide a sensitive means of studying ice-sheet surface processes that assists ice-core interpretation and can extend local observations across regional scales. Analysis of special sensor microwave/imager (SSM/I) brightness temperature ( $T_B$ ) data supports ice-core research in two specific ways. First, the summer hoar complex layers used to date the Holocene portion of the Greenland Ice Sheet Project 2 ice core can be defined temporally and spatially by SSM/I 37-GHz vertically (V) and horizontally (H) polarized  $T_B$  ratio (V/H) trends. Second, comparison of automatic weather station temperatures to SSM/I 37-GHz V  $T_B$  data shows that they are an effective proxy temperature record in this region. Also, the  $T_B$  data can be correlated with proxy temperature trends from stable-isotope-ratio ( $\delta^{18}\text{O}$  and  $\delta\text{D}$ ) profiles from snow pits and this allows the assignment of dates to specific snow depths.

### Introduction

Passive-microwave remote-sensing research has provided valuable insights on processes affecting near-surface snow and ice in central Greenland. Satellite passive-microwave sensors, with their broad spatial coverage and extensive temporal record which begins in the 1970s, provide a unique perspective on specific ice-sheet surface processes that affect the snow stratigraphy (see Figure 1). They also provide a convenient means of extending site-specific observations across regional scales. The purpose of this paper is to describe the ability of this research tool to support glaciologic and climatologic studies at ice-sheet deep drilling sites. Here we summarize and elaborate on results from research using passive-microwave data in support of the Greenland Ice Sheet Project 2 (GISP2) and, by extension, the Greenland Ice Core Project (GRIP).

### Background

The use of remote-sensing data in the study of ice sheets has an extensive history [Hall and Martinec, 1985; Massom, 1991]. Satellite passive-microwave sensor observations of

the polar regions began in 1972 with the electrically scanning microwave radiometer (ESMR) on the Nimbus 5 and Nimbus 6 satellites, followed by the scanning multichannel microwave radiometer (SMMR) on the Nimbus 7 satellite in 1978, and continuing with the special sensor microwave/imager (SSM/I) on the Defense Meteorological Satellite Program (DMSP) satellite series in 1987 [Massom, 1991]. The brightness temperature ( $T_B$ ) data produced by these sensors have provided a wealth of insight on ice-sheet surface phenomena [e.g., Chang *et al.*, 1976; Zwally, 1977; Mote *et al.*, 1993; Steffen *et al.*, 1993; Ridley, 1993; Rowe *et al.*, 1995].

The relationship of brightness temperature to physical temperature is described by the Rayleigh-Jeans approximation [Hall and Martinec, 1985]. In this approximation, brightness temperature is primarily a function of the physical temperature of the near-surface snow multiplied by its emissivity. For the 37-GHz channels used in this research, emissivity is controlled primarily by radiative scattering from the ice grains over a skin depth of a meter or so but is dominated by the top few tens of centimeters [Rott *et al.*, 1993]. The emissivity of the snow and ice is influenced by a variety of factors, but the predominant factor is grain size [Chang *et al.*, 1976; Armstrong *et al.*, 1993]. Mean grain size is known to vary over an annual period [Benson, 1962], whereas the other factors (such as crystal shape, layering, and density) are known to vary more rapidly. Satellite brightness temperatures are thus sensitive to short- and long-term changes in ice-sheet surface characteristics such as accumulation, melting, and diagenesis (see Figure 1).

The passive-microwave data used primarily in this research were derived from National Snow and Ice Data Center (NSIDC) CD-ROMs. Daily-average, 37-GHz, vertically (V) and horizontally (H) polarized brightness temperatures ( $T_B$ ) from the SSM/I sensors F8, F10, and F11, and to a lesser extent the SMMR, were compiled for grid cells covering specific locations in central Greenland (see Figure 2a). Typically, these  $T_B$  values are the result of several satellite passes per day with multiple observations per grid cell per pass, which are then averaged. The measurement accuracies of the 37-GHz V

<sup>1</sup>Oceans and Ice Branch, NASA Goddard Space Flight Center, Greenbelt, Maryland.

<sup>2</sup>Earth System Science Center and Department of Geosciences, Pennsylvania State University, University Park.

<sup>3</sup>Joint Center for Earth System Science, University of Maryland, College Park.

<sup>4</sup>Now at Department of Earth and Planetary Sciences, University of New Mexico, Albuquerque.

<sup>5</sup>Institute for Arctic and Alpine Research, University of Colorado, Boulder.

<sup>6</sup>Leibniz Labor, Christian-Albrechts-Universität, Kiel, Germany.

<sup>7</sup>Space Science and Engineering Center, University of Wisconsin, Madison.



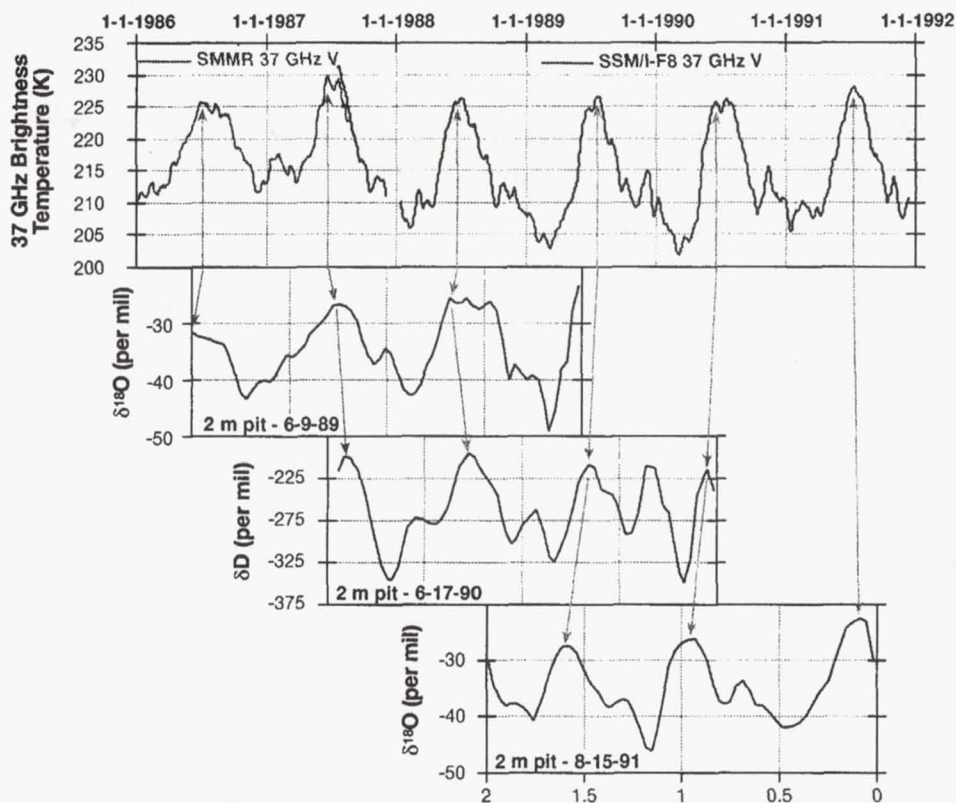


**Figure 9.** Comparison of temperature proxy records from GISP2. The similar patterns of the two types of records, 15-day smoothed 37-GHz  $V T_B$  and 2-m stable isotope ratio profiles, allow satellite observation dates to be correlated with snow pit depths. The  $\delta^{18}\text{O}$  and  $\delta\text{D}$  depth profiles have been correlated with the  $T_B$  observation time axis with the benefit of stratigraphic information, primarily hoar layers. The arrows only illustrate the general association of the profile times and depths. Multiple correlation points per year are possible which allow the rate and timing of accumulation to be assessed [Shuman *et al.*, 1995b]. Differences in the shapes of the isotope trends for common time periods indicate the spatial variability of stable isotope concentrations resulting from difficult-to-constrain factors [see Grootes and Stuiver, this issue].

The utility of 37-GHz  $T_B$  as a proxy temperature time series for ice-sheet research is further illustrated by the similar patterns of stable isotope ratios ( $\delta^{18}\text{O}$  and  $\delta\text{D}$ ) and smoothed  $T_B$  data (Figure 9, as presented in Shuman *et al.* [1995b, 1997]). Qualitative comparison shows that high-resolution snow pit isotope profiles (>20-25 samples per year) can be correlated with  $T_B$  records. As a result, density-corrected isotope profile depths can be associated with  $T_B$  dates and subseasonal data on water-equivalent accumulation rate and timing can be derived. In addition, by correlating isotope values to calibrated  $T_B$  data, isotope thermometry over recent periods can be assessed. This approach gives  $\delta/T$  slope values of about 0.5 over a multiyear period which are similar to those obtained by shallow borehole thermometry studies [Shuman *et al.*, 1995b, 1997; Cuffey *et al.*, 1994; Jouzel *et al.*, this issue]. Although these results are based on a few high-resolution profiles, more work is needed to test the technique as well as to assess the processes responsible for the spatial variability of isotope records (see Figure 9) (also see the discussion by Grootes and Stuiver [this issue]). Additional snow pit profiles from other locations are now under analysis to test the consistency of the relationship between these temperature proxy records.

## Summary

Passive-microwave brightness temperatures provide valuable data that support the paleoclimate analyses of the

GISP2 and GRIP deep cores as well as current studies of the area's climate. The repeated association of SSM/I  $T_B$  37-GHz ratio patterns with the evolution and burial of hoar complexes in central Greenland, and the persistence of these patterns across hundreds of thousands of square kilometers, confirms that they are reliable, seasonally sensitive stratigraphic markers of annual accumulation. Their association with particular meteorologic patterns and their observed formation during the summer period, primarily from mid-June to late August, allow an improved interpretation of ice-core paleoclimatic records that are dated by counting of hoar layers.

The  $T_B$  data also allow current environmental monitoring in this climatically sensitive region. Comparison of SSM/I 37-GHz  $V$  data with AWS near-surface air temperatures documents that  $T_B$  data are a valuable proxy temperature record. Using a combination of surface and satellite temperature information, a multiyear temperature record has been compiled which details 7 years of temperature history for the Greenland Summit region. This record characterizes distinctive aspects of the Summit temperature cycle, and provides a basis for comparison to general circulation model output from this region. In addition, the  $T_B$  proxy record provides a timescale for comparison to stable isotope profiles which allows short-term assessments of the reliability of isotope thermometry as well as the determination of the rate and timing of accumulation at specific ice-sheet sites. Future ice-sheet drilling sites could clearly benefit from the integration of passive-microwave data into their overall research plans.



# Comparison of satellite-derived with ground-based measurements of the fluctuations of the margins of Vatnajökull, Iceland, 1973–92

RICHARD S. WILLIAMS, JR.,<sup>1</sup> DOROTHY K. HALL,<sup>2</sup> ODDUR SIGURÐSSON,<sup>3</sup> JANET Y. L. CHIEN<sup>4</sup>

<sup>1</sup>*U.S. Geological Survey, Quissett Campus, Woods Hole, MA 02543, U.S.A.*

<sup>2</sup>*NASA, Goddard Space Flight Center, Code 974, Greenbelt, MD 20771, U.S.A.*

<sup>3</sup>*National Energy Authority, Grensásvegi 9, IS-108, Reykjavík, Iceland*

<sup>4</sup>*General Sciences Corporation, Laurel, MD 20707, U.S.A.*

**ABSTRACT.** Vatnajökull, Iceland, is the Earth's most studied ice cap and represents a classical glaciological field site on the basis of S. Pálsson's seminal glaciological field research in the late 18th century. Since the 19th century, Vatnajökull has been the focus of an array of glaciological studies by scientists from many nations, including many remote-sensing investigations since 1951. Landsat-derived positions of the termini of 11 outlet glaciers of Vatnajökull were compared with frontal positions of six of these 11 outlet glaciers determined by field observations during the period 1973–92. The largest changes during the 19 year period (1973–92) occurred in the large lobate, surge-type outlet glaciers along the southwestern, western, and northern margins of Vatnajökull. Tungnaárjökull receded  $-1413 \pm 112$  m ( $-1380 \pm 1$  m from ground observations), and Brúarjökull receded  $-1975 \pm 191$  m ( $-2096 \pm 5$  m from extrapolated ground observations) between 1973 and 1992. Satellite images can be used to delineate glacier margin changes on a time-lapse basis, if the glacier margin can be spectrally discriminated from terminal moraines and sandur deposits and if the advance/recession is larger than maximum image pixel size. "Local knowledge" of glaciers is critically important, however, in the accurate delineation of glacier margins on Landsat images.

## INTRODUCTION

During the past 25 years, many remote-sensing techniques have been applied to the study of glaciers, including measurements of (1) absolute ice thickness by radio-echo sounding from surface and airborne platforms, (2) changes in surface elevation over time with aerial photogrammetric methods and by geodetic airborne or spaceborne radar and laser altimetry, (3) delineation of the surface expression of glacier facies with satellite sensors, and (4) measurements of the fluctuations of the termini of valley glaciers and outlet glaciers (and margins) from ice fields, ice caps and ice sheets (Williams and Hall, in press). Often, satellite and airborne remote-sensing studies of glacier fluctuations do not have the benefit of ground observations to confirm the measurements. In this paper, however, we analyze Landsat images acquired between 1973 and 1992, in combination with field observations made during the same interval, to compare the measurement of changes in the termini of outlet glaciers and margin of Vatnajökull, Iceland (Figs 1 and 2). Variations of Iceland's glaciers are reported annually in *Jökull*.

The Earth's smaller glaciers have generally been receding during the 20th century (Wood, 1988; Oerlemans, 1994). This has been accompanied by an estimated  $1\text{--}3$  mm  $\text{a}^{-1}$  rise in sea level (Paterson, 1994), perhaps as much as one-third of which has been caused by reduction in glacier-ice volume primarily from southeastern Alaska (Meier, 1984). The terminus-position changes of small glaciers often occur on

a decadal time-scale, because smaller glaciers react more rapidly to climate change, according to Haeberli (1995) and Haeberli and Hoelzle (1995). Termini of Icelandic glaciers react to climate on a decadal time-scale regardless of their length (Sigurðsson and Jónsson, 1995). Sustained recession of a glacier terminus is usually indicative of a negative glacier mass balance, although it is possible for a glacier to increase in volume while its front is receding (Meier, 1984). In general, however, glaciers with a negative mass balance will retreat over time, although "large and relatively flat glaciers have a tendency of downwasting rather than retreating in case of rapid warming" (personal communication from W. Haeberli, 1996; cf. Haeberli and Hoelzle, 1995).

An ice cap is a dome-shaped mass of ice,  $<50\,000$  km<sup>2</sup> in area, that completely covers the terrain except for a few internal and marginal nunataks; it usually has one or more lobate or valley outlet glaciers. Ice caps are vulnerable to climate change, particularly those in the temperate areas of the Northern Hemisphere, because even small changes in the elevation of the equilibrium line can markedly affect the relationship of the size of the accumulation area to the ablation area. There is a marked decrease in the accumulation area in response to upward movement of the equilibrium line and a concomitant increase in the ablation area; as a result, total ice-cap area can shrink rapidly (e.g. Ok ice cap in Iceland (Williams, 1986a)), the shrinkage including recession of its outlet glaciers.



Skaftárjökull had receded  $-485 \pm 112$  m on 1973 MSS and 1987 TM images and  $-425 \pm 112$  m on 1973 MSS and 1992 TM images; there is no ground-based observation station to corroborate these measurements.

On 1973 MSS and 1987 TM images, Siðujökull had receded  $-527 \pm 112$  m in its west-central part,  $-485 \pm 112$  m in its central part, and  $-513 \pm 112$  m in its east-central part. During the same period of time, ground observations showed a recession of  $-643 \pm 1$  m on its eastern part. On 1973 MSS and 1992 TM images, Siðujökull had receded  $-1030 \pm 112$  m; ground observations showed a recession of  $-1021 \pm 1$  m for the same period. Siðujökull last surged in 1963–64 at least 0.5 km, although field evidence suggests that the total surge was probably much more.

Skeiðarárjökull (Fig. 4), on the basis of 1973 MSS and 1987 TM images, had advanced  $+257 \pm 112$  m on its western lobe and had receded  $-150 \pm 112$  m in its central part. Comparable ground observations of the western lobe during the 1973–87 period showed an advance of  $+244 \pm 1$  m. Skeiðarárjökull began a surge in 1991, so the Landsat images that postdate 1991 will show an advance. In the eastern part of its margin, 1973 MSS and 1992 TM images show an advance of  $+474 \pm 112$  m; comparable ground observations showed an advance of  $+520 \pm 1$  m. 1987 TM and 1992 TM images show an advance of its terminus of  $+480 \pm 42$  m in the west-central part and  $+223 \pm 42$  m in the eastern part. Comparable ground observations for this latter period showed an advance of  $+276 \pm 1$  m. Changes in the western part of the lobe on 1987 and 1992 TM images were too small to measure on the Landsat images.

The post-surge (surge in 1972–73, for a total advance of 1.5–2 km determined from ground observations) recession of Eyjabakkajökull has been  $-790 \pm 191$  m on 1973 MSS and 1991 TM images,  $-921 \pm 191$  m on 1973 MSS and 1992 TM images (Fig. 3). There have been no ground measurements of the terminus of Eyjabakkajökull since 1985. On the 1973 MSS image its terminus was  $2095 \pm 79$  m wide; on the 1992 TM image it was  $1387 \pm 30$  m wide, reflecting the rapid downwasting and recession of the stagnant terminus following the 1972–73 surge.

Following a surge in 1963–64 of +8 km, Brúarjökull has been actively receding. Ground observations for the period 1977–88 show that its broad terminus had receded  $-1048 \pm 5$  m. No ground observations were made during the 1972–77 and 1988–92 periods, although a linear extrapolation of downwasting and recession would give  $-2096 \pm 5$  m for the period 1972–92. Although Brúarjökull presents a difficult problem in delineating the glacier ice and terminal moraine contact, because of massive downwasting all along its stagnant terminus, measurements were made on 1973 MSS and 1992 TM images. The terminus had, during this period of time, receded  $-1975 \pm 191$  m at the approximate position of the ground-observation station.

On 1973 MSS and 1991 TM images, Dyngjujökull's margin had advanced  $+790 \pm 112$  m on the east-northeastern,  $+632 \pm 112$  m on the eastern, and  $+474 \pm 112$  m on the east-southeastern parts of its eastern margin; on the 1973

MSS and 1992 TM images its east-southeastern margin advanced  $+553 \pm 112$  m (Fig. 5). On Köldukvíslarjökull, on 1973 MSS and 1978 RBV images, it had advanced from  $+290 \pm 112$  m to  $+330 \pm 112$  m on its southern margin and  $+215 \pm 112$  m on its northern margin; on 1973 MSS and 1992 TM images its western margin had advanced between  $+285 \pm 112$  m on the north and  $+883 \pm 112$  m on the south-central part of the lobe. On 1973 MSS and 1992 TM images, Sylgjujökull receded  $-395 \pm 112$  m in the center of the lobe to between  $-553 \pm 112$  m and  $-711 \pm 112$  m on its south-western lobe.

## CONCLUSIONS

In the specific case of Iceland, Landsat images permit the monitoring of fluctuations along most of Vatnajökull's margin, not just at the 23 ground-observation stations (19 individual outlet glaciers) monitored on an annual basis at an accuracy of about 112 m with MSS images and 42 m for Landsat 3 RBV or TM images. Within the margins of error, we found good correspondence between the satellite-derived and ground-based measurements of six outlet glaciers of Vatnajökull during the period 1973–92. One aspect of our comparison of measurements of glacier fluctuations made from Landsat images vs ground-based observations is the critical importance of having "local knowledge" of glaciers to support the analysis of Landsat images.

Based on these results, we have confidence in the accuracy of the measurement of fluctuation of five additional outlet glaciers for which ground observations are not available. For four other outlet glaciers for which ground-observation stations exist, the ground-based measurements were  $\leq 110 \pm 1$  m; no fluctuation could be discerned with satellite-derived measurements of these four outlet glaciers.

For the larger glaciers, such as ice fields, ice caps and ice sheets, the capability now exists to begin to build an archive of long-term data sets of the fluctuations of large glacier margins and area on a global basis, using glaciological data based on analysis of current satellite sensor data. If the World Glacier Monitoring Service expands its area of interest from small glaciers to the larger glaciers (e.g. ice fields, ice caps, ice sheets and the outlet glaciers that comprise each), satellite images will be an important source of data for monitoring and measuring changes in glacier margins on a regional (and global) basis, in association with glaciologists who have "local knowledge" of glaciers of their specific region, and in the building of an international archive of long-term data sets. Improvements in the pixel resolution of imaging sensors, use of radar imagers, the annual acquisition of satellite images and acquisition of geodetically accurate laser altimetry from Earth-orbiting satellites will eventually provide considerably more data of value to glaciologists who are monitoring and measuring changes in glacier margins, area and volume (Williams and Hall, in press).



# ANNUAL SEA LEVEL VARIABILITY INDUCED BY CHANGES IN SEA ICE EXTENT AND ACCUMULATION ON ICE SHEETS: AN ASSESSMENT BASED ON REMOTELY SENSED DATA

H. J. ZWALLY<sup>1</sup> and M. B. GIOVINETTO<sup>2</sup>

<sup>1</sup>Goddard Space Flight Center, Code 971, Greenbelt, MD 20771, USA

<sup>2</sup>Earth Sciences 356, University of Calgary, Calgary, Alberta T2N 1N4, Canada

**Abstract.** Changes of mean annual net accumulation at the surface on the grounded ice sheets of East Antarctica, West Antarctica and Greenland in response to variations in sea ice extent are estimated using grid-point values 100 km apart. The data bases are assembled principally by bilinear interpolation of remotely sensed brightness temperature (Nimbus-5 ESMR, Nimbus-7 SMMR), surface temperature (Nimbus-7 THIR), and surface elevation (ERS-1 radar altimeter). These data, complemented by field data where remotely sensed data are not available, are used in multivariate analyses in which mean annual accumulation (derived from firm emissivity) is the dependent variable; the independent variables are latitude, surface elevation, mean annual surface temperature, and mean annual distance to open ocean (as a source of energy and moisture). The last is the shortest distance measured between a grid point and the mean annual position of the 10% sea ice concentration boundary, and is used as an index of changes in sea ice extent as well as of mean concentration. Stepwise correlation analyses indicate that variations in sea ice extent of  $\pm 50$  km would lead to changes in accumulation inversely of  $\pm 4\%$  on East Antarctica,  $\pm 10\%$  on West Antarctica, and  $\pm 4\%$  on Greenland. These results are compared with those obtained in a previous study using visually interpolated values from contoured compilations of field data; they substantiate the findings for the Antarctic ice sheets ( $\pm 4\%$  on East Antarctica,  $\pm 9\%$  in West Antarctica), and suggest a reduction by one half of the probable change of accumulation on Greenland (from  $\pm 8\%$ ). The results also suggest a reduction of the combined contribution to sea level variability to  $\pm 0.19$  mm a<sup>-1</sup> (from  $\pm 0.22$  mm a<sup>-1</sup>).

## 1. Introduction

The relationships between net surface accumulation or surface mass balance on the Greenland and Antarctic ice sheets and climatic variables such as air temperature and sea ice extent are of interest because changes in climate affect the overall mass balance of the ice sheets and, consequently, global sea level. Interannual variations in the rate of ice discharge across grounding lines are relatively small. However, interannual variations in net accumulation at the surface of the ice sheets cause a net transfer of water between the ocean and the ice sheets, which is immediately reflected in changes in global sea level. Since the annual mass input to the ice sheets is equivalent to about 8 mm yr<sup>-1</sup> in global sea level, an annual ice accumulation variation of 10% causes a global sea level change of 0.8 mm.

Current knowledge of the relationship between changes in ice accumulation and climate change is so uncertain that predicted changes in the ice mass balance could be either positive or negative (Warrick *et al.*, 1996). Part of the difficulty in deriving meaningful quantitative relationships arises because the relevant physical



Parkinson, 1991). Therefore, to estimate the change in the rate of accumulation that may be expected for a change of  $\pm 50$  km in  $D_i$ ,  $D_s$  we remove  $L$  from the models, and adjust  $T_i$ ,  $T_s$  values for same-sign changes in  $D_i$ ,  $D_s$ :

$$A_i = f\{H_i, [T_i = f(H_i, (D_i \pm 50))], (D_i \pm 50)\}, \quad (1)$$

and

$$A_d = f\{H_s, [T_s = f(H_s, (D_s \pm 50))], (D_s \pm 50)\}. \quad (2)$$

The rates of accumulation estimated using Equations (1) and (2) are listed in Table V, where several points stand out, as described below.

A. Stepwise analyses at the 90% confidence level show that:

- (i)  $D_i$ ,  $D_s$  enter all models, and are the first to enter in the determination of  $A_i$ ,  $A_d$  for West Antarctica and Greenland.
- (ii)  $T_i$ ,  $T_s$  are the first to enter in the determination of  $A_i$ ,  $A_d$  for East Antarctica, but do not enter the models to determine  $A_i$  for West Antarctica and Greenland.
- (iii)  $H_i$ ,  $H_s$  do not enter any of the models; of course, they enter the models used to adjust  $T_i$ ,  $T_s$  values for same-sign changes in  $D_i$ ,  $D_s$ .

B. The models for the Antarctic ice sheets are robust ( $r$  values between 0.86 and 0.73), and those for Greenland are weak ( $r = 0.64, 0.53$ ).

C. The changes in accumulation estimated from the models are much smaller than errors in the estimates of mean accumulation for the ice sheets (e.g. Jacobs *et al.*, 1992; Reeh, 1985); this is of no concern because we are attempting to estimate variation about a mean.

D. All the changes in accumulation suggested by the models conform with the expectation of an inverse relationship between accumulation and sea ice extent; this is internally compounded in the models, given the inverse relationship between temperature and sea ice extent (A(iii), above).

E. For the Antarctic ice sheets, the relative change in accumulation suggested by the satellite data is approximately the same as that suggested by the field data, i.e. approximately  $\pm 4\%$  for East Antarctica,  $\pm 10\%$  for West Antarctica. For Greenland, the satellite data suggest a change of  $\pm 4\%$  that is exactly one half of that suggested by the field data ( $\pm 8\%$ ).

#### 4. Conclusion

The estimates of change in annual accumulation on the ice sheets in response to changes in sea ice extent and mean concentration presented in this work based on remotely sensed data, indicate contributions to sea level variability of  $\pm 0.10$  mm  $a^{-1}$  from East Antarctica,  $\pm 0.15$  mm  $a^{-1}$  from West Antarctica, and  $\pm 0.05$  mm  $a^{-1}$  from Greenland. These results substantiate the estimates presented in a previous study based on field data for the Antarctic ice sheets (East Antarctica:  $\pm 0.12$  mm  $a^{-1}$ ; West Antarctica:  $\pm 0.15$  mm  $a^{-1}$  and suggest a one-half reduction of the Greenland contribution (from  $\pm 0.11$  mm  $a^{-1}$ ). Overall, use of remotely sensed data indicate a combined contribution of  $\pm 0.19$  mm  $a^{-1}$  (the square root of the sum of the contributions squared), which is practically the same as that indicated by analyses of field data ( $\pm 0.22$  mm  $a^{-1}$ ) since the difference is smaller than the probable error in the estimates.



# Areal distribution of the oxygen-isotope ratio in Greenland

H. JAY ZWALLY,<sup>1</sup> MARIO B. GIOVINETTO<sup>2</sup>

<sup>1</sup>Code 971, NASA/Goddard Space Flight Center, Greenbelt, MD 20771, U.S.A.

<sup>2</sup>Earth Sciences 356, University of Calgary, Calgary, Alberta T2N 1N4, Canada

**ABSTRACT.** Mean values of the oxygen-isotope ratio relative to standard mean ocean water ( $\delta^{18}\text{O}$ , in ‰) reported for 46 sites on the Greenland ice sheet are compiled together with data on mean annual surface temperature, latitude,  $\delta^{18}\text{O}$  elevation, and mean annual shortest distance to the open ocean denoted by the 10% sea-ice concentration boundary. Stepwise regression analyses, with  $\delta^{18}\text{O}$  as the dependent variable, define two robust models. In the forward mode at the 99.9% confidence level, only temperature enters the model. In the backward mode at the 95% confidence level, only temperature, latitude and distance to the open ocean remain in the model. Inversions of the models on the basis of 160 gridpoint locations 100 km apart in the area delimited by the surface equilibrium line produce four contoured distributions of  $\delta^{18}\text{O}$ . Two distributions are based on the bivariate model and two on the multivariate model. The second distribution for each model is obtained substituting mean annual surface-temperature values obtained from the Nimbus-7 Temperature Humidity Infrared Radiometer (THIR) database. All four distributions are considered valid, and differences between them are evaluated using contoured anomaly maps. It is suggested that the inversion of the multivariate model using THIR data provides the more reliable pattern for studies of atmospheric advection or for the derivation of ice-flow adjustments for  $\delta^{18}\text{O}$  series obtained from deep-core or ablation-zone sites.

## INTRODUCTION

Multi-year mean values of  $^{18}\text{O}/^{16}\text{O}$  relative to standard mean ocean water (SMOW) ( $\delta^{18}\text{O}$ , in ‰) determined from samples collected on the Greenland ice sheet are used in climatological and glaciological investigations (e.g. Reeh and others, 1987b; Clausen and others, 1988; Johnsen and others, 1989). This study presents stepwise statistical analyses based on  $\delta^{18}\text{O}$  reported for 46 sites (Fig. 1a) as the dependent variable, and four independent variables: latitude ( $L$ , in °N); surface elevation ( $H$ , in m); multi-year mean surface temperature ( $T_s$ , in K) normally determined from 10 m borehole temperature, mean surface temperature in 1979 ( $T_r$ , in K) obtained by bilinear interpolation from the Nimbus-7 Temperature Humidity Infrared Radiometer (THIR) database (Comiso, 1994); and multi-year mean shortest distance to the open ocean denoted by the 10% sea-ice concentration boundary ( $D$ , in km) obtained from the Nimbus-7 Scanning Multichannel Microwave Radiometer (Gloersen and others, 1992). Use of a different sea-ice concentration boundary to denote open ocean (e.g. 20% open water) does not introduce significant differences in the statistics. The purpose is to define multivariate models applied to a 100 km grid database (Figure 1b) and produce contoured distributions of  $\delta^{18}\text{O}$ . These distributions may be used in advection studies (e.g. Johnsen and others, 1989) or to derive ice-flow adjustments (e.g. Reeh and others, 1987a).

In the following sections, the statistics are significant at the 99.99% confidence level ( $F$  statistic under the null hypothesis showing a probability of  $P \leq 0.0001$ ) unless stated otherwise. A confidence level selected for a particular model to determine which variables contribute at that level (or better) to the explanation of variation is a separate statistic from the  $P$ -value attained by the model.

## SAMPLE SITE DATABASE

The initial compilation included data for a total of 62 sites (after the analyses were completed we were informed of a few more sites available for northern Greenland (K. Steffen, personal communication, August 1996)). Data for 46 of the 62 sites were retained for analyses; these are from Müller and others (1977), Schriber and others (1977), Clausen and Hammer (1988), Clausen and others (1988), Johnsen and others (1989), Dansgaard and others (1993), Grootes and others (1993) and Fischer and others (1995). Most of the data for 18 sites from Fischer and others (1995) were obtained by interpolation. Actual values were obtained after the analyses were completed (H. Fischer, personal communication, August 1996). The differences between the interpolated and actual values are minor. The largest differences are in elevation; differences in latitude and longitude would introduce small changes in  $D$  and  $T_r$  values. However, use of the actual values would not introduce significant changes in the statistics presented in this study.

Data for 14 sites were excluded from the analyses because the samples were collected in the ablation zone or in areas of widespread summer melt and percolation. These were Warming Land (81.50° N, 52.0° W; Reeh and others, 1987b), nine sites in the Thule area centered at approximately 76.5° N, 68° W (Reeh and others, 1990), Paakitsoq (69.75° N, 49.0° W; Reeh and others, 1991), Storstrømmen, (77.40° N, 23.0° W; Reeh and others, 1993), and Drill Sites I and II, at approximately 70.00° N, 49.5° W, and 69.92° N, 49.4° W, respectively (Clausen and Stauffer, 1988).

The reliability of  $T_r$  values interpolated from the THIR database with a resolution of approximately  $30 \times 30$  km (Comiso, 1994) was assessed by a simple regression of the form  $T = f(T)$  ( $N48$ , where  $N$  denotes the number of sites



contour map is due, in part, to the overlay of a fixed-grid pattern over maps of different projections and with different standard lines. The differences between these and the elevation values obtained from the ERS-1 database is due, in part, to round off (to 0.1°)  $L_i$  and longitude values entered in the gridpoint database. This implies an error in location of several km north to south and in most areas of at least 1 km east to west, whereas the ERS-1 data resolution is of about 500 m (Wingham, 1995). Therefore, we did not update the  $H_i$  data.

## AREAL DISTRIBUTION OF $\delta^{18}\text{O}$

The inversions of Equation (1) using the N160 database and either  $T_{si}$  or  $T_{ri}$  (i.e.  $(\delta^{18}\text{O})_{bs} = f(T_{si})$ , and  $(\delta^{18}\text{O})_{br} = f(T_{ri})$ ) result in mean, maximum and minimum values that are remarkably close to those obtained by the inversions of Equation (2) (i.e.  $(\delta^{18}\text{O})_{ms} = f(L_i, T_{si}, D_i)$ , and  $(\delta^{18}\text{O})_{mr} = f(L_i, T_{ri}, D_i)$ ) (Table 4). The correlation matrix for the N160 set (Table 2) lists the strong correlations that would be expected from Equations (1) and (2) between the derived terms  $(\delta^{18}\text{O})_{ms}$ ,  $(\delta^{18}\text{O})_{mr}$  and the input terms  $T_{si}$  and  $T_{ri}$  ( $R$  values of 0.996 and 0.994). The covariation between  $H_i$  and the temperature terms ( $R$  values of 0.633 and 0.672) is weak relative to the strong covariation noted for the sample sites data (Table 2, N46;  $R$  values of 0.873 and 0.986). This decay is also noted in the relationship between  $\delta^{18}\text{O}$  and elevation ( $R$  is 0.872 for the sample site data, and  $R$  values are 0.684 and 0.727 for the gridpoint data).

The distributions of  $(\delta^{18}\text{O})_{bs}$  and  $(\delta^{18}\text{O})_{br}$  as well as of  $(\delta^{18}\text{O})_{ms}$  and  $(\delta^{18}\text{O})_{mr}$  (Figs 2a, b and 3a, b, respectively) show that, in general, the isopleths are oriented perpendicular to flow lines (e.g. Radok and others, 1982), thus facilitating any derivation of adjustments for  $\delta^{18}\text{O}$  series obtained from deep cores.

We evaluate first the difference between bivariate models using either  $T_{si}$  or  $T_{ri}$  data (i.e.  $\Delta_b = [(\delta^{18}\text{O})_{bs} - (\delta^{18}\text{O})_{br}]$  (Fig. 2c). The distribution of  $\Delta_b$  indicates differences of -1‰ in the north-central region, changing to +1‰ in the south-central region. In these regions lie most of the length of the main drainage divides, where flow lines originate. In general,  $\Delta_b$  becomes larger toward the equilibrium line, except in four regions where it decreases to zero: these are the sectors of the Smith Sound-Nares Strait, McKinley Sea, southern North Greenland Sea-northern Iceland Sea, and southern Denmark Strait. Otherwise,  $\Delta_b$  remains positive in the southern outlying slopes, i.e. toward the equilibrium line in the sectors of the Davis Strait (+3‰), Labrador Sea (+2‰) and Irminger Sea (+4‰). It also becomes larger toward the equilibrium line, but the increases are signed in a complex pattern in the sectors of the Denmark Strait-Iceland Sea (+3‰, decreasing northward to -3‰), and around the northern outlying slopes in the sectors of Baffin Bay (+2‰), the Lincoln and western McKinley Seas (-2‰), the Wandels Sea (+1‰), and the North Greenland Sea (from +2‰ in the central part of the

sector, to -3‰ in the southern part).

Due to the dominance of the temperature term in both Equations (1) and (2), the difference between multivariate models using either  $T_{si}$  or  $T_{ri}$  data (i.e.  $\Delta_m[(\delta^{18}\text{O})_{ms} - (\delta^{18}\text{O})_{mr}]$ , is practically identical (Figure 3c). This similarity is also noted in the descriptive statistics, which show insignificant differences between  $\Delta_b$  and  $\Delta_m$  (Table 4).

We evaluate next the difference introduced by the multivariate models that include the effects of latitude and distance to the open ocean. For this, we select the models that include  $T_r$  data, and produce a contoured distribution of  $\Delta_r = (\delta^{18}\text{O})_{br} - (\delta^{18}\text{O})_{mr}$  (Fig. 4, Table 4). The difference in distribution introduced by the multivariate model is small (mean -0.22‰, std dev. 0.03). The larger  $\Delta_r$  values are noted in the northwest region of the ice sheet (between -0.50‰ and -1.15‰), decreasing to zero in a broad zone extending from the sector of Baffin Bay to the Irminger Sea sector. Values of  $\Delta_r$  increase toward the southern region of the ice sheet (between +0.10‰ and +0.35‰).

## DISCUSSION AND CONCLUSIONS

At present, given the relatively small number and sporadic areal distribution of firn-temperature measurements at depths > 10 m, and the paucity of meteorological records from the interior (manned as well as automatic weather stations), we believe that the distribution of  $(\delta^{18}\text{O})_{ms}$  (Fig. 3b) is the more reliable pattern. The reliability of this pattern, as well as that produced using  $(\delta^{18}\text{O})_{mr}$  (Fig. 2b) may be improved if  $\delta^{18}\text{O}$  values for the sample sites could be adjusted to represent only the last 10–20 years of records available at each site (some of the  $\delta^{18}\text{O}$  values entered in the database are from samples spanning at least a few centuries).

The distribution of  $(\delta^{18}\text{O})_{mr}$  is produced from the inversion of a robust multivariate model that includes Nimbus-7 THIR mean annual temperature data, latitude and mean annual shortest distance to the open ocean ( $R$  is 0.987, rms is 0.53). It shows large differences relative to the distribution produced using a bivariate model based on temperature values interpolated from surface data ( $\Delta_m = 0.34 \pm 0.12$ ‰, with a range of -3.43‰ to +4.41‰). The larger differences show in the outer slopes, i.e. the zone characterized by steep surface gradient close to the equilibrium line. These are the areas where interpolation of surface-temperature data would be least reliable. Nevertheless, in more than half the accumulation area of the ice sheet, in the interior where the main drainage divides lie, the difference is -1‰ in the north and central part, and +1‰ in the southern part.

The distribution of  $(\delta^{18}\text{O})_{mr}$  also shows differences from a distribution based on a bivariate model using only Nimbus-7 THIR data. The inclusion of latitude and distance to the open ocean induces differences ( $\Delta_r = 0.22 \pm 0.02$ ‰, with a range of -1.18 to 0.40‰) that are smaller than the error of prediction in more than three-quarters the accumulation area of the ice sheet. The only differences larger than the error are found in the northwest region of the ice sheet.



## ATMOSPHERIC OZONE

During the past 20-30 years the importance of ozone has escalated from being thought of as an interesting atmospheric trace gas because of its ability to absorb damaging ultraviolet radiation to global prominence because its devastating depletion seriously impacts human habitation. Although the ozone layer is very thin, if the total amount is compressed to a finite layer, its maintenance in the stratosphere is essential to insure the health of humans, animals, and plants. Vertical profiles of ozone are obtained using the Electrochemical Concentration Cell (ECC) ozonesonde. The pre-flight preparation and calibration of this instrument is a critical factor for understanding and validating the current state of the ozone layer. The quality of the ozone measurement is extremely dependent on how carefully pre-flight preparation of the instrument is performed. Code 972 established unique calibration procedures applicable to the ECC ozonesonde instrument. These procedures have been discussed in the literature (Torres and Bandy, 1978; Torres, 1985) and more recently Bittner, et al, 1997, discuss a number of special instrument comparisons that have been conducted. Calibrations are performed using controlled concentrations of ozone resulting in high quality measurements without distortion arising in the data from manufacturer's calibration deficiencies nor from step-changes as new instrument models appear. The latest ECC model (6A) is in use and provides a digitally formatted output approximately every 1-2 seconds. All of the ozonesondes flown from Wallops Island are calibrated against an absorption photometer (Dasibi) which previously has been calibrated against a 3-meter long solar absorption photometer maintained at Wallops Island. In addition to the long-term Wallops Island data base, short-term specific data bases are available from various sites, e.g., Panama (Schmidlin and Kloos, 1977), from Antarctica during Austral Springs of 1987, 1988, 1989, 1990, and more recently during 1994, and other locations. Cooperation between NASA and INPE in Brazil is permitting the accumulation of ozone profiles from Natal,  $\sim 6^{\circ}\text{S}$ , and more recently between NASA and the USAF from Ascension Island,  $\sim 8^{\circ}\text{S}$ .

Total-column values of ozone are also obtained from the Wallops Island Dobson spectrophotometer and are reported to the World Ozone and Ultraviolet Data Center (WOUDC) on a monthly interval. The Dobson record began in 1966 and has been continuous since 1970.







## CRISTA OZONE MEASUREMENTS/VALIDATION

M. Bittner\*, D. Offermann\*, P. Preusse\*, M. Riese\*,  
H. Claude\*\* and F. J. Schmidlin\*\*\*

\* Physics Department, University of Wuppertal, Gauss-Strasse 20, 42097 Wuppertal, Germany

\*\* Deutscher Wetterdienst, Albin-Schwaiger-Weg 10, 82383 Hohenpeissenberg, Germany

\*\*\* Observational Science Branch, NASA Goddard Space Flight Center, Code 916, Wallops Flight Facility, Wallops Island VA 23337, USA

### ABSTRACT

Seven days of global high resolution middle atmosphere ozone profiles have been measured by the CRYogenic Infrared Spectrometers and Telescopes for the Atmosphere (CRISTA) in November 1994. Measurements cover the altitude range from 10 to 80 km and latitudes from 59°S to 64°N. An example of a global ozone map is presented and demonstrates the ability of the instrument to detect medium and even small scale structures. Comparisons with ECC- and Brewer Mast balloon-sonde underflights are discussed. Reasonable agreement between CRISTA and balloon-sondes is found especially in the altitude interval between about 19km and 27km. © 1997 COSPAR. Published by Elsevier Science Ltd.

### INTRODUCTION

Recently, the CRYogenic Infrared Spectrometers and Telescopes for the Atmosphere (CRISTA) was flown on the ASTRO-SPAS satellite and operated from November 4 through November 12 1994, yielding thousands of ozone radiance profiles with excellent coverage and resolution (Riese et al., this issue). With this data set it will be possible to examine details of the dynamics of the nearly global ozone distribution from 59°S to 64°N latitude and from about 15 to 80 km in altitude (Offermann, 1993). A correlative measurement program was set up for validation studies (Bittner, 1994).

### CRISTA OZONE DATA

A representative map of global ozone density retrieved from 12.6  $\mu\text{m}$  is shown in Figure 1 (Type: B1). Given are ozone mixing ratios at an altitude of about 30 km for November 6, 1994. Due to the three simultaneously operated telescopes of CRISTA, the horizontal coverage is considerably denser than it is for other satellite instruments. The three tracks of the telescopes can easily be identified in the map. The distance of two adjacent measurement points along track is about 200 km on this day ("stratospheric mode", see Riese et al., this issue), which is near the theoretical limit of the limb technique. It should be mentioned that each dot in Figure 1 corresponds to one complete height profile. The map reflects high ozone densities near the equator and lower concentrations at higher latitudes. The region with extremely low mixing ratios in the southern part of South America reflects the elongated southern polar vortex. The data also reveal that the northern polar vortex was already well established during that period. Beyond these synoptical features, the data clearly show the ability of the instrument to detect a variety of medium and even small scale structures. For instance, the map indicates the presence of a strong streamer along the east coast of Asia apparently carrying ozone rich

\*) Now at German Aerospace Research Establishment-German Remote Sensing Data Center, 82234 Oberpfaffenhofen, Germany



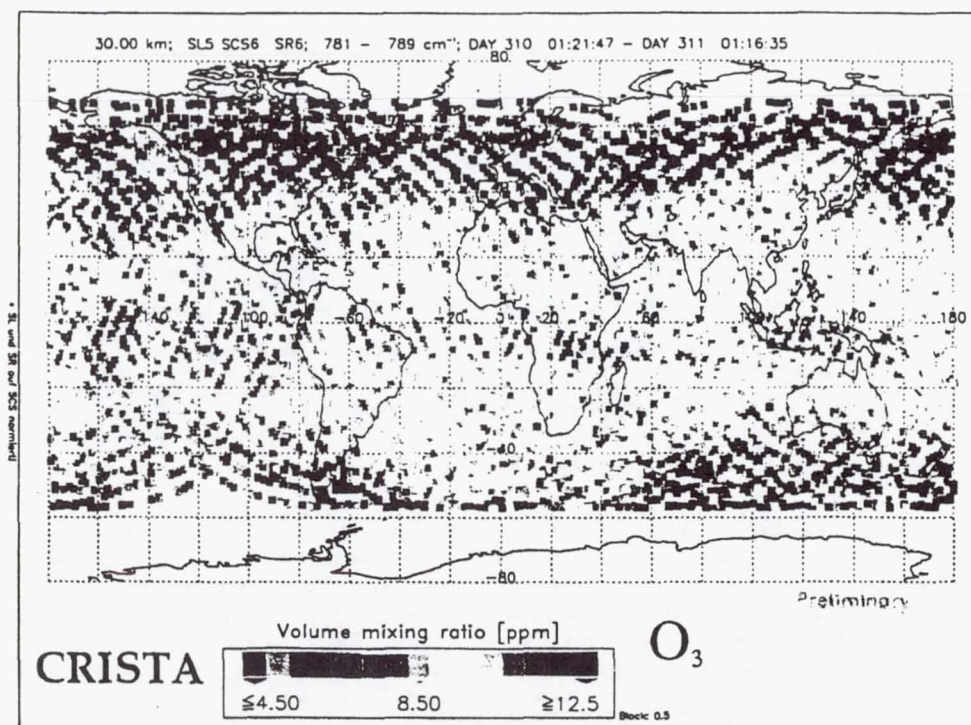


Fig. 1 Global coverage of ozone mixing ratios on 6 November 1994 for 30km altitude. (Type: B1)  
The map covers latitudes from  $-80^{\circ}$  to  $+80^{\circ}$  and longitudes from  $-180^{\circ}$  to  $+180^{\circ}$  (East). Each dot represents a complete height profile.

air from low to high latitudes. These structures are found to be highly variable on time scales of one day or so, and they are believed to play a substantial role in the understanding of the stability of vortices (e.g. Plumb et al., 1994, Waugh et al., 1994).

The presence of even smaller structures is revealed by the patchy colour pattern of the map: ozone densities can vary considerably from one measurement point to the next. (Only part of this is instrument noise.) Such trace gas fluctuations are important especially in the context of photochemistry (e.g. Tuck, 1979).

## CORRELATIVE DATA COMPARISONS

Ozone measurements close in space and time to the CRISTA tangent points were performed with balloon-borne sensors at two sites at each overpass of the CRISTA-instrument. The measurement sites were Hohenpeissenberg ( $48^{\circ}\text{N}$ ,  $12^{\circ}\text{E}$ ) and NASA's Wallops Flight Facility ( $37.5^{\circ}\text{N}$ ,  $75^{\circ}\text{W}$ ) using Brewer-Mast sondes and electrochemical concentration (ECC) sondes, respectively. Both measurements were part of the CRISTA ground-truth program: the CRISTA/MAHRSI-Campaign (Bittner, 1994).

The quality of the balloon data was checked for each ascent. To account for systematic errors, corrections were applied by normalizing the integrated ozone from the sounding to a simultaneous measurement of total column ozone by a Dobson spectrophotometer. For example, the mean correction factor for Brewer-Mast sondes at Hohenpeissenberg was found to be about 1.08 during the CRISTA/MAHRSI-Campaign. Typical values for random error in stratospheric ozone are  $\pm 4\%$  between the tropopause and about 25 km, increasing to about  $\pm 10\%$  at 30km and above (Steinbrecht et al., 1996). Random errors for the ECC sonde are estimated as being similar to those for the Brewer-

Mast sonde. Taking into account systematic errors for the Dobson instrument as well as uncertainties from the normalization procedure for the Brewer-Mast instrument the total maximum error may be estimated to range from  $-13$  to  $+20\%$  from about 16 to 26km and from  $-17$  to  $+22\%$  at 30km and above (Remsberg et al., 1984).



## SENSOR/ALGORITHM DEVELOPMENT

The papers in this section describe the efforts to improve sensor technology/measurement technique for retrieving geophysical parameters essential for a better understanding of the hydrospheric processes of the Earth. These papers cover a wide range of subject matter that can be broadly categorized into three groups: land surface, oceanic, and atmospheric studies.

In the category of land surface characteristics, four papers deal with soil moisture measurements by passive and active microwave sensors. Shi et al. and Wang et al. (1) explore in detail the potential and limitation of estimating surface soil moisture content from the L-band Shuttle Imaging Radar C measurements. Chanzy et al. discuss the multiple-frequency radiometric measurements of soil moisture in the Sahel region in central Africa and conclude that measurements at L-band are far superior compared to those in C-band in sensing soil wetness through vegetation canopy. A paper by Toll et al. makes use of data obtained from the Konza Prairie (Kansas) to develop a surface albedo model for the NOAA Advanced Very High Resolution Radiometer. Two papers are dedicated to the microwave measurement of snow. Chang et al. (2) use airborne passive microwave data to infer the snow-covered area and snow water equivalent in the forested regions, as well as the thickness of lake ice. Foster et al. compare a prototype snow algorithm and a newly revised snow algorithm to the snow depth climatology and conclude that the new algorithm significantly improved the estimation of snow depth. Roman et al. found that a new local gravity field model adequately simulates the long to intermediate wavelengths of the gravity field based on a comparison of the model derived geoid undulations and the difference in elevations from global positioning system controlled airborne laser altimetry and optical leveling surveys.

The area of oceanic studies covers a variety of subjects. New results on ocean waves are discussed by Elfouhaily et al., Liu et al., and Vandemark et al. Elfouhaily et al. combine various sources of data and works and arrive at a unified directional spectrum for short and long wind-driven waves. Liu et al. describe the efficiency of the two-dimensional wavelet transform and demonstrate, with some examples, the feasibility of the technique for coastal monitoring. Vandemark et al. use the Ku-band altimeter and *in-situ* measurements to examine the relationship between the altimeter backscatter and the magnitude of near-surface wind and friction velocities. Papers by Bliven et al. (2) and Craeye et al. discuss effects of microwave scattering from rain roughened seas. In addition, Bliven et al. (1) explore the possibility of improving the accuracy of wind speed estimation using dual frequency (C and Ku band) altimeter data. Closely associated with the altimeter measurements are the work by Bilitza et al. that attempts to improve the IRI (International Reference Ionosphere)-computed electron content for a better estimate of the ionospheric correction term in altimeter data analysis. Regarding sea ice measurements, a paper by Comiso et al. compares two different passive microwave techniques for the estimation of sea ice concentration, and another paper by St. Germain and Cavalieri explores a passive microwave approach for mapping the ice temperature in the Arctic seasonal sea ice zone. Works related to the studies of ocean color are summarized in papers by Aiken and Hooker, Fraser et al., Gregg et al., and Patt et al. Aiken and Hooker discuss the use of AMT (Atlantic Meridional Transact) cruises to calibrate and validate Sea-viewing Wide Field-of-view Sensor (SeaWiFS) data and, thereby, improve the accuracy for estimating global primary production. Fraser et al. develop an algorithm to correct the satellite measurements of ocean color for atmospheric and surface reflection effects. Gregg et al. derive a realistic simulated data set that was essential for mission readiness preparations for SeaWiFS. Closely related to the SeaWiFS project, Patt et al. develop an automated method for performing navigation assessment on satellite-based Earth sensor data.



In the area of atmospheric studies, activities in radar and radiometer measurements for rainfall estimation continue at a healthy level, in association with the TRMM (Tropical Rainfall Measuring Mission) program. Caylor et al. discuss the error in estimation of surface cross section from a meteorological radar and its impact on the rain rate retrieval. Meneghini et al. examine the data acquired by multiple-frequency airborne radar and radiometers and show the effect of drop-size distribution (DSD) of hydrometeors on the brightness temperatures measured at 34 GHz. Wang et al.(4) analyze data acquired over towering storms and illustrate how the radiometric signatures at frequencies of 90-220 GHz could be used to infer the structure and microphysics of these storm clouds. Chang and Chiu examine a number of rainfall algorithms and arrived at results suggesting the importance of sampling. Prabhakara et al. develop a method to discriminate between stratiform and convective rain systems from SSM/I observations. A paper by Wang and King assesses the effect of Rayleigh scattering in the retrieval of cloud optical thickness, and two papers by Wang et al. (2,3) explore the potential and limitation of water vapor profiling by millimeter-wave radiometry under clear and cloudy conditions. Finally, a paper by Goldberg et al. studies the global modulation of the tidal motions to study the interaction of the tidal structures with gravity waves and turbulence, and to gain a better understanding of dynamic influences and variability on the equatorial middle atmosphere.



## THE ATLANTIC MERIDIONAL TRANSECT:

### *Spatially Extensive Calibration and Validation of Optical Properties and Remotely-Sensed Measurements of Ocean Colour*

JAMES AIKEN

Plymouth Marine Laboratory,  
Prospect Place, Plymouth, PL1 3DH, U.K.  
E-mail: j.aiken@pml.ac.uk

STANFORD B. HOOKER

Goddard Space Flight Centre  
Code 970.2, Greenbelt, MD 20771, USA  
E-mail: stan@ardbeg.gsfc.nasa.gov

Twice a year, the Royal Research Ship (RRS) James Clark Ross (JCR) steams a meridional transect of the Atlantic Ocean between Grimsby (UK) and Stanley (Falkland Islands) with a port call in Montevideo (Uruguay), as part of the annual research activities of the British Antarctic Survey (BAS). In September, the JCR sails from the UK, and the following April it makes the return trip. The ship is operated by the BAS for the Natural Environment Research Council (NERC). The Atlantic Meridional Transect (AMT) Program exploits the passage of the JCR from approximately 50°N to 50°S with a primary objective to investigate physical and biological processes, as well as to measure the meso-to-basin-scale bio-optical properties of the Atlantic Ocean. The calibration and validation of remotely sensed observations of ocean colour is an inherent objective of these studies: first, by relating *in situ* measurements of water-leaving radiance to satellite measurements, and second, by measuring the bio-optically active constituents of the water.

To date, there have been four AMT cruises: AMT-1 departed Grimsby on 21 September 1995 and docked at Stanley on 24 October 1995; AMT-2 left Stanley on 18 April 1996 and arrived in Plymouth on 25 May 1996; AMT-3 departed Grimsby on 20 September 1996 and docked in Stanley on 25 October 1996; and AMT-4 started from Stanley on 21 April 1997

and ended in Grimsby on 27 May 1997. The AMT Program is led by the Plymouth Marine Laboratory (PML) in partnership with the Southampton Oceanographic Centre and BAS with contributions from University groups in the UK and Europe. The Sea-viewing Wide Field-of-view Sensor (SeaWiFS) Project has been a major partner with PML in the AMT Program, supplying state-of-the-art optical sensors and logistical support. Figure 1 depicts the AMT-2 cruise track superimposed on the major current systems of the Atlantic Ocean between 50°N to 50°S, plus a set of composite AVHRR sea surface temperature images for the cruise time period.

To exploit the passage of the JCR, the AMT Program employs three sampling strategies: 1) Continuous, underway, surface layer measurements from pumped sea water of temperature (T) and salinity (S),  $pCO_2$ , nutrients, and inherent optical properties at nine wavelengths (Wet Labs AC-9), with discrete measurements (every two hours) of phytoplankton species high performance liquid chromatography (HPLC) pigments; 2) Towed measurements (10–80 m) using the Undulating Oceanographic Recorder (UOR) with sensors for T-S, chlorophyll fluorescence, water transmission (660 nm), plus downwelling irradiance,  $E_d(\lambda)$ , and upwelling radiance,  $L_u(\lambda)$ , at seven SeaWiFS wavelengths; 3) Station measurements, made daily at local

solar noon or pre-noon, for conductivity, temperature, and depth (CTD) and water samples to 200 m, for plankton, pigments, and productivity determinations; separate casts for multispectral optical properties,  $E_d(\lambda)$  and  $L_u(\lambda)$  with the SeaWiFS Optical Profiling System (SeaOPS) and the SeaWiFS Free-falling Advanced Light Level Sensors (SeaFALLS).

All biogeochemical measurements and all optical measurements adhere to the Joint Global Ocean Flux Study [JGOFS, 1991] and SeaWiFS protocols [Mueller and Austin, 1995], respectively. Whenever possible, new instrumentation and novel technologies have been employed to enhance the data acquisition in both quantity and quality; e.g., autonomous  $pCO_2$ , the UOR, the AC-9, SeaOPS and SeaFALLS, as well as the SeaWiFS Quality Monitor (SQM) which is used to monitor the stability of the radiometers. All of the radiometers used, including spares, were manufactured by Satlantic, Inc. (Halifax, Canada) to ensure redundancy and intercalibration. Figure 2 depicts the main radiometric instruments used in the AMT Program.

The calibration and validation of ocean colour satellites, and the acquisition of data for the development of remote sensing algorithms, requires sensor and data accuracies of the highest order, generally better than those achieved until now. The same data with com-



erence devices, or fiducials, that are designed to mimic the reflectivity of the optical surface of the field sensor, but are not functioning detector units. The front surface of the fiducial is protected when not in use and is kept clean during the field experiment. A kinematically designed D-shaped collar is used on both the optical sensors and the fiducials to ensure the devices being tested view the same part of the SQM aperture each time they are used.

The SQM was deployed on the AMT-3 cruise for the first time and demonstrated the following capabilities [Hooker and Aiken, 1997]: 1. The SQM can be used to track the stability of field radiometers at less than the 1% level in terms of the radiometric response of the sensors; 2. The SQM light field is sufficiently stable to model changes in the radiometric detectors; 3. Based on the radiometers used during AMT-3, daily SQM measurements are required to resolve short-term temporal changes of the radiometric detectors; and 4. The field assessment showed that the SQM performance decayed approximately 0.6% during the course of the 36 day deployment.

SeaOPS is composed of an above-water and in-water set of instruments [Robins et al., 1996]. The in-water component is composed of a downward-looking radiance sensor (OCR-200) which measures upwelling radiance,  $L_u$ , and an upward-looking irradiance sensor (OCI-200) which measures downwelling irradiance,  $E_d$ . The in-water instruments are mounted on a T-shaped frame which is lowered and raised through the water column by a winch; data are collected during the lowering and raising of the frame. The above-water component, an OCI-200, measures the incident solar irradiance at the ocean surface,  $E_d(0+)$ . The OCI-200 and OCR-200 radiometers have seven channels, which were chosen to correspond with the SeaWiFS instrument wavelengths and bandwidths [Hooker and Esaias, 1993].

The UOR is a measurement platform which is towed approximately 400 m behind a ship [Aiken and Bellan, 1990]. It uses a programmable servo that controls the attitude of a diving plane which causes the vehicle to undulate through a preset depth range, typically 10-80 m, at tow speeds between 10 to 12 kts. At speeds in excess of 6 kts, the servo unit is powered by an alternator, which is driven by a propeller on the rear of the body. During AMT-3, an OCI-200 was fitted to the top of the UOR instrument bay to measure downwelling irradiance,  $E_d$ , and an OCR-200 was fitted to the bottom of the instrument bay to measure upwelling radiance,  $L_u$ . The OCI-200 and OCR-200 radiometers employed in the UOR and SeaOPS use 16-bit analog-to-digital (A/D) converters and are capable of detecting light over a four decade range.

SeaFALLS is composed of two subsystems: a SeaWiFS Profiling Multichannel Radiometer (SPMR) and a SeaWiFS Multichannel Surface Reference (SMSR). The former measures  $E_d$  and  $L_u$  as it falls freely through the water column, while the latter measures the incident solar irradiance just below the sea surface,  $E_d(0-)$ . The profiler receives its power and sends its data via an umbilical cable, while the reference floats just below the surface suspended from a square floating frame [Waters et al., 1990]. Both the profiler and the reference can be deployed far away from the ship, so any ship-induced disturbances to the *in situ* light field are minimized [Mueller and Austin, 1995]. Since SeaFALLS can be deployed quickly by only two people, the ship can be stopped when light conditions are optimal. SeaFALLS is equipped with 13-channel OCI-1000 and OCR-1000 radiometers, which employ 24-bit A/D converters, and are capable of detecting light over a seven decade range.

The data acquired by these means are used to validate the performance and accuracy

of algorithms for the interpretation of SeaWiFS imagery and generate new algorithms where deficiencies are detected. Along with the HPLC pigment measurements, the analysis points to the validation of the Platt-Longhurst hypothesis [Platt et al., 1995; Sathyendranath et al., 1995] of bio-optical provinces with distinct optical properties. AMT measurements show that these align precisely with physical provinces determined by T-S relationships. Significantly, the analysis shows that interprovince bio-optical variability is driven by phytoplankton accessory pigment concentrations, particularly photoprotective carotenoid (PPC) abundance, and ratio to photosynthetic carotenoids (PSC), i.e., PPC/PSC, which is highest in high-light equatorial zones; though this is as expected ecologically, the ratios are province-specific rather than intensity-specific.

With the wide diversity of ecosystems encountered (two hemispheres and two seasons are sampled over a period of 30-35 days), an AMT cruise is like many cruises rolled into one, making it inevitable that new observations and new discoveries will emerge on every transect. For the future, the project will continue to pioneer new sensors and new technology. During AMT-4, a new free-fall radiometric instrument called the Low-Cost NASA Environmental Sampling System (LoCNESS) and a new hyperspectral radiometer called SeaSPEC were both tested. By AMT-5, a Fast Repetition Rate Fluorometer (FRRF) will be deployed in the UOR to provide measurements of photosynthetic parameters in all the provinces of the Atlantic Ocean - data which are necessary to exploit remotely sensed observations of ocean colour for estimating global primary production.





## IMPROVED IRI PREDICTIONS FOR THE GEOSAT TIME PERIOD

D. Bilitza\*, S. Bhardwaj\* and C. Koblinsky\*\*

\*HSTX, GSFC, NSSDC, Code 633, Greenbelt, MD 20771, U.S.A.

\*\*NASA, GSFC, Code 971, Greenbelt, MD 20771, U.S.A.

### ABSTRACT

Single-frequency altimeter measurements require an estimate of the signal retardation effect in the ionosphere. Ionospheric models like the International Reference Ionosphere (IRI) are being used to obtain these correction factors. Incorporation of worldwide ionosonde measurements is discussed as a way towards more accurate predictions. Using measurements of the F peak critical frequency (foF2) from more than 70 ionosondes we have derived (hour and month dependent) regional and global ionospheric-effective solar indices. Replacing the solar index in IRI with these new indices we could improve the IRI estimates for the GEOSAT time period (1986-1989) by a few percent.

©1997 COSPAR. Published by Elsevier Science Ltd.

### INTRODUCTION

The ionospheric correction (signal retardation) that needs to be considered in altimeter sea surface height measurements is directly proportional to the electron content (EC) along the (vertical) signal path. EC can be described as the F peak density NmF2 times the slab thickness ST ( $EC = NmF2 \cdot ST$ ). It is well-known that EC and NmF2 are closely correlated and that most of the variability of EC is due to the variability of NmF2 (e.g., Houminer and Soicher, 1996). Measured values of NmF2 or of the critical frequency foF2 (foF2 squared is proportional to NmF2) can therefore be used to update the EC assuming that the less variable ST is well represented by a model like IRI.

Our effort is part of the Ocean Science Pathfinder project and is concentrated on the GEOSAT mission years. Ideally, for this purpose one would like to have measured ionospheric parameters in the ocean areas and then update the model predictions with the weighted mean of the closest measurement points. Since such a data source is not available, we have used all data (or a regional subset) to update the global (regional) predictions for a specific Universal Time (UT).

### THE IONOSONDE DATA (NGDC CD-ROM)

The ionosonde data used in this study were taken from the "Ionospheric Digital Database", a set of two CD-ROMs recently issued by NOAA's National Geophysical Data Center (NGDC). The set includes about 40,000 station years (1.35 Gbyte) from 1957 to 1990; mostly hourly peak parameters. We extracted all data for the GEOSAT years 1986 to 1989. At any specific hour there were data from about 75 stations available. As Figure 1 shows the global distribution of these stations is unfortunately not homogenous but is largely biased towards the European mid-latitude sector.

As a caveat for other CD users we would like to point out that we found a number of cases where we had to correct the information on the CD: for KHEYSA ISLAND the wrong coordinates were given in 1989; for several stations the time given is actually the Local Time and not the Universal Time, this includes UPPSALA for all of 1987, 1988, and 1989, TAHITI for all of 1989, and LA REUNION for all of 1989; for JOHANNESBURG (June, July, Aug and Oct of 1988) and CAPETOWN (June and Aug of 1988) the given time is shifted by a full 12 hour time period. In all these cases the error was detected because the difference to IRI-95 was larger than 50%; comparisons with IRI are thus a simple way of avoiding/pinpoint potential errors.

### IONOSONDE-DERIVED INDICES

We have used the URSI option in IRI for predicting foF2 (Rush et al., 1989). Figure 1 compares these predictions with the measurements from the CD-ROM for Jan 1986, 12 UT. We see that during this hour the discrepancy range is about  $\pm 2$  MHz with IRI underestimating northern measurements and overestimating southern measurements.



The rationale for the FLT index is, that it is based on station from the region of interest for the GEOSAT ocean data. The ZONAL indices were tested since often a distinct hemispheric difference was observed in the data-model discrepancy (see Figures 1 and 2). These differences indicate a problem in the URSI maps with the representation of hemispheric and/or seasonal variations. Because the station-volume is so heavily biased towards northern mid-latitudes, we have also used the 3ZONE index which gives equal weight to all three latitude zones. Figure 3 shows the ALL, 3ZONE, and ZONAL monthly indices in comparison to the IG12 index. All indices closely follow the general solar cycle variation of IG12 but show as expected a much higher month-to-month variability. Differences to IG12 are in the  $\pm 20$  range. Distinct zonal differences are noticeable especially during low solar activity.

## ACHIEVED IMPROVEMENT

We have studied the improvement potential of these new indices with the ionosonde data themselves and also with independent EC data. Table 1 shows the percentage improvement (PI) when using the new monthly and hourly indices instead of IG12 in IRI for the GEOSAT years 1986 to 1989. PI is defined as the difference between the RMS (root mean square of difference between data and IRI) obtained with using IG12 in IRI and the RMS obtained with using the new indices; positive values indicate an improvement when using the new index and negative values indicate that IG12 is better. Looking at the total average (TOTAL AVG) in Table 1, we note that all indices (except for ALL-HR) provide an improvement. Averaging over the whole 4-year time period the improvement is below the 1% margin, although there are months (years) where improvements of up to 2.5% (1.6%) are achieved. Best results are obtained with the ZONAL index and the worst results with the ALL-HR index. The time resolution of the indices did not have a significant effect. Both, hourly and monthly indices provided about similar results; please note that the November 1989 value for ZONAL-HR is erroneous, without this value the overall average (AVG) is the same as for the monthly ZONAL index. Clearly further improvement has to come from a better spatial resolution of the data source, i.e. more ionosonde stations more evenly distributed over the globe.

A 1-2% improvement in foF2 will translate into a 2-4% improvement of the electron content EC (and thus of the ionospheric corrections for satellite altimeters), since the EC depends on foF2 squared. We have used hourly EC data to independently verify this small improvement. The Faraday measurements were obtained from NOAA's National Geophysical Data Center (NGDC). They are hourly data for all of 1989 from 10 stations located in the modip range 20° to 60°. The results are listed in Table 2. The overall improvement with the ZONAL index is 4.5%, although there are two months (March and July) where neither of the new indices provides an improvement. The second-best index is FLT with an improvement of 2.2%. Using all stations for the index (ALL) made the discrepancy between model and data even larger than when using the IG12 index. Since the EC data were mostly from Northern mid-latitudes, it is not surprising that the 3ZONE index (that accounts evenly for all three zones) performs much worse than the FLT index (that is strongly influenced by the large number of Northern mid-latitude ionosonde stations).

## CONCLUSION

We have investigated the potential improvement of IRI predictions with the help of simultaneous ionosonde foF2 observations. The prime intent of this study was to improve the IRI-computed electron content for a better estimate of the ionospheric correction term in altimeter data analysis for the GEOSAT time period from 1986 to 1989. Using ionosonde foF2 data from more than 70 stations (from NGDC's CD-ROM) we have obtained new ionosonde-based, solar-ionospheric indices. We have considered hourly and monthly indices for the whole globe as well as for specific latitude zones.

Substituting this new indices in IRI for the IG12 index we find only a very modest improvement (a few percent) of the IRI EC predictions. Hourly indices provided only marginal (a few tenth of a percent) better results than monthly indices. Similarly, zonal indices provided only an improvement of a few tenth of a percent over the global indices.

Our study shows that going from a 12-month-running mean index (IG12) to hourly or monthly indices did not result in a significant improvement of IRI predictions. Also the usage of zonal indices to improve hemispheric and/or seasonal imperfections in the URSI maps, did not provide significantly better predictions.

We recommend using the monthly FLT index for the GEOSAT data analysis. It should result in an improvement of 2 to 4% in the ionospheric correction for GEOSAT altimeter data. To obtain significantly better predictions a direct updating of IRI with more measurements from evenly distributed stations would be required. The intent would then be to update IRI at a specific location with the weighted mean of the model-measurement differences of the closest stations.



## FRICION VELOCITY ESTIMATION USING DUAL-FREQUENCY ALTIMETER DATA

Larry F. Bliven

*NASA/Goddard Space Flight Center, Laboratory for Hydrospheric Processes, Wallops Island, VA, 23337, USA*

Piotr W. Sobieski and Albert Guissard

*Université Catholique de Louvain, Département d'Electricité, Place du Levant 2, B-1348 Louvain-la-Neuve, Belgium*

and

Hubert Branger

*Institut de Mécanique Statistique de la Turbulence, 12 av. Général Leclerc, Marseille, France*

**Abstract.** Global estimation of wind speeds near the sea-surface can be obtained using normalized radar cross sections  $\sigma_o$  from satellite-borne single-frequency altimeters. Indeed recent validation studies of Geosat altimeter-derived wind speeds show that several often cited semi-empirical algorithms yield linear trends between wind-speeds from altimeter data and wind speeds from (a) ships of opportunity (Etcheto 1992), (b) buoys (Carter 1992) and (c) atmospheric models (Guillaume 1992). Although the linear trends are striking, there is considerable scatter since the range of standard deviations is from 1.5 to 3 m s<sup>-1</sup>. In fact, the scatter of some particular measurements about the regressions is striking because they depart from the 'standard' by as much as  $\pm 5$  m s<sup>-1</sup>, which is large - even for full gale winds of 20 m s<sup>-1</sup>. These anomalies can cause serious problems for gas exchange, heat, and aerosol estimates. They can also induce considerable errors in wind-driven oceanic circulation models and sea-surface wave models. This paper explores the possibility of improving the accuracy of wind speed estimation using dual-frequency altimeters.

### 1 Introduction

Undoubtedly sea-surface morphology depends upon not only local wind conditions but also upon winds that have acted previously - both locally and faraway. Short waves rapidly adjust to the local wind and because their wavelengths are small, they damp out quickly. On the other hand, long-waves require considerable distance and/or duration to develop and because their relaxation time is large, they can last for hours after their initial cause has disappeared. They even propagate great distances from their source region. Therefore long-wave characteristics are not well correlated to the local wind. Because sea-surface morphology is not uniquely determined by the local wind, it is unlikely that a robust one-to-one relationship exists between  $\sigma_o$  and local wind speed.

Considering these factors, we assessed the effects of long-wave variability on an altimeter wind algorithm by using a multiple-parameter spectral model to represent the sea-surface. This analysis assumes normal wind-generated seas, i.e., that winds are from the direction of the long-waves. The simulations of a K<sub>u</sub>-band altimeter show that  $\sigma_o$  is predominantly a function of short-waves, which are coupled to the local wind friction velocity  $u_*$ ; however, long-wave steepness also affects  $\sigma_o$  levels. Therefore we examine a dual-frequency altimeter and the analysis of  $\sigma_o(C)$  and  $\sigma_o(K_u)$  data reveals a technique to derive long-



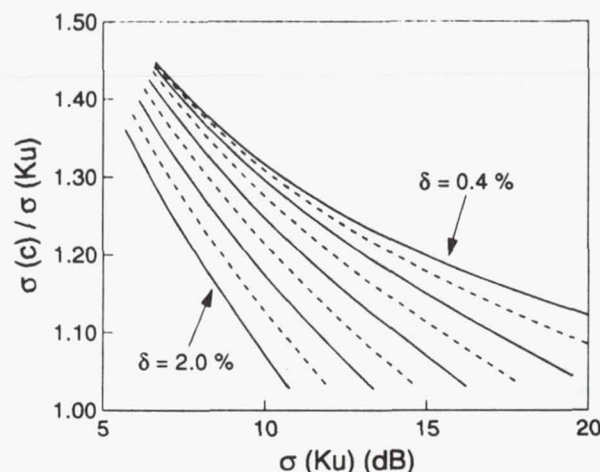


Fig. 2. Simulations with SymALT-CK reveal a technique to infer significant slope using dual-frequency data.  $\delta$  increments = 0.2 %. Thus a two-parameter friction velocity algorithm may be viable for dual-frequency altimeters such as TOPEX-POSEIDON

parameter model. For example, one can simply use the results presented in Figure 2 to infer  $\delta$ , then use Figure 1 with both  $\sigma_o(K_u)$  and  $\delta$  as input to obtain  $u_*$ . Hence for a particular  $\sigma_o(K_u)$  value,  $u_*$  is unambiguously determined with respect to long-wave conditions.

The sensitivity of the results shown in Figures 1 and 2 was examined by changing the dominant wavelength by almost an order of magnitude, *i.e.* from 25 to 200 m. The cross sections differed from those shown in Figure 1 by less than  $\sim 0.4$  dB and the ratios differed from those shown in Figure 2 by less than  $\sim 0.01$ . In both cases, this is typically smaller than the spacing between isopleths. Because the isopleths shown in these figures are only weakly dependent upon the dominant wavelength, this two-parameter model is practically insensitive to the dominant wavenumber  $k_p$  and hence this approach may lead to a useful operational algorithm.

#### 4 Summary and Recommendations

This simulation shows that both long-wave significant slope and friction velocity are important parameters affecting  $\sigma_o(K_u)$  values. Consequently we introduced a technique to use dual-frequency altimeter data to refine estimates of friction velocity by compensating for naturally occurring long-wave slope variability. The results of this analysis, however, are not intended to be applied immediately as an operational algorithm, but rather are intended to demonstrate a technique that should be further examined to assess its real potential to enhance the utilization of dual-frequency altimeter data for geophysical applications.

Accurate friction velocity values are needed for many oceanic processes to be effectively modelled and monitored. The TOPEX/POSEIDON satellite is



# A SUMMARY OF SCATTEROMETER RETURNS FROM WATER SURFACES AGITATED BY RAIN

Larry F. Bliven

*NASA/Goddard Space Flight Center, Laboratory for Hydrospheric Processes, Wallops Island,  
VA, 23337, USA*

Jean-Paul Giovanangeli and Hubert Branger

*Institut de Mécanique Statistique de la Turbulence, 12 av. Général Leclerc, Marseille, France*

and

Piotr W. Sobieski

*Université Catholique de Louvain, Département d'Electricité, Place du Levant 2,  
B-1348 Louvain-la-Neuve, Belgium*

**Abstract.** In this paper, we summarize our initial findings from  $K_a$ - and  $K_u$ -band scatterometers which include: a scaling law for backscattered power as a function of rain rate; a linear superposition model for light rains and low wind speeds; evidence of the importance of scattering from rain-generated ring-waves; and progress towards development of a scattering model for computing normalized radar cross sections from wind and rain roughened water surfaces.

## 1 Introduction

Rain modifies sea-surface roughness, so precautions must be taken to derive accurate surface winds from scatterometer data obtained in storms. Unbiased wind estimates are needed for oceanic circulation modeling and wave forecasting, which are major subjects areas because of their significant roles in heat flux and gas exchange. For weather and climate studies, it is important to minimize biases due to rain in scatterometer wind data sets. Thus, we initiated a research program with the goal of improving the understanding of microwave scattering from rain-roughened seas.

## 2 Methodology

We conducted rain experiments in the NASA wind-wave tank (20 x 1 x 1.2 m) at Wallops Island and in the IMST wind-wave tank (40 x 3 x 2.5 m) at Marseille. Scatterometer data are from  $K_a$ - and  $K_u$ -band systems like the one described by Bliven and Norcross (1988). The scatterometer data are reported in terms of relative backscattered power (RCS) by using the backscattered power from a metal sphere at the appropriate distance as the normalizing factor. We also built rain simulators: the one at NASA was at 1.5 m above the calm water surface and it produced uniformly sized 2.8 mm diameter water drops that fell from 10 nozzles (35 x 14 cm<sup>2</sup>); and the one at IMST was 1 m above the calm water surface and it produced water drops from 72 nozzles (40 x 45 cm<sup>2</sup>) distributed among six sizes that generated drops that ranged from 1.2 to 2.8 mm. For a given flow rate, each rain simulator had nearly uniform flow rates through all of its nozzles. Consequently for a given flow rate with the IMST simulator, the



### 3.3 SCATTERING FROM RING-WAVES

The component of RCS for rain-agitated water surfaces that is attributable to scattering from ring-waves rather than other features such as stalks and craters has been investigated by Bliven *et al.* (1993c). The analysis consists of a comparison of RCS measurements from solely rain to RCS measurements from solely wind conditions. Surface elevation was measured using a capacitance probe adjacent to the radar footprint on the water surface (just outside of the rain footprint). Ring-waves propagate - but craters and stalks don't propagate. Consequently for the rain cases, the radar measured scattering from all sources but the elevation probe measured only the ring-waves. On the other hand for the solely wind cases, the elevation probe measured wind-generated roughness - for which craters and stalks are not a concern. Since the data comparison shows that RCS is primarily from small-scale features, appropriate scaling factors were used to account for the directional characteristics of short wind-waves (aligned with the wind) and for rain-generated ring-waves (isotropic distribution). Thus we found evidence (Figure 3) that the component of backscattered power attributable to ring-waves is 90 % of the backscattered power from the rain-agitated water surface. The 10 % residual is ascribed to scattering from other features and to measurement error or uncertainty. This comparison indicates that scattering from ring-waves is the dominant scattering mechanism and it accounts for between 75 % and 100 % of the backscattered power from rain-agitated water surfaces.

### 3.4 NUMERICAL MODELING

The results reported herein are being used to enhance the composite scattering model of the Université Catholique de Louvain (UCL), which computes backscattered power values for altimeters and scatterometers by using various sea-surface spectral models. This simulator for wind-roughened seas is amply documented by Guissard *et al.* (1994) and Sobieski *et al.* (1994) and recent developments with respect to rain effects are presented by Sobieski *et al.* (1993).

## 4 Summary

In this paper, we have summarized our recent efforts to improve the understanding of microwave scattering from water-surfaces roughened by rain. For a more complete understanding there remain many issues to be clarified. A few examples include improved characterization: of rain generated features (crowns, stalks, ring waves); of effects related to stratification from fresh water layers above sea-water; and of interactions between rain-generated and wind-generated processes. Studies are also needed at higher rainfall rates and with drops at terminal velocity. On the other hand, radar measurements are needed at various incidence angles and polarizations. To systematically investigate many of these topics, the Rain-Sea Interaction Facility was recently established at NASA-GSFC (Bliven and Elfouhaily 1993) and we foresee collaborative studies with investigators who are engaged in measuring and modeling rain-sea interaction processes.



## Correction of Sampling Errors in Ocean Surface Cross-Sectional Estimates from Nadir-Looking Weather Radar

I. J. CAYLOR\* AND G. M. HEYMSFIELD

*Mesoscale Atmospheric Processes Branch, Laboratory for Atmospheres, NASA/Goddard Space Flight Center, Greenbelt, Maryland*

R. MENEGHINI

*Microwave Sensors Branch, Laboratory for Hydrospheric Processes, NASA/Goddard Space Flight Center, Greenbelt, Maryland*

L. S. MILLER

*Department of Physics and Astronomy, Clemson University, Clemson, South Carolina*

4 April 1996 and 25 July 1996

### ABSTRACT

The return from the ocean surface has a number of uses for airborne meteorological radar. The normalized surface cross section has been used for radar system calibration, estimation of surface winds, and in algorithms for estimating the path-integrated attenuation in rain. However, meteorological radars are normally optimized for observation of distributed targets that fill the resolution volume, and so a point target such as the surface can be poorly sampled, particularly at near-nadir look angles. Sampling the nadir surface return at an insufficient rate results in a negative bias of the estimated cross section. This error is found to be as large as 4 dB using observations from a high-altitude airborne radar. An algorithm for mitigating the error is developed that is based upon the shape of the surface echo and uses the returned signal at the three range gates nearest the peak surface echo.

### 1. Introduction

Microwave remote sensing of the ocean surface is a well-established field of research, and the design of instruments such as scatterometers and radar altimeters has been optimized to provide accurate measurements of the backscattered signal. During the last decade, airborne radar techniques have been developed in the meteorological community that require estimation of the normalized surface cross section ( $\sigma^0$ ). These techniques involve using the observed cross section as a means of validating radar calibration (Durden et al. 1994) and estimating the magnitude and direction of the surface winds (Atlas and Matejka 1985; Hildebrand 1994). Airborne radars typically operate at attenuating wavelengths, and so algorithms have been developed to correct rainfall estimates for attenuation. One such algo-

rithm, the surface reference method, involves comparing observations of the surface cross section in a cloud-free region to the cross section under regions of rain (Meneghini et al. 1983; Meneghini and Nakamura 1990; Iguchi and Meneghini 1994). However, meteorological radar systems normally are not designed for observations of point targets, and as a result, a significant error may arise in the estimate of the surface cross section for a near-nadir viewing geometry (Kozu et al. 1995).

While weather radar is designed for targets uniformly distributed in the pulse volume, the surface is a point, or impulse, target. The surface echo at nadir incidence is a narrow feature that will appear only in two or three range gates for airborne weather radars with typical gate spacing of 75–150 m. Because a meteorological radar does not digitally sample the return signal at a sufficiently high rate, only a crude stepwise approximation to the surface echo is available. The peak of the narrow surface echo will be inaccurately determined in those instances where the surface echo is located, in range time, between two gates as a consequence of variation in aircraft altitude. In such situations, the magnitude of the surface echo can be negatively biased. The theoretical source of the error is discussed in section 2. Observations obtained by the National Aeronautics and

\* Additional affiliation: Science Systems and Applications, Inc., Lanham, Maryland.

Corresponding author address: Dr. I. Jeff Caylor, NASA/GSFC, Code 912, Greenbelt, MD 20771.  
E-mail: caylor@carmen.gsfc.nasa.gov



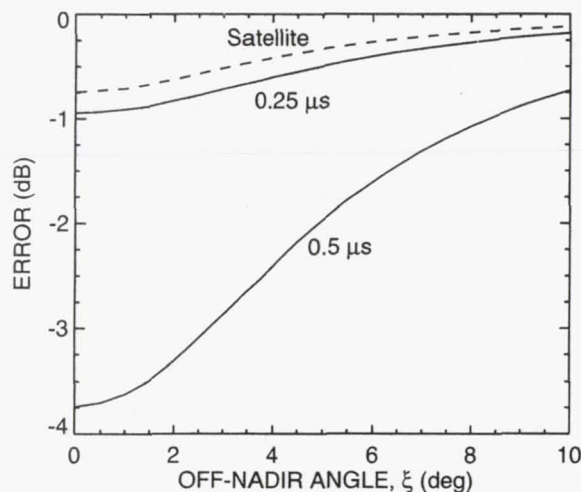


FIG. 11. Computed error as a function of the antenna angle off-nadir ( $\xi$ ) using the EDOP system parameters. Errors are shown for gate spacings of  $0.5 \mu\text{s}$  (current configuration) and  $0.25 \mu\text{s}$ . The dashed line is for a radar such as will be flown on the NASA TRMM satellite.

cross-track scanning, and because the  $0.71^\circ$  beamwidth is relatively narrow compared to the incidence angle, the surface impulse response function (1) was modified with the approximation described by Brown (1989) for  $\xi \geq 5^\circ$ . The receiver impulse response that was used is that given by Kozu (1995). In anticipation of the type of problems described in this paper, the TRMM radar will perform oversampling with gate spacing of half a pulse width, and as a result the error is expected to be less than 0.75 dB for all scan angles.

A scatterplot of  $m$  versus offset is shown in Fig. 12a for the 2200 UTC 28 August 1995 case where the mean incidence angle is  $1.2^\circ$ . At a higher incidence angle of  $3.9^\circ$  (Fig. 12b, 1757 UTC 11 January 1995), the curve is similar in shape but truncated at  $m = 15$ , which indicates the surface echo has been broadened. As the incidence angle increases, the surface return is broadened, and  $m_d$  and  $m_u$  will have a smaller dynamic range, with values approaching zero. Near  $m = 0$ , there is an approximately 0.75-dB difference between the data for the two angles, which agrees reasonably well with the 1 dB estimated from Fig. 11.

Since (5) is a combination of (3) and (4), the contributions to ratio  $m$  from  $m_d$  (+ symbols) and  $m_u$  ( $\Delta$  symbols) are differentiated in Fig. 12. The  $m_u$  contributions typically have a slightly larger ratio, that is, steeper rise, for the same offset because of the asymmetry in the surface echo as a result of the antenna sidelobes (see Fig. 5). This feature can be seen in Fig. 12a, and other EDOP observations show it more clearly. A regression fit to the  $m$  data, therefore, does not perform quite as well as the two-ratio algorithm described above since it would not distinguish between down- and up-range sides of the surface echo.

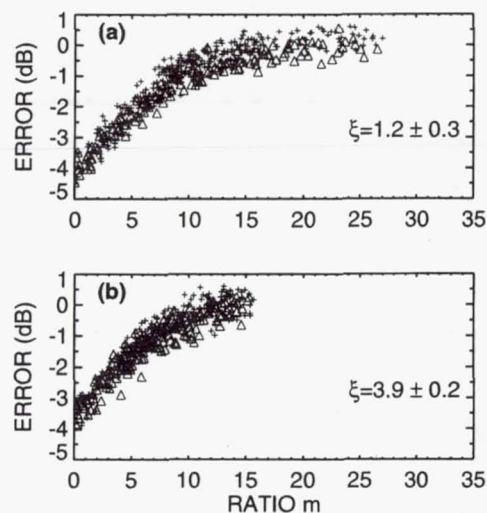


FIG. 12. (a) Scatterplot of  $m$  versus estimated error for the data shown in Fig. 4. The mean incidence angle is  $1.2^\circ$ . (b) Example of  $m$  for a case at 1757 UTC 11 January 1995, where the mean incidence angle is  $3.9^\circ$ . In both panels, the contributions are shown for  $m_d$  (+) and  $m_u$  ( $\Delta$ ).

## 5. Conclusions

Deviations of 3–4 dB in the return from the ocean surface have been observed with the EDOP airborne radar at nadir incidence. These deviations are correlated with changes in aircraft altitude and arise from the fixed gating (range sampling) normally used in a weather radar, which, at times, makes it difficult to estimate the peak value of the narrow surface echo. A number of airborne radar analysis techniques require estimates of the surface cross section; in particular, the surface reference methods for estimating path-integrated attenuation through precipitation and the observed deviations of 3–4 dB can be as large as those occurring from attenuation in precipitation. A correction, therefore, needs to be applied to the surface cross section for observations at near-nadir incidence angles.

The values of the range gates on each side of the peak return are shown to exhibit a relationship to the peak as the surface echo moves between two gates. The functional relation between the gates is a result of the surface scattering physics and the radar system characteristics such as antenna pattern, pulse shape and width, and receiver response. This empirical relationship forms the basis of a simple statistical algorithm that can be used to correct the bias in the mean surface cross section for observations in both cloud-free and rainy regions. Because wave height and surface roughness can change significantly from day to day, the most reliable results have been obtained by computing correction polynomials for each flight line. All that is required to develop a similar relationship for any particular airborne weather radar is a slowly ascending or descending flight track over cloud-free ocean.

The findings of this paper are of concern to existing





## UNCERTAINTY IN SATELLITE RAINFALL ESTIMATES: TIME SERIES COMPARISON

Alfred T. C. Chang\* and Long S. Chiu\*,\*\*

\* *Hydrological Sciences Branch, NASA Goddard Space Flight  
Center, Greenbelt MD 20771, USA*

\*\* *SAIC/General Sciences Corporation, Laurel MD 20707, USA*

### ABSTRACT

We examined nine satellite rainfall algorithms and compared the rain fields produced from these algorithms for the period of August 1987 to December 1988. Preliminary results show algorithms which use the same satellite sensor data tend to be similar, suggesting the importance of sampling. Oceanic global mean rainfall ranges from 2.7 to 3.6 mm/d. The variability in zonal mean rain rate is about 1.5-2 mm/d for these algorithms.

Published by Elsevier Science Ltd on behalf of COSPAR

### INTRODUCTION

There exist a number of operational or semi-operational climate scale satellite rainfall algorithms whose products have been used in diagnostic or comparative studies. To quantify the uncertainty in these algorithms, we compared these rain algorithms at the global and monthly climate scale. Our comparison focused on the time period during which available SSM/I measurements overlap the Atmospheric Modeling Intercomparison Project (AMIP) period, i.e., July 1987 through December 1988. During this period, the algorithms went through at least a seasonal cycle, and hence we can examine the seasonal difference between the algorithms. The responses of the algorithms to the 1986-1987 El Nino Southern Oscillation (ENSO) were evaluated using pattern correlation and paired-t statistics.

### ALGORITHMS

The satellite rain algorithms included in this study are:

1. The Goddard Scattering Algorithm by Adler et al. (1993) (denoted Adler),
2. Calibrating GPI IR data with microwave data by Huffman et al. (1993) (Huffman),
3. Monthly oceanic rainfall using SSM/I Tb histogram by Wilhelm et al. (1991) (Chang or WCC),
4. Theoretical regression method by Kummerow and Giglio (1993) (Kummerow),
5. Precipitation area dependent technique by Prabhakara et al. (1993) (Prabhakara),
6. GOES Precipitation Index (GPI) Technique by Arkin and Meisner (1987) (Arkin),
7. Oceanic rainfall from MSU by Spencer (1993) (Spencer),
8. Global precipitation from TOVS by Susskind et al (1984; 1989) (Susskind), and
9. Multi-spectral rainfall algorithm by Wu (1991) (Wu).

The characteristics of these algorithms are summarized in Table 1.



Table 1: Characteristics of rainfall algorithms

Algorithm	Objective	Technique	Input	Spatial Res.	Temporal Res.	Domain
Adler	Instant. Climate scale	MW scattering	SSM/I 19, 22, 37 & 85 GHz	0.5°x0.5°	monthly	global
Huffman	Climate scale	MW calibrated IR threshold	MW and IR	2.5°x2.5°	monthly	+/-40°
Arkin	Climate scale rainfall	IR thresholding	Geostationary and AVHRR	2.5°x2.5°	Pentad	+/-40°
Chang	Climate scale	MW emission, Lognormal pdf constraint	SSM/I 19 and 22 GHz	2.5°x2.5° & 5°x5°	monthly	+/-65° oceans
Kummerow	Instant. rainfall, Profiles	Optimal, piecewise, linear reg.	SSM/I 19, 22, 37 and 85 GHz	pixel	instant.	global
Prabhakara	Instantaneous /Climate scale	Precipitation area	SSM/I 19, 37 and 85 GHz	3°x5°	instant. monthly	+/-50° oceans
Spencer	Climate scale	Reg. using MW threshold	MSU channel 3	2.5°x2.5°	monthly	+/-50° global
Susskind	Instantaneous rainfall	Reg. using retrieved quantities	TOVS sounding products	60 km	twice daily	global
Wu	Mesoscale/Climate scale	Cloud radiative forcing	TOVS sounding products	4°x5°	10 day, monthly	global

## RESULTS AND DISCUSSIONS

Data were available for most algorithms for the period August 1987 to December 1988, except Kummerow and Huffman whose dataset consisted of data till July 1988. SSM/I data for December 1987 is missing. We resampled the data at the lowest resolution of 5° by 5° without area weighting. For example, Prabhakara's data has a resolution of 3° latitude by 5° longitude and hence latitudinal weights of [3,2], [1,3,1], or [2,3] are used where appropriate. All units are converted to mm/day. We created an ocean mask using the ETOPO5 landmask and computed statistics for oceanic and land areas, respectively. Only oceanic results are presented here.

All algorithms show the major patterns of precipitation in the right locations: the Inter-tropical Convergence Zone (ITCZ), the South Pacific Convergence Zone (SPCZ), and the oceanic dry areas in the western north Atlantic and south Pacific. The intensities at the location of the maximum and minimum are quite varied, however. Table 2 shows the pattern correlation coefficients between algorithms for August 1987. Coefficients greater than 0.85 are bolded. There are high correlation between algorithms of Adler, Chang, Huffman, and Kummerow, who use SSM/I data and those of Susskind and Wu whose algorithms are based on TOVS sounding retrieval products. Huffman's algorithm merges GPI and SSM/I data. Both Arkin and Susskind's algorithm rely on cloud estimates.

Table 2: Pattern Correlation Coefficients for August 1987 between Algorithms

	<u>Huffman</u>	<u>Prabhakara</u>	<u>Chang</u>	<u>Kummerow</u>	<u>Spencer</u>	<u>Arkin</u>	<u>Susskind</u>	<u>Wu</u>
<u>Adler</u>	<b>0.90</b>	0.66	<b>0.88</b>	<b>0.92</b>	0.74	0.82	0.83	0.79
<u>Huffman</u>		0.65	0.83	0.83	0.71	<b>0.88</b>	0.82	0.79
<u>Prabhakara</u>			0.70	0.68	0.76	0.60	0.68	0.70
<u>Chang</u>				<b>0.90</b>	0.75	0.78	0.79	0.78
<u>Kummerow</u>					0.76	0.79	0.79	0.77
<u>Spencer</u>						0.72	0.81	0.79
<u>Arkin</u>							<b>0.91</b>	<b>0.87</b>
<u>Susskind</u>								<b>0.94</b>



## Snow parameters derived from microwave measurements during the BOREAS winter field campaign

A. T. C. Chang, J. L. Foster, and D. K. Hall

NASA Goddard Space Flight Center, Hydrological Sciences Branch, Laboratory for Hydrospheric Processes, Greenbelt, Maryland

B. E. Goodison, A. E. Walker, and J. R. Metcalfe

Climate Research Branch, Atmospheric Environment Service, Downsview, Ontario, Canada

A. Harby

Norwegian Hydrotechnical Laboratory, Trondheim, Norway

**Abstract.** Passive microwave data have been used to infer the snow-covered area and snow water equivalent (SWE) over forested areas, but the accuracy of these retrieved snow parameters cannot be easily validated for heterogeneous vegetated regions. The Boreal Ecosystem-Atmosphere Study Winter Field Campaign provided the opportunity to study the effect of boreal forests on snow parameter retrieval in detail. Microwave radiometers (18, 37, and 92 GHz) were flown on board the Canadian National Aeronautical Establishment's Twin Otter. Flight lines covered both the southern study area near Prince Albert and the northern study area near Thompson, Canada. During the 1994 winter campaign, extensive ground-based snow cover information, including depth, density, and grain size, was collected along most of the flight lines, jointly by U.S. and Canadian investigators. Satellite data collected by the special sensor microwave imager are also used for comparison. Preliminary results reconfirmed the relationship between microwave brightness temperature and SWE. However, the effect of forest cover observed by the aircraft sensors is different from that of the satellite observations. This is probably due to the difference in footprint averaging. There were also several flight lines flown over Candle Lake and Waskesiu Lake to assess lake ice signatures. Preliminary results show the thickness of the lake ice may be inferred from the airborne microwave observations. The microwave signature relationship between lake ice and snow matches the results from radiative transfer calculations.

### 1. Introduction

The boreal forests that stretch across the northern tier of North America and Eurasia provide a treasure trove of natural resources. Probably the most ephemeral of these resources is the seasonal snowpack, which covers the ground for at least half of the year. The boreal areas are always snow covered during the winter months, but because the canopy can obscure much of the snowpack viewed by satellite sensors, accurate estimates of snow depth or snow water equivalent (SWE) is a challenging task.

Ground-based measurements [Edgerton *et al.*, 1971; Schanda and Hofer, 1977; Shiue *et al.*, 1978; Ulaby and Stiles, 1980] indicated that for dry snow over frozen soil the emerging brightness temperature decreases as the depth of snowpack increases. Subsequently, measurements obtained from airborne and spaceborne sensors [Chang *et al.*, 1981, 1987; Rango *et al.*, 1979] have confirmed this finding. Snowpack retrieval algorithms were later developed to infer the SWE from remote measurements [Goodison *et al.*, 1986; Chang *et al.*, 1987]. Based on an algorithm designed for global use, Chang *et al.* [1987] have generated a time series of SWE data set using the scan-

ning multichannel microwave radiometer (SMMR) data from November 1978 to August 1987. Quality of the SMMR-derived snow data set has been carefully studied and evaluated by many investigators [e.g., Barry and Schweiger, 1988; Robinson *et al.*, 1993; Tait and Armstrong, 1996]. It was found that the SMMR-derived snow data in prairie regions compared quite well with National Oceanic and Atmospheric Administration (NOAA) snow cover maps but performed poorly in parts of the boreal forest and in high-latitude tundra regions. The errors in the estimated SWE are mainly due to the effects of the forest and to snow grain size distribution. Canadian research has focused on producing regional SWE products, notably for the Canadian prairies and southern boreal regions of western Canada for real-time hydrological use and climatological studies [Goodison *et al.*, 1986, 1990; Goodison, 1989; Thirkettle *et al.*, 1991; Goodison and Walker, 1994]. SWE maps of the Canadian prairies have been produced weekly since 1988 for evaluation and use by operational water resource and agricultural agencies in western Canada. This SWE algorithm was developed for the open prairie region and enhanced to detect wet snow in these areas [Walker and Goodison, 1993; Goodison and Walker, 1994]. However, the algorithm consistently underestimates SWE in the boreal regions [Goodison *et al.*, 1990; Walker and Goodison, 1991, 1992; Goodison and Walker, 1994]. Hence the Boreal-Ecosystem Atmosphere Study (BOREAS) experiment,



tively. The closest overpass time in this case is about 3 hours after the Twin Otter takeoff (1500 LST), at which time the air temperature of 1.6°C was reported. Some melting at the surface of the snowpack during the aircraft overflight could have occurred; even a small amount of meltwater on the snowpack surface will generate the observed high brightness temperatures. It is a well-known fact that melting snow gives high microwave brightness temperatures at both 18 and 37 GHz [Chang and Gloersen, 1975; Stiles and Ulaby, 1980; Walker and Goodison, 1993].

For the forested grid, only the airborne sensors observed brightness temperature increases. Differences in the observation time may have contributed to the differences in observed brightness temperatures. Although the SSM/I grid may cover a larger area than the aircraft grid, melting could have spread to the grid and caused higher brightness temperatures. Another possibility is that the microwave emissivity of trees is greater than the value of 0.9 that we assumed, and the forested grid could have a temperature higher than 250 K without melting. Three hours later, SSM/I forest readings are similar to those of the agricultural and mixed grids. This could be due to the rapid decrease of the physical temperature of the trees. At this time, we do not fully understand the scaling effect on the measured brightness temperatures. This phenomenon will be addressed in a future paper.

#### 4.3. Lake Ice

There is a large difference between the microwave emissivity of lake ice and fresh water. The presence of layers of ice and snow on a water surface will modify the resultant reflection coefficient of the surface as a consequence of multiple reflections within the layers. Reflection coefficients of snow and ice at VHF (30–300 MHz) wavelengths was reviewed by Saxton [1950]. Depending on the depth of penetration into the ice, the observed brightness temperature at different wavelengths can provide information of the ice depth. Schmugge *et al.* [1974] reported on multichannel microwave observations over Bear Lake, Utah. Hall *et al.* [1981] reported that 5 GHz radiometer measurements were responsive to ice thickness, which ranged from 25.4 to 67.3 cm, observed on Walden Reservoir in Colorado on different days. The 18 and 37 GHz radiometers were found to be less responsive to ice thickness as compared with the lower frequency. Overlying snow cover had a greater effect on 37 GHz than on 18 GHz. Model calculations have been made with some success to simulate the observations [Schmugge *et al.*, 1974]. These calculated brightness temperatures are a strong oscillatory function of the ice thickness with a weaker snow thickness dependence.

We applied the layer radiative transfer model to calculate the brightness temperature of lake ice with snow on top and water at the bottom. Index of refraction values used are tabulated in Table 4. In this study, values of the index of ice and water are those reported by Ray [1972]. To simplify the computation, a constant thickness of snow (20 cm) is assumed.

**Table 4.** Index of Refraction for Lake Ice Calculations

	18 GHz	37 GHz
Air	$1.0 + i0.0$	$1.0 + i0.0$
Snow (density 0.2)	$1.2 + i0.0001$	$1.2 + i0.0002$
Ice (−20°C)	$1.78 + i0.0003$	$1.78 + i0.0008$
Water (0°C)	$5.40 + i2.98$	$3.84 + i2.37$

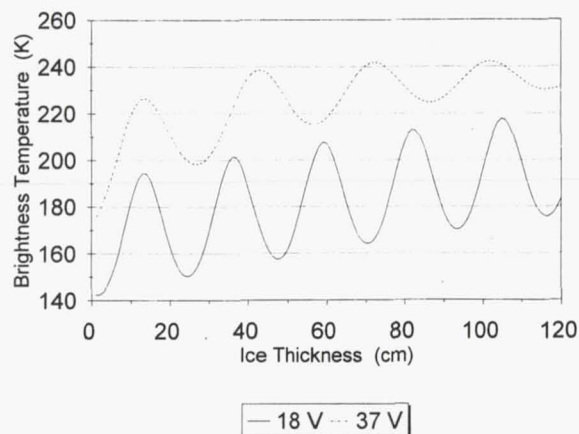


**Figure 2.** Calculated 18 and 37 GHz brightness temperatures versus ice thickness with a 20 cm snow on top of ice.

Figure 2 plots the calculated brightness temperatures of 18 and 37 GHz vertical polarization for varying ice thickness. The oscillating characteristics of brightness depend greatly on the imaginary part of the index of refraction of ice. Due to the large difference of emissivity between ice and water, the polarization factor (ratio of brightness difference and sum of the vertical and horizontal polarization) is generally less than 0.1 for ice and greater than 0.15 for water. This factor could be used as an indicator of whether the microwave radiation penetrates through the ice layer. Based on the index of refraction used in this paper, the penetration depths [Ulaby *et al.*, 1982] are approximately 10 and 1 m for 18 and 37 GHz, respectively.

Flight lines were flown over Candle and Waskesiu Lakes. The averaged brightness temperatures are given in Table 5. The average brightness temperatures are 217.5 and 196.3 K for 18 GHz and 243.4 and 216.8 K for 37 GHz vertical and horizontal polarization, respectively. The standard deviations of the observed brightness temperatures are about 2 K for 18 GHz and 4 K for 37 GHz over the entire Candle Lake line. This suggests that the ice thickness is relatively constant for the entire lake. The observed 18 and 37 GHz vertically polarized brightness temperatures match the calculated values of an ice thickness of 102 and 20 cm of snow. This is in very good agreement with the measured snow depth of 20 cm and ice thickness of 97 cm in the middle of the lake.

As indicated in Figure 2, ice thickness modulates the amplitude of the oscillation. This is to be expected on the basis of interference of the reflected components from various surfaces. The separation between adjacent brightness temperature maxima is about 20 and 30 cm for these two frequencies. Thus there may be a brightness temperature gradient of about

**Table 5.** Averaged Brightness Temperature and Polarization Factor for Lake Ice

	18 GHz			37 GHz		
	V	H	P	V	H	P
Waskesiu Lake	224.1	206.0	0.04	239.5	215.7	0.05
Candle Lake I	217.7	196.3	0.05	242.8	215.6	0.06
Candle Lake II	214.1	191.6	0.06	245.5	218.2	0.06
Candle Lake III	214.1	191.3	0.06	245.6	217.7	0.06

V, vertical polarization; H, horizontal polarization; P, polarization.



## Airborne microwave radiometry on a semi-arid area during HAPEX-Sahel

A. Chanzy<sup>a</sup>, T.J. Schmugge<sup>b,\*</sup>, J.-C. Calvet<sup>c</sup>, Y. Kerr<sup>d</sup>, P. van Oevelen<sup>e</sup>,  
O. Grosjean<sup>f</sup>, J.R. Wang<sup>g</sup>

<sup>a</sup>INRA, Unité de Science du Sol, 84914 Avignon Cédex 9, France

<sup>b</sup>USDA, Hydrology Laboratory, Beltsville, MD 20740 USA

<sup>c</sup>Météo-France–CNRM, 42 Av. G. Coriolis, 31057 Toulouse Cédex, France

<sup>d</sup>LERTS–CESBIO, 18 Av. E. Belin, 31055 Toulouse Cédex, France

<sup>e</sup>Department of Water Resources, Wageningen Agricultural University, Nieuwe Kanaal 11,  
6709 PA Wageningen, Netherlands

<sup>f</sup>CNES, 18 Av. E. Belin, 31055 Toulouse Cédex, France

<sup>g</sup>NASA Goddard Space Flight Center, Greenbelt, MD 20771, USA

---

### Abstract

Airborne microwave radiometric measurements in the framework of the HAPEX-Sahel Experiment were performed by the Push Broom Microwave Radiometer (PBMR) and the PORTOS radiometer. The flights of both radiometers produced an original set of data covering the 1.4–90 GHz range of frequency. The East and West Central Super Sites were the areas most intensively observed by the microwave radiometers. Over those sites, several brightness temperature ( $T_B$ ) maps are available at seven dates distributed over a 1 month period in the middle of the rainy season. A comparison of the two radiometers demonstrates their radiometric quality and the precision of the localization of the microwave observations. At 1.4 GHz, the vegetation had very little effect on the soil microwave emission. Maps of soil moisture were developed using a single linear relationship between  $T_B$  and the surface soil moisture. There is an important spatial heterogeneity in the soil moisture distribution, which is explained by both the soil moisture hydrodynamic properties and the localization of the precipitation fields. At 5.05 GHz, the vegetation must be accounted for to infer soil moisture from the microwave observations. A method based on a simple radiative transfer model and on microwave data has shown encouraging results. © 1997 Elsevier Science B.V. All rights reserved.

---

\* Corresponding author.



## 5. Conclusion

In the HAPEX-Sahel experiment, most of the initial goals planned for the microwave radiometric measurement campaigns were attained. During a period of 1 month, there were sufficient flights to observe a large range of soil moisture conditions. Over the Central Super Sites, which were the most intensively observed by the microwave sensors, there were seven and five low-altitude flights with PORTOS and the PBMR, respectively. The flight patterns allowed the creation of  $T_B$  maps over a 30 km by 5 km region under different microwave configurations (frequency and polarization). Several joint flights have shown the consistency in the radiometric results from both sensors and the geolocation of their measurements. Further studies involving the two radiometers are therefore possible.

At 1.4 GHz, the soil microwave emission was not significantly affected by the vegetation attenuation. It is shown that soil moisture could be accurately estimated by using a single linear regression, between  $T_B$  and the soil moisture, to cover the entire Central Super Sites. The calculated residual standard deviation in surface soil moisture is less than 2%. Such accuracy is comparable with that obtained with the ground techniques, which are affected by the soil moisture spatial variability. Therefore we have assumed that the surface soil moisture derived from the PBMR measurement are reliable enough to be used as a reference. Such a reference is very useful to analyse the vegetation effect on the microwave emission at the higher frequencies (5 GHz or more). The spatial variability in the soil moisture is significantly affected by both the precipitation heterogeneity and the soil surface hydrodynamic properties. Hence, in the HAPEX-Sahel experimental area, we cannot map the precipitation from surface soil moisture monitoring (or the soil hydrodynamic properties) without accounting for the soil hydrodynamic properties (or the amounts of precipitation).

At 5.05 GHz, the surface soil moisture cannot be inferred from the microwave observations without accounting for the vegetation influence on the microwave radiation. We have tested an approach based only on remotely sensed microwave measurements and a simple radiative transfer model. Results obtained with this approach are significantly better than a linear regression analysis between ground and microwave data. These preliminary results are encouraging, but still require improvements in the vegetation characterization. A better use of the available range of frequencies and of measurements in the optical wavelength region may be useful.

The studied area is basically divided into three major types of surface, i.e. the tiger bush, the fallow lands and the cultivated fields. Attempts to discriminate them by their microwave spectral signatures do not lead to a clear distinction of the surface type. Nevertheless, a classification performed by a principal components analysis based on PORTOS measurements at 5.05, 10.65 and 36.5 GHz and their temporal evolution fits the surface patterns well. This means that information allowing the discrimination of different targets is included in the temporal evolution of the  $T_B$  measured at different frequencies. However, in the future, the target spectral and temporal microwave signatures must be established in an analytical form to generalize the identification of the land surface type from the microwave observation of these surfaces.



# Passive Microwave Algorithms for Sea Ice Concentration: A Comparison of Two Techniques

Josefino C. Comiso,\* Donald J. Cavalieri,\* Claire L. Parkinson,\*  
and Per Gloersen\*

*The most comprehensive large-scale characterization of the global sea ice cover so far has been provided by satellite passive microwave data. Accurate retrieval of ice concentrations from these data is important because of the sensitivity of surface flux (e.g., heat, salt, and water) calculations to small changes in the amount of open water (leads and polynyas) within the polar ice packs. Two algorithms that have been used for deriving ice concentrations from multichannel data are compared. One is the NASA Team algorithm and the other is the Bootstrap algorithm, both of which were developed at NASA's Goddard Space Flight Center. The two algorithms use different channel combinations, reference brightness temperatures, weather filters, and techniques. Analyses are made to evaluate the sensitivity of algorithm results to variations of emissivity and temperature with space and time. To assess the difference in the performance of the two algorithms, analyses were performed with data from both hemispheres and for all seasons. The results show only small differences in the central Arctic in winter but larger disagreements in the seasonal regions and in summer. In some areas in the Antarctic, the Bootstrap technique shows ice concentrations higher than those of the Team algorithm by as much as 25%; whereas, in other areas, it shows ice concentrations lower by as much as 30%. The differences in the results are caused by temperature effects, emissivity effects, and tie point differences. The Team and the Bootstrap results were compared with available Landsat, advanced very high resolution radiom-*

*eter (AVHRR), and synthetic aperture radar (SAR) data. AVHRR, Landsat, and SAR data sets all yield higher concentrations than the passive microwave algorithms. Inconsistencies among results suggest the need for further validation studies. ©Elsevier Science Inc., 1997*

## INTRODUCTION

Passive microwave satellite remote sensing has been the most effective and consistent tool used for characterizing the global sea ice cover (Zwally et al., 1983; Parkinson et al., 1987; Gloersen et al., 1992). Data from passive microwave radiometers have been available since the launch of the Nimbus-5 electrically scanning microwave radiometer (ESMR) in December 1972. The ESMR was a one-channel, horizontally polarized, 19-GHz radiometer that provided good data for most of the period from December 1972 until early 1977. In 1978, the scanning multichannel microwave radiometer (SMMR) was launched onboard the Seasat and Nimbus-7 satellites and provided horizontally (H) and vertically (V) polarized data at 6.6, 10.7, 18, 21, and 37 GHz. The Seasat SMMR functioned for only 3 months, whereas the Nimbus-7 SMMR functioned for almost 9 years. Since 1987, the special sensor microwave imager (SSM/I) has been providing data to continue the historical series. The SSM/I provides dual polarized data at 19, 37, and 85 GHz and vertically polarized data at 22 GHz. The passive microwave data have been mapped into a standard polar stereographic format for convenience in storage and analysis. With more than 20 years of good spatial and temporal coverage, this data set is unique; and, in view of its importance in climate change studies, the conversion of raw data into geophysical products should be done as accurately as possible.

Among the most useful sea ice parameters that can

\*Oceans and Ice Branch, Laboratory for Hydrospheric Processes, NASA/Goddard Space Flight Center, Greenbelt

Address correspondence to Dr. J. Comiso, Laboratory for Hydrospheric Processes, NASA/Goddard Space Flight Center, Oceans and Ice Branch, Code 971, Greenbelt, MD 20771.

Received 31 January 1996; revised 11 October 1996.



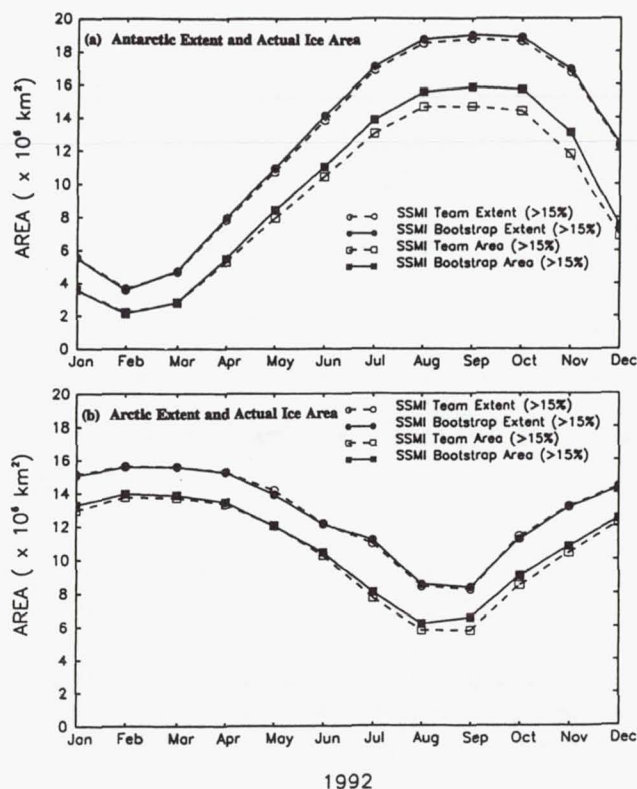


Figure 22. Comparison of monthly extent and actual ice areas derived from ice concentration maps generated by the Team and Bootstrap algorithms for the (a) Antarctic and (b) Arctic regions during 1992.

trations during the summer than those previously generated from the Bootstrap algorithm, are the ones currently in use.

## DISCUSSION AND CONCLUSIONS

In this paper, a comparison of ice concentrations derived from the Team and Bootstrap algorithms has been made. Monthly maps over an annual cycle in 1992 were compared in both the Northern and the Southern Hemispheres. The results indicate some large differences in ice concentrations, in the inner pack, in the coastal regions, and in some marginal ice areas. In some areas of the Antarctic, the Bootstrap algorithm shows 10–35% higher values than does the Team algorithm. In others, the reverse is true, especially in the coastal regions along the continent. Similar but smaller discrepancies are observed in the seasonal sea ice zones of the Arctic. Results from other years also have been examined (e.g., 1988), and the patterns of differences are similar.

Errors associated with each algorithm have been assessed. The sensitivity in the determination of ice concentration resulting from fluctuations in temperature and emissivity has been discussed. The key issue is how well each algorithm handles these fluctuations. Temperature

fluctuations are handled by the Team algorithm better than the Bootstrap algorithm. Interestingly, some of the patterns in the monthly maps of the differences (Fig. 7) are similar to the patterns in the temperature maps in Gloersen et al. (1992). Low snow-ice interface temperatures would cause an underestimate in ice concentration by the Bootstrap algorithm, whereas high ice temperatures would cause an overestimate. However, in areas of the Antarctic where large discrepancies occur between the two algorithms, in situ measurements of snow/ice interface temperatures indicate an average of  $-6^{\circ}\text{C}$  with a standard deviation of only about  $2^{\circ}\text{C}$  (Comiso et al., 1989).

Two case studies presented suggest that temperature is not the only cause of the discrepancies in the results. In these studies, the Bootstrap algorithm results are on average about 10% higher than the Team algorithm results, and analysis of Landsat, AVHRR, SAR, and aircraft photography indicate even higher ice concentrations than the Bootstrap values. If the Landsat and SAR values are correct, possible explanations for the differences are sub-surface effects, such as ice layers in the snow or near the ice surface or the presence of new and young ice types. Each of these effects would affect the horizontally polarized radiances more than the vertically polarized radiances. The problem of new ice has been addressed elsewhere for Arctic seasonal sea ice zones (Cavalieri, 1994; Wensnahan et al., 1993).

For global climate studies, it is important to examine differences in sea ice extents, actual area, and their trends as produced by the two algorithms. Estimates of ice extent from either algorithm can be done with relatively high precision because of the large contrast in emissivity between ice and ocean at 19 or 37 GHz. However, the ice edge is usually the scene of stormy weather conditions, and the locations of the ice edge as inferred from the Team and Bootstrap algorithms are not always consistent, because of different weather filter-ocean masking techniques. The ice extents and ice areas derived from both algorithms in both hemispheres are shown in Figure 22. In the Antarctic, the difference in the 15% ice extent is as large as  $0.2 \times 10^6 \text{ km}^2$  (about 1%), whereas the maximum difference in actual ice area is about  $1.2 \times 10^6 \text{ km}^2$  (about 7.5%). In the Arctic, the corresponding values are  $0.2 \times 10^6$  and  $0.8 \times 10^6 \text{ km}^2$ , respectively. The differences in ice extents may originate in part from the differences in the weather filter-ocean masks. The differences in ice concentration within the pack make a substantial difference in the estimates of ice area. A better understanding of the differences between the two algorithms would eventually lead to more accurate ice concentrations, which would improve estimates of heat, radiation, and salinity fluxes in the polar regions.

We conclude that there is a need for further validation studies, especially in areas where there are large discrepancies in ice concentrations derived from the two algorithms. The focus should be on studying spatial



# Scattering by artificial wind and rain roughened water surfaces at oblique incidences

C. CRAEYE, P. W. SOBIESKI

Université Catholique de Louvain, B-1348 Louvain-la-Neuve, Belgium

L. F. BLIVEN

NASA/GSFC/WFF, Laboratory for Hydrospheric Processes, Wallops Island, VA 23337, U.S.A.

(Received 3 July 1996; in final form 22 November 1996)

**Abstract.** Rain affects wind retrievals from scatterometric measurements of the sea surface. To depict the additional roughness caused by rain on a wind driven surface, we use a ring-wave spectral model. This enables us to analyse the rain effect on  $K_u$  band scatterometric observations from two laboratory experiments. Calculations based on the small perturbation method provide good simulation of scattering measurements for the rain-only case, whereas for combined wind and rain cases, the boundary perturbation method is appropriate.

## 1. Introduction

Rain affects wind retrieval from scatterometric measurements, through the additional roughness it causes on the surface. Wind maps from satellite radar measurements over the oceans present gaps where it rains. This highlights the importance of evaluating the surface roughness introduced by rain, and the corresponding radar return, as globally about 5 per cent of the Earth's surface is covered by rain. Locally, rain can cause ambiguities in the interpretation of weather fronts and convective storms observed from space.

Stalks and ring-waves, two splash products, have been identified as the dominant features for backscattered microwave power at grazing and scatterometric incidence angles respectively. Hansen (1986) and Rein (1993) present high speed photographs of these features. The former combined such observations with high resolution laboratory radar measurements at 9 GHz and found that stalks are the dominant feature contributing to the backscattered power at grazing incidence. Conversely from 13.5 and 36 GHz measurements performed at scatterometric incidence ( $30^\circ$  off-nadir and  $VV$  polarization) Bliven *et al.* (1993) and Sobieski and Bliven (1995) experimentally observed that the ring-waves are the major contributors to the backscattered power.

In the following, we first show that ring-wave and scatterometer data (Bliven *et al.* 1997) are consistent with results that we obtained from a small perturbation scattering model. Then to simulate the scattering measurements for wind and rain conditions that were reported by Moore *et al.* (1979), we used the ring-wave model in a boundary perturbation approach which is valid for a broader range of surface conditions.



slope (SS). The wind and rain spectral contributions are shown in figure 2 for different wind speeds and rain rates.

Experiments used here for comparison were reported by Moore *et al.* (1979); they correspond to radar responses collected in a wavetank at 14 GHz and 40° from nadir versus wind speed (defined at 19.5 m height), combined with different rain rates produced by drops of 1.5 to 2 mm diameter, falling from a 3 m height. Unfortunately, the results from Moore *et al.* were presented only in a graphical form, so it is unclear how many data points were measured for the various conditions. Those are replotted in figure 3(a). The polarization was not specified in the article, but from simulations in the wind-only case, we inferred that the polarization was VV.

Applying the combined spectrum, we calculated the radar response using the BPM. The parameters of the wind spectrum were adapted to wavetank conditions i.e.,  $K_p = 0.04 \text{ cm}^{-1}$  and  $SS = 1.5$  per cent. For the considered configuration, the relative scattering coefficients present a very weak dependence on  $K_p$  (for  $K_p = 0.08$  instead of  $0.04 \text{ cm}^{-1}$ , the maximum change is of 0.2 dB).  $SS$  has been set to a low value for wavetank conditions because (i) there was no mechanical wave generation, and hence no large surface slopes, (ii) for  $SS > 2$  per cent, the dependence of  $\sigma^0$  on wind speed in the non-rain case becomes significantly lower than in Moore's experiments. Moreover, the influence of the significant slope near 1.5 per cent is low (the maximum change for  $SS$  going from 1.5 to 1 per cent is 0.5 dB). The result of the simulation is presented in figure 3(b).

## 5. Discussion

The rain-roughened water surface spectra derived from elevation data collected in a wavetank allowed us to calculate the radar backscattering at oblique incidences. In the rain only case, calculations based upon the small perturbation method give results in good accordance with data at 13.5 GHz and 30° incidence.

In the combined wind and rain case, the boundary perturbation method was used. The results calculated for 14 GHz and 40° incidence present the same trend as the experimental data presented by Moore *et al.* (1979), with a slightly different increase of the response with the rain rate. However, note that in Moore *et al.* experiments, drops were smaller and fell from 3 m only, hence reaching the surface at a speed between 85 and 90 per cent of the terminal velocity, which has a mean value of  $6 \text{ m s}^{-1}$  for drops between 1.5 and 2 mm (instead of  $7.8 \text{ m s}^{-1}$  for drops of 2.8 mm). No scaling calculations were performed here, because the dependence of the ring-waves amplitude on drop speed and size has yet to be investigated. Further measurements should indicate, for instance, how capillarity, underwater turbulence and splash products influence the energy transfer between the falling drops and the ring-waves.

In addition, it should be stressed that the effect of rain on the measured backscattered power at high wind speeds seems to be lower than the calculated one. Recall that the calculation is based on the assumption that the wind and rain spectra simply add. Further surface experiments are needed to assess the validity range of this assumption; in particular, non-linear effects between wind and rain waves have still to be analysed. Note also that, in wavetank experiments, high winds may cause some of the rain drops to drift downstream of the measurement area, reducing their effect on the backscattered power from the surface.

The results presented here are restricted to a laboratory environment, where it was possible to control most parameters. They validate the methodology followed. This is encouraging and underlines the need of measurements in open field conditions.



## A unified directional spectrum for long and short wind-driven waves

T. Elfouhaily, B. Chapron, and K. Katsaros

Institut Français de Recherche pour l'Exploitation de la Mer, Plouzané, France

D. Vandemark

NASA Goddard Space Flight Center, Laboratory for Hydrospheric Processes, Wallops Island, Virginia

**Abstract.** Review of several recent ocean surface wave models finds that while comprehensive in many regards, these spectral models do not satisfy certain additional, but fundamental, criteria. We propose that these criteria include the ability to properly describe diverse fetch conditions and to provide agreement with in situ observations of *Cox and Munk* [1954] and *Jähne and Riemer* [1990] and *Hara et al.* [1994] data in the high-wavenumber regime. Moreover, we find numerous analytically undesirable aspects such as discontinuities across wavenumber limits, nonphysical tuning or adjustment parameters, and noncentrosymmetric directional spreading functions. This paper describes a two-dimensional wavenumber spectrum valid over all wavenumbers and analytically amenable to usage in electromagnetic models. The two regime model is formulated based on the Joint North Sea Wave Project (JONSWAP) in the long-wave regime and on the work of *Phillips* [1985] and *Kitaigorodskii* [1973] at the high wavenumbers. The omnidirectional and wind-dependent spectrum is constructed to agree with past and recent observations including the criteria mentioned above. The key feature of this model is the similarity of description for the high- and low-wavenumber regimes; both forms are posed to stress that the air-sea interaction process of friction between wind and waves (i.e., generalized wave age,  $u/c$ ) is occurring at all wavelengths simultaneously. This wave age parameterization is the unifying feature of the spectrum. The spectrum's directional spreading function is symmetric about the wind direction and has both wavenumber and wind speed dependence. A ratio method is described that enables comparison of this spreading function with previous noncentrosymmetric forms. Radar data are purposefully excluded from this spectral development. Finally, a test of the spectrum is made by deriving roughness length using the boundary layer model of *Kitaigorodskii*. Our inference of drag coefficient versus wind speed and wave age shows encouraging agreement with Humidity Exchange Over the Sea (HEXOS) campaign results.

### 1. Introduction

A reliable statistical description of wind-generated surface waves is of crucial importance for improving understanding of continuous motions and exchanges across the air-sea interface. Satellite remote sensing, engineering design of marine vessels, wave forecasting, and atmosphere-ocean interaction research are all fields where knowledge of the directional wind wave field is needed.

Among statistical descriptions of waves, spectral formulation is generally privileged stemming from the early work of *Phillips* [1958]. There is a wealth of theoretical and empirical studies detailing candidate equilibrium wind wave spectra in the literature [e.g., *Toba*, 1973; *Hasselmann et al.*, 1973; *Mitsuyasu and Honda*, 1974; *Kitaigorodskii et al.*, 1975; *Kahma*, 1981; *Donelan et al.*, 1985; *Phillips*, 1985]. Presently, it is well-accepted that the long-wave spectrum resulting from the Joint North Sea Wave Project (JONSWAP [*Hasselmann et al.*, 1973]) reasonably represents fetch-limited wind wave development. In the high-frequency regime, present models are tenuous in both theory

and observation. Extensive attention has been given to both aspects [e.g., *Kitaigorodskii et al.*, 1975; *Phillips*, 1985]. *Banner* [1990] observed that for the full range of wavenumbers, theory and observation remain unreconciled.

It is recognized that for remote sensing studies, precise knowledge of the short-scale wave roughness is the prime requirement. As a first-order approximation, studies often present a spectrum for only high wavenumbers. However, it is now accepted that short waves are intimately coupled with intermediate- and long-scale waves necessitating the need for full wavenumber models such as those developed by *Donelan and Pierson* [1987], *Bjerkaas and Riedel* [1979], and *Apel* [1994]. These models are widely used in microwave radar scattering studies because of their attention to high-frequency spectral definition.

It is our contention that regardless of the means of construction (theoretical or empirical), a wave spectrum should be capable of reproducing certain observations. In the high-frequency regime, integration of the slope spectrum should provide wind-dependent mean square slope results of *Cox and Munk* [1954]. It should also well-represent the dynamics of gravity-capillary wave curvature as seen in laboratory measurements by *Jähne and Riemer* [1990] and by *Hara et al.* [1994]. For long waves, wave age and extended fetch are needed. In addi-



exponential term in (63), only short-gravity and gravity-capillary waves support the total integral term. *Geernaert* [1990] came to the same conclusion when reviewing relevant roughness models. *Makin et al.* [1995] by developing a wave boundary model based on *Miles*' [1957, 1959] and *Janssen's* [1989] theories, concluded that short-gravity waves are responsible for almost all the downward momentum flux.

*Maat et al.* [1991] and *Smith et al.* [1992] proposed a relationship between the roughness parameter  $z_0$  and the related wave age parameter ( $u^*/c_p$ ). Their HEXOS results can be summarized (including rms uncertainty of the fit to data) as

$$\frac{gz_0}{u^{*2}} = (0.45 \pm 0.05) \frac{u^*}{c_p} \quad (65)$$

This formulation indicates that young seas (low  $c_p$ ) are rougher than mature ones (high  $c_p$ ). Similar results were obtained recently by *Donelan et al.* [1993]. Based on in situ measurements, *Donelan et al.* [1993] proposed however a slightly different model for  $z_0$ ,

$$z_0 = 3.7 \times 10^{-5} \frac{U_{10}^2}{g} \left( \frac{U_{10}}{c_p} \right)^{0.9} \quad (66)$$

Figure 11a shows friction velocity function of wind speed and wave age as inferred from our unified spectrum by utilizing iterative scheme based on *Kitaigorodskii's* [1973] model (64) and a  $u^*-U_{10}$  relationship (61) along with in situ results. Overall agreement can easily be seen with both in situ models and *Garratt's* [1977] model for mature seas. These results strengthen the idea that our unified spectrum is consistent with wind stress measurements.

## 8. Conclusion

In this paper we have attempted to derive from several recent experimental results a relatively simple closed-form model for the surface wave directional spectrum. The latter has been developed solely from in situ or tank measurements. Thus no radar data have been included in elaborating this model.

Our directional wave spectrum satisfactorily models surface waves from near the main spectral peak up to the gravity-capillary peak. Nondeveloped seas were also modeled by using the modified JONSWAP formulation for long waves together with a new fetch versus wave age relationship that extends its validity to large fetch values in open ocean. The secondary gravity-capillary peak increases with the wind friction velocity as a two-regime logarithmic function as derived from *Jähne and Riemer* [1990] and *Hara et al.* [1994] tank data. The omnidirectional spectral model reproduces significant wave height for developing seas and measured mean square slopes (mss) for both clean and oil-slick covered water surfaces (Figure 7b). Moreover, when combined with our simple spreading function, upwind-crosswind asymmetry also verifies for both clean and slick mss to within experimental errors. By combining all former equations, our improved unified directional spectrum can then be written as

$$\Psi(k, \varphi) = \frac{1}{2\pi} k^{-4} [B_l + B_h] [1 + \Delta(k) \cos(2\varphi)] \quad (67)$$

Where  $B_l$ ,  $B_h$ , and  $\Delta$  are from (31), (40), and (57) and their subsequent formulas. If we use (17) instead of (40) for the omnidirectional curvature spectrum of short waves, one obtains a modified *Donelan and Pierson* [1987] spectrum that

improves mss predictions as reported in Figure 7a (dashed curve). With this modification, the curvature secondary peak moves over to 1.7 cm wavelength (Figure 7b). New parameters that improve on the *Donelan and Pierson* spectrum are suggested here to be,  $n + 1 = 3$  from *Phillips* [1985] and  $\ln \alpha = n \{ (k/k_m - 1)^2 + 4.4 \}$  from the current development.

The main feature of our spectrum is the equilibrium range dependence on the generalized wave age ( $u/c$ ) for which  $u$  is the wind speed at a height of 10 m from the water surface ( $U_{10}$ ) for the long-wave spectral domain [*Kahma*, 1981; *Donelan et al.*, 1985; *Dobson et al.*, 1989] and the friction velocity ( $u^*$ ) for the short-gravity and gravity-capillary wave spectral domain [*Toba*, 1973; *Kitaigorodskii*, 1983; *Phillips*, 1985]. Short-gravity and gravity-capillary waves are responsible for most of the wave-induced stress. When using our unified spectrum in the boundary layer model proposed by *Kitaigorodskii* [1973], the inferred form drag agrees with HEXOS campaign measurements [*Smith et al.*, 1992]. Therefore our unified spectrum is consistent with wind stress measurements.

The only remote-sensing data used in our development are optical data. Our approach is very flexible and can be used in conjunction with future in situ data to refine these initial findings.

## Appendix: Spectral Definitions

By definition, the elevation spectrum is the Fourier transform of the autocovariance function of the surface displacements.

$$\Psi(\mathbf{k}) = \text{FT} \{ \langle \eta(\mathbf{r}_0) \eta(\mathbf{r}_0 + \mathbf{r}) \rangle \} \quad (\text{A1})$$

FT being the Fourier transform operator, angle bracket are the ensemble average operator,  $\eta$  is the surface elevation with zero mean, and  $\mathbf{r}$  is horizontal lag over the surface.

In our analysis, only spatial variability is considered. Temporal or frequency dependence of wave spectra is outside the scope of this study. The directional spectrum is normalized as

$$\begin{aligned} \sigma_\eta^2 &= \langle \eta^2 \rangle = \int_{-\infty}^{\infty} \int_{-\infty}^{\infty} \Psi(k_x, k_y) dk_x dk_y \\ &= \int_0^{\infty} \int_{-\pi}^{\pi} \Psi(k, \varphi) k dk d\varphi = \int_0^{\infty} S(k) dk \end{aligned} \quad (\text{A2})$$

where  $\sigma_\eta$  is the standard deviation of surface elevations and  $\Psi(k_x, k_y)$  and  $\Psi(k, \varphi)$  are directional spectrum in Cartesian and polar coordinates, respectively. The wind is assumed to be blowing in the positive  $x$  axis. The omnidirectional spectrum  $S(k)$  is

$$S(k) = \int_{-\pi}^{\pi} \Psi(k, \varphi) k d\varphi \quad (\text{A3})$$

The mean square slope in the upwind direction is

$$\begin{aligned} \text{mss}_x &= \int_{-\infty}^{\infty} \int_{-\infty}^{\infty} k_x^2 \Psi(k_x, k_y) dk_x dk_y \\ &= \int_0^{\infty} \int_{-\pi}^{\pi} k^2 \cos^2 \varphi \Psi(k, \varphi) k dk d\varphi \end{aligned} \quad (\text{A4})$$



# Comparison of Snow Mass Estimates from a Prototype Passive Microwave Snow Algorithm, a Revised Algorithm and a Snow Depth Climatology

J. L. Foster,\* A. T. C. Chang,\* and D. K. Hall\*

While it is recognized that no single snow algorithm is capable of producing accurate global estimates of snow depth, for research purposes it is useful to test an algorithm's performance in different climatic areas in order to see how it responds to a variety of snow conditions. This study is one of the first to develop separate passive microwave snow algorithms for North America and Eurasia by including parameters that consider the effects of variations in forest cover and crystal size on microwave brightness temperature. A new algorithm (GSFC 1996) is compared to a prototype algorithm (Chang et al., 1987) and to a snow depth climatology (SDC), which for this study is considered to be a standard reference or baseline. It is shown that the GSFC 1996 algorithm compares much more favorably to the SDC than does the Chang et al. (1987) algorithm. For example, in North America in February there is a 15% difference between the GSFC 1996 algorithm and the SDC, but with the Chang et al. (1987) algorithm the difference is greater than 50%. In Eurasia, also in February, there is only a 1.3% difference between the GSFC 1996 algorithm and the SDC, whereas with the Chang et al. (1987) algorithm the difference is about 20%. As expected, differences tend to be less when the snow cover extent is greater, particularly for Eurasia. The GSFC 1996 algorithm performs better in North America in each month than does the Chang et al. (1987) algorithm. This is also the case in Eurasia, except in April and May when the Chang et al.

(1987) algorithm is in closer accord to the SDC than is the GSFC 1996 algorithm. Published by Elsevier Science Inc.

## INTRODUCTION

Snow cover and snow depth data sets may be useful indicators of regional or global climate change and basin-scale water storage in mountainous areas. Thus, it is important to ensure that they are accurate and as free as possible of any known biases. Visible satellite data have been utilized to map the extent of snow cover for about 30 years. Microwave satellite data have been used to map snow extent and snow depth for over 20 years.

National Oceanic and Atmospheric Administration (NOAA) visible satellite data of snow permit direct observation of snow extent and afford direct comparisons with climatological data. However, because passive microwave satellite data require algorithms to derive snow extent and thickness, the estimates are not as direct as those from the visible data. Consequently, the ability of the passive microwave data to provide reliable snow depth, snow water equivalent (SWE), and snow extent information need to be evaluated. Only when there is a high degree of confidence that the snow extent and snow depth data sets are reliable can they be used for predicting snow water yield, analyzing climate trends or validating the performance of general circulation models (GCMs). Bromwich et al. (1994) and Foster et al. (1996) among others have shown that GCMs do not simulate the present arctic climate very well. Development of passive microwave algorithms to derive snow extent and depth is an evolutionary process. Algorithms will become more precise as input ancillary data and our understand-

\* NASA Goddard Space Flight Center, Hydrological Sciences Branch, Laboratory for Hydrospheric Processes, Greenbelt

Address correspondence to J. L. Foster, NASA/GSFC, Hydrological Sciences Br., Lab. for Hydrospheric Processes, Code 974, Greenbelt, MD 20771.

Received 17 January 1997; revised 2 May 1997.



ness; however, there are very few places with mean areal depths of 125 cm at the microwave pixel scale ( $1/2^\circ$  latitude  $\times$   $1/2^\circ$  longitude).

The above-discussed error sources depend on how microwave energy interacts with snow. Another source of error that should not be overlooked results from constraints imposed upon the algorithm. The density of the snow is assumed to be  $300 \text{ kg m}^{-3}$ . Newly fallen snow may have a density that is closer to  $100 \text{ kg m}^{-3}$ , whereas aging snow in a ripe snowpack may have a density of  $500 \text{ kg m}^{-3}$ . Firm or snow that does not melt from one year to the next has a density between about  $400 \text{ kg m}^{-3}$  to about  $800 \text{ kg m}^{-3}$ . The  $300 \text{ kg m}^{-3}$  value used for the Chang et al. (1987) algorithm is what might be measured in snowpacks during the months of January, February, and March in much of the Northern Hemisphere. Higher densities would typically occur in April and May while lower densities would be the rule during the autumn season.

Finally, the argument that the snowpack in interior areas of Eurasia consists of crystals or grains having a slightly larger size than exists for North America is crucial to the validity of the GSFC 1996 algorithm. Using the larger grain size brings the new algorithm into better accord with the SDC data. Of course, this does not necessarily mean that the snow grains are in fact larger, and if they are larger, their size difference may be greater or smaller than that specified in the GSFC 1996 algorithm. This can only be confirmed by large-scale spatial sampling for different months and for enough years to ensure the sampling results are meaningful.

## CONCLUSIONS

Although passive microwave satellite data have been used to generate snow depth products globally and for different regions, the main advantage of using this data set is that it is only snow depth data set that varies from year to year. However, derived algorithms applicable for use over the entire globe which use only a single set of coefficients and the differences between two microwave channels have been shown to be neither very accurate nor very reliable. This study is one of the first to develop separate algorithms for North America and Eurasia by incorporating parameters that take into account the effects of forest cover and differences in crystal size on the microwave response. Other problems remain, though, which to some degree influence snow cover and snow-depth derivations. These include the existence of wet snow (liquid water in the snowpack), signal saturation (very deep snow), mixed pixels (microwave contributions from varying sources), effects of snow metamorphism (melt and refreeze), and the effects of crystal shape (Goodison et al., 1993).

Nevertheless, it is believed that the derived passive-microwave snow-cover and snow-depth information is

now of sufficient quality that climate models can use it to confirm their simulations and improve their predictions. The performance of GCMs in predicting snow fields needs to be tested to quantitatively study the effects of snow on climate. Simulations of atmospheric flow using GCMs have achieved a high level of quality; however, evaluation of model parameters such as snow has thus far been hindered by the lack of quality large-scale data for snow thickness (Arpe et al., 1993). Regardless of the level of sophistication of the GCMs, realistic results cannot be assured unless reliable input data sets are utilized (Foster et al., 1996).

In terms of future directions, measurements and modeling are still needed and are fundamental to learning more about the remote sensing of snowpack properties. Ground-based and airborne microwave radiometric efforts need to be continued to understand better how microwaves interact with and respond to varying snow conditions.

The next generation of passive-microwave sensors, including the Advanced Microwave Sounding Radiometer (AMSR), is tentatively scheduled for a 1998 launch. This instrument will sense from 89 GHz to 6.8 GHz with a spatial resolution of from  $5 \text{ km}^2$  to  $20 \text{ km}^2$  and an incidence angle of  $55^\circ$ . By the time this instrument is operational, working snow algorithms need to be in place (Goodison et al., 1993). The algorithms which have been developed in this article can perhaps be a starting point for future algorithm development.



# Algorithm for atmospheric and glint corrections of satellite measurements of ocean pigment

Robert S. Fraser,<sup>1</sup> Shana Mattoo,<sup>2</sup> Eueng-Nan Yeh,<sup>3</sup> and C. R. McClain<sup>1</sup>

**Abstract.** An algorithm is developed to correct satellite measurements of ocean color for atmospheric and surface reflection effects. The algorithm depends on taking the difference between measured and tabulated radiances for deriving water-leaving radiances. The tabulated radiances are related to the measured radiance where the water-leaving radiance is negligible (670 nm). The tabulated radiances are calculated for rough surface reflection, polarization of the scattered light, and multiple scattering. The accuracy of the tables is discussed. The method is validated by simulating the effect of different wind speeds than that for which the lookup table is calculated, and aerosol models different from the maritime model for which the table is computed. The derived water-leaving radiances are accurate enough to compute the pigment concentration with an error of less than  $\pm 15\%$  for wind speeds of 6 and 10 m/s and an urban atmosphere with aerosol optical thickness of 0.20 at 443 nm and decreasing to 0.10 at 670 nm. The pigment accuracy is less for wind speeds less than 6 m/s and is about 30% for a model with aeolian dust. On the other hand, in a preliminary comparison with coastal zone color scanner (CZCS) measurements this algorithm and the CZCS operational algorithm produced values of pigment concentration in one image that agreed closely.

## 1. Introduction

The current Nimbus 7 coastal zone color scanner (CZCS) algorithm for making atmospheric corrections [Gordon *et al.*, 1988] is not generally applied when the aerosol optical thicknesses exceed 0.2, or when pixels are in the fringe of the sea glint. The aerosol optical thickness frequently exceeds 0.2 off the east coasts of Asia and the United States due to urban pollution, during outflows of dust from Asia and Africa, and in smoke from biomass burning. Evans and Gordon [1994] eliminate regions of surface glint for estimates of pigment concentration where  $L_g/F_0 > 0.005$  ( $L_g$  is the radiance of the surface glint at a sea surface and  $F_0$  is the solar spectral irradiance above the Earth's atmosphere). As an example, if the surface wind speed were 10 m/s when the Sun is at the zenith, a region within  $40^\circ$  of the nadir would be excluded. An algorithm to overcome the glint and large aerosol optical thickness conditions is developed.

A method had been developed previously for making atmospheric corrections over land utilizing lookup tables [Fraser *et al.*, 1992]. Also, a radiative transfer code already exists for ocean-atmosphere models that account for rough surface reflection, an arbitrary atmosphere, degree of polarization of the light, and multiple scattering [Ahmad and Fraser, 1982]. In this report we describe the theory, the ocean-atmosphere model, the lookup tables (LUT), and use of them. Simulations are made to derive the water-leaving radiance in the glint region, and when dust or urban aerosols are present. Finally, a comparison is made of one image of water-leaving radiances and pigment concentrations derived with the LUT and the CZCS algorithm.

## 2. Radiative Transfer

The radiance of the ocean-atmosphere system measured at a satellite ( $L_t$ ) can be expressed as

$$L_t = L_0(\lambda; \theta, \phi; \theta_0, \phi_0; \tau_a) + L_{\text{sfc}}(\lambda; \theta, \phi; \theta_0, \phi_0; W; \tau_a) t(\lambda; \theta; \tau_a) + L_w(\lambda; \theta, \phi; \theta_0, \phi_0; W; \tau_a; C) t'(\lambda; \theta; \tau_a), \quad (1)$$

where  $L_0$  is the radiance of the atmosphere, if the radiance just above the sea surface were zero;  $L_{\text{sfc}}$  is the radiance of the light reflected from the surface; and  $L_w$  is the water-leaving radiance of light scattered from beneath the surface and penetrating it. All four radiances are vectors representing the four Stokes parameters, in order to account for the polarization properties of the scattered light.  $L_w$  contains the information about the sea particles and absorbers;  $t$  and  $t'$  are the transmissions through the atmosphere of  $L_{\text{sfc}}$  and  $L_w$ , respectively. The independent parameters in (1) are defined as follows:

- $\lambda$  wavelength;
- $\theta, \phi$  polar and azimuth angles of the line of sight at a spacecraft;
- $\theta_0, \phi_0$  polar and azimuth angles of the direct sunlight;
- $W$  surface wind speed;
- $\tau_a$  aerosol optical thickness;
- $C$  pigment concentration.

The surface reflection accounts for both a rough sea and a foam:

$$L_{\text{sfc}} = (1 - f) L_g + A_f f F_d / \pi, \quad (2)$$

where  $f$  is the fraction of the surface covered by foam,  $(1 - f) L_g$  is the radiance of light reflected from a rough surface but minus coverage by foam,  $A_f$  is the foam reflectance,  $F_d$  is the total downward flux (equation (13)). Light reflected by the foam is assumed to be unpolarized. The water-leaving

<sup>1</sup>NASA Goddard Space Flight Center, Greenbelt, Maryland.

<sup>2</sup>Applied Research Corporation, Landover, Maryland.

<sup>3</sup>General Sciences Corporation, Laurel, Maryland.



values derived with the CZCS algorithm. The CZCS radiances were measured over the Gulf of Mexico in December 1979; the solar zenith angle was  $48^\circ$ – $49^\circ$ ; and the scattering angle between the direct sunlight and the line of sight ranged between  $121^\circ$  and  $131^\circ$ .

The relative contribution of the radiance of light reflected from rough surface reflection to the total radiance at the top of a Rayleigh atmosphere is given in Figure 9. As the CZCS channel 1 (443 nm) scans from nadir to the Earth's limb, surface reflection would decrease from 9% to 5% of the total radiance. This contribution to the total radiance is about the same as either the water-leaving or the aerosol radiance.

The lookup water-leaving radiances are generally a few counts higher than those of the CZCS algorithm (Figure 10). A generally positive difference of two counts and increasing difference with decreasing wavelength suggests the possibility of calibration bias, because the vicarious calibration is tuned to the CZCS algorithm [Evans and Gordon, 1994]. The goal is to get the water-leaving radiances derived by the two methods to differ by less than one count. Because the differences are well correlated among the three wavelengths, the errors tend to cancel when the pigment concentration is computed with ratio of radiances (equation (24)).

The pigment concentrations for the operational and lookup-table algorithms are strongly correlated (Figure 11); but there is a bias in the regression line determined by 17 points, since the slope is not 1. The LUT estimates higher concentrations for small amounts of pigment; for example, if the operational concentration is  $0.1 \text{ mg/m}^3$ , the LUT value is  $0.13 \text{ mg/m}^3$ .

## 5. Discussion

This preliminary study indicates that we cannot expect to estimate water-leaving radiances with an error less than 10%, because of 1% errors in the radiances tabulated in these lookup tables. The simulations for modest surface reflection and aerosol perturbations resulted in pigment concentration with an error in the range of  $\pm 15\%$  where the simulated

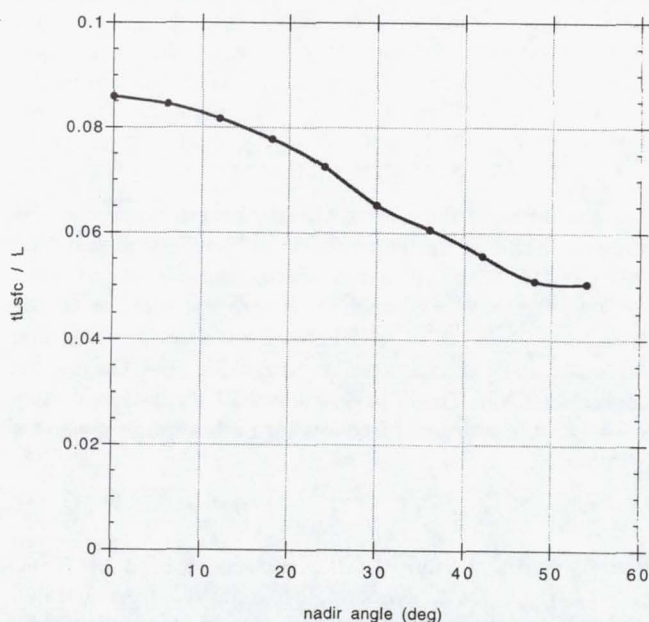


**Figure 9.** Relative contribution of surface reflection to total radiance;  $\tau_a = 0.0$ ,  $\theta_0 = 48^\circ$ ,  $\phi = 88^\circ$ .

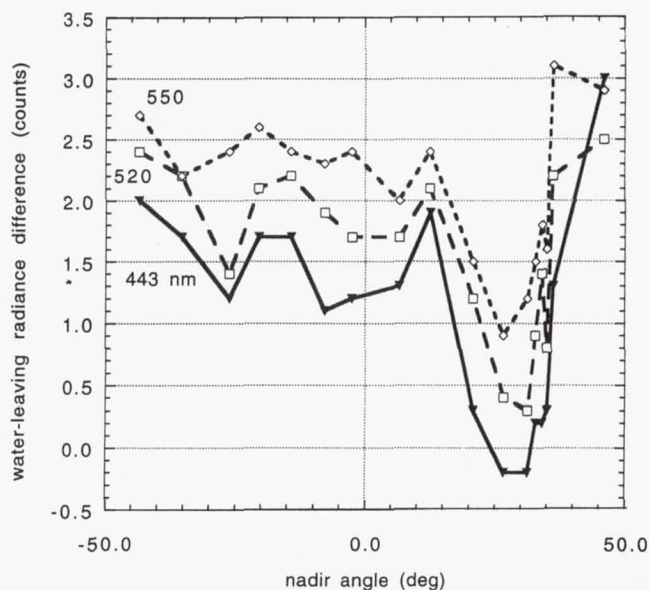


**Figure 10.** Water-leaving difference in counts:  $L_w$  from LUT minus that from the coastal zone color scanner (CZCS) algorithm. Gain = 0 [Hovis et al., 1980].

radiance fell within the range of the LUT, because of the strong correlation of the water-leaving radiance errors for 443 and 550 nm. With wind speeds less than the value used for calculating the LUT (6 m/s), measured radiances may be less than the LUT radiances in the glint pattern, and atmospheric corrections cannot be made. For wind speeds of 6 and 10 m/s the glint correction is encouraging. Chlorophyll errors for an urban aerosol are small but relatively large for aeolian dust. In principle, a separate lookup table for dust could be calculated, but its reliability would be uncertain because the optical properties of aeolian dust are poorly known. A preliminary comparison of pigment concentrations derived with this algorithm and the CZCS operational algorithm are strongly correlated.

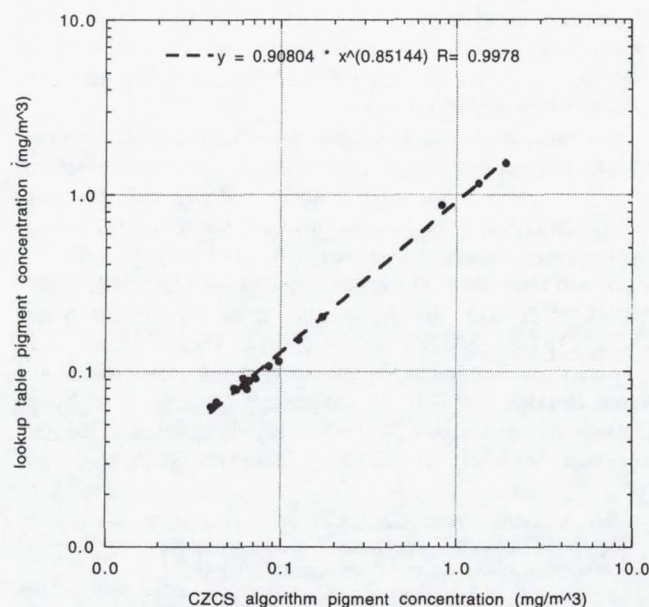


**Figure 11.** Comparison of pigment concentrations ( $\text{mg/m}^3$ ) as derived from the LUT and the CZCS operational algorithm.



# Equatorial dynamics observed by rocket, radar, and satellite during the CADRE/MALTED campaign

## 1. Programmatics and small-scale fluctuations

Richard A. Goldberg,<sup>1</sup> Gerald A. Lehmacher,<sup>1,2</sup> Frank J. Schmidlin,<sup>3</sup> David C. Fritts,<sup>4,5</sup> J. D. Mitchell,<sup>6</sup> C. L. Croskey,<sup>6</sup> M. Friedrich,<sup>7</sup> and W. E. Swartz<sup>8</sup>

**Abstract.** In August 1994, the Mesospheric and Lower Thermospheric Equatorial Dynamics (MALTED) Program was conducted from the Alcântara rocket site in northeastern Brazil as part of the International Guará Rocket Campaign to study equatorial dynamics, irregularities, and instabilities in the ionosphere. This site was selected because of its proximity to the geographic (2.3°S) and magnetic (~0.5°S) equators. MALTED was concerned with planetary wave modulation of the diurnal tidal amplitude, which exhibits considerable amplitude variability at equatorial and subtropical latitudes. Our goals were to study this global modulation of the tidal motions where tidal influences on the thermal structure are maximum, to study the interaction of these tidal structures with gravity waves and turbulence at mesopause altitudes, and to gain a better understanding of dynamic influences and variability on the equatorial middle atmosphere. Four (two daytime and two nighttime) identical Nike-Orion payloads designed to investigate small-scale turbulence and irregularities were coordinated with 20 meteorological falling-sphere rockets designed to measure temperature and wind fields during a 10-day period. These in situ measurements were coordinated with observations of global-scale mesospheric motions that were provided by various ground based radars and the Upper Atmosphere Research Satellite (UARS) through the Coupling and Dynamics of Regions Equatorial (CADRE) campaign. The ground-based observatories included the Jicamarca radar observatory near Lima, Peru, and medium frequency (MF) radars in Hawaii, Christmas Island, and Adelaide. Since all four Nike-Orion flights penetrated and overflew the electrojet with apogees near 125 km, these flights provided additional information about the electrodynamics and irregularities in the equatorial ionospheric *E* region and may provide information on wave coupling between the mesosphere and the electrojet. Simultaneous with these flights, the CUPRI 50-MHz radar (Cornell University) provided local sounding of the electrojet region. A description of the campaign logistics and the measurements performed with the Nike-Orion instrumentation and their implications for turbulence due to gravity waves and tidal instability in the mesosphere and lower thermosphere (MLT) are presented here. From a study of electron density fluctuations measured by rocket probes, we have found evidence for equatorial mesospheric neutral-atmospheric turbulence between 85 and 90 km. Furthermore, falling-sphere data imply that gravity wave breaking was a source for this turbulence. Mean motions and the various planetary, tidal, and gravity wave structures and their coherence and variability are the subjects of a companion paper.

## Introduction

The Guará Rocket Campaign was conducted at the rocket range at Alcântara, Brazil, from August to October 1994. The

overall program, which consisted of four independent elements, was designed to study various aspects of the equatorial ionosphere including electrodynamics of the electrojet and upper ionosphere and dynamics of the equatorial mesosphere. The Mesospheric and Lower Thermospheric Equatorial Dynamics/Coupling and Dynamics of Regions Equatorial (MALTED/CADRE) Program, which concentrated on the latter, was successfully completed as the first element of the series. The MALTED/CADRE 24-rocket sequence began on August 16 and was completed on August 25, 1994. During that period, four Nike-Orion payloads and 20 Viper-Dart meteorological falling-sphere payloads were launched to study the equatorial mesosphere and lower thermosphere, concentrating on large- and small-scale dynamics of the mesopause region (~80–120 km) but also measuring some properties of the daytime and nighttime electrojet. These flights were coordinated with the CADRE program using ground-based radar measurements from the Jicamarca Observatory in Peru and MF radars in Hawaii, Christmas Island, and Adelaide and with the High Resolution Doppler Imager (HRDI) aboard the

<sup>1</sup>Laboratory for Extraterrestrial Physics, NASA Goddard Space Flight Center, Greenbelt, Maryland.

<sup>2</sup>Now at Department of Physics, University of Wuppertal, Wuppertal, Germany.

<sup>3</sup>Wallops Flight Facility, NASA Goddard Space Flight Center, Wallops Island, Virginia.

<sup>4</sup>Laboratory for Atmospheric and Space Physics, University of Colorado, Boulder.

<sup>5</sup>Now at Colorado Research Associates, Boulder.

<sup>6</sup>Communications and Space Sciences Laboratory, Pennsylvania State University, University Park.

<sup>7</sup>Institute für Nachrichtentechnik und Wellenausbreitung, Technical University of Graz, Graz, Austria.

<sup>8</sup>School of Electrical Engineering, Cornell University, Ithaca, New York.



**Table 2.** List of Falling-Sphere Launches

Flight	Date	Time UT
NRO1874	Aug. 16, 1994	1422
NRO1876	Aug. 17, 1994	1540
NRO1877	Aug. 18, 1994	1408
NRO1878	Aug. 19, 1994	1424
NRO1879	Aug. 19, 1994	2000
NRO1881	Aug. 20, 1994	0356
NRO1882	Aug. 20, 1994	0800
NRO1883	Aug. 20, 1994	0835
NRO1892	Aug. 20, 1994	1432
NRO1894	Aug. 21, 1994	1439
NRO1896	Aug. 22, 1994	1627
NRO1897	Aug. 23, 1994	1346
NRO1898	Aug. 24, 1994	1352
NRO1899	Aug. 24, 1994	2002
NRO1901	Aug. 25, 1994	0244
NRO1902	Aug. 25, 1994	0926

Local time (LT) is UT - 3 hours.

diurnal tide was not sufficiently large in amplitude to account for this instability in the absence of gravity waves during this key day.

Referring to the temperature profile obtained at the beginning of the first key day (NRO 1878; August 19 in Figure 8) and the corresponding tidal thermal amplitude inferred from these data, however, we arrive at somewhat different conclusions. The temperature gradient inferred from the Atlas track of the first meteorological rocket during this series exhibits a temperature gradient in excess of  $-20$  K/km above 85 km, far above what is required for convective instability of the motion field. In this case, the inferred tidal thermal response is also  $\sim 37$  K between 85 and 90 km, suggesting that the diurnal tide exceeds the amplitude for convective instability with a mean gradient in the mesosphere of  $-2$  K/km. Here, the presence of gravity waves only enhances the occurrence of instability and turbulence. Thus, to the extent that the Atlas temperature profiles displayed here and by *Fritts et al.* [this issue] are representative of true wave perturbations at upper mesospheric altitudes, they imply that the diurnal tide often approaches, and on occasion exceeds, the amplitude required for convective instability for the motion field, but to account for the large negative thermal gradients measured by meteorological rockets at certain times, we cannot rely exclusively on tidal thermal perturbations. These observations suggest an important role for gravity waves in modulating tidal instability and the turbulence and mixing that this implies. To be more quantitative, however, we will need to perform measurements using instruments simultaneously sensitive to the larger tidal amplitudes and scales and the gravity waves acting on smaller spatial scales.

### Electrojet Considerations

Because electrojet fluctuations in the lower thermosphere and turbulence in the mesosphere could exhibit properties indicating some interaction between the two regions, we planned our experiment to include measurements of the electrojet to estimate its strength and extent. The eight passes through the electrojet (four upleg, four downleg; 4 day, 4 night) have provided probe data to compare with results from the CUPRI VHF radar, which was operational at the Alcântara rocket range during the four Nike-Orion flights [cf. *Gold-*

*berg et al.*, 1995]. CUPRI measured strong electrojet patterns, particularly during the two Nike-Orion daytime flights, which will enable us to learn about plasma-wave interactions and density fluctuations in the electrojet region. Plate 2 provides a range-time-intensity (RTI) plot of the CUPRI radar echo data encompassing the period of the second daytime flight (31.105). For this period CUPRI was operating with a  $4\text{-}\mu\text{s}$  pulse length to achieve an altitude resolution of 600 m. The transmitter power was about 17 kW. The antennas were directed vertically with portions of the beams perpendicular to the Earth's magnetic field throughout the electrojet region. For this overview plot the data were averaged for 9.6 s to reduce the number of pixels plotted to a reasonable number, even though 2-s averages are usually sufficient for such strong daytime electrojet data. Considerable structure is evident in the plot with the strongest echoes occurring between 1015 and 1045 LT and between 100 and 103 km altitude. Rocket 31.105 was launched at 1039 LT during the time of strongest echoes. The radar echoes result from vertically structured 3-m irregularities aligned along the magnetic field, while structures seen by the rocket are direction independent. The radar data show that electrojet fluctuations penetrate to altitudes as low as 92 km, yet the rocket data show additional fluctuations that continue below this altitude and down to 85 km. This may imply a region of overlap between electrojet instabilities and mesospheric turbulence (compare Figure 6a). Details of these features are now under study to seek evidence for wave coupling between the regions.

### Conclusions

The data from the MALTED Nike-Orion payloads provide a multitude of electron and ion density measurements in the equatorial  $D$  and lower  $E$  region and help us to compare various probe techniques under daytime and nighttime conditions. From the spectral analysis of electron density fluctuations for the daytime flights, we find evidence for neutral turbulence at 85–90 km. The altitude and magnitude of our results agree well with other in situ measurements. We have found that the mesospheric instabilities may be characterized as turbulence and show similar features to those observed in Peru by *Røyrvik and Smith* [1984]. Both daytime and nighttime flights give us the opportunity to study instabilities of the equatorial electrojet, particularly in comparison with the CUPRI radar observations. From the falling sphere payloads, which are used to obtain mesospheric winds and temperatures, and the small-scale instabilities measured by the Nike-Orion probes, we have detected evidence for gravity wave breaking in the mesosphere above 85 km. From future comparisons of the meteorological rocket data together with radar and satellite wind measurements, we expect to detect changes in the gravity wave momentum flux and associate them to variations of the tidal amplitude. Comparison of the rocket results along with VHF radar and satellite results are made by *Fritts et al.* [this issue].



# Development of a Simulated Data Set for the SeaWiFS Mission

Watson W. Gregg, Frederick S. Patt, and Robert H. Woodward

**Abstract**—A realistic simulated data set is essential for mission readiness preparations and can potentially assist in all phases of ground support for a future mission. Such a data set was created for the Sea-viewing Wide Field-of-view Sensor (SeaWiFS), a global ocean color mission due for launch in 1997. This data set incorporates a representation of virtually every known aspect of the flight mission. Thus, it provides a high fidelity data set for testing most phases of the ground system, including data processing, data transfers, calibration and validation, quality control, and mission operations. The data set is constructed for a seven-day period, March 25–31, 1994. Specific features of the data set: it includes Global Area Coverage (GAC), recorded Local Area Coverage (LAC), and real-time High Resolution Picture Transmission (HRPT) data for the seven-day period; it includes a realistic orbit which is propagated using a Brouwer–Lyddane model with drag; the data correspond to a command schedule based on the orbit for this seven-day period; it includes total (at-satellite) radiances for ocean, land, clouds, and ice; it utilizes a high-resolution land/sea mask; it includes actual SeaWiFS spectral responses; it includes the actual sensor saturation responses; it is formatted according to current onboard data structures; and it includes corresponding telemetry (instrument and spacecraft) data. The methods are described and some examples of the output are given.

## I. INTRODUCTION

THE AVAILABILITY of simulated data is essential for preparation in a remote sensing mission. The usefulness of the simulated data for mission preparation activities depends upon the thoroughness with which the data are prepared, the adherence to format/content specifications, and the realism of the data. For example, data transfer speeds, storage capabilities, and computer memory requirements can usually be tested using only dummy data sets of the expected volume. Unpacking algorithms, computer processing requirements, and intricacies of storing the data require correct data structures and formats. More advanced mission preparation activities, such as quality control, algorithm development, mission health and safety monitoring, and the initiation of an awareness of potential in-flight problems and discoveries, require a realistic data set containing observations similar to the expected flight data, with the correct volumes and structures. Such a simulated data set can potentially increase the success of the mission by exposing problems in sensor design, spacecraft operations, orbit anomalies, etc., well in advance of launch, allowing repair

(if detected in time) or compensation by developing algorithms or revising the sensor/spacecraft operations scenario.

The development of a realistic simulated data set is simplified if a predecessor sensor/mission exists. If the predecessor mission is an exact copy of the future mission, of course, then development of simulated data is simply a matter of using the previous data. This is frequently not the case, however, since the predecessor mission often yielded insights that led to an improved sensor design and capability, or perhaps a different spacecraft or orbit configuration. In most cases, additional effort and data are required for development of the simulated data set.

The Sea-viewing Wide Field-of-view Sensor (SeaWiFS) mission, due for launch in 1997, is an example of a mission that has a predecessor sensor (the Nimbus-7 Coastal Zone Color Scanner, or CZCS), but contains many improvements in sensor design that preclude direct use of the predecessor data for mission preparation. The most important differences are the spectral band placement and the global, routine operations scenario for SeaWiFS (the CZCS was a limited duty sensor). Additional differences include the sensor scan parameters and the overall data content, especially the telemetry.

Our method for constructing a simulated SeaWiFS data set takes advantage of the fact that the eight years of accumulated CZCS data led to many insights into the processes of radiative transfer in the oceans, and the relationship of these processes to remote sensing principles. By emphasizing this knowledge, we may develop a realistic simulated data set for a similar, but not identical, sensor without relying excessively on manipulation of previous (and only approximately valid) data sets.

Although the data set described here was developed specifically for the SeaWiFS mission, the methods can easily be used for any ocean color sensor, and may be extrapolated for use by most Earth-viewing sensors that use the visible and near-infrared wavelengths. The methods for constructing the data set will be described in the following, along with examples of data output.

## II. BACKGROUND

The primary scientific goal of the SeaWiFS mission is to provide global monitoring of ocean color. However, because the spacecraft contains limited storage capacity ( $125 \times 10^6$  Bytes), onboard subsampling of the data is required to obtain global coverage. Thus, SeaWiFS will produce two different resolutions of data: local area coverage (LAC) and global area coverage (GAC). LAC data is full sensor resolution data (1.12 km at nadir) and is used for regional observations and calibration activities. GAC data is simply LAC data

Manuscript received February 9, 1995; revised July 15, 1996. This work was supported by NASA Grant 902-579-11-04 (WWG) and the SeaWiFS Project.

W. W. Gregg is with the NASA/Goddard Space Flight Center, Code 902, Greenbelt, MD 20771 USA.

F. S. Patt and R. H. Woodward are with General Sciences Corporation, Laurel, MD 20707 USA.

Publisher Item Identifier S 0196-2892(97)00384-7.



satellite radiances are dominated by the atmosphere ( $\approx 90\%$  of the total), particularly Rayleigh scattering. An image of Band 8 shows that land produces very large radiances at this wavelength, usually over the ocean saturation threshold (Fig. 5). There is significant sun glint contamination near the center of the image south of Haiti, before obscuration by clouds.

### B. Stored LAC Data

Stored LAC data collection in the simulated data set follows the command schedule described earlier. It includes short-duration Earth observations (which appear as shorter and wider segments than GAC data), and calibration data. A depiction of solar calibration/intergain check LAC data is shown in Fig. 6. The procedure involves acquiring data in solar mode off the solar diffuser at specified gains first, followed by inter-gain checks using the so-called calibration pulse. The truncated object on the left represents the solar calibration data, while the perpendicular stripe represents the results of the calibration pulse, which is solid in color until completion of the solar calibration. Then the intergain check begins, represented by alternating bands of 6 scans at selected gains. The TDI check is shorter in duration than the solar calibration activity, but is otherwise similar, so it is not shown here.

A full moon event occurs during the period of the simulated data set. The required  $7^\circ$  phase angle for data acquisition actually occurs in the GMT morning of March 27, 1994. A representation of the lunar data is taken from actual observations from the SeaWiFS sensor from the ground in Band 1 (Fig. 7). For the simulated data set, these actual moon data were packaged into a realistic scan of 2 minutes duration, showing the actual size of the moon within the downlinked SeaWiFS scan data (Fig. 8).

### C. Real-Time HRPT Data

Simulated real-time data are comprised of LAC data taken when SeaStar is in view of the GSFC HRPT station. The GSFC visibility mask nearly overlaps the Wallops visibility mask shown in Fig. 4. A nonmapped view of simulated real-time HRPT data is selected for display (Fig. 9) that corresponds with the GAC scene shown earlier (Fig. 5). The Florida peninsula is visible at the upper western edge of the scan, with Cuba, Haiti/Dominican Republic, and Puerto Rico successively west-to-east along the southern portion of the image. One may note very large radiances, exceeding the ocean saturation radiance, along the extreme edges of the scans, due to large scan angle (the spacecraft zenith angle is nearly  $72^\circ$  at the scan edge when tilted). This large scan angle results in a longer atmospheric path length, and consequently more scattered radiance. HRPT data for Band 8 shows once again that land saturates at this wavelength (Fig. 9). What is particularly notable is the high resolution of land features, resulting from the use of the high resolution WVS land mask.

### D. Sensor Saturation Response

The sensor saturation response is fairly subtle and can be seen around clouds, particularly in the HRPT data (Fig. 9), but otherwise is not readily apparent in the images discussed up to now. We provide here a closeup view of a portion of an HRPT image to better illustrate the saturation response effects. The image portion chosen is a segment on the east coast of Puerto Rico, where a number of saturating islands and coastlines occur. We choose Band 8 because it is the most sensitive over these land features (Bands 1–5 most likely will remain within the ocean saturation radiance here). The saturation effects appear as an elongation of island features and land edges in the direction of the scan, both preceding (stray light effects) and following (bright target recovery effects) small land objects (Fig. 10).

## V. DISCUSSION

Undertaking of a complete simulation for a mission can be a daunting task, and consequently many simplifications may be required in order to keep costs under control and reduce the time required to develop the data set. In addition, many of the characteristics of the sensor or spacecraft are not initially known, and detailed information comes in at infrequent intervals. This necessitates a continuing revision of the data set to preserve realism. In the SeaWiFS case, the data set described here represents the third version, and still does not contain a full representation of the actual on-board telemetry.

Some of the most apparent simplifications in this data set include lack of a variable aerosol concentration, lack of aerosol-Rayleigh interactions over the oceans, lack of a scattering atmosphere over land, simplified cloud and ice radiative transfer, low spatial resolution of the input data sets, and a simplified solar calibration. These are clearly areas in which a more thorough treatment would improve the realism of the data, and increase its usefulness especially for pre-launch algorithm development and testing. However, this increase in realism comes at a cost of an increase in complexity and time required for development of the data set. In the SeaWiFS mission, we faced an extremely short preparation period (initially 18 months, but later increased due to launch slips), so we had to make a choice about including more complexity and providing a simple, but reasonably realistic data set, that is complete in the production of all required operations, data formats and structures, telemetry, and scientific radiances. Missions with longer lead times and/or more personnel can take the time and develop a more inclusive data set. Nevertheless, this data set has been used extensively by the SeaWiFS project personnel, and has greatly benefitted many aspects of system development, especially ground operations, data system, and calibration/validation efforts. The methods used here are certainly applicable at least as starting points for future missions in ocean color, and perhaps other Earth-viewing satellites.



# Wavelet Analysis of Satellite Images for Coastal Watch

Antony K. Liu, Chich Y. Peng, and Steve Y.-S. Chang

**Abstract**—The two-dimensional wavelet transform is a very efficient bandpass filter, which can be used to separate various scales of processes and show their relative phase/location. In this paper, algorithms and techniques for automated detection and tracking of mesoscale features from satellite imagery employing wavelet analysis are developed. The wavelet transform has been applied to satellite images, such as those from synthetic aperture radar (SAR), advanced very-high-resolution radiometer (AVHRR), and coastal zone color scanner (CZCS) for feature extraction. The evolution of mesoscale features such as oil slicks, fronts, eddies, and ship wakes can be tracked by the wavelet analysis using satellite data from repeating paths. Several examples of the wavelet analysis applied to various satellite images demonstrate the feasibility of this technique for coastal monitoring.

**Index Terms**—Marine technology, marine vehicle detection and tracking, process monitoring, satellite applications, wavelet transforms.

## I. INTRODUCTION

MESOSCALE oceanic processes, such as internal waves, ship wakes, fronts, ice-edge meanders, oil spills, surface slicks, upwelling, and eddies have been imaged by synthetic aperture radar (SAR), coast zone color scanner (CZCS), and advanced very-high-resolution radiometer (AVHRR), although the sea state conditions involved in this imaging have not been well calibrated due to lack of ground truth. The objectives of this paper are to develop algorithms and techniques for automated detection and tracking of mesoscale features in satellite imagery by wavelet analysis and to relate the evolution of these features to oceanic processes in coastal waters. Reliable imaging of such mesoscale features, combined with a definition of the conditions under which imaging is feasible, would lead to an important data product: satellite-derived maps for tracking mesoscale features in the coastal zone.

The combined use of sensors from several satellites, such as AVHRR, SeaWiFS (Sea-viewing Wide Field-of-view Sensor), OCTS (ocean color temperature sensor), and ERS-2 or RADARSAT SAR can provide frequent high-resolution coverage of the coastal zone. Coastal processes affecting sea surface temperature, pigment concentration, or surface roughness can be studied using IR (infrared), ocean color, or

SAR data, respectively. Simultaneous satellite images, *in situ* measurements from moorings and ship operations, and wind records from buoys and meteorological stations can be used to detect and monitor the ocean environment. By using repeat satellite coverage, mesoscale features associated with coastal processes can be tracked from a sequence of satellite images through multitemporal satellite data analysis.

A new method for time-varying signal analysis, called the wavelet transform, has been developed for application at NASA/GSFC during the past three years and provides spectral decompositions via the scale concept. Basically, wavelet transforms are analogous to Fourier transforms, but are localized both in frequency and time, i.e., they enable the study of transient processes by localizing their properties in both time and frequency [1]. Recent investigations in physical oceanography [2] justify the efficiency and abilities of these transforms to analyze nonlinear dynamical ocean systems. Wavelet analysis of wind fluctuations over the wave groups and the long-short wave interaction have been reported [3], [4] using the one-dimensional (1-D) Morlet wavelet transform. The wavelet transform has proved to be a convenient tool for studying the details of transient air-sea interaction processes.

The two-dimensional (2-D) wavelet transform is a highly efficient bandpass filter, which can be used to separate various scale processes and show their relative phase/location information, e.g., in SAR imagery [5]. The 2-D Gaussian wavelet transform (often referred to as the "Mexican hat") of a SAR image for the extraction of small-scale features can be used as an edge detector [6]. In a marginal ice zone study [7], the ice edge in each SAR image has been delineated by using a 2-D wavelet transform. The wavelet transforms of satellite images can be used for near real-time "quick look" screening of satellite data (feature detection), data reduction (binary image), and image enhancement (edge linking).

In this paper, the 2-D Gaussian wavelet transform will be briefly described in the next section. Wavelet analyses for feature tracking, such as oil spills, fronts, eddies, and ship wakes are then presented, along with some detailed discussion of algorithms and models. The application of satellite images to coastal monitoring and the results of wavelet analysis are discussed in the final section.

## II. TWO-DIMENSIONAL GAUSSIAN WAVELET

The wavelet transform,  $W_s(a, b)$ , of a function,  $s(r)$ , where  $r = (x, y)$ , is expressed in terms of the complex valued

Manuscript received May 7, 1996; revised October 30, 1996. This work was supported by the National Aeronautics and Space Administration, National Oceanic and Atmospheric Administration, and the Office of Naval Research.

The authors are with the Oceans and Ice Branch, NASA Goddard Space Flight Center, Greenbelt, MD 20771 USA.

Publisher Item Identifier S 0364-9059(97)01262-4.



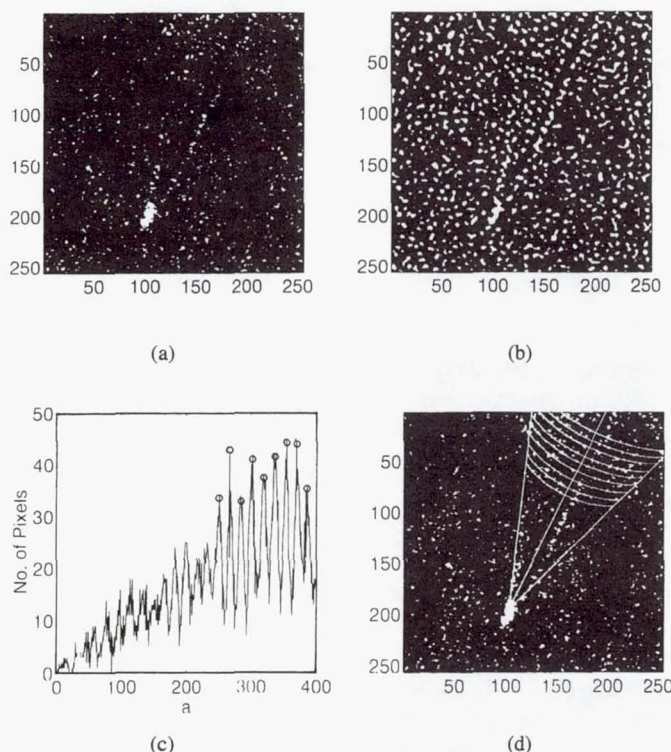


Fig. 10. (a) ERS-1 SAR subscene of ship transverse waves, (b) the wavelet transform with a small scale, (c) the result of Hough transform to the wavelet-transformed image, and (d) ship transverse waves detected by the Hough transform, indicated by open circles for the peaks in (c), which is overlaid on the SAR subscene.

wake phase function [14]:

$$X = A(1 - 0.5 \cos^2 \theta) \quad (4)$$

where  $A$  is the axis behind the ship wake along the ship's direction of motion. When  $\theta = 0$ ,  $A/2$  is the wavelength of the transverse wave. The peaks of the Hough transform are shown in Fig. 10(c) as a function of  $A$  (pixels) along the ship's direction of motion. The sequential transverse wave can be easily identified by open circles in Fig. 10(c). The wavelength is estimated to be 106.3 m. Based on the dispersion relation,  $V$  is defined as

$$V = \left( \frac{gA}{4\pi} \right)^{1/2} \quad (5)$$

The ship speed is approximately 12.86 m/s. According to the ship powering and steering survey, this is probably a fast cargo vessel or a huge passenger liner. Fig. 10(d) shows the detected transverse wave and ship wake overlaid on the SAR subscene, with an almost perfect match.

#### IV. COASTAL MONITORING AND DISCUSSION

The NOAA (National Oceanic and Atmospheric Administration) CoastWatch provides near real-time mapped satellite and *in situ* data and information for U.S. coastal waters suitable for hazard warning, ice and ocean monitoring, and environmental management [15]. A development project is underway to add SAR data and products to the CoastWatch

product suite. One of the major areas of interest will be the coast of Alaska [11]. The use of wavelet transform techniques for the automated analysis of SAR, AVHRR, and SeaWiFS images to detect ocean features will be evaluated for CoastWatch applications.

The coastal zone is a highly productive and dynamic environment. Because of the fast growth of industry, pollution is one of the major issues for environmental protection [16]. Increasingly, coastal regions need reliable, high-quality resource and environmental information from remote sensing to better manage this vital area. Remote sensing with repeated coverage is the most efficient method to monitor and study marine productivity and pollution. The mapping of mesoscale ocean features in the coastal zone is a major potential application for satellite SAR data, especially for the ScanSAR on RADARSAT with 500-km swath. The use of SAR-derived observations to track eddies, surface temperature-related features, and river and estuarine plumes can aid in the management of fisheries. Especially in subtropical and tropical regions, uniform sea surface temperatures and cloud cover preclude AVHRR measurements of surface structure and obscure ocean color observations.

The wavelet transforms of satellite images can be used for near real-time "quick look" screening of satellite data (feature detection), data reduction (binary image), and image enhancement (edge linking). By combining ocean color (SeaWiFS or OCTS), SAR (ERS-2 or RADARSAT), and infrared (AVHRR) images (wavelet-transformed binary images) using some data fusion techniques, mesoscale features of various physical processes such as oil spills, surface slicks, fronts, upwelling, and eddies can be detected and tracked in the coastal zone. Wavelet analysis can provide a more cost-effective monitoring program that would keep track of changes in important elements of the coastal watch system.

In this paper, the wavelet transform has been applied to satellite SAR, AVHRR, and CZCS images, and the feasibility of this technique for feature extraction has been demonstrated. Several examples of wavelet analysis from various satellite images have been studied for the extraction of mesoscale features such as fronts, ice-edge meanders, oil slicks, ship wakes, and eddies. Algorithms and techniques for automated detection and tracking of mesoscale features from satellite imagery by wavelet analysis have been developed. While further development is needed to establish the automated system, the techniques developed here should remain valid for any image data. Reliable imaging of such mesoscale features by various sensors and definition of the conditions under which imaging is possible will provide a better understanding of oceanic processes influencing by sea surface temperature (IR), pigment concentration (ocean color), or surface roughness (SAR).



# Microphysical Retrievals over Stratiform Rain Using Measurements from an Airborne Dual-Wavelength Radar-Radiometer

Robert Meneghini, *Member, IEEE*, Hiroshi Kumagai, James R. Wang, *Senior Member, IEEE*, Toshio Iguchi, and Toshiaki Kozu, *Member, IEEE*

**Abstract**—The need to understand the complementarity of the radar and radiometer is important not only to the Tropical Rain Measuring Mission (TRMM) program but to a growing number of multi-instrumented airborne experiment that combine single or dual-frequency radars with multichannel radiometers. The method of analysis used in this study begins with the derivation of dual-wavelength radar equations for the estimation of a two-parameter drop size distribution (DSD). Defining a “storm model” as the set of parameters that characterize snow density, cloud water, water vapor, and features of the melting layer, then to each storm model there will usually correspond a set of range-profiled drop size distributions that are approximate solutions of the radar equations. To test these solutions, a radiative transfer model is used to compute the brightness temperatures for the radiometric frequencies of interest. A storm model or class of storm models is considered optimum if it provides the best reproduction of the radar and radiometer measurements. Tests of the method are made for stratiform rain using simulated storm models as well as measured airborne data. Preliminary results show that the best correspondence between the measured and estimated radar profiles usually can be obtained by using a moderate snow density ( $0.1\text{--}0.2\text{ g/cm}^3$ ), the Maxwell-Garnett mixing formula for partially melted hydrometeors (water matrix with snow inclusions), and low to moderate values of the integrated cloud liquid water (less than  $1\text{ kg/m}^2$ ). The storm-model parameters that yield the best reproductions of the measured radar reflectivity factors also provide brightness temperatures at 10 GHz that agree well with the measurements. On the other hand, the correspondence between the measured and modeled values usually worsens in going to the higher frequency channels at 19 and 34 GHz. In searching for possible reasons for the discrepancies, it is found that changes in the DSD parameter  $\mu$ , the radar constants, or the path-integrated attenuation can affect the high frequency channels significantly. In particular, parameters that cause only modest increases in the median mass diameter of the snow, and which have a minor effect on the radar returns or the low frequency brightness temperature, can produce a strong cooling of the 34 GHz brightness temperature.

## I. INTRODUCTION AND BACKGROUND

AS THE instruments aboard the Tropical Rain Measuring Mission (TRMM) will include both the TRMM Microwave Imager (TMI) and the first spaceborne precipitation radar (PR), there is a need to develop methods for the analysis

of radar and radiometer data [1]–[5]. Even apart from the instruments of TRMM, the growing number of airborne data sets that include both radar and radiometer data has prompted a number of researchers to examine how best to combine them to obtain a more complete characterization of the precipitation.

The analysis method used in this work can be divided into two parts. The first objective is to generalize a dual-wavelength airborne radar method; the second is to use radiometric data to determine the storm parameters that enter the radar retrievals as unknown parameters. As these methods are related to dual-wavelength radar as well as radar-radiometer methods, we present a brief background on both approaches. In Section II solution methods for the dual-wavelength radar equations are presented along with a description of how these solutions can be used to estimate the corresponding radiometric brightness temperatures. To understand the performance and limitations of the method, simulations are given in Section III. Tests of the method using experimental airborne data are presented in Section IV.

### A. Radar-Radiometer Methods

Lu and Lin [6] appear to have been the first to develop and test a combined radar-radiometer algorithm. The essence of the procedure is to solve simultaneously the radar and the radiative transfer equation by the use of an iterative procedure. Tests of the method for the estimation of cloud liquid water and rain water content using a ground-based dual-wavelength radar-radiometers at 9.375 and 35 GHz were reported by Lin *et al.* [7]. The method of Lu and Lin is related to the modified Hitschfeld-Bordan method [8] in which an independent estimate of path attenuation is used to avoid the instabilities in the estimated rain rate profile to which single-attenuating wavelength retrievals are subject. In cases where only airborne or spaceborne radar data are available, the path attenuation can be estimated by the surface reference method [9] or by the “slope” method [10], [11]. With the addition of a radiometer that has approximately the same field of view as the radar, the radiometer-derived path attenuation can be used in place of the radar-derived value. Thus, the final-value or  $\alpha$ - and  $C$ -adjustment methods [12], [13] can be reconstituted as radar-radiometer methods by the replacement of path-attenuation estimates [14].

A somewhat similar approach has been described by Kumagai *et al.* [15], [16] who extended a radar-derived two-scale

Manuscript received October 26, 1995; revised August 23, 1996.

R. Meneghini and J. R. Wang are with NASA Goddard Space Flight Center, Greenbelt, MD 20771 USA.

H. Kumagai, T. Iguchi, and T. Kozu are with the Communications Research Laboratory, Koganei, Tokyo 184, Japan.

Publisher Item Identifier S 0196-2892(97)02108-6.



To show how well the 3 approaches reproduce the brightness temperatures, a 90 sec segment of data ( $\approx 18$  km) is chosen from the flight of 24 September, 1990 from 5:53:30 to 5:55 UT. Note that this segment of data includes the radar measurements discussed in the previous example. Comparisons of the estimated (dashed lines) and measured (solid lines)  $T_b$  for 10 and 34 GHz are shown in Figs. 16 and 17, respectively. For both sets of plots, a snow density of  $0.2 \text{ g/cm}^{-3}$  and  $\mu = 8$  is assumed (for the MP distribution,  $\mu = 0$ ); the lower and upper bounds of the estimated  $T_b$  shown in the plots correspond to  $I_{CLW} = 0$  and  $I_{CLW} = 0.9 \text{ kg/m}^{-2}$ , respectively. Shown in Fig. 16(a) and (b) are the values of  $T_b$  estimated from the composite solution (method 2) and the backward recursion (method 1), respectively, while Fig. 16(c) corresponds to the  $T_b$  derived from the MP size distribution. The plots of Fig. 17, for  $T_b$  (34 GHz), are displayed in the same sequence. Comparisons between the results of Fig. 17(a) and (b) ( $f = 34$  GHz) show that the two methods yield similar results; at the lower frequency, however, Fig. 16(a) and (b) indicate that the composite solution gives values of  $T_b$  that are typically 1 to 5 K higher than the backward recursion results. The MP-derived brightness temperatures (Figs. 16(c) and 17(c)) show significant positive biases at both 10 and 34 GHz. The primary reason for the error appears to be the fact that the  $D_0$  values are underestimated and the  $N_T$  are overestimated in the snow region. This can be understood by examining the estimated profiles of Fig. 15(c): the overestimates of  $Z_m$  (34.45 GHz) in the snow region corresponds to smaller values of  $D_0$  and larger values of  $N_T$  than the corresponding dual-wavelength estimates [Fig. 15(a) and (b)]. This problem of large overestimates can be corrected by recognizing that (46) and (50), although approximate, are applicable to any exponential distribution. This implies that  $N_0$  can be adjusted so that the estimated ( $N_0, D_{0j}; j = 1, \dots, n$ ) profiles accurately reproduce the measured  $Z_m$  profiles at both 10 and 34.45 GHz. Applying this idea to the radar data in Fig. 15 shows that a value of  $N_0$  of  $2000 \text{ mm}^{-1}/\text{m}^{-3}$  (i.e.,  $1/4$  of the MP value) not only gives a better reproduction of the  $Z_m$  profiles but yields  $T_b$  values significantly closer to the measured values (not shown). The idea of modifying  $N_0$  to obtain a better match with the dual-wavelength radar profiles (and with the measured  $T_b$ ) can be considered a dual-wavelength analog of the method of Kumagai *et al.* [15], [16]. Unlike the method considered in this paper, an advantage of the approach is that it does not require the surface reference method. On the other hand, a single value of  $N_0$  can reproduce the measured  $Z_m$  profiles only approximately.

## V. DISCUSSION AND SUMMARY

In this study, an airborne or spaceborne dual-wavelength radar method was described for the estimation of a two parameter size distribution of rain and snow. To incorporate the radiometric measurements into the retrieval, it was recognized

that there are a number of free parameters in the solution to the dual-wavelength radar equations which include cloud liquid water content, relative humidity, snow density, the dielectric mixing formula for partially melted particles, and various parameters of the melting layer model. In particular, for each fixed set of these "storm model" parameters, solutions to the radar equations for the DSD parameters ( $N_0, D_0$ ) can be sought and usually found. In turn, from each storm model and the associated DSD parameters, the corresponding brightness temperatures, at any frequency, can be generated from a radiative transfer model. The apparent radar reflectivities and the path-integrated attenuations can also be generated and compared to the radar measurements. In principle, this procedure allows an identification of a storm model or class of storm models and their associated DSD parameters that best reproduce the measured radar and radiometer data. To test the method, a simple stratiform storm model was constructed from measured DSD's and a melting layer model. In general, the method performs well on the simulated data in the sense that the input storm model, or one similar to it, was usually identified. However, the simulations were carried out in the absence of errors such as offsets in the path attenuations or radar constants: only errors arising from the unknown values of snow density, the amount and location of the cloud water and variability in the DSD were included.

In the final part of the study the technique was applied to airborne radar-radiometer data taken during the typhoon mission of September 1990. Application of the method to selected segments of stratiform rain suggests that, by the use of the dual-wavelength radar data, a profile of the DSD and the associated set of storm parameters (cloud water, water vapor, snow density and parameters of the melting layer) can generally be found that accurately reproduces the measured radar data and the low frequency brightness temperatures. At the higher frequency of 34 GHz, however, discrepancies between the modeled and measured  $T_b$  values become apparent. Possible sources of error are radar and radiometer calibration errors, errors in the SRT-derived path attenuations, and the choice of the  $\mu$  parameter. Unfortunately, modest errors in the radar calibration constants or path integrated attenuation of 1–2 dB can have a significant effect on the 34 GHz  $T_b$  estimates; in particular, small changes in the snow DSD can have a strong cooling (increasing  $D_0$ , decreasing  $N_T$ ) or warming effect (decreasing  $D_0$ , increasing  $N_T$ ). Because of this, a complete specification of the storm parameters may be too ambitious a goal and the best that can be obtained, with the present approach, is a class of storm models (and a corresponding range of possible storm parameters) that are approximately consistent with the measured data. Future work on the existence/uniqueness issues associated with the dual-wavelength radar equations, generalizations of the melting layer model, and comparisons with the alternative approach outlined in Section IV may lead to improved methods of analysis. It should also serve to illuminate the complex relationships between precipitation parameters and the corresponding radar-radiometer response.



## **An automated method for navigation assessment for Earth survey sensors using island targets**

F. S. PATT and R. H. WOODWARD

General Sciences Corporation, Laurel, Maryland 20702, U.S.A.

W. W. GREGG

Global Change Data Center, Goddard Space Flight Center,  
National Aeronautics and Space Administration (NASA), Greenbelt,  
Maryland 20771, U.S.A.

*(Received 4 July 1995; in final form 20 December 1996)*

**Abstract.** An automated method has been developed for performing navigation assessment on satellite-based Earth sensor data. The method utilizes islands as targets which can be readily located in the sensor data and identified with reference locations. The essential elements are an algorithm for classifying the sensor data according to source, a reference catalogue of island locations, and a robust pattern-matching algorithm for island identification. The algorithms were developed and tested for the Sea-viewing Wide Field-of-view Sensor (SeaWiFS), an ocean colour sensor. This method will allow navigation error statistics to be automatically generated for large numbers of points, supporting analysis over large spatial and temporal ranges.

### **1. Introduction**

Assessing navigation accuracy has been a challenge for nearly every Earth sensing satellite mission since the beginning of the space program. Extensive analysis efforts have been devoted to this problem, as evidenced by many publications in the open literature (e.g., Emery *et al.* 1989, Marsouin and Brunel 1991). By and large, navigation assessment has relied on manual selection of ground control points based on overlaying coastlines in sensor image co-ordinates (Krasnopolsky and Breaker 1994, Rosborough *et al.* 1994). However, the effort required to perform manual navigation quality control is considerable, and requires human resources which are better used for other purposes. Manual assessment is also extremely tedious and error-prone. For a global survey mission, these problems are exacerbated.

In developing a navigation assessment strategy for the Sea-viewing Wide Field-of-view Sensor (SeaWiFS), a global ocean colour sensor to be launched in 1995, we sought to develop a system to minimize the need for manual intervention. Automated methods based on autocorrelation techniques have been developed, but with limited success (O'Brien and Turner 1992). One method based upon a catalogue of features (islands, capes) over a local area has met with considerable success (Bordes *et al.* 1992).

However, an automatic navigation assessment technique must meet stringent requirements. Earth features to be used for computing navigation errors must be



candidates, matches, and the median position differences in longitude and latitude between the located and catalogued positions of the matches islands. The total number of islands is significantly greater than for the unperturbed data, due to the fragmentation effect of the random errors. The median latitude and longitude difference show a clear negative trend in latitude, with significant scatter around this trend. The direction and magnitude of this trend is consistent with the effect of the systematic orbit errors, demonstrating that the method was able to correctly discern the error. The longitude differences show scatter and possibly a smaller negative trend.

A plot of latitude differences vs. longitude differences for one of the orbits (figure 10) shows large scatter compared to the unperturbed data (figure 9). This scatter raises questions about the reliable matching of any but the largest islands in the data; in particular, we were concerned about the number of random matches among the small islands in the data and the catalog. We re-ran the tests using a smaller reference catalogue, limited to islands with a minimum dimension of at least  $0.05^\circ$  and a minimum separation of  $0.2^\circ$  (measured on the Earth's surface). The resultant catalogue contained 1155 islands (vs. nearly 4300 for the standard GAC catalogue). The effect of the smaller catalog is apparent in both the number of islands with candidates and the number of matches; in this case, orbit 5 did not produce any matches (table 9). The overall trend is still clear. The differences between the two tests are less than one GAC pixel ( $0.04^\circ$ ) for a given orbit. This test shows, albeit with a limited amount of data, that the system is capable of detecting navigation trends even in the presence of large random errors.

Table 9. Navigation assessment results with perturbed orbit and attitude: small catalogue.

Orbit	Total islands/ islands with candidates	Matches	Median position differences	
			Longitude ( $^\circ$ )	Latitude ( $^\circ$ )
1	107/44	27	-0.0287	-0.0232
4	76/28	11	-0.0115	-0.0464
8	86/31	25	0.0085	-0.0886
11	32/7	6	-0.0110	-0.1185
13	92/30	21	-0.0372	-0.1183
14	165/41	34	-0.0081	-0.1285
15	150/50	38	-0.0068	-0.1037

#### 4. Conclusion

We have developed a system for automated assessment of satellite-based Earth sensor navigation using island targets. The method involved filtering the sensor data to locate islands, and matching them with reference island locations in a catalogue. We developed algorithms for classifying sensor data and locating the islands using the results of classification; generated a global catalogue of island locations and sizes based on a precise vector shoreline database; and adapted pattern-matching software to perform robust matching of located and reference islands. We tested the methods using simulated SeaWiFS sensor data representing both GAC and direct-broadcast HRPT data collection. The targets located in the GAC data are reasonably well distributed, with islands found in nearly every orbit and distributed over the full range of latitudes and longitudes. The tests with the simulated HRPT data, most of which included parts of the Caribbean Sea, produced large numbers of islands. The island matching algorithm succeeded in matching almost half of the islands found in the GAC data, and about one quarter of those in the HRPT data; the unmatched islands correspond to congested coastal regions or barrier islands. Methods were discussed for detecting and eliminating mismatched islands. The average number of correctly matched islands is about 17 per GAC orbit or 44 per HRPT pass. This represents a substantial number of targets which can be generated automatically for navigation assessment during the SeaWiFS mission. The methods were also shown to perform effectively in the presence of large systematic and random errors.



# STRATIFORM AND CONVECTIVE RAIN DISCRIMINATION FROM MICROWAVE RADIOMETER OBSERVATIONS

C. Prabhakara\*, M. Cadeddu†, D.A. Short\*,  
J.A. Weinman\*, J.L. Schols‡, J. Haferman†

## ABSTRACT

A criterion based on the SSM/I observations is developed to discriminate rain into convective and stratiform types. This criterion depends on the microwave polarization properties of the flat melting snow particles that fall slowly in the stratiform clouds. Utilizing this criterion and some spatial and temporal characteristics of hydrometeors in TOGA-COARE area revealed by ship borne radars, we have developed an algorithm to retrieve convective and stratiform rain rate from SSM/I data.

## 1. RADAR OBSERVATIONS

Radar observations over the TOGA-COARE region in the equatorial Pacific ( $1^{\circ}$  N to  $4^{\circ}$  S and  $153^{\circ}$  E to  $158^{\circ}$  E) reveal several useful properties of the maritime tropical rain. Since these radars operated continuously we can follow the life cycle of the Mesoscale Convective Systems (MCS) in this region that lasts for several hours. In the early phase of the MCS rain from convective cells, on a scale of a few kilometers, dominates. As a result, in the rain area, averaged convective rain rate is greater than the averaged stratiform rain rate. This character reverses with aging of the MCS. In the later stages radar data show, over extensive area, enhancement of reflectivity around 4.5 Km altitude due to flat melting snow particles that fall slowly in the stratiform clouds. The spatial distribution of rain at any time during the life cycle of the MCS follows a probability distribution that is analogous to the log-normal type.

## 2. RAIN DISCRIMINATION AND ESTIMATION FROM SSM/I DATA

Absorption, emission and scattering due to various hydrometeors (cloud liquid drops, rain drops, dry and

melting snow and ice particles) can significantly influence the Special Sensor Microwave/Imager (SSM/I) radiometer observations over the TOGA-COARE region. The sea surface can introduce polarization effect in the SSM/I observations. In addition, scattering by aspherical melting snow and ice particles can also polarize the microwave radiation (Wu and Weinman, 1984, Kummerow and Weinman, 1988). Besides these extinction effects due to hydrometeors, their spatial and temporal variations can profoundly impact the SSM/I measurements. A key objective of the multi frequency ( $\nu = 19, 37$  and  $85$  GHz) dual polarization SSM/I radiometer is to retrieve rain rate taking into account all these factors. Based on radiative transfer theory we find, from a simple analysis of the SSM/I measured brightness temperature  $T_b$  and the polarization  $P_v$  (the difference between the  $T_b$  measured in the vertical and horizontal polarization) in the 19 and 37 GHz channels, there is one dominant information component (Prabhakara et al., 1992) in these low frequency channels. We can interpret this dominant information in terms of an effective area of the hydrometeors in the radiometer field of view (*fov*) that can mask the sea surface from the view of the radiometer. This interpretation is consistent with the SSM/I data that show  $P_v$  decreases as  $T_b$  increases. In these low frequency channels scattering effects are weak over the maritime areas and hence we cannot get more information about rain. Because in the 85 GHz channel of the SSM/I scattering effects over the TOGA-COARE region are quite pronounced, additional information about rain is available.

From radiative transfer theory we expect in the SSM/I channels, mainly because of absorption due to clouds and rain that contain nearly spherical particles,  $P_v$  decreases from 19 to 85 GHz. However, when there are flat melting snow particles in the clouds,  $P_{19}$  and  $P_{37}$  decrease mainly due to enhanced absorption, while  $P_{85}$  increases because of the enhanced scattering. Based on these properties, a parameter  $r = C(P_{85}/P_{37})$  can dis-

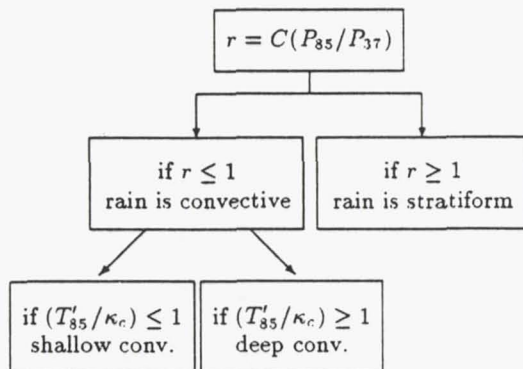
\*NASA/Goddard Space Flight Center, Greenbelt, MD, 20771, USA

†USRA NASA/Goddard Greenbelt, MD 20771, USA

‡GSC/SAIC, Laurel, MD 20707, USA



The following decision tree explains our retrieval scheme:



It may be noted that, in order to estimate three different types of rain, in the above scheme we have introduced the constants  $R'_c (=20)$ ,  $R'_s (=12)$ ,  $\kappa_c (=30)$ ,  $\kappa_s (=100)$ ,  $\kappa_a (=10)$  and the exponent 0.2 in Eq. (2). These quantities are optimized with the help of SSM/I and radar rain rate observations from a few rain events. Thus these constants are not deduced from radiative transfer theory. The complexity of the dynamics that governs the rain processes is introduced in a crude way in the scheme, i.e. Eqs. (1) to (4), through these constants.

### 3. RESULTS

We have retrieved rain rate from SSM/I data for 30 cases in the TOGA-COARE area and compared them with the radar rain rate at a resolution of 15 Km.

The correlation coefficient between retrieved and radar rain rate is, on average, about 0.6. The area average of retrieved rain rate is within about  $\pm 60\%$ . In Figs. 1 and 2 we compare rain patterns over TOGA-COARE region retrieved from SSM/I and radar for Dec. 24, 1992, and Feb. 15, 1993. Gray scale for rain rate in mm/h is given at bottom of each rain map.

In Fig. 3 the probability distribution of rain rate retrieved from SSM/I is compared with that of radar rain. From this comparison we note that, in the retrievals, the sharp rain maxima are not precisely placed and are underestimated. This is obviously a limitation of the crude resolution of the 85 GHz SSM/I data.

### 4. CONCLUSIONS

With the help of four parameters,  $r$ ,  $P_{85}$ ,  $T'_{85}$  and  $\epsilon$  deduced from SSM/I data and maximum convective and stratiform rain rates at 15 Km resolution adopted from radar observations, we have derived rain rate distribution over TOGA-COARE region. This approach demonstrates how we can tune, in the TOGA-COARE region,

a microwave rain retrieval algorithm with radar data from few rain events, and then use that tuned algorithm to retrieve rain for many events. Such a procedure can be helpful in the Tropical Rain Measurement Mission (TRMM) where there will be radar observations over a limited area, and microwave radiometer observations over a much larger region.

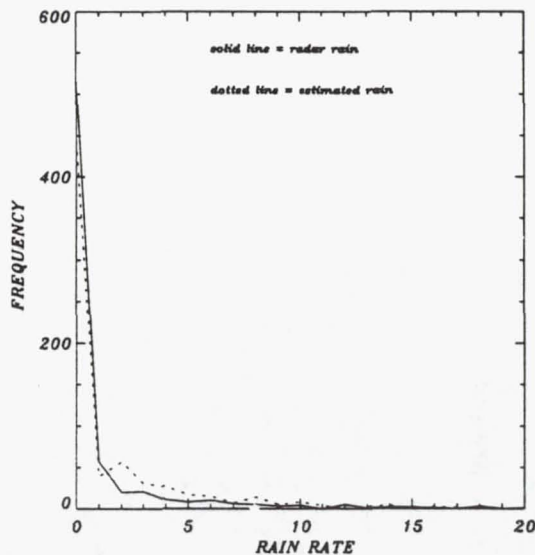


Fig. 3a Feb. 15, 1993: probability distribution of radar and SSM/I retrieved rain rate (mm/h)

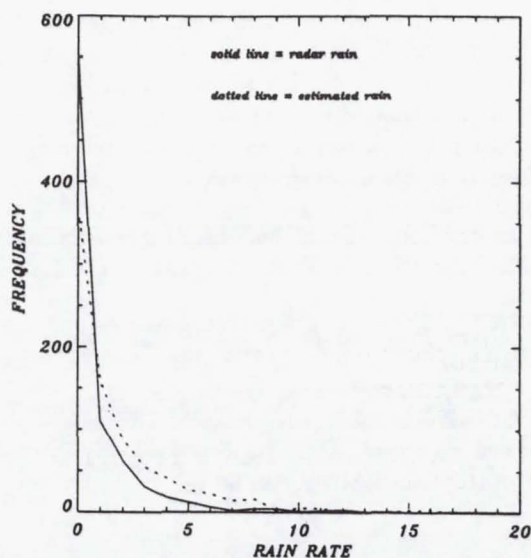


Fig. 3b Dec. 24, 1992: probability distribution of radar and SSM/I retrieved rain rate (mm/h)



## A comparison of geoid undulations for west central Greenland

Daniel R. Roman,<sup>1</sup> Beata Csathó,<sup>1</sup> Kenneth C. Jezek,<sup>1</sup> Robert H. Thomas,<sup>2</sup> William B. Krabill,<sup>3</sup> Ralph R. B. von Frese,<sup>4</sup> and Rene Forsberg<sup>5</sup>

**Abstract.** The accuracy of a new local gravity field model, GEOID94A, is examined at a site on the western Greenland ice sheet. The model, developed by the Danish National Survey and Cadastre, incorporates several new gravity data sets including an extensive amount of airborne gravity data. Model-derived geoid undulations were compared to independently determined undulations found by differencing the elevations from Global Positioning System controlled airborne laser altimetry and optical leveling surveys. Differences between the two sets of undulations were less than  $\pm 6$  cm RMS. The comparison improved ( $\pm 5$  cm RMS) when GEOID94A undulations were adjusted by local gravity observations also acquired at the site. Our comparisons demonstrate that GEOID94A adequately models the long to intermediate wavelengths of the gravity field. We conclude that GEOID94A constitutes a reliable reference model for studies of Greenland's gravity field.

### Introduction

Gravity field models provide a reference for interpreting local and regional gravity data. However, current global models (OSU91A, JGM2, etc.) are derived based on only limited observations for remote regions [Rapp *et al.*, 1991; Nerem *et al.*, 1994]. Hence the reliability and utility of these models are reduced for those regions. A new model, the Danish GEOID94A [Forsberg, 1994], incorporates data from an airborne gravity survey over most of interior Greenland. The inclusion of this new data warrants a closer examination of the model.

To evaluate GEOID94A, a comparison was made with a profile of independently determined geoid undulation differences measured along a 42 km survey line located on the western flank of the Greenland ice sheet (Figure 1). Figure 1 shows a main NE-SW trending profile with two crossing profiles. Only the NE-SW profile is examined here. The independent undulations were derived from the topographic difference of airborne laser altimetry and optical leveling survey measurements.

The laser system measured the height of the ice surface above the ellipsoid (ellipsoidal height). The leveling surveys measured the relative height change above the geoid (relative orthometric height). The difference of the two heights was the relative geoid undulation [e.g., Heiskanen and Moritz, 1967; Rapp and Pavlis, 1990].

Relative gravity observations were made at about 1 km intervals along the 42 km line. These measurements were combined with GEOID94A values through a point mass inversion technique [von Frese *et al.*, 1981] to obtain better estimates of local geoid undulations. These adjusted undulations were then compared with the laser/leveling-derived undulations.

### Airborne Oceanographic Lidar (AOL) System

Airborne laser altimetry is particularly suited for fast and precise elevation measurements in remote areas. It can provide submeter accuracy by using Global Positioning System (GPS) and inertial navigation system (INS) measurements to determine aircraft position and attitude. Laser profiling systems have only one laser element pointing at nadir and a single range measurement is performed for each laser pulse. Laser scanning systems contain movable optics or multiple laser elements. These are superior when aerial coverage, precise overflight of known surface points, or repeat flights (mapping surface changes) are needed.

NASA has developed several different airborne and spaceborne laser systems over the years. The airborne oceanographic lidar (AOL) system was originally designed and developed for shallow water bathymetry, but it has been successfully used for various applications on land (Krabill *et al.*, 1984; Krabill and Swift, 1987) and

<sup>1</sup> Byrd Polar Research Center, Ohio State University, Columbus.

<sup>2</sup> NASA Headquarters, Washington, D.C.

<sup>3</sup> Observational Science Branch, Laboratory for Hydro-spheric Processes, Goddard Space Flight Center/Wallops Flight Facility, NASA, Wallops Island, Virginia.

<sup>4</sup> Geological Sciences Department, Ohio State University, Columbus.

<sup>5</sup> National Survey and Cadastre, Geodetic Division, Copenhagen, Denmark.



## Undulations Derived From Laser Altimetry and Leveling

Relative geoid undulations were estimated by differencing coincident ellipsoidal and orthometric heights. No absolute geoid undulations could be determined from our topographic data, because the orthometric heights were referenced to an arbitrary point (N10). Undulations were computed for both leveling lines using the six AOL flights (12 combinations). As an example, the one computed using the September 18, 1991, AOL flight along the 1991 leveling line is shown in Figure 5.

Also shown are estimates of the geoid undulations derived by differencing the simultaneously acquired surface GPS measurements (positions noted in Figure 1) and optical leveling data sets [Sohn *et al.*, 1994]. The good agreement between the AOL- and GPS-derived undulations suggested that there were minimal time dependent processes, such as variable snow accumulation, affecting the study.

Lines were fit to the AOL/leveling-derived geoid undulations (Table 1). The slope of the fitted line, its bias relative to N10, the RMS of the fit, and the total height difference over the 42 km section have been computed for the different AOL/leveling combinations. The slope of the fitted lines approximated the slope of the local geoid undulations. The RMS error of the fit was due to errors in AOL and leveling heights. The causes of the large (20 cm) differences in biases between AOL elevation profiles were discussed above.

We estimated the AOL/leveling-derived geoid undulations in the following fashion. The biases calculated in Table 1 were removed from the data and then all the 1991 and 1992 observations are averaged. The random noise is reduced by using a 13-term moving average filter, and the data set is thinned by calculating the undulations only at the gravity station positions.

In Figures 6a and 6b, the relative undulations are plotted using the averaged AOL data and the 1991 and 1992 leveling data, respectively. The smoothed AOL/leveling-derived undulations are shown with the thick line. For reference, the original (unsmoothed) AOL/leveling-derived undulations are overplotted in a dotted line. The individual gravity stations are shown as triangles. The gravity-adjusted GEOID94A derived undulations are plotted as a dashed-dotted line for comparison. The RMS difference was  $\pm 5$  cm between the gravity-adjusted GEOID94A undulations and the 1992 AOL/leveling-derived undulations. The RMS difference for the 1991 data set comparison was  $\pm 8$  cm. Biases between the adjusted GEOID94A-derived undulations and the AOL/leveling-derived undulations were caused by the selection of N10 as an arbitrary reference height point. Consequently, biases should be ignored.

The 1991 AOL/leveling-derived undulations included a 10 km wavelength feature with a 15 cm amplitude (Figure 6a). This wavelength corresponds to the glacier surface topography. It is not observed in the 1992 undulations. We attributed this feature to operator errors

that occurred during the more difficult 1991 measurements season. Subsequent discussion will focus on the 1992 data set.

## Comparisons

Gravity-adjusted GEOID94A undulations (Figure 7a) are compared to the 1992 AOL/leveling-derived undulations (Figure 7b). The residuals are shown in Figure 7c. The slopes of the two geoid undulation profiles are similar (Figures 7a and 7b). The height difference between the ends of the residual profile is about 10 cm (Figure 7c). The relatively large 20 cm signal approximately 10 km south of station N10 (to the left in Figure 7c) is located near the stations that had incompletely removed tares. The RMS difference between the gravity-adjusted GEOID94A undulations and the 1992 AOL/leveling-derived undulations is  $\pm 5$  cm.

The differences between the GEOID94A model undulations uncorrected for observed gravity (Figure 8a) and the 1992 AOL/leveling-derived undulations (Figure 8b) are shown in Figure 8c. Many of the high-frequency features observed in the residuals in Figure 7c are seen in Figure 8c. We attributed the 10 km wavelength features in Figures 7c and 8c to leveling uncertainties and stochastic changes in snow accumulation patterns weakly coupled with surface topography. These 10 km features were similar to those observed in the 1991 leveling data (Figure 6a) but not of the same amplitude.

The height difference between the ends of the residual profile is about 20 cm (Figure 8c). A distinct slope from the southern to the northern ends of the profile (left to right in Figure 8c) is more clearly visible than in Figure 7c. The RMS difference between the GEOID94A model undulations (without gravity observations) and the 1992 AOL/leveling-derived undulations is  $\pm 6$  cm.

## Conclusions

Our comparisons show that the GEOID94A model approximates the gravity field in our study area for intermediate and long wavelengths ( $\pm 6$  cm RMS differences). By using additional local gravity data to adjust GEOID94A, we observe a better comparison because a small slope and bias in the modeled field is removed ( $\pm 5$  cm RMS differences). We conclude that the GEOID94A undulations adequately approximate the gravity field in intermediate and long wavelengths. Inclusion of our local gravity data appears to correct a shorter wavelength term, resulting in a small improvement in the predicted undulations.

The gravity data discussed in this study were collected as part of a much larger and ongoing NASA project that has now acquired surface topography and surface gravity data around the entire Greenland Ice Sheet. The small, centimeter scale differences detected in our comparison between modeled and measured undulations indicate that GEOID94A will provide a satisfactory reference model for incorporating these new data in studies of Greenland's subglacial crust.



# Estimation of Bare Surface Soil Moisture and Surface Roughness Parameter Using L-band SAR Image Data

Jiancheng Shi, *Member, IEEE*, James Wang, Ann Y. Hsu, Peggy E. O'Neill, and Edwin T. Engman

**Abstract**—An algorithm based on a fit of the single-scattering Integral Equation Method (IEM) was developed to provide estimation of soil moisture and surface roughness parameter (a combination of rms roughness height and surface power spectrum) from quad-polarized synthetic aperture radar (SAR) measurements. This algorithm was applied to a series of measurements acquired at L-band (1.25 GHz) from both AIRSAR (Airborne Synthetic Aperture Radar operated by the Jet Propulsion Laboratory) and SIR-C (Spaceborne Imaging Radar-C) over a well-managed watershed in southwest Oklahoma. Prior to its application for soil moisture inversion, a good agreement was found between the single-scattering IEM simulations and the L band measurements of SIR-C and AIRSAR over a wide range of soil moisture and surface roughness conditions. The sensitivity of soil moisture variation to the co-polarized signals were then examined under the consideration of the calibration accuracy of various components of SAR measurements. It was found that the two co-polarized backscattering coefficients and their combinations would provide the best input to the algorithm for estimation of soil moisture and roughness parameter. Application of the inversion algorithm to the co-polarized measurements of both AIRSAR and SIR-C resulted in estimated values of soil moisture and roughness parameter for bare and short-vegetated fields that compared favorably with those sampled on the ground. The root-mean-square (rms) errors of the comparison were found to be 3.4% and 1.9 dB for soil moisture and surface roughness parameter, respectively.

**Index Terms**—Algorithm, soil moisture, surface roughness, synthetic aperture radar (SAR).

## I. INTRODUCTION

SOIL moisture is a key parameter in numerous environmental studies, including hydrology, meteorology, and agriculture. It plays an important role in the interactions between the land surface and the atmosphere, as well as the partitioning of precipitation into runoff and ground water storage. In spite of its importance, soil moisture has not found a widespread application in the modeling of hydrological and biogeochemical processes and related ecosystem dynamics, in part because soil moisture is a difficult parameter to measure on a large area, cost-effective, and routine basis. However, recent advances in microwave remote sensing have demonstrated the potential to measure soil moisture quantitatively on bare and short vegetated surfaces [1]. This raises the feasibility

of developing algorithms for the retrieval of this important parameter through microwave remote measurements.

It is well known that return signals from synthetic aperture radar (SAR) are affected by surface characteristics such as the roughness, correlation length, and dielectric constant of the soil. Some earlier studies [2], [3] using single frequency and single polarization SIR-B (Shuttle Imaging Radar-B) imagery could only describe the dependence of backscattering coefficient  $\sigma^\circ$  on these surface parameters separately. Estimation of surface soil wetness was usually obtained by employing an empirical relationship to convert the measured  $\sigma^\circ$  into volumetric soil moisture  $m_v$  [4]. The inversion of soil moisture information from radar backscatter became more rigorous after the availability of polarimetric radar data. For example, Oh *et al.* [5] developed a model to estimate  $m_v$  and rms roughness height  $s$  from simultaneous ratio measurements of  $\sigma_{hh}^\circ/\sigma_{vv}^\circ$  and  $\sigma_{hv}^\circ/\sigma_{vh}^\circ$ , where the subscripts  $h$  and  $v$  stand for horizontal and vertical polarizations, respectively, in either transmit or receive mode of radar operation. The model is based on the data collected by their truck-mounted scatterometer system over bare soils of different roughness and moisture conditions. Its applicability to SAR imagery remains to be verified.

More recently, Dubois *et al.* [6] developed an empirical model that only requires measurements of  $\sigma_{hh}^\circ$  and  $\sigma_{vv}^\circ$  at a frequency between 1.5 and 11 GHz to retrieve both rms roughness height  $s$  and soil moisture  $m_v$  from bare soils. They used two sets of ground based scatterometer data collected by Oh *et al.* [5] and by the University of Berne's RASAM [7] system. They applied the new model to the L-band data acquired by both AIRSAR and SIR-C over a test site in Chickasha, Oklahoma and found a reasonable agreement between the retrieved and measured values of  $m_v$  and  $s$ .

Both of these empirical models did not take into account the surface power spectrum which is closely related to the surface roughness correlation function and correlation length. This is not consistent with all theoretical surface backscattering model predictions; i.e., the backscattering coefficients are sensitive not only to  $m_v$  and  $s$  but also to the surface roughness power spectrum. In addition, these empirical models developed from a limited number of observations might have site-specific problem due to the nonlinear response of backscattering to the soil moisture and surface roughness parameters.

Besides the empirical models described above, progress in theoretical modeling such as the Integral Equation Method (IEM) [8], [9] offers an alternative approach for the retrieval of  $m_v$  from SAR data. Although the IEM model is valid for a wider range of surface roughness conditions when

Manuscript received December 5, 1995; revised December 30, 1996.

J. Shi is with the Institute for Computational Earth System Science, University of California, Santa Barbara, CA 93106 USA (e-mail: shi@icess.ucsb.edu).

J. Wang, A. Y. Hsu, P. O'Neill, and E. T. Engman are with the Laboratory for Hydrospheric Processes, NASA Goddard Space Flight Center, Greenbelt, MD 20771 USA.

Publisher Item Identifier S 0196-2892(97)05512-5.



soil conditions, sometimes accompanied by standing water, could be found in a number of places. The  $m_v$  image on June 10 (at the first row and the first column) shows values in excess of 24% (in red and green) for a number of fields. By June 18 (at the third row and the second column),  $m_v$  values from most of these fields decrease to less than 12% (in light brown and yellow). It clearly shows the trend of drying down situation. In addition, the number of pixels that cannot be inverted to  $m_v$  by the algorithm increases from near range to far range indicating the effect of vegetation cover to the algorithm as a function of incidence angle. The images of the inferred surface roughness parameter  $S_R$  (right two columns) generally show a decrease with slant range as a result of its strong dependence on  $\theta$ . This is because  $S_R$  is a product of  $(ks)^2$  and the surface power spectrum  $W$ . The patterns of the inferred  $S_R$  show little change with time. There are exceptions for some vegetated fields where the estimated  $S_R$  values can not be trusted, however. For example, the region with green color on the June 10 image (pointed with a white color arrow on the third and fourth columns) were covered by healthy corn. The algorithm apparently overestimates  $S_R$  on June 10 and, thereafter, could not provide a solution for an increasing number of pixels as the soils became drier.

Fig. 11 shows the spatial distribution of  $m_v$  retrieved from the SIR-C measurements over a region of about 10.7 km by 12.6 km on April 12, 13, 15–17 and 18, of 1994. The time sequence of these six images of  $m_v$  goes from left to right in the first row and continues on to the second row in the same order. These images are geometrically corrected and geo-coded. The color codes for  $m_v$  values are again specified in Table V. The moisture condition of the soil during this series of SIR-C measurements was very similar to that of AIRSAR flights in June 1992. During April 10–11, a moderate amount of rain (about 2 cm on average) fell over most of the Little Washita watershed. No rainfall occurred thereafter and throughout the entire mission. Thus, the whole region underwent a drying-down sequence as clearly displayed by the six  $m_v$  images. There was a significant decrease in  $m_v$  from April 12 (image on top left) to April 18 (image on bottom of right), as most pixels initially in red, green and blue changed to brown and yellow.

## VI. CONCLUSION

An algorithm based on the regression analysis of the simulated surface backscattering coefficients by the single scattering IEM model was developed to provide estimation of soil moisture and surface roughness parameter from L-band SAR co-polarized measurements over bare and short vegetated fields. Although the multiple scattering terms in the original expression for backscattering coefficients have been ignored, the single scattering IEM remained quite complex and its simplification was deemed necessary for practical applications. This simplification procedure presented in this paper took the form of a regression between the calculated backscattering

coefficients and surface parameters (i.e., soil moisture, rms roughness height, surface correlation function and correlation length). The results were equations that would relate the backscattering coefficients directly with surface parameters through some constants depending only on the incidence angle. The inverse models were checked against the single scattering IEM for its applicability by comparing the values of calculated backscattering coefficients over a wide range of soil moisture and surface roughness conditions. By going through a series of sensitivity tests and a consideration of SAR calibration accuracy, it was found that the co-polarized backscattering coefficients and their combinations were the best measurements for input to the algorithm for the retrieval of surface parameters. It was also established that the absolute calibration accuracy of both AIRSAR and SIR-C [16]–[18] was adequate for providing a reasonable estimation of soil moisture and roughness parameters.

This algorithm was applied to a series of AIRSAR and SIR-C measurements obtained over the Little Washita River watershed near Chickasha, Oklahoma in June 1992, and April and October 1994. The results from this effort were summarized in two different ways. First, the values of retrieved soil moisture and surface roughness parameter for a number of bare and short-vegetated fields were compared with those sampled on the ground in near concurrence with the AIRSAR and SIR-C measurements. A reasonable agreement was found between the retrieved and measured values. The rms errors of the comparison were estimated to be 3.4% and 1.9 dB for soil moisture and surface roughness parameter, respectively. Next, the retrieved surface parameters on a regional scale were examined for their temporal changes. Two dry-down sequences, one derived from AIRSAR measurements in June 1992 and the other from SIR-C measurements in April 1994, showed the expected changes in soil moisture in sparsely vegetated areas. The retrieved surface roughness parameter remained relatively constant with time in these areas as expected. However, the algorithm either failed to provide a solution or gave unreliable estimation of surface parameters over regions associated with moderate or tall vegetation.

It is concluded from this study that the algorithm derived from the regression analysis of the data generated by the single scattering IEM could provide a reasonable estimation of soil moisture and roughness parameters from co-polarized SAR measurements over bare and sparsely vegetated surfaces. The main advantage of the algorithm is that the regression analysis was performed on a large data set simulated for a wide range of surface parameters at very fine intervals, it is expected not to have the site-specific problem commonly associated with an empirical model derived from a limited observations. However, it will be necessary to test the algorithm on other test sites with SAR and ground measurements to determine its usefulness in different areas. Furthermore, since its applicability is currently limited to bare or sparsely vegetated regions, the algorithm will have to be improved by taking into account the effect of vegetation in order to have a wider range of applications.



# A Microwave Technique for Mapping Ice Temperature in the Arctic Seasonal Sea Ice Zone

Karen M. St. Germain, *Member, IEEE*, and Donald J. Cavalieri

**Abstract**—A technique for deriving ice temperature in the Arctic seasonal sea ice zone from passive microwave radiances has been developed. The algorithm operates on brightness temperatures derived from the Special Sensor Microwave/Imager (SSM/I) and uses ice concentration and type from a previously developed thin ice algorithm to estimate the surface emissivity. Comparisons of the microwave derived temperatures with estimates derived from infrared imagery of the Bering Strait yield a correlation coefficient of 0.93 and an RMS difference of 2.1 K when coastal and cloud contaminated pixels are removed. SSM/I temperatures were also compared with a time series of air temperature observations from Gambell on St. Lawrence Island and from Point Barrow, AK weather stations. These comparisons indicate that the relationship between the air temperature and the ice temperature depends on ice type.

## I. INTRODUCTION

POLAR SEA ICE covers approximately 7% of the world's oceans. In the Arctic, the sea ice spatial extent varies between a minimum of  $7.8 \times 10^6$  km<sup>2</sup> in summer and a maximum of  $14.8 \times 10^6$  km<sup>2</sup> in winter. Sea ice acts as an insulator between the relatively warm ocean and the cold Arctic atmosphere during the winter and, as such, controls the heat exchange between ocean and atmosphere. Sea ice temperature is needed to calculate both the conductive heat flux through the ice and the heat flux from ice to atmosphere.

Sea ice surface temperature estimation has largely been the domain of satellite-based infrared sensors such as the AVHRR [1], [2]. The algorithms for these sensors provide excellent estimates under clear air conditions but are susceptible to contamination by cloud cover and ice crystal precipitation conditions, both of which are common in the Arctic [3], [4]. A temperature product derived from microwave frequencies would be more robust because microwaves pass easily through the polar atmosphere. Of course, the price of this advantage is the relatively poor spatial resolution. With this trade-off in mind, a microwave-derived temperature field should be viewed as a complement to Advanced Very High Resolution Radiometer (AVHRR) derived fields.

Manuscript received September 11, 1996; revised March 6, 1997. This work was supported in part by the NASA-ASEE Summer Faculty Fellowship Program at the Goddard Space Flight Center, the NASA Polar Program (RTOP 622-82-13), and the NASA EOS Project (229-04-15).

K. M. St. Germain is with the Remote Sensing Division, Code 7223, Naval Research Laboratory, Washington, DC 20375-5351 USA, on leave from the Department of Electrical Engineering, University of Nebraska, Lincoln, NE 68508 USA (e-mail: ksaint@ultraimg.nrl.navy.mil; kst.germain@unl.edu).

D. J. Cavalieri is with the Laboratory for Hydrospheric Processes, Code 971, NASA Goddard Space Flight Center, Greenbelt, MD 20771 USA (e-mail: don@cavalieri.gsfc.nasa.gov).

Publisher Item Identifier S 0196-2892(97)04483-5.

Deriving a remotely sensed temperature field requires the ability to estimate the ice emissivity at the appropriate frequency. This is more difficult at microwave frequencies than at infrared frequencies. There are many types of sea ice, from the thin ice types (grease ice, nilas, pancake ice, etc.) to thick multiyear ice. The physical characteristics of sea ice are determined by the environmental conditions that exist as the ice forms and ages. The microwave emission of each type depends on the ice structure and dielectric constant, which is a function of both the temperature profile and salinity. Because salinity and structure change over the life cycle of an ice floe, it is possible to classify ice in terms of three broad categories; thin ice, first-year ice and multiyear ice, which are distinguishable from satellite-based sensors [5], [6]. The thin ice can be categorized further by stage of development [7], [8]. Typically the characterization is accomplished through the use of ratios, which are independent of temperature. The algorithm described herein uses microwave radiances as measured by the Defense Meteorological Satellite Program (DMSP) Special Sensor Microwave/Imager (SSM/I) and the characterization provided by previously developed algorithms to estimate the scene emissivity. The emissivity and a simple radiative transfer model is then used to calculate the ice temperature.

## II. THEORETICAL CONSIDERATIONS

Radiative transfer theory predicts that the brightness temperature observed by a satellite based radiometer will be:

$$T_B = \epsilon T_S e^{-\kappa} + T_{Up} + (1 - \epsilon) T_{Down} e^{-\kappa} + (1 - \epsilon) T_{Cosmic} e^{-2\kappa} \quad (1)$$

where

$T_B$	measured brightness temperature;
$\epsilon$	total surface emissivity;
$T_S$	physical temperature of the radiating portion of the ice;
$\kappa$	atmospheric opacity;
$T_{Up}$	total atmospheric upwelling radiation;
$T_{Down}$	total atmospheric downwelling radiation;
$T_{Cosmic}$	cosmic background radiation, 2.7 K at microwave frequencies.

The upwelling and downwelling atmospheric radiation can be approximated as

$$\begin{aligned} T_{up} &\cong T_{Down} \\ &\cong T_{Atm} \\ &= \langle T \rangle (1 - e^{-\kappa}) \end{aligned} \quad (2)$$



the temperatures retrieved from the SSM/I for first year ice north of the Bering Strait are remarkably close to the AVHRR derived temperatures. However, buoys in the Beaufort and Chukchi Seas indicate air temperatures of 242.4 and 249.2 K, respectively, indicating that the air temperatures are much colder than the AVHRR derived skin temperature. This seems to be inconsistent with our expectation. However, because of the particular coastal station data that were used to develop the AVHRR algorithm [2], it is possible that the AVHRR temperatures derived over pack ice are too warm. Alternately, ice crystal precipitation in the region also could cause the AVHRR derived temperatures to be several degrees too warm [4].

Recall that within a 25-km SSM/I pixel, there is presumably a mix of ice and water. We use an ice concentration algorithm to obtain an areal measure in percent of the amount of sea ice within the pixel. The physical temperature of the open water is assumed to be at the freezing point. We are now left with the problem of determining the physical temperature of a mix of sea ice types. Because we limit the application of the algorithm to seasonal sea ice zones, the ice, by definition is first year or younger. We make use of an ice type algorithm to determine the emissivity and determine the ice temperature. This ice temperature, then, represents an average temperature for the mix of first-year ice and new ice or a 100% young ice cover. There is an ambiguity within the ice type algorithm. For example, we cannot discriminate between a 50-50 mix of first year ice and new ice or a 100% young ice cover. We do not think this is a serious limitation, because the heat losses in both cases are approximately equal.

A second question centers on the atmospheric correction. To assess the importance of including a model of the atmosphere in this algorithm, we calculated the error in retrieved temperature that would result from the use of a simpler, first order algorithm such as the one used by Gloersen *et al.* [9] based on the SMMR 6.6-GHz channel. At 19 GHz, such an approach could yield significant errors whenever the scene emissivity is low because of contamination principally by atmospheric water vapor. Fig. 8 shows the retrieval error, as a function of actual surface temperature, resulting from a temperature retrieval algorithm that simply divided brightness temperature by emissivity. The parameter is ice concentration where, of course, lower concentrations imply a decrease in scene emission. This plot indicates that the errors in retrieved temperature could be as much as 5 K if the effect of the atmosphere is ignored. Once again, this model assumes a vapor saturated atmosphere. If the atmosphere deviates from this model, then errors would also be introduced.

Currently, this algorithm has been tested only for the Beaufort/Bering/Chukchi region of the Arctic. This is the simplest area to study because we can be reasonably sure that any pixel passing the Spectral Gradient Ratio threshold test in the Thin Ice Algorithm does not contain any multiyear ice. The same is not necessarily true in the Greenland or Kara Seas. Therefore, more analysis, and perhaps refinement, is necessary before this approach can be considered applicable to the entire Arctic seasonal ice zone. The approach also has not been tested

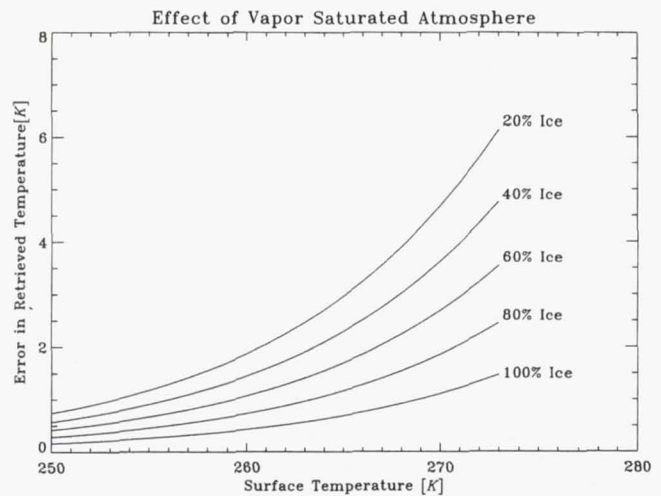


Fig. 8. Error introduced in temperature retrieval if the effect of the atmosphere is ignored. The parameter is ice concentration, where low ice concentration corresponds to low surface emissivity.

yet on Antarctic sea ice, and we expect that refinement will be needed there as well.

## VI. CONCLUSIONS

Here we present a method for measuring the physical temperature of sea ice. The technique uses a thin ice algorithm developed previously for obtaining ice concentration and ice type information that is used to compute an effective surface emissivity. This, when combined with the observed radiometric temperature from the SSM/I 19 GHz vertically polarized channel, allows for a solution for the physical temperature of the sea ice within the scene. The approach is similar to one taken by Gloersen *et al.* [9] that used the 6 GHz SMMR channel. Although the SSM/I 19.4 GHz channel does see some variability due to the atmosphere, the spatial resolution is significantly better than that possible at the lower frequency, and the emitting layer of the ice is significantly thinner.

The temperature product has been compared with skin temperature estimates derived from the AVHRR and air temperatures from Gambell Station and Point Barrow Station. In thin ice regions, the passive microwave and infrared derived temperatures are strongly correlated when cloud cover is not present, with the exception of pixels adjacent to land, which, for the SSM/I, appear to be contaminated by mixed pixel effects. In the presence of clouds, the correlation between the temperatures decreases significantly, with the AVHRR temperatures becoming significantly colder. In the cloud-free case, the RMS difference between the two estimates is 2.1 K, which is within the estimated uncertainty of the AVHRR temperatures. A linear regression suggests a bias of less than 0.3 K, which means that for thin ice, the microwave and infrared temperatures are comparable.

The temperature estimate provided by the SSM/I is more difficult to interpret than the skin temperature provided by the AVHRR and should, therefore, be used with the ice classification in mind. Currently, this product has been evaluated only in the Pacific seasonal sea ice zone, and further work is



## NOAA AVHRR land surface albedo algorithm development

D. L. TOLL

Hydrology Branch (Code 974), Laboratory for Hydrospheric Processes,  
NASA/GSFC, Greenbelt, MD 20771, U.S.A.

D. SHIREY

Department of Geography, University of Maryland, College Park, MD 20742,  
U.S.A.

and D. S. KIMES

Biospheric Branch (Code 923), Laboratory for Terrestrial Physics,  
NASA/GSFC, Greenbelt, MD 20771, U.S.A.

(Received 6 February 1996; in final form 7 November 1996)

**Abstract.** The primary objective of this research is to develop a surface albedo model for the National Oceanic and Atmospheric Administration (NOAA) Advanced Very High Resolution Radiometer (AVHRR). The primary test site is the Konza prairie, Kansas (U.S.A.), used by the International Satellite Land Surface Climatology Project (ISLSCP) in the First ISLSCP Field Experiment (FIFE). In this research, high spectral resolution field spectrometer data was analyzed to simulate AVHRR wavebands and to derive surface albedos. Development of a surface albedo algorithm was completed by analysing a combination of satellite, field spectrometer, and ancillary data. Estimated albedos from the field spectrometer data were compared to reference albedos derived using pyranometer data. Variations from surface anisotropy of reflected solar radiation were found to be the most significant albedo-related error. Additional error or sensitivity came from estimation of a shortwave mid-IR reflectance ( $1.3\text{--}4.0\text{ }\mu\text{m}$ ) using the AVHRR red and near-IR bands. Errors caused by the use of AVHRR spectral reflectance to estimate both a total visible ( $0.4\text{--}0.7\text{ }\mu\text{m}$ ) and near-IR ( $0.7\text{--}1.3\text{ }\mu\text{m}$ ) reflectance were small. The solar spectral integration, using the derived ultraviolet, visible, near-IR and SW mid-IR reflectivities, was not sensitive to many clear-sky changes in atmospheric properties and illumination conditions.

### 1. Introduction

Land surface albedo is a primary control on land surface net radiation, and thus controls both the warming rate of ground and lower atmosphere, and the amount of energy expended for evapotranspiration. Sud *et al.* (1993), Laval and Picon (1986), Sud and Fennessy (1982), Vukovich *et al.* (1987), and Henderson-Sellers and Gornitz (1984) have indicated that land surface changes in albedo may significantly influence climate. The derivation of a global surface albedo monitored dynamically over time is an important objective of Earth system science (CEES 1992). In principle, the synoptic and repetitive viewing capabilities of Earth orbiting satellite sensors provide a comprehensive method for estimating and monitoring surface albedo over large areas.



clear sky changes in illumination angle and atmospheric properties. Hence, analysis of solar radiation results in tables 10 and 11 (see § 5.4) indicates time-specific solar radiation measurements are not required, but either modelled or general spectral transformation coefficients may be used for many atmospheres.

## **6. Summary and conclusions**

The NOAA AVHRR may provide spatially extensive and repetitive estimates of albedo over large areas, which are useful for surface energy balance calculations and climate modeling. The NOAA AVHRR provides repetitive cover two times a day with near daily overpasses (defined by view angle limitations), making a monitoring effort of albedo practical. Corrections for the atmosphere, clouds and radiometric calibration were not emphasized for this effort.

The following summarizes the conclusions from this study.

1. Single directional reflectance data used to estimate hemispherical reflectance yields the most significant error of the factors studied. Other factors include: AVHRR waveband to total visible and near-IR reflectance estimation, SW mid-IR and ultraviolet reflectance estimation, and spectral region reflectance integration. Correction for anisotropy of reflected solar radiation, using an appropriate conversion technique, should substantially improve results. More accurate results will be obtained with multiple directional reflectance values compared to a single directional acquisition.
2. Conversion of NOAA AVHRR waveband to broad band visible and near-IR reflectance does not provide closer results to the reference data. Analysis of coefficients for various grasses and agriculture indicate similar results. Preliminary results indicate that the spectral transformation coefficients may be representative for broad selection of herbaceous land cover (i.e., grasses and agriculture).
3. Visible (0.4–0.7  $\mu\text{m}$ ) or AVHRR band 1 (red) reflectance may be used to estimate an ultraviolet reflectance for albedo estimation. Although ultraviolet reflectance only comprises approximately 5 per cent of the reflective solar radiation, the high leaf absorption of ultraviolet radiation (and subsequently the small proportion of ultraviolet radiation at the sensor) combined with similar leaf optical properties for visible radiation, result in a negligible effect on albedo when using a visible reflectance to represent solar reflectance at less than 0.70  $\mu\text{m}$ .
4. Neglecting SW mid-IR reflectance (i.e., assuming AVHRR band 2 represents the reflected radiation above 0.7  $\mu\text{m}$ ) may introduce albedo errors from ~10–20 per cent, worsening with increased vegetation density. The AVHRR visible reflectance may be used in a transformation to represent a mid-IR reflectance. Adding a near-IR reflectance does not provide a significantly improved estimator of mid-IR, and does not adequately represent the spectral variation of SW mid-IR radiation for plant canopies.
5. Modelled or representative estimates of the incident global radiation at the surface, categorized by the major spectral region in the analysis (ultraviolet, visible, near-IR, and SW mid-IR) may be used to integrate the derived hemispherical reflectivities for estimating albedo. There is a strong compensating effect between diffuse and direct radiation for many clear sky atmospheres,



## Altimeter Estimation of Sea Surface Wind Stress for Light to Moderate Winds

DOUGLAS VANDEMARK

*NASA/Goddard Space Flight Center, Wallops Island, Virginia*

JAMES B. EDSON

*Woods Hole Oceanographic Institution, Woods Hole, Massachusetts*

BERTRAND CHAPRON

*Institut Français de Recherche pour l'Exploitation de la Mer, Plouzane, France*

3 May 1996 and 10 September 1996

### ABSTRACT

Aircraft altimeter and in situ measurements are used to examine relationships between altimeter backscatter and the magnitude of near-surface wind and friction velocities. Comparison of altimeter radar cross section with wind speed is made through the modified Chelton–Wentz algorithm. Improved agreement is found after correcting 10-m winds for both surface current and atmospheric stability. An altimeter friction velocity algorithm is derived based on the wind speed model and an open-ocean drag coefficient. Close agreement between altimeter- and in situ-derived friction velocities is found. For this dataset, quality of the altimeter inversion to surface friction velocity is comparable to that for adjusted winds and clearly better than the inversion to true 10-m wind speed.

### 1. Introduction

Relationships between ocean wind speed, wind stress, and microwave remote sensing are both elementary and complicated. Because of the relative ease and availability of wind speed measurements, ocean wind speed algorithms for the scatterometer, altimeter, and radiometer have been the first developed. Wind models for these three sensors have been demonstrated with uncertainty of order  $2 \text{ m s}^{-1}$  (Stoffelen and Anderson 1993; Witter and Chelton 1991; Wentz 1992). The physics behind these semiempirical wind algorithms is quite different for each sensor. For each case, it is clear they cannot directly map their respective measurement to the 10-m wind speed. For radar scatterometers, known contamination of wind speed inversion can come from nonwind geophysical effects such as atmospheric stratification, current or SST fronts, surfactant, and sea state. To account for these influences, some have suggested relating scatterometer measurements directly to surface friction velocity  $u_*$ , a measure of wind stress that implicitly carries a response to near-surface phenomena. A major limitation here has been that wind stress measurements are not available on anywhere near the scale

of buoy and ship wind speed data. Field data have just recently become available (Colton et al. 1995; Weismann et al. 1994) that indicate Ku-band scatterometer backscatter is more closely correlated with  $u_*$  than with 10-m wind speed.

A clear connection between altimeter radar cross section ( $\sigma_0$ ) and sea surface wind stress is not yet established. Wu (1992) proposed an altimeter algorithm for wind stress based on the physical relationship of altimeter response to changes in ocean ripples and on examination of the modified Chelton–Wentz (MCW) (Witter and Chelton 1991) altimeter wind speed retrieval algorithm. However, aside from several studies on sea state effects (Glazman and Greysukh 1993; Queffeulou et al. 1995), there is little published data to support or deny measurable nonwind effects on the altimeter–wind speed relationship. This may be because of a scarcity of altimeter measurements collected over well-instrumented research sites. Nonetheless, theory suggests a strong parallel between surface wind stress and altimeter backscatter in that both are formed through partial integration of the wave slope distribution (Brown 1979; Kitaigorodskii 1973). If a satellite altimeter can reliably retrieve wind stress, this may aid refinement of other satellite sensor and general circulation model wind stress estimates.

Recently, aircraft altimeter backscatter data were collected over open-ocean research platforms during the High Resolution Remote Sensing program. Our objec-

---

Corresponding author address: Douglas Vandemark, NASA/GSFC, Bldg. N-159, Wallops Island, VA 23337.  
E-mail: vandemark@gsfc.nasa.gov



ficients ( $\alpha = 16.5$ ,  $\beta = 3.1$ ) suggested by Wu for optical mean-square slope data of Hwang and Schemdin (1988). These values predict very strong slope growth (suppression) with instability (stability). As notably, they suggest a *large* departure between optically derived slope and wind stress response. The solid curve in Fig. 4b is that suggested for C-band (Keller et al. 1989), 45° incidence, scatterometer  $\sigma_0$  ratio data; having a much smaller value in unstable conditions ( $\alpha = 0.50$ ,  $\beta = 2.75$ ). These values also appear too drastic for the present  $S_r$  data. Best fit for the Ku-band altimeter data is  $\alpha = 0.17$  and  $\beta = 0.47$  (dashed curve) with large scatter that clearly limits our confidence in these values. However, the data do indicate less departure than for the optical and scatterometer results.

The considerable scatter found in Fig. 4 points to the limited size and constraints of our dataset. Further data are needed to confirm or deny the slightly differing responses of altimeter  $mss_{ku}$  and direct covariance  $u_*$  measurements to these nonwind parameters. The main point is that there is not a big divergence between them; nominally less than 15% for a broad range of both surface current and stability conditions.

For atmospheric stability, these data appear to support the idea of enhancement (suppression) with atmospheric instability (stability) beyond that of friction velocity's response, but altimeter-derived  $u_*$  has much closer agreement with in situ  $u_*$  than was found for scatterometer or optical slope measurements. We note that one primary difference between sensors is that the microwave altimeter is somewhat "blind" to very short-scale gravity capillary waves (Brown 1978), while the scatterometer and optical slope sensor are very sensitive to them. Thus, previous results (Wu 1991) may imply this narrow gravity-capillary wave regime (waves less than approximately 6-cm wavelength) is more responsive to stratification effects than are the respective integrated slope domains that are thought to dictate altimeter  $\sigma_0$  (Brown 1978) and wind stress (Kitaigorodskii 1973).

#### 4. Concluding remarks

Results of the Ku-band altimeter-in situ wind speed comparisons indicate that MCW-derived altimeter wind speed is most closely related to an adjusted 10-m wind speed, not the true wind speed. Adjusting wind estimates for surface current and atmospheric stability effects provided clear improvement in the wind data comparison. There was a factor of 2 reduction in bias and of 1.6 in rms error. This result is not fully supported or agreed upon in the literature. For example, when developing a statistical altimeter wind model, Freilich and Challenor (1995) assumed a monotonic relationship between wind speed and  $\sigma_0$  and also assumed near-surface influences are negligibly small. The present dataset was of limited size, but collected over a region with strong current and for a fairly broad range of stratification. These local nonwind influences will be present in a global sampling, and our data suggest they will be an error source in satellite altimeter wind speed retrieval.

Perhaps the more fundamental finding is derived from

the altimeter-in situ friction velocity comparisons. These measurements indicate that Ku-band altimeter  $\sigma_0$  is more highly correlated with  $u_*$  than with the 10-m wind speed. A single parameter (current, stratification, or other ancillary data not required) mapping between altimeter  $\sigma_0$  and  $u_*$  shows very good agreement for  $u_*$  ranging from 0.0 to 0.4 m s<sup>-1</sup>. A drag coefficient from Wu (1992) and the MCW wind speed algorithm were used for our altimeter- $u_*$  algorithm (3), but we find that the general characteristics of Table 1 hold for other light-to-moderate wind altimeter routines (e.g., Brown et al. 1981) and drag coefficients (e.g., Smith 1988). In summary, these field data suggest that Ku-band altimeter backscatter data would be better used for direct wind stress derivation rather than for wind speed.

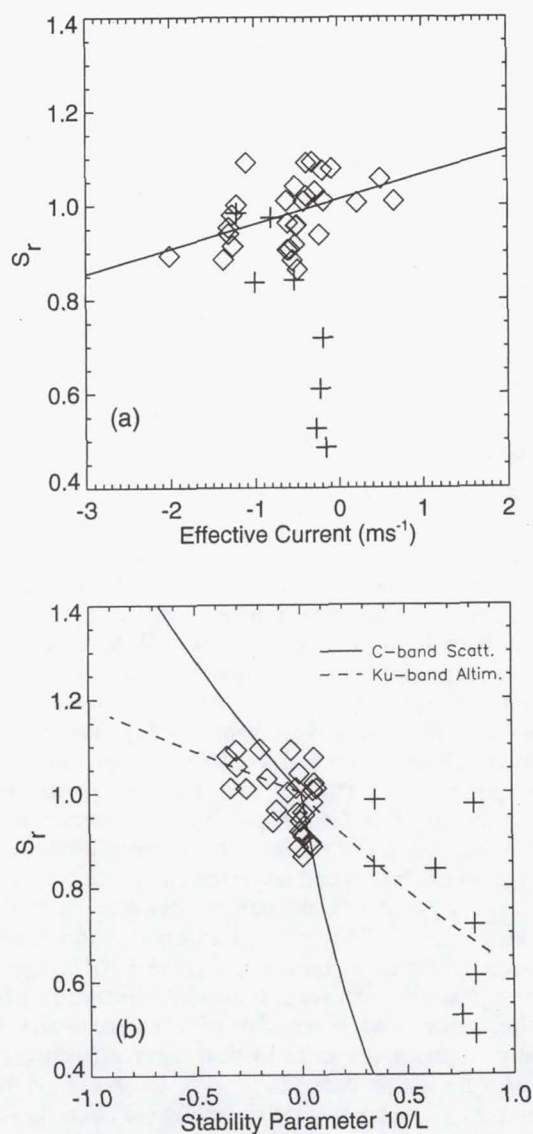


FIG. 4. Environmental parameters (a) effective current, and (b) stability vs altimeter measurement deviation, Eq. (5), from the  $u_{*MCW}$  algorithm. Measurements in stable stratification are denoted with the "+" symbol. In (a) a linear regression for  $S_r$  vs current is shown. In (b), solid curve is (6) and (7) with exponents from the C-band scatterometer. Dashed curve is the present data fit to (6) and (7) giving  $\alpha = 0.17$  and  $\beta = 0.47$ .



# A Comparison of Soil Moisture Retrieval Models Using SIR-C Measurements over the Little Washita River Watershed

J. R. Wang,\* A. Hsu,† J. C. Shi,‡ P. E. O'Neill,\* and E. T. Engman\*

**S**IR-C L-band measurements over the Little Washita River watershed in Chickasha, Oklahoma during 11–17 April 1994 have been analyzed for studying the change of soil moisture in the region. Two algorithms developed recently for estimation of moisture content in bare soil were applied to these measurements and the results were compared with those sampled on the ground. There is a good agreement between the values of soil moisture estimated by either one of the algorithms and those measured from ground sampling for bare or sparsely vegetated fields. The standard error from this comparison is on the order of  $0.05\text{--}0.06\text{ cm}^3/\text{cm}^3$ , which is comparable to that expected from a regression between backscattering coefficients and measured soil moisture. Both algorithms provide a poor estimation of soil moisture or fail to give solutions to areas covered with moderate or dense vegetation. Even for bare soils the number of pixels that bear no numerical solution from the application of either one of the two algorithms to the data is not negligible. Results from using one of these algorithms indicate that the fraction of these pixels becomes larger as the bare soils become drier. The other algorithm generally gives a larger fraction of these pixels when the fields are vegetation-covered. The implication and impact of these features are discussed in this article. ©Elsevier Science Inc., 1997.

## INTRODUCTION

Experimental studies on the relationship between radar backscatter and soil moisture have been conducted for nearly three decades (Ulaby and Batlivala, 1976; Ulaby et al., 1978; Dobson and Ulaby, 1986a, 1986b; Wang et al., Engman and Wang, 1987; Oh et al., 1992; Dubois et al., 1995). Most of these studies can be categorized as a forward problem because they mainly establish the correlation between radar backscattering coefficients and soil moisture with surface conditions, such as vegetation cover and roughness, as well as with other variables. For example, Ulaby and Batlivala (1976) and Ulaby et al. (1978) reported from their analyses of early ground-based scatterometer measurements over bare soils that there is a positive correlation between the backscattering coefficients ( $\sigma^\circ$ ) in the frequency range of 1–12 GHz and soil moisture. This positive correlation holds for any polarization of HH (horizontal transmit and horizontal receive), VV (vertical transmit and vertical receive), VH, or HV. At incidence angles  $>20^\circ$ , an increase in surface roughness increases the radar backscatter, but the positive correlation between  $\sigma^\circ$  and soil moisture remains. At low frequencies  $\sim 1$  GHz, the positive correlation also holds for observations over short-vegetated fields (Ulaby et al., 1979). These results received confirmation from the more recent and extensive measurements of Shuttle Imaging Radar B (SIR-B) (Dobson and Ulaby, 1986b; Wang et al., 1986). The SIR-B measurements at 1.28 GHz and HH polarization also imply that  $\sigma^\circ$  could change by as much as 10 dB when soil moisture changes from dry to wet conditions. On the other hand,  $\sigma^\circ$  could vary over a 20 dB range when surface roughness height changes from  $\sim 0$  to 4 cm (Wang et al., 1986). The changes in  $\sigma^\circ$  caused by a variety of vegetation covers could also be on the order of 15 dB (Dobson and Ulaby, 1986b). Thus, to estimate soil moisture from radar back-

\*NASA Goddard Space Flight Center, Greenbelt

†Scientific Systems and Application, Inc., Lanham, Maryland

‡Institute for Computational Earth System Science, University of California, Santa Barbara

Address correspondence to J. R. Wang, Laboratory for Hydro-spheric Processes, NASA/Goddard Space Flight Center, Code 675, Greenbelt, MD 20771.

Received 22 January 1996; revised 21 May 1996.



this effect based on the lightly vegetated fields that were sampled for soil moisture in the region given by the image in Figure 7. Here  $N_0$  and  $N_f$  resulting from applying the algorithms of Dubois et al. (1995) and Shi et al. (1995) to the SIR-C data for these six fields are plotted for 11, 12, 13, 15, 16, and 17 April. The change in  $N_0$  from day to day is due to the changes in both  $\theta$  and  $\varphi$  between the SIR-C data takes. It is clear that in four out of six days the algorithm of Shi et al. (1995) gives a higher  $N_f$  than that of Dubois et al. (1995) which suggests a poorer performance of the algorithm of Shi et al. (1995) for vegetated fields. The same conclusion is reached when the retrieval results of the SIR-C L-band data over the entire watershed are examined and shown in the bottom panel of Figure 13. For three days of 12, 13, and 15 April, the  $N_f$ 's resulted from the algorithm of Shi et al. (1995) are substantially higher than those of Dubois et al. (1995).

Referring back to Figure 6b, we notice that the parameter  $p$  (in dB) or the difference  $\sigma_{HH}^0 - \sigma_{VV}^0$  increases as  $\varepsilon$  (or  $m_v$ ) decreases. This appears to be closely associated with the observed increase in  $N_f$  (Fig. 12) as soils lose moisture in the study region, which has been discussed in the previous section in reference to Figures 8 and 10. To establish this association, we have examined all 6 days of SIR-C L-band images over the entire watershed for changes in the distribution of  $p$ . We found that the pattern of pixels with  $p \geq 0$  showed a resemblance to the black areas in the images of Figures 8 and 10, and the fraction of pixels with  $p \geq 0$  increased as soils became drier. This fraction changes from 0.26 on 12 April to 0.31 on 15 April, and to 0.47 on 17 April.

The pixels with no solution from the algorithm of either Dubois et al. (1995) or Shi et al. (1995) are not included in the averaging process to estimate  $m_v$ . When  $N_f$  is not small with respect to  $N_0$ , like the one in Figure 12a, the question arises about the representativeness of the estimated  $m_v$  values. Here we have to consider several factors. First, a substantial portion of the region under study is covered with modest or dense vegetation, which cannot be effectively dealt with by either algorithm. Many areas in the images of 12 April in both Figures 8 and 10 that are associated with low estimated  $m_v$  or large  $N_f$  belong to this category. An adequate algorithm needs to be developed in the future to deal with the estimation of  $m_v$  under vegetation cover. Next, for the bare soils, it is quite clear that by ignoring  $N_f$  pixels in the process of estimation using the algorithm of Dubois et al. (1995), we estimate  $m_v$  values larger than they should be. If we take the pixel averages of  $\sigma_{VV}^0$  and  $\sigma_{HH}^0$  by window larger than  $4 \times 8$  and then apply the algorithm, we compromise the spatial resolution of the imaging radar and also obtain lower  $m_v$  values than those which appear in Figures 9 and 12a. This will result in a general underestimation of  $m_v$  in comparison to the measured one. The algorithm of Shi et al. (1995) appears to pose a less severe problem for bare soils, but  $N_f$  is not

negligible for some days of SIR-C measurements. The problem needs to be evaluated further in the future analysis.

## CONCLUSION

Six SIR-C L-band images acquired at incidence angles of  $28^\circ$ – $50^\circ$  over the Little Washita River watershed near Chickasha, Oklahoma during 11–17 April 1994 were used to study the change of soil moisture in the region. The watershed was blessed with moderate rain showers with a total average amount of rainfall about 1.5 cm during 10–11 April and experienced no more rainfall through the rest of the 11-day SIR-C mission. The combined data set of SIR-C and ground measurements thus provides a unique means to study the dry-down of soils with an imaging radar. Two algorithms for the estimation of moisture content for bare soils recently reported in the literature were tested on this data set. The results of applying either one of the two algorithms showed a general drying of the study region from 12 April to 17 April as expected. A comparison between the estimated and measured values of soil moisture for a number of sampled fields, which were bare or lightly vegetated showed a good agreement. The standard deviation of the comparison was found to be  $\pm 0.059 \text{ cm}^3/\text{cm}^3$  or  $\pm 0.053 \text{ cm}^3/\text{cm}^3$  when either the algorithm of Dubois et al. (1995) or that of Shi et al. (1995) was used in the estimation. These values were reasonable considering that the regression between like-polarized backscattering coefficients at incidence angle of  $\sim 42^\circ$  and soil moisture gave a standard deviation of  $\sim \pm 0.05$ – $0.06 \text{ cm}^3/\text{cm}^3$ .

However, a few shortcomings were found from the application of both algorithms to the SIR-C data over our study region. First, more than 80% of the watershed is covered with vegetation. Both algorithms were developed for application to bare soils, and, when applied to moderately or densely vegetated areas in the study region, result in no solution or unreliable estimation of soil moisture. Next, even for bare soils, the number of pixels that bear no solution from the estimation process is not negligible; these pixels are particularly substantial when the algorithm of Dubois et al. (1995) is applied to dry soils. The problem could be lessened to some degree by averaging the backscattering coefficients before the application of the Dubois et al. (1995) algorithm, but this would entail a sacrifice of spatial resolution. Although the problem associated with moisture estimation for bare soils appears to be less severe in the algorithm of Shi et al. (1995), this algorithm seems to break down even for areas covered with short vegetation. An algorithm needs to be developed in the future so that moisture content can be estimated with confidence not only for bare soils but also for soils covered with moderate vegetation. Only then will a region like the Little Washita watershed benefit from radar remote sensing for hydrological applications.



# MIR Measurements of Atmospheric Water Vapor Profiles

J. R. Wang, P. Racette, and L. A. Chang

**Abstract**—Three subjects related to atmospheric water vapor profiling using the 183.3 GHz absorption line are discussed in this paper. First, data acquired by an airborne millimeter-wave imaging radiometer (MIR) over ocean surface in the western Pacific are used to estimate three-dimensional (3-D) distribution of atmospheric water vapor. The instrument's radiometric measurements with mixed vertical and horizontal polarizations require modifications to the retrieval algorithm used in the past. It is demonstrated that, after the modifications, the new algorithm can provide adequate retrieval of water vapor profiles, even though the measured data are of mixed polarizations. Next, the retrieved profiles, in terms of water vapor mixing ratio  $\rho$  (g/kg), are compared with those measured in near concurrence by dropsondes from a research aircraft in the western Pacific and by a ground-based Raman lidar at Wallops Island, Virginia. The ratio of the standard deviation to the mean  $\rho$  is found to be 0.12 at 0.25 km altitude and gradually degraded to 0.67 at the highest altitude of the retrieval of 10.25 km. Finally, the effect of the "initial guess" relative humidity profile on the final retrieved product is analyzed with respect to the condition for the convergent retrieval. It is found that the effect is minimal if the initial profile is not unrealistically different from the true one. If the initial profile is very different from the true one, the final retrieved product could be subject to a substantial error. Tightening of the convergent condition in the retrieval helped reduce magnitude of the error, but not remove it totally. It is concluded that an initial profile based on climatology is likely to provide most reliable retrieval results.

## I. INTRODUCTION

A SIX-CHANNEL, total-power, airborne millimeter-wave imaging radiometer (MIR) has recently been built jointly by NASA Goddard Space Flight Center and Georgia Institute of Technology to measure atmospheric water vapor profiles, clouds, and precipitation [1]–[2]. It measures microwave radiation at three side-band frequencies ( $183.3 \pm 1$ ,  $183.3 \pm 3$ , and  $183.3 \pm 7$  GHz) near the strong water vapor line of 183.31 GHz and at another three frequencies (89, 150, and 220 GHz) in window regions of the microwave absorption spectrum [3]. It is a cross-track scanner that covers an angular swath of 100 degrees centered at nadir. It has a temperature sensitivity ( $\Delta T$ ) of  $\leq 0.5$  K, and a measurement accuracy of  $\leq \pm 2$  K in the brightness temperature ( $T_b$ ) range of 240–300 K [2]. At  $T_b$  values  $< 240$  K, the errors of radiometric measurements

could be larger; at  $T_b \sim 80$  K, the measurement accuracy was estimated to be  $\sim \pm 3$  K [2]. The sensor was installed onto the NASA ER-2 aircraft and flown for the first time on May 14, 1992 in the coastal region of California for a satellite sensor validation program [4]. It has since participated numerous field experiments and acquired about 150 h of excellent data. Some results from these experiments have been reported by Jackson and Gasiewski [5] and Wang *et al.* [6]. The sensor was recently upgraded to include three additional channels near another strong water vapor line of 325 GHz [7].

Profiling of the atmospheric water vapor has been made with radiometric measurements from the Airborne Microwave Moisture Sounder (AMMS) in the past decade [8]–[13]. AMMS is a cross-track imager that measures microwave radiation at four frequencies of 92, 183.3,  $\pm 2$ , 183.3,  $\pm 5$ , and  $183.3 \pm 9$  GHz. Because of the available microwave technology in the late 1970's and the system design philosophy at that time, the sensor inherently had a poor  $\Delta T$  from the very beginning. The measured  $\Delta T$  was about 4 K at all four frequency channels although the calibration accuracy was comparable to that of MIR [12]–[13]. To reduce the errors in the retrieved water vapor profiles caused by the fluctuation of radiometric signals, a number of measured  $T_b$  values were averaged before the retrieval algorithm was applied [12]–[13]. As a consequence, studies of the retrieval processes were limited to radiometric measurements obtained from the nadir direction [8]–[13]. Furthermore, most of these studies were limited to measurements over regions of clear sky. An attempt by Wang *et al.* [13] to retrieve water vapor profiles from AMMS measurements under a cloudy condition did not yield promising results. These authors suggested that measurements with more frequency channels than those provided by the AMMS might be required to obtain reliable water vapor profiles in the presence of clouds.

The new MIR provides radiometric measurements with a much improved temperature sensitivity and with more frequency channels compared to the old AMMS. It has the potential of overcoming the difficulty experienced by the AMMS. Recent studies with this new instrument [5], [6] emphasized the forward calculations and comparisons of the measured radiometric outputs with those calculated from Raman lidar and rawinsondes. Retrieval of water vapor profiles was limited to nadir-viewing and to a small region in proximity to the Raman lidar site [6]. In this paper, the retrieval algorithm used by Wang and Chang [12] was extended to estimate the water vapor profiles from MIR measurements over ocean surfaces at

Manuscript received March 11, 1994; revised July 19, 1996.

J. R. Wang and P. Racette are with the Laboratory for Hydrospheric Processes, NASA Goddard Space Flight Center, Greenbelt, MD 20771 USA.

L. A. Chang is with Futurtech Corporation, Gaithersburg, MD, 20878 USA.

Publisher Item Identifier S 0196-2892(97)00382-3.



and M3 are comparable, the difference at each level being less than or equal to about 3%. The average RH profile from M2 (plot b) is markedly different from the other two, and also represents a significant deviation from a typical clear-sky RH profile observed in the tropical region. At  $h = 0.25$  km, the average RH derived from M2 is lower than that from M1 by about 17%. At  $h = 2.75$  km and  $h = 4.75$  km the average RH values from M2 are higher than those from M1 by about 11% and 18%, respectively. These results suggest that using an initial profile unrealistically different from the true profile, like the constant 10% RH in this case, would not provide an adequate retrieval. Tightening of the condition for the convergent retrieval,  $\delta T_b \leq 1$  K, is not sufficient to alter this conclusion as demonstrated below.

To explore the effect of  $\delta T_b$  on the final products, another sequence of retrieval was performed on the MIR data over the same region with the condition of  $\delta T_b \leq 0.5$  K. The number of iterations in the retrieval were also raised to 65. It was found that the number of cases satisfying this condition of convergence is reduced when compared to that with  $\delta T_b \leq 1$  K; the  $\delta T_b$  values for a significant fraction of cases were inbetween 0.5 K and 1 K. The average RH profiles derived from this new constraint for convergence are compared in Fig. 12(a), (b), and (c) for M1, M2, and M3, respectively. At all six levels, there are only minor changes in the differences of RH values between M1 and M3 compared with those in Fig. 11(a) and (c). The new average RH profile from M2 shows a significant improvement at all levels with respect to those from M1. At  $h = 0.25$ , 2.75, and 4.75 km the differences between the RH values from M1 and M2 are reduced to about 9.5%, 6.2%, and 6.9% respectively. This effect of  $\delta T_b$  and initial input profile on the final retrieval products is more clearly illustrated in Fig. 13, where the averages of the relative humidity differences and their standard deviations are plotted for two different convergent conditions. Standard deviations of some data points are so small that they cannot be displayed in the figure. To arrive at these averages and standard deviations for each convergent condition, the retrievals using all three methods M1, M2 and M3 are performed from each of the 70 sets of MIR measurements over the same region (at times  $>0224$  UTC in Fig. 5). Then for each of the six altitude levels, the differences from the 70 pairs (M1-M2 and M1-M3) of retrieved RH values are tabulated and their average and standard deviation computed and entered in the figure. It is quite clear from the plots (a) and (c) in Fig. 5 that the average RH differences are reduced appreciably at all levels when the convergent condition is changed from  $\delta T_b \leq 1$  K to  $\leq 0.5$  K. The differences between plots (b) and (d) are minimal, which suggest a lack of improvement in the results by imposing a more stringent condition for convergence when either a constant 50% or 90% RH profile is used as initial input in the retrieval.

These results suggest that one should choose an initial profile resembling the climatology of the geographical location for input to the retrieval algorithm. If the initial profile is markedly different from the true one, the retrieved products could be subject to significant errors. Applying a more stringent condition for convergence than the one we normally used,

$\delta T_b \leq 1$  K, in the retrieval algorithm would significantly improve the final results, but this requires more iterations and computer time.

## VI. CONCLUSION

Radiometric measurements obtained from the airborne MIR during TOGA/COARE were used to demonstrate the retrieval of 3-D water vapor distribution over ocean surfaces. The polarization vector of the instrument was in the horizontal plane and perpendicular to the direction of the aircraft flight. As a consequence, the measured brightness temperature was a mixture of vertical and horizontal polarizations when the view angle is in the off-nadir direction, and the retrieval would have to take this factor into account. Modifications to the algorithm used in the early studies [8], [12] were made to take care of the instrument's mixed-polarization measurements. Results of retrieval using the modified algorithm suggested that adequate water vapor profiles could be obtained even though the radiometric measurements were made with mixed vertical and horizontal polarizations.

The water vapor profiles retrieved from the MIR measurements were compared with those measured in near concurrence by dropsondes and Raman lidar. A good agreement between the retrieved and measured water vapor mixing ratios was found at low altitudes  $<1.5$  km. The comparison became poorer with increase in altitudes. The ratio of the standard deviation to the mean was found to increase from 0.12 at 0.25 km to 0.67 at 10.25 km altitude.

The assumed water vapor profile used to initiate the retrieval algorithm was found to have a certain impact on the final retrieved product. The extent of this impact depends on the condition set for a convergent retrieval, which is determined by the root mean square ( $\delta T_b$ ) of the differences between the brightness temperatures measured by the MIR and those calculated from the water vapor profiles generated during the iteration process. Three different sets of relative humidity profiles were used as initial inputs to the retrieval algorithm to illustrate this impact; these were constant profiles at 10%, 50%, and 90% relative humidities. When the condition for convergence was set with  $\delta T_b \leq 1$  K, the average differences of the relative humidity profiles retrieved from the same MIR measurements with initial profiles of 50% and 90% were found to be  $\leq 3\%$  at all six altitude levels between 0.25 and 10.25 km. Only small changes in these differences were noticed when the condition for convergence was tightened to  $\delta T_b \leq 0.5$  K. When the 10% relative humidity profile was used as initial input to the algorithm, the resultant profiles were found to be significantly different (as much as 18% at the altitude level of 4.75 km) from those of the other two sets. The tightening of convergent condition to  $\delta T_b \leq 0.5$  K reduced these differences by about a factor of two, but required more iterations and computing time. A choice of an initial input profile based on the climatology of the location at hand would probably provide the most efficient and accurate results in the retrieval process.



## The Effect of Clouds on Water Vapor Profiling from the Millimeter-Wave Radiometric Measurements

J. R. WANG, J. D. SPINHIRNE, AND P. RACETTE

*Earth Sciences Directorate, NASA/Goddard Space Flight Center, Greenbelt, Maryland*

L. A. CHANG

*Futuretech Corporation, Gaithersburg, Maryland*

W. HART

*Science Systems and Applications, Inc., Lanham, Maryland*

(Manuscript received 30 September 1996, in final form 21 March 1997)

### ABSTRACT

Simultaneous measurements with the millimeter-wave imaging radiometer (MIR), cloud lidar system (CLS), and the MODIS airborne simulator (MAS) were made aboard the NASA ER-2 aircraft over the western Pacific Ocean on 17–18 January 1993. These measurements were used to study the effects of clouds on water vapor profile retrievals based on millimeter-wave radiometer measurements. The CLS backscatter measurements (at 0.532 and 1.064  $\mu\text{m}$ ) provided information on the heights and a detailed structure of cloud layers; the types of clouds could be positively identified. All 12 MAS channels (0.6–13  $\mu\text{m}$ ) essentially respond to all types of clouds, while the six MIR channels (89–220 GHz) show little sensitivity to cirrus clouds. The radiances from the 12- $\mu\text{m}$  and 0.875- $\mu\text{m}$  channels of the MAS and the 89-GHz channel of the MIR were used to gauge the performance of the retrieval of water vapor profiles from the MIR observations under cloudy conditions. It was found that, for cirrus and absorptive (liquid) clouds, better than 80% of the retrieval was convergent when one of the three criteria was satisfied; that is, the radiance at 0.875  $\mu\text{m}$  is less than 100  $\text{W cm}^{-2} \text{sr}^{-1}$ , or the brightness at 12  $\mu\text{m}$  is greater than 260 K, or brightness at 89 GHz is less than 270 K (equivalent to cloud liquid water of less than 0.04  $\text{g cm}^{-2}$ ). The range of these radiances for convergent retrieval increases markedly when the condition for convergent retrieval was somewhat relaxed. The algorithm of water vapor profiling from the MIR measurements could not perform adequately over the areas of storm-related clouds that scatter radiation at millimeter wavelengths.

### 1. Introduction

Profiling of atmospheric water vapor with radiometric measurements near the 183.3-GHz strong water vapor line has been explored quite extensively for more than a decade (Schaerer and Wilheit 1979; Rosenkranz et al. 1982; Wang et al. 1983, 1993, 1995, 1997a; Wang and Chang 1990; Kakar 1983; Kakar and Lambrigtsen 1984; Lambrigtsen and Kakar 1995; Wilheit 1990; Lutz et al. 1991; Kuo et al. 1994). The studies by Schaerer and Wilheit (1979), Rosenkranz et al. (1982), and Kuo et al. (1994) were either theoretical or based on synthetic datasets; no real measurements were involved. The remaining studies above used radiometric measurements obtained by the airborne MIR (millimeter-wave imaging

radiometer) or AMMS (airborne microwave moisture sounder). The AMMS is a four-channel (90, 183.3  $\pm$  2, 183.3  $\pm$  5, and 183.3  $\pm$  9 GHz) cross-track scanner built around 1980 (Gagliano and McCheehy 1981), which has a temperature sensitivity ( $\Delta T_b$ ) of approximately 4 K. The MIR is a six-channel (89, 150, 183.3  $\pm$  1, 183.3  $\pm$  3, 183.3  $\pm$  7, and 220 GHz), total power, cross-track scanner that was built in 1992 with a much improved  $\Delta T_b$  of less than or equal to 1 K (Racette et al. 1996). Both radiometers use external calibration targets to derive the scene brightness temperature  $T_b$ . The calibration accuracy for the MIR is estimated to be better than  $\pm 2$  K in the  $T_b$  range of 240–300 K.

Studies made with the AMMS measurements (Lutz et al. 1991; Wang and Chang 1990; Wang et al. 1993) have shown that profiling of atmospheric water vapor profiles from radiometric measurements using the 183.3-GHz absorption line is definitely affected by the presence of a cloud cover. The retrieval was in general found to be divergent under mostly cloudy conditions

---

Corresponding author address: Dr. J. R. Wang, Earth Sciences Directorate, NASA/Goddard Space Flight Center, Greenbelt, MD 20771.  
E-mail: wang@sensor.gsfc.nasa.gov



figure shows the distribution of the number of events concurrently measured by the MIR and MAS within the ranges of  $I(0.875 \mu\text{m})$  and  $T(12 \mu\text{m})$ . The middle and bottom portions of the figure give, in each category of  $I(0.875 \mu\text{m})$  and  $T(12 \mu\text{m})$ , the percentage of convergent retrieval of water vapor profiles based on the MIR measurements when the conditions of the convergence  $\delta T_b$ 's are set to less than or equal to 1 K and less than or equal to 1.5 K, respectively. It is noted that more than 80% of the events occur with  $T(12 \mu\text{m})$  greater than 270 K or  $I(0.875 \mu\text{m})$  less than  $60 \text{ W cm}^{-3} \text{ sr}^{-1}$ . Even under practically clear-sky conditions with  $T(12 \mu\text{m})$  greater than 290 K or  $I(0.875 \mu\text{m})$  less than  $20 \text{ W cm}^{-3} \text{ sr}^{-1}$ , there is about 5% of nonconvergent events when  $\delta T_b \leq 1 \text{ K}$ ; these events disappear when  $\delta T_b \leq 1.5 \text{ K}$ . These clear-sky, nonconvergent events can be attributed to measurement noise such as that displayed by some data points in the 220-GHz channel in Fig. 4. Based on the distribution of Fig. 12, it appears that adequate water vapor profiling can be performed from the MIR measurements when  $T(12 \mu\text{m})$  is greater than 250 K or  $I(0.875 \mu\text{m})$  is less than  $100 \text{ W cm}^{-3} \text{ sr}^{-1}$ . When the condition of convergent retrieval is relaxed to  $\delta T_b \leq 1.5 \text{ K}$ , adequate water vapor profiling can be obtained with  $T(12 \mu\text{m})$  greater than 220 K or  $I(0.875 \mu\text{m})$  less than  $140 \text{ W cm}^{-3} \text{ sr}^{-1}$ . It is noted that there are not many events with either  $I(0.875 \mu\text{m})$  greater than  $100 \text{ W cm}^{-3} \text{ sr}^{-1}$  or  $T(12 \mu\text{m})$  less than 250 K. Analysis with more concurrent measurements from these instruments is needed to arrive at a firm conclusion.

An examination of Fig. 4 clearly indicates that the 89-GHz channel is particularly sensitive to the low-level liquid clouds over the ocean surface. It is therefore interesting to examine the relation between the convergent retrievals and the  $T_b(89)$  values. Figure 13a shows the frequency distribution of MIR measurements based on the categories of  $T_b(89)$  values in 10-K steps from 230 to 290 K. Again, the events associated with the scattering cell in region C (Fig. 4) are not included in the figure. Figures 13b and 13c, respectively, give the percentage of convergent retrievals within each category when the conditions of  $\delta T_b \leq 1 \text{ K}$  and  $\delta T_b \leq 1.5 \text{ K}$  are applied. It is clear that profiling of water vapor under cloudy condition begins to deteriorate only when  $T_b(89) \geq 270 \text{ K}$ . If the condition for convergent retrieval is relaxed to  $\delta T_b \leq 1.5 \text{ K}$ , then the histogram of Fig. 13c suggests a better than 80% of convergent water vapor profiling from the MIR measurements under a variety of absorptive clouds.

It is also interesting to look at the dependence of  $T_b(89)$  on the total cloud liquid water required by the algorithm to satisfy a convergent retrieval of water vapor profile. Figure 14 shows the scatterplot between  $T_b(89)$  and the estimated CLW from the retrieval algorithm. The data points on the vertical axis correspond to clear-sky condition as viewed by the MIR. Generally, there is a nonlinear dependence of  $T_b(89)$  on CLW and  $T_b(89)$  reaches a saturated value of about 280 K at CLW

$\geq 0.09 \text{ g cm}^{-2}$ . These estimated CLWs are not validated; they are the by-product of the MIR water vapor profiling. Their usefulness needs to be explored in the future.

## 5. Conclusions

During January–February 1993 a host of instruments were placed aboard the NASA ER-2 aircraft, which made a number of observations over a region in the western Pacific Ocean in support of the TOGA COARE mission. Among these instruments were MIR, CLS, and MAS, whose simultaneous measurements were analyzed to study the effects of clouds on water vapor profiling from the radiances observed at the millimeter wavelengths. The measurements for this particular study were obtained from a long flight segment covering a region stretching from near Townsville, Australia, where the aircraft was stationed, to a waypoint near the equator on 17–18 January 1993. All three instruments functioned well over the 2-h plus interval and made observations over a variety of clouds, both scattering and absorptive in the millimeter wavelengths. There were a total of 2377 events with simultaneous measurements from the three instruments. A retrieval algorithm was applied to the nadir-viewing measurements from the MIR to estimate profiles of water vapor mixing ratio along the flight segment. It was found that the estimated profiles showed a general enhancement from high latitude to equatorial region as expected. Normal retrievals could be performed from the MIR measurements over the areas of cirrus clouds or moderate liquid clouds. Over the areas of heavy cloud covers with the presence of atmospheric hydrometeors that scatter radiation at the MIR frequencies, retrievals would experience difficulty and the estimated water vapor profiles became unreliable.

All six channels of the MIR measurements show little sensitivity to cirrus clouds from this flight; they all respond to convective clouds. The 89-GHz channel shows most sensitivity to the absorptive (liquid) clouds. To quantify the effects of absorptive clouds on the water vapor profiling from the MIR radiometric measurements, radiances obtained by the  $12\text{-}\mu\text{m}$  and  $0.875\text{-}\mu\text{m}$  channels of the MAS and the 89-GHz channel of the MIR were used as classifiers. It was found that more than 80% of the retrieval of water vapor profiles from the MIR measurements was convergent (defined as the root-mean-square value of the measured and calculated brightness temperatures  $\delta T_b \leq 1 \text{ K}$ ) when the brightness at  $12 \mu\text{m}$  was greater than or equal to 260, or the radiance at  $0.875 \mu\text{m}$  less than or equal to  $100 \text{ W cm}^{-3} \text{ sr}^{-1}$ , or the brightness at 89 GHz less than or equal to 270 K. When the condition of convergent retrieval was relaxed to  $\delta T_b \leq 1.5 \text{ K}$ , reasonable water vapor profiles could be obtained when the radiance at  $0.875 \mu\text{m}$  is less than  $140 \text{ W cm}^{-3} \text{ sr}^{-1}$ , or the brightness at  $12 \mu\text{m}$  greater than 220 K; adequate retrievals could be performed regardless of the brightness temperature values at 89 GHz.



# Storm-Associated Microwave Radiometric Signatures in the Frequency Range of 90–220 GHz

J. R. WANG

*Laboratory for Hydrospheric Processes, NASA/Goddard Space Flight Center, Greenbelt, Maryland*

J. ZHAN

*Caelum Research Corporation, Silver Spring, Maryland*

P. RACETTE

*Laboratory for Hydrospheric Processes, NASA/Goddard Space Flight Center, Greenbelt, Maryland*

(Manuscript received 8 December 1995, in final form 20 June 1996)

## ABSTRACT

Radiometric measurements were made by a millimeter-wave imaging radiometer (MIR) at the frequencies of 89, 150,  $183.3 \pm 1$ ,  $183.3 \pm 3$ ,  $183.3 \pm 7$ , and 220 GHz aboard the NASA ER-2 aircraft at an altitude of about 20 km over two rainstorms: one in the western Pacific Ocean on 19 January 1993 and another in southern Florida on 5 October 1993. These measurements were complemented by nearly simultaneous observations by other sensors aboard the same aircraft and another aircraft flying along the same path. Analysis of data from these measurements, aided by radiative transfer and radar reflectivity calculations of hydrometeor profiles, which are generated by a general cloud ensemble model, demonstrates the utility of these frequencies for studying the structure of frozen hydrometeors associated with storms. Particular emphasis is placed on the three water vapor channels near 183.3 GHz. Results show that the radiometric signatures measured by these channels over the storm-associated scattering media bear a certain resemblance to those previously observed over a clear and fairly dry atmosphere with a cold ocean background. Both of these atmospheric conditions are characterized by a small amount of water vapor above a cold background. Radiative transfer calculations were made at these water vapor channels for a number of relative humidity profiles characterizing dry atmospheres over an ocean surface. The results are compared with the measurements to infer some characteristics of the environment near the scattering media. Furthermore, radiometric signatures from these channels display unique features for towering deep convective cells that could be used to identify the presence of such cells in storms.

## 1. Introduction

Microwave radiometric measurements of precipitation have been conducted from both aircraft and satellite platforms for nearly two decades (Wilheit et al. 1977, 1982; Rodgers et al. 1979; Prabhakara et al. 1986; Spencer 1986; Spencer et al. 1989; Adler et al. 1990; Weinman and Guetter 1977; Chang et al. 1993; Vivekanandan et al. 1993). Radiative transfer calculations based on simple hydrometeor profiles or more sophisticated profiles derived from general cloud ensemble models have been made to interpret the observed radiometric signatures (Wilheit et al. 1977, 1991; Smith and Mugnai 1988; Yeh et al. 1990). Furthermore, from the activities associated with the Tropical Rainfall Measuring Mission (TRMM) program (Simpson et al. 1988), a number of

algorithms have been developed to retrieve the rain rate from microwave radiometric measurements (Weinman et al. 1990; Wilheit et al. 1991; Smith et al. 1992; Kummerow et al. 1989; Kummerow and Giglio 1994). Most of these efforts emphasize using radiometric signatures at frequencies below 90 GHz. The signatures of rain are mainly caused by the emission of microwave radiation by liquid hydrometeors that gives rise to warm radiometric brightness over a cold ocean background (Wilheit et al. 1977). Moderate signatures caused by scattering processes at 37 and 85 GHz are also used to estimate rain rate over land surface (Spencer 1986; Spencer et al. 1989; Adler et al. 1993; Negri et al. 1994).

Radiometric signatures of precipitating systems at frequencies of 90 GHz or greater have not been explored as extensively; to the best of our knowledge, only a few studies have been reported in the literature. Wilheit et al. (1982), Hakkarinen and Adler (1988), and Adler et al. (1990) have examined radiometric signatures at both 90- and 183-GHz frequencies from, respectively, Trop-

---

Corresponding author address: Dr. James R. Wang, NASA/Goddard Space Flight Center, Code 975, Greenbelt, MD 20771.  
E-mail: wang@sensor.gsfc.nasa.gov



## 6. Conclusions

Radiometric measurements from an MIR aboard the NASA ER-2 aircraft were made from an altitude of 20 km at the frequencies of 89, 150,  $183.3 \pm 1$ ,  $183.3 \pm 3$ ,  $183.3 \pm 7$ , and 220 GHz over two different storms; one was located in the Pacific Ocean near  $1^\circ\text{S}$ ,  $156^\circ\text{E}$  on 19 January 1993 and another in southern Florida on 5 October 1993. These measurements are complemented by observations from other sensors aboard the same aircraft or in the NASA DC-8 aircraft flying along the same path at a lower altitude of 11 km. In the first case on 19 January a host of microwave radiometers covering a frequency range of 18–183 GHz were aboard the DC-8 aircraft, and the MODIS Airborne Simulator was aboard the same ER-2 aircraft. In the second case on 5 October only the ER-2 aircraft carrying a 9.7-GHz Doppler radar (EDOP) and MAMS was involved. The analysis of the MIR data from the measurements of three water vapor channels near 183.3 GHz was emphasized because these channels were found to contain very useful information and were least explored in the previous studies on rain storms. Radiative transfer and radar reflectivity calculations based on the hydrometeor profiles generated by the RAMS cloud model (Smith et al. 1992) were made to help interpret the observed data. It was found from both observations and calculations that, over the storm cells, the differences in brightness temperatures from pairs of water vapor channels correlated with the brightness temperatures themselves. Because of the double side-band measurements of these channels, this correlation was proven to be caused by water vapor in and over the scattering media.

From the thermal infrared channel of MAS or MAMS and the sounding data, the cloud top over the storm area was estimated to be at an altitude of about 13–14 km for both measurement cases. The brightness temperatures of the thermal infrared channel did not show much variation, while those from all the MIR channels were found to vary significantly. This suggests the potential of using these channels to map regions of frozen hydrometeors associated with storms. The differences in brightness temperatures from pairs of the water vapor channels showed a definite correlation with the average radar reflectivity in the 6–12-km altitude range, similar to the correlation between brightness temperatures at millimeter wavelengths and radar reflectivity reported from previous studies (Wang et al. 1994; Heymsfield et al. 1996). For both cases of observations, the ER-2 aircraft flew over a deep convective cell that was characterized by MAMS (MAS) thermal infrared temperatures of less than 190 K. These cells were also characterized by small differences in the MIR water vapor channels at very low brightness temperatures.

There is an analogy between the radiometric signatures of the water vapor channels observed over the storm-associated scattering media and those over a dry atmosphere with a cold ocean background. The ob-

served behavior of the brightness temperature differences from these channels, when entering the scattering cells, corresponds well to that entering the region of dry atmosphere. The changes of these brightness temperature differences follow the same particular sequence as the total precipitable water decreases over the ocean background or above the scattering media. Even for the two deep convective cells, it is possible to compare the measured brightness temperature differences and relatively infer the amount of water vapor above the scattering media. However, a quantitative estimation of water vapor above the scattering media cannot be obtained from the analogy of radiometric signatures from these two very different atmospheric conditions. Systematic calculations based on a variety of model-generated hydrometeor and water vapor profiles, as well as more observations, are needed to learn more about the radiometric signatures from these and other millimeter-wave channels.



## Correction of Rayleigh scattering effects in cloud optical thickness retrievals

Menghua Wang

University of Maryland Baltimore County, NASA Goddard Space Flight Center, Greenbelt, Maryland

Michael D. King

Earth Sciences Directorate, NASA Goddard Space Flight Center, Greenbelt, Maryland

**Abstract.** We present results that demonstrate the effects of Rayleigh scattering on the retrieval of cloud optical thickness at a visible wavelength ( $0.66\ \mu\text{m}$ ). The sensor-measured radiance at a visible wavelength ( $0.66\ \mu\text{m}$ ) is usually used to infer remotely the cloud optical thickness from aircraft or satellite instruments. For example, we find that without removing Rayleigh scattering effects, errors in the retrieved cloud optical thickness for a thin water cloud layer ( $\tau_c = 2.0$ ) range from 15 to 60%, depending on solar zenith angle and viewing geometry. For an optically thick cloud ( $\tau_c \geq 10$ ), on the other hand, errors can range from 10 to 60% for large solar zenith angles ( $\theta_0 \geq 60^\circ$ ) because of enhanced Rayleigh scattering. It is therefore particularly important to correct for Rayleigh scattering contributions to the reflected signal from a cloud layer both (1) for the case of thin clouds and (2) for large solar zenith angles and all clouds. On the basis of the single scattering approximation, we propose an iterative method for effectively removing Rayleigh scattering contributions from the measured radiance signal in cloud optical thickness retrievals. The proposed correction algorithm works very well and can easily be incorporated into any cloud retrieval algorithm. The Rayleigh correction method is applicable to cloud at any pressure, providing that the cloud top pressure is known to within  $\pm 100$  hPa. With the Rayleigh correction the errors in retrieved cloud optical thickness are usually reduced to within 3%. In cases of both thin cloud layers and thick clouds with large solar zenith angles, the errors are usually reduced by a factor of about 2 to over 10. The Rayleigh correction algorithm has been tested with simulations for realistic cloud optical and microphysical properties with different solar and viewing geometries. We apply the Rayleigh correction algorithm to the cloud optical thickness retrievals from experimental data obtained during the Atlantic Stratocumulus Transition Experiment (ASTEX) conducted near the Azores in June 1992 and compare these results to corresponding retrievals obtained using  $0.88\ \mu\text{m}$ . These results provide an example of the Rayleigh scattering effects on thin clouds and further test the Rayleigh correction scheme. Using a nonabsorbing near-infrared wavelength ( $0.88\ \mu\text{m}$ ) in retrieving cloud optical thickness is only applicable over oceans, however, since most land surfaces are highly reflective at  $0.88\ \mu\text{m}$ . Hence successful global retrievals of cloud optical thickness should remove Rayleigh scattering effects when using reflectance measurements at  $0.66\ \mu\text{m}$ .

### 1. Introduction

In the remote sensing of cloud microphysical, optical, and radiative properties from aircraft or satellite sensors, the sensor-measured radiance at visible wavelengths ( $0.66\ \mu\text{m}$ ) is primarily a function of cloud optical thickness, whereas near-infrared (NIR) radiances ( $1.6$ ,  $2.1$ , and  $3.7\ \mu\text{m}$ ) are sensitive both to optical thickness and, especially, to cloud particle size [Foot, 1988; Nakajima and King, 1990; Nakajima and Nakajima, 1995; Platnick and Valero, 1994; Twomey and Cocks, 1982, 1989]. As a consequence, Rayleigh scattering in the atmosphere above the cloud primarily affects the cloud optical thickness retrieval since the Rayleigh optical thickness in the near-infrared is negligible. Because the Rayleigh optical thickness in the visible wavelength region is small (about  $0.044$  at

$0.66\ \mu\text{m}$ ), it has previously been neglected in retrieving cloud optical thickness. In principle, one can also retrieve the cloud optical thickness using a nonabsorbing NIR band (e.g.,  $0.88\ \mu\text{m}$ ) over the ocean. Rayleigh scattering has much less effect on cloud optical thickness retrievals at  $0.88\ \mu\text{m}$  than at  $0.66\ \mu\text{m}$  since the Rayleigh optical thickness is much smaller ( $\tau_r \sim 0.015$  at  $0.88\ \mu\text{m}$ ). Over land, however, it is preferable to use visible wavelengths ( $0.66\ \mu\text{m}$ ) because the surface reflectance of land is low at this wavelength, in contrast to NIR bands where the surface reflectance can reach  $0.5$  over vegetation areas. In this paper we investigate the Rayleigh scattering effects on cloud optical thickness retrievals at a visible ( $0.66\ \mu\text{m}$ ) wavelength for various cloud microphysical and optical properties and different solar and viewing geometries. We then propose a scheme to effectively remove the Rayleigh scattering contributions. Finally, we extensively test the Rayleigh correction algorithm with simulations and provide results of retrieving cloud optical thickness from experimental measurements



tion (PDF) (in percent) of retrieved cloud optical thickness and effective particle radius for various retrievals obtained using the MAS measurements shown in Figure 7. This includes a total of  $2.29 \times 10^4$  retrievals in the range  $2 \leq \tau_c \leq 5$  and  $4 \leq r_e \leq 26 \mu\text{m}$ . Figure 8a shows that the shape of the PDF for the retrieved cloud optical thickness is very similar for all three retrievals. However, there is clear evidence indicating that the Rayleigh scattering effects lead to overestimates of the cloud optical thickness at  $0.66 \mu\text{m}$  for the optically thin paths of the cloud scene. Results from both  $0.66 \mu\text{m}$  (with correction) and  $0.88 \mu\text{m}$  retrievals (without correction) are really identical, while the retrievals at  $0.66 \mu\text{m}$  obtained without Rayleigh correction are shifted toward large values of  $\tau_c$ . The PDF of  $\tau_c$  was shifted about 0.3 at  $\tau_c = 3$  ( $\Delta\tau_c = 10\%$ ) and 0.4 at  $\tau_c = 4.4$  ( $\Delta\tau_c = 9\%$ ), which is consistent with the results from our simulations. Figure 8b shows that for thin clouds, without making a Rayleigh correction at visible wavelength ( $0.66 \mu\text{m}$ ), the retrieved cloud effective particle radius is also overestimated due to the overestimation of the cloud optical thickness. This phenomenon is easy to understand. For thin clouds the cloud effective particle radius increases as the cloud optical thickness increases for a given measured reflected radiance at the absorbing NIR  $2.1 \mu\text{m}$  band. Increasing the cloud optical thickness enhances the reflected radiance contribution. Therefore the cloud needs to absorb more through increasing the water droplet size to keep the measured radiance at  $2.1 \mu\text{m}$  unchanged. For thick clouds, however, the reflected radiance reaches its maximum in the asymptotic range for a given cloud effective particle radius, that is, photons can only "see" the cloud layer up to a maximum optical thickness value. Therefore, any more increase of  $\tau_c$  does not change the reflected radiance at the TOC. It should be pointed out that the cloud optical thickness retrievals using a NIR wavelength ( $0.88 \mu\text{m}$ ) are not completely error free, though they are much reduced over retrievals at  $0.66 \mu\text{m}$  due to the much smaller Rayleigh scattering contributions at  $0.88 \mu\text{m}$ . The errors in retrieved  $\tau_c$  at  $0.88 \mu\text{m}$  ranges from about 1 to 5% for  $\tau_c$  between 2 and 5. We can see some differences in the PDF in retrieved  $\tau_c$  between using band  $0.66 \mu\text{m}$  (with Rayleigh correction) and  $0.88 \mu\text{m}$  (without Rayleigh correction).

## 8. Discussion

As presented in section 7, Rayleigh scattering effects can be observed with satellite and/or airborne multichannel measurements. This can also be observed and validated with satellite multiangle measurements, e.g., the Multiangle Imaging Spectroradiometer (MISR) [Diner *et al.*, 1989] scheduled to be flown on the same platform as MODIS in 1998 [King *et al.*, 1995]. MISR consists of a set of nine cameras that view the Earth at nine angles ( $0, \pm 26.1^\circ, \pm 45.6^\circ, \pm 60.0^\circ$ , and  $\pm 70.5^\circ$  to the Earth's surface normal, where positive and negative angles refer to directions ahead of and behind the spacecraft, respectively) and in four spectral bands ( $0.443, 0.555, 0.670$ , and  $0.865 \mu\text{m}$ ). Thus, for a particular MISR band (e.g.,  $0.670 \mu\text{m}$ ) we expect to observe Rayleigh scattering effects by looking at clouds with different viewing angles, that is, the smallest Rayleigh scattering effects are expected for nadir viewing ( $\theta = 0^\circ$ ) and the largest effects are expected for large viewing angles ( $\theta = 70.5^\circ$ ).

Our objective in this work is to accurately remove the Rayleigh scattering effects in cloud optical thickness retrievals. These unwanted Rayleigh scattering contributions, however,

can be related to the cloud top pressure. It is particularly useful to relate Rayleigh scattering to cloud top pressure in remote sensing of cloud height and could potentially be utilized for this purpose by estimating the amount of Rayleigh scattering contributions above the cloud from visible radiance measurements. Obviously, for this purpose, one would like to use measured radiances at a short visible wavelength, e.g., the blue band, since the Rayleigh scattering contributions at this wavelength are more significant. Therefore it provides a sensitivity that could be applied to the remote retrieval of cloud top height using the measured radiance at the blue band. This will, however, be the topic of a future paper.

Since Rayleigh corrections have heretofore not been incorporated into satellite retrievals of cloud optical thickness, reported results are expected to be highly biased, especially at high latitudes. This effect will be incorporated into the cloud optical thickness and effective radius retrieval using MODIS data in 1998, where retrievals will be made using  $0.65 \mu\text{m}$  over land,  $0.86 \mu\text{m}$  over oceans, and  $1.24 \mu\text{m}$  over snow and ice surface.

## 9. Conclusions

From studies of Rayleigh scattering effects on cloud optical thickness retrievals, we conclude that it is important to correct for Rayleigh scattering effects when retrieving cloud optical thickness for optically thin clouds and for thick clouds with large solar zenith angles ( $\theta_0 \geq 60^\circ$ ). For thin clouds, however, errors in cloud optical thickness lead to errors in remotely retrieved cloud effective particle radius as well. By using a nonabsorbing NIR band ( $0.88 \mu\text{m}$ ) in cloud optical thickness retrievals over oceans, the Rayleigh effects are much reduced because of the much smaller Rayleigh optical thickness. However, for cases with large solar zenith angles ( $\theta_0 \geq 60^\circ$ ),  $\Delta\tau_c$  in retrieved cloud optical thickness at  $\lambda = 0.88 \mu\text{m}$  still range between 5 and 25%. On the basis of single scattering theory, we have developed an iterative method to effectively remove the Rayleigh scattering contributions in cloud optical thickness retrievals. The iteration scheme is efficient and can be easily incorporated into any cloud retrieval algorithm. The correction scheme has been extensively tested with simulations for realistic cloud microphysical and optical properties and for a wide range of solar and viewing geometries. We conclude that the proposed Rayleigh correction algorithm can reduce the error in the retrieved cloud optical thickness in most cases from 20% to 2% for thin clouds. The error in retrieved  $\tau_c$  was improved from a maximum of 28% in some cases to better than 4%. On the other hand, for optically thick clouds ( $\tau_c \geq 10$ ) and large solar zenith angles ( $\theta_0 \approx 70^\circ$ ) the error in  $\tau_c$  was reduced in most cases from 12% to 2%. The improvements are even more substantial for cases of large  $\tau_c$  and  $\theta_0 = 80^\circ$ . Finally, we have validated the correction algorithm for thin clouds with experimental data obtained from the MODIS airborne simulator during ASTEX in June 1992.



## Other Contributions







# **NASA Technical Memorandum 104566, Vol. 40**

## **SeaWiFS Technical Report Series**

**Stanford B. Hooker, Editor**

*NASA Goddard Space Flight Center*

*Greenbelt, Maryland*

**Elaine R. Firestone, Technical Editor**

*General Sciences Corporation*

*Laurel, Maryland*

## **Volume 40, SeaWiFS Calibration Topics, Part 2**

**Robert A. Barnes**

**Robert E. Eplee, Jr.**

**Eueng-nan Yeh**

*General Sciences Corporation*

*Laurel, Maryland*

**Wayne E. Esaias**

*NASA Goddard Space Flight Center*

*Greenbelt, Maryland*



National Aeronautics and  
Space Administration

**Goddard Space Flight Center**

*Greenbelt, Maryland 20771*

**1997**



## ABSTRACT

For Earth-observing satellite instruments, it was standard to consider each instrument band to have a spectral response that is infinitely narrow, i.e., to have a response from a single wavelength. The SeaWiFS bands, however, have nominal spectral bandwidths of 20 and 40 nm. These bandwidths effect the SeaWiFS measurements on orbit. The effects are also linked to the manner in which the instrument was calibrated and to the spectral shape of the radiance that SeaWiFS views. The spectral shape of that radiance will not be well known on orbit. In this technical memorandum, two source spectra are examined. The first is a 12,000 K Planck function, and the second is based on the modeling results of H. Gordon at the University of Miami. By comparing these spectra, the best available corrections to the SeaWiFS measurements for source spectral shape, plus estimates of the uncertainties in these corrections, can be tabulated.

## PROLOGUE

The Sea-viewing Wide Field-of-view Sensor (SeaWiFS) measures the Earth's upwelling radiance at eight wavelengths. These bands have finite spectral bandwidths, ranging from 20–40 nm. As a result, there is a dependence of the SeaWiFS measurements on the spectral shape of the Earth-exiting radiance that it measures. The manner in which this dependence manifests itself in the SeaWiFS data derives from the radiometric calibration of the instrument before launch.

There are two methods of interpreting the SeaWiFS calibration data. In the first method, the digital counts from each band of the instrument are related to the spectral radiance at the nominal center wavelength for that band. By definition, the center wavelengths for the bands are fixed. For this method, the relationship between the counts and the radiance varies with the spectral shape of the source that is measured. Since the laboratory calibration source has a spectral shape that is markedly different from the upwelling Earth radiance, there must be a correction factor to convert the laboratory calibration to the calibration on orbit.

In the second method, the digital counts from each band of the instrument are related to the band-averaged spectral radiance. Since the band-averaged spectral radiance is taken over the full spectral response of the band, there is no source shape dependence in the counts to radiance relationship for the band. However, the wavelength for the band-averaged center wavelength will change with different source spectral shapes. Fundamentally, it is not possible to determine both the radiance responses of the SeaWiFS bands and their center wavelengths during the laboratory calibration. Depending on the type of laboratory calibration, one of them will vary on-orbit with the spectral shape of the Earth-exiting radiance.

A previous volume in this technical memoranda series (Barnes et al. 1996) included several sensitivity studies to examine the effects of different source spectral shapes on the output of the SeaWiFS bands. These studies used

Planck function curves with a wide range of color temperatures (2,000–38,000 K) covering the full range of laboratory and ocean scenes that SeaWiFS is expected to view. Using these Planck curves and the typical SeaWiFS spectral radiances from the sensor's specifications, it was determined that a 12,000 K Planck function curve best represented the Earth-exiting radiance spectrum for ocean scenes (Barnes et al. 1996).

In this technical memorandum, a model from H. Gordon (at the University of Miami) of the upwelling Earth radiance for an ocean scene and a clear atmosphere is adapted to provide a prelaunch top-of-the-atmosphere (TOA) radiance spectrum for SeaWiFS. Comparisons of the responses of the SeaWiFS bands, using this model TOA spectrum to those for the 12,000 K Planck function, give an estimate of the uncertainty in the SeaWiFS measurements that comes from a lack of knowledge of the actual spectral shape of the upwelling Earth radiance on-orbit. These differences are investigated for the two types of instrument calibrations described above.

In addition, the LOWTRAN and MODTRAN7 atmospheric radiative transfer codes were modified and combined with the Gordon model to allow estimates of the effects of atmospheric water vapor and oxygen A-band absorption on the SeaWiFS measurements. Again, these effects are investigated for the two types of instrument calibrations described above. The laboratory measurements from November 1993 calibration were also used to provide a calibration in terms of band-averaged spectral radiances. These results were used for comparison with the postthermal-vacuum calibration of the SeaWiFS instrument and spacecraft at the conclusion of environmental testing. This took place at the spacecraft manufacturer—Orbital Sciences Corporation (OSC)—on 23–24 January 1997. The results of the second SeaWiFS radiometric calibration will be published in a future volume in this series. Preliminary calculations suggest a consistency between the two SeaWiFS calibrations at the 3% level.

A short synopsis of each chapter in this volume is given below.



## **SeaWiFS Technical Report Series**

**Stanford B. Hooker, Editor**  
*NASA Goddard Space Flight Center*  
*Greenbelt, Maryland*

**Elaine R. Firestone, Technical Editor**  
*General Sciences Corporation*  
*Laurel, Maryland*

## **Volume 40, SeaWiFS Calibration Topics, Part 2**

**Robert A. Barnes**  
**Robert E. Eplee, Jr.**  
**Eueng-nan Yeh**  
*General Sciences Corporation*  
*Laurel, Maryland*

**Wayne E. Esaias**  
*NASA Goddard Space Flight Center*  
*Greenbelt, Maryland*



National Aeronautics and  
Space Administration

**Goddard Space Flight Center**  
Greenbelt, Maryland 20771

**1997**



---

## Chapter 1

---

### A Nominal Top-of-the-Atmosphere Spectrum for SeaWiFS

ROBERT A. BARNES

*General Sciences Corporation  
Laurel, Maryland*

WAYNE E. ESAIAS

*Goddard Space Flight Center  
Greenbelt, Maryland*

#### ABSTRACT

This chapter presents a TOA radiance spectrum to be used in modeling studies of the interaction of the SeaWiFS relative spectral responses with the radiance spectrum that they view. The TOA spectrum presented here was developed from previous modeling work by H. Gordon at the University of Miami. It covers the full wavelength range of the relative spectral responses for the SeaWiFS bands (380–1,150 nm), and it can be modified using LOWTRAN absorption spectra for atmospheric water vapor and oxygen to account for the effects of these absorbers. In addition, it includes the MODTRAN7 spectrum for atmospheric oxygen A-band absorption, which occurs in the band pass of SeaWiFS band 7 (765 nm). These spectra are available on the SeaWiFS Web site (Barnes 1997a).

---

#### 1.1 INTRODUCTION

For filter radiometers with finite bandpasses, there is a fundamental interaction between the spectral responses of the instrument bands and the spectral shape of the radiance spectrum that they measure. For instruments with narrow bandpasses of 10 nm or less, such as the SeaWiFS Transfer Radiometer (SXR), the effects of source spectral shape are negligibly small. For SeaWiFS, which has bandwidths of 20 and 40 nm, different source spectral shapes lead to different output from the instrument.

The effects of source spectral shape were studied in Barnes et al. (1996), using normalized Planck function (i.e., blackbody) curves to provide TOA radiance spectra. These were combined with the published spectral response curves for the SeaWiFS bands from Barnes (1994) to examine changes to the in-band and out-of-band responses of the instrument, as well as to the total band responses. For those studies, it was assumed that the TOA spectrum for SeaWiFS measurements was best approximated by a 12,000 K Planck function curve. In addition, the Planck function curves in those studies did not include any accommodation for absorption features in the TOA spectrum.

Using models of atmospheric radiative transfer, it is possible to provide more realistic TOA spectra. The model results of H. Gordon from the University of Miami (Hooker et al. 1992) are the basis for the refinement presented here.

They are used to create a baseline TOA spectrum, that is, a TOA spectrum with no absorption features. This base spectrum covers the wavelength range from 380–1,150 nm at 1 nm intervals covering the range for the measured spectral responses of the SeaWiFS bands. In addition, the LOWTRAN tropical model has been adapted to provide spectra for atmospheric water vapor and oxygen A-band absorption features over the wavelength range of the base spectrum.

A high resolution (MODTRAN7) oxygen A-band absorption spectrum has also been created to examine the effects of oxygen absorption on the output of SeaWiFS band 7. A more detailed spectrum is required, since oxygen absorption occurs at the peak of the spectral response for band 7 (as shown in the Prologue to Barnes et al. 1996). The absorption spectrum presented here is provided at 0.1 nm intervals. To use this spectrum, the base radiance profile and the spectral response values for SeaWiFS band 7 have been set to the same wavelength interval via interpolation.

#### 1.2 BASELINE SPECTRUM

This nominal spectrum is based on the model results of H. Gordon as given in Fig. 3 of Hooker et al. (1992). Those results cover wavelengths from 400–890 nm for a nadir view with a 60° solar zenith angle. The model includes absorption by oxygen, ozone, and water vapor, plus scattering by



## **SeaWiFS Technical Report Series**

**Stanford B. Hooker, Editor**

*NASA Goddard Space Flight Center*

*Greenbelt, Maryland*

**Elaine R. Firestone, Technical Editor**

*General Sciences Corporation*

*Laurel, Maryland*

## **Volume 40, SeaWiFS Calibration Topics, Part 2**

**Robert A. Barnes**

**Robert E. Eplee, Jr.**

**Eueng-nan Yeh**

*General Sciences Corporation*

*Laurel, Maryland*

**Wayne E. Esaias**

*NASA Goddard Space Flight Center*

*Greenbelt, Maryland*



National Aeronautics and  
Space Administration

**Goddard Space Flight Center**

Greenbelt, Maryland 20771

**1997**



---

## Chapter 2

---

### SeaWiFS Measurements in Orbit: Spectral Radiances at the Nominal Center Wavelengths

ROBERT A. BARNES  
ROBERT E. EPLEE, JR.  
EUENG-NAN YEH

*General Sciences Corporation, Laurel, Maryland*

#### ABSTRACT

In November 1993, SeaWiFS was calibrated using a technique in which the digital counts from the instrument were paired with the spectral radiances from a laboratory integrating sphere at the nominal center wavelengths for the SeaWiFS bands. The conversion of this type of laboratory calibration to orbit requires three factors linked to the spectral shape of the source that SeaWiFS views. First, the total band response to the laboratory source must be converted to that for the source viewed on orbit. In this case, the nominal TOA spectrum of Barnes and Esaias (1997) is used. Second, the effects of water vapor and the oxygen A-band on the upwelling atmospheric radiance must be removed; and third, the out-of-band response of the SeaWiFS bands to the upwelling radiance must also be removed. These factors are presented in a tabular form as the basis for an efficient correction algorithm for on-orbit measurements.

## 2.1 INTRODUCTION

The radiometric calibration of SeaWiFS in November 1993 was based on spectral radiances at eight wavelengths, i.e., the nominal center wavelengths for the SeaWiFS bands (412, 443, 490, 510, 555, 670, 765, and 865 nm). The SIS in the laboratory was, itself, calibrated at these wavelengths. A calibration of this sort works well for radiometric instruments that measure at one (or several) individual wavelengths. The SeaWiFS bands, however, have nominal spectral bandwidths (FWHM response) of 20 and 40 nm. For instruments with finite spectral bandwidths such as these, this type of calibration creates a dependence of the instrument's response on the spectral shape of the source that is measured.

According to the manufacturer of SeaWiFS, the SIS used in calibrating the instrument has the spectral shape of a 2,850 K blackbody. The analysis behind this assumption was not a required part of the laboratory calibration data for SeaWiFS. For measurements of a similar SIS, however, the SeaWiFS output were equivalent to those for a Planck function with the same temperature (Barnes et al. 1996). For the current radiometric calibration of SeaWiFS (Barnes et al. 1994b), the manufacturer's calibration source is assumed to have the spectral shape of a 2,850 K blackbody.

The initial prelaunch calibration of SeaWiFS used the relative spectral responses (RSRs) of the eight SeaWiFS

bands to convert the instrument's responses from a 2,850 K blackbody spectral shape in the laboratory, to an on-orbit response for a 5,900 K blackbody (Table 12 of Barnes et al. 1994b). This is the spectral shape for the solar output and is the spectral shape found in the SeaWiFS Performance Specifications (Barnes et al. 1994a). In a series of modelling studies (Barnes et al. 1995 and Barnes and Yeh 1996), it was determined that a 12,000 K Planck function (blackbody) curve is more representative of the spectral shape for the upwelling radiance from the ocean scenes that will be viewed by SeaWiFS. The factors to convert the output from the eight instrument bands for a 2,850 K laboratory source to those for a 12,000 K on-orbit source are listed in Table 17 of Barnes and Yeh (1996). Neither the 12,000 K nor the 5,900 K TOA spectra include the absorption features found in the upwelling Earth radiance.

More recently, Barnes and Esaias (1997) developed a TOA radiance spectrum based on the atmospheric radiative transfer model results of H. Gordon at the University of Miami (Hooker et al. 1992). The TOA spectrum includes a baseline component, extending from 380–1,150 nm in 1 nm increments, which has no absorption features. The LOWTRAN tropical model was also adapted by Barnes and Esaias (1997) to provide spectra for atmospheric water vapor and oxygen A-band absorption features. In addition, a higher resolution spectrum, based on MODTRAN7, was adapted to examine the effects of oxygen A-band absorption on the output of SeaWiFS band 7. The TOA



## **SeaWiFS Technical Report Series**

**Stanford B. Hooker, Editor**  
*NASA Goddard Space Flight Center*  
*Greenbelt, Maryland*

**Elaine R. Firestone, Technical Editor**  
*General Sciences Corporation*  
*Laurel, Maryland*

## **Volume 40, SeaWiFS Calibration Topics, Part 2**

**Robert A. Barnes**  
**Robert E. Eplee, Jr.**  
**Eueng-nan Yeh**  
*General Sciences Corporation*  
*Laurel, Maryland*

**Wayne E. Esaias**  
*NASA Goddard Space Flight Center*  
*Greenbelt, Maryland*



National Aeronautics and  
Space Administration

**Goddard Space Flight Center**  
Greenbelt, Maryland 20771

**1997**



---

## Chapter 3

---

### The Effect of Atmospheric Absorption on the Output of SeaWiFS Band 7

ROBERT A. BARNES  
General Sciences Corporation  
Laurel, Maryland

#### ABSTRACT

Oxygen A-band absorption in SeaWiFS band 7 (765 nm) has been investigated twice previously. Fraser (1995) calculated the ozone equivalent bandwidth for two pathlengths through the atmosphere, and Ding and Gordon (1995) provided an analysis in which ozone absorption was imbedded in their radiative transfer model. Here, ozone absorption is presented using the relative spectral responses from Barnes (1994), the nominal TOA spectrum from Barnes and Esaias (1997), and the ozone absorption spectrum from MODTRAN7. The study presented here is compared with the previous studies. The MODTRAN7 spectrum has much higher wavelength resolution than the LOWTRAN spectrum used by Barnes et al. (1997), and Table 16 in this paper completes Table 9 in Barnes et al. (1997). The uncertainty in the correction for oxygen absorption in SeaWiFS band 7 is estimated to be 0.8%.

### 3.1 INTRODUCTION

SeaWiFS was designed with near-infrared bands at 765 and 865 nm. These bands will provide the basis for the atmospheric correction algorithm used in the procedure to deduce water-leaving radiances from the SeaWiFS data (Gordon and Wang 1994). The band edges for the two bands, that is, the half-maximum response points, are located at 744.7 and 785.0 nm for the nominal 765 nm band, and at 845.7 and 887.0 nm for the nominal 865 nm band (Barnes et al. 1994a). The bandwidths, or the wavelength intervals between the half-maximum response points, for these bands were specified to be 40 nm to allow measurements from the instrument with sufficiently large signal-to-noise ratios. In addition, the two bands have been placed in spectral regions that are relatively free of atmospheric water vapor absorption; however, the 765 nm band encompasses a region of atmospheric oxygen absorption, the oxygen A-band, that extends from approximately 758–771 nm.

Atmospheric oxygen A-band absorption was a consideration in the design of SeaWiFS. The original specification for the 765 nm band included a notch in the spectral response for the band. The design specification called for a bimodal response from the interference filter, with near zero transmission in the wavelength region for the oxygen absorption. Studies by the instrument manufacturer showed that such a feature would make the filter nearly impossible to fabricate, because of the narrowness of the notch and the sharp changes in transmission on either side.

In addition, any filter that could be made would have low overall transmission, creating a major reduction in the optical throughput for the band. The reduction in radiance at the detectors for band 7 would have required a greatly increased electronic gain for the band, reducing the band's signal-to-noise ratio and compromising other design specifications. As a result, the SeaWiFS Project decided that SeaWiFS band 7 would have a *standard shaped* spectral response and that the effects of the oxygen A-band would be included in the processing of the on-orbit data.

### 3.2 OZONE BANDWIDTH

Fraser (1995) used the concept of ozone equivalent bandwidth to calculate the effects of oxygen A-band absorption on SeaWiFS band 7. In that analysis, the relative spectral response for the band,  $R(\lambda)$ , normalized to unity, is integrated to give the bandwidth

$$B = \int_{\lambda_1}^{\lambda_2} R(\lambda) d\lambda, \quad (3)$$

where  $B$  is the bandwidth (in nanometers),  $\lambda_1$  is 380 nm, and  $\lambda_2$  is 1,150 nm. These integration limits encompass the wavelength region over which the SeaWiFS photodiodes have a significant quantum efficiency. Using the relative spectral response values from Barnes (1994), the bandwidth for SeaWiFS band 7 is 40.99 nm. This bandwidth corresponds to that for the total band response ( $R_T$ ), described in Barnes et al. (1997), where changes to  $R_T$  for



## **SeaWiFS Technical Report Series**

**Stanford B. Hooker, Editor**  
*NASA Goddard Space Flight Center*  
*Greenbelt, Maryland*

**Elaine R. Firestone, Technical Editor**  
*General Sciences Corporation*  
*Laurel, Maryland*

## **Volume 40, SeaWiFS Calibration Topics, Part 2**

**Robert A. Barnes**  
**Robert E. Eplee, Jr.**  
**Eueng-nan Yeh**  
*General Sciences Corporation*  
*Laurel, Maryland*

**Wayne E. Esaias**  
*NASA Goddard Space Flight Center*  
*Greenbelt, Maryland*



National Aeronautics and  
Space Administration

**Goddard Space Flight Center**  
Greenbelt, Maryland 20771

1997



## Chapter 4

### The 1993 SeaWiFS Calibration Using Band-Averaged Spectral Radiances

ROBERT A. BARNES

ROBERT E. EPLEE, JR.

*General Sciences Corporation, Laurel, Maryland*

#### ABSTRACT

The radiometric calibration of SeaWiFS in November 1993 used a calibration technique that paired the digital counts from the instrument bands, with the spectral radiances from the laboratory SIS at the nominal center wavelengths for those bands. Using the spectral shape of the output of the laboratory radiance source, as provided by the manufacturer, it is possible to provide a radiometric calibration of SeaWiFS in terms of band-averaged spectral radiances. That calibration is presented here. It is given for three wavelength ranges, 380–940 nm, 380–1,150 nm, and for the in-band response ranges for the SeaWiFS bands.

#### 4.1 INTRODUCTION

The data for the 1993 calibration of SeaWiFS at SBRS were provided by the instrument's manufacturer in terms of the digital counts from the instrument bands versus the spectral radiances at the nominal center wavelengths for the bands. Those data can be found in Table 8 of Barnes et al. (1994b). A series of instrument modelling studies (Barnes and Yeh 1996 and Barnes et al. 1997) examined the effects of this calibration method. When an instrument with finite bandwidths, such as SeaWiFS, is calibrated at one fixed wavelength, the relationship between the instrument output and the spectral radiance at that wavelength changes with the spectral shape of the source that is measured. This effect has been included in the current SeaWiFS radiometric calibration (Barnes et al. 1994b), where the laboratory calibration, for a source with the spectral shape of a 2,850 K blackbody, was transferred into an on-orbit calibration, for a source with the spectral shape of a 5,900 K blackbody, by revising the calibration coefficients.

There is an alternate calibration method, in which the band-averaged (or band-weighted) spectral radiance is calculated. This requires knowledge of the radiance from the laboratory source over the wavelength region at which the instrument responds. For SeaWiFS, the spectral responses of the bands were measured from 380–1,150 nm (Barnes 1994 and Barnes et al. 1994b). The band-averaged (or band-weighted) spectral radiance is calculated using

$$L_B(\lambda_B) = \frac{\int_{\lambda_1}^{\lambda_2} L_s(\lambda) R(\lambda) d\lambda}{\int_{\lambda_1}^{\lambda_2} R(\lambda) d\lambda}, \quad (9)$$

and

$$\lambda_B = \frac{\int_{\lambda_1}^{\lambda_2} \lambda L_s(\lambda) R(\lambda) d\lambda}{\int_{\lambda_1}^{\lambda_2} L_s(\lambda) R(\lambda) d\lambda}, \quad (10)$$

where  $L_B(\lambda_B)$  is the band-averaged spectral radiance for the band at wavelength,  $\lambda_B$ ;  $\lambda_1$  and  $\lambda_2$  are the lower and upper integration wavelengths (380 nm and 1,150 nm for SeaWiFS);  $L_s(\lambda)$  is the spectral radiance from the source at wavelength  $\lambda$ ; and  $R(\lambda)$  is the response of the band at wavelength  $\lambda$ .

In (9), the spectral response of the band,  $R(\lambda)$ , is the weighting function. For SeaWiFS,  $R(\lambda)$  is given as the current of the band's photodiode (in picoamperes) at each nanometer from 380–1,150. This current is amplified and quantized to give a digital output. It is possible to normalize this spectral response to an integral value of unity, where unity represents the entire output from the photodiode. This normalization shows the link between the spectral response and the digital output from the band. The integral of the relative spectral response is transformed to the total number of digital counts from the band; however,  $R(\lambda)$  appears in both the numerator and denominator of (9), so any normalizing constant for  $R(\lambda)$  falls out of the calculation.

The band-averaged spectral radiance and the band-averaged center wavelength are tied together. Once calibrated using the laboratory source, the output from each band will give the band-averaged spectral radiance for any other source spectral shape. However, the band-averaged center wavelength (that is, the wavelength associated with the band-averaged spectral radiance) will vary with source spectral shape.



## **SeaWiFS Technical Report Series**

**Stanford B. Hooker, Editor**

*NASA Goddard Space Flight Center  
Greenbelt, Maryland*

**Elaine R. Firestone, Technical Editor**

*General Sciences Corporation  
Laurel, Maryland*

## **Volume 40, SeaWiFS Calibration Topics, Part 2**

**Robert A. Barnes**

**Robert E. Eplee, Jr.**

**Eueng-nan Yeh**

*General Sciences Corporation  
Laurel, Maryland*

**Wayne E. Esaias**

*NASA Goddard Space Flight Center  
Greenbelt, Maryland*



National Aeronautics and  
Space Administration

**Goddard Space Flight Center**  
Greenbelt, Maryland 20771

**1997**



---

## Chapter 5

---

### SeaWiFS Measurements in Orbit: Band-Averaged Spectral Radiances

ROBERT A. BARNES

*General Sciences Corporation, Laurel, Maryland*

#### ABSTRACT

This paper presents the culmination of the source spectra shape studies in Barnes et al. (1996) and in this technical memorandum. The SeaWiFS band-averaged spectral radiances are independent of the spectral shape of the source that the instrument measures; however, the band-averaged center wavelengths associated with them do have such a dependence. The current radiometric calibration (Barnes et al. 1994b) does not use band-averaged measurements. The adoption of band-averaged spectral radiances awaits analysis of the radiometric recalibration of SeaWiFS at the spacecraft manufacturer, which was done during the first quarter of 1997. For measurements of on-orbit band-averaged spectral radiances, it is recommended that the in-band results be used. A modification of the technique of Barnes and Yeh (1996), for use with band-averaged measurements, is presented. Since band-averaged center wavelengths are not part of the SeaWiFS level-1b processing, the best estimates for these wavelengths are given here. In addition, estimates are provided of the uncertainties in the on-orbit band-averaged spectral radiances and center wavelengths that derive from the lack of information on the spectral shape of the Earth-exiting radiance.

### 5.1 INTRODUCTION

The band-averaged spectral radiance and center wavelength for SeaWiFS measurements of the Earth-exiting radiance are defined as

$$L_B(\lambda_B) = \frac{\int_{\lambda_1}^{\lambda_2} L_e(\lambda) R(\lambda) d\lambda}{\int_{\lambda_1}^{\lambda_2} R(\lambda) d\lambda}, \quad (12)$$

and

$$\lambda_B = \frac{\int_{\lambda_1}^{\lambda_2} \lambda L_e(\lambda) R(\lambda) d\lambda}{\int_{\lambda_1}^{\lambda_2} L_e(\lambda) R(\lambda) d\lambda}, \quad (13)$$

where  $L_B(\lambda_B)$  is the band-averaged spectral radiance for the band at wavelength,  $\lambda_B$ ;  $\lambda_1$  and  $\lambda_2$  are the lower and upper integration wavelengths (380 nm and 1,150 nm for SeaWiFS);  $L_e(\lambda)$  is the spectral radiance from the source at wavelength  $\lambda$ ; and  $R(\lambda)$  is the response of the band at wavelength  $\lambda$ .

In (12), the integral in the numerator is the total band response. In Barnes et al. (1997), the total band response was calculated as the total current from the photodiode (in picoamperes). With electronic amplification and digitization within the instrument, this current is converted into digital counts. There is no spectral dependence in this amplification, and it can be treated as a constant multiplier

in the term  $R(\lambda)$ . Since  $R(\lambda)$  is found in the numerators and denominators for (12) and (13), the amplification and digitization constant falls out of both equations.

In (12), the relative spectral response in the denominator has been calculated for each SeaWiFS band as the response to a source with a constant spectral radiance of  $1 \text{ mW cm}^{-2} \text{ sr}^{-1} \mu\text{m}^{-1}$  (Barnes et al. 1994b). For solutions to (12), the denominator is a constant for each SeaWiFS band. As a result, the sensitivity studies of total band response ( $R_T$ ) in Barnes et al. (1997) can be directly applied to the band-averaged spectral responses, as calculated using (12). This applies both to the effects of source spectral shape and atmospheric absorption.

For the sensitivity studies in Barnes et al. (1997), the wavelengths for the SeaWiFS bands were the nominal center wavelengths as given in the performance specification for the instrument (Barnes et al. 1994a). In the current calibration of SeaWiFS (November 1993) the digital counts from each band are linked to the spectral radiance at the nominal center wavelength for that band. In this type of calibration, the relationship of counts to spectral radiance also includes a dependence on the spectral shape of the radiance source (Barnes et al. 1994b and Barnes et al. 1996a).

For calculations of the band-averaged spectral response using (12), the numerator of the equation gives the total band output. Since the integral in the numerator of (12)



# PROCEEDINGS OF SPIE



SPIE—The International Society for Optical Engineering

## *Earth Observing Systems II*

**William L. Barnes**

*Chair/Editor*

**28–29 July 1997**

**San Diego, California**

*Sponsored and Published by*

SPIE—The International Society for Optical Engineering



**Volume 3117**

SPIE is an international technical society dedicated to advancing engineering and scientific applications of optical, photonic, imaging, electronic, and optoelectronic technologies.



# Contents

vii *Conference Committee*

---

## SESSION 1 REMOTE SENSING SYSTEMS

---

- 2 **Atmospheric lidar predevelopment program (ATLID) [3117-02]**  
D. Morancais, Matra Marconi Space (France); A. E. Marini, European Space Agency/ESTEC (Netherlands)
- 11 **Stratospheric aerosol and gas experiment III [3117-04]**  
W. P. Chu, NASA Langley Research Ctr.; M. P. McCormick, Hampton Univ.; J. M. Zawodny, L. E. Mauldin, NASA Langley Research Ctr.
- 19 **SFINX: a far-infrared limb sounding spectrometer for stratospheric trace-gas measurement (OH, HCl) [3117-05]**  
R. W. M. Hoozeveen, J. J. Wijnbergen, M. J. M. E. de Nivelle, A. R. W. de Jonge, A. P. H. Goede, P. A. J. de Korte, Space Research Organization Netherlands
- 30 **Wide-angle Earth sensor [3117-06]**  
M. R. Rost, Servo Corp. of America

---

## SESSION 2 REMOTE SENSING TECHNIQUES

---

- 36 **Imaging spectrometers for future Earth observing systems [3117-07]**  
J. J. Puschell, P. A. Tompkins, ITT Industries
- 49 **Early test results from the uncooled thermal imaging radiometer (TIR) [3117-08]**  
J. W. Hoffman, Space Instruments, Inc.
- 61 **Approaches to developing Earth observing systems based on the tunable acousto-optic filter and separate photon counter with a microchannel plate [3117-10]**  
I. D. Rodionov, I. P. Rodionova, Reagent Research and Development Ctr. (Russia); M. Ovchinnikov, Keldysh Institute of Applied Mathematics (Russia)

---

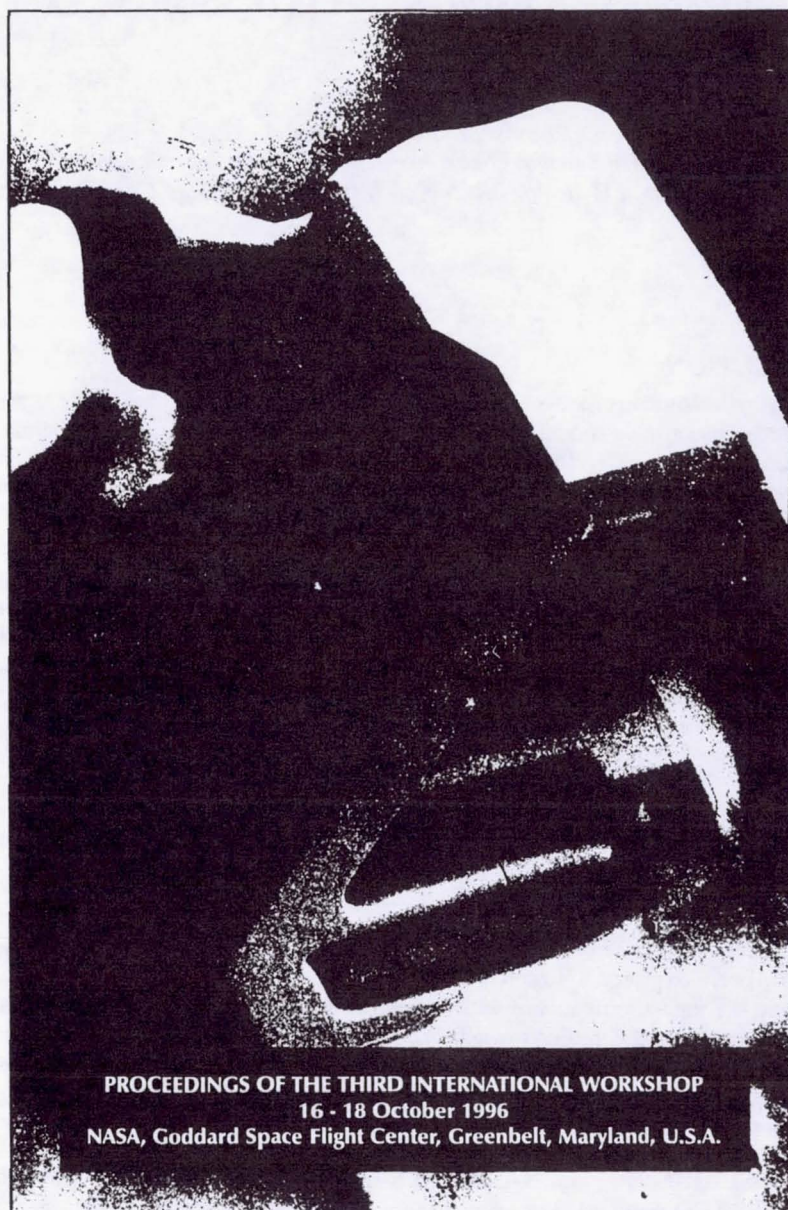
## SESSION 3 NSCAT: EARLY RESULTS

---

- 72 **Wind scatterometry and the status of the NASA scatterometer [3117-13]**  
D. G. Long, Brigham Young Univ.
- 81 **Antarctic ice edge detection using NSCAT data [3117-14]**  
Q. P. Remund, D. G. Long, Brigham Young Univ.
- 90 **Preliminary evaluation of NASA scatterometer data and its application to ocean surface analysis and numerical weather prediction [3117-15]**  
R. Atlas, NASA Goddard Space Flight Ctr.
- 98 **Wind measurement accuracy for the NASA scatterometer [3117-16]**  
D. G. Long, T. E. Oliphant, Brigham Young Univ.



APPLICATIONS OF  
**REMOTE SENSING**  
IN HYDROLOGY



PROCEEDINGS OF THE THIRD INTERNATIONAL WORKSHOP  
16 - 18 October 1996  
NASA, Goddard Space Flight Center, Greenbelt, Maryland, U.S.A.

Editors G.W. Kite, A. Pietroniro and T.J. Pultz



## DERIVATION OF LAKE AREAS AND ELEVATIONS FOR THE MACKENZIE BASIN USING SATELLITE REMOTE SENSING

Charon Birkett<sup>1</sup> and Geoff Kite<sup>2</sup>

<sup>1</sup>Mullard Space Science Laboratory, University College London, U.K.

<sup>2</sup>National Hydrology Research Institute, Saskatoon, Canada

### INTRODUCTION

Modelling hydrological processes in large watersheds flowing to the Arctic ocean is one step towards larger-scale modelling of the global water and energy cycles. Models of the Mackenzie River Basin (Northern Canada) are currently available but omit explicit routing of river flows through the three main lakes - Athabasca, Great Slave Lake and Great Bear Lake (Kite *et al.*, 1994). These lakes occupy an area of 65,000 km<sup>2</sup> but little gauge information is available. The levels of the lakes are only measured at a few points on the circumferences and river flows are only measured downstream. The hydraulic relationships between level/discharge and level/area/volume are uncertain. It has been previously shown that satellite remote sensing can be utilised in providing measurements of both lake surface area using imaging techniques and lake level using radar altimetry (Birkett, 1994). Here, we explore the application of these techniques to derive the lake levels and areas for the Mackenzie Basin lakes.

### THE DERIVATION OF LAKE LEVEL CHANGES

#### Background

The derivation of lake level changes using satellite radar altimeter measurements has previously been explored (Birkett, 1994, Birkett, 1995). This method has two main advantages; the measurements are with respect to a single reference datum, and they can provide information for regions where access to a lake is restricted or the data are unobtainable. Several altimeters have been operational during the 1990's and TOPEX/POSEIDON (T/P) is currently obtaining the best surface elevation measurements to an accuracy of 3-4cm rms (Tapley *et al.*, 1994).

TOPEX/POSEIDON is a joint NASA/CNES mission which carries two radar altimeters (NRA and SSALT) onboard. The satellite was launched in September 1992 and operates in an orbit which has global coverage to  $\pm 66^\circ$  latitude with a 10 day repeat cycle. During one orbital cycle (also termed "erm") the satellite undergoes 254 ascending and



**NASA Technical Memorandum 104606, Vol. 12**

# **Technical Report Series on Global Modeling and Data Assimilation**

**Max J. Suarez, Editor**  
*Goddard Space Flight Center  
Greenbelt, Maryland*

## **Volume 12**

# **Comparison of Satellite Global Rainfall Algorithms**

**Alfred T. C. Chang**  
**Long S. Chiu**  
*Goddard Space Flight Center  
Greenbelt, Maryland*



National Aeronautics and  
Space Administration

**Goddard Space Flight Center**  
Greenbelt, Maryland  
**1997**



## Abstract

Seventeen months of rainfall data (August 1987–December 1988) from nine satellite rainfall algorithms (Adler, Chang, Kummerow, Prabhakara, Huffman, Spencer, Susskind, and Wu) were analyzed to examine the uncertainty of satellite-derived rainfall estimates. The variability among algorithms, measured as the standard deviation computed from the ensemble of algorithms, shows regions of high algorithm variability tend to coincide with regions of high rain rates. The ratio of the annual mean algorithm variability to the annual mean (August 1987–July 1988) rain rate is generally less than 0.5 over most of the regions between 50°N and 50°S. Exceptions are found in the oceanic dry zones and the Himalayan region. High algorithm variability in the oceanic dry zones points to the different approaches in the treatment of low rain rates. Arkin's algorithm, which uses cloud top temperature, tend to over-estimate in the mountainous Himalayas and in the Indian monsoon region. The over-estimate over the Himalayas is attributed to the cold surface. Over the Indian Ocean, the frequent occurrence of non-raining high clouds contributed to the high estimates. The global annual rainfall (over the latitude belts  $\pm 50^\circ$  and for August 1987–July 1988) ranges from 2.5 to 3.5 mm/day, with higher variability over land than over ocean. The variability of zonal averaged rain rates is in the range of about 0.5 mm/day in the subtropical dry zones and increases to 2 mm/day in the tropical rain belts. Histograms of pattern correlation (PC) between algorithms suggest a bimodal distribution, with separation at a PC value of about 0.85. Applying this threshold as a criteria for similarity, our analyses show that algorithms using the same sensor or satellite input tend to be similar, suggesting the dominance of sampling errors in these satellite estimates.

The sensitivity of the algorithms to the 1986–87 El Niño Southern Oscillation event was examined using paired-t tests and PC analyses. Paired-t statistics results indicate that the algorithms of Chang, Prabhakara, and Spencer show significant difference between August 1987 and 1988, assuming the difference field is spatially uncorrelated. This assumption needs to be further examined.

## 1 INTRODUCTION

The reality of Global Circulation Models (GCMs) to predict future climate changes hinges on their ability to realistically reproduce current climate. Although most of the GCMs are based on the same laws of thermodynamics and dynamics, they emphasize different physical processes or used different parameterization schemes for many of the important climate components. The Atmospheric Model Intercomparison Project (AMIP) was established to evaluate the operational GCMs and to diagnostically compare products of the GCMs. Ten years (1979–1988) of GCM runs were performed in a controlled situation for the cases with and without actual sea surface temperature forcing.

Precipitation is an important climate parameter. Theoretical studies have shown the importance of the release of latent heat of condensation associated with precipitation in driving atmospheric circulation. Observational studies have also demonstrated the association between precipitation pattern changes and climate variations. However, the spatial and temporal variability of rainfall at all scales poses a great challenge in estimating space/time rainfall.

In response to this challenge, the National Aeronautics and Space Administration (NASA) of the United States (U.S.) and the National Space Development Agency (NASDA) of Japan jointly sponsored the Tropical Rainfall Measuring Mission (TRMM). With TRMM well underway, the science community saw the opportunity for improved global rainfall estimation.





# IGARSS'97

1997 International Geoscience and  
Remote Sensing Symposium

03-08 August 1997

Singapore International Convention & Exhibition Centre • Singapore

Remote Sensing -- A Scientific Vision for  
Sustainable Development

IEEE Catalog Number: 97CH36042  
Library of Congress Number: 97-70575



## Temperature Corrected Bootstrap Algorithm

Joey C. Comiso and H. Jay Zwally

Laboratory for Hydrospheric Processes, Code 971

NASA/Goddard Space Flight Center, Greenbelt, MD 20771

Tel: 301-286-9135, FAX: 301-286-1761, e-mail: comiso@joey.gsfc.nasa.gov

**Abstract** -- A temperature corrected Bootstrap Algorithm has been developed using Nimbus-7 Scanning Multichannel Microwave Radiometer data in preparation to the upcoming AMSR instrument aboard ADEOS and EOS-PM. The procedure first calculates the effective surface emissivity using emissivities of ice and water at 6 GHz and a mixing formulation that utilizes ice concentrations derived using the current Bootstrap algorithm but using brightness temperatures from 6 GHz and 37 GHz channels. These effective emissivities are then used to calculate surface ice temperatures which in turn are used to convert the 18 GHz and 37 GHz brightness temperatures to emissivities. Ice concentrations are then derived using the same technique as with the Bootstrap algorithm but using emissivities instead of brightness temperatures. The results show significant improvements in areas where ice temperature is expected to vary considerably such as near the continental areas in the Antarctic, where the ice temperature is colder than average, and in marginal ice zones.

### INTRODUCTION

The most important parameter derived from satellite data that has been used for sea ice cover studies is ice concentration. Ice concentration is used to calculate the extent and actual area of the ice pack which are useful for assessing the state of the ice cover and its seasonal and interannual variabilities [1,2,3]. It is also used to characterize the marginal ice zones, the divergence zones, and polynya areas in relation to air-sea-ice interaction and heat flux studies.

Ice concentration has been defined as the percentage of open water within the field of view of the sensor. In the late spring and summer period when surface air temperatures are above freezing and open water are distinctly free of ice, the definition is exact. In the winter, the definition is not as clearcut because under freezing conditions, open water surfaces undergoes continuous transition to grease ice through pancakes or nilas (depending on the state of the ocean), and to young and the thicker ice types. During this time period, the emissivity of the surface changes from that of open water to that of thick ice.

Ice concentrations are derived using a mixing formulation because of the large footprint (>25km) of the satellite sensors [4,5,6,7]. Because of the high correlation of data from the different channels [7,8], the number of

surfaces that can be unambiguously classified by SMMR data is three: two ice types and open water. The most dominant ice types are first year ice and multiyear ice which are found in the seasonal and the perennial ice regions, respectively. These two ice types have been shown to have distinctly different emissivities but the emissivity values can overlap [9,10]. The third type, which is abundant in leads, polynyas and marginal ice zones, is generally called thin ice but can be grease ice, pancake, or nilas. The ice concentration algorithms do not handle the thin ice types well because the emissivity is not well defined as stated earlier. But some have tried to calculate concentrations of thin ice in high ice production areas like the Bering Sea [11,12] where thick ice with snow cover is assumed to be minimal. In most ice algorithms, three surfaces (first year, multiyear, and open water) are used in a mixing formulation to derive ice concentration. In the Bootstrap algorithm, the high correlation of the emissivities of the different ice surfaces in some sets of channels is utilized and within the footprint of the sensor, the surface is assumed to be either ice or water. The presence of thin ice within the footprint, causes an error, the magnitude of which depends on thickness or emissivity [13].

The Bootstrap algorithm [14] makes use of two sets of channels: the HV37 set, consisting of the horizontally and vertically polarized data at 37 GHz, and the V1837 set, which makes use of the vertically polarized 18 and 37 GHz data. The HV37 set is generally insensitive to spatial variations in surface temperature and is most effective in the perennial ice regions while the V1837 is found to be most effective in the seasonal sea ice regions. The concurrent use of the two sets provides optimum accuracy in the retrieval of global sea ice parameters although the second set shows more sensitivity to surface temperature as described in [14]. In this paper, we present a technique that overcomes the latter weakness.

### TEMPERATURE INDEPENDENT TECHNIQUE

The Nimbus-7 SMMR sensor has dual polarized channels at 5 frequencies ranging from 6 GHz through 37 GHz. The 6 GHz data have not been used for ice concentration algorithms, although they provide the largest contrast between open water and ice at this frequency, because of its large footprint (about 70 by 150 km). The latter causes some of the important features of the ice cover to be smeared out.





# IGARSS'97

1997 International Geoscience and  
Remote Sensing Symposium

03-08 August 1997

Singapore International Convention & Exhibition Centre • Singapore

Remote Sensing -- A Scientific Vision for  
Sustainable Development

IEEE Catalog Number: 97CH36042  
Library of Congress Number: 97-70575



# Antarctic Surface Temperatures using Satellite Infrared Data from 1979 Through 1995

Josefino C. Comiso and Larry Stock

Laboratory for Hydrospheric Processes, Code 971,

NASA/Goddard Space Flight Center, Greenbelt, MD, U.S.A. 20771

Telephone: 301-286-9135; FAX: 301-286-1761; E-mail: comiso@joey.gsfc.nasa.gov

**ABSTRACT** — The large scale spatial and temporal variations of surface ice temperature over the Antarctic region are studied using infrared data derived from the Nimbus-7 Temperature Humidity Infrared Radiometer (THIR) from 1979 through 1985 and from the NOAA Advanced Very High Resolution Radiometer (AVHRR) from 1984 through 1995. Enhanced techniques suitable for the polar regions for cloud masking and atmospheric correction were used before converting radiances to surface temperatures. The observed spatial distribution of surface temperature is highly correlated with surface ice sheet topography and agrees well with ice station temperatures with 2K to 4K standard deviations. The average surface ice temperature over the entire continent fluctuates by about 30K from summer to winter while that over the Antarctic Plateau varies by about 45K. Interannual fluctuations of the coldest temperatures are observed to be as large as 15K. Also, the interannual variations in surface temperatures are highest at the Antarctic Plateau and the ice shelves (e.g., Ross and Ronne) with a periodic cycle of about 5 years and standard deviations of about 11K and 9K, respectively. Despite large temporal variability, however, especially in some regions, a regression analysis that includes removal of the seasonal cycle shows no apparent trend in temperature during the period 1979 through 1995.

## INTRODUCTION

Surface air temperatures from ice stations in the Antarctic region have been observed to be highly variable [1,2,3]. Also, in many areas, significant positive trends are observed whereas in some other areas negative trends are apparent. The effect of a rising temperature can be alarming, especially since the West Antarctic Ice Sheet is on the average about -5K in the summer. It is also known that an early signal of a potential increase in global temperatures induced by greenhouse effects may be observed in the polar regions [4,5]. Station data may be separated into manned data and unmanned (stand alone) data. The quality control of the manned data is usually very good since the necessary maintenance and attention are provided to assure that the thermistors used for temperature measurements are working properly. For unmanned stations, however, the data sets are less consistent and gaps in the data record usually occur due

to constant malfunction of the sensor. Unmanned stations have been used to supplement the small number of manned stations to obtain a better general overview of the continent. But considering the large extent of the ice sheet and its varying topography, the available number of ice stations, some of which are clustered together in the same general areas do not provide good spatial coverage of the entire continent. Surface temperature information over sea ice around the continent is even more limited since most of the information is derived from buoy and/or ship data.

In this study, satellite infrared data are used to produce surface temperature maps and to study large scale spatial and temporal variability of surface temperatures in the polar open ocean, sea ice, and continental ice sheet. Thermal infrared systems operate during both day and night thereby providing continuous coverage except that clouds are persistent in the region. Since clouds are usually difficult to discriminate from snow covered surfaces, non-conventional means of masking them has to be implemented but errors due to masking limitations are sometimes not negligible. However, the technique may be the only way to obtain spatially coherent and synoptic measurements of surface temperatures in the region.

## INFRARED DATA, CLOUD MASKING AND RETRIEVAL TECHNIQUES

The Advanced Very High Resolution Radiometer (AVHRR) aboard NOAA satellites is a cross track scanner operating at the following wavelengths: 0.58-0.68  $\mu\text{m}$  (channel 1), 0.73-1.1  $\mu\text{m}$  (channel 2), 3.5-3.9  $\mu\text{m}$  (channel 3), 10.3-11.3  $\mu\text{m}$  (channel 4) and 11.5-12.5  $\mu\text{m}$ . At nadir, the resolution of the Local Area Coverage (LAC) data is about 1  $\text{km}^2$ , but since the LAC data record is not complete, we use global area coverage (GAC) data in this study. GAC data have an effective resolution of 5 by 3  $\text{km}^2$  and are constructed as follows. Along the 2048-pixel scan line, the radiances from 4 successive spots are averaged while the next spot is skipped. Also, only every third scan line is recorded while skipping two scan lines. We also use data from the 11.5  $\mu\text{m}$  channel of THIR data which has a resolution of 6.7 by 6.7 km. Some techniques for retrieving surface temperatures from AVHRR and THIR have been reported [5,7,8,9].



# **WORLD METEOROLOGICAL ORGANIZATION**

## **Programme on Physics and Chemistry of Clouds and Weather Modification Research**

**WMP REPORT No 30**



### **PROCEEDINGS**

## **WMO Workshop on Measurements of Cloud Properties for Forecasts of Weather and Climate**

**Mexico City, 23-27 June 1997**



**D. Baumgardner and G. Raga, Editors**



## Rainfall Estimation over Tropical Oceans: 1) Area average rain rate

Prabhakara Cuddapah, Maria Cadeddu, R. Meneghini, David A. Short, Jung-Moon Yoo,  
G. Dalu, J. L. Schols and J. A. Weinman

NASA Goddard, Greenbelt, MD  
cuddapah@climate.gsfc.nasa.gov

### Abstract

*Multichannel dual polarization microwave radiometer SSM/I observations over oceans do not contain sufficient information to differentiate quantitatively the rain from other hydrometeors on a scale comparable to the radiometer field of view ( $\sim 30$  km). For this reason we have developed a method to retrieve average rain rate over a mesoscale grid box of  $\sim 300 \times 300$  km<sup>2</sup> area over the TOGA COARE region where simultaneous radiometer and radar observations are available for four months (Nov 92 to Feb 93). The rain area in the grid box, inferred from the scattering depression due to hydrometeors in the 85 GHz brightness temperature, constitutes a key parameter in this method. Then the spectral and polarization information contained in all the channels of the SSM/I is utilized to deduce a second parameter. This is the ratio  $S/E$  of scattering index  $S$ , and emission index  $E$  calculated from the SSM/I data. The rain rate retrieved from this method over the mesoscale area can reproduce the radar observed rain rate with a correlation coefficient of about 0.85. Furthermore monthly total rainfall estimated from this method over that area has an average error of about 15 %.*

### 1. Introduction

Radar observations over the TOGA-COARE region (1°N to 4°S and 153°E to 158°E) in the equatorial Pacific (Short et al., 1997) reveal several useful properties of the maritime tropical rain. Since these radars operated continuously we can follow the life cycle of the Mesoscale Convective Systems (MCS's) in this region that lasts for several hours. Observations made in the Winter Monsoon Experiment (Churchill and Houze, 1984), among others, also reveal this life cycle over the South China Sea. In the early phase of the MCS rain from convective cells, on a scale of  $\sim 1$  to 2 Km, dominates. As a result, average convective rainfall is greater than the average stratiform rainfall. This character reverses with the aging of the MCS. In the later stages radar data show, over extensive areas, enhancement of reflectivity (bright band) around 4.5 Km altitude due to aspherical melting snow particles (Meneghini and Kumagai, 1994) that fall slowly in the stratiform clouds. The spatial distribution of rain at any time during the life cycle of the MCS follows a probability distribution that is analogous to the log-normal type (Jones and Sims, 1978). Meteorological conditions, such as the vertical distribution of winds, humidity, and temperature, play an important role in determining the intensity of rain, and growth and distribution of various hydrometeors in the convective and stratiform cloud systems (Takahashi et al, 1995; McGaughey and Zipser, 1996).

In order to sense the rain information from the SSM/I<sup>a</sup> satellite borne microwave radiometer theoretical models have been developed. In such models the brightness temperatures,  $T_b$ 's, measured by this

---

<sup>a</sup> Special Sensor Microwave Imager (SSM/I) radiometer of the Defense Meteorological Satellite Program (DMSP) has 19.37 and 85 GHz channels in dual polarization and 22 GHz channel in a single, i.e. vertical, polarization. This radiometer observed the earth's surface and atmosphere in a conical scan with an incidence angle of  $\sim 50^\circ$ . (for more details see Hollinger et al 1985).



# RECUEIL DES ACTES / PROCEEDINGS

SYMPOSIUM INTERNATIONAL / INTERNATIONAL SYMPOSIUM

15 - 16 - 17 Octobre 1997 / October, 15 - 16 and 17, 1997  
BIARRITZ - FRANCE



CENTRE NATIONAL D'ETUDES SPATIALES



## SURVEILLANCE DES OCEANS A L'HORIZON 2000 : UNE APPROCHE INTEGREE *MONITORING THE OCEANS IN THE 2000s: AN INTEGRATED APPROACH*



El Niño 1994 vu par TOPEX/POSEIDON (source : NASA)  
*El Niño 1994 as seen by TOPEX/POSEIDON (courtesy of NASA)*



CENTRE NATIONAL D'ETUDES SPATIALES

Réunion du Groupe Scientifique TOPEX/POSEIDON

*TOPEX/POSEIDON Science Team Meeting*

13 et 14 octobre 1997 / October 13 and 14, 1997





## ZONAL AND MERIDIONAL MASS REDISTRIBUTION IN THE TROPICAL PACIFIC DURING EL NINO SOUTHERN OSCILLATION EVENTS

Thierry DELCROIX, Lionel GOURDEAU, Pierre RUAL  
Groupe SURTROPAC, Centre ORSTOM de Nouméa,  
BP A5, 98848 Nouméa, New Caledonia

Raghuram MURTUGUDDE  
NASA/GSFC  
Greenbelt, MD20771, USA

### 1. INTRODUCTION

This note aims at documenting the ENSO-related sea level changes for the whole tropical Pacific, and for the 1979-1996 period which covers numerous El Niño and La Niña events. For this purpose, we rely on (a) 0/450 dbar surface dynamic height anomaly (an alias for sea level) derived from XBT and TOGA-TAO measurements during 1979-1996, (b) TOPEX/Poseidon derived sea level anomaly during 1993-1996, and (c) Murtugudde et al. [1996] model sea level output during 1979-1995.

### 2. DATA AND METHODS

*Surface dynamic height anomaly.* About 250,000 temperature profiles were collected in the tropical Pacific during 1979-1996. After validation tests, the irregularly distributed temperature data, both in space and time, were gridded onto bi-monthly field with a resolution of 1°-latitude by 5°-longitude. The gridding procedure was performed through an objective analysis routine (courtesy of P. deMey) in which the spatial and temporal decorrelation scales were based on Meyers et al. [1991]. For each grid point, the temperature profile was converted into 0/450 dbar dynamic height anomaly using local mean T-S curves from Levitus et al. [1994]. *Topex/Poseidon data.* Gridded files of T/P sea level data (1°x1°x10-days) were obtained via internet from the University of Texas Center for Space Research. *Model.* The OGCM is a reduced gravity, primitive equation, sigma coordinate model coupled to an advective atmospheric mixed layer [Murtugudde et al. 1996] which allows accurate SST simulation without restoring to any feedbacks to observed SSTs. The tropical Pacific simulation is carried out from 1975-1995 forced with FSU winds, Xie and Arkin [1996] precipitation, and climatological ISCCP cloudiness and ERBE radiation. Freshwater forcing is included as a natural boundary condition [Murtugudde and Busalacchi, 1997]. The correlation between the ENSO indices from model SSTs and Reynolds' reanalysis SST is above 0.8 for both NINO3 and NINO4. *Southern Oscillation Index.* The SOI is the CAC version (as detailed in the March 1986 issue of the Climate Diagnostic Bulletin). *Computation of ENSO-related variations.* The interannual variations in sea level were estimated by filtering the time series with a Hanning filter [Blackman and Tukey, 1958]. The filter lengths were chosen in order to pass almost no signal at periods of one year and shorter, and to pass about 90% of the signal at periods of 4 years which is the mean El Niño return interval [Enfield and Cid, 1991]. An Empirical Orthogonal Function (EOF) analysis was performed on the interannual variations in order to extract the ENSO-related variations.

### 3. ENSO-RELATED SEA LEVEL CHANGES

Two EOF were necessary to extract the interannual variability associated with ENSO. For the first EOF, Figure 1 (right panels) shows a very good agreement between the EOF time functions and the filtered SOI. The prominent feature in the spatial patterns (Figure 1; left panels) is the presence of positive values in the west and negative values in the east. This means that during El Niño events (1982-83, 1987, 1991-94) the sea level was lower than average in the western half of the basin, whereas it was higher than average in the eastern half; the reverse situation was observed during La Niña events (1988-89, 1996). This results in a somewhat zonal "seesaw" structure almost in phase with the SOI, with a "fulcrum" near 170°W. Such a "seesaw" was already documented from observations [Wyrtki, 1977; Chao et al., 1993] and model results [Busalacchi and O'Brien, 1981; Zebiak and Cane, 1987].



PROCEEDINGS OF SPIE REPRINT

**EUROPTO**  
SERIES

*Reprinted from*

## *Earth Surface Remote Sensing*

22–25 September 1997  
London, UK



Volume 3222



# Potential for Remotely Sensed Soil Moisture Data in Hydrologic Modeling

Edwin T. Engman

Hydrological Sciences Branch,  
Laboratory for Hydrospheric Processes, NASA,  
Goddard Space Flight Center, Greenbelt, MD 20771, USA

## ABSTRACT

Many hydrologic processes display a unique signature that is detectable with microwave remote sensing. These signatures are in the form of the spatial and temporal distributions of surface soil moisture and portray the spatial heterogeneity of hydrologic processes and properties that one encounters in drainage basins. The hydrologic processes that may be detected include ground water recharge and discharge zones, storm runoff contributing areas, regions of potential and less than potential ET, and information about the hydrologic properties of soils and heterogeneity of hydrologic parameters. Microwave remote sensing has the potential to detect these signatures within a basin in the form of volumetric soil moisture measurements in the top few cm.. These signatures should provide information on how and where to apply soil physical parameters in distributed and lumped parameter models and how to subdivide drainage basins into hydrologically similar sub-basins.

## 1. INTRODUCTION

The hydrologic cycle's interaction with the Earth's land surface occurs within a thin reservoir that stores and distributes (spatially and temporally) water that falls on the surface in the form of rain or melting snow. This reservoir is commonly referred to as *soil moisture*. Soil moisture integrates much of the land surface hydrology, acts as the interface between the land surface and the atmosphere, the land surface and the ground water reservoir, and controls the infiltration and surface runoff processes. The production of surface water through the runoff process is to a large degree controlled by the antecedent soil moisture and ground water recharge is also controlled by soil moisture.

Although soil moisture physically represents only the surface layer of soil, much of the time it is highly correlated with the total water in the soil profile and is an indicator of total water availability. Unfortunately, soil moisture is not a uniform variable in either a spatial or temporal sense. The very large spatial variability of soil moisture is the result of variable inputs (rain or snow melt), land cover, highly variable soil properties and topography. The temporal patterns of soil moisture respond to the spatial distribution and variable atmospheric forcing. The net result of this is that soil moisture is a difficult variable to measure, not necessarily at one point in time, but in a temporally consistent and spatially comprehensive basis. Because it exhibits such large spatial and temporal variability; a snap shot or point measurements have had very little meaning in a hydrologic sense.

This paper reviews the various hydrologic processes and how they are reflected in the changes or patterns in soil moisture. Examples of how remotely sensed soil moisture has been used in hydrologic analysis are presented. The paper makes the case for interpreting the patterns of remotely sensed soil moisture as a hydrologic signature that can be used to identify runoff areas, recharge areas, and the general hydrologic processes in a spatial sense. These spatial and temporal signatures of soil moisture may provide the key for an objective means for modeling the natural heterogeneity found in hydrologic systems.

## 2. LAND SURFACE HYDROLOGY

Land surface hydrology refers to the spatial and temporal storage and redistribution of rainfall and snow melt as it falls on or enters into the soil. The various processes that occur define the hydrologic response of a



## **SeaWiFS Technical Report Series**

**Stanford B. Hooker, Editor**  
*NASA Goddard Space Flight Center*  
*Greenbelt, Maryland*

**Elaine R. Firestone, Technical Editor**  
*General Sciences Corporation*  
*Laurel, Maryland*

## **Volume 40, SeaWiFS Calibration Topics, Part 2**

**Robert A. Barnes**  
**Robert E. Eplee, Jr.**  
**Eueng-nan Yeh**  
*General Sciences Corporation*  
*Laurel, Maryland*

**Wayne E. Esaias**  
*NASA Goddard Space Flight Center*  
*Greenbelt, Maryland*



National Aeronautics and  
Space Administration

**Goddard Space Flight Center**  
Greenbelt, Maryland 20771

**1997**



## Chapter 6

### The SeaWiFS Temperature Calibration

ROBERT E. EPLEE, JR.

ROBERT A. BARNES

*General Sciences Corporation, Laurel, Maryland*

#### ABSTRACT

The radiometric calibration of SeaWiFS data includes a correction for the temperature dependence of the individual detector sensitivities. The detector temperatures are measured by temperature sensors mounted on the instrument focal planes. Processing of the temperature sensor output by an onboard instrument computer introduces a nonlinear response into the temperature data. This chapter describes the calibration of the temperature sensor output and the computation of the temperature corrections for the radiometric calibration of the instrument.

#### 6.1 INTRODUCTION

The radiometric calibration equation for SeaWiFS data includes a correction for the temperature dependence of the sensitivity of the individual detectors. This multiplicative correction to the calibration has the form (Barnes et al. 1994b):

$$F(T) = 1.0 + K_3(T - T_{\text{ref}}), \quad (16)$$

where  $K_3$  is the temperature dependency coefficient for the detector,  $T$  is the detector temperature, and  $T_{\text{ref}}$  is the reference temperature for the detector (Table 33).

**Table 33.** These temperature parameters are detector-specific. The data are from the SeaWiFS Calibration and Acceptance Data Package.

Band Number	$K_3$ [(°C) <sup>-1</sup> ]	$T_{\text{ref}}$ [°C]
1	0.000901	20.0
2	0.000585	20.0
3	0.000420	20.0
4	0.000390	20.0
5	0.000391	20.0
6	0.000151	20.0
7	0.000106	20.0
8	0.000078	20.0

The detector temperatures are measured by temperature sensors mounted on the instrument focal planes. Since two detectors are located on each focal plane, the detector temperatures for bands 1 and 2 are the same, as are those for bands 3 and 4, 5 and 6, and 7 and 8. The SeaWiFS temperature calibration entails deriving the focal plane tem-

peratures from the temperature sensors and computing the temperature corrections for the radiometric calibration of the data.

#### 6.2 TEMPERATURES

A SeaWiFS focal plane temperature sensor is composed of a precision negative temperature coefficient thermistor, in parallel with a load resistor, which is driven by a current source diode and buffered by a noninverting unity-gain operational amplifier. The output of the sensor is the voltage across the thermistor-resistor pair and has a range of 0.0–5.1 V. The SeaWiFS Interface Unit (SIU), an onboard instrument computer, uses an analog-to-digital converter (ADC) to change the analog temperature sensor voltages into 8-bit digital telemetry data.

The sensor calibration data provided by SBRS, the instrument builder, in the SeaWiFS Calibration and Acceptance Data Package (an SBRS internal document) shows that there should be a linear relationship between the focal plane temperatures and the temperature sensor voltages output from the SIU. The temperature sensor voltage is defined by:

$$V_T = K_5 C_T + K_6, \quad (17)$$

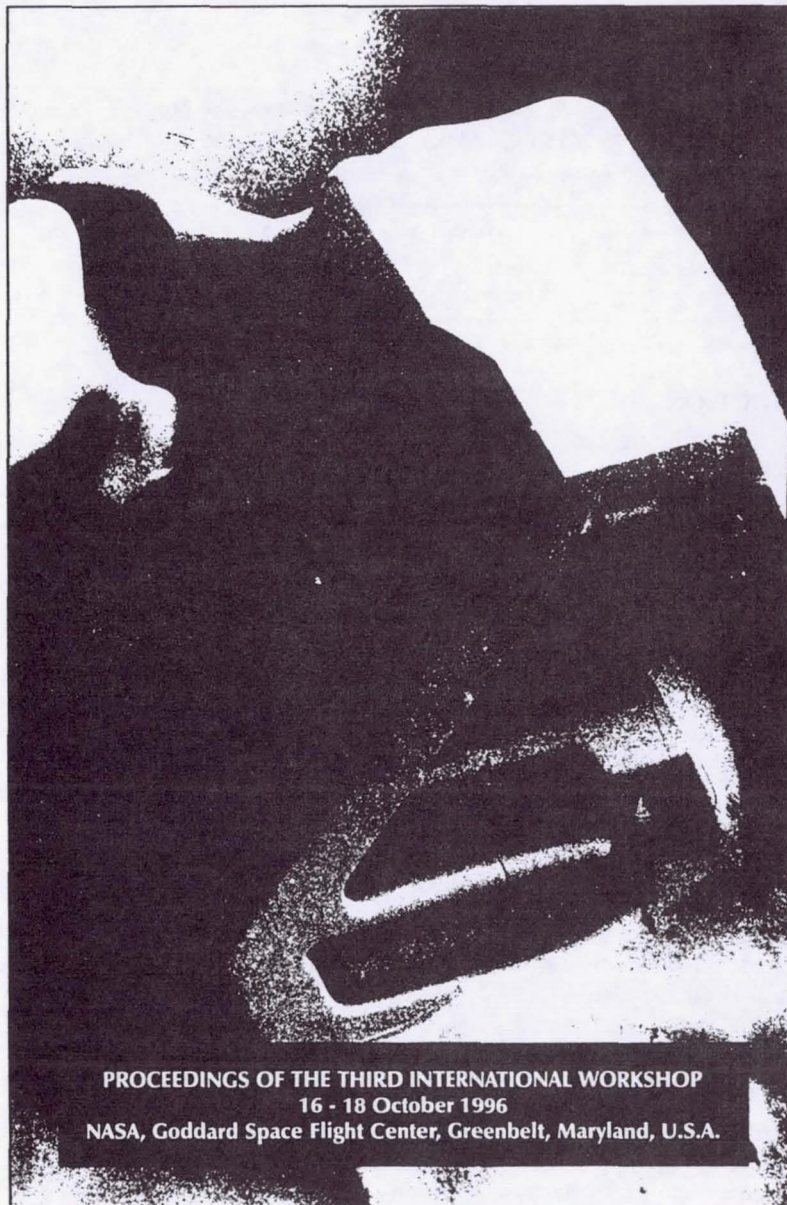
where  $K_5$  is the ADC conversion factor for temperature sensors,  $K_6$  is the ADC offset for the temperature sensors (Table 34), and  $C_T$  is the 8-bit temperature sensor voltage in counts.

$V_T$  runs from 0.0–5.1 V as  $C_T$  runs from 0–255 counts. An approximate relationship between the temperature sensor voltages and the corresponding focal plane temperatures, in degrees Celsius, is given by:

$$T_C = (5.0 - V_T) \frac{40.0}{3.0}. \quad (18)$$



APPLICATIONS OF  
**REMOTE SENSING**  
IN HYDROLOGY



Editors G.W. Kite, A. Pietroniro and T.J. Pultz



## IMPROVED PASSIVE MICROWAVE ALGORITHMS FOR NORTH AMERICA AND EURASIA

*James Foster, Alfred Chang and Dorothy Hall  
NASA Goddard Space Flight Center  
Laboratory for Hydrospheric Processes  
Hydrological Sciences Branch  
Greenbelt, MD 20771, USA*

### INTRODUCTION

Microwave algorithms simplify complex physical processes in order to estimate geophysical parameters such as snow cover and snow depth. The microwave radiances received at the satellite sensor and expressed as brightness temperatures are a composite of contributions from the Earth's surface, the Earth's atmosphere and from space. Owing to the coarse resolution inherent to passive microwave sensors, each pixel value represents a mixture of contributions from different surface types including deep snow, shallow snow, forests and open areas. Algorithms are generated in order to resolve these mixtures. The accuracy of the retrieved information is affected by uncertainties in the assumptions used in the radiative transfer equation (Steffen *et al.*, 1992). One such uncertainty in the Chang *et al.* (1987) snow algorithm is that the snow grain radius is 0.3 mm for all layers of the snowpack and for all physiographic regions. However, this is not usually the case. The influence of larger grain sizes appears to be of more importance for deeper snowpacks in the interior of Eurasia. Based on this consideration and the effects of forests, a revised SMMR snow algorithm produces more realistic snow mass values.

The purpose of this study is to present results of the revised algorithm (referred to for the remainder of this paper as the GSFC 94 snow algorithm) which incorporates differences in both fractional forest cover and snow grain size. Results from the GSFC 94 algorithm will be compared to the original Chang *et al.* (1987) algorithm and to climatological snow depth data as well.

### MICROWAVE SCATTERING AND GRAIN SIZE

With regard to satellite remote sensing, the spatial variation in grain size is basically averaged over the total pixel area, hence reducing the effect of extreme variations which may exist on a local scale. Because scattering is sensitive to grain size, without detailed grain size information to a precision of about 0.1 mm, theory suggests that accurate snow water equivalent estimates from microwave remote sensing are difficult (Armstrong *et al.*,





# IGARSS'97

1997 International Geoscience and  
Remote Sensing Symposium

03-08 August 1997

Singapore International Convention & Exhibition Centre • Singapore

*Remote Sensing -- A Scientific Vision for  
Sustainable Development*

IEEE Catalog Number: 97CH36042  
Library of Congress Number: 97-70575



## Snow Crystal Shape and Microwave Scattering

J.L. Foster, D.K. Hall and A.T.C. Chang  
NASA Goddard Space Flight Center, Code 974  
Hydrological Sciences Branch  
Laboratory for Hydrological Processes  
Greenbelt, MD 20771  
phone: 301-286-7096, fax: 301-286-1758  
e-mail: jfoster@glacier.gsfc.nasa.gov

A. Rango, W. Wergin and E. Erbe  
U.S. Department of Agriculture, Hydrology Laboratory  
Agricultural Research Service  
Beltsville, MD

### INTRODUCTION AND BACKGROUND

No two snow crystals look exactly the same because their histories are different. Precipitating snow crystals grow into forms according to how water molecules fit together as they fall through the atmosphere and encounter different temperature, pressure and humidity conditions. Impurities or defects on the surface of the crystals affect their growth by helping them to attract water vapor more efficiently. The crystals may take the form of plates, columns, needles, or dendrites, all of which are based on a hexagonal lattice structure. Competition for water vapor plays a big role in determining the shape of the falling crystals [1]. This is also the case for snow crystals which survive their fall to the ground, where the process of constructive metamorphism increases their size and alters their shape. In addition, the constant jostling of the crystals within the snowpack (destructive metamorphism) result in shapes having fewer protuberances.

Microwave emission from a layer of snow over a ground medium consists of contributions from the snow itself and from the underlying ground. Both contributions are governed by the transmission and reflection properties of the air-snow and snow-ground boundaries and by the absorption/emission and scattering properties of the snow layer [2]. Most of the attention in algorithm development has been directed towards the effects of snow crystal size and effective size [3] in scattering microwave energy, and relatively little effort has been given to the role that crystal shape plays in this regard. A better understanding of the physics of snow and how microwave energy interacts with snow crystals is needed to make the snow/microwave algorithms more reliable.

In this study, which is a follow-up of the work presented at the 1996 IGARSS meeting in Lincoln, Nebraska [4], a hand-held 35 GHz radiometer was used to make microwave measurements of snowpacks in both north-central Wisconsin and west-central Wyoming. Because the climate conditions are different for these areas, the characteristics of the snow crystals are somewhat different in regards to their shape and size. Microwave brightness temperatures (TB), in each area were related to physical properties of the snow, including snow depth, snow density, snow water equivalent (SWE), and crystal size and shape. Coincident with the field observations, an aircraft instrumented with a gamma-ray sensor made measurements of the SWE of the snowpack. These measurements are compared with the SWE as derived using the passive microwave techniques and the "ground truth" measurements.

A particle scattering model is used to assess the scattering properties of differently-shaped snow crystals and to determine if spherically-shaped crystals adequately mimic the extinction and absorption of microwave energy. Crystals were collected from the field sites and brought to a scanning electron microscopy (SEM) laboratory in order to examine and measure them in detail.

A cryosystem has been developed [5] to preserve snow crystals collected in the field (Figure 1) so that they can be imaged using low-temperature SEM. This technique uses liquid nitrogen as a coolant and special pre-cooled dewars to store and transport the snow crystal samples, which are virtually undisturbed, to the SEM laboratory in Beltsville, Maryland.





# IGARSS'97

1997 International Geoscience and  
Remote Sensing Symposium

03-08 August 1997

Singapore International Convention & Exhibition Centre • Singapore

**Remote Sensing -- A Scientific Vision for  
Sustainable Development**

IEEE Catalog Number: 97CH36042  
Library of Congress Number: 97-70575



# Combined High-Resolution Active and Passive Imaging of Ocean Surface Winds from Aircraft

A.J. Gasiewski and J.R. Piepmeier

School of Electrical and Computer Engineering  
Georgia Institute of Technology, Atlanta, GA 30332-0250  
(404) 894-2934; (404) 894-2984  
ag14@prism.gatech.edu; gt2930b@prism.gatech.edu

R.E. McIntosh, C.T. Swift, J.R. Carswell, W.J. Donnelly, and E. Knapp

Microwave Remote Sensing Laboratory  
University of Massachusetts, Amherst, MA 01003  
(413) 545-4858; FAX: (413) 545-4652  
mcintosh@ecs.umass.edu; klemyk@ecs.umass.edu; carswell@alex.ecs.umass.edu;  
donnelly@alex.ecs.umass.edu; knapp@alex.ecs.umass.edu

E.R. Westwater, V.I. Irisov, and L.S. Fedor

NOAA Environmental Technology Laboratory, Boulder, CO 80303  
(303) 497-6527; (303) 497-3577  
ewestwater@etl.noaa.gov; virisov@etl.noaa.gov; lfedor@etl.noaa.gov

D.C. Vandemark

Laboratory for Hydrospheric Processes  
NASA Goddard Space Flight Center, Wallops Island, VA 23337  
(757) 824-2038; (757) 824-1036  
vandemark@gsfc.nasa.gov

**Abstract** – A unique complement of passive and active microwave imaging and sensing instruments for observing ocean surface emission and scattering signatures were integrated onto the NASA Wallops Flight Facility's Orion P-3B aircraft (N426NA) for the purpose of studying the signature of ocean surface winds. The complement included: (i) a four-band (X, K, Ka, and W) tri-polarimetric scanning radiometer (PSR) (ii) a C-band ocean surface scatterometer (CSCAT), (iii) a Ka-band conical-scanning polarimetric radiometer (KASPR), (iv) a nadir-viewing Ka-band polarimetric radiometer, (KAPOL) (v) a 21- and 31-GHz zenith-viewing cloud and water vapor radiometer (CWVR), and (vi) a radar ocean wave spectrometer (ROWS). The above Ocean Winds Imaging (OWI) complement was flown during January-March, 1997 over the Labrador Sea. Conically-scanned brightness temperature and backscatter imagery were observed over open ocean for a variety of wind speeds and cloud conditions. Presented herein are the results of a preliminary intercomparison of data from several of the OWI instruments.

## 1. INTRODUCTION

Aircraft and satellite measurements have pointed to the possibility of building passive microwave sensors to mea-

sure both ocean surface wind speed and direction using the anisotropic nature of the emission from a wind-driven ocean. Such measurements would likely complement and improve upon wind vector maps available from active instruments (e.g., the NASA scatterometer - NSCAT). The need for complementarity is particular acute in high-wind conditions. Accordingly, the primary goal of the Ocean Winds Imaging (OWI) experiment was to collect data to verify the utility of passive polarimetric ocean wind vector sensing in high seas, with secondary goals being to better characterize the thermal emission and scattering signatures of a wind-driven ocean surface. The complement was flown under a variety of meteorological conditions in coordinated patterns over both ocean buoys along the eastern U.S. coast near Virginia and an instrumented research vessel - the *R.V. Knorr* - within the Labrador Sea. Local overflights of several NOAA ocean buoys near Wallops Island, VA and within the Gulf of Maine, and an extensive set of overflights of the Knorr located in the Labrador Sea during March 1-10, 1997 within the vicinity of 57°N, 53°W were performed. The conditions represented a wide range of surface wind speeds, cloud and water vapor states, and fetch lengths.

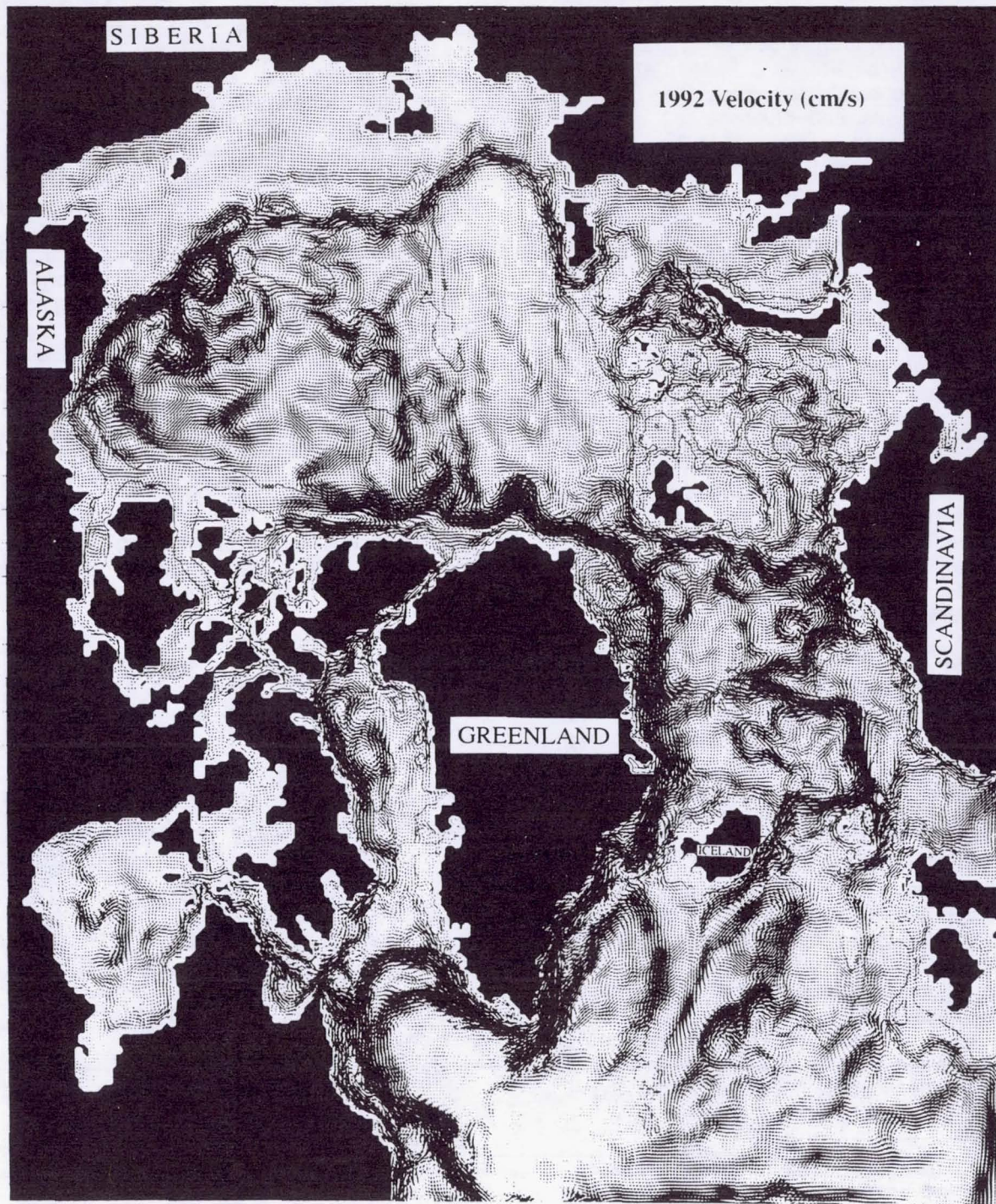
The OWI complement included two active radar scat-



# WORKSHOP ON POLAR PROCESSES IN GLOBAL CLIMATE

13-15 November 1996

Cancun, Mexico



AMERICAN METEOROLOGICAL SOCIETY



Cathleen A. Geiger\*

Thayer School of Engineering, Dartmouth College, Hanover, NH

## 1. INTRODUCTION

Reproduction of current day large-scale physical features and processes is a critical test of global climate model performance. Without this benchmark, prognoses of future climate conditions are at best speculation. A fundamental question relevant to this issue is, which processes and observations are both robust and sensitive enough to be used for model validation and furthermore are they also indicators of the problem at hand? In the case of global climate, one of the problems at hand is to distinguish between anthropogenic and naturally occurring climate responses. The polar regions provide an excellent testing ground to examine this problem because few humans make their livelihood there, such that anthropogenic influences in the polar regions usually spawn from global redistribution of a source originating elsewhere. Concomitantly, polar regions are one of the few places where responses to climate are non-anthropogenic. Thus, if an anthropogenic effect has reached the polar regions (e.g. the case of upper atmospheric ozone sensitivity to CFCs), it has most likely had an impact globally but is more difficult to sort out from local effects in areas where anthropogenic activity is high.

Within this context, sea ice has served as both a monitoring platform and sensitivity parameter of polar climate response since the time of Fridtjof Nansen. Sea ice resides in the polar regions at the air-sea interface such that changes in either the global atmospheric or oceanic circulation set up complex non-linear responses in sea ice which are uniquely determined. Sea ice currently covers a maximum of about 7% of the earth's surface but was completely absent during the Jurassic Period and far more extensive during the various ice ages. It is also geophysically very thin (typically <10m in Arctic, <3m in Antarctic) compared to the troposphere (roughly 10km) and deep ocean (roughly 3 to 4 km). Because of these unique conditions, polar researchers regard sea ice as one of the more important features to monitor in terms of heat, mass and

momentum transfer between the air and sea and furthermore, the impact of such responses to global climate.

Given this information, an important question to pose is, what are the critical variables of sea ice that are both robust enough to be monitored easily on a large-scale and yet sensitive enough to indicate a change in either the oceanic or atmospheric circulation? In terms of the large-scale physics of the problem, sea ice responds uniquely to atmospheric and oceanic forces through four measurable variables: sea ice thickness, areal extent/compactness, drift and internal ice deformation. A simple flow diagram shown in Figure 1 depicts this relationship. Basically, atmospheric and oceanic forcing serve as inputs to initiate sea ice response through a coupled set of sea ice equations which include a mass balance, momentum balance and constitutive relation (see for example Hibler, 1979 for mathematical formulation). The four sea ice parameters of thickness ( $h$ ), compactness ( $A$ ), velocity or drift ( $\mathbf{v}$ ) and deformation components ( $\dot{\epsilon}_{ij}$ ,  $\sigma_{ij}$ ,  $P$ ) can be regarded as responses to the imposed forcing or outputs (Figure 1). While a number of feedback processes ensue between the air, ice

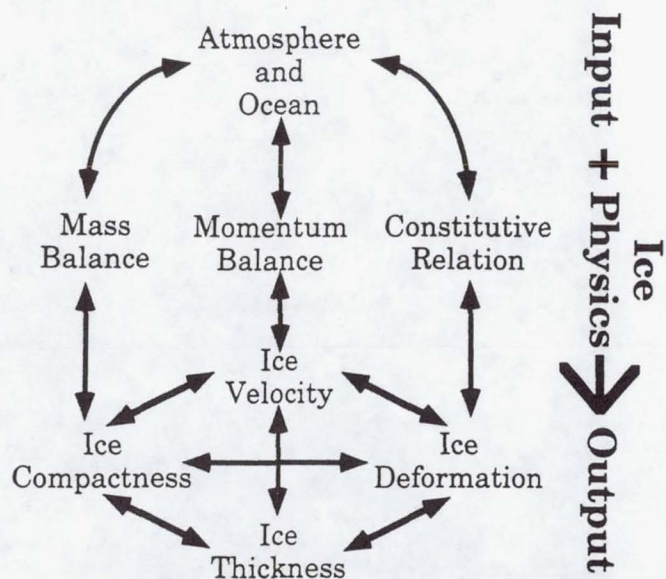


**Figure 1:** Diagram of the relationship between the physics of sea ice, its measurable quantities of drift, deformation, thickness and compactness with external forcing from the air and ocean.

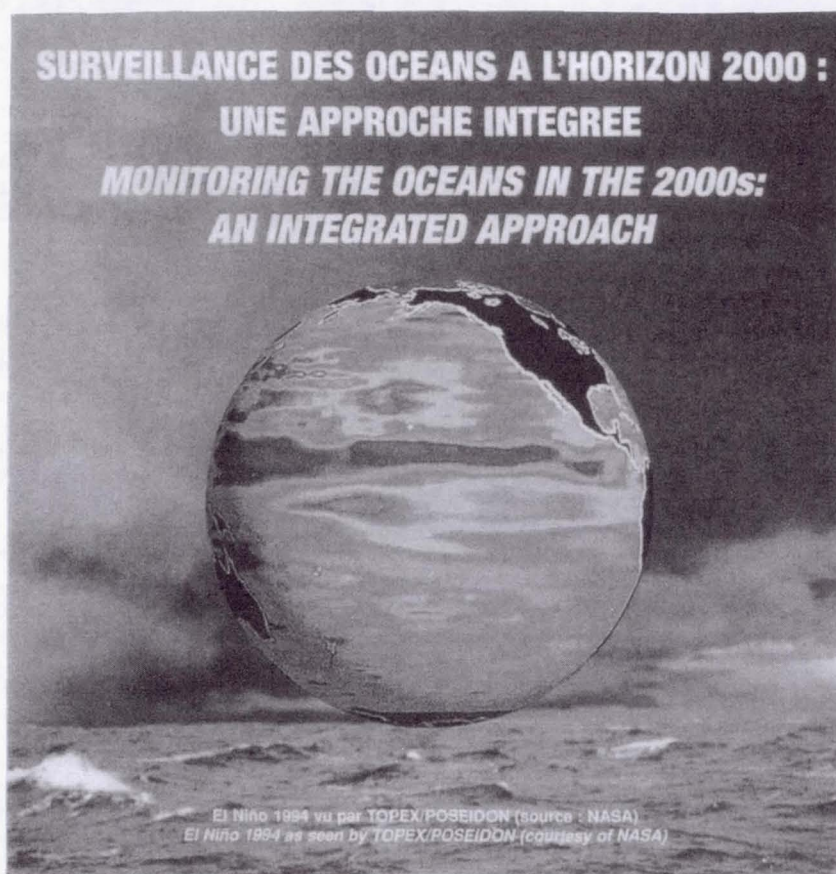
\* Corresponding author address: Cathleen A. Geiger, Goddard Space Flight Center, Code 971, Greenbelt, MD 20771



# RECUEIL DES ACTES / PROCEEDINGS

SYMPOSIUM INTERNATIONAL / INTERNATIONAL SYMPOSIUM

15 - 16 - 17 Octobre 1997 / October, 15 - 16 and 17, 1997  
BIARRITZ - FRANCE



Réunion du Groupe Scientifique TOPEX/POSEIDON  
TOPEX/POSEIDON Science Team Meeting  
13 et 14 octobre 1997 / October 13 and 14, 1997





# AN EXTENDED KALMAN FILTER TO ASSIMILATE ALTIMETRIC DATA INTO A NON-LINEAR MODEL OF THE TROPICAL PACIFIC

L. Gourdeau <sup>1</sup>, J. Verron <sup>2</sup>, R. Murtugudde <sup>3</sup>, A.J. Busalacchi <sup>3</sup>

<sup>1</sup> ORSTOM, BPAS, Nouméa, 98848 New Caledonia

<sup>2</sup> LEGI, UMR 5519 CNRS, BP53X, 38041 Grenoble Cedex, France

<sup>3</sup> LHP, NASA Goddard Space Flight Center, Greenbelt, MD 20771, USA

**RESUME** - Une méthode d'assimilation, basée sur le filtrage de Kalman étendue, a été développée pour l'assimilation d'observations altimétriques dans un modèle aux équations primitives de l'océan Pacifique. L'originalité de la méthode consiste à définir les erreurs dans une base de dimension réduite évoluant avec la dynamique du système. La méthode a été testée avec succès dans le cadre d'expériences jumelles proches de conditions réelles. Les données du niveau de la mer des 2 premières années de la mission Topex/Poseidon ont été assimilées dans le modèle de Gent & Cane [1989]. Les résultats sont confrontés aux observations in situ indépendantes des mouillages TAO.

**ABSTRACT**- A new implementation of the extended Kaman filter is developed for the purpose of assimilating altimetric observations into a primitive equation model of the tropical Pacific. Its specificity consists in defining the errors into a reduced basis that evolves in time with the model dynamic. Validation by twin experiments is conducted and the method is shown to be efficient in quasi real conditions. Data from the first 2 years of the Topex/Poseidon mission are assimilated into the Gent & Cane [1989] model. Assimilation results are evaluated against independant in situ data, namely TAO mooring observations.

## 1 - INTRODUCTION

For geophysical applications, the dimension of the system gives the Extended Kalman Filter (EKF) untractable and we must deal with some form of sub-optimality. The key limitation was actually related to the prediction error evolution; several recent studies have considered this point by, for example, propagating this error on a reduced space/basis [Cane et al., 1996]. In the present paper, the reduced basis is able to evolve in time as in the standard EKF. This is the basic concept of the Singular Evolutive Extended Kalman (SEEK) filter introduced by [Pham et al., 1996]. Applications use the primitive equation reduced gravity model of Gent & Cane [1989] for the tropical Pacific ocean and altimetric data. The challenge of observability of altimetry is a particular interest from a data assimilation perspective as the 3D-content of the ocean signal should be recovered by the sea surface height (SSH). The problem of the downward penetration of information is addressed by a projection based on a multivariable EOF analysis. More details on the method and its validation can be found in Verron et al. [1997]. A first series of assimilation are based on the concept of twin experiments in which the "true" state of the ocean is known. Then, assimilation of two years of Topex/Poseidon (T/P) data is assessed against independant measurements from the TAO array moorings.

## 2 - THE SEEK FILTER AND THE GENT & CANE MODEL

The basic idea of the SEEK filter is to discard corrections in the directions where the errors are naturally strongly attenuated by the system because of the "attractive" nature of this one. This idea of selective correction is simply realized by the use of a low-rank error covariance matrix that has the dimension of the "attractor". The rank and the initial error are determined through an EOF analysis of a free model run sampling every 10 days. The underlying approximation is that the error statistics should have the same properties than the model natural variability. The number of retained EOFs, to define the initial reduced basis, explains 99.% of the signal variance, either 32 EOFs for a two years period. The model error is crudely represented in the reduced basis, as proportional to the analysis error. The observation error is represented by a white noise of 5 cm amplitude in accordance with the budget error on T/P data.

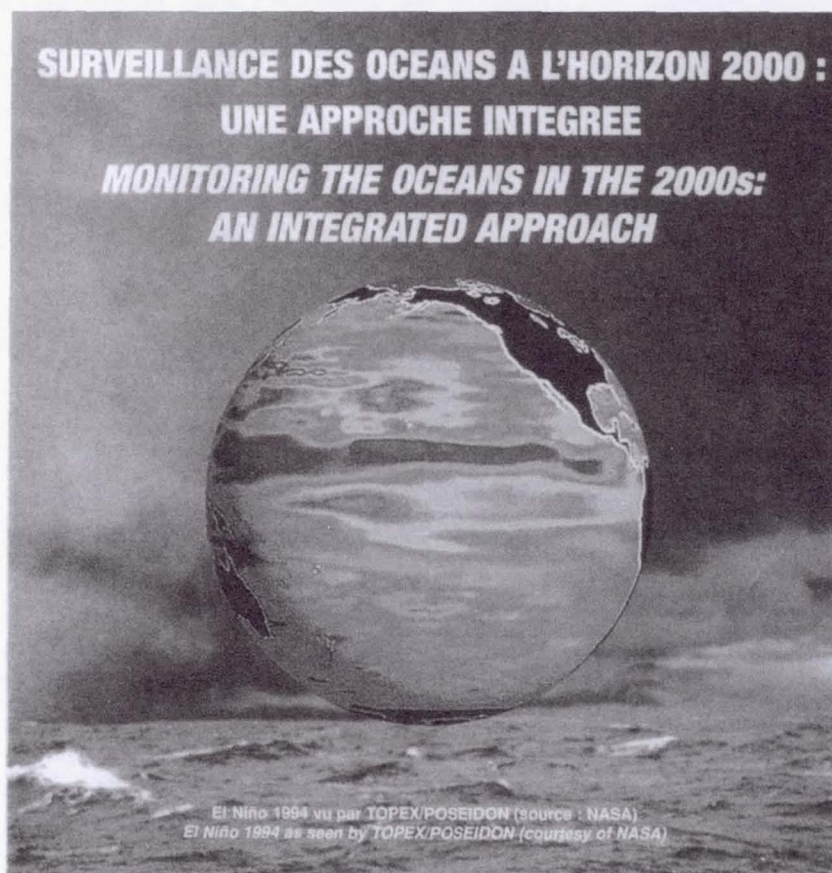
The OGCM used is the reduced gravity, primitive equation,  $\sigma$  coordinate model of Gent & Cane [1989] with an embedded hybrid mixing scheme for the upper mixed layer. This model has no flux



# RECUEIL DES ACTES / PROCEEDINGS

SYMPOSIUM INTERNATIONAL / INTERNATIONAL SYMPOSIUM

15 - 16 - 17 Octobre 1997 / October, 15 - 16 and 17, 1997  
BIARRITZ - FRANCE



Réunion du Groupe Scientifique TOPEX/POSEIDON  
*TOPEX/POSEIDON Science Team Meeting*  
13 et 14 octobre 1997 / October 13 and 14, 1997





# COMPARISON OF TOPEX/POSEIDON SEA LEVEL AND LINEAR MODEL RESULTS FORCED BY VARIOUS WIND PRODUCTS FOR THE TROPICAL PACIFIC

Eric C. HACKERT

*Hughes STX Corporation and Laboratory for Hydrospheric Processes,  
NASA Goddard Space Flight Center, Greenbelt, Maryland 20771.*

Antonio J. BUSALACCHI

*Laboratory for Hydrospheric Processes,  
NASA Goddard Space Flight Center, Greenbelt, Maryland 20771.*

**ABSTRACT** - The goal of this paper is to compare TOPEX/Poseidon (T/P) sea level with sea level results from linear ocean model experiments forced by several different wind products for the tropical Pacific. During the period of this study (October 1992 - October 1995), available wind products include satellite winds from the ERS-1 scatterometer product of [HALP 97] and the passive microwave analysis of SSMI winds produced using the variational analysis method (VAM) of [ATLA 91]. In addition, atmospheric GCM winds from the NCEP reanalysis [KALN 96], ECMWF analysis [ECMW 94], and the Goddard EOS-1 (GEOS-1) reanalysis experiment [SCHU 93] are available for comparison. The observed ship wind analysis of FSU [STRI 92] is also included in this study.

The linear model of [CANE 84] is used as a transfer function to test the quality of each of these wind products for the tropical Pacific. The various wind products are judged by comparing the wind-forced model sea level results against the T/P sea level anomalies. Correlation and RMS difference maps show how well each wind product does in reproducing the T/P sea level signal. These results are summarized in a table showing area average correlations and RMS differences. The large-scale low-frequency temporal signal is reproduced by all of the wind products. However, significant differences exist in both amplitude and phase on regional scales. In general, the model results forced by satellite winds do a better job reproducing the T/P signal (i.e. have a higher average correlation and lower RMS difference) than the results forced by atmospheric model winds.

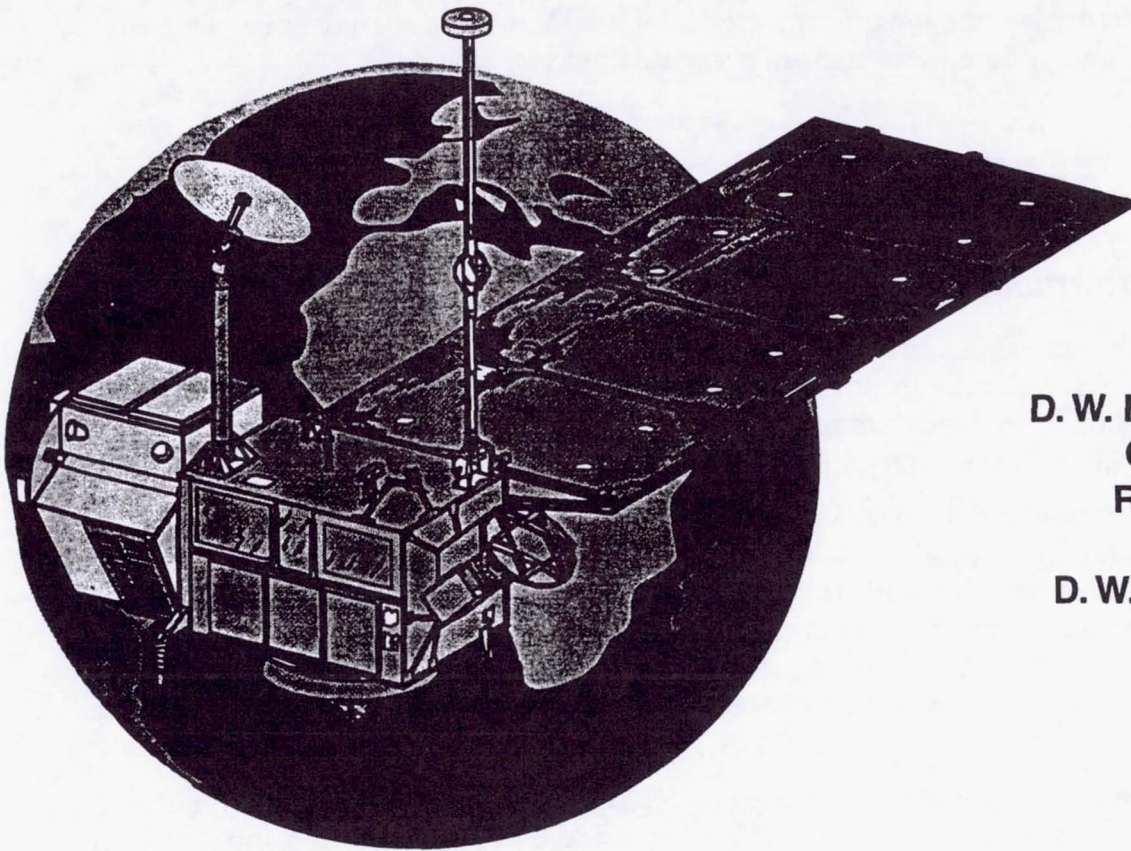
## 1 - INTRODUCTION

During the recent period, the unprecedented accuracy and coverage of the T/P satellite has allowed us to have a long term data set of sea level variability to verify our ocean models. In this project we use the T/P product to assess available wind products for forcing linear ocean models. First we process the T/P data like [BUSA 94] using the standard corrections and compare the wind forced model results against this T/P data. Then for each wind product, monthly mean wind stress is calculated using the highest temporal and spatial resolution of the wind data. Wind data are first converted to wind stress using a simple bulk formula with a drag coefficient of  $1.2 \times 10^{-3}$  and then monthly means are formulated. The data are then linearly interpolated to a  $2^\circ \times 2^\circ$  grid. Wind stress anomalies were then calculated from the October 1992 to October 1995 mean. Each of the wind products are then used to force the linear model of Cane and Patton [CANE 84]. This model uses linear shallow water equations on the equatorial  $\beta$  plane, subject to the long-wave approximation and finite differences in the horizontal directions to describe the evolution of each baroclinic mode.



# TOPEX Radar Altimeter Engineering Assessment Report

Update: Launch to January 1, 1997



D. W. Hancock, III  
G. S. Hayne  
R. L. Brooks  
J. E. Lee  
D. W. Lockwood

March 1997



Observational Science Branch  
Laboratory for Hydrospheric Processes  
NASA Goddard Space Flight Center  
Wallops Flight Facility



## Introduction

### 1.1 Identification of Document

The initial TOPEX Mission Radar Altimeter Engineering Assessment Report, in February 1994, presented performance results for the NASA Radar Altimeter on the TOPEX/POSEIDON spacecraft, from its launch in August 1992 to February 1994. There have been supplemental Engineering Assessment Reports, issued in March 1995 and again in May 1996, which updated the performance results through the end of calendar years 1994 and 1995, respectively. This supplement updates the altimeter performance to the end of calendar year 1996, and describes significant events that occurred during 1996.

As the performance data base has expanded, and as analysis tools and techniques continue to evolve, the longer-term trends of the altimeter data have become more apparent. The updated findings are presented here.

## Section 4

## Engineering Assessment Synopsis

### 4.1 Performance Overview

After nearly four-and-a-half years of on-orbit operations, the NASA Radar Altimeter on the TOPEX/POSEIDON spacecraft remains healthy and its performance meets or is better than all pre-launch requirements. The performance requirements are listed in Section 4.0 of the February 1994 Engineering Assessment Report.

The primary pre-launch specification for the altimeter is to monitor and maintain range calibration to the  $\pm 1.5$  cm level. We are well aware that TOPEX science investigators are achieving extraordinary results with this altimeter data set, and are seeking unprecedented range measurement accuracy. With our improved analysis techniques, we believe that we are achieving range calibration (i.e., internal range consistency) at the one-centimeter level, and are making strides towards the sub-centimeter level.

A recommendation we have is for the Project to consider operating Side B for about 5% of the cycles. This would give us insight to Side B performance and the characteristics of the stored parts. More importantly, it would provide some data points to be used to help cross-calibrate Side B relative to Side A, calibration data that would be very important to have if there were to be a failure on Side A. The commands to switch from Altimeter Side A to Altimeter Side B would, among a number of other things, switch receiver units and would switch to the different internal chains within the single C-Band MTU. At least one of the switch functions has been operated (toggled) each time the Altimeter has been switched off by the spacecraft as part of the Altimeter turn on procedure. However, it is proper to remind ourselves that Side B has never been powered-on in space.

We are continuing our NASA Radar Altimeter performance assessment on a daily basis, and are continuing to develop improved analysis techniques. Our performance assessment techniques are relevant not only for the NASA Radar Altimeter, but should be very applicable to other altimeters, as well.





# IGARSS'97

1997 International Geoscience and  
Remote Sensing Symposium

03-08 August 1997

Singapore International Convention & Exhibition Centre • Singapore

Remote Sensing -- A Scientific Vision for  
Sustainable Development

IEEE Catalog Number: 97CH36042  
Library of Congress Number: 97-70575



## **Geosynchronous Technology Infusion Studies**

**L. Hilliard, D. Jenstrom, D. Chesters, P. Racette**  
**National Aeronautics and Space Administration**  
**Goddard Space Flight Center**  
**Greenbelt, MD 20771**

**<http://www701.gsfc.nasa.gov/ags/ags.htm>**

Abstract -- NASA and NOAA are now sponsoring Advanced Geosynchronous Studies (AGeoS), technology work that will lead to the next generation of space sensors located in geosynchronous orbit.

### **INTRODUCTION**

In the early 1990's, NASA commissioned a Geostationary Earth Observatory (GEO) team [1] to study the utility of environmental observations from geostationary orbit. This GEO study concluded that: "In many respects, the polar-orbiting instruments study the effects of processes, whereas the geostationary instruments can study the process itself."

Indeed, research in climate change consists of determining how the long-term changes affect short-term processes, and how those altered short-term processes, in turn, establish new long-term behavior. Because the diurnal cycle drives so many energetic short-term processes, it is necessary to directly measure rapidly changing components like winds, clouds, aerosols and precipitation on a global scale. While a polar-orbiting satellite can observe the entire globe at high resolution, it cannot resolve the diurnal cycle. While a geosynchronous satellite can resolve the diurnal cycle, it is limited about one-quarter of the earth's surface. Therefore, a combination of remote sensing data from both platforms yields a synergistic system for studying both the processes and the resulting changes in weather and climate.

For the last 25 years, National Oceanic and Atmospheric Administration (NOAA) has been flying Geosynchronous Operational Environmental Satellites (GOES) to observe weather. In the mid-1990's, a new generation GOES imager and infrared Sounder came on-line with accurate radiometric calibration and

earth-location, with performance similar to the NOAA polar-orbiting instruments.

Up to the early 1980's, NASA's Operational Satellite Improvement Program (OSIP) orchestrated changes in the NOAA satellites [2]. Since that time, there is a next-generation National Polar-Orbiting Environmental Satellite System (NPOESS) being planned, but there is no corresponding effort to infuse advanced technology into the GOES program for improved weather and climate monitoring, or to coordinate the polar- and geo-systems [3]. To deal with this issue, an AGeoS team has been formed to consider improvements in future GOES missions[4].

NASA's Mission to Planet Earth (MTPE) has developed a low earth orbit imager called the Moderate Resolution Imaging Spectrometer (MODIS) carrying 36 spectral channels from 0.4 to 13.3  $\mu\text{m}$  in wavelength [5]. MTPE will also fly, on the Earth Observing System (EOS) missions, microwave sensors that probe to lower levels of the atmosphere when clouds are present. With similar imaging and sounding data from geostationary orbit, numerical modelers would have access to the diurnal drivers of climate change.

In addition to imaging and sounding, AGeoS will consider requirements for a lightning mapper, more efficient ground distribution and autonomous spacecraft control systems, spaceborne architecture tradeoffs (i.e. constellation studies), and the science algorithms associated with all of these enhancements so they can be effectively used by the scientific community. To address all of these issues joint NASA/NOAA Management and Science Teams have been established to oversee the AGeoS effort. This report briefly describes the initial steps being taken to investigate the high priority geosynchronous measurement needs identified so far.





# IGARSS'97

1997 International Geoscience and  
Remote Sensing Symposium

03-08 August 1997

Singapore International Convention & Exhibition Centre • Singapore

Remote Sensing -- A Scientific Vision for  
Sustainable Development

IEEE Catalog Number: 97CH36042  
Library of Congress Number: 97-70575



# Examination of Soil Moisture Retrieval Using SIR-C Radar Data and a Distributed Hydrological Model

A.Y. Hsu

SSAI, Code 974, NASA/GSFC, Greenbelt, MD 20771 USA

Tel: 301-286-8909, Fax: 301-286-1758, E-mail: hsu@hydro.gsfc.nasa.gov

P.E. O'Neill

Hydrological Sciences Branch/974, Laboratory for Hydrospheric Processes

NASA/Goddard Space Flight Center, Greenbelt, MD 20771 USA

Tel: 301-286-8237, Fax: 301-286-1758, E-mail: peggy@hydro4.gsfc.nasa.gov

E.F. Wood, M. Zion

Department of Civil Engineering, Princeton University, Princeton, NJ 08544 USA

Tel: 609-258-4675, Fax: 609-258-1270, E-mail: efwood@pucc.princeton.edu

## INTRODUCTION

A major objective of soil moisture-related hydrological research during NASA's SIR-C/X-SAR mission was to determine and compare soil moisture patterns within humid watersheds using SAR data, ground-based measurements, and hydrologic modeling. Currently available soil moisture inversion methods using active microwave data are only accurate when applied to bare and slightly vegetated surfaces [1]. Moreover, as the surface dries down, the number of pixels that can provide estimated soil moisture by these radar inversion methods decreases, leading to less accuracy and confidence in the retrieved soil moisture fields at the watershed scale. The impact of these errors in microwave-derived soil moisture on hydrological modeling of vegetated watersheds has yet to be addressed.

In this study a coupled water and energy balance model operating within a topographic framework is used to predict surface soil moisture for both bare and vegetated areas. In the first model run, the hydrological model is initialized using a standard baseflow approach, while in the second model run, soil moisture values derived from SIR-C radar data are used for initialization. The results, which compare favorably with ground measurements, demonstrate the utility of combining radar-derived surface soil moisture information with basin-scale hydrological modeling.

## SIR-C WASHITA '94 EXPERIMENT

The Little Washita River watershed is situated in southwest Oklahoma in the Great Plains region of the United States and covers an area of approximately 600 km<sup>2</sup>. Two intensive field measurement campaigns were conducted in the watershed in 1994 coincident with the two Shuttle Radar Laboratory (SRL) missions in April and October. During the SRL-1 experiment (April 5-18, 1994), field conditions were initially dry, became wet as a result of a heavy rainstorm on

the afternoon of 4/10/94 and morning of 4/11/94, and then gradually dried down throughout the remainder of the experimental period (a change in volumetric soil moisture of 15%). In contrast, during the SRL-2 experiment, most of the watershed remained dry except for localized rainfall in the northwest and north central part of the watershed. Thus, this study has focused on data collected during SRL-1 because of the favorable hydrologic conditions in the watershed at that time.

## HYDROLOGICAL MODELING

The model used in this study is known as TOPLATS for TOPMODEL-based Land surface-Atmosphere Transfer Scheme [2]. It assumes that subsurface moisture flows are driven by topographic gradients as described by the soil-topographic index with diffusion formulation for vertical moisture movement, and uses Brooks-Corey equations to relate soil moisture, matrix potential, and unsaturated hydraulic conductivity [3]. The unsaturated soil column is divided into two layers: a 5-cm thin upper layer and a deeper transmission zone; vegetation roots can be distributed between both layers. Canopy interception storage is included in the flux calculations for vegetated pixels. Meteorological forcings used in the model include available energy (net radiation minus ground heat flux), air temperature, relative humidity, wind, and precipitation. Previous work with a statistical version of the Princeton TOPLATS model using data from the Washita '92 experiment with the passive microwave ESTAR aircraft sensor demonstrated that initializing the hydrological model with surface soil moisture estimated from microwave remote sensing produced more accurate surface soil moisture fields compared to a more traditional initialization via baseflow analysis [4].

## ANALYSES AND CONCLUSIONS

During the Washita '94 experiment, radiation and meteorological data were measured at 43 Micronet sites





# IGARSS'97

1997 International Geoscience and  
Remote Sensing Symposium

03-08 August 1997

Singapore International Convention & Exhibition Centre • Singapore

Remote Sensing -- A Scientific Vision for  
Sustainable Development

IEEE Catalog Number: 97CH36042  
Library of Congress Number: 97-70575



# Rain Profiling Algorithm for the TRMM Precipitation Radar

Toshio Iguchi<sup>1</sup>, Toshiaki Kozu<sup>1</sup>, Robert Meneghini<sup>2</sup>, and Ken'ichi Okamoto<sup>1</sup>

<sup>1</sup>Communications Research Laboratory

Nukui Kitamachi 4-2-1, Koganei, Tokyo 184, Japan

Phone: +81-423-27-7551, Fax: +81-423-27-6666, E-mail: iguchi@crl.go.jp

<sup>2</sup>NASA/Goddard Space Flight Center, Code 975

Greenbelt, Maryland 20771

**Abstract** – This paper describes an outline of the algorithm that estimates the instantaneous profiles of the true radar reflectivity factor and rainfall rate from the radar reflectivity profiles observed by the Precipitation Radar (PR) onboard the TRMM satellite. The major challenge of the algorithm lies in the correction of rain attenuation with the non-uniform beam filling effect. The algorithm was tested with synthetic data and the result is shown.

## INTRODUCTION

The TRMM (Tropical Rainfall Measuring Mission) radar team has been developing several standard algorithms which will be used to generate standard TRMM products from the TRMM Precipitation Radar data. Among these algorithms, the level 2 standard algorithm that retrieves the instantaneous vertical profiles of rainfall and attenuation corrected radar reflectivity factor is designated as 2A-25 in the TRMM project. The algorithm reads the measured vertical profiles of reflectivity factor ( $Z_m$ ) from 1C-21 and estimates the true reflectivity factor ( $Z_e$ ) at each radar resolution cell. The rainfall rate is then calculated from the estimated true reflectivity factor. The major challenges in the algorithm lie in the corrections for the effects of rain attenuation and non-uniform beam filling (NUBF). Another important element in the algorithm is the identification of precipitating particles, because the phase state and the drop size distribution affect the relations between reflectivity and attenuation and between reflectivity and rainfall rate.

The attenuation due to heavy rain comes from the use of a relatively short wavelength (2.2 cm, 13.8 GHz) for the precipitation radar. The surface reference method, which attributes the decrease of apparent surface return power to the propagation loss, is used to determine the correction needed. As long as the rain is horizontally uniform, this method generally works well when the attenuation is significant. When the rain is not uniform, however, the actual surface return may be significantly different from that expected with the same amount of rain distributed uniformly. Consequently, the NUBF may become a source of serious bias in estimating the vertical rain structure of horizontally non-uniform rain. Since the TRMM precipitation radar has a large footprint size of 4 km, the NUBF

may affect the attenuation estimates at storm edges and within convective storms. In order to compensate for the NUBF effect, we need to know the variation structure of rain within the footprint. Since it is impossible to obtain a structure more detailed than the radar resolution, we estimate its statistical variances inside a footprint from variations of radar reflectivities and surface attenuations of larger scales in the vicinity of the footprint.

## PROCESSING FLOW

A simplified flow chart of the 2A-25 algorithm is shown in Fig. 1. It first opens the three input files (1C-21, 2A-21, and 2A-23) and two output files (2A-25 and verification file) given in the command line. It also inputs the parameters used in the program such as initial coefficients for  $k$ - $Z$  relationship from the parameter files. The input data are read scan by scan. Within the scan, data in each angle bin (each radar beam) are processed independently except in the estimation of NUBF effect.

The range bins for processing in 2A-25 are first defined according to the storm top range bin, the earth ellipsoid, the actual surface range bin, and the surface clutter by the antenna main lobe.

The attenuation correction is carried out assuming a power law between the true radar reflectivity factor  $Z$  and the specific attenuation coefficient  $k$ :  $k = \alpha Z^\beta$ .  $\beta$  may change from one angle bin to another depending on the rain type, but is assumed constant for each angle bin (radar beam).  $\alpha$  varies according to the rain type, the relative height from the estimated freezing level, and the absolute altitude from the earth ellipsoid in order to take into account the dependence of  $k$ - $Z$  relationship on the drop size distribution, and the phase state and temperature of precipitating particles.

The NUBF effect is estimated from the normalized standard deviation of the 9 path-integrated attenuations (PIA) in  $3 \times 3$  radar beams with the beam in question at the center [1]. To calculate such a quantity, it is necessary to read one scan ahead of the scan that is to be processed. The path-integrated attenuation for non-uniformity calculation is estimated by using the hybrid of the Hitschfeld-Bordan and surface reference methods [2]. The hybrid method is used to avoid a large relative error when the





# IGARSS'97

1997 International Geoscience and  
Remote Sensing Symposium

03-08 August 1997

Singapore International Convention & Exhibition Centre • Singapore

Remote Sensing -- A Scientific Vision for  
Sustainable Development

IEEE Catalog Number: 97CH36042  
Library of Congress Number: 97-70575



## Passive Microwave Observation of Soil Water Infiltration

Thomas J. Jackson, Thomas J. Schmugge, Walter J. Rawls  
USDA ARS Hydrology Lab  
104 Bldg., 007 BAR-West  
Beltsville, MD 20705  
(301) 504-8511  
fax (301) 504-8931  
tjackson@hydrolab.arsusda.gov

Peggy E. O'Neill  
NASA Goddard Space Flight Center

Marc B. Parlange  
Johns Hopkins University

**Abstract** -- Infiltration is a time varying process of water entry into soil. Experiments were conducted here using truck based microwave radiometers to observe small plots during and following sprinkler irrigation. Experiments were conducted on a sandy loam soil in 1994 and a silt loam in 1995. Sandy loam soils typically have higher infiltration capabilities than clays. For the sandy loam, the observed brightness temperature (TB) quickly reached a nominally constant value during irrigation. When the irrigation was stopped the TB began to increase as drainage took place. The irrigation rates in 1995 with the silt loam soil exceeded the saturated conductivity of the soil. During irrigation the TB values exhibited a pattern that suggests the occurrence of coherent reflection, a rarely observed phenomena under natural conditions. These results suggested the existence of a sharp dielectric boundary (wet over dry soil) that was increasing in depth with time.

### INTRODUCTION

In this investigation the role of remote sensing in infiltration studies is considered. One reason for our interest is that remote sensing provides a spatially integrated measurement. Another is the increased availability of sensors which have the potential of providing soil water information, i.e. microwave. Previous research in this area has been very limited [1 and 2]. Several recent investigations have examined new approaches to estimating infiltration parameters which depend upon temporal observations of soil moisture {3, 4 and 5}.

The work described here focuses on the results obtained in a series of experiments using passive microwave radiometers installed on a truck based observing platform. Unique aspects of these studies include multi frequency microwave measurements, high temporal resolution (as compared with typical remote sensing field observations) and a spatial resolution on the order of 1 to 2 m.

### S AND L BAND MICROWAVE RADIOMETER SYSTEM (SLMR)

The S and L Microwave Radiometer (SLMR) is a dual frequency passive sensor system operating at S band (2.65 GHz or 11.3 cm) and L band (1.413 GHz or 21.2 cm) [6]. For the 1994 experiments the SLMR system was mounted on a 1966 Ford hydraulic boom truck belonging to the Hydrological Sciences Branch at NASA's Goddard Space Flight Center. The antennas were mounted to observe horizontal polarization. At the nominal operating height of 5 m with the specified field of view of the radiometers (20°), the footprint size was 1.5 m at a viewing angle of 10° off nadir. The centers of the S and L band radiometers are offset by approximately 1 m in the installation, therefore, the centers of the ground footprints will be offset. The beams do overlap but there is the potential for some variation in target properties in the area contributing to the two individual measurements.

In 1995, a different truck system was used. This was a 1990 Navstar hydraulic boom with a maximum height of 19 m. The observations in 1995 were made at a slightly higher elevation of 8 m which results in footprints closer to 2.5 m for the sensors.

### EXPERIMENT DESCRIPTIONS

The experiments were conducted at two sites using sprinkler irrigation to apply water. In 1994, plots at the Beltsville Agricultural Research Center (BARC) were used. The soil was a sandy loam (70% sand, 6% clay) with a smooth surface. Bulk density averaged 1.45 g/cm<sup>3</sup>. Hydraulic conductivity was measured using disc permeameters at 4 cm tension as 0.338 cm/hr. From this the saturated hydraulic conductivity was estimated as 22 cm/hr.

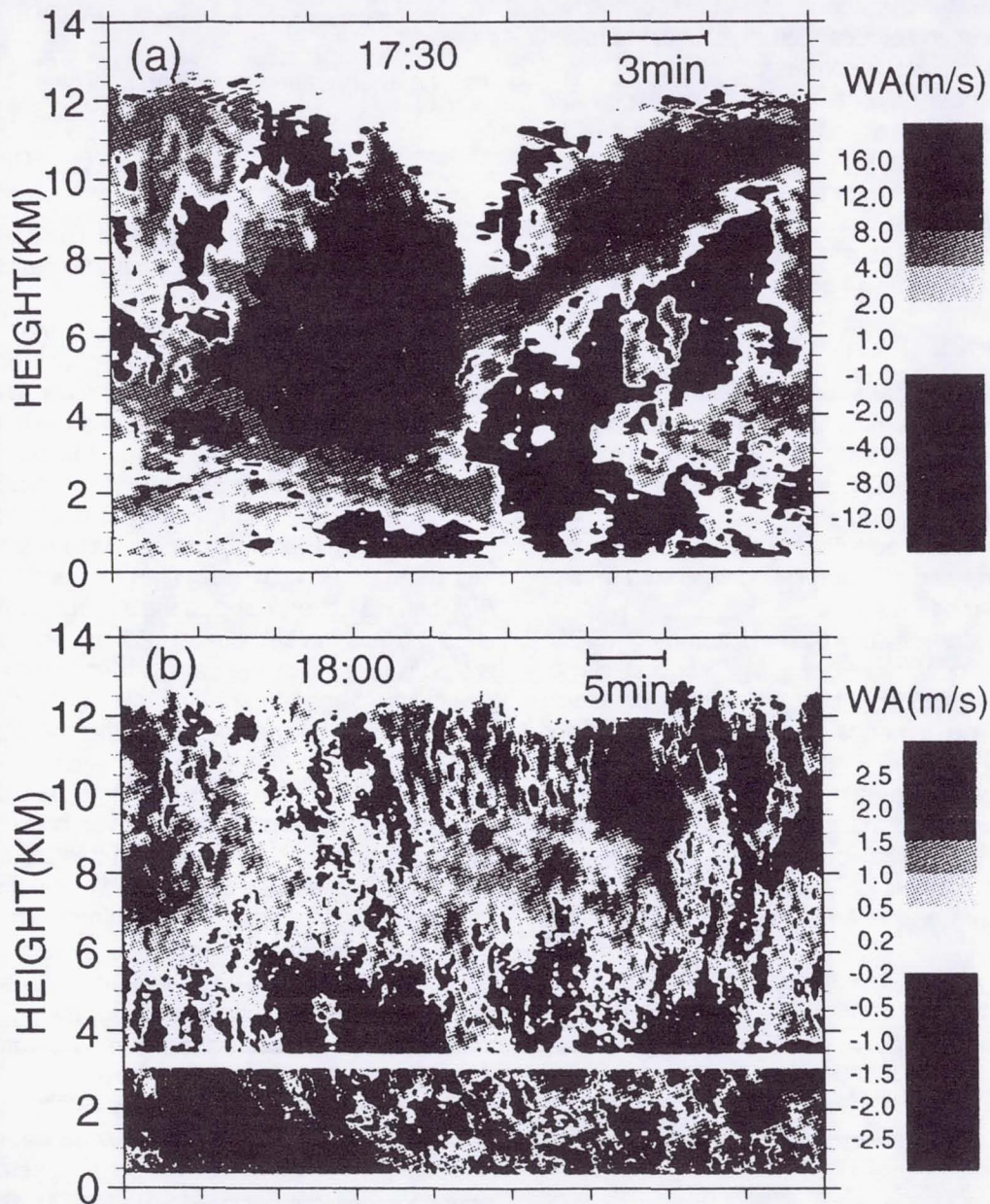
In 1995, the experiments were conducted at facilities of the



# 28th Conference on Radar Meteorology

September 7-12, 1997

Austin, Texas



AMERICAN METEOROLOGICAL SOCIETY



Jeffrey A. Jones\*, Hughes STX Corp., Greenbelt, MD

Robert Meneghini, NASA/GSFC, Greenbelt, MD

Toshio Iguchi, Communications Research Laboratory, Tokyo, Japan

Wei-Kuo Tao, NASA/GSFC, Greenbelt, MD

## 1 INTRODUCTION

Test data are required to test algorithms for the TRMM Precipitation Radar. These data are needed to test the design of the computer codes under development for the operational phase of the mission, and also to test and evaluate alternative or improved precipitation retrieval algorithms.

Over a number of years we have developed and used a 3-dimensional radar model for simulating spaceborne precipitation radars. We have adapted this code to produce data files as close as possible to the TRMM file specifications. In this paper, we will describe the model as it is currently implemented, and show some samples of the synthetic data sets.

## 2 THE MODEL

The input to the radar simulation is a storm model that specifies the particle size distributions for various hydrometeor species, on a 3-dimensional grid. Using the size distributions, the reflectivity and attenuation can be computed at each grid point. The return power observed with a hypothetical radar can now be computed by integrating these quantities over the radar beam.

The Goddard Cumulus Ensemble (GCE) mesoscale model developed by Tao and Simpson (1993) provides the 3-dimensional storm data. We use a series of GCE runs made for TOGA-COARE, consisting of a grid of  $128 \times 128$  1-km squares horizontally, and 28 variably spaced vertical levels, from the surface to 19 km height. The GCE specifies the liquid water content for rain, snow, graupel, cloud ice, and cloud water, as well as temperature and relative humidity at each grid cell.

Using representative values for  $N_0$ , and for mass density,  $\rho$ , the size distribution,  $N(D)$ , is derived from the liquid water content,  $M$ ,

$$N(D) = N_0 \exp(-\Lambda D) \quad (1)$$

where

$$\Lambda = \left( \frac{\pi \rho N_0}{M} \right)^{1/4} \quad (2)$$

Now, for each species, and at each grid cell, we can compute the radar reflectivity factor and attenuation coefficient. The reflectivity factor,  $Z$ , is given by

$$Z = \frac{\lambda^4}{|K|^2 \pi^5} \int_0^{D_{max}} \sigma_{bks}(D) N(D) dD \quad (3)$$

and the attenuation coefficient,  $k$ , is given by

$$k = \frac{1}{\ln 10} \int_0^{D_{max}} \sigma_{ext}(D) N(D) dD. \quad (4)$$

The backscattering and extinction cross sections,  $\sigma_{bks}(D)$  and  $\sigma_{ext}(D)$ , respectively, are derived from Mie theory.

The GCE does not include partially melted particles; instead, ice-phase and liquid-phase drops are modeled as separate particles. As a consequence, a radar bright-band is not produced even in stratiform regions. A bright-band model is crucial for a number of research objectives. In particular, one of the TRMM algorithms concerns bright-band detection, and the lack of a bright-band would mean that parts of the code could not be tested. To correct this, we have extended the storm model to simulate partially melted drops. When rain and snow are both present in the same storm model grid element, the separate species are replaced by partially melted hydrometeors, such that the total mass contents of rain and snow are conserved. The fractional melt water as a function of total particle mass is based on a melting model derived by Yokoyama and Tanaka (1984). The result of this procedure is a qualitatively realistic bright-band in the vicinity of the  $0^\circ$  isotherm in regions of stratiform rain.

The surface return is modeled by computing a surface reflectivity,  $\sigma^0$ , as a function of incidence angle. We use values appropriate for the ocean; the angular dependence is based on results from a Skylab experiment, reported by Ulaby et al. (1982). A random component is included to simulate variability of  $\sigma^0$ . The log of  $\sigma^0$  is assumed to be normally distributed; the standard deviation is a function of incidence angle, also derived from the Skylab experiments.

The radar profile is found by transforming the storm coordinates onto the local radar coordinates

\*Jeffrey A. Jones, Hughes STX Corp., Code 690.2, Goddard Space Flight Center, Greenbelt, MD, 20771, email: Jeffrey.A.Jones.1@gsfc.nasa.gov





# IGARSS'97

1997 International Geoscience and  
Remote Sensing Symposium

03-08 August 1997

Singapore International Convention & Exhibition Centre • Singapore

**Remote Sensing -- A Scientific Vision for  
Sustainable Development**

IEEE Catalog Number: 97CH36042  
Library of Congress Number: 97-70575



# Improving the MODIS Global Snow-Mapping Algorithm

Andrew G. Klein, USRA

Dorothy K. Hall, NASA Goddard Space Flight Center  
George A. Riggs, Research and Data Systems Corporation

Hydrological Sciences Branch Mail Code 974

Laboratory for Hydrospheric Processes

NASA/Goddard Space Flight Center, Greenbelt, MD 20771

tel: 301-286-3314

fax: 301-286-1758

email: aklein@glacier.gsfc.nasa.gov

**Abstract** -- An algorithm (Snowmap) is under development to produce global snow maps at 500 meter resolution on a daily basis using data from the NASA MODIS instrument. MODIS, the Moderate Resolution Imaging Spectroradiometer, will be launched as part of the first Earth Observing System (EOS) platform in 1998. Snowmap is a fully automated, computationally frugal algorithm that will be ready to implement at launch. Forests represent a major limitation to the global mapping of snow cover as a forest canopy both obscures and shadows the snow underneath. Landsat Thematic Mapper (TM) and MODIS Airborne Simulator (MAS) data are used to investigate the changes in reflectance that occur as a forest stand becomes snow covered and to propose changes to the Snowmap algorithm that will improve snow classification accuracy forested areas.

## INTRODUCTION

In the Northern Hemisphere winter, over 40% of the globe may be covered with seasonal snow. The high albedo of snow coupled with its large areal extent make it a strong influence on the Earth's radiation budget. Snow cover also has important societal ramifications. Runoff from snowmelt is an important water resource in many regions of the world and heavy late season snowfalls can cause disastrous flooding [1]. However monitoring of snow cover extent is not currently performed on a global basis.

MODIS, The Moderate Resolution Imaging Spectroradiometer, is scheduled for launch in 1998 aboard the first NASA Earth Observing System (EOS) platform. MODIS is designed to provide quantitative measurements of important geophysical parameters on a global basis [2]. Its high spatial resolution and numerous spectral bands in the 0.4 to 2.5  $\mu\text{m}$  wavelength region allow for more accurate monitoring of snow cover than is possible using currently operational satellites. A prototype algorithm (Snowmap) has been developed to produce daily snow maps with 500 meter resolution at the global scale using MODIS visible to short-wave infrared reflectances [3].

Aside from cloud cover, forests present the most serious limitation to monitoring snow-cover extent using visible to short-wave infrared satellite imagery as much of the world's seasonally snow-covered area contains forests. For example, in North America 40% of the area north of the continental snowline is forest covered. Validation efforts using Landsat

Thematic Mapper (TM) and MODIS Airborne Simulator (MAS) images indicate that classification accuracy in forests, especially dense forests, is lower than in biomes where vegetation is sparse or of low stature. Because of their large extent, accurate snow mapping in forests is vital to maximize the accuracy of mapping snow cover in forests.

## THE SNOWMAP ALGORITHM

Snowmap is a fully automated and computational frugal algorithm that will be ready to implement by the launch of the EOS AM-1 spacecraft in 1998 [3]. It builds on nearly on two decades of remote sensing research and represents a significant improvement over existing operational products because of the cloud screening ability of MODIS, its unique spectral bands and the planned 500 m resolution of the future MODIS snow cover products. Snowmap uses at-satellite reflectances in the 0.4 to 2.5  $\mu\text{m}$  wavelengths (Fig. 1) to determine if a pixel is snow-covered using two classification criteria. The first is a Normalized Difference Snow Index (NDSI) value of greater or equal to 0.40. The NDSI is akin

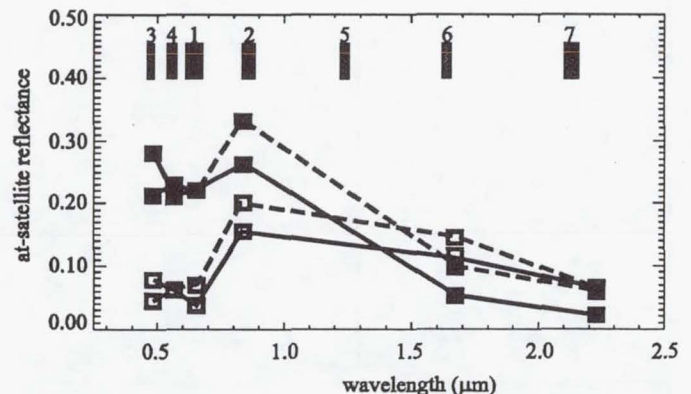


**Fig. 1:** Observed (solid line) and modeled (dashed line) spectra for a leafless deciduous forest stand. Open symbols are for snow free conditions and filled symbols for snow covered conditions. The model results were produced using the GeoSAIL model for a leafless aspen stand and illumination conditions corresponding to the August and February TM acquisitions. MODIS bands are indicated by the gray boxes





# IGARSS'97

1997 International Geoscience and  
Remote Sensing Symposium

03-08 August 1997

Singapore International Convention & Exhibition Centre • Singapore

Remote Sensing -- A Scientific Vision for  
Sustainable Development

IEEE Catalog Number: 97CH36042  
Library of Congress Number: 97-70575



# Effects of Faraday Rotation on Microwave Remote Sensing from Space at L-Band

D.M. Le Vine and M. Kao

Laboratory for Hydrospheric Processes/Code 975

NASA/Goddard Space Flight Center

Greenbelt, Maryland 20771

Phone: 301-286-8059; FAX: 301-286-0294; Email: dmlvine@meneg.gsfc.nasa.gov

**Abstract** — The effect of Faraday rotation on the remote sensing of soil moisture from space is investigated using the International Reference Ionosphere (IRI) to obtain electron density profiles and the International Geomagnetic Reference Field (IGRF) to model the magnetic field. With a judicious choice of satellite orbit (6 am, sunsynchronous) the errors caused by ignoring Faraday rotation are less than 1 K at incidence angles less than 40 degrees.

## INTRODUCTION

An L-band radiometer in space could provide global maps of surface soil moisture and contribute to the measurement of other important parameters of the earth surface [1]. Furthermore, advances in technology such as the development of aperture synthesis [2] and inflatable structures [3] have enhanced the prospect that a practical sensor can be deployed in space in the near future. Among the concerns associated with operating at this low frequency is rotation of the polarization vector due to the ionosphere (Faraday rotation). Faraday rotation can result in errors for conical scanners and cross-track imagers which view the surface at non-nadir incidence angles (i.e. where the emissivity at vertical and horizontal polarization differ).

At frequencies near L-band (1.4 GHz) the change in direction of the polarization vector of a linearly polarized wave propagating through the ionosphere can be written [4]:

$$\Delta\phi = (\pi/cv^2) \int v_p^2 v_B \cos(\theta_B) ds \quad (1)$$

where  $\Delta\phi$  is the change in direction (radians),  $ds$  is distance along the ray path,  $v$  = frequency (Hz),  $v_p$  = electron plasma frequency (Hz)  $\approx 9/N_e$ , where  $N_e$  is the electron density in  $\#/cm^3$ ,  $v_B$  = electron 'cyclotron' frequency (Hz) =  $qB/(2\pi m_e)$ , and  $\theta_B$  is the angle between the magnetic field,  $B$ , and the direction of propagation,  $\theta$ .

The effect of  $\Delta\phi$  on a linearly polarized radiometer is to mix horizontally and vertically polarized emissions received from the surface. For example, in the case of a horizontally polarized receiver, the apparent brightness temperature,  $T_B$ , is:

$$T_B = [\epsilon_h \cos^2(\Delta\phi) + \epsilon_v \sin^2(\Delta\phi)] T_s \quad (2)$$

and the error incurred by ignoring Faraday rotation is:

$$\Delta T_B = T_s [\epsilon_h - \epsilon_v] \sin^2(\Delta\phi) \quad (3)$$

where  $T_s$  is the physical temperature of the surface and  $\epsilon_h$  and  $\epsilon_v$  are the emissivities of the surface for horizontal and vertical polarization, respectively.

## EXAMPLES OF FARADAY ROTATION

Faraday rotation,  $\Delta\phi$ , has been computed using the International Reference Ionosphere [5] to generate electron density profiles and the International Geomagnetic Reference Field (IGRF) to model the earth's magnetic field. Figure 1 shows Faraday rotation as a function of local time for a hypothetical sensor at an altitude of 675 km and at 35° N. latitude and 75° W. longitude. Curves are shown for summer and winter of 1995 (solar minimum) and 1990 (solar maximum). Notice that  $\Delta\phi$  is minimum near 6 am and that the evening (6 pm) is somewhat worse than the morning. A sun-synchronous orbit is advantageous for the measurement of soil moisture (to avoid diurnal effects), and the 6 am crossing clearly is a good choice as far as Faraday rotation is concerned. Figure 2 shows Faraday rotation as a function of longitude for latitude of 20 and 60 degrees. These examples are for 6 am, 675 km altitude and for the summer of 1990 and 1995. Summer 1990 (solar maximum) is a worse case. The  $\Delta\phi$  for 1995 (solar minimum) is much less. The angles,  $\Delta\phi$ , shown in this case (1995) are also representative of the values of Faraday rotation obtained in winter for both 1990 and 1995 at latitudes between 20-60 degrees. Faraday rotation also depends on orbit altitude and this is illustrated in Figure 3 for local time of 6 am. Note that the  $\Delta\phi$  in Figures 1-3 are for a nadir directed ray path ( $\theta = 0$ ). The results can be corrected approximately for incidence angle,  $\theta$ , using:  $\Delta\phi(\theta) \approx \Delta\phi(0)/\cos(\theta)$ .

## EFFECT ON BRIGHTNESS TEMPERATURE

The effect of Faraday rotation on observed brightness temperature, depends on the emissivities,  $\epsilon_{h,v}$ , of the surface as shown in (2) and (3). Assuming a flat, homogenous half-space and neglecting effects such as roughness and vegetation cover:

$$\epsilon_{h,v}(\theta) = 1 - |R_{h,v}(\theta)|^2 \quad (4)$$

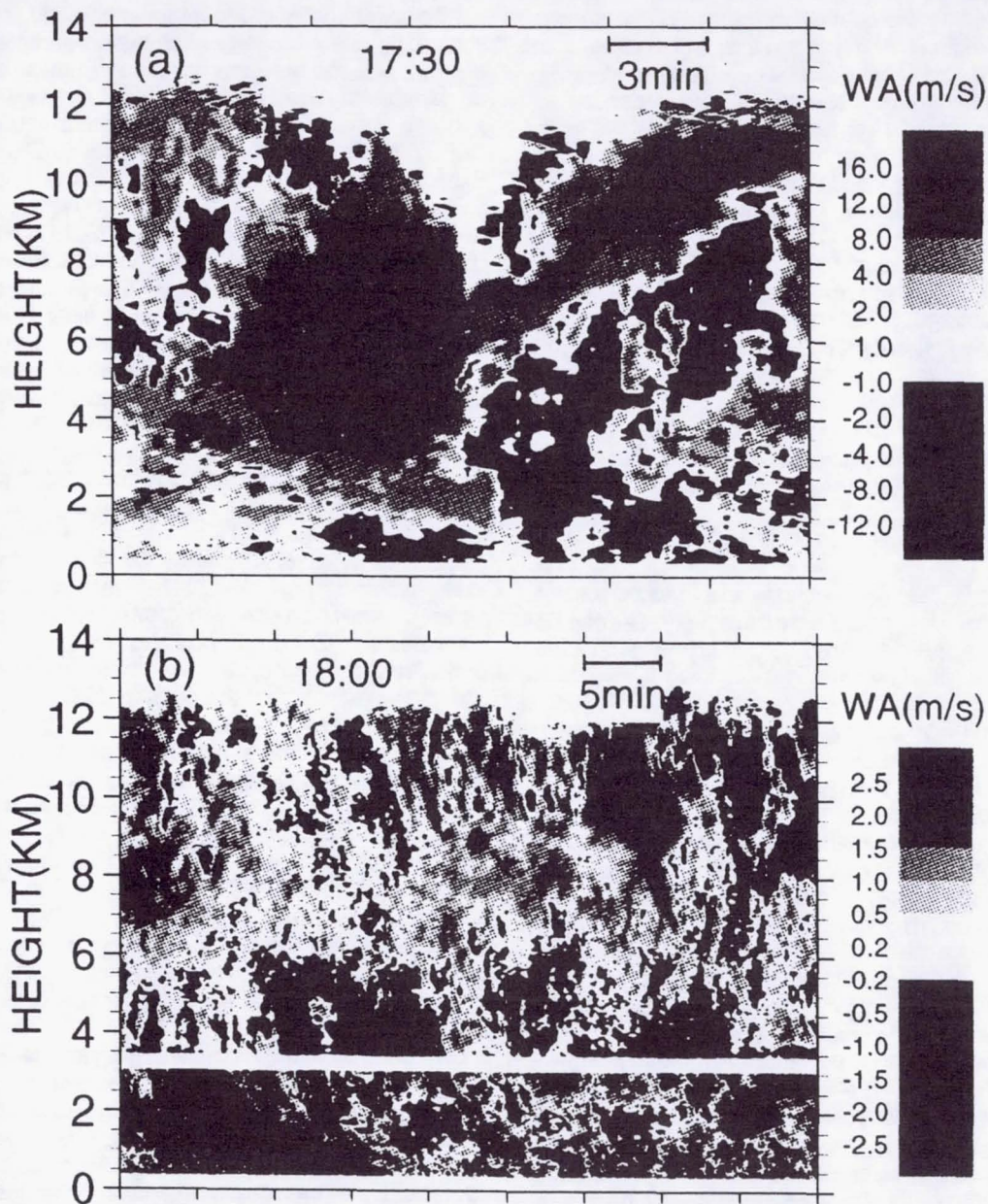
where  $R_{h,v}(\theta)$  is the Fresnel reflection coefficient of the surface. For the ideal (i.e. flat) surface the Fresnel reflection coefficients are



# 28th Conference on Radar Meteorology

September 7-12, 1997

Austin, Texas



AMERICAN METEOROLOGICAL SOCIETY



Liang Liao, Caelum Research, NASA/GSFC, Greenbelt, MD 20771

Robert Meneghini, NASA/GSFC, Greenbelt, MD 20771

Toshio Iguchi, Communications Research Lab., Tokyo Japan, 184

Andrew Detwiler, South Dakota School of Mines & Technology, Rapid City, SD, 57701

## 1. INTRODUCTION

Estimation of snow characteristics from airborne radar measurements would complement in-situ measurements. While in-situ data provide more detailed information than radar, they are limited in their space-time sampling. In the absence of significant cloud water contents, dual-wavelength radar data can be used to estimate 2 parameters of a drop size distribution if the snow density is assumed. To estimate, rather than assume, a snow density is difficult, however, and represents a major limitation in the radar retrieval. There are a number of ways that this problem can be investigated: direct comparisons with in-situ measurements, examination of the large scale characteristics of the retrievals and their comparison to cloud model outputs, use of LDR measurements, and comparisons to the theoretical results of Passarelli (1978) and others. In this paper we address the first approach and, in part, the second.

## 2. METHOD

Assuming that the snow size distribution,  $N(D_s)$ , is exponentially distributed, then

$$N(D) = N_0 \exp(-3.67 D_s/D_{0s})$$

where  $D_s$  and  $D_{0s}$  are the diameter and median volume diameter of the snow particles, respectively.  $D_{0s}$  can be estimated from the measured values of the radar dual frequency ratio (DFR) where

$$DFR = 10 \log(Z_x/Z_{ka})$$

where  $Z_x$  and  $Z_k$  are the radar reflectivity factors at  $X$  and  $K_a$  bands, respectively. For the region of dry snow in stratiform rain the attenuation from the snow and cloud water is usually negligible at these wavelengths. Moreover, if the particles are randomly oriented the DFR is relatively insensitive to the shape distribution. The particle number concentration,  $N_t$ , which is a function of  $N_0$  and  $D_{0s}$ , can be easily derived from the radar reflectivity at either wavelength once  $D_{0s}$  is known. Plots of DFR versus  $D_{0s}$  for different values of constant snow density show that this relationship is nearly independent of the snow density if  $D_{0s}$  is less than about 3.5 mm [Matrosov, 1992]. This is not the

case, however, for  $N_0$  or  $N_t$  which are highly sensitive to the snow density. Note that the independence of the DFR on snow density does not hold if the snow density is correlated with size. In this paper, only the constant snow density case is considered, however.

## 3. COMPARISON WITH IN-SITU MEASUREMENTS

To examine the algorithm described above for estimating the snow size distribution parameters,  $D_{0s}$  and  $N_t$ , we compare the estimates of these quantities as derived from dual-wavelength radar data with in-situ airborne measurements. The data are taken from CaPE (Convective and Precipitation-Electrification Experiment). The airborne radar was built by Japan and mounted on NASA T-39 aircraft while the in situ particle measurements were made using a PMS 2D-P probe mounted on the T-28 aircraft of the South Dakota School of Mines & Technology. On 19 July 1991 the T-39 and T-28 coordinated several flight lines over a weak convective cell (UT: 18:15-18:45). During these flights the T-39 and T-28 flew at altitudes of approximately 11 km and 5-6 km, respectively. Figure 1 shows an example of results of the  $D_{0s}$  and  $N_t$  as derived from the radar data at the height of the T-28 and the in-situ results from the PMS 2D-P probe. To account for the different aircraft speeds, the distance scale,  $s$ , used in Fig.1 is the relative distance with respect to a point of the T-28 flight track. An examination of the PMS 2D-P images show two main types of snow particles in this region. For the distances  $s < 6$  km, the particles appear to be almost exclusively aggregates; at  $s = 6$  km an abrupt transition occurs to particles that are smaller and more spherical. These particles are assumed to be graupel. To compare the 2 sets of results, an approximation is necessary: the 2D-P processing gives the maximum dimension of the particle,  $D_{max}$ , either along the  $X$  or  $Y$  axis, whichever length is larger. The relationship between this  $D_{max}$  and  $D_{0s}$  depends on the shape and orientation distribution of the particles. In Fig. 1 we have assumed that the ratio of  $D_{max}$  to  $D_{0s}$  is equal to 2. Although this value appears to work well for the 3 comparisons that were made, derivation of this ratio from the size and shape distributions is desirable. In the estimation of  $D_{0s}$  and  $N_t$  from the T-39 radar data, snow densities of  $0.2 \text{ g/cm}^3$  and  $0.8 \text{ g/cm}^3$  are taken to characterize the particles in the 2 regions ( $s < 6$  km,  $s > 6$  km). As can be seen in Fig.1, the values of  $D_{0s}$  as estimated from the T-39 radar data are in fairly good agreement with those from the PMS probes on the T-28. These and the results of 2 other comparisons (not shown) indicate that the  $D_{0s}$  agreement is fairly good

Liang Liao, Caelum Research, Code 975, NASA/GSFC, Greenbelt, MD, 20771; lliao@meneg.gsfc.nasa.gov



Antony K. Liu

Oceans and Ice Branch, NASA/Goddard Space Flight Center, Greenbelt, Maryland, USA

phone: (301)286-8534, fax: (301)286-0240, e-mail: liu@neptune.gsfc.nasa.gov

Ming-K. Hsu

Department of Oceanography, National Taiwan Ocean University, Keelung, Taiwan

Nai K. Liang

Institute of Oceanography, National Taiwan University, Taipei, Taiwan

## ABSTRACT

Synthetic Aperture Radar (SAR) images from ERS-1 have been used to study the characteristics of internal waves northeast and south of Taiwan in the East China Sea, and east of Hainan Island in the South China Sea. Rank-ordered packets of internal solitons propagating shoreward from the edge of the continental shelf were observed in the SAR images. Based on the assumption of a semidiurnal tidal origin, the wave speed can be estimated and is consistent with the internal wave theory. By using the SAR images and hydrographic data, internal waves of elevation have been identified in shallow water due to a thicker mixed layer as compared with the bottom layer on the continental shelf. The generation mechanism includes the influences of the tide and the Kuroshio intrusion across the continental shelf for the formations of elevation internal waves. The effects of water depth on the evolution of solitons and wave packets are modeled by nonlinear Kortweg-deVries (KdV) type equation and linked to satellite image observations. The numerical calculations of internal wave evolution on the continental shelf have been performed and compared with the SAR observations. For a case of depression waves in deep water, the solitons first disintegrate into dispersive wave trains and then evolve to a packet of elevation waves in the shallow water area after they pass through a "turning point" of approximately equal layer depths has been observed in the SAR image and simulated by numerical model.

## 1. INTRODUCTION

The tidal flow over topographic features such as a sill or continental shelf in a stratified ocean can produce nonlinear internal waves of tidal frequency and has been studied by many investigators (Apel et al., 1985). Their observations provide insight into the soliton generation process and explain the role they play in the transfer of energy from tides to ocean mixing. However, almost all of the nonlinear internal waves observed in nature previously were mode-one depression waves. Salusti et al. (1989) first observed two moving internal wave packets consisting of elevation waves and depression waves separated by a 12 hours period, using

thermistor chain in eastern Mediterranean Sea during a pilot experiment in the Rio-Antirio strait, Western Greece in July 1986. The change of polarity in internal waves is caused by the change of the mean thermocline depth. Similar change of internal wave polarity was observed by Serebryany (private communication, 1995) at the shelf of the Sea of Japan in September 1982. These nonlinear internal waves were apparently generated by internal turbulent mixing or baroclinic shear instability over bottom features.

It has been known for over two decades that internal waves have surface signatures recognizable in satellite images of sea surface (Fu and Holt, 1982). The synthetic aperture radar (SAR) images from the First European Remote Sensing Satellite, ERS-1, have been used to study the characteristics of internal waves northeast of Taiwan by Liang et al. (1995). Rank-ordered packets of internal solitons propagating shoreward from the edge of the continental shelf were observed in many SAR images. By using the SAR images and hydrographic data, internal waves of elevation can be identified because of a thicker mixed layer as compared with the bottom layer on the continental shelf. The effects of water depth on the parameters of solitons and wave packets can be linked to the observations from SAR images.

A solitary wave theory that describes the evolution of nonlinear internal waves has been developed and expanded to include effects of vertical shear, variable bottom topography, radial spreading, and dissipation by Liu et al. (1985) for the Sulu Sea internal soliton study (Apel et al., 1985). Internal solitary waves on a shelf with shoaling effects have been studied by Liu (1988) in the New York Bight. All these mechanisms of wave evolution can be simulated numerically by solving the nonlinear Kortweg-deVries-type equation with varying coefficients corresponded to the changing environments as demonstrated by Liu et al. (1985) and Liu (1988). For the case of depression waves, the disintegration of solitons into dispersive wave packets after they pass through a "turning point" of approximately equal layer depths (critical depth) has been studied numerically by Helfrich et al., (1984).



The Kuroshio moving north from Philippine Basin branches out near the south tip of Taiwan. A part of the Kuroshio intrudes into the South China Sea through the Bashi Channel and the Luzon Strait. The internal tides and internal waves have been generated by the shallow ridges (200-300 m) in the Luzon Strait. Surface signature pattern of huge internal soliton packets has been observed in the ERS-1 SAR image collected on June 16, 1995. The crest of soliton is more than 200 km long and each packet contains more than ten rank-ordered solitons with a packet width of 25 km. Within a wave packet, the wavelengths appear to be monotonically decreasing, front to rear, from 5 km to 500 m. These are the biggest internal waves that have been observed in this area. The internal wave amplitude is larger than 100 m based on the CTD casts from Taiwan's research ship during their South China Sea expedition (Wang, private communication, 1995). These huge wave packets propagate and evolve into the deep South China Sea and will reach the continental shelf of southern China. It is possible that the internal wave packets observed in the South China Sea east of Hainan is due to the evolution of these waves. The distance and degree of intrusion of Kuroshio (with high temperature and high salinity water) into the Taiwan Strait and the South China Sea with heat flux and momentum flux are still an open issues.

#### 4. NUMERICAL RESULTS

A series of numerical experiments were performed by solving the initial value problem described by Eq. (1) with a well developed soliton solution as an initial condition. The steady state depression wave solution of KdV equation is given by

$$A(x, t) = -A_0 \operatorname{sech}^2((x - Ct)/\ell), \quad (5)$$

where  $A_0$  is the wave amplitude, the wave speed  $C$  is

$$C = C_0 \left(1 + \frac{A_0(H_2 - H_1)}{2H_1H_2}\right), \quad (6)$$

and the half width  $\ell$  is

$$\ell = 2H_1H_2(3A_0(H_2 - H_1))^{-1/4}. \quad (7)$$

In the north of Taiwan area, the density contrast  $\Delta\rho/\rho = 10^{-3}$ . The first case was made for a initial profile corresponding to a single depression soliton in finite/deep water of depth  $H$  propagating towards a cosine-shaped transition to shallow water:

$$H_2 = \begin{cases} H_{20} & x < 0 \\ H_{20} + 0.5(H_{20} - H_{2e})(\cos(\pi x/L) - 1) & 0 < x < L \\ H_{2e} & x > L \end{cases}, \quad (5)$$

where  $L$  is a characteristic length of the depth variation.

The numerical simulation of nonlinear internal wave evolution on the shelf shows the change of polarity through

critical depth (Figure 5). A solitary depression wave is used as the initial condition at water depth of 160 m with  $A_0 = 10$  m. The mixed layer thickness,  $H_1 = 60$  m, the initial bottom layer thickness  $H_{20} = 100$  m, the final bottom layer thickness  $H_{2e} = 40$  m, and the characteristic length  $L = 3$  Km are chosen. Note that the critical depth is reached after 6 hours (at  $x = 0.6 L$ ) approximately. However, the solitary wave disintegrates into a wave packet after 10 hours (near  $x = L$ ), and it continues to evolve as a train of rank-ordered elevation internal solitons. It's found that from a single depression soliton more than five elevation solitons can merge.

Next, the case of two rank-ordered depression solitons ( $A_0 = 10$  and 7 m) separated by 25 km is studied. Two wave packets start to evolve and merge after 11 hours near the critical depth. The dissipation effects are expected to be important in this situation since the interaction of wave packets may steepen the wave amplitude. Thus the eddy viscosity could be eroding the sharp peaks of the large solitons, reducing their amplitudes and increasing their half-widths at the same time. Figure 6 shows the evolution of two depression solitons through the critical depth with a

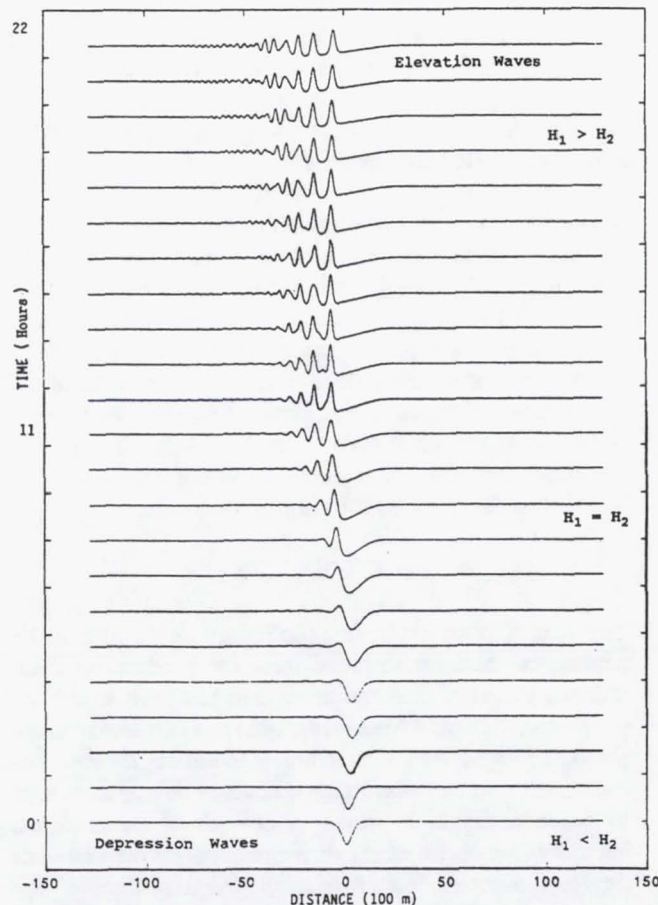


Figure 5. Numerical simulation of nonlinear internal wave evolution on the shelf showing the change of polarity through critical depth.





# IGARSS'97

1997 International Geoscience and  
Remote Sensing Symposium

03-08 August 1997

Singapore International Convention & Exhibition Centre • Singapore

Remote Sensing -- A Scientific Vision for  
Sustainable Development

IEEE Catalog Number: 97CH36042  
Library of Congress Number: 97-70575



# Microwave Remote Sensing of Soil Moisture for Estimation of Soil Properties

Nandish M. Mattikalli\*, and Edwin T. Engman  
NASA Goddard Space Flight Center, Laboratory for Hydrospheric Processes  
Hydrological Sciences Branch, Code 974 (\*Hughes STX/Code 974)  
Greenbelt, MD 20771, USA  
Tel: (301) 286-7696 Fax: (301) 286-1758 E-mail: nandish@hydro5.gsfc.nasa.gov

Thomas J. Jackson  
USDA Agricultural Research Service, Hydrology Laboratory  
Beltsville, MD 20705, USA

**Abstract** – Surface soil moisture dynamics was derived using microwave remote sensing, and employed to estimate soil physical and hydraulic properties. The L-band ESTAR radiometer was employed in an airborne campaign over the Little Washita watershed, Oklahoma during June 10-18, 1992. Brightness temperature (TB) data were employed in a soil moisture inversion algorithm which corrected for vegetation and soil effects. Analyses of spatial TB and soil moisture dynamics during the dry-down period revealed a direct relationship between changes in TB, soil moisture and soil texture. Extensive regression analyses were carried out which yielded statistically significant quantitative relationships between ratio of percent sand to percent clay (RSC, a term derived to quantify soil texture) and saturated hydraulic conductivity (Ksat) in terms of change components of TB and surface soil moisture. Validation of results indicated that both RSC and Ksat can be estimated with reasonable accuracy. These findings have potential applications for deriving spatial distributions of RSC and Ksat over large areas.

## INTRODUCTION

Surface soil moisture is of great significance to hydrologic research for partitioning rainfall into runoff and infiltration. Soil properties such as soil texture and saturated hydraulic conductivity (Ksat) play a key role in the drainage and redistribution of soil moisture, but these properties are difficult to obtain in the field and/or laboratory. Therefore, methods based on remote sensing will have capabilities of deriving spatial distribution of Ksat. Earlier studies have employed brightness temperature (TB) data obtained from passive remote sensing and soil hydrology models for estimation of soil hydraulic parameters [1, 2]. Such approaches require information on several hydrologic and meteorological parameters, and therefore might not be ideally suited for application to large areas.

Reference [3] established highly significant relationships between changes in moisture content of the surface soil, 2 days after a thorough wetting, and average Ksat of the soil profile. The log-log transformations of an effective profile-average Ksat and the initial two-day drainage of the soil were valuable to obtain estimates of an average Ksat. These findings have a potential to obtain quick estimates of the spatial distribution of Ksat from the soil moisture contents if

microwave remote sensing observations are made at two day temporal resolution after saturation [4]. The objective of the present study was to test the approach of [3] for the field conditions of a medium-sized watershed, and to evaluate if soil physical properties (viz. soil texture and Ksat) can be estimated from the temporal variability of microwave remotely sensed TB and soil moisture data.

## MATERIALS AND METHODS

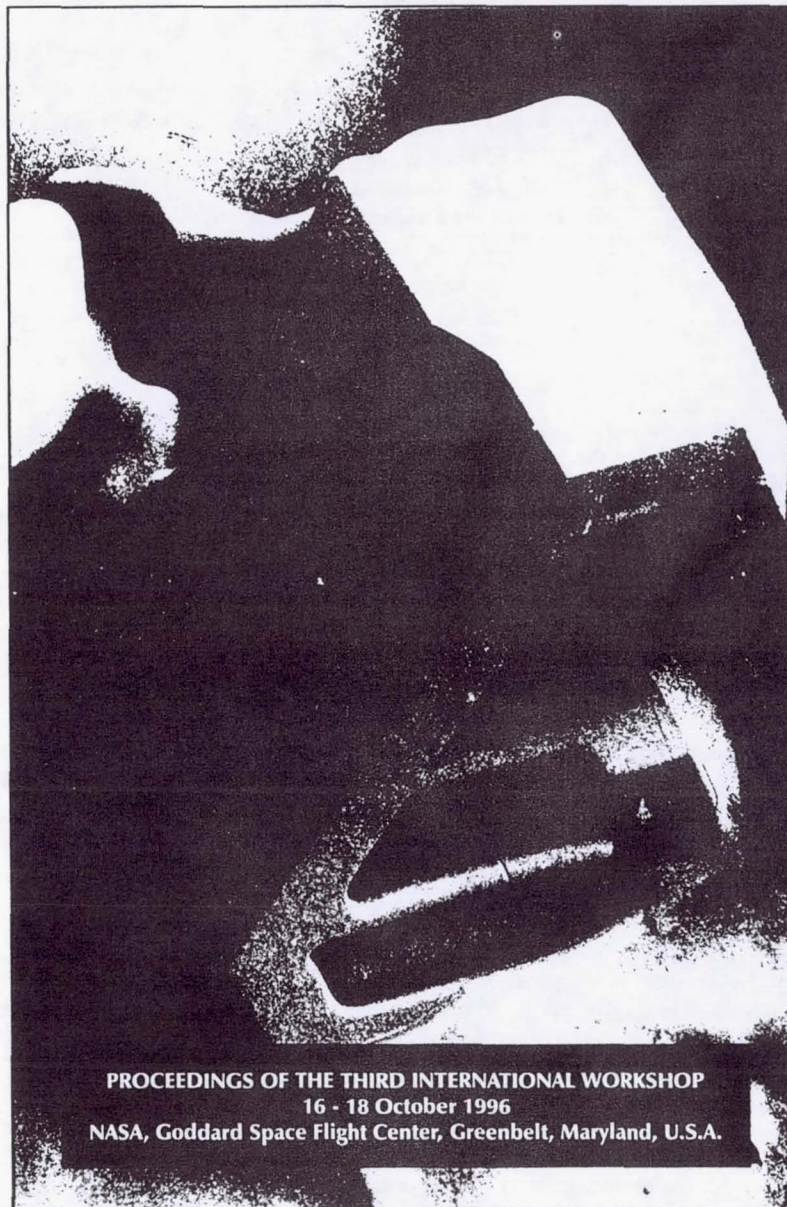
The Washita'92 research experiment was carried out during June 10-18, 1992 in the Little Washita watershed, Oklahoma. The climate of Little Washita region is moist and sub-humid with an average annual rainfall of about 750 mm [5]. During the experiment, land cover in the Little Washita watershed was dominated by pasture and senesced or harvested winter wheat with some other agricultural crops including corn and alfalfa [5]. Forest cover within the watershed is very sparse and constitutes a small proportion of the watershed.

Multitemporal airborne microwave data were collected using the L band (21 cm wavelength, or 1.4 GHz frequency) synthetic aperture Electronically Steered Thinned Array Radiometer (ESTAR) [6]. A large number of ground soil moisture measurements were carried out to support and validate microwave remotely sensed data. The study area experienced heavy rainfall (more than 30 mm) on June 5, 1992, and the rainfall continued till June 9, 1992. However, there was no rainfall in the watershed for the entire duration of the Washita'92 experiment [7]. Therefore, the hydrologic conditions in the watershed were ideal to follow a drying period from very wet (about 30%) to dry (about 10%) over a period of nine days.

Temporal soil moisture information was derived from the ESTAR TB images. The soil moisture retrieval algorithm corrects thermal emission records for vegetation cover and surface roughness, and estimates the real part of the soil dielectric constant based on the Fresnel assumptions [7]. Soil texture effects were corrected before inverting a dielectric mixing model for soil moisture determination. Vegetation parameters (i.e., type and water content) and soil texture data were derived from land-use data base and soils map, respectively. The ESTAR derived soil moisture values were validated by comparing them with the field measured soil moisture values, and the standard error of estimates were within 3.5% for the bare fields and 5.7% for the vegetated



APPLICATIONS OF  
**REMOTE SENSING**  
IN HYDROLOGY



PROCEEDINGS OF THE THIRD INTERNATIONAL WORKSHOP  
16 - 18 October 1996  
NASA, Goddard Space Flight Center, Greenbelt, Maryland, U.S.A.

Editors G.W. Kite, A. Pietroniro and T.J. Pultz



## APPLICATION OF MULTITEMPORAL REMOTELY SENSED SOIL MOISTURE FOR THE ESTIMATION OF SOIL PHYSICAL PROPERTIES

N. M. Mattikalli<sup>1</sup>, E. T. Engman<sup>1</sup>, T. J. Jackson<sup>2</sup>, and L. R. Ahuja<sup>3</sup>

<sup>1</sup>NASA Goddard Space Flight Center, Hydrological Sciences Branch  
Code 974, Greenbelt, MD 20771

<sup>2</sup>USDA-ARS, Hydrology Laboratory, Beltsville, MD 20705

<sup>3</sup>USDA-ARS, GPSR, 301 South Howes, PO Box E, Fort Collins, CO 80522

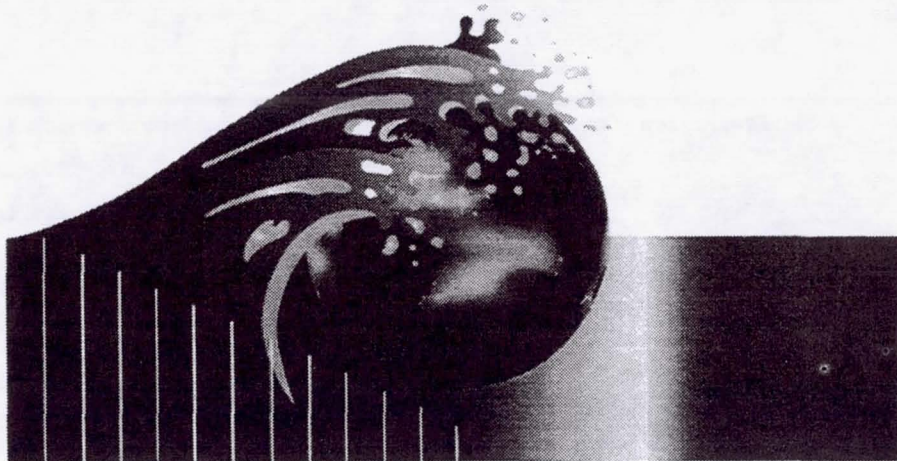
### ABSTRACT

This paper demonstrates the use of multitemporal soil moisture derived from microwave remote sensing to estimate soil physical properties. The passive microwave ESTAR instrument was employed during June 10-18, 1992, to obtain brightness temperature ( $T_B$ ) and surface soil moisture data in the Little Washita watershed, Oklahoma. Analyses of spatial and temporal variations of  $T_B$  and soil moisture during the dry-down period revealed a direct relationship between changes in  $T_B$  and soil moisture and soil physical (viz. texture) and hydraulic (viz. saturated hydraulic conductivity,  $K_{sat}$ ) properties. Statistically significant regression relationships were developed for the ratio of percent sand to percent clay (RSC) and  $K_{sat}$  in terms of change components of  $T_B$  and surface soil moisture. Validation of results using field measured values and soil texture map indicated that both RSC and  $K_{sat}$  can be estimated with reasonable accuracy. These findings have long term potential applications of microwave remote sensing to obtain quick estimates of the spatial distributions of  $K_{sat}$  over large areas for input parameterization of hydrologic models.

### INTRODUCTION

Surface soil moisture is of great significance to hydrologic research for partitioning rainfall into runoff and infiltration. Soil is an important reservoir of fresh water, where non continuous precipitation is transformed into a normally continuous flow of water to plant roots. Soil properties such as soil texture and saturated hydraulic conductivity ( $K_{sat}$ ) play key roles in the drainage and redistribution of soil moisture, but these properties are difficult to obtain in the field and/or laboratory. Therefore, methods based on remote sensing will have capabilities of deriving spatial distribution of  $K_{sat}$ . Earlier studies have employed brightness temperature ( $T_B$ ) data obtained from passive remote sensing and soil hydrology models for estimation of soil hydraulic parameters [Camillo *et al.*, 1986; Van de Griend and O'Neill, 1986]. Such approaches require information on several hydrologic and meteorological parameters, and therefore might not be ideally suited for application to large areas.





*Reprinted from*

# OCEAN OPTICS XIII

22-25 October 1996  
Halifax, Nova Scotia, Canada

 SPIE Volume 2963



## **Field evaluation of anti-biofouling compounds on optical instrumentation**

Scott McLean and Bryan Schofield

Satlantic Inc., Halifax, Nova Scotia, Canada, B3K 5X8

Giuseppe Zibordi

Space Applications Institute, Joint Research Center, Ispra, 21020, VA, Italy

Marlon Lewis

Department of Oceanography, Dalhousie University, Halifax, Nova Scotia, Canada, B3J 1R2

Stanford Hooker

NASA Goddard Space Flight Center, Greenbelt, MD, USA, 20771

Alan Weidemann

Naval Research Laboratory, Stennis Space Center, MS, USA

### **ABSTRACT**

Biofouling has been a serious question in the stability of optical measurements in the ocean, particularly in moored and drifting buoy applications. Many investigators coat optical surfaces with various compounds to reduce the amount of fouling; to our knowledge, however, there are no objective, in-situ comparative testing of these compounds to evaluate their effectiveness with respect to optical stability relative to untreated controls.

We have tested a wide range of compounds at in-situ locations in Halifax Harbour and in the Adriatic Sea on passive optical sensors. Compounds tested include a variety of TBT formulations, antifungal agents, and low-friction silicone-based compounds; time-scales of up to four months were evaluated. The results of these experiments are discussed.

### **1. HALIFAX HARBOUR EXPERIMENT**

#### **1.1 Objective**

The objective of the Halifax Experiment was to evaluate several commercially available anti-biofouling compounds for their effectiveness and stability when exposed to high productivity seawater. This experiment is unique in that the effectiveness of these types of compounds has never been evaluated in a quantitative method which preserves the in-water optical properties of the fouling organisms.

#### **1.2 Experimental Setup**

Test samples consisting of glass and acrylic, coated with various test compounds, were placed in Halifax Harbour for several months and periodically removed for evaluation. For the in-situ component, the sample holders suspended eleven test samples at a depth of one meter on a floating dock in 8 meters of water 10 meters from a 1.1 meter diameter untreated sewer outlet which provided a nutrient rich environment for the experiment.

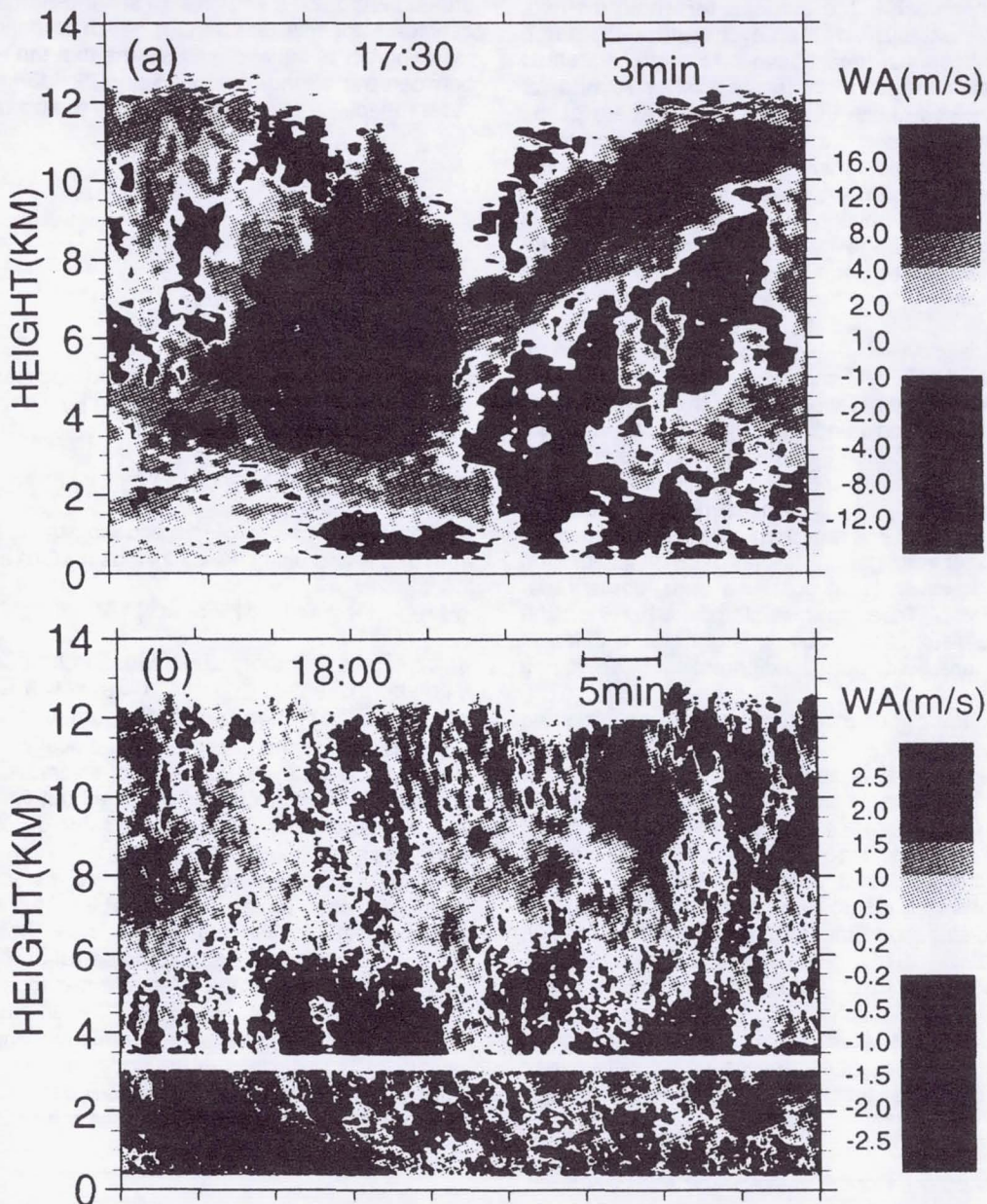
The in-situ sample holders held the test sample (a 2 inch diameter acrylic or glass substrate) with the anti-biofoulant coated side exposed to the seawater. The substrate was held in place with a delrin faceplate (which was also coated) as it would be on a typical Satlantic OCR-100 radiance sensor. A plug blocked the back of the window from being exposed to the



# 28th Conference on Radar Meteorology

September 7-12, 1997

Austin, Texas



AMERICAN METEOROLOGICAL SOCIETY



Robert Meneghini<sup>1</sup> and Jeffrey A. Jones  
Goddard Space Flight Center, Greenbelt, MD  
Hughes STX Corp, Greenbelt, MD

## 1. INTRODUCTION

One of the TRMM radar products of interest is the monthly-averaged rain rates over 5 x 5 degree cells. Clearly, the most directly way of calculating these and similar statistics is to compute them from the individual estimates made over the instantaneous field of view of the instrument (4.3 km horizontal resolution). An alternative approach is the use of a threshold method. It has been established that over sufficiently large regions the fractional area above a rain rate threshold and the area-average rain rate are well correlated for particular choices of the threshold [e.g., Kedem et al., 1990]. A straightforward application of this method to the TRMM data would consist of the conversion of the individual reflectivity factors to rain rates followed by a calculation of the fraction of these that exceed a particular threshold. Previous results indicate that for thresholds near or at 5 mm/h, the correlation between this fractional area and the area-average rain rate is high.

There are several drawbacks to this approach, however. At the TRMM radar frequency of 13.8 GHz the signal suffers attenuation so that the negative bias of the high resolution rain rate estimates will increase as the path attenuation increases. To establish a quantitative relationship between fractional area and area-average rain rate, an independent means of calculating the area-average rain rate is needed such as an array of rain gauges. This type of calibration procedure, however, is difficult for a spaceborne radar such as TRMM. To estimate a statistic other than the mean of the distribution requires, in general, a different choice of threshold and a different set of tuning parameters.

In a previous paper a multiple thresholding method was described [Meneghini and Jones, 1993]. The idea behind the method is that, because of attenuation effects at high rain rates and low signal to noise ratios at light rain rates, there will exist an intermediate region, an effective dynamic range (EDR), over which the rain rate estimates are most accurate. Using only these estimates and an assumption as to the form of the probability distribution function (log-normal or gamma), the parameters of the distribution can be found by minimizing the rms difference between the hypothesized distribution and the values of the distribution obtained directly from the measurements. In previous work the EDR was assumed rather than calculated from the data; for attenuating-wavelength

data, however, the selection criterion is a critical part of the method.

## 2. ALGORITHM

To apply the method, it is necessary to identify a measurable quantity that can be used to distinguish between reliable and unreliable rain rate estimates. For the standard Z-R and the Hitschfeld-Bordan a good candidate for this task is  $Q(r)$  which is defined by the following set of equations. Assume that the relationship between the attenuation coefficient,  $k$  (dB/km) and the radar reflectivity factor,  $Z$ , is given by the power law:

$$k = \alpha Z^\beta$$

By definition,

$$Q(r) = c \int_0^r \alpha(s) Z_m^\beta ds$$

where  $c = 0.2\beta \ln 10$  and where the apparent,  $Z_m$ , and true,  $Z$ , reflectivity factors are related by

$$Z_m(r) = Z(r) \exp[-0.2 \ln 10 \int_0^r k ds]$$

Multiplying both sides of this equation by  $\alpha$ , integrating from 0 to  $r$ , and using the definitions for  $Q(r)$  and  $k$  gives

$$Q(r) = 1 - \exp[-c \int_0^r k(s) ds]$$

which shows that the path-attenuation from the radar to  $r$ , can be expressed in terms of  $Q(r)$  which is a function only of the  $Z_m(s)$ ,  $s < r$  and the parameters  $\alpha(s)$  and  $\beta$ . Note that  $Q$  increases monotonically with path attenuation and, in the absence of errors, is asymptotic to 1 as the attenuation increases without limit. As both the standard Z-R and the Hitschfeld-Bordan (HB) estimates of rain rate degrade with increasing attenuation,  $Q$  can be used to classify the estimates into reliable or unreliable. This establishes an upper bound; the lower bound is determined by the minimum acceptable signal to noise ratio. It should be noted that for the surface reference methods, a suitable threshold variable is not  $Q$  but the difference in dB between the estimated path attenuation and standard deviation of the surface return under no-rain conditions. It can be shown that the HB and Z-R estimates of path-averaged rain rate can be written as a function of  $Q(r_s)$

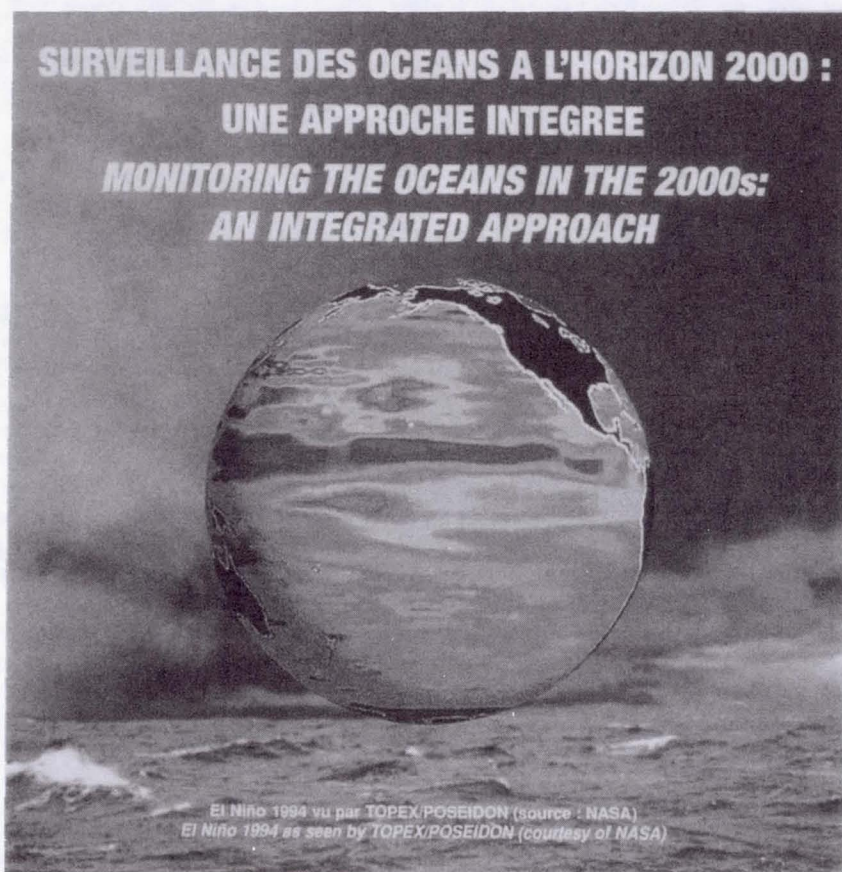
<sup>1</sup> Robert Meneghini, Code 975, NASA/GSFC, Greenbelt, MD 20771; email: bob@meneg.gsfc.nasa.gov.



# REGUEIL DES ACTES / PROCEEDINGS

SYMPOSIUM INTERNATIONAL / INTERNATIONAL SYMPOSIUM

15 - 16 - 17 Octobre 1997 / October, 15 - 16 and 17, 1997  
BIARRITZ - FRANCE



Réunion du Groupe Scientifique TOPEX/POSEIDON  
TOPEX/POSEIDON Science Team Meeting  
13 et 14 octobre 1997 / October 13 and 14, 1997





## Can TOPEX/Poseidon data be used for monitoring the Indonesian throughflow?

Ragu MURTUGUDDE

*University of Maryland, Laboratory for Hydrospheric Processes, NASA/GSFC, MD 20771*

Antonio J. BUSALACCHI, James BEAUCHAMP

*Laboratory for Hydrospheric Processes, NASA/GSFC, Greenbelt, MD 20771*

**ABSTRACT**-The effects of the Indonesian throughflow (ITF) are studied in a reduced gravity, primitive equation, sigma coordinate model. The surface heat fluxes are provided by coupling the ocean GCM to an advective atmospheric mixed layer model. There is an ENSO related signal in the ITF but the correlation with the Southern Oscillation Index (SOI) is only -0.31. When the winds over the Indian Ocean are held to climatology, this correlation jumps to -0.65 indicating that the non- ENSO signal in the ITF is caused by the downstream winds. On interannual time-scales the ITF can be explained in terms of sea level differences between the western Pacific and eastern Indian Oceans when appropriate representative locations are chosen as demonstrated in both model and TOPEX data. It is shown that the main climatological effect of the ITF is to warm the Indian Ocean and cool the Pacific. While the main ENSO indices, NINO3 and NINO4, are almost identical with and without the ITF, the total SSTs show significant ENSO dependence.

### 1-INTRODUCTION

A comprehensive review of the current knowledge of the effect the ITF on ocean circulation and heat exchange with the atmosphere is provided by [Godf 96]. Some attempts have been made to quantify the effects of the ITF on the wind-driven circulation of the global ocean [Hirs 93] and of the tropical Indo-Pacific basin [Vers 95]. The role of the ITF in the global climate system was explored in a coupled ocean-atmosphere model experiment by [Schn 97]. Very few studies have been reported thus far which address both the interannual dynamics and thermodynamics in the Indo-Pacific basin with a mass and heat exchange between them. Our model configuration allows us to address the interannual changes in the mass/heat transport and surface heatflux and their effects on wind-driven tropical Indian and Pacific Oceans. The surface flux formulation we employ allows free evolution of SST given the observed winds, cloudiness, and solar radiation. We use a multi-layer, reduced gravity, primitive equation, sigma coordinate model coupled to an advective atmospheric mixed layer model [Murt 96]. Fresh water fluxes are fully accounted for as a natural boundary condition.

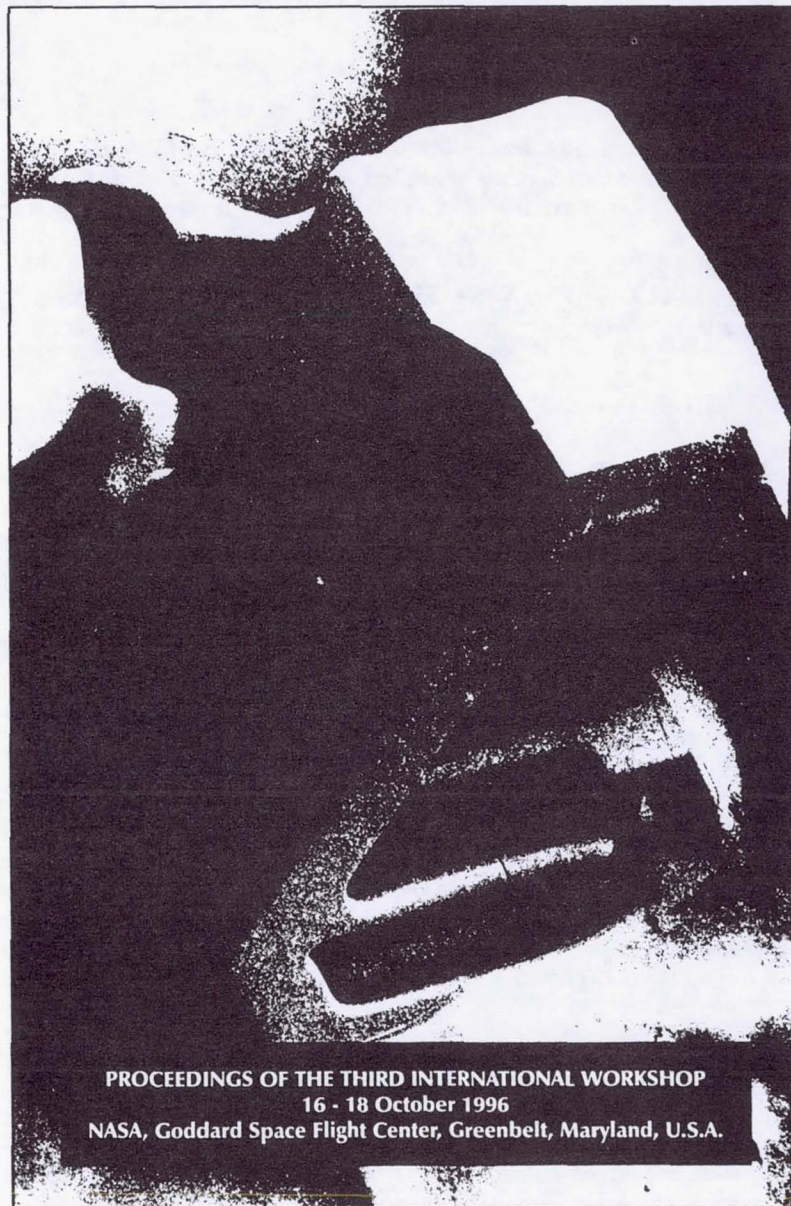
### 2- SEA-LEVEL INDEX FOR THE INDONESIAN THROUGHFLOW

The model performance in terms of SST errors, seasonal variability of the currents and thermal structure are reported for an identical model configuration in [Murt 97]. In brief, a spin up of 25 model years from rest provides model climatology. The interannual simulation is initiated from the climatology. The FSU wind-stresses in the tropics are combined with the NCEP reanalysis product for higher latitudes and the wind speeds are computed from these blended wind-stresses. As in [Murt 97], climatological ISCCP cloudiness and ERBE solar radiation are employed for surface fluxes.

The anomalies of the various transports for 1980-1995 are shown in Fig. 1. The total tran-



APPLICATIONS OF  
**REMOTE SENSING**  
IN HYDROLOGY



PROCEEDINGS OF THE THIRD INTERNATIONAL WORKSHOP  
16 - 18 October 1996  
NASA, Goddard Space Flight Center, Greenbelt, Maryland, U.S.A.

Editors G.W. Kite, A. Pietroniro and T.J. Pultz



## **THE IMPACT OF MICROWAVE-DERIVED SURFACE SOIL MOISTURE ON WATERSHED HYDROLOGICAL MODELING**

*P.E. O'Neill*

*Hydrological Sciences Branch/974, Laboratory for Hydrospheric Processes,  
NASA/Goddard Space Flight Center, Greenbelt, MD 20771 USA,  
Tel: 301-286-8273, Fax: 301-286-1758, E-mail: peggy@hydro2.gsfc.nasa.gov*

*A.Y. Hsu*

*SSAI, Code 974, NASA/GSFC, Greenbelt, MD 20771 USA,  
Tel: 301-286-8909, Fax: 301-286-1758, E-mail: hsu@hydro.gsfc.nasa.gov*

*T.J. Jackson*

*USDA/ARS Hydrology Laboratory, 104 Bldg 007 BARC-West,  
Beltsville, MD 20705 USA  
Tel: 301-504-8511, Fax: 301-504-8931, E-mail: tjackson@hydrolab.arsusda.gov*

*E.F. Wood, M. Zion*

*Department of Civil Engineering, Princeton University, Princeton, NJ 08544 USA  
Tel: 609-258-4675, Fax: 609-258-1270, E-mail: EFWOOD@pucc.princeton.edu*

### **ABSTRACT**

The usefulness of incorporating microwave-derived soil moisture information in a semi-distributed hydrological model was demonstrated for the Washita '92 experiment in the Little Washita River watershed in Oklahoma. Initializing the hydrological model with surface soil moisture fields from the ESTAR airborne L-band microwave radiometer on a single wet day at the start of the study period produced more accurate model predictions of soil moisture than a standard hydrological initialization with streamflow data over an eight-day soil moisture drydown.

### **INTRODUCTION**

During 1992 and 1994 NASA/GSFC, USDA, and Princeton University conducted hydrology field experiments in the Little Washita River watershed near Chickasha, Oklahoma with a goal of characterizing the spatial and temporal variability of soil moisture using microwave sensors from ground, aircraft, and space platforms. A major objective of these activities included the subsequent incorporation of the microwave-derived soil moisture patterns in models of larger scale water balance and partial area hydrology.



APPLICATIONS OF  
**REMOTE SENSING**  
IN HYDROLOGY



PROCEEDINGS OF THE THIRD INTERNATIONAL WORKSHOP  
16 - 18 October 1996  
NASA, Goddard Space Flight Center, Greenbelt, Maryland, U.S.A.

Editors G.W. Kite, A. Pietroniro and T.J. Pultz



## GROUND-BASED MICROWAVE RADIOMETER MEASUREMENTS OVER VARIOUS SURFACE COVERS

Manfred Owe\*, Jan de Ruiter\*\*, Ben Gouweleeuw\*\*, and Adriaan van de Griend\*\*

\*Code 974 NASA/Goddard Space Flight Center, Greenbelt, MD 20771 USA  
and \*\*Faculty of Earth Sciences, Vrije Universiteit, Amsterdam NL

### ABSTRACT

Microwave brightness temperatures were measured over a young wheat crop of varying canopy density during the First NOPEX Concentrated Field Effort near Uppsala, Sweden. Measurements were made with a portable ground-based microwave radiometer system at a frequency of 1.4 GHz. The brightness temperature at each wavelength was measured at horizontal and vertical polarization, and at incidence angles ranging from nadir to 60 degrees. Three measuring sequences were made; at full canopy, after the partial harvest, and of the bare soil. Supporting data such as soil and canopy temperature, soil moisture, other soil physical properties, and canopy biomass were also collected. Preliminary results of some of the field measurements and comparisons with theoretical calculations are presented.

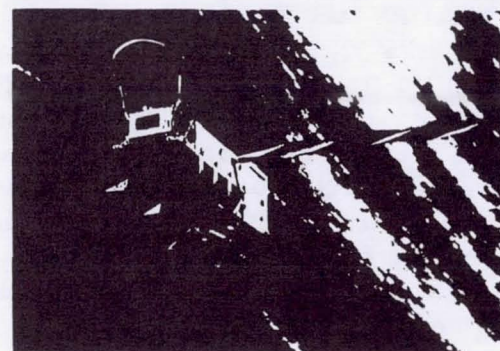
### INTRODUCTION

While the importance of surface moisture in water and energy balance modelling is well understood (Shukla and Mintz, 1982) the reliability of large scale estimates, especially when measurements are made by conventional ground sampling methods, is often suspect. A major reason is the high variability of soil moisture (Bell *et al.*, 1980; Hills and Reynolds, 1969; Nielsen *et al.*, 1973). While large scale spatial differences are generally due to differences in climatology, small scale variations are often due to changes in surface characteristics and also localized variability in precipitation. Remotely sensed observations represent an integrated measure of the surface over a resolution cell, and therefore will help relieve the uncertainty associated with extrapolating and averaging point measurements. Such data are a logical input to regionally-based energy balance models and global climate models. Furthermore microwave technology is the only method which has been shown to offer the possibility of direct measurement of variations in surface moisture from remote platforms with a certain accuracy and consistency.

Vegetation may affect the emitted microwave radiation in several ways. It may absorb, reflect, and scatter the emission from the soil surface. The relative magnitude of each



# PM Science Working Group Meeting on Spacecraft Maneuvers



— **Claire L. Parkinson** (clairep@neptune.gsfc.nasa.gov), PM Project Scientist, NASA Goddard Space Flight Center

The EOS PM Science Working Group met on May 6, 1997, to examine the issue of spacecraft maneuvers. The meeting was held at NASA Goddard Space Flight Center and was attended by the Team Leaders of all four instrument science teams with instruments on the PM-1 spacecraft, additional representatives from each of the four teams, the PM Project management, and random others. The meeting was chaired by the PM Project Scientist and open to all.

The meeting was called in order to untangle some of the concerns raised over the past several months regarding whether or not the PM-1 spacecraft should undergo spacecraft maneuvers to allow the instruments to obtain deep-space views. Two of the Science Teams, those for the Moderate-Resolution Imaging Spectroradiometer (MODIS) and the Clouds and the Earth's Radiant Energy System (CERES), had strongly expressed the need for deep-space views in order to calibrate their instruments properly and conveniently. The other two teams, those for the Advanced Microwave Scanning Radiometer (AMSR-E) and the Atmospheric Infrared Sounder (AIRS), the Advanced Microwave Sounding Unit (AMSU), and the Humidity Sounder for Brazil (HSB), had expressed concerns that the maneuvers involve risks to the instruments and undesired gaps in the data sets.

The meeting began with introductory statements by the PM Project Scientist, Claire Parkinson, the PM Project Manager, Marty Donohoe, and the EOS Program Scientist, Ghassem Asrar. Parkinson opened the meeting by briefly summarizing the basic positions of the four teams and expressing the desirability of coming to a resolution on the maneuver issue early, so that each team can proceed accordingly. Donohoe explained that the spacecraft contractor's (TRW's) specifications include the possibility of a maneuver, and that the Project management will task TRW to

study whatever consensus maneuver the scientists decide upon. Asrar reiterated the importance of the maneuver issue, explained that he is anxious to hear the arguments of each of the teams, and mentioned that we cannot ignore the international dimension and must be particularly sensitive to concerns the Japanese have raised concerning the AMSR-E instrument that they are providing for the PM-1 mission. All other instruments on the PM-1 spacecraft are from the U.S. with the exception of the HSB, which is being provided by Brazil.

The introductory statements by Parkinson, Donohoe, and Asrar were followed by a short presentation by the AIRS/AMSU/HSB (or AIRS for short) Team Leader, Mous Chahine, laying out what he sees as the appropriate metric for making a decision. In particular, although he is convinced that the MODIS and CERES calibrations will be helped by a maneuver, Chahine feels that the decision on whether or not to have a maneuver should be based, in part, on the quantitative impact on the accuracy of the derived geophysical parameters, specifically the Level 2 products. Bruce Barkstrom, the CERES Team Leader, indicated that it would be best to add Level 3 products to the metric, and Chahine readily agreed.

The setting-the-scene presentation by Chahine was followed by presentations by each of the four science teams, detailing their respective positions.

## The MODIS Team Position

The MODIS Team Leader, Vince Salomonson, began the MODIS presentation by explaining that he and his team have been considering whether they need a maneuver for quite some time and are convinced that a maneuver is essential for them in order to meet their most visible Level 1 requirement, which is to obtain sea surface temperatures (SSTs) to an accuracy of 0.3-



### The AIRS Team Position

The AIRS Project Scientist, George Aumann, presented the AIRS Team position. He emphasized that from what is known about the AIRS instrument as of May 1997, the AIRS does not need a deep-space view and that, because of the data losses and risks involved with a maneuver, the preference of the AIRS Team is that no maneuver be done. He explained three significant differences in the AIRS and MODIS situations in spite of their both having a Denton coating:

1. AIRS uses a Denton coating only on the scan mirror, with all other AIRS mirrors being gold-coated. Furthermore, the AIRS scan mirror is used at a fixed angle of  $45^\circ$ . In contrast, the MODIS mirrors are all Denton coated, and the MODIS scan mirror is used at angles of incidence ranging from  $-11^\circ$  to  $+65^\circ$ .
2. The required absolute calibration accuracies for the two instruments differ significantly, that for AIRS being 3% and that for MODIS being 0.5%.
3. The AIRS data processing uses routine daily checking of the calibration and, on a monthly timescale, tuning of geophysical parameters relative to a global set of co-located radiosondes.

In response to a query on whether the AIRS would be turned off in the event of a maneuver, Aumann replied that this would not be done. The maneuver itself, if executed as planned, might not pose a risk to the AIRS instrument, but it is expected to shift the spectral response of the AIRS outside the range permissible for normal Level 2 data processing. Aumann fears that the resulting disruption of the data processing would likely appear as an artifact in the long-term AIRS Level 2 data record, a situation that would not be acceptable for the AIRS mission objectives.

### Decision and Remaining Issues

By the end of the meeting, it was agreed to request that the PM Project have TRW do a feasibility study for having a single maneuver at about day 45 of the mission, after turning on the MODIS and CERES instruments but prior to turning on the AIRS and AMSR-E instruments. All parties agreed to this as an appropriate first step, recognizing that the issue will have to be readdressed later, after additional information is obtained. In addition to the TRW study, the

Japanese will be examining the issue further for the AMSR-E instrument, and the AIRS Team has decided to undertake a study of the AIRS mirror similar to the study done by the MODIS Team for the MODIS mirror, with the possibility that the AIRS Team position could thereby be revised. Also, both the MODIS and CERES Teams will have a better handle on the value of the maneuver and the desired frequency after the EOS AM-1 spacecraft is launched, and they have a chance to analyze the effects on their data sets of the AM-1 maneuvers.

At the end of the meeting, David Starr, the EOS Validation Scientist, briefly discussed the major steps in the upcoming validation planning exercise for PM-1. Draft plans are due from the AIRS and AMSR-E Teams on August 15, following which a workshop will be held in September and revised plans will be due in December. An NRA for validation studies, specifically for PM-1, can be expected to be released in about two years.





# RECUEIL DES ACTES / PROCEEDINGS

SYMPOSIUM INTERNATIONAL / INTERNATIONAL SYMPOSIUM

15 - 16 - 17 Octobre 1997 / October, 15 - 16 and 17, 1997  
BIARRITZ - FRANCE



**SURVEILLANCE DES OCEANS A L'HORIZON 2000 :**  
**UNE APPROCHE INTEGREE**  
**MONITORING THE OCEANS IN THE 2000s:**  
**AN INTEGRATED APPROACH**



Réunion du Groupe Scientifique TOPEX/POSEIDON  
*TOPEX/POSEIDON Science Team Meeting*  
13 et 14 octobre 1997 / October 13 and 14, 1997





## ENSO MECHANISMS

Joël PICAUT

Groupe SURTROPAC  
ORSTOM

Nouméa, New Caledonia

present address:

Laboratory for Hydrospheric and Atmospheric Processes  
NASA/Goddard Space Flight Center  
Greenbelt, Maryland, USA

**ABSTRACT** - *The current leading theory of the El Niño-Southern Oscillation (ENSO) phenomenon involves reflection of equatorial waves on the western ocean boundary to shift the ENSO phase from El Niño to La Niña and vice versa. However, recent satellite altimetry and in situ observations indicate that this theory has several flaws. These include imperfect equatorial wave reflection on the western ocean boundary, a maxima of the simulated coupled wind-sea surface temperature (SST) interaction located too far into the eastern equatorial Pacific, and an excessive role of thermocline displacement on SST in this region. We show that the central equatorial Pacific SST is fundamental in driving the ENSO ocean-atmosphere coupled system, through the east-west displacement of the eastern edge of the warm pool, perfectly related with ENSO. Within the equatorial wave-guide, the dominance of surface zonal advection in these displacements is demonstrated with four different satellite and in situ datasets and three ocean models. This demonstration is supported by the evidence of a convergence of water masses into the eastern edge of the warm pool, resulting in a well-defined salinity front. All these results lead us to propose a notable modification of the leading delayed-action oscillator theory for the oscillatory nature of ENSO. Simulations with a linearized coupled ocean-atmosphere model result in 3-6 year ENSO-like oscillations, with many of the variable model parameters found very close to their observed values. This simple model suggests that ocean processes ignored or underestimated in the delayed action oscillator theory, such as zonal current convergence, zonal advection of sea surface temperature and equatorial wave reflection from the eastern-ocean boundary, are fundamental to the development of ENSO, in particular to its manifestations in the central equatorial Pacific.*

### 1 - INTRODUCTION

Most of the results presented at the Biarritz meeting have been published recently in two Science reports. The first one, entitled "Mechanism of the zonal displacement of the Pacific warm pool: implications for ENSO" by J. Picaut, M. Ioualalen, C. Menkes, T. Delcroix and M. J. McPhaden, was published in the 29 November 1996 issue of Science; the other, entitled "An advective-reflective conceptual model for the oscillatory nature of the ENSO" by J. Picaut, F. Masia and Y. du Penhoat, was published in the 1 August 1997 issue of Science. Rather than summarizing these two reports in the meeting proceeding, we have decided to illustrate our recent findings on ENSO mechanisms through the presentation of recent TOPEX/POSEIDON data analysis and of a few figures already published in Science.



# PROCEEDINGS OF SPIE



SPIE—The International Society for Optical Engineering

## *Earth Observing Systems II*

**William L. Barnes**

*Chair/Editor*

**28–29 July 1997**

**San Diego, California**

*Sponsored and Published by*

SPIE—The International Society for Optical Engineering



**Volume 3117**

SPIE is an international technical society dedicated to advancing engineering and scientific applications of optical, photonic, imaging, electronic, and optoelectronic technologies.



# MODIS snow and ice products from the NSIDC DAAC

Greg R. Scharfen<sup>a</sup>, Dorothy K. Hall<sup>b</sup>, and George A. Riggs<sup>c</sup>

<sup>a</sup>National Snow and Ice Data Center, Campus Box 449, University of Colorado, Boulder, CO 80309

<sup>b</sup>Goddard Space Flight Center, Greenbelt MD 20771

<sup>c</sup>Research and Data System Corp., 7855 Walker Drive #460, Greenbelt, MD 20770

## ABSTRACT

The National Snow and Ice Data Center (NSIDC) Distributed Active Archive Center (DAAC) provides data and information on snow and ice processes, especially pertaining to interactions among snow, ice, atmosphere and ocean, in support of research on global change detection and model validation, and provides general data and information services to the cryospheric and polar processes research community. The NSIDC DAAC is an integral part of the multi-agency-funded support for snow and ice data management services at NSIDC.

The Moderate Resolution Imaging Spectroradiometer (MODIS) will be flown on the first Earth Observation System (EOS) platform (AM-1) in 1998. The MODIS Instrument Science Team is developing geophysical products from data collected by the MODIS instrument, including snow cover and sea ice products which will be archived and distributed by the NSIDC DAAC. The MODIS snow and ice mapping algorithms will generate global snow, lake ice and sea ice cover products on a daily basis. These products will augment the existing record of satellite-derived snow cover and sea ice products that began about 30 years ago. The characteristics of these products, their utility, and comparisons to other data sets are discussed. Current developments and issues are summarized.

**Keywords:** EOSDIS, MODIS, NSIDC, snow, ice, sea ice, cryosphere

## 1. INTRODUCTION

The EOS Project Science Office has identified 24 critical science measurements that are important for scientific research aimed at the understanding, analysis and monitoring of global climate change<sup>1</sup>. Two of these are snow cover (including snow cover extent and water equivalent) and sea ice (including sea ice extent, concentration, motion and temperature). Snow cover extent, sea ice extent and sea ice surface temperature will be provided as EOS Standard Products, using MODIS data, at the time of launch of the AM-1 satellite, or shortly thereafter. This paper describes the MODIS snow and ice products which have been developed by the MODIS Instrument Science Team and will be archived and distributed as part of the EOS Data and Information System (EOSDIS) by the NSIDC DAAC.

## 2. THE IMPORTANCE OF SNOW AND ICE IN CLIMATE

The global extent of snow cover is an important variable in the hydrologic cycle and is a key indicator of changes in the global climate system. Due to its high albedo and large spatial variability, snow cover is a primary factor controlling the amount of solar energy absorbed at the surface. Changes in the extent of snow cover have a direct effect on the earth's radiation budget. Snow cover also has significant effects on the seasonal temperature cycle due to its high latent heat of fusion. In many areas of the world, snow cover represents an important resource in terms of water supply and hydroelectric power. The U.S. National Weather Service and other agencies monitor snowpacks during the winter and spring months to forecast water supply and flooding potential<sup>2</sup>. The devastating 1997 flood event in the Red River Valley of the U.S. Upper Midwest was primarily due to an abnormally deep snow pack. Links between snow cover extent and atmospheric circulation have been demonstrated<sup>3</sup>, and the extent of snow cover has been found to be inversely related to hemispheric surface air temperature<sup>4</sup>.



European Space Agency  
Programme Advisory Committee (PAC)  
on the Special Project  
Concerning the Launching of Sounding Rockets

*Proceedings*

**13th ESA Symposium on  
European Rocket and Balloon Programmes  
and Related Research**

Öland, Sweden  
26 - 29 May 1997



# VERTICAL OZONE PROFILE COMPARISONS BETWEEN OZONESONDES AND REMOTE INSTRUMENTATION

F. J. Schmidlin<sup>1</sup>, S. McCarthy<sup>2</sup>, W. Michel<sup>3</sup>, E. David Ross<sup>4</sup>

- 1/ Laboratory for Hydrospheric Processes, Observational Science Branch, NASA GSFC/Wallops Flight Facility, Wallops Island, Virginia 23337 USA; Tel: 757 824-1618; Fax: 757 824-1036; e-mail: fjs@osb1.wff.nasa.gov
- 2/ Computer Sciences Corp., NASA GSFC/Wallops Flight Facility, Wallops Island, Virginia 23337 USA
- 3/ Science and Engineering Services, Inc., NASA GSFC/Wallops Flight Facility, Wallops Island, Virginia 23337 USA
- 4/ Mantech Environmental Technology, Inc., NASA GSFC/Wallops Flight Facility, Wallops Island, Virginia 23337 USA

## Abstract

Ozonesonde measurement quality is a critical factor for insuring measurement accuracy and is fundamentally indispensable for validating remotely measured ozone. Reasonable results from such ozone profile comparisons are best obtained by maintaining the smallest possible spatial and time differences between ozonesonde and remote measurement observations. Ozone profiles measured with the Halogen Occultation Experiment (HALOE) instrument and the Microwave Limb Sounder (MLS) instrument on NASA's Upper Atmosphere Research Satellite (UARS) are compared with ECC profiles. Comparisons with the GSFC ozone lidar also demonstrate good agreement. In this paper we show 1) the process used by NASA to secure quality ozonesonde measurements, 2) comparisons of ozonesondes with various remote sensing instruments and, 3) the reliability obtained when both measurement types are obtained close in time and, when possible, in space.

## Introduction

Vertical profiles of ozone have been measured from Wallops Island, Virginia since the latter half of the 1960's using the Electrochemical Concentration Cell (ECC) ozonesonde. The preparation and calibration of the ECC instrument enables consistent time series data to be made available. . Acquisition of improved ground equipment necessary to receive, record, and process ECC data now allow digital ozonesondes to be employed. As a result, more detailed data are possible revealing a number of measurement inconsistencies. These inconsistencies have been addressed in the laboratory and results have led to an

improvement to the procedures used at Wallops; however, further improvement of ECC measurements is necessary. Tests of ECC ozonesondes from different manufacturers indicated that small differences in resulting measurements could easily be reconciled. Comparisons of satellite remote measurements of ozone with ECC measurements give diverse results. As we show, ECC measurements at the ozone peak compare with lidar relatively well, while comparisons with HALOE and MLS do not.

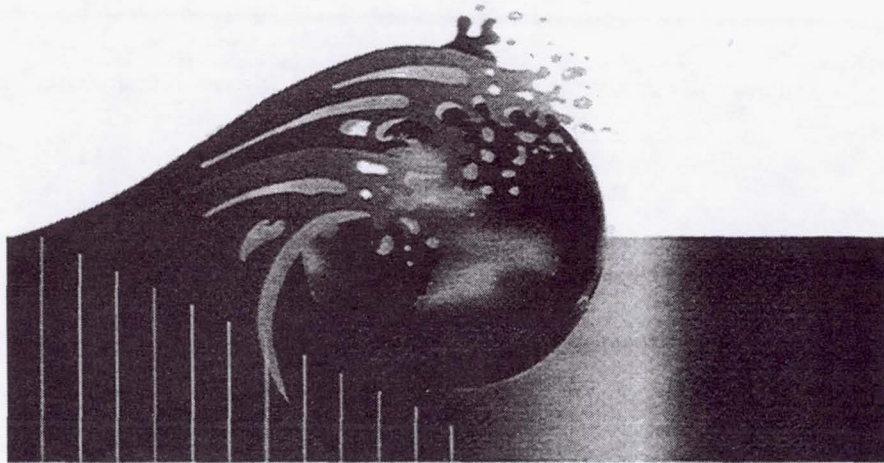
## Procedures

Pre-flight preparation and calibration procedures include: individually derived corrections for pump efficiency, pre-flight flow rate determination, minimization of spurious background currents, and checks against a secondary calibration standard (Dasibi uv photometer).

Pump Efficiency - A specially equipped pressure chamber (usually a bell-jar) is used to determine individual pump efficiency corrections for each ozone instrument (Torres, 1985). Using a pre-calibrated evacuated chamber air is pumped through the ozone instrument; the pump efficiency is determined and then factored into the ozone reduction equation.

The differences, in the mean, of the pump efficiency for three different lots of ozonesondes and the manufacturers recommended optimized curve (Komyhr, 1986) is shown in Figure 1. It is evident that the pump efficiency varies for each instrument type and, from this figure, it can be seen that they all disagree with the manufacturer's recommended curve (Komhyr, 1986). Although the recommended pump efficiency curve was originally developed using measurements made with the 4A series of instruments, the pump itself is essentially unchanged. We





*Reprinted from*

# OCEAN OPTICS XIII

22-25 October 1996  
Halifax, Nova Scotia, Canada



**SPIE Volume 2963**



## **The SeaWiFS Quality Monitor - a portable field calibration light source**

Ping-Shine Shaw and B. Carol Johnson

Optical Technology Division  
National Institute of Standards and Technology  
Gaithersburg, MD 20899 USA

Stanford B. Hooker

NASA/Goddard Space Flight Center, Code 970.2  
Greenbelt, MD 20771 USA

Don Lynch

Reyer Corporation, 11847-B Lime Plant Road  
New Market, MD 21774 USA

### **ABSTRACT**

A portable and stable source, the Sea-viewing Wide Field-of-view Sensor (SeaWiFS) Quality Monitor, has been developed for use as a field instrument. The source can be used with either radiance- or irradiance-measuring sensors to transfer the laboratory calibration to the field so that the stability of the sensors can be monitored during the experiment. Temperature-controlled silicon photodiodes with colored glass filters are used to monitor the stability of the SeaWiFS Quality Monitor.

**Keywords:** calibration, field instrument, portable source, radiometric source, SeaWiFS

### **1. INTRODUCTION**

Oceanographic field studies are an essential component of the Sea-Viewing Wide Field-of-View Sensor (SeaWiFS) Calibration and Validation Program.<sup>1,2</sup> Ocean-color data collected during cruises will be used to assist in the analysis of the data collected by the SeaWiFS satellite, with the ultimate goal to improve the atmospheric correction and bio-optical algorithms. The quality of these ocean-color data is critical to the success of the SeaWiFS project, and protocols have been established for the measurements.<sup>3</sup> To ensure data quality, each marine radiometer is generally calibrated before and after the field experiment. Ideally, the stability of the calibration should be monitored during the cruise. Because on-board calibration facilities are difficult to realize in practice, current investigative cruises rely on the manufacturer's calibration data or pre- and post-cruise calibration data. Considering the severe environmental changes encountered by marine radiometers, especially during shipment, the stability of the radiometer is in question and that, in turn, raises the concern that the data are not accurate enough for the success of the project.

In response to the requirement to monitor the stability of the marine radiometers, the National Institute of Standards and Technology (NIST) along with National Aeronautics and Space Administration's Goddard Space Flight Center



APPLICATIONS OF

# REMOTE SENSING

IN HYDROLOGY



Editors G.W. Kite, A. Pietroniro and T.J. Pultz



## **ESTIMATION OF BARE SURFACE SOIL MOISTURE AND SURFACE ROUGHNESS PARAMETER USING L-BAND SAR IMAGE DATA**

*Jiancheng Shi*

*Institute for Computational Earth System Science*

*University of California, Santa Barbara*

*Tel: 805-893-2309, Fax: 805-893-2578, E-mail: shi@icess.ucsb.edu*

*James Wang, Ann Hsu, Peggy O'Neill and Edwin T. Engman*

*Laboratory for Hydrospheric Processes*

*NASA Goddard Space Flight Center, Greenbelt, MD*

### **ABSTRACT**

An algorithm based on a fit of the single-scattering Integral Equation Method (IEM) was developed to provide estimation of soil moisture and surface roughness parameter (a combination of rms. roughness height and surface power spectrum) from quad-polarized synthetic aperture radar (SAR) measurements. This algorithm was applied to a series of measurements acquired at L-band (1.25 GHz) from both AIRSAR (Airborne Synthetic Aperture Radar operated by Jet Propulsion Laboratory) and SIR-C (Spaceborne Imaging Radar-C) over a well-managed watershed in southwest Oklahoma. It was found that the two co-polarized backscattering coefficients and their combinations would provide the best input to the algorithm for estimation of soil moisture and roughness parameter. Application of the inversion algorithm to the co-polarized measurements of both AIRSAR and SIR-C resulted in estimated values of soil moisture and roughness parameter for bare and short-vegetated fields that compared favorably with those sampled on the ground. The root-mean-square (rms.) errors of the comparison were found to be 3.4% and 1.9 dB for soil moisture and surface roughness parameter, respectively.

### **INTRODUCTION**

Soil moisture is a key parameter in numerous environmental studies, including hydrology, meteorology, and agriculture. It plays an important role in the interactions between the land surface and the atmosphere, as well as the partitioning of precipitation into runoff and ground water storage. In spite of its importance, soil moisture has not found a widespread application in the modeling of hydrological and biogeochemical processes and related ecosystem dynamics, in part because soil moisture is a difficult parameter to measure on a large area, cost-effective, and routine basis. However, recent advances in microwave





# IGARSS'97

1997 International Geoscience and  
Remote Sensing Symposium

03-08 August 1997

Singapore International Convention & Exhibition Centre • Singapore

Remote Sensing -- A Scientific Vision for  
Sustainable Development

IEEE Catalog Number: 97CH36042  
Library of Congress Number: 97-70575



# Estimation of Soil Moisture for Vegetated Surfaces Using Multi-Temporal L-band SAR Measurements

Jiancheng Shi

*Institute for Computational Earth System Science*

*University of California, Santa Barbara*

*Tel: 805-893-8116, Fax: 805-893-2578, E-mail: shi@icess.ucsb.edu*

*G. Sun, A. Hsu, J. Wang, P. O'Neill, J. Ranson and E. T. Engman*

*NASA Goddard Space Flight Center, Greenbelt, MD*

**Abstract** - This paper demonstrates the technique to estimate ground surface and vegetation scattering components, based on the backscattering model and the radar decomposition theory, under configuration of multi-temporal L-band polarimetric SAR measurement. This technique can be used to estimate soil moisture of vegetated surface.

## INTRODUCTION

Soil moisture is a key parameter in numerous environmental studies, including hydrology, meteorology, and agriculture. It plays an important role in interactions between the land surface and the atmosphere, as well as in the partitioning of precipitation into runoff and ground water storage. In spite of its importance, soil moisture has not found a widespread application in the modeling of hydrological and biogeochemical processes and related ecosystem dynamics, in part because soil moisture is a difficult parameter to measure on a large area, cost-effective, and routine basis.

In attempting to use active microwave remote sensors to estimate soil moisture, we are facing two major problems: effects of surface roughness and vegetation cover. Recently, several algorithms have been developed for measuring bare surface soil moisture quantitatively using dual-polarization L-band SAR image data [1,2] or three-polarization SAR measurements [3]. All of these algorithms use weighted combinations of different polarization signatures to minimize the effect of surface roughness so that soil moisture can be directly inferred from SAR image data. However, the effect of vegetation cover has not been included in the currently available algorithms. It is clear that the presence of vegetation will cause an under-estimation of soil moisture and an over-estimation of

surface roughness when we apply the algorithm for bare surface soil moisture to vegetated regions.

In this study, we take one step further to estimate soil moisture accurately for vegetated surfaces using a multi-temporal L-band polarimetric SAR approach. An algorithm has been developed to reduce the vegetation effect on the estimation of soil moisture based on a radar backscattering model and decomposition theory. We will demonstrate the physical principles and development of this algorithm.

## BASIC PRINCIPLE OF THE ALGORITHM

A backscattering model [4] for a vegetated surface can be written as

$$\sigma_t^{pp}(\theta) = \sigma_v^{pp}(\theta) + \sigma_{sv}^{pp}(\theta) + \sigma_s^{pp}(\theta)L_{pp}^2 \quad (1)$$

where  $L_{pp}^2 = \exp(-2k_e^{pp}d \sec(\theta))$  is the double pass attenuation factor.  $\kappa_e$  is the volume extinction coefficient which depends on the polarization configuration  $pp$  (for HH or VV).  $d$  is the thickness of the vegetation layer and  $\theta$  is the radar incidence angle. The subscripts  $t$ ,  $v$ ,  $s$ , and  $sv$  are for total, volume, surface, and surface-volume interaction terms. The direct volume scattering and the surface-volume interaction scattering terms in (1) can be written as

$$\sigma_{sv}^{pp}(\theta) = 0.5\eta_{pp}(1 - L_{pp}^2) / \kappa_e^{pp} \quad (2)$$

and

$$\sigma_s^{pp}(\theta) = 2\eta_{pp}dR_{pp}L_{pp}^2 \quad (3)$$

where  $\eta$  is the volume scattering coefficient depending also on the polarization.  $R$  is the surface reflectivity.





# IGARSS'97

1997 International Geoscience and  
Remote Sensing Symposium

03-08 August 1997

Singapore International Convention & Exhibition Centre • Singapore

Remote Sensing -- A Scientific Vision for  
Sustainable Development

IEEE Catalog Number: 97CH36042  
Library of Congress Number: 97-70575



# **A Comparison of Sea Ice Type, Sea Ice Temperature, and Snow Thickness Distributions in the Arctic Seasonal Ice Zones with the DMSP SSM/I**

**Karen St.Germain<sup>1</sup>, Donald J. Cavalieri<sup>2</sup> and Thorsten Markus<sup>2,3</sup>**

<sup>1</sup> Remote Sensing Division, Code 7223

Naval Research Laboratory, Washington DC 20375-5351  
(202)767-3443; (202)767-9194 FAX; ksaint@ultraimg.nrl.navy.mil

<sup>2</sup> Laboratory for Hydrospheric Processes, Code 971

NASA Goddard Space Flight Center, Greenbelt, MD; (301)286-2444; (301)286-0240 FAX;  
don@cavalieri.gsfc.nasa.gov

<sup>3</sup> Research Associate at the Joint Center of Earth System Science (JCESS)  
University of Maryland at College Park, College Park, MD

## **INTRODUCTION**

Global climate studies have shown that sea ice is a critical component in the global climate system through its effect on the ocean and atmosphere, and on the earth's radiation balance. Polar energy studies have further shown that the distribution of thin ice and open water largely controls the distribution of surface heat exchange between the ocean and atmosphere within the winter Arctic ice pack. The thickness of the ice, the depth of snow on the ice, and the temperature profile of the snow/ice composite are all important parameters in calculating surface heat fluxes. In recent years, researchers have used various combinations of DMSP SSM/I channels to independently estimate the thin ice type (which is related to ice thickness), the thin ice temperature, and the depth of snow on the ice. In each case validation efforts provided encouraging results, but taken individually each algorithm gives only one piece of the information necessary to compute the energy fluxes through the ice and snow. In this paper we present a comparison of the results from each of these algorithms to provide a more comprehensive picture of the seasonal ice zone using passive microwave observations.

## **THE ALGORITHMS**

The three algorithms used in this study were developed to operate on the brightness temperatures available from the DMSP SSM/I sensor. In addition, we make use of surface temperature estimates generated by Massom and Comiso from AVHRR radiances [1].

The thin ice algorithm [2] uses the 19.4 GHz vertical and horizontal, and the 37.0 GHz vertical channels of the SSM/I to obtain an improved measure of ice concentration and to determine the distribution of new, young, and first-year ice types in seasonal sea ice zones.

This algorithm was validated by high resolution AVHRR imagery and aircraft observations. The ice temperature algorithm [3], makes use of the radiances at 19.4 GHz vertical polarization as well as the ice type and corrected concentration output from the thin ice algorithm to determine the physical temperature of the surface. By assuming that the physical temperature of any open water within the satellite footprint is at the freezing point, the physical temperature of the ice can be calculated. The temperature algorithm was validated with surface temperature estimates from AVHRR and air temperature observations from Point Barrow and Gambell Stations. The snow thickness algorithm uses the ice concentration information and the 37 and 19.4 GHz horizontal polarization radiance data to estimate snow depth [4]. The validation for this algorithm was provided by in situ observations over similar ice in the sea ice around Antarctica.

## **COMPARISON OF ALGORITHM PRODUCTS**

The initial comparison of products was made for April 4, 1988 in the Bering Sea. Ice type retrievals for the area of interest are shown in Figure 1.

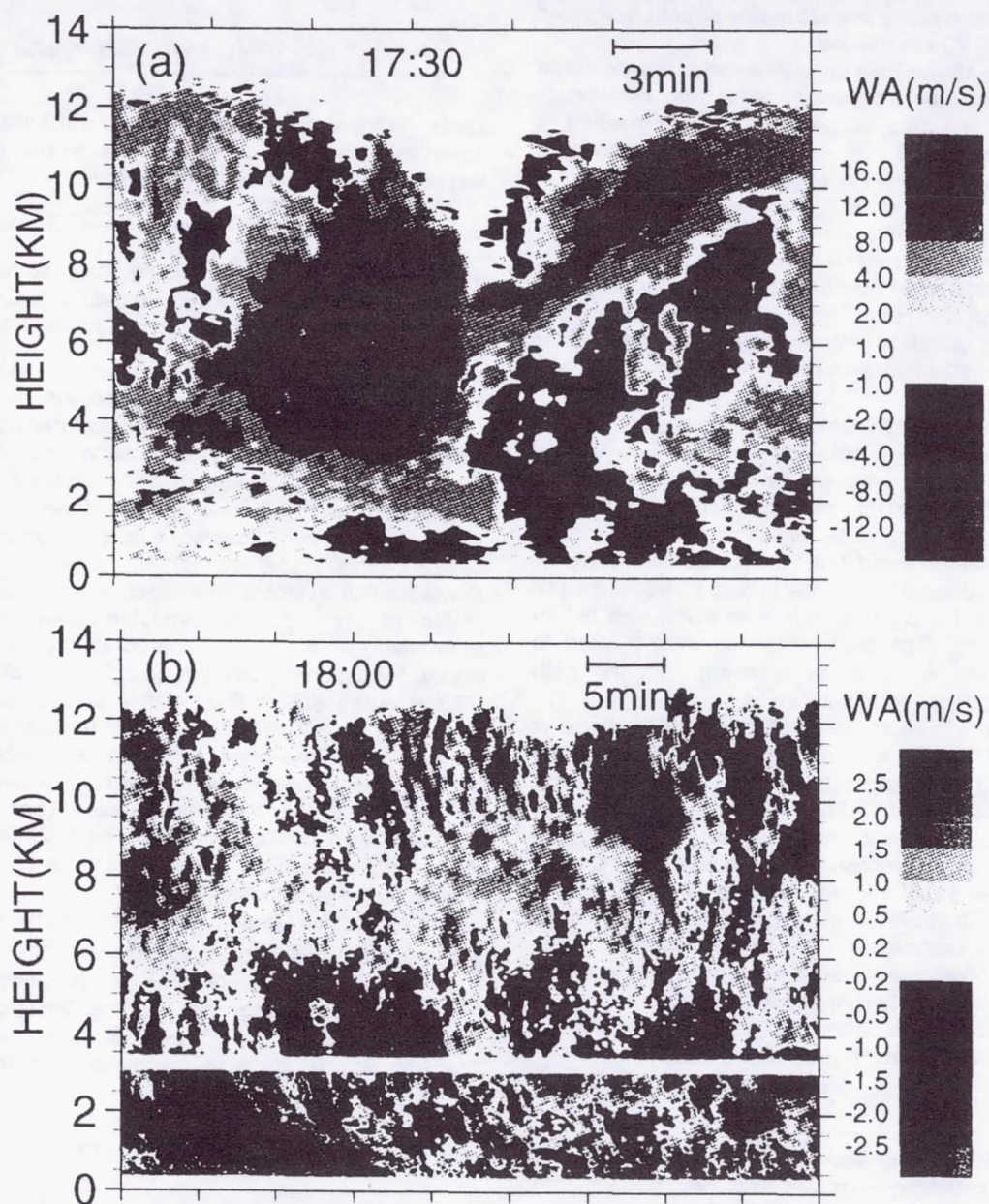
To focus our comparisons in this initial study, we limited ourselves to a small area around St. Lawrence Island. Ice type, ice temperature, and snow depth are shown in Figures 2, 3, and 4 respectively.



# 28th Conference on Radar Meteorology

September 7-12, 1997

Austin, Texas



AMERICAN METEOROLOGICAL SOCIETY



Nobuhiro Takahashi<sup>1</sup>, Hiroaki Horie<sup>2</sup> and Robert Meneghini<sup>3</sup>

1 Universities Space Research Association  
2 Communications Research Laboratory, Japan  
1,3 NASA Goddard Space Flight Center

## 1. INTRODUCTION

Dual frequency methods are one of the most useful ways to estimate precise rainfall rates ( $R$ ) (e.g. Fujita (1983), Iguchi and Meneghini (1995)). However, there are some difficulties in applying this method to ground based radars because of the existence of a blind zone and possible errors in the radar calibration. Because of these problems, supplemental observations such as rain gauges or satellite link estimates of path integrated attenuation (PIA) are needed.

This study shows how to estimate rainfall rate with a ground based dual frequency radar with rain gauge and satellite link data. Applications of this method to stratiform rainfall is also shown. This method is compared with single wavelength method.

Data were obtained from a dual frequency (10 GHz and 35 GHz) mutiparameter radar radiometer built by the Communications Research Laboratory (CRL), Japan, and located at NASA/GSFC during the spring of 1997. Optical rain gauge (ORG) data and broadcasting satellite signal data near the radar location were also utilized for the calculation.

## 2. DATA AND ANALYTICAL METHOD

Radar data were obtained at about one second intervals for both frequencies with 30 m range resolution. Data are not available within the first 20 range bins (600 m). The region is called the blind zone. In order to avoid the computational instability, data were averaged over time (9 sec.) and range (10 gates) and clutter signals were also eliminated before the calculation. The radar antennas were pointed to  $az. = 228^\circ$  and  $el. = 38^\circ$ , to compare with the path integrated attenuation of satellite link.

From the measurement of the satellite downlink signal, the PIA at 12 GHz is derived by subtracting the observed signal strength from that measured during clear-air conditions. The estimated PIA has uncertainties because the signal strength is affected by the wetness of the receiver antenna surface. Careful data treatment is needed for the analysis. The resolution of the data varies with signal strength. Data are recorded every three seconds. Optical rain gauge data are also obtained over three second intervals with a minimum detectable  $R$  of about 0.5 mm/h.

Calculation was performed to retrieve the range profile of a two parameter drop size distribution (DSD;  $N(D) = N_0 D^\mu \exp(-\Lambda D)$  with fixed  $\mu$ ) using the

procedure by Iguchi and Meneghini (1995). Unknown parameters  $N_0$  and  $\Lambda$  are calculated from the differential equations

$$\frac{d\Lambda}{dr} = \frac{\frac{d}{dr}(dBZ_x) - \frac{d}{dr}(dBZ_k) + CN_0(f_x - f_k)}{g_x - g_k}$$

$$\frac{d(10\log(N_0))}{dr} = \frac{g_k \frac{d}{dr}(dBZ_x) - g_x \frac{d}{dr}(dBZ_k) + CN_0(f_x g_k - f_k g_x)}{g_k - g_x}$$

where  $r$  is the radar range,  $dBZ_x$  and  $dBZ_k$  express the observed reflectivity factor for X-band and Ka-band, respectively,  $C$  is constant, and  $g_x(k)$  is

$$g_x(k) = \frac{d}{d\Lambda} (10\log(\int \sigma_{x(k)} C_{x(k)} \exp(-\Lambda D) dD))$$

where  $\sigma_x(k)$  is the backscattering cross section of the particle diameter  $D$  for X-(Ka) band, and  $C_x(k)$  is a function of the refractive index.  $f_x(k)$  is

$$f_x(k) = \int Q_{x(k)} \exp(-\Lambda D) dD,$$

where  $Q_x(k)$  is the extinction cross section.

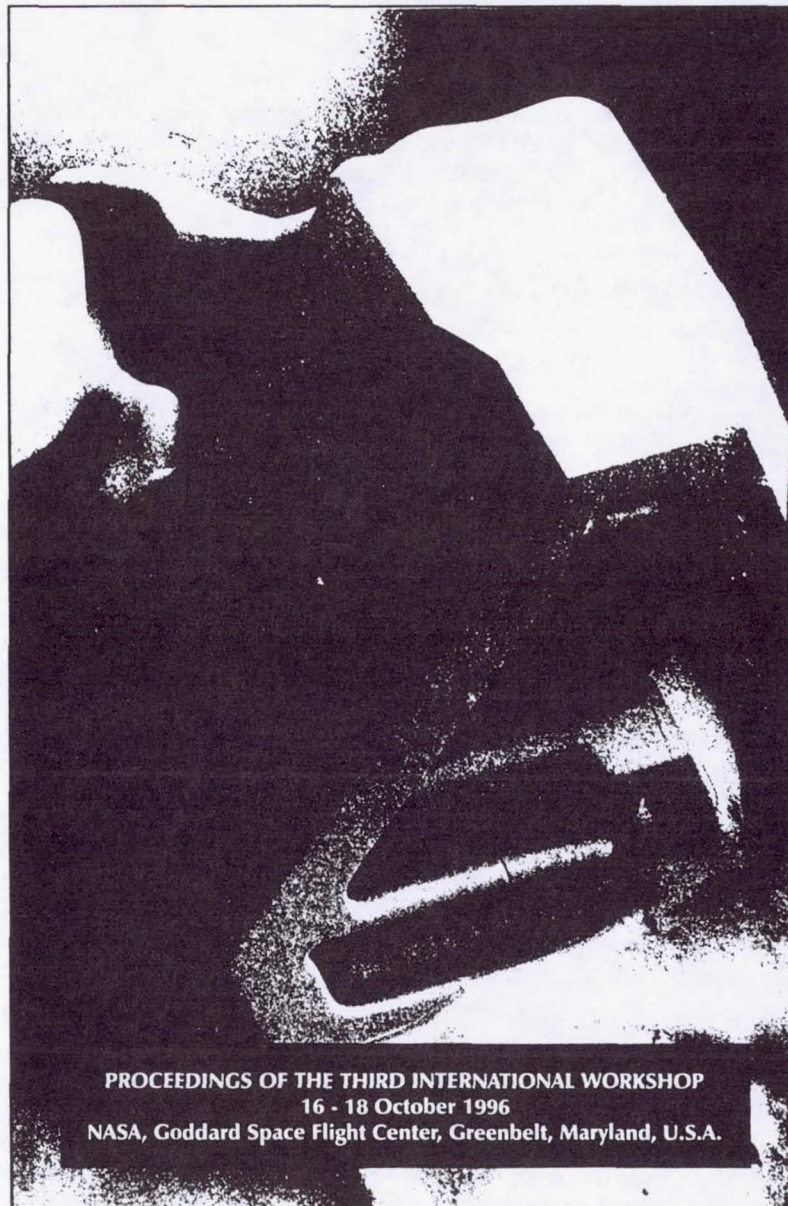
Range profiles of  $N_0$  and  $\Lambda$  are calculated from these differential equation with given initial values. To obtain the appropriate initial value, the PIA is utilized. In Iguchi and Meneghini (1995), the PIA is estimated from the sea surface echo of downward looking airborne radar data. In this study, we use the broadcast satellite signal for PIA estimate. For each initial value, a new profile of the DSD is computed from which the estimated PIA at 12 GHz is calculated using Mie theory. By assuming that the near field (in blind zone) DSD is same as the first reliable data point (in our case, 20th gate = 600 m), and that the attenuation of far field where Ka-band data fully attenuated to be below the noise level is approximated with k-R (and Z-R) relationship, the total attenuation (one way) is compared with satellite link PIA. The DSD profile that yields a PIA closest to the measured value of 12 GHz is chosen as the final result.

The rainfall rate is calculated from the DSD assuming the rain drop fall speed ( $w \approx 386D^{0.67}$ ) and is compared with the ORG data. The distance between the nearest radar range bin and the ORG location is about 470 m in the horizon and 360 m in the vertical. The PIA and  $R$  are also compared with the single

\* Corresponding author address: Nobuhiro Takahashi, CODE 975 NASA/GSFC Greenbelt, MD 20771;  
e-mail: ntaka@meneg.gsfc.nasa.gov



APPLICATIONS OF  
**REMOTE SENSING**  
IN HYDROLOGY



PROCEEDINGS OF THE THIRD INTERNATIONAL WORKSHOP  
16 - 18 October 1996  
NASA, Goddard Space Flight Center, Greenbelt, Maryland, U.S.A.

Editors G.W. Kite, A. Pietroniro and T.J. Pultz



## **SURFACE ENERGY HEAT FLUXES USING REMOTELY SENSED PARAMETERS**

David L. Toll

Laboratory for Hydrospheric Processes (Code 974)  
NASA/Goddard Space Flight Center, Greenbelt, MD 20771, USA  
ph 301-286-9256 fax 301-286-1758  
Email toll@toll.gsfc.nasa.gov

Fred M. Vukovich

SSAI, Suite 300, 615 Oberlin Rd., Raleigh, NC 27605 USA  
ph 919-832-7242

Elizabeth G. Pontikes

Physics Department, Yale University, New Haven, CT 06520 USA

### **ABSTRACT**

Realistic estimates of surface energy heat fluxes are needed for the study of water and energy interactions between the land and atmosphere. The primary objective of this work is to study the estimation of surface heat energy fluxes using remote sensing derived parameters under different spatial and temporal conditions. Surface energy fluxes and remote sensing derived data from two sources were analyzed. First, we used surface heat flux, remote sensing, and ancillary data from the International Satellite Land Surface Climatology Project (ISLSCP), mapped at a  $1^\circ \times 1^\circ$  grid. Second, we used NOAA AVHRR (1 km), weather station, and ancillary data to derive estimates of surface latent and sensible heat energy fluxes over a 100 sq kilometer area for three test sites: 1) First ISLSCP Field Experiment (FIFE) grassland site, Konza Prairie, Kansas; 2) Howland, Maine Forest Ecosystem Dynamics Site; and 3) Walnut Gulch, scrubland site, surrounding Tombstone, Arizona. Satellite derived estimates of land surface temperature, surface albedo, and spectral vegetation index are used in selected models to provide estimates of surface heat fluxes.

Analysis of results from the  $1^\circ \times 1^\circ$  grid for North America indicated there were similar, overall correlations between sensible and latent heat energy fluxes versus remotely sensed vegetation index and ground temperature during dry and wet year conditions. However, there were significant differences in correlations between years when stratified by land cover class. Analysis of 100 km x 100 km data (1 km resolution) indicated partitioning the areas in to primary versus secondary cover, with the secondary cover comprising less than 5% of the area, significantly improved surface heat energy flux estimates. Analysis of grid





# IGARSS'97

1997 International Geoscience and  
Remote Sensing Symposium

03-08 August 1997

Singapore International Convention & Exhibition Centre • Singapore

Remote Sensing -- A Scientific Vision for  
Sustainable Development

IEEE Catalog Number: 97CH36042  
Library of Congress Number: 97-70575



# Airborne Millimeter-wave Radiometric Observations of Cirrus Clouds

J. R. Wang and P. Racette

Laboratory for Hydrospheric Processes

NASA Goddard Space Flight Center, Greenbelt, MD 20771, U.S.A

Tel: 301-286-8949/FAX: 301-286-1762/e-mail: wang@sensor.gsfc.nasa.gov

## ABSTRACT

This paper reports the first radiometric measurements of cirrus clouds in the frequency range of 89-325 GHz from a high-altitude aircraft flight. The measurements are conducted with a Millimeter-wave Imaging Radiometer (MIR) on board the NASA ER-2 aircraft over a region in northern Oklahoma. Aboard the same aircraft are a cloud lidar system and a multichannel radiometer operating at the visible and infrared wavelengths. The instrument ensemble is well suited for identifying cirrus clouds. It is shown that the depressions in brightness temperatures associated with a few intense cirrus clouds occur at all frequency channels of the MIR. Estimates of total ice water path of the cirrus clouds are derived from comparisons of radiative transfer calculations and observed brightness depressions.

## INTRODUCTION

Remote measurements of cirrus clouds have mostly been made in the visible and infrared regions of the electromagnetic wave spectrum [1]. Observations in the microwave and millimeter-wave regions were limited to ground-based radars [2]. At aircraft altitudes, there are measurements [3] over storms in which the brightness temperatures ( $T_b$ ) in the frequency range of 90-220 GHz are  $\leq 150$  K. The modest decreases in  $T_b$  values at millimeter wavelengths expected from radiative transfer modeling of cirrus clouds [4], to the best of our knowledge, have not been observed and reported.

The following gives a brief description of MIR observations of cirrus clouds in the frequency range of 89-325 GHz [5]. The measurements were made over northern Oklahoma during the SUCCESS (SUBsonic aircraft: Contrail and Cloud Effects Special Study) mission of April-May 1996. The MIR was on board the NASA ER-2 aircraft, which was flown at an altitude of about 20 km and generally above the tops of most clouds. Data from two other instruments aboard the same aircraft, the Cloud Lidar System (CLS) and the MODIS (Moderate-resolution Imaging Spectrometer) Airborne Simulator (MAS), were used to help identify the presence of cirrus clouds. Three events of cirrus clouds are discussed in the following; they are among the most intense ones observed by the MIR during the mission.

## OBSERVATIONS

The data reported in this paper were acquired on April 16, 1996 when the aircraft made 12 repeated passes over the same

region in northern Oklahoma along the  $36.6^\circ\text{N}$  latitude line and between the two endpoints defined by the longitude lines of  $95.9^\circ\text{W}$  and  $98.5^\circ\text{W}$ . Figure 1 shows the backscatter profiles from the CLS and brightness temperatures  $T(11\ \mu\text{m})$  measured by the thermal infrared channel ( $11\ \mu\text{m}$ ) of the MAS over a straight 135-km path with two endpoints at geographic locations of  $(36.6^\circ\text{N}, 97.5^\circ\text{W})$  and  $(36.6^\circ\text{N}, 96.0^\circ\text{W})$ . Four plots (A, B, C, and D) in the figure represent four consecutive measurements over the same path. The endpoint at  $(36.6^\circ\text{N}, 97.5^\circ\text{W})$  always begins from the left side of each plot; thus, the time axes in plots (A) and (C) run from right to left. The top portion of each plot gives the heights of cloud layers and surface ( $\sim 0$  km) as detected by the CLS, which appear to be closely correlated to the  $T(11\ \mu\text{m})$  values measured by the MAS displayed in the bottom portion of the plot. In each of the plots (A), (B), and (C), there is a region where the values of  $T(11\ \mu\text{m})$  are  $< 250$  K. In this region the CLS fails to observe the return signals from the surface; the region is covered with dense cirrus clouds that totally attenuate the lidar signals. In the fourth pass over the region between 1938-1949 UTC, shown in plot (D),  $T(11\ \mu\text{m})$  are  $\geq 250$  K, suggesting the presence of thin cirrus clouds only.

The corresponding variations of  $T_b(\nu)$ 's at frequency  $\nu$  from the MIR for the same four consecutive passes are shown in Figure 2. Only the  $T_b(\nu)$  values from six channels at 150, 220,  $183.3 \pm 3$ ,  $183.3 \pm 7$ ,  $325 \pm 3$ , and  $325 \pm 8$  GHz are plotted in order to maintain the simplicity of the figure. The two horizontal dotted lines in each plot, at  $T_b(\nu)$  values of 225 K and 250 K, provide a reference of  $T_b(\nu)$  variations for the 183.3 GHz and 325 GHz channels, respectively. The two vertical dotted lines in plots (A), (B), and (C) identify the areas of dense cirrus where the CLS fails to observe signal return from the surface; in these areas a strong depression in  $T_b(\nu)$ 's are observed at all six channels. This depression in  $T_b(\nu)$  displays a frequency dependence characteristic of wave scattering by ice particles: the higher the frequency of observations the stronger the  $T_b(\nu)$  depression [4]. At the location of the strongest  $T_b(\nu)$  depression in plot (C), for example, the changes in  $T_b(\nu)$ 's from their nominal values





# IGARSS'97

1997 International Geoscience and  
Remote Sensing Symposium

03-08 August 1997

Singapore International Convention & Exhibition Centre • Singapore

Remote Sensing -- A Scientific Vision for  
Sustainable Development

IEEE Catalog Number: 97CH36042  
Library of Congress Number: 97-70575



# Simultaneous Measurements of Water Vapor Profiles From Airborne MIR and LASE

J. R. Wang, P. Racette, and M. E. Triesky  
Laboratory for Hydrospheric Processes

NASA Goddard Space Flight Center, Greenbelt, MD 20771, U. S. A.  
Tel: 301-286-8949/FAX: 301-286-1762/e-mail: wang@sensor.gsfc.nasa.gov

E. V. Browell and S. Ismail  
Atmospheric Sciences Division  
NASA Langley Research Center, Hampton, VA 23681, U. S. A.

L. A. Chang  
Futuretech Corporation, 14232 Masterpiece Lane, Gaithersburg, MD 20878, U. S. A.

## ABSTRACT

A NASA ER-2 aircraft flight with both Millimeter-wave Imaging radiometer (MIR) and Lidar Atmospheric Sensing Experiment (LASE) was made over ocean areas in the eastern United States on September 25, 1995. The water vapor profiles derived from both instruments under both clear and cloudy conditions are compared in this paper. It is shown that good agreement is found between the MIR-derived and the LASE-measured water vapor profiles over the areas of clear-sky condition. In the cloudy areas, the MIR-retrieved values at the altitudes of the cloud layers and below are generally higher than those measured by the LASE.

## INTRODUCTION

During September 9-26, 1996, a number of NASA ER-2 aircraft flights were conducted both over land and ocean surfaces in the eastern United States for the LASE validation experiment. LASE can provide measurements of high-precision water vapor profiles as well as profiles of scattering ratio that can be used to derive parameters associated with aerosols and cirrus clouds. On board the same aircraft is another instrument, MIR, that is capable of measuring atmospheric water vapor profiles under both clear and cloudy conditions [1-2]. Previously, the MIR-retrieved water vapor profiles could only be compared with those measured by the Raman lidar system and radiosondes at fixed times and locations. The simultaneous measurements of LASE and MIR on board the same aircraft provide the means of validating MIR-retrieved water vapor profiles over extended time and space.

MIR is a total-power cross-track scanning radiometer that measures millimeter-wave radiation at 9 frequency channels of 89, 150,  $183.3 \pm 1$ ,  $183.3 \pm 3$ ,  $183.3 \pm 7$ , 220,  $325 \pm 1$ ,  $325 \pm 3$ , and  $325 \pm 8$  GHz [4]. It has a frequency-independent beamwidth of 3.5 degrees and provides brightness temperature images with an angular swath of 100 degrees centered at nadir. The temperature sensitivities for the six low-frequency channels are  $\leq 1$  K based on a 70-msec integration time, while those for the three 325 GHz channels are on the order of 7-8 K. The

measurements from the three high-frequency channels are not used in the present study.

## MEASUREMENTS

The data presented below were acquired from the flight on September 25, 1995. Figure 1 shows the results from a 20-minute segment of the LASE measurements, expressed in gray scale; the top panel gives the aerosol backscatter and

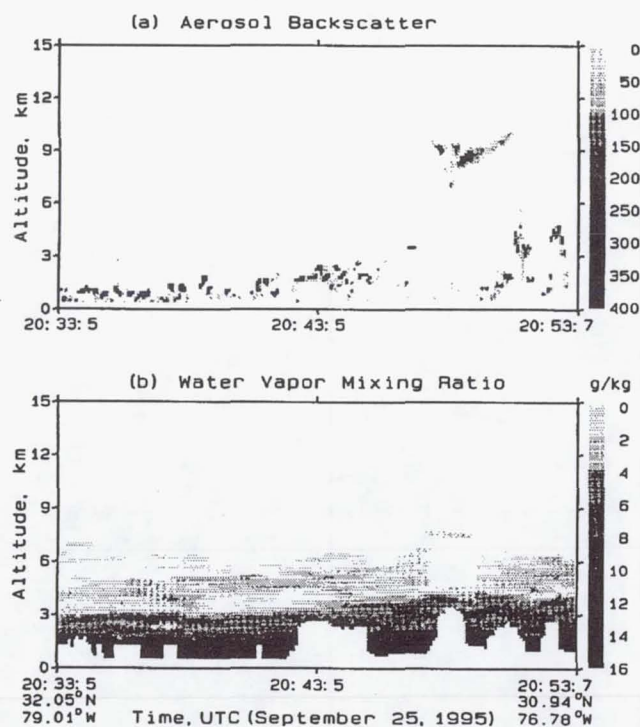


Figure 1. Profiles from the LASE measurements: (a) aerosol backscatter and (b) water vapor mixing ratio.



## **SeaWiFS Technical Report Series**

**Stanford B. Hooker, Editor**  
*NASA Goddard Space Flight Center*  
*Greenbelt, Maryland*

**Elaine R. Firestone, Technical Editor**  
*General Sciences Corporation*  
*Laurel, Maryland*

## **Volume 41, Case Studies for SeaWiFS Calibration and Validation, Part 4**

**Eueng-nan Yeh**  
**Robert A. Barnes**  
**Michael Darzi**  
*General Sciences Corporation*  
*Laurel, Maryland*

**Edward A. Early**  
**B. Carol Johnson**  
*National Institute of Standards and Technology*  
*Gaithersburg, Maryland*

**Lakshmi Kumar**  
*Hughes STX*  
*Landover, Maryland*

**James L. Mueller**  
**Charles C. Trees**  
*Center for Hydro-Optics and Remote Sensing/SDSU*  
*San Diego, California*



National Aeronautics and  
Space Administration

**Goddard Space Flight Center**  
Greenbelt, Maryland 20771

1997



## Chapter 3

### A Simplified Out-of-Band Correction Algorithm for SeaWiFS

EUENG-NAN YEH  
ROBERT A. BARNES  
*General Sciences Corporation  
Laurel, Maryland*

#### ABSTRACT

The SeaWiFS instrument will scan through a broad area of known radiance, and the measurement for each band may contain signals from outside of the desired bandwidth. A calculation that will quickly remove the out-of-band contamination is presented here.

### 3.1 INTRODUCTION

SeaWiFS is an eight-band filter radiometer. For SeaWiFS, as well as for other satellite instruments managed at GSFC, the spectral response of the instrument is divided into in-band and out-of-band responses. The in-band response includes the wavelength region where the response of the band is greater than 1% of the maximum response; at all other wavelengths, the response is out-of-band.

For each SeaWiFS band, the out-of-band response is within the specification for the instrument (Barnes et al. 1994a). These out-of-band responses, however, must be accommodated in the data reduction algorithms for on-orbit SeaWiFS measurements. The original out-of-band correction algorithm was derived for measurements by SeaWiFS from a radiant source with the spectral shape of a 5,900 K blackbody (Barnes et al. 1994b). This is the reference source spectral shape in the SeaWiFS performance specifications (Barnes et al. 1994a). Subsequently, an out-of-band correction scheme was developed that uses SeaWiFS measurements to determine the spectral shape of the upwelling Earth radiances which SeaWiFS measures (Barnes et al. 1995). Although this correction technique gives accurate out-of-band responses, the technique requires an algorithm that uses a great deal of computation time. As a result, Barnes et al. (1996) derived an alternate approach that produces out-of-band calculations much faster in terms of computer time. The equations in Barnes et al. (1996) are the basis for the computer code presented here. A benchmark test of 200 SeaWiFS scan lines has shown that the new algorithm operates about 120 times faster than its predecessor. In addition, the benchmark test showed the calculated results from the two algorithms to be equivalent at the 0.1% level.

### 3.2 THE out\_bandsub ALGORITHM

Prior to the application of atmospheric correction to derive geophysical values, the level-1 radiances from SeaWiFS need an out-of-band correction. The corrections for out-of-band response range from about 0.5% to more than 5%. The level-1 data correction routine, `out_bandsub`, takes an array of calibrated level-1b radiances and, after applying the out-of-band correction, returns a corresponding array of corrected level-1b data. This subroutine is designed to work one scan line with eight bands at a time. This procedure is written in C.

The input arguments for this algorithm are:

- 1) `rad` (real number, array size  $8 \times 1285$ ): the level-1b radiances (bands 1–8) per line;
- 2) `oxygen` (real number): the oxygen absorption correction factor; equals 1 if `rad`(76 nm) is already corrected, otherwise it equals 1.12;
- 3) `xsample` (integer): number of pixels per line (maximum of 1,285).

There is only one output argument, which is:

`rad` (real number, array size  $8 \times 1285$ ): the level-1b out-of-band corrected radiances (bands 1–8).

This simplified out-of-band method applies the ratio of in-band response to the total band response as an out-of-band correction factor ( $k_b$ , Table 11, Barnes et al. [1996]) for each band. This process will go through each pixel of a line:

```
for (m = 0; m < xsample; m++) {\n  original_input_8 = rad[7][m];\n  original_input_6 = rad[5][m];\n  original_input_5 = rad[4][m];\n  for (n = 0; n < 8; n++) rad[n][m] *= Kb[n];\n}
```



## **SeaWiFS Technical Report Series**

**Stanford B. Hooker, Editor**  
*NASA Goddard Space Flight Center*  
*Greenbelt, Maryland*

**Elaine R. Firestone, Technical Editor**  
*General Sciences Corporation*  
*Laurel, Maryland*

## **Volume 41, Case Studies for SeaWiFS Calibration and Validation, Part 4**

**Eueng-nan Yeh**  
**Robert A. Barnes**  
**Michael Darzi**  
*General Sciences Corporation*  
*Laurel, Maryland*

**Edward A. Early**  
**B. Carol Johnson**  
*National Institute of Standards and Technology*  
*Gaithersburg, Maryland*

**Lakshmi Kumar**  
*Hughes STX*  
*Landover, Maryland*

**James L. Mueller**  
**Charles C. Trees**  
*Center for Hydro-Optics and Remote Sensing/SDSU*  
*San Diego, California*



National Aeronautics and  
Space Administration

**Goddard Space Flight Center**  
Greenbelt, Maryland 20771

**1997**



## ABSTRACT

This document provides brief reports, or case studies, on a number of investigations sponsored by the Calibration and Validation Team (CVT) within the Sea-viewing Wide Field-of-view Sensor (SeaWiFS) Project. Chapter 1 describes the calibration and characterization of the GSFC sphere, which was used in the recent recalibration of the SeaWiFS instrument. Chapter 2 presents a revision of the diffuse attenuation coefficient,  $K(490)$ , algorithm based on the SeaWiFS wavelengths. Chapter 3 provides an implementation scheme for an algorithm to remove out-of-band radiance when using a sensor calibration based on a finite width (truncated) spectral response function, e.g., between the 1% transmission points. Chapter 4 describes the implementation schemes for the stray light quality flag (local area coverage [LAC] and global area coverage [GAC]) and the LAC stray light correction.

## Prologue

The purposes of the Sea-viewing Wide Field-of-view Sensor (SeaWiFS) Project is to obtain valid ocean color data of the world ocean for a five-year period, to process that data in conjunction with ancillary data to meaningful biological parameters, and to make that data readily available to researchers. The National Aeronautics and Space Administration (NASA) Goddard Space Flight Center (GSFC) will develop a data processing and archiving system in conjunction with the Earth Observing System Data and Information System (EOSDIS), which includes a ground receiving system. In addition, the SeaWiFS Project will oversee a calibration and validation effort which is designed to ensure the integrity of the final products.

The Calibration and Validation Team (CVT) has three main tasks:

- 1) Calibration and characterization of the SeaWiFS instrument;
- 2) Development and validation of the operational atmospheric correction algorithm; and
- 3) Development and validation of the derived product algorithms, such as chlorophyll *a* concentration.

Some of this work will be done internally at GSFC, while the remainder will be done externally at other institutions. NASA and the Project place the highest priority on ensuring the accuracy of derived water-leaving radiances globally, and over the duration of the entire mission. If these criteria are met, the development of global and regional biogeochemical algorithms can proceed on many fronts. These various activities are discussed in detail in *The SeaWiFS Calibration and Validation Plan* (McClain et al. 1992).

Because many of the studies and other works undertaken with the Calibration and Validation Program are not extensive enough to require dedicated volumes of the *SeaWiFS Technical Report Series*, the CVT has decided to publish volumes composed of brief, but topically specific, chapters. Volume 13 is the first volume, and consists

primarily of contributions related to atmospheric correction methodologies, ancillary data sets required for level-2 processing of Coastal Zone Color Scanner (CZCS) and SeaWiFS data, laboratory techniques for instrument calibration relevant to calibration round-robins, and field observations designed for transferring the prelaunch calibration to orbit, and in interpreting the on-orbit lunar calibration data. The second case studies volume, Volume 19, contains chapters on atmospheric and glint corrections; solar-, lunar-, and integrating sphere optical measurements; data format considerations; and the use of ancillary data (including surface wind velocities) in SeaWiFS processing. Volume 27 is the third in the set of such volumes and contains chapters on measuring immersion coefficients, oxygen absorption, solar calibration experiments, ship shadow effects on radiance and irradiance measurements, and the definition of the SeaWiFS data day for level-3 data binning. Volume 41 is the fourth of the case studies volumes. A short synopsis of each chapter in this volume is given below.

### 1. Calibration and Characterization of the GSFC Sphere

A large integrating sphere source, which is owned and maintained by the Sensor Development and Calibration Branch at GSFC, was calibrated and characterized by the Optical Technology Division at the National Institute of Standards and Technology (NIST). This effort, in support of the GSFC SeaWiFS Project, is part of an inter-agency agreement between NASA and NIST. The spectral radiance was measured for four different lamp settings of the sphere source from 370–1,100 nm every 10 nm using a NIST standard tungsten strip lamp and a prism-grating monochromator which was equipped with a silicon photodiode. The results are presented as a function of wavelength with a relative standard uncertainty of 0.29–2.6% ( $k=1$ ), depending on the measurement conditions. During these measurements, the SeaWiFS Transfer Radiometer (SXR) was used to determine the spectral radiance of the sphere source at six fixed wavelengths. In



## **SeaWiFS Technical Report Series**

**Stanford B. Hooker, Editor**  
*NASA Goddard Space Flight Center*  
*Greenbelt, Maryland*

**Elaine R. Firestone, Technical Editor**  
*General Sciences Corporation*  
*Laurel, Maryland*

## **Volume 41, Case Studies for SeaWiFS Calibration and Validation, Part 4**

**Eueng-nan Yeh**  
**Robert A. Barnes**  
**Michael Darzi**  
*General Sciences Corporation*  
*Laurel, Maryland*

**Edward A. Early**  
**B. Carol Johnson**  
*National Institute of Standards and Technology*  
*Gaithersburg, Maryland*

**Lakshmi Kumar**  
*Hughes STX*  
*Landover, Maryland*

**James L. Mueller**  
**Charles C. Trees**  
*Center for Hydro-Optics and Remote Sensing/SDSU*  
*San Diego, California*



National Aeronautics and  
Space Administration

**Goddard Space Flight Center**  
Greenbelt, Maryland 20771

1997



---

## Chapter 4

---

### SeaWiFS Stray Light Correction Algorithm

EUENG-NAN YEH AND MICHAEL DARZI

*General Sciences Corporation*

*Laurel, Maryland*

LAKSHMI KUMAR

*Hughes STX*

*Lanham, Maryland*

#### ABSTRACT

SeaWiFS will scan through not only the dark ocean surface, but also the bright land, clouds, and ice objects. Because of stray light in the SeaWiFS instrument, light from these bright sources can contaminate ocean measurements several pixels away from a bright source. A mathematical formula that can be used to correct this contamination is discussed here.

#### 4.1 INTRODUCTION

Two routines were developed, `stray_light_lac` and `stray_light_gac`, to apply a stray light correction to SeaWiFS level-1 LAC and GAC data, respectively. The routines are integrated as part of the operational level-1a read routine; their algorithms are based on the methodology described by Barnes et al. (1995). The routines perform radiance manipulations to label pixels that are bright sources or are in the vicinity of bright sources. In addition, the radiances of pixels that are along scan to, and near, a bright source are corrected for stray light contamination from that bright source. Because the input data to the routines are radiances, the calibrated level-1 data, i.e., level-1b data, must be used.

The labelling identifies pixels that are part of a bright source, near a bright source in the along-track direction, diagonal to the ends of a bright source, or near a bright source in the along-scan direction. These along-scan pixels are correctable for stray light contamination as a function of their distance from the bright source. For this reason, they are labelled by their pixel distance from the nearest edge of a bright source to the right of that pixel and from the nearest edge of a bright source to the left of that pixel. For LAC, 14 pixels to the left and 12 pixels to the right of a bright source edge are considered to be affected by stray light from that bright source. For GAC, 3 pixels on each side of a bright source are so considered. If a stray light pixel is within this range between two bright sources, the pixel distance to the bright source on the right is multiplied by 1,000; the product is then added to the pixel distance to the bright source on the left.

Both routines are designed to work on individual scan lines even though along-track processing is required. This is accomplished by using a buffer that retains a rolling window of consecutive scan lines.

#### 4.2 LAC CORRECTION

There are two major steps involving the SeaWiFS LAC image stray light correction for level-1b data (Fig. 10). The first step is to identify the left and right bright source edges. Two conditions, radiance value and gradient value, are applied to SeaWiFS level-1 band 8 (865 nm) radiance ( $L8$ ) to identify these edges. The radiance of a pixel has to exceed a certain threshold, `Stray_thresh`, which is defined as a fraction of the value of  $L8$  at knee 1. The value of the typical stray light fraction, `Styp_frac`, is given as 0.9. The radiance gradient,  $\Delta_L$ , is defined as the  $L8$  difference between two adjacent pixels  $n + 1$  and  $n$ . The left edge is found if the radiance value is greater than `Stray_thresh` and  $\Delta_L$  is greater than the typical gradient threshold value. This value is defined as a fraction of the bigger one of the following two quantities:  $L_{\text{typical}}(8)$ , or the difference between  $L8$  of pixel  $n + 1$ , i.e.,  $L8[n + 1]$ , and  $L_{\text{typical}}(8)$ . The  $L_{\text{typical}}(8)$  is the typical quantity of sea surface radiance measured by band 8 and the value is  $1.09 \text{ mW cm}^{-2} \mu\text{m}^{-1} \text{ sr}^{-1}$ . The radiance fraction `Ltyp_frac` is given as 0.25. The right edge is found if the radiance value is greater than `Stray_thresh` and  $\Delta_L$  is greater than the typical gradient threshold value, which is defined as a fraction of the bigger one of the following two quantities:  $L_{\text{typical}}(8)$ , or the difference between  $L8$  of pixel  $n$ , i.e.,  $L8[n]$ , and  $L_{\text{typical}}(8)$ .



# AUTHOR INDEX

## A

Abdalati, W. 75, 81  
Arrigo, K. 5

## B

Barnes, R. 173, 175, 177, 179, 181, 183, 201, 273, 275  
Barnes, W. 185  
Beauchamp, J. 243  
Bindschadler, R. 99  
Birkett, C. 187  
Bliven, L. 35, 117, 119, 131  
Brooks, R. 215  
Busalacchi, A. 19, 23, 43, 57, 211, 213, 243

## C

Cavalieri, D. 21, 129, 155, 263  
Chang, A. 77, 87, 123, 125, 135, 189, 203, 205  
Chang, L. 163, 165, 271  
Chang, S. 143  
Chien, J. 101  
Chiu, L. 77, 123, 189  
Choudhury, B. 29, 49, 51, 53, 67  
Comiso, J. 21, 39, 47, 129, 191, 193

## E

Engman, E. 7, 9, 153, 161, 199, 235, 237, 259, 261  
Eplee, R. 173, 177, 181, 201  
Esaias, W. 173, 175

## F

Fahnestock, M. 89, 99  
Foster, J. 87, 125, 135, 203, 205

## G

Geiger, C. 31, 209  
Gloersen, P. 21, 129  
Gregg, W. 141, 147

## H

Hackert, E. 57, 213  
Häkkinen, S. 91  
Hall, D. 87, 101, 125, 135, 203, 205, 227, 253  
Hancock, D. 215  
Hayne, G. 215  
Hooker, S. 37, 113, 237, 257  
Hsu, A. 153, 161, 219, 245, 259, 261

## J

Jones, J. 225, 241

## K

Kao, M. 229  
Klein, A. 227  
Koblinsky, C. 71, 115  
Koster, R. 27, 41, 45, 65  
Krabill, W. 93, 151  
Kumar, L. 275, 277

## L

Lee, J. 215  
Le Vine, D. 229  
Liao, L. 231  
Liu, A. 55, 143, 233  
Lockwood, D. 215

## M

Markus, T. 263  
McClain, C. 15, 137  
Meneghini, R. 121, 145, 195, 221, 225, 231, 241, 265  
Murtugudde, R. 15, 85, 97, 197, 211, 243

## O

O'Neill, P. 11, 153, 161, 219, 223, 245, 259, 261  
Owe, M. 247



## AUTHOR INDEX (Con't)

### P

Parkinson, C. 21, 59, 95, 129, 249  
Patt, F. 141, 147  
Picaut, J. 13, 61, 63, 251

### R

Racette, P. 163, 165, 167, 217, 269, 271  
Riggs, G. 227, 253  
Ross, E. 255

### S

Schmidlin, F. 109, 139, 255  
Shuman, C. 41, 83, 99  
Stock, L. 193

### T

Takahashi, N. 265  
Toll, D. 69, 157, 267

Triesky, M. 271

### V

Vandemark, D. 25, 133, 159, 207

### W

Wang, J. 67, 127, 145, 153, 161, 163, 165,  
167, 259, 261, 269, 271  
Wang, L. 71  
Wang, M. 169  
Weinman, J. 149, 195  
Woodward, R. 141, 147  
Worthen, D. 5

### Z

Zwally, H. 21, 33, 103, 105, 191